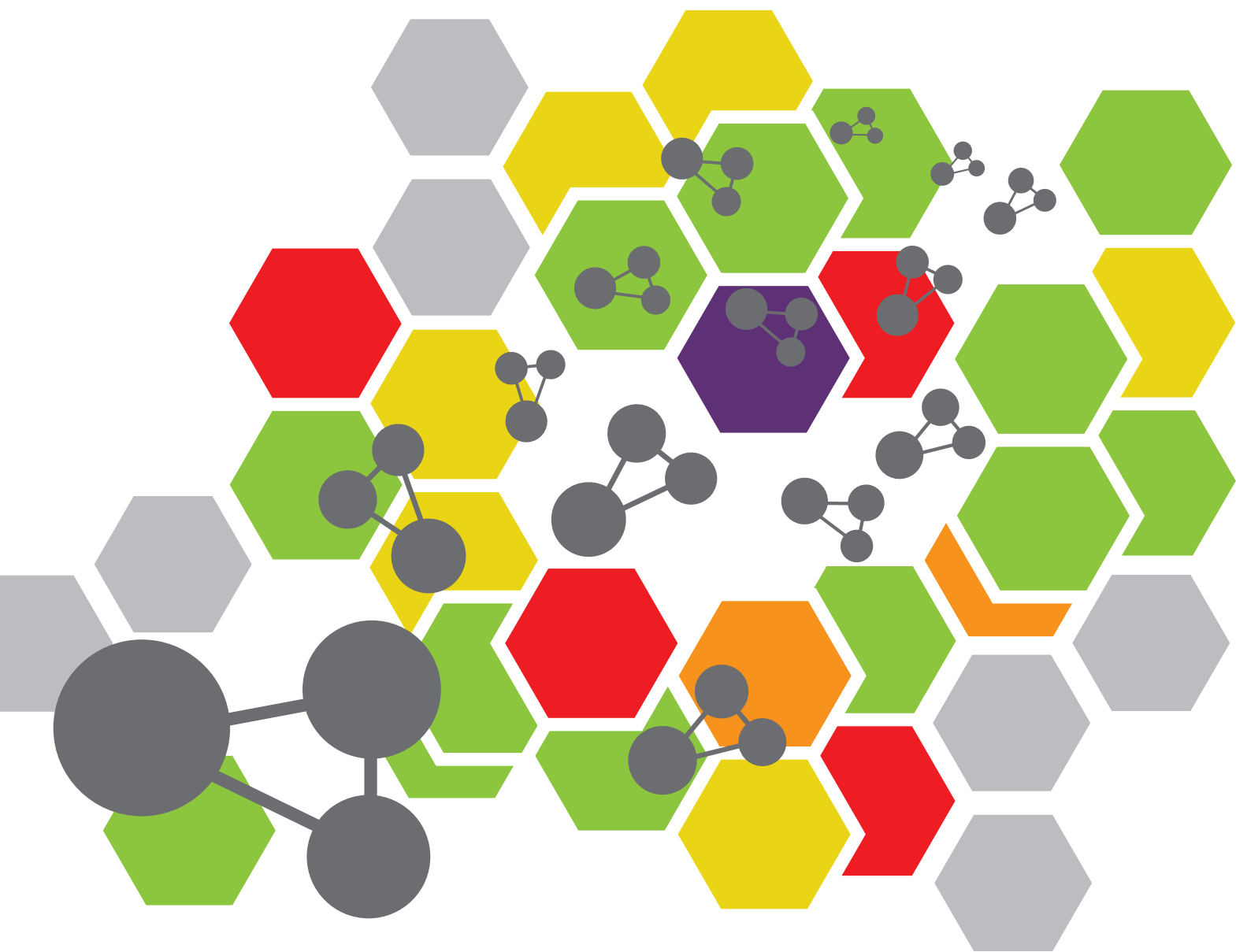


LOW-DIMENSION SENSING NANOMATERIALS

EDITED BY: Mingshui Yao, Jiandong Pang, Weiwei Wu, Jiaqiang Xu and Wen Zeng
PUBLISHED IN: Frontiers in Chemistry





frontiers

Frontiers eBook Copyright Statement

The copyright in the text of individual articles in this eBook is the property of their respective authors or their respective institutions or funders. The copyright in graphics and images within each article may be subject to copyright of other parties. In both cases this is subject to a license granted to Frontiers.

The compilation of articles constituting this eBook is the property of Frontiers.

Each article within this eBook, and the eBook itself, are published under the most recent version of the Creative Commons CC-BY licence.

The version current at the date of publication of this eBook is CC-BY 4.0. If the CC-BY licence is updated, the licence granted by Frontiers is automatically updated to the new version.

When exercising any right under the CC-BY licence, Frontiers must be attributed as the original publisher of the article or eBook, as applicable.

Authors have the responsibility of ensuring that any graphics or other materials which are the property of others may be included in the CC-BY licence, but this should be checked before relying on the CC-BY licence to reproduce those materials. Any copyright notices relating to those materials must be complied with.

Copyright and source acknowledgement notices may not be removed and must be displayed in any copy, derivative work or partial copy which includes the elements in question.

All copyright, and all rights therein, are protected by national and international copyright laws. The above represents a summary only. For further information please read Frontiers' Conditions for Website Use and Copyright Statement, and the applicable CC-BY licence.

ISSN 1664-8714

ISBN 978-2-88966-857-1

DOI 10.3389/978-2-88966-857-1

About Frontiers

Frontiers is more than just an open-access publisher of scholarly articles: it is a pioneering approach to the world of academia, radically improving the way scholarly research is managed. The grand vision of Frontiers is a world where all people have an equal opportunity to seek, share and generate knowledge. Frontiers provides immediate and permanent online open access to all its publications, but this alone is not enough to realize our grand goals.

Frontiers Journal Series

The Frontiers Journal Series is a multi-tier and interdisciplinary set of open-access, online journals, promising a paradigm shift from the current review, selection and dissemination processes in academic publishing. All Frontiers journals are driven by researchers for researchers; therefore, they constitute a service to the scholarly community. At the same time, the Frontiers Journal Series operates on a revolutionary invention, the tiered publishing system, initially addressing specific communities of scholars, and gradually climbing up to broader public understanding, thus serving the interests of the lay society, too.

Dedication to Quality

Each Frontiers article is a landmark of the highest quality, thanks to genuinely collaborative interactions between authors and review editors, who include some of the world's best academicians. Research must be certified by peers before entering a stream of knowledge that may eventually reach the public - and shape society; therefore, Frontiers only applies the most rigorous and unbiased reviews.

Frontiers revolutionizes research publishing by freely delivering the most outstanding research, evaluated with no bias from both the academic and social point of view. By applying the most advanced information technologies, Frontiers is catapulting scholarly publishing into a new generation.

What are Frontiers Research Topics?

Frontiers Research Topics are very popular trademarks of the Frontiers Journals Series: they are collections of at least ten articles, all centered on a particular subject. With their unique mix of varied contributions from Original Research to Review Articles, Frontiers Research Topics unify the most influential researchers, the latest key findings and historical advances in a hot research area! Find out more on how to host your own Frontiers Research Topic or contribute to one as an author by contacting the Frontiers Editorial Office: frontiersin.org/about/contact

LOW-DIMENSION SENSING NANOMATERIALS

Topic Editors:

Mingshui Yao, Kyoto University, Japan

Jiandong Pang, Texas A&M University, United States

Weiwei Wu, Xidian University, China

Jiaqiang Xu, Shanghai University, China

Wen Zeng, Chongqing University, China

Citation: Yao, M., Pang, J., Wu, W., Xu, J., Zeng, W., eds. (2021).

Low-Dimension Sensing Nanomaterials. Lausanne: Frontiers Media

SA. doi: 10.3389/978-2-88966-857-1

Table of Contents

- 05 Editorial: Low-Dimension Sensing Nanomaterials**
Ming-Shui Yao, Wei-Wei Wu, Wen Zeng, Jian-Dong Pang and Jia-Qiang Xu
- 07 Systematic Theoretical Study on Structural, Stability, Electronic, and Spectral Properties of Si_2Mg_n^Q ($Q = 0, \pm 1$; $n = 1-11$) Clusters of Silicon-Magnesium Sensor Material**
Ben-Chao Zhu, Ping-Ji Deng and Lu Zeng
- 23 Hollow WO_3/SnO_2 Hetero-Nanofibers: Controlled Synthesis and High Efficiency of Acetone Vapor Detection**
Hongyun Shao, Minxuan Huang, Hao Fu, Shaopeng Wang, Liwei Wang, Jie Lu, Yinghui Wang and Kefu Yu
- 33 Controlled Synthesis of Pt Doped SnO_2 Mesoporous Hollow Nanospheres for Highly Selective and Rapidly Detection of 3-Hydroxy-2-Butanone Biomarker**
Haijie Cai, Haiquan Liu, Tianjun Ni, Yingjie Pan, Yong Zhao and Yongheng Zhu
- 46 Exonuclease III-Regulated Target Cyclic Amplification-Based Single Nucleotide Polymorphism Detection Using Ultrathin Ternary Chalcogenide Nanosheets**
Yanling Hu, Chaoliang Tan, Xin Lin, Zhuangchai Lai, Xiao Zhang, Qipeng Lu, Ning Feng, Dongliang Yang and Lixing Weng
- 54 Current Applications of Gas Sensor Based on 2-D Nanomaterial: A Mini Review**
Liang Ge, Xiaolin Mu, Guiyun Tian, Qi Huang, Junaid Ahmed and Ze Hu
- 61 NO_2 Sensing Properties of Cr_2WO_6 Gas Sensor in Air and N_2 Atmospheres**
Yi Wu, Meng Yan, Chen Tian, Yuhang Liu and Zhongqiu Hua
- 68 Qualitative Detection Toward Military and Improvised Explosive Vapors by a Facile TiO_2 Nanosheet-Based Chemiresistive Sensor Array**
Yushu Li, Wenyi Zhou, Baiyi Zu and Xincun Dou
- 80 Gas-Sensing Performances of Metal Oxide Nanostructures for Detecting Dissolved Gases: A Mini Review**
Wei Guan, Na Tang, Kuang He, Xiaoying Hu, Mingshan Li and Kaiming Li
- 85 Simultaneously Optimize the Response Speed and Sensitivity of Low Dimension Conductive Polymers for Epidermal Temperature Sensing Applications**
Cheng Zhou, Ning Tang, Xiaoshuang Zhang, Ye Fang, Yang Jiang, Hainan Zhang and Xuexin Duan
- 95 Application of WO_3 Hierarchical Structures for the Detection of Dissolved Gases in Transformer Oil: A Mini Review**
Zhijie Wei, Lingna Xu, Shudi Peng and Qu Zhou

- 101 ***The Functionalized Single-Walled Carbon Nanotubes Gas Sensor With Pd Nanoparticles for Hydrogen Detection in the High-Voltage Transformers***
Sirui Tang, Weigen Chen, He Zhang, Zihao Song, Yanqiong Li and Yu Wang
- 109 ***Study on Interaction Between TATA-Box Binding Protein (TBP), TATA-Box and Multiprotein Bridging Factor 1(MBF1) in Beauveria bassiana by Graphene-Based Electrochemical Biosensors***
Chi Song, Zhijia Peng, Xiaogang Lin, Haoyue Luo, Min Song, Lifeng Jin, Xiangyue Xiao and Hong Ji
- 118 ***Application of Zero-Dimensional Nanomaterials in Biosensing***
Zhengdi Wang, Tingting Hu, Ruizheng Liang and Min Wei
- 137 ***A Fast and Highly Selective Nitrite Sensor Based on Interdigital Electrodes Modified With Nanogold Film and Chrome-Black T***
Haoyue Luo, Xiaogang Lin, Zhijia Peng, Yong Zhou, Shibin Xu, Ming Song, Lifeng Jin and Xiaodong Zheng
- 144 ***Study on AgInZnS-Graphene Oxide Non-toxic Quantum Dots for Biomedical Sensing***
Chi Song, Haoyue Luo, Xiaogang Lin, Zhijia Peng, Lingdong Weng, Xiaosheng Tang, Shibin Xu, Ming Song, Lifeng Jin and Xiaodong Zheng
- 154 ***Recent Advances of SnO₂-Based Sensors for Detecting Volatile Organic Compounds***
Baoliang Li, Qu Zhou, Shudi Peng and Yiming Liao
- 160 ***Asymptomatic Diagnosis of Huanglongbing Disease Using Metalloporphyrin Functionalized Single-Walled Carbon Nanotubes Sensor Arrays***
Hui Wang, Pankaj Ramnani, Tung Pham, Claudia Chaves Villarreal, Xuejun Yu, Gang Liu and Ashok Mulchandani
- 171 ***Interface Design of SnO₂@PANI Nanotube With Enhanced Sensing Performance for Ammonia Detection at Room Temperature***
Anqiang Jia, Bitao Liu, Haiyan Liu, Qiufeng Li and Yingxia Yun
- 180 ***Anisotropic Thermal Expansion in an Anionic Framework Showing Guest-Dependent Phases***
Zhu Zhuo, You-Gui Huang, Krista S. Walton and Osamu Sato
- 188 ***Low-Dimension Nanomaterial-Based Sensing Matrices for Antibiotics Detection: A Mini Review***
Yucan Dong, Fengting Li and Ying Wang



Editorial: Low-Dimension Sensing Nanomaterials

Ming-Shui Yao^{1*}, Wei-Wei Wu², Wen Zeng³, Jian-Dong Pang⁴ and Jia-Qiang Xu⁵

¹Institute for Integrated Cell-Material Sciences, Kyoto University Institute for Advanced Study, Kyoto University, Kyoto, Japan, ²School of Advanced Materials and Nanotechnology, Interdisciplinary Research Center of Smart Sensors, Xidian University, Shaanxi, China, ³College of Materials Science and Engineering, Chongqing University, Chongqing, China, ⁴Texas A and M University, College Station, TX, United States, ⁵Department of Chemistry, College of Science, Shanghai University, Shanghai, China

Keywords: low-dimension, sensor, nanomaterials, data processing, theoretical calculations

Editorial on the Research Topic

Low-Dimension Sensing Nanomaterials

Sensing is the art of seeing things invisible (Fourkas, 2011; Yao et al., 2021). Specifically, sensors help human beings collect chemical/physical/bio-stimulus or variations in the environment, and transduce them into readable signals that can be further processed and analyzed (Hu W. et al., 2019; Broza et al., 2019; Xie et al.). In the last 2 decades, the intensive studies on low dimension nanomaterials have indicated the advantages of such materials on developing new sensors with ultrahigh sensitivity, specificity, low-power consumption, multi-functionality, and miniaturized size (Choi and Kim, 2018; Ge et al.; Meng et al., 2019; Qiu and Tang, 2020; Yang et al., 2020).

The Frontiers research topic “Low-Dimension Sensing Nanomaterials” comprises a collection of original research and review articles dealing with the synthesis, chemistry, and applications of low-dimension sensing nanomaterials. This special issue consists of 15 research articles and five mini-reviews, reflecting recent developments on sensing materials, data processing, and theoretical calculations. The collected papers cover the broad applications of sensors in fields of environmental monitoring/cleaning (Li B. et al.; Dong et al.; Luo et al.; Tang et al.), disease diagnosis (Cai et al.; Wang H. et al.), biosensing (Song et al.; Wang Z. et al.), public security affairs (Li Y. et al.), etc.

The rich history of sensing materials has made it possible to predict with a relatively high degree of confidence what sensing performances might result if certain well-studied materials are used individually or jointly. However, there are still many worthwhile directions to be pursued to overcome the difficulty to fulfill the “4S” requirements (i.e., sensitivity (response), selectivity, speed (response/recovery time) and stability) at the same time. Firstly, the newly emerging sensing materials (e.g., metal organic framework/porous coordination polymers (MOF/PCPs), black phosphorus, covalent-organic frameworks (COFs), conducting polymers, Mxenes) or hybrid materials always bring new understanding of what the sensor can or cannot do (Hu Y. et al.; Cai et al.; Zhou et al.; Zhuo et al.), which can be further applied to guide the development of existed sensing materials. Secondly, the boosting developments of characterization techniques triggered various in-depth and fundamental studies on both atomic/nanoscale level structure-properties relationships

OPEN ACCESS

Edited and reviewed by:

Zoe Pikramenou,
University of Birmingham,
United Kingdom

*Correspondence:

Ming-Shui Yao
mingshuiyao@gmail.com

Specialty section:

This article was submitted to
Nanoscience,
a section of the journal
Frontiers in Chemistry

Received: 20 September 2020

Accepted: 18 February 2021

Published: 12 April 2021

Citation:

Yao M-S, Wu W-W, Zeng W, Pang J-D
and Xu J-Q (2021) Editorial: Low-
Dimension Sensing Nanomaterials.
Front. Chem. 9:608327.
doi: 10.3389/fchem.2021.608327

and in-/ex-situ sensing mechanisms characterization (Hu Y. et al.; Shao et al.; Song et al.; Wang H. et al.; Jia et al.; Wu et al.). Its great challenge is how to move forward the qualitative measurements to quantitative measurements, summarize the individual cases into general rules via data processing, and thus guide the design of high performance sensors. Last but not the least, the theoretical calculations have contributed greatly to the understanding of sensing mechanisms in the past few decades (Ji et al., 2019; Zhu et al.). With the fast development of simulation theories and computing power, greater contributions on both confirmation and prediction can be expected.

REFERENCES

- Broza, Y. Y., Zhou, X., Yuan, M., Qu, D., Zheng, Y., Vishinkin, R., et al. (2019). Disease detection with molecular biomarkers: from chemistry of body fluids to nature-inspired chemical sensors. *Chem. Rev.* 119, 11761–11817. doi:10.1021/acs.chemrev.9b00437
- Choi, S.-J., and Kim, I.-D. (2018). Recent developments in 2D nanomaterials for chemiresistive-type gas sensors. *Electron. Mater. Lett.* 14, 221–260. doi:10.1007/s13391-018-0044-z
- Fourkas, J. T. (2011). Nanosensing: the art of seeing things invisible. *J. Phys. Chem. Lett.* 2, 2945. doi:10.1021/jz201284e
- Hu, W., Wan, L., Jian, Y., Ren, C., Jin, K., Su, X., et al. (2019). Electronic noses: from advanced materials to sensors aided with data processing. *Adv. Mater. Technol.* 4, 1800488. doi:10.1002/admt.201800488
- Ji, H., Zeng, W., and Li, Y. (2019). Gas sensing mechanisms of metal oxide semiconductors: a focus review. *Nanoscale* 11, 22664–22684. doi:10.1039/c9nr07699a
- Meng, Z., Stolz, R. M., Mendecki, L., and Mirica, K. A. (2019). Electrically-Transduced chemical sensors based on two-dimensional nanomaterials. *Chem. Rev.* 119, 478–598. doi:10.1021/acs.chemrev.8b00311

We hope the contributions here can give the inquisitive reader a primer and a springboard that inspires further new ideas in this exciting and challenging research area, in which many more discoveries will be made.

AUTHOR CONTRIBUTIONS

MY prepare this editorial. MY, WW, WZ, JP and JX discussed the editorial.

- Qiu, Z., and Tang, D. (2020). Nanostructure-based photoelectrochemical sensing platforms for biomedical applications. *J. Mater. Chem. B* 8, 2541–2561. doi:10.1039/C9TB02844G
- Yang, T., Liu, Y., Wang, H., Duo, Y., Zhang, B., Ge, Y., et al. (2020). Recent advances in 0D nanostructure-functionalized low-dimensional nanomaterials for chemiresistive gas sensors. *J. Mater. Chem. C* 8, 7272–7299. doi:10.1039/D0TC00387E
- Yao, M.-S., Li, W.-H., and Xu, G. (2021). Metal-organic frameworks and their derivatives for electrically-transduced gas sensors. *Coord. Chem. Rev.* 426, 213479. doi:10.1016/j.ccr.2020.213479

Conflict of Interest: The authors declare that the research was conducted in the absence of any commercial or financial relationships that could be construed as a potential conflict of interest.

Copyright © 2021 Yao, Wu, Zeng, Pang and Xu. This is an open-access article distributed under the terms of the Creative Commons Attribution License (CC BY). The use, distribution or reproduction in other forums is permitted, provided the original author(s) and the copyright owner(s) are credited and that the original publication in this journal is cited, in accordance with accepted academic practice. No use, distribution or reproduction is permitted which does not comply with these terms.



Systematic Theoretical Study on Structural, Stability, Electronic, and Spectral Properties of Si_2Mg_n^Q ($Q = 0, \pm 1$; $n = 1-11$) Clusters of Silicon-Magnesium Sensor Material

Ben-Chao Zhu^{1,2}, Ping-Ji Deng^{1,2} and Lu Zeng^{3*}

¹ School of Public Health and Management, Hubei University of Medicine, Shiyan, China, ² Center for Environment and Health in Water Source Area of South-to-North Water Diversion, Hubei University of Medicine, Shiyan, China, ³ College of Materials Science and Engineering, Chongqing University, Chongqing, China

OPEN ACCESS

Edited by:

Weiwei Wu,
Xidian University, China

Reviewed by:

Cheng Lu,
China University of Geosciences
Wuhan, China
Xiaoyu Kuang,
Sichuan University, China

*Correspondence:

Lu Zeng
zool@foxmail.com

Specialty section:

This article was submitted to
Nanoscience,
a section of the journal
Frontiers in Chemistry

Received: 28 August 2019

Accepted: 24 October 2019

Published: 12 November 2019

Citation:

Zhu B-C, Deng P-J and Zeng L (2019)
Systematic Theoretical Study on
Structural, Stability, Electronic, and
Spectral Properties of Si_2Mg_n^Q ($Q = 0, \pm 1$; $n = 1-11$) Clusters of
Silicon-Magnesium Sensor Material.
Front. Chem. 7:771.
doi: 10.3389/fchem.2019.00771

By using CALYPSO searching method and Density Functional Theory (DFT) method at the B3LYP/6-311G (d) level of cluster method, a systematic study of the structures, stabilities, electronic and spectral properties of Si_2Mg_n^Q ($n = 1-11$; $Q = 0, \pm 1$) clusters of silicon-magnesium sensor material, is performed. According to the calculations, it was found that when $n > 4$, most stable isomers in Si_2Mg_n^Q ($n = 1-11$; $Q = 0, \pm 1$) clusters of silicon-magnesium sensor material are three-dimensional structures. Interestingly, although large size Si_2Mg_n^Q clusters show cage-like structures, silicon atoms are not in the center of the cage, but tend to the edge. The $\text{Si}_2\text{Mg}_{1,5,6,8}^{-1}$ and $\text{Si}_2\text{Mg}_{13,4,7,9,10}^{+1}$ clusters obviously differ to their corresponding neutral structures, which are in good agreement with the calculated values of VIP, AIP, VEA, and AEA. $|\text{VIP-VEA}|$ values reveal that the hardness of Si_2Mg_n clusters decreases with the increase of magnesium atoms. The relative stabilities of neutral and charged Si_2Mg_n^Q ($n = 1-11$; $Q = 0, \pm 1$) clusters of silicon-magnesium sensor material is analyzed by calculating the average binding energy, fragmentation energy, second-order energy difference and HOMO-LUMO gaps. The results reveal that the Si_2Mg_3^0 , $\text{Si}_2\text{Mg}_3^{-1}$, and $\text{Si}_2\text{Mg}_3^{+1}$ clusters have stronger stabilities than others. NCP and NEC analysis results show that the charges in Si_2Mg_n^Q ($n = 1-11$; $Q = 0, \pm 1$) clusters of silicon-magnesium sensor material transfer from Mg atoms to Si atoms except for $\text{Si}_2\text{Mg}_1^{+1}$, and strong sp hybridizations are presented in Si atoms of Si_2Mg_n^Q clusters. Finally, the infrared (IR) and Raman spectra of all ground state of Si_2Mg_n^Q ($n = 1-11$; $Q = 0, \pm 1$) clusters of silicon magnesium sensor material are also discussed.

Keywords: silicon-magnesium sensor material, $\text{Si}_2\text{Mg}_n^{0,\pm 1}$ clusters, geometrical structures, electronic properties, spectral properties

INTRODUCTION

Silicon and magnesium are abundant elements on the earth and are widely used in sensor industry. In particular, silicon, as the main material of semiconductor sensors, has always been the research frontier in the field of sensors. As the only stable compound in Mg-Si binary system, Mg_2Si , which has the characteristics of high melting point, high hardness, high modulus of

elasticity and environmentally friendly, is an *n*-type semiconductor material with a band gap of 0.68–1.03 eV (Atanasov and Baleva, 2007). There are many experimental and theoretical studies on silicon-magnesium sensor materials. For example, theoretically, Morris et al. (1958) first used graphite crucible to melt stoichiometric components to prepare high purity single crystal Mg_2Si materials, they found the band gap of Mg_2Si is 0.78 eV. Aymerich and Mula (2010) and Imai et al. (2003) studied the band structure of Mg_2Si using empirical and first-principles pseudopotentials, respectively. Chen et al. (2010) studied the band structure of Mg_2Si and doped Ag, Al elements by using the first-principles pseudopotential plane wave method based on density functional theory (DFT). By using DFT, they obtained the real part, imaginary part and Photoconductivity of Mg_2Si dielectric function as a function of photon energy. Experimentally, the main work on Mg_2Si is focused on the preparation of thin film materials. Wittmer et al. (1979) was the first to fabricate Mg_2Si semiconductor thin films on Si (111) substrates by evaporating Mg atoms films with different thicknesses using an electron gun at a speed of about 40 Å/s in vacuum. Boher et al. (1992) used radio frequency magnetron sputtering technology to sputter Mg_2Si targets onto glass materials and Si (111) substrates, and obtained amorphous Mg_2Si films. Song et al. (2003) used pulsed laser deposition (PLD) method to grow Mg_2Si crystal semiconductor thin films nearly 380 nanometers thick on stainless steel substrates at 500° annealing temperature.

All the above theoretical and experimental studies have greatly enriched the research results on the properties of silicon-magnesium sensor material. However, these studies have not touched the fundamental problem, how do the physical and chemical properties of silicon-magnesium compounds change from small systems (several or dozens of atoms) to large systems? Fortunately, small clusters provide a new way to study this system, which can provide insight into the strength and properties of metal bonds (Ju et al., 2015; Sun et al., 2017, 2018; Bole et al., 2018). Cluster material scale is a concept of nanomaterials. It is a relatively stable micro or sub-micro aggregate composed of several or even thousands of atoms, molecules or ions. Its physical and chemical properties usually vary with the number of atoms contained. Cluster studies have successfully helped us to in-depth understand the structure, stability, electronic states and spectral properties of many materials (Jin et al., 2015a,b; Xia et al., 2015; Xing et al., 2016a,b). There are many reports about sensor material study by using cluster method. For example, Yang et al. (2006) used full-muffin-tin-orbital molecular-dynamics (FP-LMTO-MD) method to study the electronic and geometric structures of Ga_nAs_n ($n = 4, 5, 6$) cluster ions. They found that some of the lowest energy structures for the cluster ions are different from those of the corresponding neutral clusters. Dmytruk et al. (2009) produced zinc oxide clusters by laser ablation of bulk powder zinc peroxide in vacuum and studied them by time-of-flight mass spectrometry. By comparing the experimental results with the theoretical calculations of clusters, the most stable structure of $(\text{ZnO})_n$ clusters was verified at $n = 34, 60$, and 78.

However, most of the studies on sensor material clusters are carried out in a crystal growth mode, such as AsGa and ZnO,

where the number of different atoms increases in harmony. In this paper, doped clusters will be used to study the materials of silicon-magnesium sensors. To be exact, we doped a small amount of silicon into magnesium element, which increased the number of magnesium atoms around two silicon atoms from 1 to 11, and made them neutral charged, negative charged and positive charged, respectively. Then, we will study the structure, stability, electronic and spectral properties of Si_2Mg_n^Q ($n = 1-11$; $Q = 0, \pm 1$) clusters of silicide-magnesium materials in detail. The paper is organized as follows: Section Computation Methods describes the computational details, the results are presented and completely discussed in section Results and discussions, and the final conclusions are summarized in section Conclusion.

COMPUTATION METHODS

All structural optimization and infrared Raman spectrum analysis are carried out by using DFT at B3LYP/6-311G (d) basis set level in Gauss 09 program package (Frisch et al., 2014). In order to find the lowest energy state structure of Si_2Mg_n^Q ($n = 1-11$; $Q = 0, \pm 1$) clusters of silicon-magnesium sensor material, it is necessary to prepare enough initial configurations of Si_2Mg_n clusters. We used the particle swarm optimization (CALYPSO) method (Wang et al., 2010, 2012; Lv et al., 2012) to get the initial structures of pure magnesium clusters. Then, replacing any two Mg atoms with Si atom in the initial Mg_n clusters' structures. CALYPSO method has successfully predicted structures for various systems ranging from clusters to crystal structures (Lu et al., 2013, 2017, 2018; Lu and Chen, 2018; Xiao et al., 2019). In the process of geometric optimization in Gauss 09 package, for neutral clusters, the spin multiplicity of electrons takes into account 1, 3, 5 states, while for charged clusters, it is 2, 4, 6 states, and there is no constraint on the symmetry. Finally, if the optimization results include virtual frequencies, the coordinates of the virtual mode are relaxed until the real local minimum is obtained. On the basis of eliminating imaginary frequency, the potential energy of all optimized ground state structures will reach absolute local minimum.

In order to prove the reliability of the selected B3LYP/6-311G (d) basis set level, the calculated bond length, vibrational frequency, vertical ionization potential (VIP) and vertical electron affinity (VEA) of the neutral Mg_2 , Si_2 , SiMg clusters by using different methods at the same 6-311G (d) basis set are shown in Table 1. As showed in Table 1, the calculated values $r(\text{Mg}_2) = 3.93 \text{ \AA}$, $\omega(\text{Mg}_2) = 44.96 \text{ cm}^{-1}$, $r(\text{Si}_2) = 2.17 \text{ \AA}$, $\omega(\text{Si}_2) = 540.82 \text{ cm}^{-1}$, $\text{VIP}(\text{Si}_2) = 9.13 \text{ eV}$, and $\text{VEA}(\text{Si}_2) = 2.02 \text{ eV}$, these conclusions are quite agree with the existed experimental results (Huber, 1979; de Heer et al., 1987; Kitsopoulos et al., 1991; Ruetten et al., 2005).

RESULTS AND DISCUSSIONS

Geometrical Structures of Si_2Mg_n^Q ($n = 1-11$; $Q = 0, \pm 1$) Clusters of Silicon-Magnesium Sensor Material

The geometries of Si_2Mg_n^Q ($n = 1-11$; $Q = 0, \pm 1$) clusters of silicon-magnesium sensor material are optimized by using

TABLE 1 | Calculated values of bond length r (Å), frequency ω (cm^{-1}), vertical ionization potential VIP (eV) and vertical electron affinity VEA (eV) for the Mg_2 , Si_2 , and SiMg clusters by different methods.

Methods	Mg_2				Si_2				SiMg			
	r	ω	VIP	VEA	r	ω	VIP	VEA	r	ω	VIP	VEA
B3LYP	3.93	44.96	8.16	0.43	2.17	540.82	9.13	2.02	2.57	288.31	6.77	0.61
B3PW91	3.61	85.29	6.20	0.22	2.31	476.71	8.53	2.79	2.54	325.98	5.84	1.70
PBE	2.78	263.51	4.75	1.68	2.18	531.49	8.15	2.08	2.56	311.01	6.91	0.96
BPV86	2.78	259.56	7.71	0.69	2.18	527.65	7.84	2.08	2.55	306.74	7.94	1.32
MP1PW91	3.60	88.05	6.16	0.21	2.30	484.06	8.54	2.79	2.54	327.96	5.80	1.71
Expt	3.89 ^a	45 ^a	–	–	2.25 ^b	511 ^b	>8.49 ^c	2.176 ± 0.002 ^d	–	–	–	–

^aRuette et al. (2005).^bHuber (1979).^cde Heer et al. (1987).^dKitsopoulos et al. (1991).

the computational method in section Computation Methods. Due to the existence of so many initial structures, the relative energies of all the initial isomers with different spin multiplicities are optimized, but only the lowest energies and a few low-lying energy isomers are given in **Figures 1–3**. In addition, in **Figures 1–3**, in order to compare the effect of Si-doped Mg clusters on the original structure of pure Mg clusters, we also list the lowest energy state structure Mg_{n+2} ($n = 1-11$) of pure Mg clusters optimized by the same method, while the lowest energy state and two metastable structures of neutral Si_2Mg_n^0 , anionic $\text{Si}_2\text{Mg}_n^{-1}$, cationic $\text{Si}_2\text{Mg}_n^{+1}$ ($n = 1-11$) clusters are given. Under each isomer structure, there are three information about the energy difference between the metastable structure and the lowest energy state structure, the symmetry, and the electronic spin state. So, the first structure of Si_2Mg_n^Q clusters are all labeled as 0.00 eV, indicating that this structure is the lowest energy state. The latter two are two metastable structures, and the energy difference with the lowest energy state is directly expressed as a non-zero value. It is noteworthy that when n is determined, there are three energy differences on the right side of the lowest energy structure of Mg_{n+2} , they are $\Delta E_1 = E(\text{Si}_2\text{Mg}_n^0) - E(\text{Mg}_{n+2})$, $\Delta E_2 = E(\text{Si}_2\text{Mg}_n^{-1}) - E(\text{Mg}_{n+2})$, and $\Delta E_3 = E(\text{Si}_2\text{Mg}_n^{+1}) - E(\text{Mg}_{n+2})$, notably, E means the ground state energy. Since there are too many structures, we first give a brief introduction to each structure, and then analyze and discuss their growth patterns shortly below.

$n = 1$: Si_2Mg_1 , $\text{Si}_2\text{Mg}_1^{-1}$, $\text{Si}_2\text{Mg}_1^{+1}$, and Mg_3

The lowest energy structure of neutral Si_2Mg_1 with spin singlet and C_s symmetry is an isosceles triangle, which are the similar as the ground state of cationic $\text{Si}_2\text{Mg}_1^{+1}$ and pure Mg_3 clusters. For anionic $\text{Si}_2\text{Mg}_1^{-1}$, the linear chain (C_s , $^6A'$) in which the Mg atom is in the middle position is found to be the most stable isomer. For metastable isomers, two triangular structures for $\text{Si}_2\text{Mg}_1^{+1}$, two linear chain structures for $\text{Si}_2\text{Mg}_1^{-1}$, and one triangular, one linear chain structures for neutral Si_2Mg_1 .

$n = 2$: Si_2Mg_2 , $\text{Si}_2\text{Mg}_2^{-1}$, $\text{Si}_2\text{Mg}_2^{+1}$, and Mg_4

The ground states of Si_2Mg_2 (D_{2H} , 1AG) and $\text{Si}_2\text{Mg}_2^{-1}$ (C_{2H} , 2AG) are parallelograms with a little different shapes. Replacing

any two Mg atoms with Si atoms in the tetrahedral structure of Mg_4 (T_D , 1A_1) forms the lowest energy isomer structure of $\text{Si}_2\text{Mg}_2^{+1}$ (C_{2V} , 2B_2). All metastable isomers are planar structures, such as trapezoids, triangles and parallelograms.

$n = 3$: Si_2Mg_3 , $\text{Si}_2\text{Mg}_3^{-1}$, $\text{Si}_2\text{Mg}_3^{+1}$, and Mg_5

It is impossible to replace two magnesium atoms in the ground state structure of Mg_5 (C_1 , 1A) with silicon atoms to directly form any Si_2Mg_3 ($Q = 0, \pm 1$) cluster structure. But the lowest energy isomer structures of Si_2Mg_3 (C_s , $^1A'$) and $\text{Si}_2\text{Mg}_3^{-1}$ (C_s , $^2A'$) can be formed by the second metastable isomer structure of Si_2Mg_2 , in where attracting a Mg atom in the same plane outside the trapezoidal silicon-silicon bond. The lowest energy isomer structure of $\text{Si}_2\text{Mg}_3^{+1}$ (C_1 , 2A) is formed by the ground state of $\text{Si}_2\text{Mg}_2^{+1}$ with a magnesium cap at the top of a magnesium atom. In addition, all metastable isomers exhibit planar structures.

$n = 4$: Si_2Mg_4 , $\text{Si}_2\text{Mg}_4^{-1}$, $\text{Si}_2\text{Mg}_4^{+1}$, and Mg_6

The lowest energy structure of Mg_6 (C_1 , 1A) is an octahedron. When the two magnesium atoms at the octahedron vertex are replaced by silicon atoms and the lower silicon atoms float up to the plane where the four magnesium atoms are located, the lowest energy state structures of Si_2Mg_4 (C_1 , 1A) and $\text{Si}_2\text{Mg}_4^{-1}$ (C_1 , 2A) are formed. The ground state structure of $\text{Si}_2\text{Mg}_4^{+1}$ (C_1 , 2A) can be formed by the ground state of $\text{Si}_2\text{Mg}_2^{+1}$ attracting a Mg-Mg bond parallel to the Si-Si bond. All metastable isomers are three-dimensional structures and are directly related to the structure of isomers with small n values.

$n = 5$: Si_2Mg_5 , $\text{Si}_2\text{Mg}_5^{-1}$, $\text{Si}_2\text{Mg}_5^{+1}$, and Mg_7

The ground state structure of Mg_7 (C_1 , 1A) can be directly formed from Mg_6 with a magnesium atom cap on one side of the octahedron. The ground state structures of $\text{Si}_2\text{Mg}_5^{-1}$ (C_1 , 2A) and $\text{Si}_2\text{Mg}_5^{+1}$ (C_1 , 2A) are similar, their main body is a triangular prism with a magnesium-silicon-magnesium triangle at the top and bottom, and then a magnesium atom cap at different distances from the side. The lowest energy structure of neutral Si_2Mg_5 (C_1 , 2A) is formed when the ground state structure of Si_2Mg_4 attracting one magnesium atom. It is easy to see that the first metastable structure of cationic $\text{Si}_2\text{Mg}_5^{+1}$ is the lowest energy state structure of neutral Si_2Mg_5 . Interestingly, the

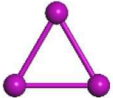
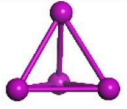
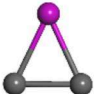
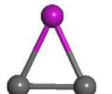
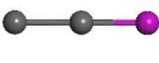
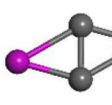
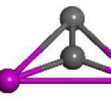

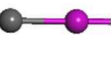
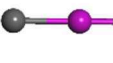
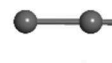
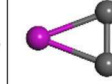

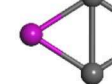


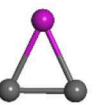
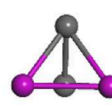
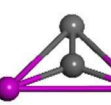

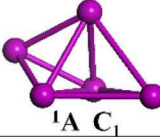
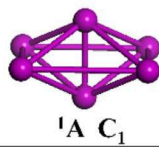
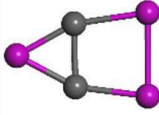
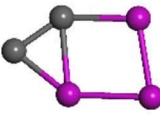
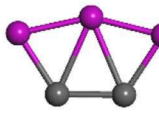
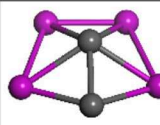
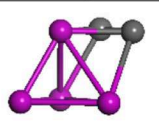
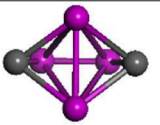

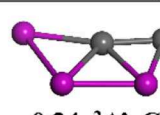
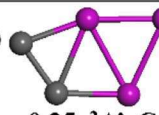
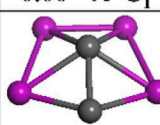
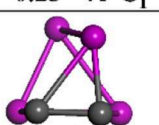
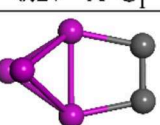
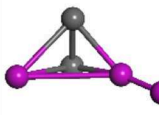

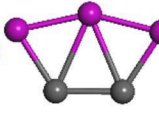
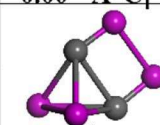
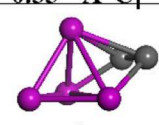

Mg₃	 $^5A'' C_S$ $\Delta E_1=-4867.41$ $\Delta E_2=-4867.22$ $\Delta E_3=-4860.23$	Mg₄	 $^1A_1 T_D$ $\Delta E_1=-4864.22$ $\Delta E_2=-4865.96$ $\Delta E_3=-4857.66$
Si₂Mg₁	 0.00 $^1A' C_S$  1.84 $^5A'' C_S$  2.04 $^5A' C_S$	Si₂Mg₂	 0.00 $^1AG D_{2H}$  0.28 $^3A' C_S$  0.42 $^1A_1 C_{2V}$
Si₂Mg₁⁻	 0.00 $^6A' C_S$  0.56 $^4A'' C_S$  0.64 $^6A'' C_S$	Si₂Mg₂⁻	 0.00 $^2AG C_{2H}$  0.07 $^2A_1 C_{2V}$  0.80 $^2AG D_{2H}$
Si₂Mg₁⁺	 0.00 $^2A'' C_S$  0.54 $^4A'' C_S$  0.94 $^4A'' C_S$	Si₂Mg₂⁺	 0.00 $^2B_2 C_{2V}$  0.13 $^4A'' C_S$  0.18 $^2B_1 C_{2V}$
Mg₅	 $^1A C_1$ $\Delta E_1=-4865.03$ $\Delta E_2=-4866.73$ $\Delta E_3=-4859.01$	Mg₆	 $^1A C_1$ $\Delta E_1=-4865.20$ $\Delta E_2=-4867.07$ $\Delta E_3=-4859.64$
Si₂Mg₃	 0.00 $^1A' C_S$  0.12 $^1A' C_S$  0.16 $^1A' C_S$	Si₂Mg₄	 0.00 $^1A C_1$  0.23 $^1A C_1$  0.27 $^1A C_1$
Si₂Mg₃⁻	 0.00 $^2A' C_S$  0.24 $^2A' C_S$  0.25 $^2A' C_S$	Si₂Mg₄⁻	 0.00 $^2A C_1$  0.33 $^2A C_1$  0.37 $^2A C_1$
Si₂Mg₃⁺	 0.00 $^2A C_1$  0.07 $^2A' C_S$  0.11 $^2A' C_S$	Si₂Mg₄⁺	 0.00 $^2A C_1$  0.07 $^2A C_1$  0.08 $^2A C_1$

FIGURE 1 | Optimized geometries of Mg_{n+2} and $Si_2Mg_n^Q$ ($n = 1-4$; $Q = 0, \pm 1$) clusters of silicon-magnesium sensor material at B3LYP/6-311+G(d) level. The pink and gray balls present the Mg and Si atoms, respectively.

difference between the first metastable state structure of neutral Si_2Mg_5 and the lowest energy state structure of anionic $Si_2Mg_5^{-1}$ is the orientation of the cap with magnesium atom, the former at the bottom and the latter at the side.

$n = 6$: Si_2Mg_6 , $Si_2Mg_6^{-1}$, $Si_2Mg_6^{+1}$, and Mg_8

The lowest energy structure of Mg_8 (C_1 , 1A) is formed by adding a Mg atom cap to the up down mirror symmetry of Mg_7 . When adding a Mg atom cap to the right left mirror symmetry of the lowest energy structure of $Si_2Mg_5^{+1}$, the ground state structures of $Si_2Mg_6^{+1}$ (C_1 , 2A) is formed. The lowest energy structure of neutral Si_2Mg_6 (C_1 , 1A) is as the same as its first metastable structure. The ground state of $Si_2Mg_6^{-1}$ (C_1 , 2A) is an

irregular polyhedral cylinder, but its metastable state structures show certain irregularity.

$n = 7$: Si_2Mg_7 , $Si_2Mg_7^{-1}$, $Si_2Mg_7^{+1}$, and Mg_9

The lowest energy state structure of the cationic $Si_2Mg_7^{+1}$ (C_1 , 2A), which is as the same as its second metastable state structure, can be formed by substituting the upper and lower mirror symmetrical Mg atoms for the silicon atoms in the lowest energy state Mg_9 (C_1 , 1A) structure. The ground state of $Si_2Mg_7^{-1}$ (C_1 , 2A) is similar as the first metastable state structure $Si_2Mg_7^{+1}$. The lowest energy structure of the neutral Si_2Mg_7 (C_1 , 2A) has the same main body as the ground state structure of Si_2Mg_4 . Interestingly, the second metastable state structure of Si_2Mg_7

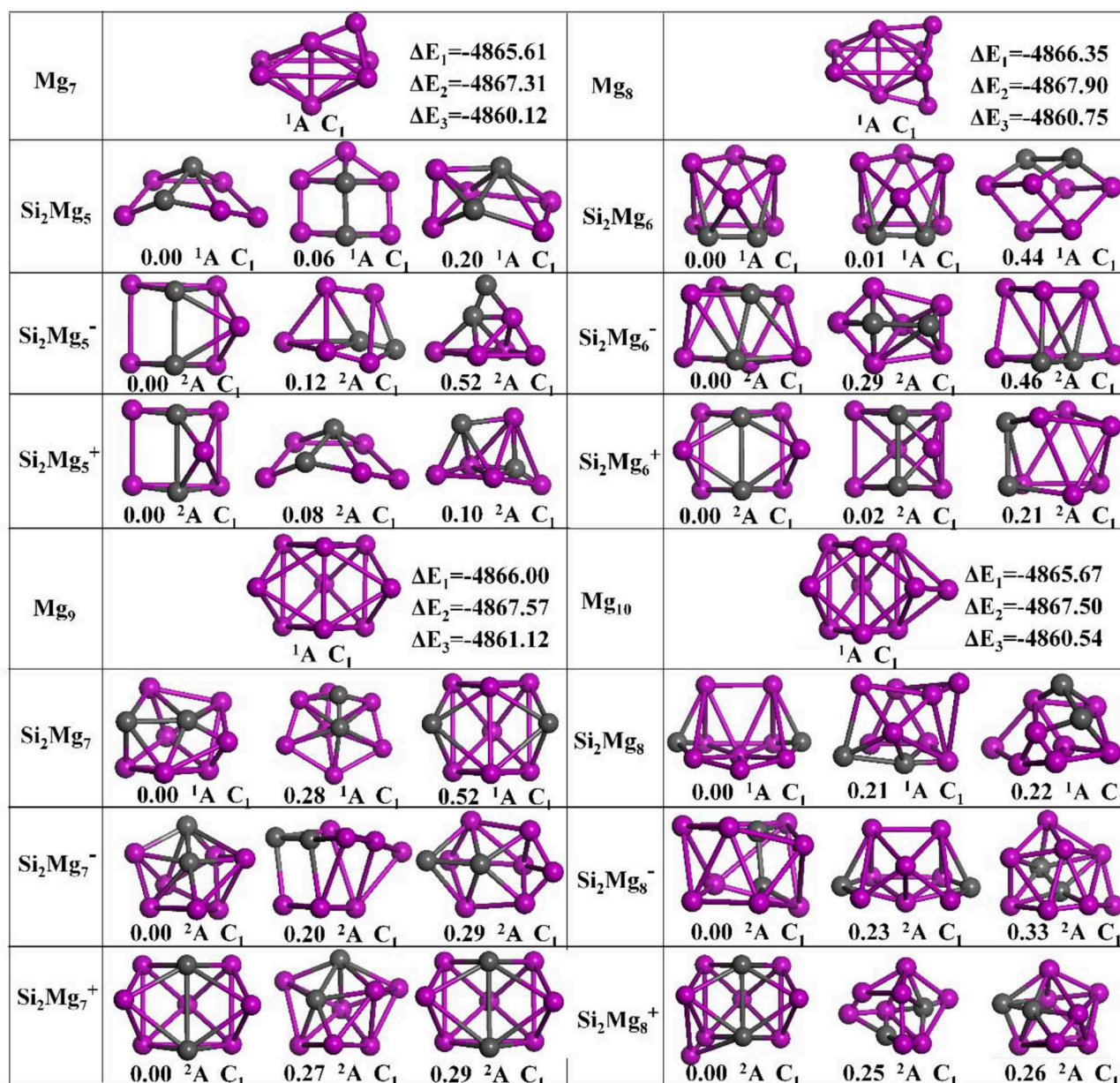


FIGURE 2 | Optimized geometries of Mg_{n+2} and Si₂Mg_n^Q ($n = 5-8$; $Q = 0, \pm 1$) clusters of silicon-magnesium sensor material at B3LYP/6-311+G(d) level. The pink and gray balls present the Mg and Si atoms, respectively.

is similar as the ground state structure of Si₂Mg₇⁺¹, the only difference is the two silicon atoms are bonded from top to bottom to left.

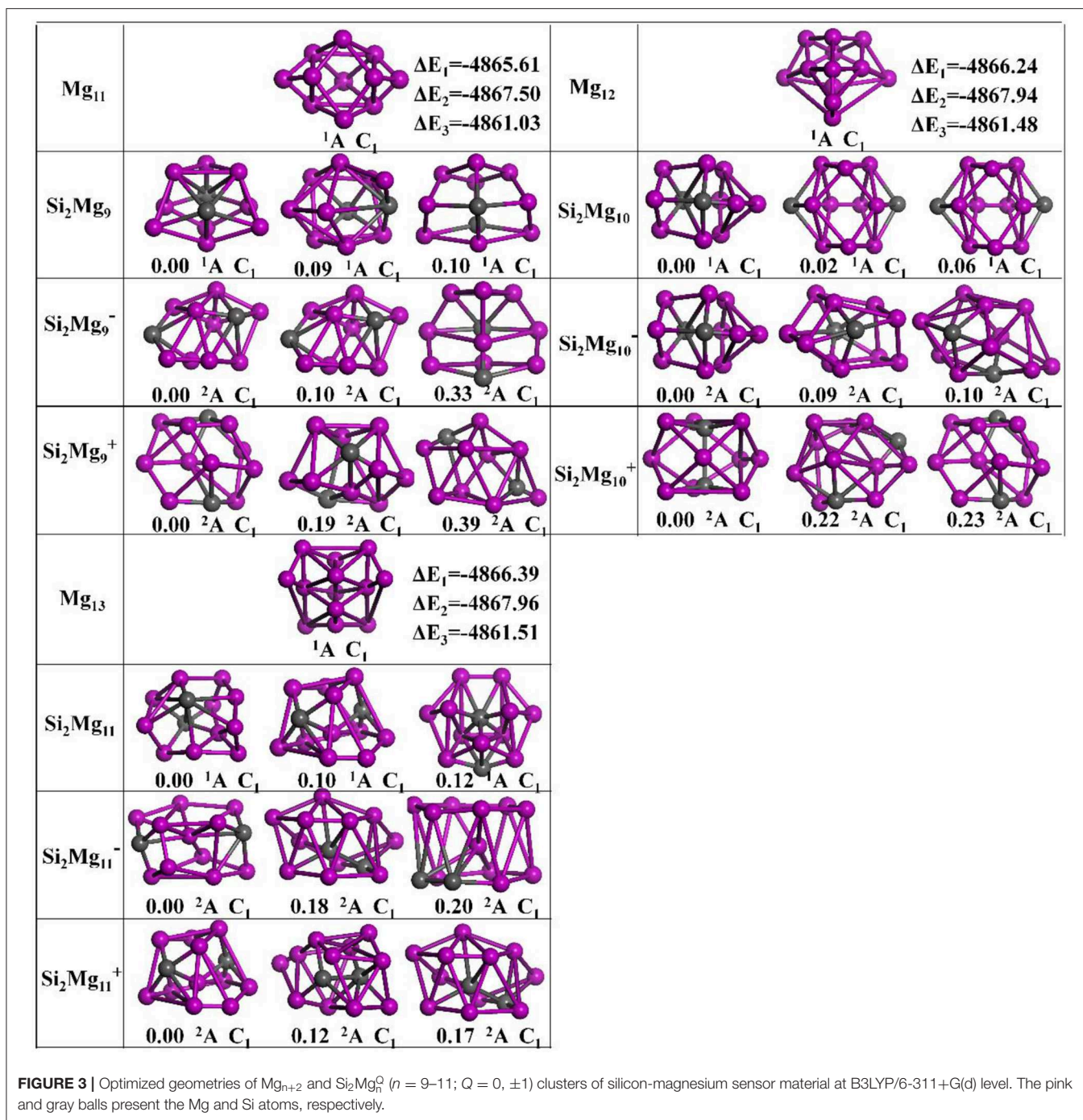
$n = 8$: Si₂Mg₈, Si₂Mg₈⁻¹, Si₂Mg₈⁺¹, and Mg₁₀

The lowest energy state structure of the Mg₁₀ (C_1 , 1A_1) is formed by Mg₉ with a magnesium atom on right side. The ground state structure of Si₂Mg₈⁻¹ (C_1 , 2A_1) can be formed by ground state structure of Si₂Mg₇⁺¹ with a magnesium cap on left-down side. The lowest energy state structure of neutral Si₂Mg₈ (C_1 , 2A_1) is similar as the first metastable state structure of Si₂Mg₈⁻¹. The

ground state of Si₂Mg₈⁻¹ (C_1 , 2A_1) is cage-like structure with one silicon atom trapped on the upper surface. Interestingly, other metastable state structures also present cage-like structures.

$n = 9$: Si₂Mg₉, Si₂Mg₉⁻¹, Si₂Mg₉⁺¹, and Mg₁₁

When Mg₁₀ attracting a magnesium on the left side, it is the lowest energy structure of Mg₁₁ (C_1 , 1A_1). From $n = 9$, it is easy found that no structure of Si₂Mg_n^Q ($Q = 0, \pm 1$) can be formed by substituting two magnesium atoms for silicon atoms in Mg_{n+2}. The ground state of Si₂Mg₉⁻¹ (C_1 , 2A_1) is similar as its first metastable state structure. They can be formed based on



the first metastable structure of $\text{Si}_2\text{Mg}_8^{+1}$ with a Mg atomic cap. The ground state structure of neutral Si_2Mg_9 (C_1 , ^2A) is similar as its second metastable structure and the second metastable structure of Si_2Mg_9^- . The lowest energy state structure of $\text{Si}_2\text{Mg}_9^{+1}$ (C_1 , ^2A) is a complex 3D cage-like structure based on the second metastable state of Si_2Mg_4 with attracting more five Mg atoms.

$n = 10$: $\text{Si}_2\text{Mg}_{10}$, $\text{Si}_2\text{Mg}_8^{-1}0$, $\text{Si}_2\text{Mg}_8^{+1}0$, and Mg_{12}

The ground state structures of neutral $\text{Si}_2\text{Mg}_{10}$ (C_1 , ^1A) and $\text{Si}_2\text{Mg}_8^{-1}0$ (C_1 , ^2A) are the same and can be formed by the

lowest energy state structure of $\text{Si}_2\text{Mg}_9^{+1}$ with a magnesium cap. The lowest energy state structure of $\text{Si}_2\text{Mg}_8^{+1}0$ (C_1 , ^2A) is formed by the ground state structure of $\text{Si}_2\text{Mg}_8^{-1}$ with adding two magnesium atoms. All the metastable structures present 3D structures, and some of them can easily be found to be associated with the cluster structure discussed earlier. For example, the metastable structure of neutral $\text{Si}_2\text{Mg}_{10}$ can be formed by the ground state of neutral Si_2Mg_8 with adding two Mg atoms.

$n = 11$: $\text{Si}_2\text{Mg}_{11}$, $\text{Si}_2\text{Mg}_8^{-1}1$, $\text{Si}_2\text{Mg}_8^{+1}1$, and Mg_{13}

The lowest energy structures of $\text{Si}_2\text{Mg}_{11}$ (C_{1v} , 1A), $\text{Si}_2\text{Mg}_9^{-1}1(C_{1v}, ^2A)$, $\text{Si}_2\text{Mg}_9^{+1}1(C_{1v}, ^2A)$ show cage structures, but no silicon atom located the cage center. By using the ground state structure of $\text{Si}_2\text{Mg}_9^{-1}$ with adding two magnesium atoms, the lowest energy structure of $\text{Si}_2\text{Mg}_9^{-1}1(C_{1v}, ^2A)$ is got. The ground state structure of $\text{Si}_2\text{Mg}_{11}$ (C_{1v} , 1A) can be formed by the first metastable structure of Si_2Mg_9 with two more magnesium attracted. The lowest energy structure of $\text{Si}_2\text{Mg}_9^{+1}1(C_{1v}, ^2A)$ is the same as the first metastable structure of $\text{Si}_2\text{Mg}_{11}$, and they are quite similar as the first metastable structure of $\text{Si}_2\text{Mg}_9^{+1}$. Other metastable structures exhibit 3D cage-like structure.

Energy Difference Between Structures

As shown in **Figures 1–3**, the energy differences ΔE_1 (from -4867.41 to -4864.22 eV), ΔE_2 (from -4867.96 to

-4865.96 eV), and ΔE_3 (from -4861.51 to -4857.66 eV) are quite stable and reasonable. Because the energy difference between the free neutral Si_2 and Mg_2 , $E(\text{Si}_2)-E(\text{Mg}_2) = -4864.42$ eV, is quite near to the ΔE_1 . In addition, $\Delta E_2 < \Delta E_1 < \Delta E_3$ is consistent with the following conclusion: if the neutral charged cluster is negatively charged, the cluster will lose energy, and if the neutral charged cluster is positively charged, the cluster will get energy. In addition, the energy differences between all metastable state structures and their corresponding ground state structures are also listed under each metastable state structure, they are all very small (from 0.01 to 2.04 eV) and reasonable.

Growth Pattern

According to the structural characteristics of the lowest energy state structures mentioned above, the growth mechanism of

TABLE 2 | The shortest bond length (Å) of Mg_{n+2} , neutral and charged Si_2Mg_n^Q ($n = 1-11$; $Q = 0, \pm 1$) clusters.

Clusters	The shortest bond length (Å)			Clusters	The shortest bond length (Å)
	Anionic	Cationic	Neutral		
Si_2Mg_1	$d_{\text{Si-Si}} = 5.27$ $d_{\text{Si-Mg}} = 2.63$	$d_{\text{Si-Si}} = 2.31$ $d_{\text{Si-Mg}} = 2.70$	$d_{\text{Si-Si}} = 2.21$ $d_{\text{Si-Mg}} = 2.54$	Mg_3	$d_{\text{Mg-Mg}} = 2.91$
Si_2Mg_2	$d_{\text{Si-Si}} = 2.37$ $d_{\text{Si-Mg}} = 2.66$ $d_{\text{Mg-Mg}} = 4.76$	$d_{\text{Si-Si}} = 2.47$ $d_{\text{Si-Mg}} = 2.66$ $d_{\text{Mg-Mg}} = 2.99$	$d_{\text{Si-Si}} = 2.22$ $d_{\text{Si-Mg}} = 2.79$ $d_{\text{Mg-Mg}} = 5.13$	Mg_4	$d_{\text{Mg-Mg}} = 3.17$
Si_2Mg_3	$d_{\text{Si-Si}} = 2.25$ $d_{\text{Si-Mg}} = 2.67$ $d_{\text{Mg-Mg}} = 3.01$	$d_{\text{Si-Si}} = 2.21$ $d_{\text{Si-Mg}} = 2.66$ $d_{\text{Mg-Mg}} = 2.96$	$d_{\text{Si-Si}} = 2.32$ $d_{\text{Si-Mg}} = 2.53$ $d_{\text{Mg-Mg}} = 3.00$	Mg_5	$d_{\text{Mg-Mg}} = 3.45$
Si_2Mg_4	$d_{\text{Si-Si}} = 2.23$ $d_{\text{Si-Mg}} = 2.77$ $d_{\text{Mg-Mg}} = 3.03$	$d_{\text{Si-Si}} = 2.75$ $d_{\text{Si-Mg}} = 2.59$ $d_{\text{Mg-Mg}} = 2.99$	$d_{\text{Si-Si}} = 2.27$ $d_{\text{Si-Mg}} = 2.68$ $d_{\text{Mg-Mg}} = 2.93$	Mg_6	$d_{\text{Mg-Mg}} = 3.00$
Si_2Mg_5	$d_{\text{Si-Si}} = 2.32$ $d_{\text{Si-Mg}} = 2.69$ $d_{\text{Mg-Mg}} = 3.05$	$d_{\text{Si-Si}} = 2.59$ $d_{\text{Si-Mg}} = 2.58$ $d_{\text{Mg-Mg}} = 2.98$	$d_{\text{Si-Si}} = 2.22$ $d_{\text{Si-Mg}} = 2.60$ $d_{\text{Mg-Mg}} = 2.88$	Mg_7	$d_{\text{Mg-Mg}} = 3.15$
Si_2Mg_6	$d_{\text{Si-Si}} = 2.33$ $d_{\text{Si-Mg}} = 2.65$ $d_{\text{Mg-Mg}} = 2.99$	$d_{\text{Si-Si}} = 2.56$ $d_{\text{Si-Mg}} = 2.64$ $d_{\text{Mg-Mg}} = 2.99$	$d_{\text{Si-Si}} = 2.74$ $d_{\text{Si-Mg}} = 2.60$ $d_{\text{Mg-Mg}} = 2.87$	Mg_8	$d_{\text{Mg-Mg}} = 3.14$
Si_2Mg_7	$d_{\text{Si-Si}} = 2.29$ $d_{\text{Si-Mg}} = 2.67$ $d_{\text{Mg-Mg}} = 3.03$	$d_{\text{Si-Si}} = 2.36$ $d_{\text{Si-Mg}} = 2.67$ $d_{\text{Mg-Mg}} = 3.02$	$d_{\text{Si-Si}} = 2.23$ $d_{\text{Si-Mg}} = 2.66$ $d_{\text{Mg-Mg}} = 2.90$	Mg_9	$d_{\text{Mg-Mg}} = 3.12$
Si_2Mg_8	$d_{\text{Si-Si}} = 2.39$ $d_{\text{Si-Mg}} = 2.67$ $d_{\text{Mg-Mg}} = 3.01$	$d_{\text{Si-Si}} = 2.69$ $d_{\text{Si-Mg}} = 2.65$ $d_{\text{Mg-Mg}} = 2.99$	$d_{\text{Si-Si}} = 5.15$ $d_{\text{Si-Mg}} = 2.54$ $d_{\text{Mg-Mg}} = 2.89$	Mg_{10}	$d_{\text{Mg-Mg}} = 3.04$
Si_2Mg_9	$d_{\text{Si-Si}} = 5.02$ $d_{\text{Si-Mg}} = 2.64$ $d_{\text{Mg-Mg}} = 2.98$	$d_{\text{Si-Si}} = 2.39$ $d_{\text{Si-Mg}} = 2.65$ $d_{\text{Mg-Mg}} = 3.03$	$d_{\text{Si-Si}} = 5.72$ $d_{\text{Si-Mg}} = 2.58$ $d_{\text{Mg-Mg}} = 2.92$	Mg_{11}	$d_{\text{Mg-Mg}} = 3.08$
$\text{Si}_2\text{Mg}_{10}$	$d_{\text{Si-Si}} = 5.90$ $d_{\text{Si-Mg}} = 2.64$ $d_{\text{Mg-Mg}} = 3.03$	$d_{\text{Si-Si}} = 2.45$ $d_{\text{Si-Mg}} = 2.67$ $d_{\text{Mg-Mg}} = 3.02$	$d_{\text{Si-Si}} = 5.84$ $d_{\text{Si-Mg}} = 2.55$ $d_{\text{Mg-Mg}} = 2.88$	Mg_{12}	$d_{\text{Mg-Mg}} = 3.09$
$\text{Si}_2\text{Mg}_{11}$	$d_{\text{Si-Si}} = 5.17$ $d_{\text{Si-Mg}} = 2.64$ $d_{\text{Mg-Mg}} = 2.96$	$d_{\text{Si-Si}} = 5.22$ $d_{\text{Si-Mg}} = 2.67$ $d_{\text{Mg-Mg}} = 2.96$	$d_{\text{Si-Si}} = 6.04$ $d_{\text{Si-Mg}} = 2.68$ $d_{\text{Mg-Mg}} = 2.93$	Mg_{13}	$d_{\text{Mg-Mg}} = 3.03$

Si_2Mg_n^Q ($n = 1-11$; $Q = 0, \pm 1$) clusters of silicon-magnesium sensor material can be summarized as following: (i) The lowest energy state Si_2Mg_n^Q clusters favor 3D and low spin multiplicity for $n = 4-11$. (ii) Compared with neutral Si_2Mg_n clusters, charged $\text{Si}_2\text{Mg}_n^{\pm 1}$ clusters formed when they get or lose electrons will change their structures in most cases. (iii) Larger size clusters $\text{Si}_2\text{Mg}_n^{0\pm 1}$ show cage-like geometries, but silicon atoms are not in the center of the cage, but tend to the edge, which is different from some reports (Zhang et al., 2015). This may be related to the distribution of electrons outside the nucleus of magnesium and silicon atoms. Through the above structure optimization, we can find that the shortest chemical bond length of clusters tends to be smaller when silicon doped with magnesium. **Table 2** shows the shortest chemical bond lengths of Mg-Mg, Si-Si, Si-Mg for all Si_2Mg_n

clusters as the number of magnesium atoms increases. For comparison, **Table 2** also lists the shortest chemical bond lengths of Mg-Mg clusters with corresponding atomic numbers of pure magnesium clusters. From **Table 2**, it can be seen clearly that silicon doping into magnesium can indeed make the cluster structure more compact when the total number of atoms is the same.

The Relative Stabilities of Si_2Mg_n^Q ($n = 1-11$; $Q = 0, \pm 1$) Clusters of Silicon-Magnesium Sensor Material

In order to study the relativity stabilities of neutral and charged Si_2Mg_n^Q ($n = 1-11$; $Q = 0, \pm 1$) clusters of silicon-magnesium sensor material, the average binding energy E_b , fragmentation energy E_f , the second-order energy differences Δ_2E , and the

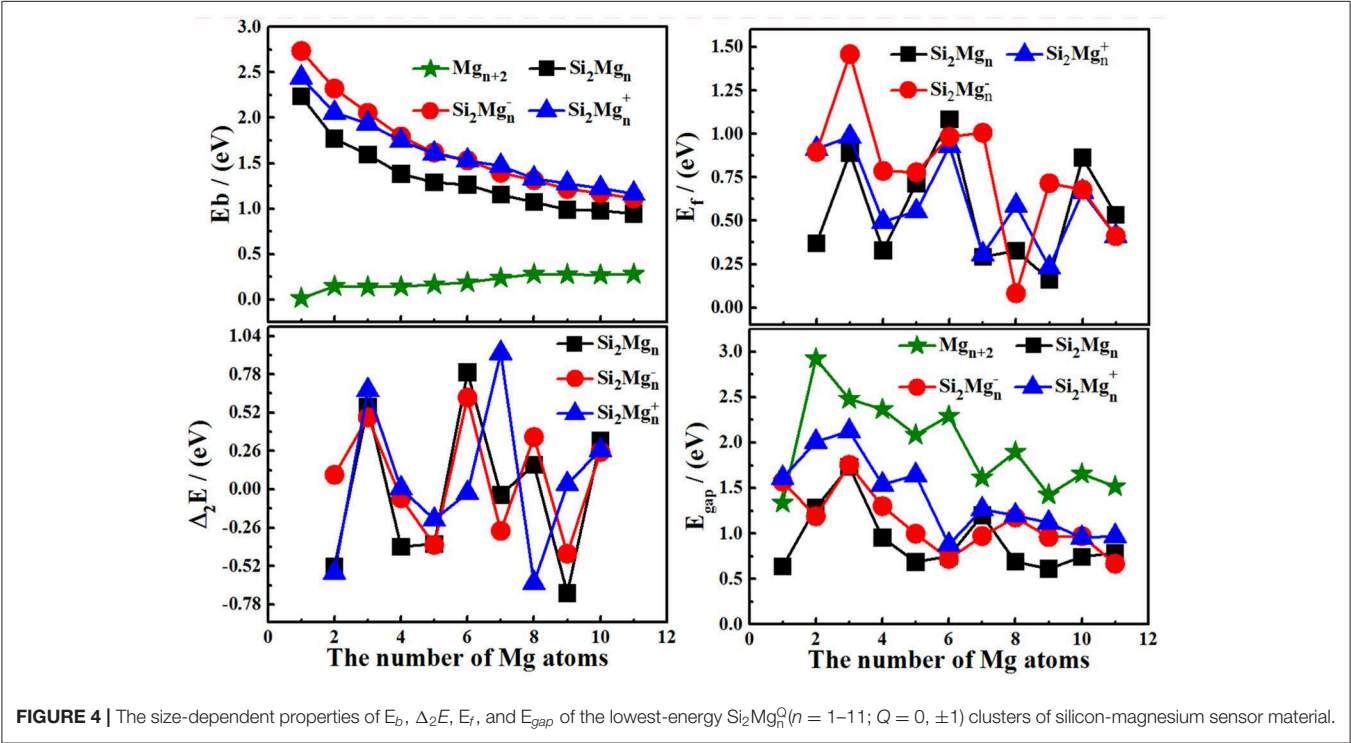


FIGURE 4 | The size-dependent properties of E_b , Δ_2E , E_f , and E_{gap} of the lowest-energy Si_2Mg_n^Q ($n = 1-11$; $Q = 0, \pm 1$) clusters of silicon-magnesium sensor material.

TABLE 3 | NCP of the lowest-energy structures for neutral SiMg_n ($n = 1-11$) clusters of silicon-magnesium sensor material.

Clusters/Atom	Si-1	Si-2	Mg-1	Mg-2	Mg-3	Mg-4	Mg-5	Mg-6	Mg-7	Mg-8	Mg-9	Mg-10	Mg-11
Si_2Mg_1	−0.36	−0.36	0.72										
Si_2Mg_2	−0.55	−0.55	0.55	0.55									
Si_2Mg_3	−0.88	−0.89	0.45	0.45	0.86								
Si_2Mg_4	−0.59	−1.14	0.57	0.29	0.29	0.57							
Si_2Mg_5	−0.92	−0.76	0.26	0.27	0.23	0.46	0.45						
Si_2Mg_6	−0.89	−0.89	0.23	0.42	0.42	0.00	0.23	0.49					
Si_2Mg_7	−1.34	−0.68	0.43	0.22	0.15	0.45	0.52	0.00	0.25				
Si_2Mg_8	−1.89	−1.89	0.51	0.59	0.30	0.51	0.51	0.51	0.59	0.25			
Si_2Mg_9	−1.37	−1.53	0.61	0.25	0.22	0.42	0.49	0.25	0.22	−0.04	0.49		
$\text{Si}_2\text{Mg}_{10}$	−1.69	−1.61	0.49	0.00	0.16	0.34	0.37	0.35	0.37	0.48	0.15	0.59	
$\text{Si}_2\text{Mg}_{11}$	−1.70	−1.73	0.37	0.52	0.41	0.30	0.04	0.53	−0.03	0.30	0.22	0.58	0.19

HOMO-LUMO energy gap E_{gap} are calculated, which can be read as below:

$$E_b(\text{Si}_2\text{Mg}_n) = [nE_k(\text{Mg}) + 2E_k(\text{Si}) - E_k(\text{Si}_2\text{Mg}_n)]/(n+2) \quad (1)$$

$$E_b(\text{Si}_2\text{Mg}_n^{\pm 1}) = [(n-1)E_k(\text{Mg}) + E_k(\text{Mg}^{\pm}) + 2E_k(\text{Si}) - E_k(\text{Si}_2\text{Mg}_n^{\pm 1})]/(n+2) \quad (2)$$

$$E_f(\text{Si}_2\text{Mg}_n^{0,\pm 1}) = E_k(\text{Si}_2\text{Mg}_{n-1}^{0,\pm 1}) + E_k(\text{Mg}) - E_k(\text{Si}_2\text{Mg}_n^{0,\pm 1}) \quad (3)$$

$$\Delta_2 E(\text{Si}_2\text{Mg}_n^{0,\pm 1}) = E_k(\text{Si}_2\text{Mg}_{n-1}^{0,\pm 1}) + E_k(\text{Si}_2\text{Mg}_{n+1}^{0,\pm 1}) - 2E_k(\text{Si}_2\text{Mg}_n^{0,\pm 1}) \quad (4)$$

$$E_{\text{gap}}(\text{Si}_2\text{Mg}_n^{0,\pm 1}) = E_{\text{LUMO}}(\text{Si}_2\text{Mg}_n^{0,\pm 1}) - E_{\text{HOMO}}(\text{Si}_2\text{Mg}_n^{0,\pm 1}) \quad (5)$$

E_k in Equations (1–4) are the total energy of the corresponding atom and ground state clusters. E_{HOMO} and E_{LUMO} in Equation (5) are the energies of highest occupied molecular orbital (HOMO) and the lowest unoccupied molecular orbital (LUMO).

The motivation for comparing pure magnesium clusters must be explained here. Physically, the most ideal (simplest) silicon doping is to replace two magnesium atoms with silicon atoms in pure magnesium clusters, and then to optimize the structure. Therefore, comparing some properties of silicon-doped magnesium clusters, we always habitually compare pure magnesium clusters with the total number of corresponding

atoms in our research. The size-dependent properties of E_b , E_f , $\Delta_2 E$, and E_{gap} for the lowest energy state Si_2Mg_n^Q ($n = 1-11$; $Q = 0, \pm 1$) clusters of silicon-magnesium sensor material are presented in **Figure 4**. We can summarize the properties as the following:

- 1) The E_b values of all Si_2Mg_n^Q ($n = 1-11$; $Q = 0, \pm 1$) clusters of silicon-magnesium sensor material decrease followed by same tendency with the size increases, but the E_b values of pure Mg_{n+2} clusters are gradually increase. In addition, the E_b values of cationic $\text{Si}_2\text{Mg}_n^{+1}$ are always the highest, while the E_b values of neutral Si_2Mg_n^0 are the lowest all the time. It means that electron removal can enhance the chemical properties of Si_2Mg_n clusters.
- 2) The E_f curves of neutral and charged Si_2Mg_n^Q ($n = 1-11$; $Q = 0, \pm 1$) clusters of silicon-magnesium sensor material have a similar oscillating tendency. For neutral Si_2Mg_n^0 clusters, the stronger relative stability clusters are Si_2Mg_3^0 , Si_2Mg_6^0 , and $\text{Si}_2\text{Mg}_{10}^0$ based on the maxim of E_f values. For anionic $\text{Si}_2\text{Mg}_n^{-1}$ clusters, three significant maxima are found at $n = 3, 7, 9$, which indicate that $\text{Si}_2\text{Mg}_3^{-1}$, $\text{Si}_2\text{Mg}_7^{-1}$, and $\text{Si}_2\text{Mg}_9^{-1}$ clusters are the most stable clusters. For cationic $\text{Si}_2\text{Mg}_n^{+1}$ clusters, three local peaks can be found from the E_f curve, it

TABLE 4 | NCP of the lowest-energy structures for anionic $\text{Si}_2\text{Mg}_n^{-1}$ ($n = 1-11$) clusters of silicon-magnesium sensor material.

Clusters/Atom	Si-1	Si-2	Mg-1	Mg-2	Mg-3	Mg-4	Mg-5	Mg-6	Mg-7	Mg-8	Mg-9	Mg-10	Mg-11
Si_2Mg_1^-	−0.73	−0.73	0.46										
Si_2Mg_2^-	−0.81	−0.81	0.31	0.31									
Si_2Mg_3^-	−0.88	−0.88	0.38	0.19	0.19								
Si_2Mg_4^-	−0.65	−1.07	0.27	0.09	0.09	0.27							
Si_2Mg_5^-	−0.98	−0.98	0.23	0.07	0.23	0.35	0.07						
Si_2Mg_6^-	−0.53	−0.53	−0.07	0.08	0.08	−0.07	0.03	0.03					
Si_2Mg_7^-	−0.79	−1.46	0.22	0.05	0.35	0.19	0.09	−0.02	0.37				
Si_2Mg_8^-	−1.47	−1.49	0.30	0.27	0.17	0.39	0.19	0.21	0.17	0.26			
Si_2Mg_9^-	−1.52	−1.67	0.41	0.27	0.04	0.29	0.00	0.33	0.38	0.34	0.12		
$\text{Si}_2\text{Mg}_{10}^-$	−1.83	−1.74	0.46	0.05	0.02	0.31	0.30	0.31	0.30	0.38	0.02	0.43	
$\text{Si}_2\text{Mg}_{11}^-$	−1.88	−1.80	0.35	−0.19	0.44	0.45	0.04	0.09	0.04	0.43	0.49	0.30	0.25

TABLE 5 | NCP of the lowest-energy structures for cationic $\text{Si}_2\text{Mg}_n^{+1}$ ($n = 1-11$) clusters of silicon-magnesium sensor material.

Clusters/Atom	Si-1	Si-2	Mg-1	Mg-2	Mg-3	Mg-4	Mg-5	Mg-6	Mg-7	Mg-8	Mg-9	Mg-10	Mg-11
Si_2Mg_1^+	0.02	0.03	0.95										
Si_2Mg_2^+	−0.34	−0.34	0.84	0.84									
Si_2Mg_3^+	−0.38	−0.37	0.55	0.65	0.55								
Si_2Mg_4^+	−1.16	−1.16	0.99	0.99	0.67	0.67							
Si_2Mg_5^+	−1.37	−1.29	0.67	0.66	0.64	1.09	0.61						
Si_2Mg_6^+	−1.15	−1.15	0.44	0.44	0.78	0.44	0.44	0.78					
Si_2Mg_7^+	−1.09	−1.09	0.65	0.42	0.42	0.42	0.42	0.21	0.65				
Si_2Mg_8^+	−1.33	−1.14	0.35	0.49	0.85	−0.12	0.43	0.81	0.30	0.36			
Si_2Mg_9^+	−1.43	−1.49	0.55	0.55	0.35	0.53	0.53	0.19	0.19	0.69	0.35		
$\text{Si}_2\text{Mg}_{10}^+$	−1.51	−1.51	0.49	0.38	0.48	0.40	0.22	0.41	0.48	0.49	0.41	0.26	
$\text{Si}_2\text{Mg}_{11}^+$	−2.06	−2.06	0.12	0.45	0.59	0.66	0.52	0.52	0.59	0.28	0.28	0.45	0.66

means that $\text{Si}_2\text{Mg}_3^{+1}$, $\text{Si}_2\text{Mg}_6^{+1}$, $\text{Si}_2\text{Mg}_8^{+1}$ clusters are more stable than their neighbors.

3) The irregular oscillation behaviors are the most prominent feature of Δ_2E curves of all Si_2Mg_n^Q ($n = 1-11$; $Q = 0, \pm 1$) clusters of silicon-magnesium sensor material. The maxima are found at $n = 3$ for all Si_2Mg_n^Q clusters, $n = 6$ and 8 for both neutral Si_2Mg_n^0 and anionic $\text{Si}_2\text{Mg}_n^{-1}$ clusters, $n = 7$ for cationic $\text{Si}_2\text{Mg}_n^{+1}$ clusters. It means that the $\text{Si}_2\text{Mg}_3^{-1}$, $\text{Si}_2\text{Mg}_6^{-1}$, $\text{Si}_2\text{Mg}_8^{-1}$, $\text{Si}_2\text{Mg}_3^{+1}$, $\text{Si}_2\text{Mg}_6^{+1}$, and $\text{Si}_2\text{Mg}_7^{+1}$ clusters have slightly stronger relative stabilities and have large abundances in mass spectroscopy in comparison with the corresponding neighbors. For neutral clusters, Si_2Mg_3^0 , Si_2Mg_6^0 , and Si_2Mg_8^0 clusters are more stable than other clusters.

4) The pure Mg_{n+2} clusters have the highest E_{gap} is an unexpected conclusion, because pure magnesium has higher chemical stability than silicon magnesium. For Si_2Mg_n^Q ($n = 1-11$; $Q = 0, \pm 1$) clusters, the E_{gap} of cationic $\text{Si}_2\text{Mg}_n^{+1}$ clusters is always the higher one. It means that $\text{Si}_2\text{Mg}_n^{+1}$ clusters have higher chemical stability than the neutral and anionic Si_2Mg_n^Q clusters. The curves of E_{gap} show that the maxima values appear at $n = 3$ for all Si_2Mg_n^Q ($Q = 0, \pm 1$) clusters, $n = 7$ for both neutral Si_2Mg_n^0 and cationic $\text{Si}_2\text{Mg}_n^{+1}$, and $n = 8$ for anionic $\text{Si}_2\text{Mg}_n^{-1}$ clusters, which implies that the higher chemical stability clusters are Si_2Mg_3^0 , $\text{Si}_2\text{Mg}_3^{-1}$, $\text{Si}_2\text{Mg}_3^{+1}$, Si_2Mg_6^0 , $\text{Si}_2\text{Mg}_7^{+1}$, and $\text{Si}_2\text{Mg}_8^{-1}$.

Based on the discussions about E_b , E_f , Δ_2E , and E_{gap} , we can conclude that the magic numbers of neutral and charged Si_2Mg_n^Q ($n = 1-11$; $Q = 0, \pm 1$) clusters of silicon-magnesium sensor material are Si_2Mg_3^0 , $\text{Si}_2\text{Mg}_3^{-1}$, $\text{Si}_2\text{Mg}_3^{+1}$.

The Charge Transfer of Si_2Mg_n^Q ($n = 1-11$; $Q = 0, \pm 1$) Clusters of Silicon-Magnesium Sensor Material

Natural charge population (NCP) and natural electron population (NEC) of clusters are two important parameters

to study the localization of charges in clusters (Trivedi et al., 2014). In order to study internal charge transfer of neutral and charged Si_2Mg_n^Q ($n = 1-11$; $Q = 0, \pm 1$) clusters of silicon-magnesium sensor material, we calculate NCP and NEC for the ground state structures of Si_2Mg_n^Q ($n = 1-11$; $Q = 0, \pm 1$), and the results are summarized in the **Tables 3–6**. We can find that the charges of silicon atoms in Si_2Mg_n^Q ($n = 1-11$; $Q = 0, \pm 1$) clusters is very significant from the **Tables 3–5**. Specifically, except for $\text{Si}_2\text{Mg}_1^{+1}$, silicon atoms are negatively charged in the range of -0.34 to -2.06 electrons, and most magnesium atoms are positively charged in the range of $0.02-0.99$ electrons. This result is consistent with expectation, because electrons are always transferred from magnesium atoms to silicon atoms in Si_2Mg_n^Q clusters. In short, the NCP of Si atoms indicates that silicon atoms are electron acceptors in Si_2Mg_n^Q clusters. The NEC of silicon atoms can be found in the **Table 6**, the electronic configuration for silicon atoms ($3s^13p^3$) shows that $3p$ orbital get

TABLE 7 | AIP, VIP, AEA, VEA of ground state Si_2Mg_n^Q ($n = 1-11$; $Q = 0, \pm 1$) clusters of silicon-magnesium sensor material.

<i>n</i>	AIP (eV)	VIP (eV)	AIP- VIP (eV)	AEA (eV)	VEA (eV)	AEA- VEA (eV)	VIP- VEA (eV)
1	7.11	7.04	0.07	1.44	0.91	0.53	6.13
2	6.59	6.33	0.25	1.61	1.24	0.37	5.09
3	6.02	6.37	0.36	1.70	1.59	0.11	4.78
4	5.56	5.92	0.36	1.87	1.78	0.08	4.14
5	5.50	5.68	0.18	1.71	1.20	0.50	4.48
6	5.60	5.79	0.19	1.55	1.21	0.34	4.58
7	4.88	5.57	0.69	1.57	1.34	0.23	4.23
8	5.13	5.42	0.29	1.83	1.36	0.47	4.06
9	4.57	5.34	0.77	1.90	1.66	0.24	3.68
10	4.76	5.32	0.57	1.70	1.52	0.18	3.80
11	4.88	5.03	0.15	1.58	1.40	0.18	3.63

TABLE 6 | NEC of the lowest-energy structures for neutral and charged Si_2Mg_n^Q ($n = 1-11$; $Q = 0, \pm 1$) clusters of silicon-magnesium sensor material.

Clusters	Neutral		Anionic		Cationic	
	Si-1	Si-2	Si-1	Si-2	Si-1	Si-2
Si_2Mg_1	$3s^{1.75}3p^{2.60}$	$3s^{1.75}3p^{2.59}$	$3s^{1.89}3p^{2.83}$	$3s^{1.89}3p^{2.83}$	$3s^{1.85}3p^{2.11}$	$3s^{1.85}3p^{2.10}$
Si_2Mg_2	$3s^{1.76}3p^{2.77}$	$3s^{1.76}3p^{2.77}$	$3s^{1.71}3p^{3.07}$	$3s^{1.71}3p^{3.07}$	$3s^{1.81}3p^{2.51}$	$3s^{1.81}3p^{2.51}$
Si_2Mg_3	$3s^{1.68}3p^{3.19}$	$3s^{1.67}3p^{3.19}$	$3s^{1.65}3p^{3.21}$	$3s^{1.65}3p^{3.21}$	$3s^{1.73}3p^{2.62}$	$3s^{1.73}3p^{2.62}$
Si_2Mg_4	$3s^{1.69}3p^{2.88}$	$3s^{1.63}3p^{3.48}$	$3s^{1.66}3p^{2.96}$	$3s^{1.59}3p^{3.45}$	$3s^{1.74}3p^{3.40}$	$3s^{1.74}3p^{3.40}$
Si_2Mg_5	$3s^{1.59}3p^{3.311}$	$3s^{1.62}3p^{3.11}$	$3s^{1.62}3p^{3.32}$	$3s^{1.62}3p^{3.32}$	$3s^{1.71}3p^{3.64}$	$3s^{1.72}3p^{3.55}$
Si_2Mg_6	$3s^{1.61}3p^{3.25}$	$3s^{1.61}3p^{3.25}$	$3s^{1.59}3p^{3.39}$	$3s^{1.59}3p^{3.39}$	$3s^{1.67}3p^{3.45}$	$3s^{1.67}3p^{3.45}$
Si_2Mg_7	$3s^{1.54}3p^{3.76}$	$3s^{1.62}3p^{3.03}$	$3s^{1.59}3p^{3.17}$	$3s^{1.53}3p^{3.89}$	$3s^{1.61}3p^{3.44}$	$3s^{1.61}3p^{3.44}$
Si_2Mg_8	$3s^{1.64}3p^{4.24}$	$3s^{1.64}3p^{4.24}$	$3s^{1.60}3p^{3.83}$	$3s^{1.59}3p^{3.85}$	$3s^{1.62}3p^{3.68}$	$3s^{1.65}3p^{3.46}$
Si_2Mg_9	$3s^{1.63}3p^{3.72}$	$3s^{1.60}3p^{3.92}$	$3s^{1.62}3p^{3.88}$	$3s^{1.59}3p^{4.07}$	$3s^{1.60}3p^{3.80}$	$3s^{1.56}3p^{3.89}$
$\text{Si}_2\text{Mg}_{10}$	$3s^{1.59}3p^{4.09}$	$3s^{1.62}3p^{3.98}$	$3s^{1.60}3p^{4.21}$	$3s^{1.61}3p^{4.11}$	$3s^{1.60}3p^{3.87}$	$3s^{1.60}3p^{3.87}$
$\text{Si}_2\text{Mg}_{11}$	$3s^{1.61}3p^{4.08}$	$3s^{1.59}3p^{4.13}$	$3s^{1.59}3p^{4.28}$	$3s^{1.58}3p^{4.21}$	$3s^{1.61}3p^{4.43}$	$3s^{1.61}3p^{4.43}$

0.10–2.28 electrons, while 3s orbital loses 0.11–0.47 electrons. Obviously, charge transfer occurs only in the outermost electron orbit, and strong s-p hybridizations are presented in silicon atoms of Si_2Mg_n^Q clusters. Notably, the contributions of 4s and 5d orbitals are almost zero and can be ignored. Moreover, the charges of 3s and 3p orbitals for two silicon atoms in the ground state of Si_2Mg_n^Q clusters are equal except for $\text{Si}_2\text{Mg}_{3-5}^-$, Si_2Mg_7^- , $\text{Si}_2\text{Mg}_{9-11}^-$, Si_2Mg_4^+ , $\text{Si}_2\text{Mg}_{7-11}^+$, Si_2Mg_5^+ , and $\text{Si}_2\text{Mg}_{8-9}^+$.

Ionization Potential and Electron Affinity of Si_2Mg_n^Q ($n = 1-11$; $Q = 0, \pm 1$) Clusters of Silicon-Magnesium Sensor Material

Adiabatic ionization potential (AIP), vertical ionization potential (VIP), adiabatic electron affinity (AEA), and vertical electron affinity (VEA) are important characteristics of the electronic properties for clusters. On the basis of optimizing the structure, AIP, VIP, AEA, and VEA are calculated and listed in the Table 7 with the following formulas (Deka et al., 2014):

$$\text{AIP} = E_{(\text{optimized cation})} - E_{(\text{optimized neutral})} \quad (6)$$

$$\text{VIP} = E_{(\text{cation at optimized neutral geometry})} - E_{(\text{optimized neutral})} \quad (7)$$

$$\text{AEA} = E_{(\text{optimized neutral})} - E_{(\text{optimized anion})} \quad (8)$$

$$\text{VEA} = E_{(\text{optimized neutral})} - E_{(\text{anion at optimized neutral geometry})} \quad (9)$$

It should be pointed out that the properties of neutral clusters are related to the values of VIP and VEA, while the properties of anionic and cationic clusters are related to AEA and AIP. Figures 5A,B show the size dependence of the AIP, VIP, AEA, and VEA. As Figure 5A showed, the curves of AIP and VIP have the same tendencies as the cluster size increases except for $n = 3, 8, 10$. This result means that most cations are similar to the corresponding neutrals. In addition, from the Table 7, we can find that except for $n = 3, 4, 7, 9, 10$, the $|\text{AIP-VIP}|$ values are in the range of 0.07–0.29 eV, which implies that the deformation of these structures corresponding to their neutral clusters are not big. The relation between AEA and VEA is showed in the Figure 5B, one can find that they also have the same tendencies and the $|\text{AEA-VEA}|$ values are all small except for $n = 1, 2, 5, 6$, and 8, which means that these structures of $\text{Si}_2\text{Mg}_{n-1}^-$ clusters do not differ greatly from the corresponding Si_2Mg_n clusters. In addition, as one knows that $|\text{VIP-VEA}|$ can present the chemical hardness and is always used to characterize the stability of clusters (Pearson, 1997). Table 7 also shows the hardness of Si_2Mg_n ($n = 1-11$) clusters, and one can find that the hardness of Si_2Mg_n clusters decreases with the increase of magnesium atoms. It is noteworthy that when $n = 6$, the hardness of the corresponding clusters is obviously larger than that of the adjacent clusters, which indicates that the stability of Si_2Mg_6 is higher. This conclusion is consistent with that of the Δ_2E in Figure 4.

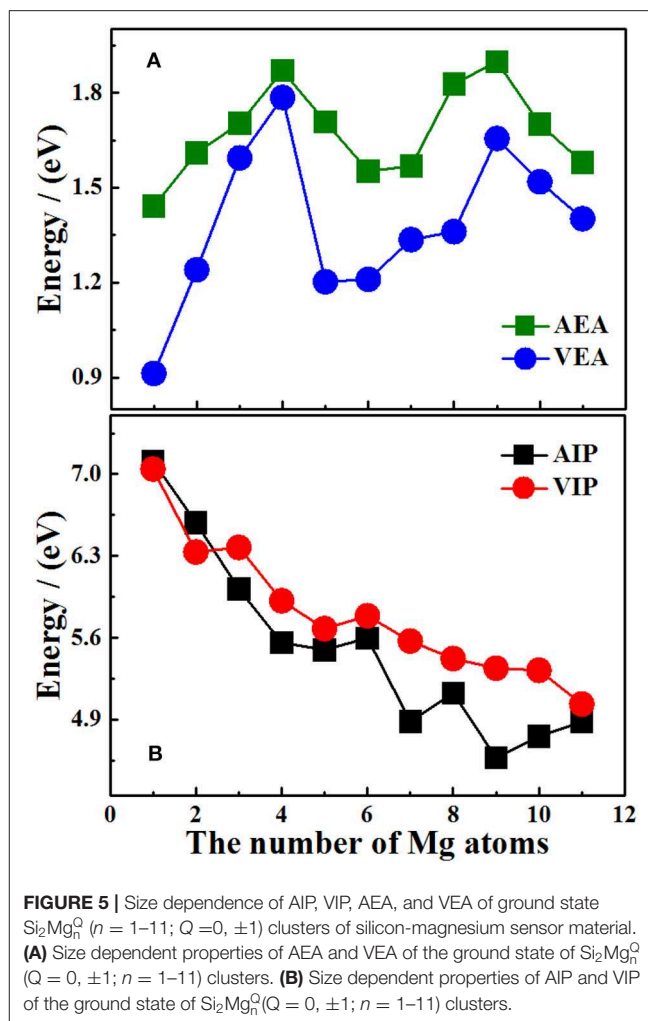


FIGURE 5 | Size dependence of AIP, VIP, AEA, and VEA of ground state Si_2Mg_n^Q ($n = 1-11$; $Q = 0, \pm 1$) clusters of silicon-magnesium sensor material. **(A)** Size dependent properties of AEA and VEA of the ground state of Si_2Mg_n^Q ($Q = 0, \pm 1$; $n = 1-11$) clusters. **(B)** Size dependent properties of AIP and VIP of the ground state of Si_2Mg_n^Q ($Q = 0, \pm 1$; $n = 1-11$) clusters.

Infrared and Raman Spectra of Si_2Mg_n^Q ($n = 1-11$; $Q = 0, \pm 1$) Clusters of Silicon-Magnesium Sensor Material

In order to further determine the stability of silicon-magnesium semiconductor sensor material, we calculate the infrared and Raman spectra of ground state of pure Mg_{n+2} and all Si_2Mg_n^Q ($n = 1-11$; $Q = 0, \pm 1$) clusters at B3LYP/6-311G (d) level, and present them in Figures 6–9. Figure 6 presents the infrared spectra of the lowest energy structure of Mg_{n+2} ($n = 1-11$) and Si_2Mg_n^Q ($n = 1-5$; $Q = 0, \pm 1$) clusters. It is necessary to point out that the vibration spectra (intensity ratio, line width, wave number, and location) are related to the calculation methods and basis groups. For example, the IR spectra of Mg_{2-31} clusters are calculated and showed by two different basis sets under B3PW1 function (Belyaev et al., 2016), but the overall trend of the spectra is similar. By our calculation, the main absorption bands of Mg_{n+2} clusters ($n = 1-11$) are located at $60-230 \text{ cm}^{-1}$, which is similar as the results of the existing report (Belyaev et al., 2016). From Figures 6, 7, one can find that the IR strong peaks frequencies are in the range of $40-500 \text{ cm}^{-1}$ for neutral Si_2Mg_n^0 clusters, $80-460 \text{ cm}^{-1}$ for anionic $\text{Si}_2\text{Mg}_n^{-1}$ clusters and

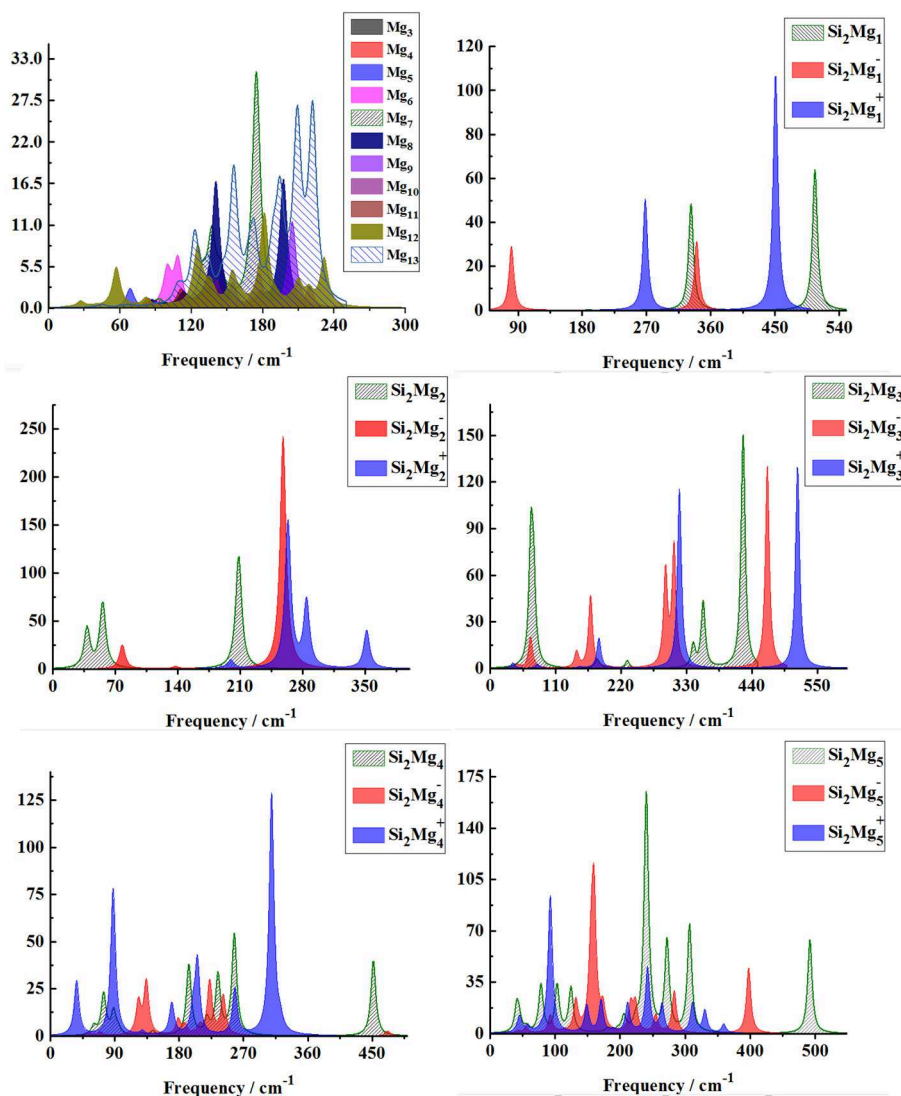


FIGURE 6 | Infrared spectra of the lowest-energy structure of Mg_{n+2} clusters ($n = 1-11$) and $Si_2Mg_n^Q$ ($n = 1-5$; $Q = 0, \pm 1$) clusters of silicon-magnesium sensor material calculated at B3LYP/6-311G (d) level. Horizontal axes is wave number; vertical axes is IR intensity, km/mol.

$30-540\text{ cm}^{-1}$. In small size ($n \leq 5$) clusters, the IR strong vibration spectra of neutral, anionic and cationic $Si_2Mg_n^Q$ ($n = 1-11$; $Q = 0, \pm 1$) clusters are easily distinguished from each other. While, in large size ($n = 6-11$) clusters, the frequency of IR strong vibration spectra of these clusters is relatively close from mid-frequency to the high-frequency region. As we know that the electron-absorbing base moves the infrared absorption peak to the high frequency region, and the electron-supplying base moves the infrared absorption peak to the low frequency region. In addition, the tension property of materials shows that the larger the tension of structures, the higher the infrared absorption frequency. Therefore, we can find that two interesting conclusions from **Figures 6, 7**. (i) The electron-absorbing base structure of neutral cluster materials is stronger than that of charged clusters, and this trend decreases with the increase

of the number of magnesium atoms. (ii) With the increase of magnesium atoms around silicon atoms, the peak infrared absorption frequency shifts from relative high frequency to relative low frequency. This indicates that the tension properties of cluster materials with high Mg atoms are not good. The vibration modes of IR spectra of $Si_2Mg_n^Q$ ($n = 1-11$; $Q = 0, \pm 1$) clusters are very numerous and complex, and as the results discussed above show that magic number clusters of $Si_2Mg_3^0$, $Si_2Mg_3^{-1}$, $Si_2Mg_3^{+1}$ are more stable than other clusters. Therefore, here we only focus on these three clusters' vibration modes. As **Figure 6** showed, the highest intensity IR frequency of neutral $Si_2Mg_3^0$ locates at 425.28 cm^{-1} , and its vibration mode is assigned as stretching of Si2-Si1 bond. The frequency of the strongest peak of anionic $Si_2Mg_3^{-1}$ cluster at 465.87 cm^{-1} , and its vibrational mode is as the same as the highest peak of neutral $Si_2Mg_3^0$. The

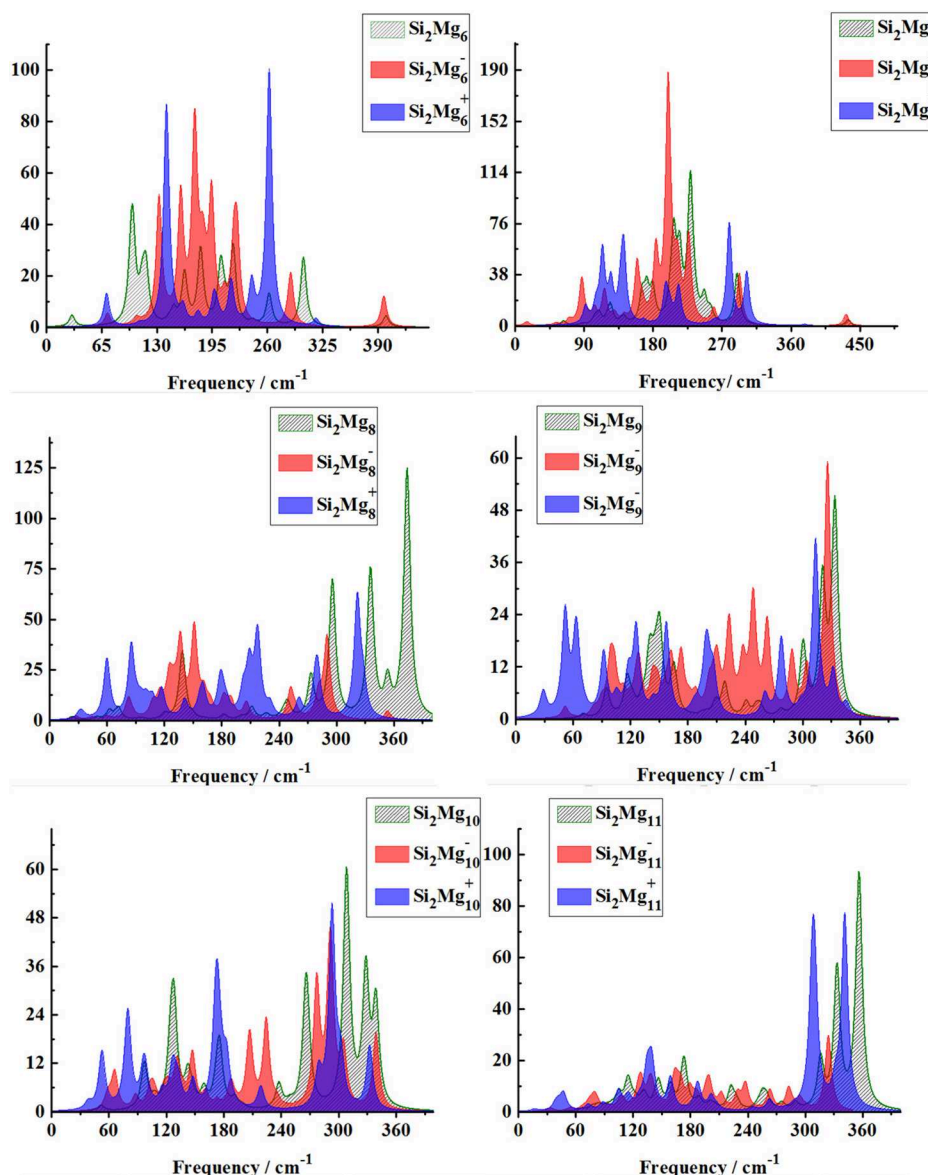


FIGURE 7 | Infrared spectra of the lowest-energy structure of Si_2Mg_n^Q ($n = 6-11$; $Q = 0, \pm 1$) clusters of silicon-magnesium sensor material calculated at B3LYP/6-311G (d) level. Horizontal axes is wave number; vertical axes is IR intensity, km/mol .

strong peaks of IR spectra of cationic $\text{Si}_2\text{Mg}_3^{+1}$ cluster at 516.55 cm^{-1} resulted from the stretching of Si2-Si1 bond.

From **Figures 8, 9**, one can find Raman spectra of Mg_{n+2} and Si_2Mg_n^Q ($n = 1-11$; $Q = 0, \pm 1$) clusters. Raman spectra activity of Mg_{n+2} ($n = 1-11$) clusters show a fairly low frequency (in the range of $25-180 \text{ cm}^{-1}$) nature except for Mg_3 . Raman spectra activity properties of Si_2Mg_n^Q ($n = 1-11$; $Q = 0, \pm 1$) clusters are rather different from their IR absorption properties. In small size clusters ($n = 1-3$), the Raman activity of cationic Si_2Mg_n^Q clusters is fairly high in Mid-frequency and high-frequency regions. When $n = 4, 5$, the Raman activity of the clusters is widely distributed, and it is easy to distinguish them from each other. However, after $n > 5$, the Raman activity of the clusters begin to

shift slowly from the high-frequency region to the mid-frequency region and close to each other. The Raman activity frequency of Si_2Mg_n^Q ($Q = 0, \pm 1$) clusters are $50-480 \text{ cm}^{-1}$ for neutral Si_2Mg_n^0 , $40-480 \text{ cm}^{-1}$ for anionic $\text{Si}_2\text{Mg}_n^{-1}$ and $40-450 \text{ cm}^{-1}$, respectively. When studying the vibration information of Raman spectra with specific magic number structure, we can find that the maximum Raman activity of neutral Si_2Mg_3^0 cluster at the frequency of 179.66 cm^{-1} with the stretching of Mg3-Mg4 bond, the frequency of the highest peak of anionic $\text{Si}_2\text{Mg}_3^{-1}$ cluster at 308.76 cm^{-1} is assigned as stretching of Si1-Mg3 and Si2-Mg3 bonds and the highest Raman activity frequency peak of cationic $\text{Si}_2\text{Mg}_3^{+1}$ cluster at 182.25 cm^{-1} vibrated as stretching of Si1-Mg4, Si2-Mg4 bonds.

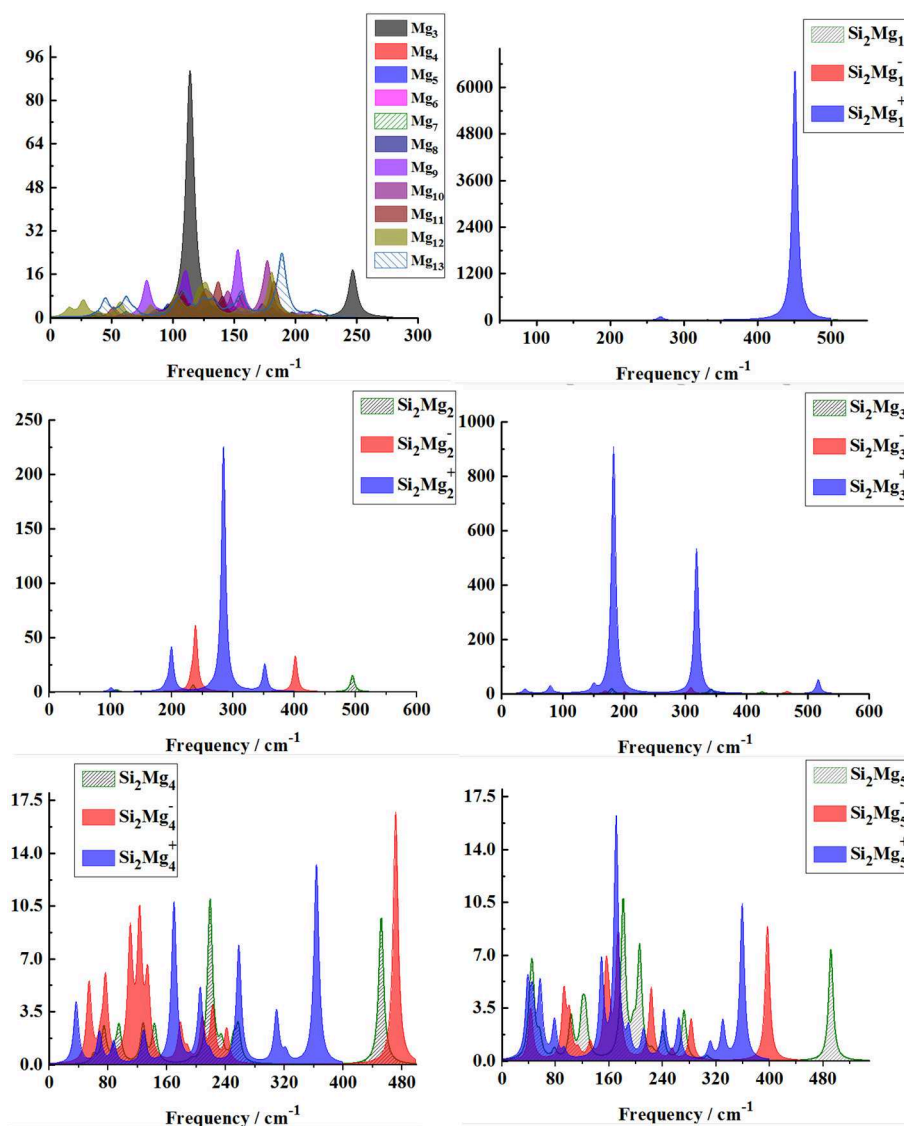


FIGURE 8 | Raman spectra of the lowest-energy structure of Mg_{n+2} clusters ($n = 1-11$) and $Si_2Mg_n^Q$ ($n = 1-5$; $Q = 0, \pm 1$) clusters of silicon-magnesium sensor material calculated at B3LYP/6-311G (d) level. Horizontal axes is wave number; vertical axes is Raman activity, A^4/AMU .

CONCLUSION

The structural, stability, electronic structure and spectral properties of silicon-magnesium semiconductor sensor materials are systematically studied by $Si_2Mg_n^Q$ ($n = 1-11$; $Q = 0, \pm 1$) clusters in this paper. By using the CALYPSO searching method and B3LYP at 6-311G (d) basis set of DFT, the results can be summarized below:

- (i) The results of $Si_2Mg_n^Q$ ($n = 1-11$; $Q = 0, \pm 1$) clusters' structure of silicon-magnesium semiconductor sensor material reveal that only a few of the lowest-energy anionic and cationic geometries are similar as their corresponding neutral ones, most of them are deformation. This conclusion is in good agreement with the changes of

their AIP, VIP, AEA, and VEA. $|VIP-VEA|$ values reveal that the hardness of Si_2Mg_n clusters decreases with the increase of magnesium atoms.

- (ii) For the stability of $Si_2Mg_n^Q$ ($n = 1-11$; $Q = 0, \pm 1$) clusters of silicon-magnesium semiconductor sensor materials, the average bonding energy of neutral $Si_2Mg_n^0$ clusters are always smaller than the anionic and cationic ones show that attachment or detachment of one electron can enhance chemical stabilities of $Si_2Mg_n^0$ clusters. Based on the calculations of E_b , E_f , Δ_2E , and E_{gap} , we find that $Si_2Mg_3^0$, $Si_2Mg_3^{-1}$, $Si_2Mg_3^{+1}$ clusters have stronger stabilities than other clusters.
- (iii) The cluster electronic structure of silicon-magnesium semiconductor sensor materials is analyzed. The results of

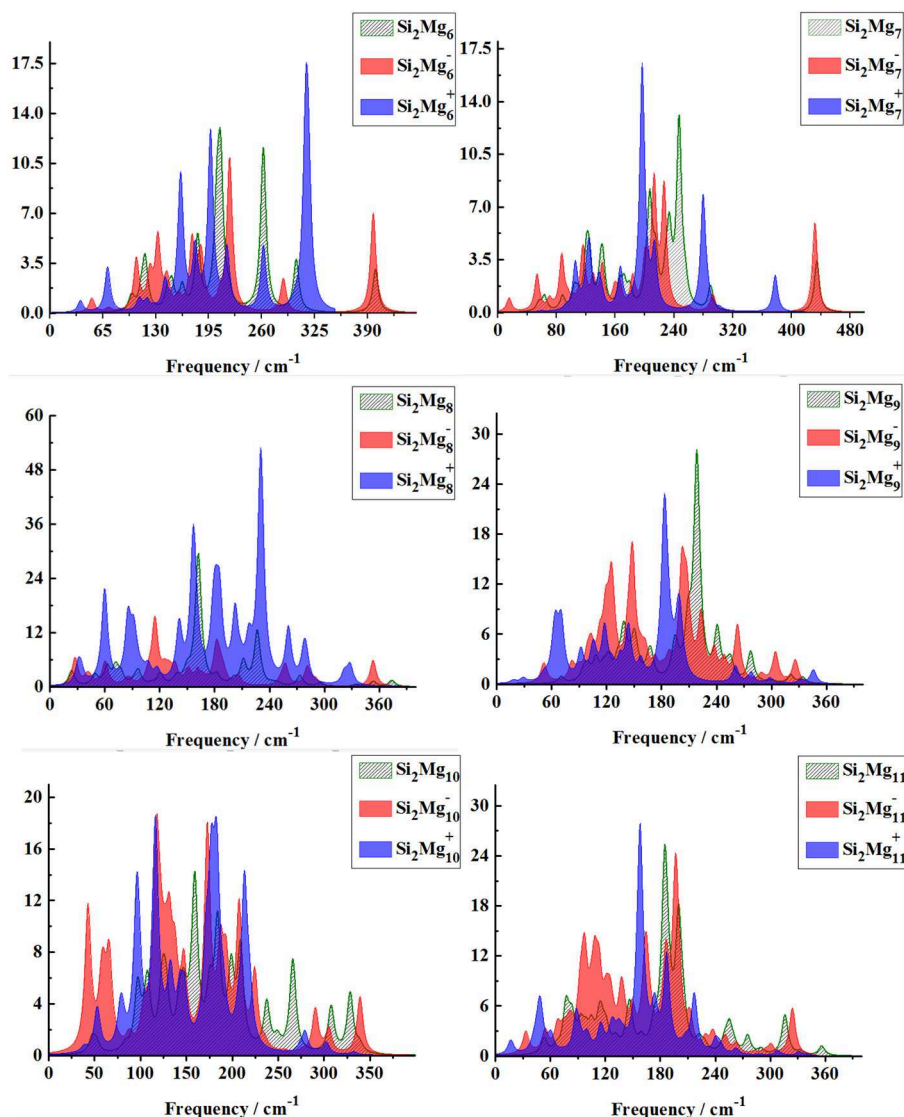


FIGURE 9 | Raman spectra of the lowest-energy structure of Si_2Mg_n^Q ($n = 6-11$; $Q = 0, \pm 1$) clusters of silicon-magnesium sensor material calculated at B3LYP/6-311G (d) level. Horizontal axes is wave number; vertical axes is Raman activity, $\text{\AA}^4/\text{AMU}$.

NCP and NEC show that the charges in Si_2Mg_n^Q ($n = 1-11$; $Q = 0, \pm 1$) clusters transfer from Mg atoms to Si atoms, and the sp hybridization is existed in Si atoms in the clusters.

- (iv) The infrared (IR) and Raman spectra of Si_2Mg_n^Q ($n = 1-11$; $Q = 0, \pm 1$) clusters of silicon-magnesium semiconductor sensor materials show different properties. Both IR and Raman spectra can be easily distinguished each other in small size clusters, however, in large clusters, IR spectra converge and concentrate at high frequencies, while Raman spectra converge and concentrate at mid-frequency region.

DATA AVAILABILITY STATEMENT

All datasets generated for this study are included in the article/supplementary material.

AUTHOR CONTRIBUTIONS

All authors listed have made a substantial, direct and intellectual contribution to the work, and approved it for publication.

FUNDING

This work was partly supported by the Cultivating Project for Young Scholar at Hubei University of Medicine (No. 2013QDJZR03), partly supported by the Basic Science and Preface Technology Project of Chongqing (cstc2017cyjAX0315). The project of Fundamental Research Funds for the Central Universities (No. 2019CDYGYB011).

REFERENCES

- Atanassov, A., and Baleva, M. (2007). On the band diagram of $\text{Mg}_2\text{Si}/\text{Si}$ heterojunction as deduced from optical constants dispersions. *Thin Solid Films* 515, 3046–3051. doi: 10.1016/j.tsf.2006.08.015
- Aymerich, F., and Mula, G. (2010). Pseudopotential band structures of Mg_2Si , Mg_2Ge , Mg_2Sn , and of the solid solution $\text{Mg}_2(\text{Ge}, \text{Sn})$. *Phys. Status Solidi* 42, 697–704. doi: 10.1002/pssb.19700420224
- Belyaev, S. N., Pantelev, S. V., Ignatov, S. K., and Razuvaev, A. G. (2016). Structural, electronic, thermodynamic and spectral properties of Mg_n ($n = 2-31$) clusters. A DFT study. *Comput. Theor. Chem.* 1079, 34–46. doi: 10.1016/j.comptc.2016.01.011
- Boher, P., Houdy, P., Kühne, M., Müller, P., Barchewitz, R., and Delaboudiniere, J. P., et al. (1992). Tungsten/magnesium silicide multilayers for soft x-ray optics. *J. Xray. Sci. Technol.* 3, 118–132. doi: 10.1016/0895-3996(92)90004-4
- Bole, C., Weiguo, S., Xiao-Yu, K., Cheng, L., Xinxin, X., Hongxiao, S., et al. (2018). Structural stability and evolution of medium-sized tantalum-doped boron clusters: a half-sandwich-structured tab_{12} -cluster. *Inorg. Chem.* 57, 343–350. doi: 10.1021/acs.inorgchem.7b02585
- Chen, Q., Xie, Q., Zhao, F., Cui, D., and Li, X. (2010). First-principles calculations of electronic structure and optical properties of strained Mg_2Si . *Chin. Sci. Bull.* 55, 2236–2242. doi: 10.1007/s11434-010-3280-7
- de Heer, W. A., Knight, W. D., Chou, M. Y., and Cohen, M. L. (1987). Electronic shell structure and metal clusters. *Solid State Phys.* 40, 93–181. doi: 10.1016/S0081-1947(08)60691-8
- Deka, R. C., Bhattacharjee, D., Chakrabartty, A. K., and Mishra, B. K. (2014). Catalytic oxidation of NO by Au_2^- dimers: a DFT study. *RSC Adv.* 4, 5399–5404. doi: 10.1039/c3ra42240b
- Dmytruk, A., Dmitruk, I., Blonsky, I., Belosludov, R., Kawazoe, Y., and Kasuya, A. (2009). ZnO clusters: laser ablation production and time-of-flight mass spectroscopic study. *Microelectron. J.* 40, 218–220. doi: 10.1016/j.mejo.2008.07.010
- Frisch, M., Trucks, G., Schlegel, H., Scuseria, G., Robb, M., Cheeseman, J., et al. (2014). *Gaussian 09*. Wallingford, CT: Gaussian, Inc., 481.
- Huber, K. P. (1979). “Constants of diatomic molecules,” in *Molecular Spectra and Molecular Structure*.
- Imai, Y., Watanabe, A., and Mukaida, M. (2003). Electronic structures of semiconducting alkaline-earth metal silicides. *J. Alloys Comp.* 358, 257–263. doi: 10.1016/S0925-8388(03)00037-9
- Jin, Y., Maroulis, G., Kuang, X., Ding, L., Lu, C., Wang, J., et al. (2015a). Geometries, stabilities and fragmental channels of neutral and charged sulfur clusters: $\text{Sn}(q)$ ($n = 3-20$, $q = 0, \pm 1$). *Phys. Chem. Chem. Phys.* 17, 13590–13597. doi: 10.1039/C5CP00728C
- Jin, Y., Tian, Y., Kuang, X., Zhang, C., Lu, C., Wang, J., et al. (2015b). Ab initio search for global minimum structures of pure and boron doped silver clusters. *J. Phys. Chem. A* 119, 6738–6745. doi: 10.1021/acs.jpca.5b03542
- Ju, M., Lv, J., Kuang, X. Y., Ding, L. P., Lu, C., Wang, J. J., et al. (2015). Systematic theoretical investigation of geometries, stabilities and magnetic properties of iron oxide clusters $(\text{FeO})_n \mu$ ($n = 1-8$, $\mu = 0, \pm 1$): insights and perspectives. *RSC Adv.* 5, 6560–6570. doi: 10.1039/C4RA12259C
- Kitsopoulos, A., Chick, C. J., Zhao, Y., and Neumark, D. M. (1991). Study of the low-lying electronic states of Si_2 and Si_2^- using negative ion photodetachment techniques. *J. Chem. Phys.* 95, 1441–1448. doi: 10.1063/1.461057
- Lu, C., and Chen, C. (2018). High-pressure evolution of crystal bonding structures and properties of feoh. *J. Phys. Chem. Lett.* 9, 2181–2185. doi: 10.1021/acs.jpclett.8b00947
- Lu, C., Li, Q., Ma, Y., and Chen, C. (2017). Extraordinary indentation strain stiffening produces superhard tungsten nitrides. *Phys. Rev. Lett.* 119:115503. doi: 10.1103/PhysRevLett.119.115503
- Lu, C., Maximilian, A., and Changfeng, C. (2018). Unraveling the structure and bonding evolution of the newly discovered iron oxide FeO_2 . *Phys. Rev. B* 98:054102. doi: 10.1103/PhysRevB.98.054102
- Lu, C., Miao, M., and Ma, Y. (2013). Structural evolution of carbon dioxide under high pressure. *J. Am. Chem. Soc.* 135, 14167–14171. doi: 10.1021/ja404854x
- Lv, J., Wang, Y., Zhu, L., and Ma, Y. (2012). Particle-swarm structure prediction on clusters. *J. Chem. Phys.* 137:084104. doi: 10.1063/1.4746757
- Morris, R. G., Redin, R. D., and Danielson, G. C. (1958). Semiconducting properties of Mg_2Si single crystals. *Phys. Rev. B* 109:1916. doi: 10.1103/PhysRev.109.1909
- Pearson, R. G. (1997). *Chemical Hardness - Applications From Molecules to Solids*. Weinheim: Wiley-VCH, 198.
- Ruette, F., Sánchez, M., Anez, R., Bermúdez, A., and Sierraalta, A. (2005). Diatomic molecule data for parametric methods. I. *J. Mol. Struct. THEOCHEM* 729, 19–37. doi: 10.1016/j.theochem.2005.04.024
- Song, S. W., Striebel, K., and Cairns, E. (2003). Electrochemical studies of the Mg_2Si thin films prepared with pulsed laser deposition. *J. Electrochem. Soc.* 153, A12–A19. doi: 10.1149/1.1527937
- Sun, W., Xia, X., Lu, C., Kuang, X., and Hermann, A. (2018). Probing the structural and electronic properties of zirconium doped boron clusters: Zr distorted B 12 ligand framework. *Phys. Chem. Chem. Phys.* 20, 23740–23746. doi: 10.1039/C8CP03384F
- Sun, W. G., Wang, J. J., Lu, C., Xia, X. X., Kuang, X. Y., and Hermann, A. (2017). Evolution of the structural and electronic properties of medium-sized sodium clusters: a honeycomb-like na_{12} cluster. *Inorg. Chem.* 56, 1241–1248. doi: 10.1021/acs.inorgchem.6b02340
- Trivedi, R., Dhaka, K., and Bandyopadhyay, D. (2014). Study of electronic properties, stabilities and magnetic quenching of molybdenum-doped germanium clusters: a density functional investigation. *RSC Adv.* 4, 64825–64834. doi: 10.1039/C4RA11825A
- Wang, Y., Lv, J., Zhu, L., and Ma, Y. (2010). Crystal structure prediction via particle-swarm optimization. *Phys. Rev. B* 82:094116. doi: 10.1103/PhysRevB.82.094116
- Wang, Y., Lv, J., Zhu, L., and Ma, Y. (2012). CALYPSO: a method for crystal structure prediction. *Comput. Phys. Commun.* 183, 2063–2070. doi: 10.1016/j.cpc.2012.05.008
- Wittmer, M., Lüthy, W., and Allmen, M. V. (1979). Laser induced reaction of magnesium with silicon. *Phys. Lett. A* 75, 127–130. doi: 10.1016/0375-9601(79)90300-1
- Xia, X. X., Hermann, A., Kuang, X. Y., Jin, Y. Y., Lu, C., and Xing, X. D. (2015). Study of the structural and electronic properties of neutral and charged niobium-doped silicon clusters: niobium encapsulated in silicon cages. *J. Phys. Chem. C* 120, 677–684. doi: 10.1021/acs.jpcc.5b09453
- Xiao, T., Weiguo, S., Yuantong, G., Lu, C., Liangzhi, K., and Changfeng, C. (2019). CoB_6 monolayer: a robust two-dimensional ferromagnet. *Phys. Rev. B* 99:045445. doi: 10.1103/PhysRevB.99.045445
- Xing, X., Hermann, A., Kuang, X., Ju, M., Lu, C., Jin, Y., et al. (2016a). Insights into the geometries, electronic and magnetic properties of neutral and charged palladium clusters. *Sci. Rep.* 6:19656. doi: 10.1038/sre19656
- Xing, X., Wang, J., Kuang, X., Xia, X., Lu, C., and Maroulis, G. (2016b). Probing the low-energy structures of aluminum–magnesium alloy clusters: a detailed study. *Phys. Chem. Chem. Phys.* 18, 26177–26183. doi: 10.1039/C6CP05571K
- Yang, J., Li, B., and Zhan, S. (2006). Study of gaas cluster ions using fp-lmto md method. *Phys. Lett. A* 348, 416–423. doi: 10.1016/j.physleta.2005.08.071
- Zhang, S., Zhang, Y., Yang, X., Lu, C., Li, G., and Lu, Z. (2015). Systematic theoretical investigation of structures, stabilities, and electronic properties of rhodium-doped silicon clusters: Rh_2Si_n ($n = 1-10$; $q = 0, \pm 1$). *J. Mater. Sci.* 50, 6180–6196. doi: 10.1007/s10853-015-9175-x

Conflict of Interest: The authors declare that the research was conducted in the absence of any commercial or financial relationships that could be construed as a potential conflict of interest.

Copyright © 2019 Zhu, Deng and Zeng. This is an open-access article distributed under the terms of the Creative Commons Attribution License (CC BY). The use, distribution or reproduction in other forums is permitted, provided the original author(s) and the copyright owner(s) are credited and that the original publication in this journal is cited, in accordance with accepted academic practice. No use, distribution or reproduction is permitted which does not comply with these terms.



Hollow WO₃/SnO₂ Hetero-Nanofibers: Controlled Synthesis and High Efficiency of Acetone Vapor Detection

Hongyun Shao^{1,2}, Minxuan Huang^{1,2}, Hao Fu^{1,2}, Shaopeng Wang^{1,2,3}, Liwei Wang^{1,2,3*}, Jie Lu^{4*}, Yinghui Wang^{1,2} and Kefu Yu^{1,2*}

¹ School of Marine Sciences, Guangxi University, Nanning, China, ² Guangxi Laboratory on the Study of Coral Reefs in the South China Sea, Nanning, China, ³ Guangxi Key Laboratory of Processing for Nonferrous Metallic and Featured Materials, Nanning, China, ⁴ College of Life Science and Technology, Guangxi University, Nanning, China

OPEN ACCESS

Edited by:

Mingshui Yao,
Kyoto University, Japan

Reviewed by:

Xiaogan Li,
Dalian University of Technology
(DUT), China
Fanli Meng,
Northeastern University, China

*Correspondence:

Liwei Wang
wangliwei0427@163.com
Jie Lu
jlu92@163.com
Kefu Yu
kefuyu@scsio.ac.cn

Specialty section:

This article was submitted to
Nanoscience,
a section of the journal
Frontiers in Chemistry

Received: 27 September 2019

Accepted: 31 October 2019

Published: 19 November 2019

Citation:

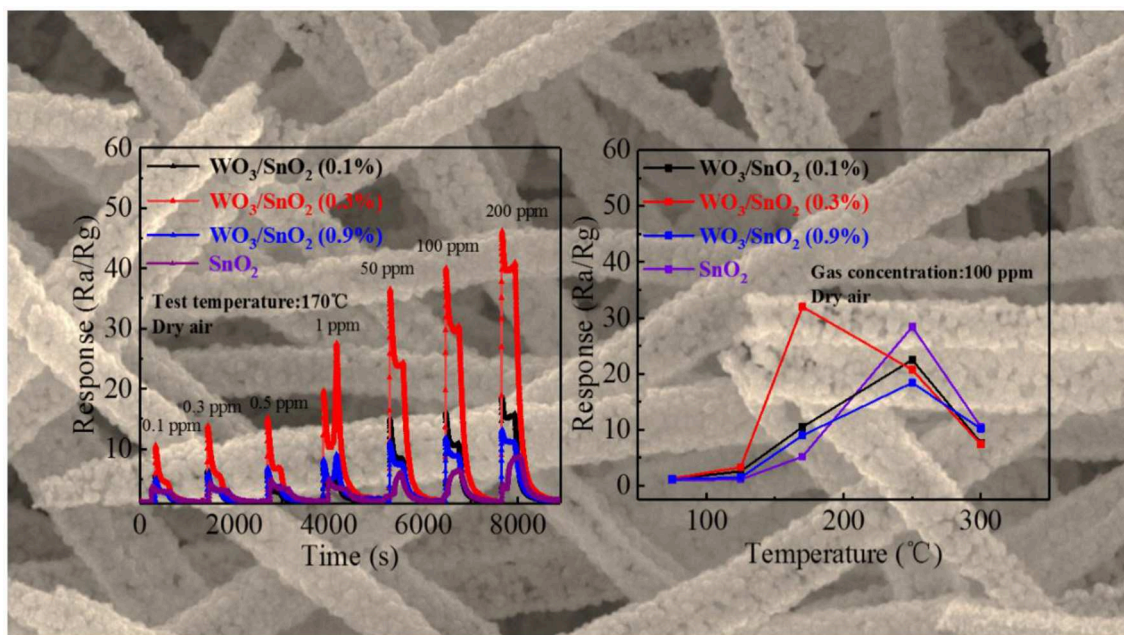
Shao H, Huang M, Fu H, Wang S,
Wang L, Lu J, Wang Y and Yu K
(2019) Hollow WO₃/SnO₂
Hetero-Nanofibers: Controlled
Synthesis and High Efficiency of
Acetone Vapor Detection.
Front. Chem. 7:785.
doi: 10.3389/fchem.2019.00785

Metal oxide hetero-nanostructures have widely been used as the core part of chemical gas sensors. To improve the dispersion state of each constituent and the poor stability that exists in heterogeneous gas sensing materials, a uniaxial electro-spinning method combined with calcination was applied to synthesize pure SnO₂ and three groups of WO₃/SnO₂ (WO₃ of 0.1, 0.3, 0.9 wt%) hetero-nanofibers (HNFs) in our work. A series of characterizations prove that the products present hollow and fibrous structures composed of even nanoparticles while WO₃ is uniformly distributed into the SnO₂ matrix. Gas sensing tests display that the WO₃/SnO₂ (0.3 wt%) sensor not only exhibits the highest response (30.28) and excellent selectivity to acetone vapor at the lower detection temperature (170°C), 6 times higher than that of pure SnO₂ (5.2), but still achieves a considerable response (4.7) when the acetone concentration is down to 100 ppb with the corresponding response/recovery times of 50/200 s, respectively. Such structure obviously enhances the gas sensing performance toward acetone which guides the construction of a highly sensitive acetone sensor. Meanwhile, the enhancement mechanism of such a special sensor is also discussed in detail.

Keywords: electrostatic spinning, hollow nanofiber, WO₃/SnO₂ heterojunction, acetone, gas sensor

INTRODUCTION

The air quality in the workplace and living environment is closely related to people's health, it is therefore urgent to detect air pollution quickly and accurately. Acetone, a common organic volatile solvent, is widely used in laboratories and industries, posing a threat to the nose, eyes, and central nervous system of the human body when the concentration in the environment reaches 0.90 ppm (Hygienic Standard for Design of Industrial Enterprises) (Yang C. et al., 2019). Additionally, clinical data indicate that certain components of exhaust gases can be regarded as diagnostic markers of certain diseases, to that end acetone can be used as a marker of diabetes (Parthibavarman et al., 2018). Therefore, chemical gas sensors have emerged as many advantages such as portable, real-time and online detection are required (Meng et al., 2017; Yuan et al., 2019). Thus the development of acetone gas sensor can supply better service for safety control and human health (Meng et al., 2019).



GRAPHICAL ABSTRACT | Response curves of hollow WO_3/SnO_2 hetero-nanofibers at different concentrations and temperatures.

To date, a great deal of research still focuses on fabricating high performance metal oxide semiconductor (MOS) gas sensing materials due to their many irreplaceable advantages such as their stability and their reliable sensing (Kucheyev et al., 2006; Das and Jayaraman, 2014; Yang and Guo, 2016; Teng et al., 2019), especially in improving the gas sensing properties of SnO_2 -based nanomaterials through the assembly into heterojunctions (Das and Jayaraman, 2014; Koohestani, 2019; Teng et al., 2019). It is known that pristine SnO_2 -based sensors often work at higher temperatures ($>300^\circ\text{C}$) with poor selectivity, a lack of reproducibility, and an inadequate detection limit, thereby restricting their practical application (Wang et al., 2016; Wang L. et al., 2019). Hetero-junction constructing has become attractive since it produces intimate interface-contact directly between two different semiconductor materials, thus balancing the Fermi level, forming the thicker depletion layer on the interface, and finally increasing the sensor performances (Wang et al., 2016; Zhao et al., 2019).

Furthermore, SnO_2 composed of a hollow/porous nanostructure can help increase the surface area remarkably, and provide more channels to transfer electrons (Lu et al., 2011). 1D nanofibers (NFs) possess a high surface area-to-volume ratio, excellent stability, and can easily be modified which are favorable for enhancing response signals (Xia et al., 2010), while WO_3 has been widely studied in gas sensors with advantages of low temperature, high sensitivity, and low detection limit (Joshi et al., 2018; Li et al., 2018; Sukunta et al., 2018). By combining the advantages of 1D and hollow/porous structures, more attention is now being focused on the construction of the WO_3/SnO_2 heterojunction. In comparison with other synthetic methods, like the hydrothermal or impregnation method, electro-spinning is the most effective method to uniformly control one-dimensional

hetero-nanofibers (HNFs) with a high yield and favorable stability (Ma et al., 2010; Wang et al., 2013).

Inspired by the newly reported 1D HNFs and with the intention of artificially tuning the gas-sensing performances, electro-spinning was used to construct hollow WO_3/SnO_2 HNFs with different weight ratios of WO_3 (Patil et al., 2017; Wang K. et al., 2019). Herein, the synthesized sensor based on WO_3/SnO_2 (0.3 wt%) could be a good candidate for acetone pollutant monitoring. Its gas sensing properties and working mechanism in particular will be evaluated and discussed systematically.

EXPERIMENTAL SECTION

Synthesis of Hollow WO_3/SnO_2 HNFs

All the reagents used in the experiment, including Tin(II) chloride dehydrate ($\text{SnCl}_2 \cdot 2\text{H}_2\text{O}$, AR, $\geq 98\%$), N,N-dimethylformamide (DMF, AR, 99.5%) and polyvinylpyrrolidone (PVP, K = 1300000, K88-96) were purchased from Aladdin Industrial Corporation (Shanghai, China). Sinopharm Chemical Reagent Co. Ltd. (Shanghai, China) provides ammonium tungstate hydrate ($(\text{NH}_4)_{10}\text{W}_{12}\text{O}_{41} \cdot x\text{H}_2\text{O}$, AR) and ethanol ($\text{CH}_3\text{CH}_2\text{OH}$, AR). Furthermore, distilled water was used in the synthesis procedures.

An electrostatic spinning method was applied for the preparation. Typically, 1 mmol of $\text{SnCl}_2 \cdot 2\text{H}_2\text{O}$ and a certain amount of $(\text{NH}_4)_{10}\text{W}_{12}\text{O}_{41} \cdot x\text{H}_2\text{O}$ was dissolved in 2.32 ml of DMF and 2.79 ml of anhydrous ethanol under stirring. Then, 0.0003 mmol of PVP (K = 1300000) was added before the precursor solution was prepared. By controlling the amount of $(\text{NH}_4)_{10}\text{W}_{12}\text{O}_{41} \cdot x\text{H}_2\text{O}$, we designed different mass percentages of WO_3 as 0, 0.1, 0.3, 0.9 wt% respectively in the WO_3/SnO_2 products, which were denoted as pure SnO_2 , WO_3/SnO_2 (0.1%),

WO₃/SnO₂ (0.3%), and WO₃/SnO₂ (0.9%). Then the configured solution was transferred in the 5 ml syringe, then 20–22 kV of positive voltage was added to the needle and 3–4 kV of negative voltage to the receiver of the sample. The distance between the needles and the receiver was 15 cm, and the jet velocity of the fluid from the syringe was kept 2.32 mL of DMF and 2.79 mL as 0.2 mm/min under a high voltage electric field. In the whole electrostatic spinning process, the temperature was kept at 60°C and humidity of 10%. Afterwards, the white film was collected and calcined at 600°C, for 2 h in the air state, and finally different HNFs products were obtained.

Characterization of Hollow WO₃/SnO₂ HNFs

The samples were characterized by means of powder XRD analysis (Rigaku Ultima IV, Japan; Cu K α radiation, λ = 1.5418 Å), Field-emission SEM (Hitachi SU5000, Japan), TEM and HRTEM with EDS (FEI Tecnai G2 f20 s-twin, 200 KV), XPS (Thermo SCIENTIFIC ESCALAB 250Xi, Al K α X-ray monochromator), BET (Autosorb-IQ, USA).

Preparation of Gas Sensor and Sensing Test

The detailed manufacturing process of gas sensors can be found in our previous reports (Wang L. et al., 2019). Briefly, the sample was mixed with deionized water and ground until it became sticky and was then coated onto the surface of the ceramic tube, which was welded to the pedestal and inserted into the test channel. A gas-sensing test was carried out using the CGS-8 intelligent test system (Beijing Elite Tech Co. Ltd., China). The response value (*S*) of sensors based on n-type semiconductor is defined as $S = R_a/R_g$, where R_a and R_g represent the resistance value of the sensor in air and in target gas, respectively, while the p type is the opposite. Response time is defined as the time taken by the sensor to reach 90% of the final equilibrium value, or the recovery time for gas desorption. Most tests were carried out under dry air conditions, except the discussion of RHs effect on the response of different sensors (Xia et al., 2010; Wang et al., 2013; Wang L. et al., 2019).

RESULTS AND DISCUSSION

Characterization

X-ray diffraction was utilized to confirm the crystal structure of as-prepared samples. As shown in **Figure 1a**, the sharp diffraction peaks represent the pure tetragonal SnO₂ phase (JCPDS file No. 41-1445) with high crystallinity and large crystal size. Additionally, the main diffraction patterns in **Figures 1b–d** can also be indexed to tetragonal SnO₂, but no obvious WO₃ peak presents due to its low content or highly dispersed amorphous state in the HNFs. Then the grain sizes of WO₃/SnO₂ (0.1%, 0.3%, 0.9%) and pure SnO₂ samples were calculated by the Scherrer formula taken from $2\theta = 26.6^\circ$ of the XRD data, which were 17.53, 15.71, 20.56, and 22.70 nm, respectively. It means that the grain size was smallest in the sample of WO₃/SnO₂ (0.3%) HNFs. It is overwhelmingly known that when crystallite sizes approach Debye length (λ_D , usually several nm), the sensor

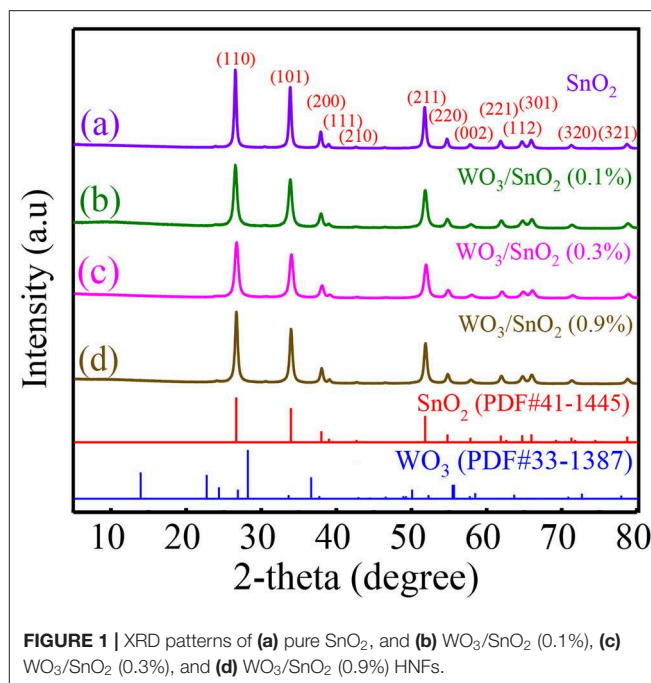


FIGURE 1 | XRD patterns of (a) pure SnO₂, and (b) WO₃/SnO₂ (0.1%), (c) WO₃/SnO₂ (0.3%), and (d) WO₃/SnO₂ (0.9%) HNFs.

response will drastically increase, and the smaller the better (Miller et al., 2014; Nan et al., 2019). The conclusion can therefore be drawn from the XRD results that the WO₃/SnO₂ (0.3%) sample with the smallest grain size, 15.71 nm, would exhibit excellent gas sensing performance in the following tests, and all the other characterizations were taken based on this example.

The morphology of each sample, namely the pure SnO₂, and WO₃/SnO₂ (0.1, 0.3, and 0.9%) HNF samples, respectively, were investigated by FESEM. As can be seen in **Figure 2a**, a uniform and hollow SnO₂ NF is composed of large numbers of nanoparticles with an average diameter of ~ 18 nm, which is derived from the electro-spinning and heat treatment. Regarding the WO₃/SnO₂ HNF samples in **Figures 2b–d**, they show similar morphologies to that of the pristine SnO₂ NF (**Figure 2a**), but as the amount of WO₃ increases, the average diameters of the particle-like construction units increase gradually to 22, 48, and 52 nm respectively. SEM results showed that the surface structure of SnO₂ NF had been changed by the doping of WO₃, which may indirectly prove the existence of WO₃. Such results are also proven through other investigations (HRTEM and XPS) in the following sections. Since the WO₃/SnO₂ composite is comprised of aggregated nanoparticles with porous structures, the N₂ adsorption–desorption method (**Figure 3**) was applied on WO₃/SnO₂ (0.3%) to confirm the speculation, as can be calculated from the data in **Figure 3** which shows that the specific surface area is 22.05 m²/g with a pore size diameter in the range of 3.4–45 nm averaged at 12.4 nm, proving its mesoporous structure for the composite. Therefore, the porosity of the sensing materials could improve its sensitivity due to the high surface area and rapid gas diffusion.

To more clearly provide insight into the microstructure, TEM & HRTEM were taken on the WO₃/SnO₂ (0.3%) HNFs.

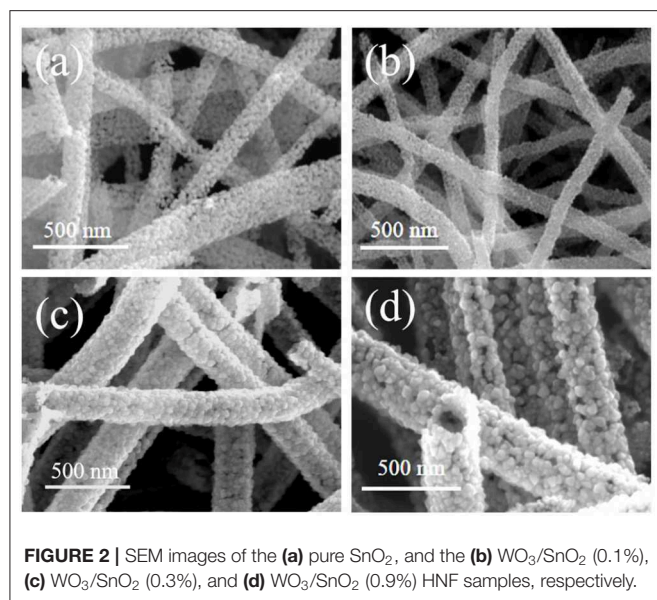


FIGURE 2 | SEM images of the (a) pure SnO₂, and the (b) WO₃/SnO₂ (0.1%), (c) WO₃/SnO₂ (0.3%), and (d) WO₃/SnO₂ (0.9%) HNF samples, respectively.

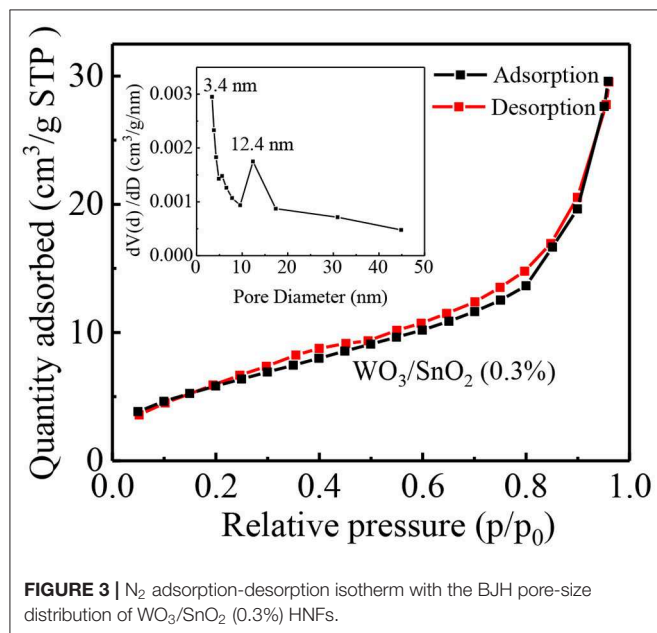


FIGURE 3 | N₂ adsorption-desorption isotherm with the BJH pore-size distribution of WO₃/SnO₂ (0.3%) HNFs.

Corresponding to the SEM image in **Figure 4a**, the sample in the enlarged (**Figure 4b**) presents a hollow structure composed of various crossly-dispersed and stereoscopic nanofibers with width of ~ 200 nm. In addition, it can be seen in **Figure 4c** that the interplanar spacings of the SnO₂ (110) and WO₃ (200) are 0.334 and 0.316 nm, respectively. The SAED pattern (**Figure 4d**) displays the polycrystal characteristic of the composite, while the elemental mapping shown in **Figures 4e–g** proves the existence of Sn, O and W elements in the final composite; in particular, W is uniformly distributed along the SnO₂ matrix. The corresponding EDS spectrum image and content of Sn, O and W elements were exhibited in **Figure S1**.

As is known, combining of the W element should bring interface change that then affects the chemical state of the SnO₂ substrate (Tang et al., 2014; Stojadinović et al., 2016). In order to obtain a clearer vision the elemental chemical status of pure SnO₂ and WO₃/SnO₂ (0.9%) HNFs were confirmed by XPS in **Figure 5**. Besides the peaks of Sn, O and C, a tiny peak of W 4f can be seen in the XPS spectra of the WO₃/SnO₂ (0.3%) composite (**Figures 5A,D**), consistent with the results shown in **Figure 4d**. The binding energy of Sn 3d_{3/2} (494.98 eV) and Sn 3d_{5/2} (486.58 eV) in particular, are displayed in the pure SnO₂, but a minor negative shift of 0.18 eV can be noted for the Sn 3d_{3/2} (494.8 eV) and Sn 3d_{5/2} (486.4 eV) in the WO₃/SnO₂ (0.3%) composite (**Figure 5B**) (Lavacchi et al., 2000; Liu et al., 2016). Furthermore, a minor negative shift of the binding energy is also observed for the element of O 1s (**Figure 5C**), i.e., the lattice oxygen [530.38 eV (O_I)] and chemisorbed oxygen (531.24 eV (O_{II})) for pure SnO₂, while 530.38 eV (O_I) and 531.11 eV (O_{II}) are the values for the WO₃/SnO₂ (0.3%) composite, wherein the chemisorbed oxygen of O_{II} shifts negatively for 0.13 eV (Yang and Guo, 2016; Yang C. et al., 2019). Note that the gas sensing property is quite relative to the content of chemisorbed oxygen which increases by 9% after W modification, so the sensing performance would be remarkably improved (Teng et al., 2019). Finally, in **Figure 5D**, W 4f in the WO₃/SnO₂ (0.3%) composite gives a spin orbital dipole with two binding energies of 36.38 and 38.48 eV, respectively. The calculation results show that the spin orbit jet energy is 2.1 eV, which reaches a similar agreement with the theoretical calculation value (Nayak et al., 2015; Bai et al., 2016; Tofighi et al., 2019). According to the XPS results, interaction with the decoration of WO₃ is clearly witnessed, leading to the modification of the chemical state of the WO₃/SnO₂ (0.3%) composite. In particular, the improved gas properties will be compared with pure SnO₂ and discussed in detail in the gas sensitivity test section.

Gas Sensing Test

As mentioned, the WO₃/SnO₂ (0.3%) HNF could be a good gas sensor candidate, since its hollow channel and porous structure may accelerate the gas diffusion and reaction on the active sites. Moreover, the interaction of W nanoparticles with the SnO₂ substrate can promote the O₂ chemisorption and generate a higher response when exposed to an acetone pollutant at low concentrations. Consequently, the optimal working temperature of the gas sensitive materials, based on various WO₃/SnO₂ HNFs with acetone as the target gas was first determined with pure SnO₂ HNFs included for comparison. **Figure 6** shows that all the four response curves gradually increase when increasing the working temperature from 50°C, and decline at only 170°C for WO₃/SnO₂ (0.3%), but 250°C for the other three samples. Additionally, the sensor that is based on WO₃/SnO₂ (0.3%) provides the highest response (32) compared with other sensors. Just as expected, WO₃/SnO₂ (0.3%) is a promising choice and all the following tests were carried out at the optimal operating temperature of 170°C.

Additionally, four dynamic response change curves of pure SnO₂ and WO₃/SnO₂ sensor devices of different concentrations (0.1–200 ppm) of acetone at 170°C have been provided in

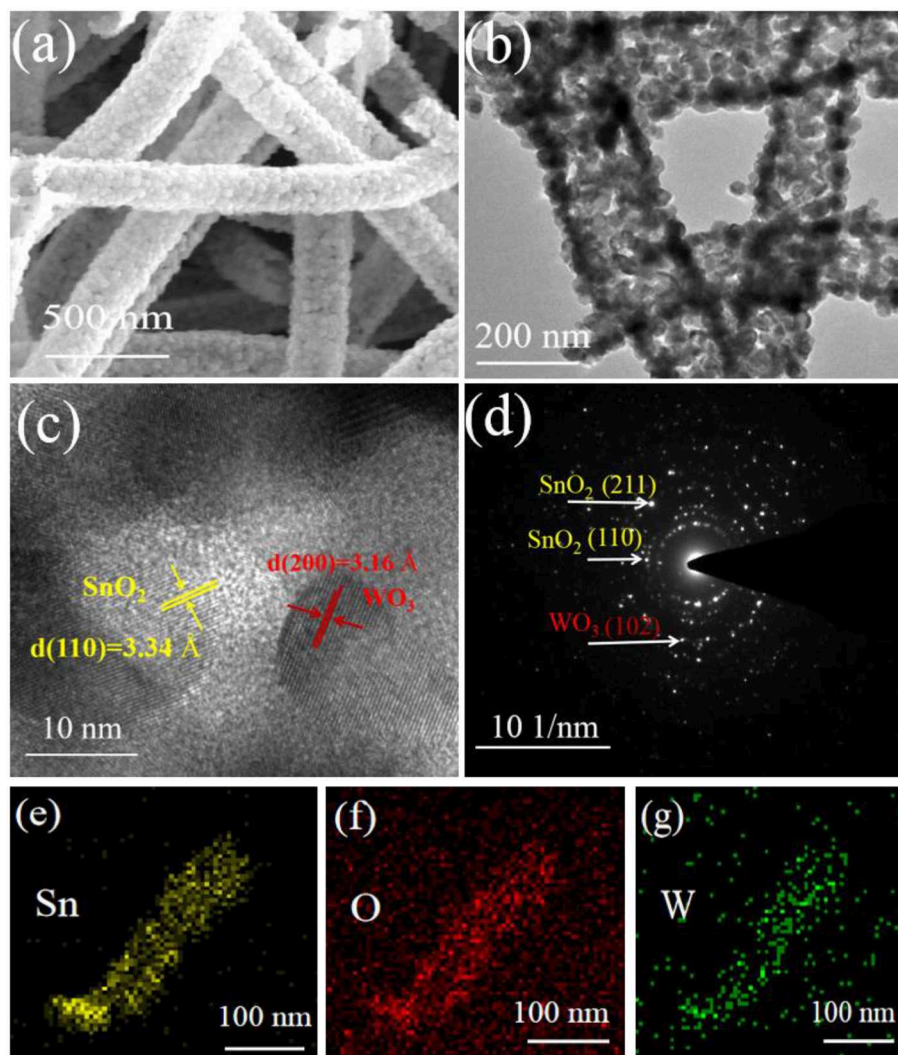


FIGURE 4 | (a) SEM image, (b) TEM image, (c) HRTEM image and (d) SAED of WO_3/SnO_2 (0.3%) sample, with the (e–g) elemental mappings of Sn, O, and W elements.

Figure 7. As can be seen in **Figure 7A**, WO_3/SnO_2 (0.3%) presents the highest response amplitude compared with the others, as well as the fastest instantaneous response speeds (≤ 6 s), which proves its favorable response properties. (**Figure S3**) enlarged response–recovery curve for 100 ppb acetone gas was explored to determine the response/recovery time. At 170°C , for as-fabricated WO_3/SnO_2 (0.3%) based sensor toward 100 ppb acetone gas, the response/recovery time was 50 and 200 s, respectively. Furthermore, the sensors display a better fold linear relationship between the response signal vs. acetone concentration (**Figure 7B**). Such a result clearly indicates that the gas sensitivity of SnO_2 has been significantly improved through the synergistic effect of the hetero-junction formed by WO_3 doping, which is also consistent with the results from **Figures 4, 5**. However, the doping amount of WO_3 also displays an important role in the synergistic effect, thus affecting the surficial gas catalytical sensing properties.

In order to further confirm the selectivity of the WO_3/SnO_2 (0.3%)-based sensor, 100 ppm of industrial gases such as methanol, formaldehyde, triethylamine, ethylenediamine and toluene were chosen to test at 170°C . **Figure 8A** shows that the WO_3/SnO_2 (0.3%) sample not only exhibits excellent selectivity to acetone gas (32), three times more than other polluting gases, but also the highest response value compared to the other three sensors types. The sensor selectivity was influenced by many factors. On the one hand, the bond dissociation energy of $\text{CH}_3\text{-COCH}_3$ (352 kJ/mol) is smaller than that of $\text{C}_2\text{H}_5\text{O-H}$, $\text{CH}_3\text{O-H}$ (462 kJ/mol), H-COH (368 kJ/mol), $\text{H-CH}_2\text{C}_6\text{H}_5$ (371 kJ/mol), therefore, acetone is more likely to react with the adsorbed oxygen species than other gas molecules. On the other hand, the polar nature of the surface of the WO_3/SnO_2 (0.3 wt%) would accelerate the adsorption of polar molecules. Acetone is much easier to be adsorbed on the surface of WO_3/SnO_2 (0.3 wt%) than triethylamine. Consequently, more acetone molecules

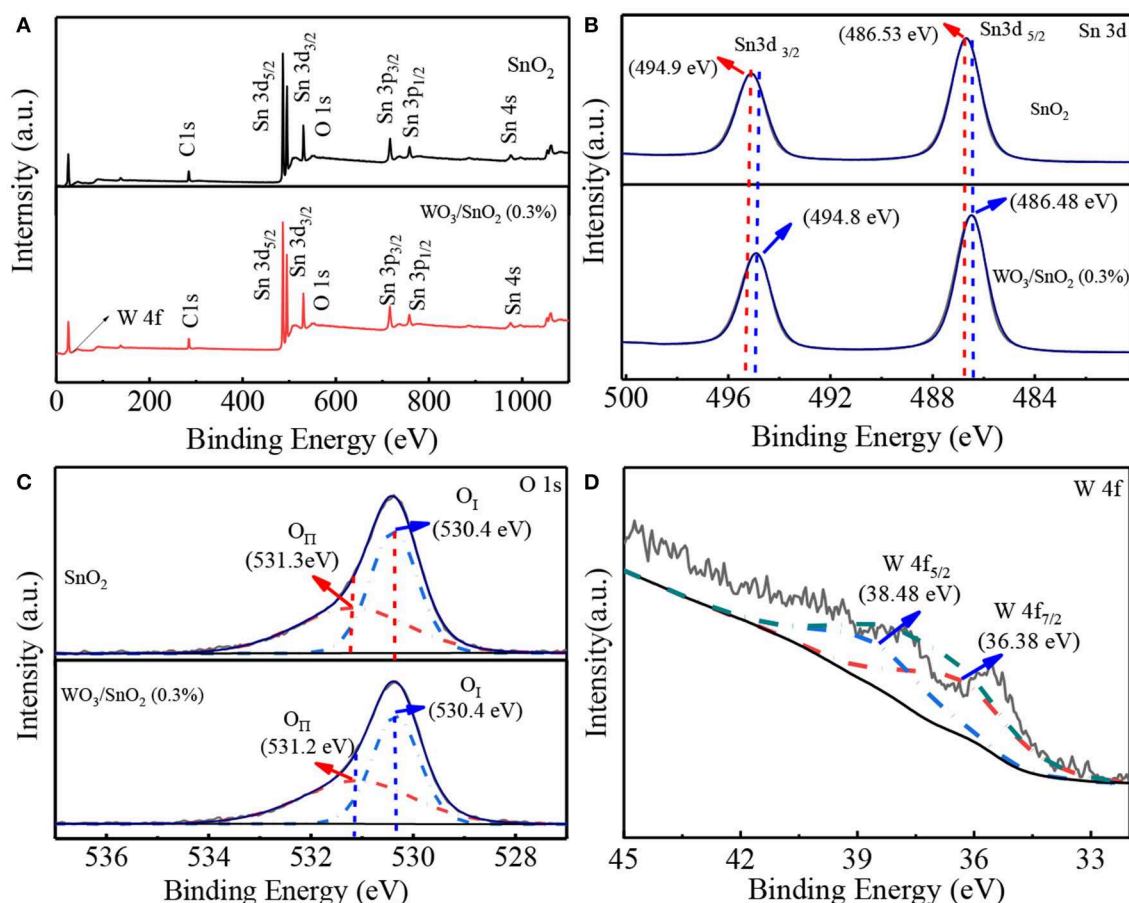


FIGURE 5 | (A) Survey spectra, and high magnification XPS spectra of (B) Sn 3d, (C) O 1s based on pure SnO₂ and WO₃/SnO₂ (0.3%) HNF samples, as well as (D) W 4f in WO₃/SnO₂ (0.3%) HNF, respectively.

can react with the adsorbed oxygen species which releases more electrons than any other gas molecule. As a result, the WO₃/SnO₂ (0.3 wt%) hetero-nanofibers had a good sensing response and selectivity to acetone gas (Li et al., 2016; Zhang et al., 2017). The more detailed mechanism of adsorption and reaction using DFT calculation and *in situ* instruments, will be discussed in our future work. In **Figure 8B**, the corresponding desirable repeatability can also be witnessed for the four sensors to 100 ppm of acetone after five circles, especially the most attractive component of WO₃/SnO₂ (0.3%). In general, the sensor based on WO₃/SnO₂ (0.3%) HNF in this study is a promising candidate for trace indoor or industrial acetone gas sensing.

Last but not the least, to verify the stability of the prepared acetone sensor, the sensitivity of pure SnO₂ and three groups of WO₃/SnO₂ (0.1, 0.3, 0.9 wt%) HNFs were detected every 6 days for 1 month. **Figure S2** shows that all the sensors nearly keep their response states, especially the sensor based on WO₃/SnO₂ (0.3%) which exhibits quite high and stable response values. Such a result also indicates that the acetone gas sensor has good stability and prospective application.

To give a clear vision on the sensing properties of gas sensors to acetone, comparisons were made in **Table 1**. As can be seen, the gas sensor based on our WO₃/SnO₂ (0.3%) HNF material displays the improved performance in a certain way, such as a lower working temperature of only 170°C. Generally, this work is valuable in enhancing the gas sensing properties by preparation of hollow hetero-structures.

Gas Sensing Mechanism

The basic sensing principle for the n-type semiconductor metal oxides is based on the conductivity changes which are caused by surface gas adsorption and desorption (Wang Q. et al., 2019). In short, oxygen molecules in the air are adsorbed on the metal oxide surfaces. The different oxygen species including O⁻, O₂²⁻, and O₂⁻ will form at different temperatures by capturing free electrons from the conduction bands of WO₃ and SnO₂, e.g., the stable oxygen species on the surface of the sensing material is mainly O⁻ below 300°C (Yamazoe et al., 2003; Rakshit et al., 2012). Thus, the electron concentration will be reduced to form an electron depletion layer, resulting in a higher resistance. When the sensor is exposed to the reduced gas like acetone, it can react with the adsorbed O⁻ and release the captured electrons back,

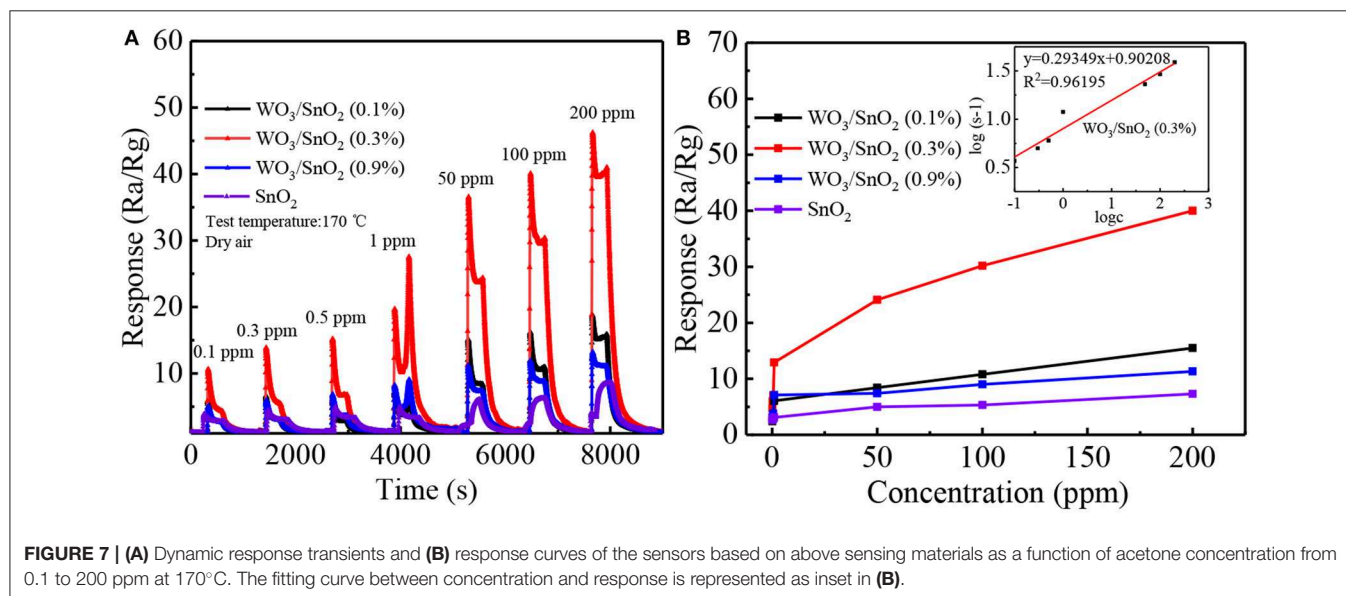
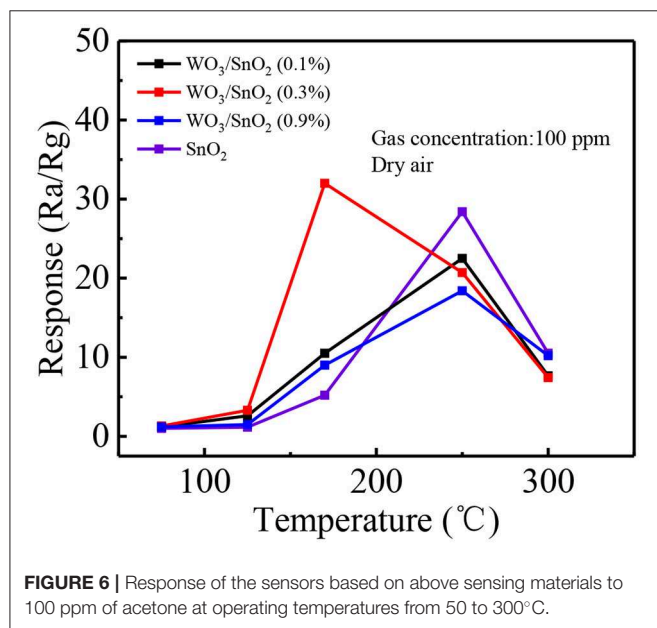
thus decreasing the resistance (Das and Jayaraman, 2014; Yang and Guo, 2016).

On the basis of the above theory, the improved sensing performances for the sensor based on WO_3/SnO_2 (0.3%) HNF can be attributed to three factors. First, as shown in **Figure 9**, the band gap and work function of SnO_2 is 3.6 and 4.9 eV, while that for WO_3 it is 2.6 and 4.8 eV, respectively. As the work functions of both are imbalanced, the electrons will transfer from the Fermi level of WO_3 (higher Fermi level) to that of SnO_2 (lower Fermi level) until they reach a balance, as displayed in **Figures 9A,B**. At the equilibrium point, the Schottky barrier with an additional depletion layer between WO_3 and SnO_2 are formed, controlling the electron transport efficiency of the

heterojunction (Rakshit et al., 2012; Koohestani, 2019). The WO_3/SnO_2 hetero-structure provides more electrons to oxygen than pure SnO_2 , then produces more O^- species on the materials surface. Therefore, the hetero-structure exhibits better sensing properties (Wal et al., 2009; Lingyue and Shantang, 2018; Yang et al., 2018).

Second, it's also the key factor that the synergetic effect between the interfaces can improve their sensing performances (Gu et al., 2011). It can be concluded from the TEM and XPS results in **Figures 4, 5** that, WO_3 nanoparticles have been incorporated into the SnO_2 HNFs successfully, thus both of them become highly accessible for the adsorption of oxygen species, add the thickness of the depletion layer at the interfaces and join in the reaction with acetone to a greater extent. This promotes the sensing response but helps reduce the working temperature of pure SnO_2 (Parthibavarman et al., 2018; Wang L. et al., 2019). However, the heterojunctions with different contents of WO_3 showed different gas sensing properties during the test, which also indicates that the optimal proportion of dopant is quite important in the construction of heterojunctions (Stojadinović et al., 2016).

The last factor has a lot to do with the morphology of the heterojunction. Many advantages exist in the HNFs produced by the electro-spinning method, since compared to the other three dimensions, the first characteristic of 1D nanostructure is its smaller dimension structure and high aspect ratio, which could efficiently transport electrical carriers along one controllable direction, making it highly suitable for moving charges in integrated nanoscale systems (Wal et al., 2009; Gu et al., 2011; Lu et al., 2011; Yuan et al., 2011; Wang et al., 2016). Additionally, the grain size also greatly affects the gas sensitivity. The region within a Debye length of the surface is known as the depletion region because it is depleted of its normal charge carriers. The Debye length may change to more or less when oxygen is adsorbed on the surface, which in turn causes a



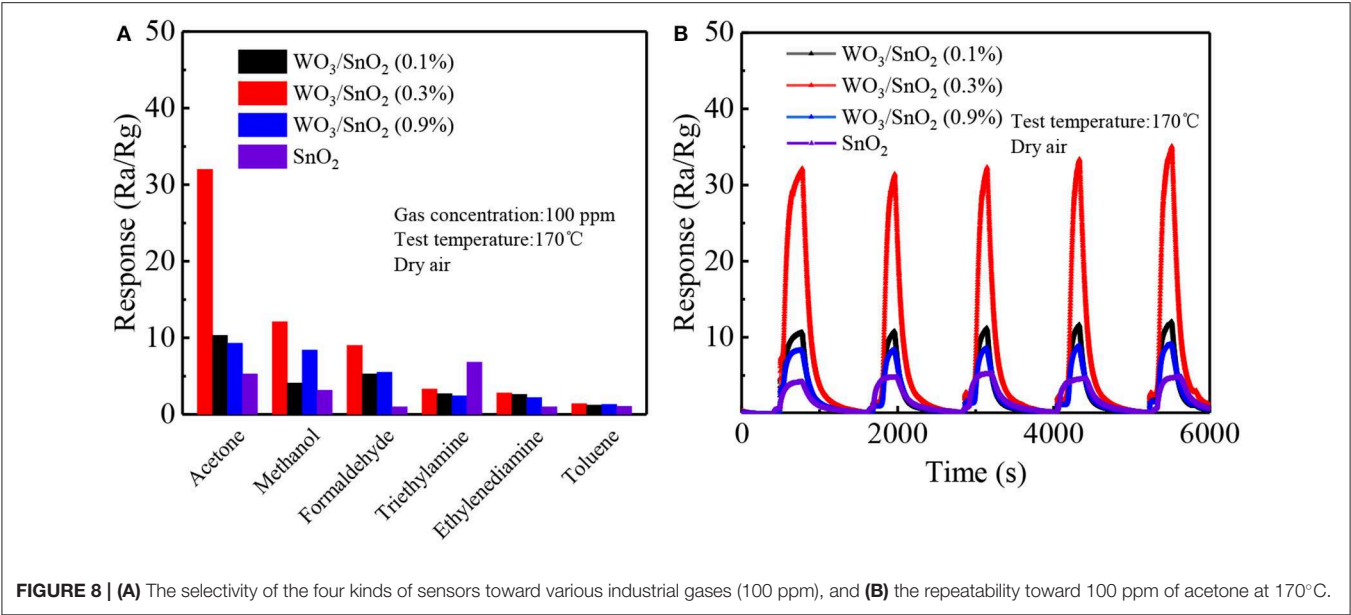
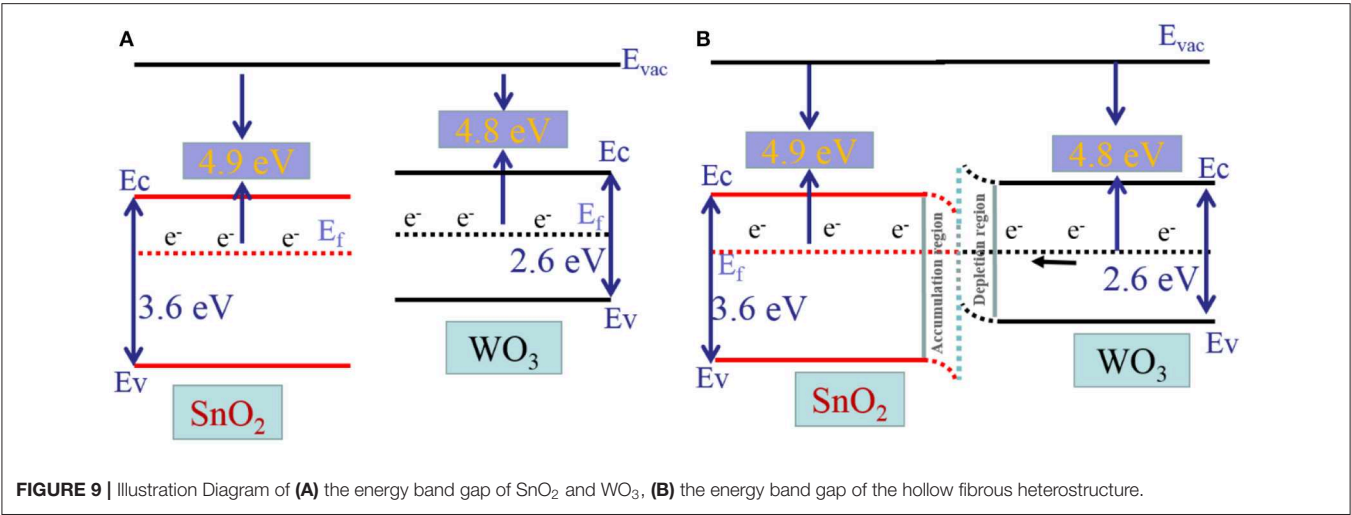


TABLE 1 | Sensing performance of various gas sensors toward acetone.

Materials	Method	W.T. (°C)	LOD (ppm)	Response	References
Ag@CuO-TiO ₂	Hydrothermal	200	1	11	Wang G. et al., 2019
Pt-decorated Fe ₂ O ₃ nanocubes	Hydrothermal	139	1	1.8	Zhang et al., 2019a
CoFe ₂ O ₄ nanoparticles (SM)	Solvothermal	220	50	16	Zhang H. et al., 2019
Porous NiFe ₂ O ₄ microspheres	Hydrothermal	250	0.2	1.2	Zhang et al., 2019b
0.5 wt% Au-ZnO	Sol-geltechnique	172	15	10	Yang M. et al., 2019
BiFeO ₃ nanoparticles	Hydrothermal	350	1	1.8	Chakraborty and Pal, 2019
WO ₃ /SnO ₂ heterostructure	Electrospinning	170	0.1	4.7	This work



measurable change in the resistance. It has been overwhelmingly shown that when crystallite sizes are below about 20 nm, sensor response drastically increases (Miller et al., 2014), similar to the explanation presented in the XRD part, where the grain size calculations of various heterojunctions at 17.53, 15.71, and 20.56 nm in the WO_3/SnO_2 (0.1%, 0.3%, 0.9%) composite, and the smallest grain size of 15.71 nm in the WO_3/SnO_2 (0.3%), contributes to its best gas sensitivity among all the samples. The gas sensitivity was not controlled by the grain size of the main phase alone, but also the particle size, density, and distribution of the doped catalyst WO_3 . As the doping amount of WO_3 is 0.1 wt%, small WO_3 nanoparticles are sparsely dispersed in SnO_2 nanotubes with a lower density and less heterogeneous nodes. The increased charge carrier density would have little impact on depletion regions and the overall electrical conduction in the WO_3/SnO_2 heterostructure. When the doping of WO_3 is higher than 0.3 wt%, the crystallization of WO_3 is accompanied by the growth of SnO_2 crystallite size and the loss in specific surface area, leading to a less effective target gas diffusion, less reduction of depletion regions and deteriorated sensor response. Motivated by such facts, when the content of WO_3 is above 0.3 wt% results in a weakened gas response.

CONCLUSION

The heterogeneous structure and pure SnO_2 of three components of WO_3/SnO_2 hollow nanofibers (HNF) were prepared by electro spinning in this study. The grain size measured by TEM and calculated by scherrer formula also proved that the group with the best gas sensitivity was WO_3/SnO_2 (0.3%) HNF. Moreover, the large specific surface area characteristic of the hollow structure and the enhanced surface activity as the grain size decreases to the nanometer level providing a good way for the gas to enter the semiconductor material. The sample of the WO_3/SnO_2 (0.3%) component has the best selectivity

for acetone in several representative industrial waste gases at the optimal operating temperature of 170°C. In particular, while the acetone concentration is as low as 100 ppb a good response was shown as well (4.7), and the response/recovery time was 50/200 s, respectively. This research can provide significant references for acetone gas sensors with low temperature and low detection limits.

DATA AVAILABILITY STATEMENT

All datasets generated for this study are included in the article/**Supplementary Material**.

AUTHOR CONTRIBUTIONS

HS initiated the experiments and draft. MH, HF, and SW helped prepare the samples. LW, JL, and KY contributed equally to this work, and they designed and completed the manuscript. YW offered useful comments on the technical methods.

FUNDING

This work was funded by the National Natural Science Foundation of China (NO. 51762005, 91428203, and 61771267), Science and Technology Major Project of Guangxi (NO. AA17204074, AA17202020, AA17204100), and the Natural Science Foundation of Guangxi Province, China (2017GXNSFAA198254).

SUPPLEMENTARY MATERIAL

The Supplementary Material for this article can be found online at: <https://www.frontiersin.org/articles/10.3389/fchem.2019.00785/full#supplementary-material>

REFERENCES

- Bai, S., Guo, W., Sun, J., Li, J., Tian, Y., Chen, A., et al. (2016). Synthesis of SnO_2 -CuO heterojunction using electrospinning and application in detecting of CO. *Sens. Actuators B*. 226, 96–103. doi: 10.1016/j.snb.2015.11.028
- Chakraborty, S., and Pal, M. (2019). Highly selective and stable acetone sensor based on chemically prepared bismuth ferrite nanoparticle. *J. Alloy. Compd.* 787, 1204–1211. doi: 10.1016/j.jallcom.2019.02.153
- Das, S., and Jayaraman, V. (2014). SnO_2 : A comprehensive review on structures and gas sensors. *Prog. Mater. Sci.* 66, 112–255. doi: 10.1016/j.pmatsci.2014.06.003
- Gu, L., Zheng, K., Zhou, Y., Li, J., Mo, X., Patzke, G. R., et al. (2011). Humidity sensors based on ZnO/TiO_2 core/shell nanorod arrays with enhanced sensitivity. *Sens. Actuators B*. 159, 1–7. doi: 10.1016/j.snb.2010.12.024
- Joshi, N., Hayasaka, T., Liu, Y., Liu, H., Oliveira, O. N., and Lin, L. (2018). A review on chemiresistive room temperature gas sensors based on metal oxide nanostructures, graphene and 2D transition metal dichalcogenides. *Microchim. Acta* 185, 213–214. doi: 10.1007/s00604-018-2750-5
- Koohestani, H. (2019). Characterization of TiO_2/WO_3 composite produced with recycled WO_3 nanoparticles from W Ni Fe alloy. *Mater. Chem. Phys.* 229, 251–256. doi: 10.1016/j.matchemphys.2019.03.027
- Kucheyev, S. O., Baumann, T. F., Sterne, P. A., Wang, Y. M., Van Buuren, T., Hamza, A. V., et al. (2006). Surface electronic states in three-dimensional SnO_2 nanostructures. *Phys. Rev. B*. 72, 1–5. doi: 10.1103/PhysRevB.72.035404
- Lavacchi, C. B., Rovida, G., Bardi, U., Atrei, A., Angelucci, R., Dori, L., et al. (2000). Composition and structure of tin/vanadium oxide surfaces for chemical sensing applications. *Sens. Actuators B*. 71, 123–126. doi: 10.1016/S0925-4005(00)00596-7
- Li, F., Gao, X., Wang, R., and Zhang, T. (2018). Design of WO_3 - SnO_2 core-shell nanofibers and their enhanced gas sensing performance based on different work function. *Appl. Surf. Sci.* 442, 30–37. doi: 10.1016/j.apsusc.2018.02.122
- Li, J., Tang, P., Zhang, J., Feng, Y., Luo, R., Chen, A., et al. (2016). Facile synthesis and acetone sensing performance of hierarchical SnO_2 hollow microspheres with controllable size and shell thickness. *Ind. Eng. Chem. Res.* 55, 3588–3595. doi: 10.1021/acs.iecr.6b00060
- Lingyue, L., and Shantang, L. (2018). Oxygen vacancies as an efficient strategy for promotion of low concentration SO_2 Gas Sensing: the case of Au modified SnO_2 . *ACS Sustain. Chem. Eng.* 6, 13427–13434. doi: 10.1021/acssuschemeng.8b03205
- Liu, J., Xin, L., Xiang, C., Hao, N., Xiao, H., Zhang, T., et al. (2016). Synthesis of $\text{SnO}_2/\text{In}_2\text{O}_3$ hetero-nanotubes by coaxial-electrospinning method for enhanced formaldehyde response. *New J. Chem.* 40, 1756–1764. doi: 10.1039/C5NJ02337H
- Lu, X., Zhang, W., Wang, C., Wen, T., and Wei, Y. (2011). One-dimensional conducting polymer nanocomposites: Synthesis, properties and applications. *Prog. Polym. Sci.* 36, 671–712. doi: 10.1016/j.progpolymsci.2010.07.010

- Ma, H., Yoon, K., Rong, L., Mao, Y., Mo, Z., Fang, D., et al. (2010). High-flux thin-film nanofibrous composite ultrafiltration membranes containing cellulose barrier layer. *J. Mater. Chem.* 20, 4692–4704. doi: 10.1039/b922536f
- Meng, F., Qin, W., Li, B., Zhang, H., Wang, S., Chang, Y., et al. (2019). Synthesis of Au nanoparticle-modified spindle shaped α -Fe₂O₃ nanorods and their gas sensing properties to N-butanol. *IEEE T Nanotechnol.* 18, 911–920. doi: 10.1109/TNANO.2019.2933569
- Meng, F., Zheng, H., Sun, Y., Li, M., and Liu, J. (2017). Trimethylamine sensors based on Au-modified hierarchical porous single-crystalline ZnO nanosheets. *Sensors* 17, 1–12. doi: 10.3390/s17071478
- Miller, D., R., and Akbar, S., A., Morris, P., A. (2014). Nanoscale metal oxide-based heterojunctions for gas sensing: a review. *Sens. Actuators B* 204, 250–272. doi: 10.1016/j.snb.2014.07.074
- Nan, H., Guofeng, P., Jie, Z., and Ru, W. (2019). Co₃O₄-ZnO p-n Heterostructure low temperature acetone gas sensor. *Semicond. Technol.* 44, 379–385. doi: 10.13290/j.cnki.bdtjs.2019.05.010
- Nayak, A. K., Ghosh, R., Santra, S., Guha, P. K., and Pradhan, D. (2015). Hierarchical nanostructured WO₃-SnO₂ for selective sensing of volatile organic compounds. *Nanoscale* 7, 12460–12473. doi: 10.1039/C5NR02571K
- Parthibavarman, M., Karthik, M., and Prabhakaranc, S. (2018). Facile and one step synthesis of WO₃ nanorods and nanosheets as an efficient photocatalyst and humidity sensing material. *Vacuum* 155, 224–232. doi: 10.1016/j.vacuum.2018.06.021
- Patil, J. V., Mali, S. S., Kamble, A. S., Hong, C. K., Kim, J. H., and Patil, P. S. (2017). Electrospinning: a versatile technique for making of 1D growth of nanostructured nanofibers and its applications: an experimental approach. *Appl. Surf. Sci.* 423, 641–674. doi: 10.1016/j.apsusc.2017.06.116
- Rakshit, T., Mondal, S. P., Manna, I., and Ray, S. K. (2012). CdS-decorated ZnO nanorod heterostructures for improved hybrid photovoltaic devices. *ACS Appl. Mater. Inter.* 4, 6085–6095. doi: 10.1021/am301721h
- Stojadinović, S., Vasilčić, R., Radić, N., Tadić, N., Stefanov, P., and Grbić, B. (2016). The formation of tungsten doped Al₂O₃/ZnO coatings on aluminum by plasma electrolytic oxidation and their application in photocatalysis. *Appl. Surf. Sci.* 377, 37–43. doi: 10.1016/j.apsusc.2016.03.104
- Sukunta, J., Wisitsoraat, A., Tuantranont, A., Phanichphant, S., and Liewhiran, C. (2018). WO₃ nanotubes-SnO₂ nanoparticles heterointerfaces for ultrasensitive and selective NO₂ detections. *Appl. Surf. Sci.* 458, 319–332. doi: 10.1016/j.apsusc.2018.07.096
- Tang, W., Wang, J., Yao, P., and Li, X. (2014). Hollow hierarchical SnO₂-ZnO composite nanofibers with heterostructure based on electrospinning method for detecting methanol. *Sens. Actuators B* 192, 543–549. doi: 10.1016/j.snb.2013.11.003
- Teng, L., Liu, Y., Ikram, M., Liu, Z., Ullah, M., Ma, L., et al. (2019). One-step synthesis of palladium oxide-functionalized tin dioxide nanotubes: Characterization and high nitrogen dioxide gas sensing performance at room temperature. *J. Colloid. Interface Sci.* 537, 79–90. doi: 10.1016/j.jcis.2018.11.001
- Tofighi, G., Degler, D., Junker, B., Müller, S., Lichtenberg, H., Wang, W., et al. (2019). Microfluidically synthesized Au, Pd and AuPd nanoparticles supported on SnO₂ for gas sensing applications. *Sens. Actuators B* 292, 48–56. doi: 10.1016/j.snb.2019.02.107
- Wal, R. L. V., Berger, G. M., Kulis, M. J., Hunter, G. W., Xu, J. C., and Laura, E. (2009). Synthesis methods, microscopy characterization and device integration of nanoscale metal oxide semiconductors for gas sensing. *Sensors-Basel* 9, 7866–7902. doi: 10.3390/s91007866
- Wang, G., Fu, Z., Wang, T., Lei, W., Sun, P., Sui, Y., et al. (2019). A rational design of hollow nanocages Ag@CuO-TiO₂ for enhanced acetone sensing performance. *Sens. Actuators B* 295, 70–78. doi: 10.1016/j.snb.2019.05.075
- Wang, K., Wei, W., Lou, Z., Zhang, H., and Wang, L. (2019). 1D/2D heterostructure nanofiber flexible sensing device with efficient gas detectivity. *Appl. Surf. Sci.* 479, 209–215. doi: 10.1016/j.apsusc.2019.02.094
- Wang, L., Fu, H., Jin, Q., Jin, H., Haick, H., Wang, S., et al. (2019). Directly transforming SnS₂ nanosheets to hierarchical SnO₂ nanotubes: towards sensitive and selective sensing of acetone at relatively low operating temperatures. *Sens. Actuators B* 292, 148–155. doi: 10.1016/j.snb.2019.04.127
- Wang, Q., Bai, J., Huang, B., Hu, Q., Cheng, X., Li, J., et al. (2019). Design of NiCo₂O₄@SnO₂ heterostructure nanofiber and their low temperature ethanol sensing properties. *J. Alloy. Compd.* 791, 1025–1032. doi: 10.1016/j.jallcom.2019.03.364
- Wang, X., Ding, B., Sun, G., Wang, M., and Yu, J. (2013). Electro-spinning/netting: a strategy for the fabrication of three-dimensional polymer nano-fiber/nets. *Prog. Mater. Sci.* 58, 1173–1243. doi: 10.1016/j.pmatsci.2013.05.001
- Wang, Y., He, B., Wang, H., Xu, J., Ta, T., Li, W., et al. (2016). Transparent WO₃/Ag/WO₃ electrode for flexible organic solar cells. *Mater. Lett.* 188, 107–110. doi: 10.1016/j.matlet.2016.11.054
- Xia, Y. N., Yang, P. D., Sun, Y. G., W. U. Y. Y., Mayers, B., Gates, B., et al. (2010). One-dimensional nanostructures: synthesis, characterization, and applications. *Adv. Mater.* 15, 353–389. doi: 10.1002/adma.200390087
- Yamazoe, N., Sakai, G., and Shimanoe, K. (2003). Oxide semiconductor gas sensors. *Catal. Surv. Asia* 7, 63–75. doi: 10.1023/A:1023436725457
- Yang, C., Miao, G., Pi, Y., Xia, Q., Wu, J., Li, Z., et al. (2019). Abatement of various types of VOCs by adsorption/catalytic oxidation: a review. *Chem. Eng. J.* 370, 1128–1153. doi: 10.1016/j.cej.2019.03.232
- Yang, F., and Guo, Z. (2016). Tuning SnO₂ architectures with unitary or composite microstructure for the application of gas sensor. *J. Colloid Interface Sci.* 462:140–147. doi: 10.1016/j.jcis.2015.09.074
- Yang, M., Zhang, S., Qu, F., Gong, S., Wang, C., Qiu, L., et al. (2019). High performance acetone sensor based on ZnO nanorods modified by Au nanoparticles. *J. Alloy. Compd.* 797, 246–252. doi: 10.1016/j.jallcom.2019.05.101
- Yang, W., Feng, L., He, S., Liu, L., and Liu, S. (2018). Density gradient strategy for preparation of broken In₂O₃ microtubes with remarkably selective detection of triethylamine vapor. *ACS Appl. Mater. Interfaces* 10, 27131–27140. doi: 10.1021/acsami.8b09375
- Yuan, J., Xu, Y., and A., Müller, H. E. (2011). One-dimensional magnetic inorganic-organic hybrid nanomaterials. *Chem. Soc. Rev.* 40, 640–655. doi: 10.1039/c0cs00087f
- Yuan, Z., Zhao, J., Meng, F., Qin, W., Chen, Y., Yang, M., et al. (2019). Sandwich-like composites of double-layer Co₃O₄ and reduced graphene oxide and their sensing properties to volatile organic compounds. *J. Alloy. Compd.* 793, 24–30. doi: 10.1016/j.jallcom.2019.03.386
- Zhang, H., Liu, L., Zhang, X., Zhang, S., and Meng, F. (2019). Microwave-assisted solvothermal synthesis of shape-controlled CoFe₂O₄ nanoparticles for acetone sensor. *J. Alloy. Compd.* 788, 1103–1112. doi: 10.1016/j.jallcom.2019.03.009
- Zhang, S., Jiang, W., Li, Y., Yang, X., Sun, P., Liu, F., et al. (2019b). Highly-sensitivity acetone sensors based on spinel-type oxide (NiFe₂O₄) through optimization of porous structure. *Sens. Actuators B* 291, 266–274. doi: 10.1016/j.snb.2019.04.090
- Zhang, S., Song, P., Zhang, J., Yan, H., Li, J., Yang, Z., et al. (2017). Highly sensitive detection of acetone using mesoporous In₂O₃ nanospheres decorated with Au nanoparticles. *Sens. Actuators B* 242, 983–993. doi: 10.1016/j.snb.2016.09.155
- Zhang, S., Yang, M., Liang, K., Turak, A., Zhang, B., Meng, D., et al. (2019a). An acetone gas sensor based on nanosized Pt-loaded Fe₂O₃ nanocube. *Sens. Actuators B* 290, 59–67. doi: 10.1016/j.snb.2019.03.082
- Zhao, S., Shen, Y., Zhou, P., Zhong, X., Han, C., Zhao, Q., et al. (2019). Design of Au@WO₃ core-shell structured nanospheres for ppb-level NO₂ sensing. *Sens. Actuators B* 282, 917–926. doi: 10.1016/j.snb.2018.11.142

Conflict of Interest: The authors declare that the research was conducted in the absence of any commercial or financial relationships that could be construed as a potential conflict of interest.

Copyright © 2019 Shao, Huang, Fu, Wang, Wang, Lu, Wang and Yu. This is an open-access article distributed under the terms of the Creative Commons Attribution License (CC BY). The use, distribution or reproduction in other forums is permitted, provided the original author(s) and the copyright owner(s) are credited and that the original publication in this journal is cited, in accordance with accepted academic practice. No use, distribution or reproduction is permitted which does not comply with these terms.



Controlled Synthesis of Pt Doped SnO₂ Mesoporous Hollow Nanospheres for Highly Selective and Rapidly Detection of 3-Hydroxy-2-Butanone Biomarker

Haijie Cai^{1,2,3}, Haiquan Liu^{1,2,3}, Tianjun Ni⁴, Yingjie Pan^{1,2,3}, Yong Zhao^{1,2,3*} and Yongheng Zhu^{1,2,3*}

¹ College of Food Science and Technology, Shanghai Ocean University, Shanghai, China, ² Laboratory of Quality & Safety Risk Assessment for Aquatic Products on Storage and Preservation (Shanghai), Ministry of Agriculture, Shanghai, China,

³ Shanghai Engineering Research Center of Aquatic-Product Processing & Preservation, Shanghai, China, ⁴ School of Basic Medicine, Xinxiang Medical University, Xinxiang, China

OPEN ACCESS

Edited by:

Mingshui Yao,
Kyoto University, Japan

Reviewed by:

Yingming Xu,
Heilongjiang University, China
Jing-Hui He,
Soochow University, China

*Correspondence:

Yong Zhao
yzhao@shou.edu.cn
Yongheng Zhu
yh-zhu@shou.edu.cn

Specialty section:

This article was submitted to
Nanoscience,
a section of the journal
Frontiers in Chemistry

Received: 11 October 2019

Accepted: 19 November 2019

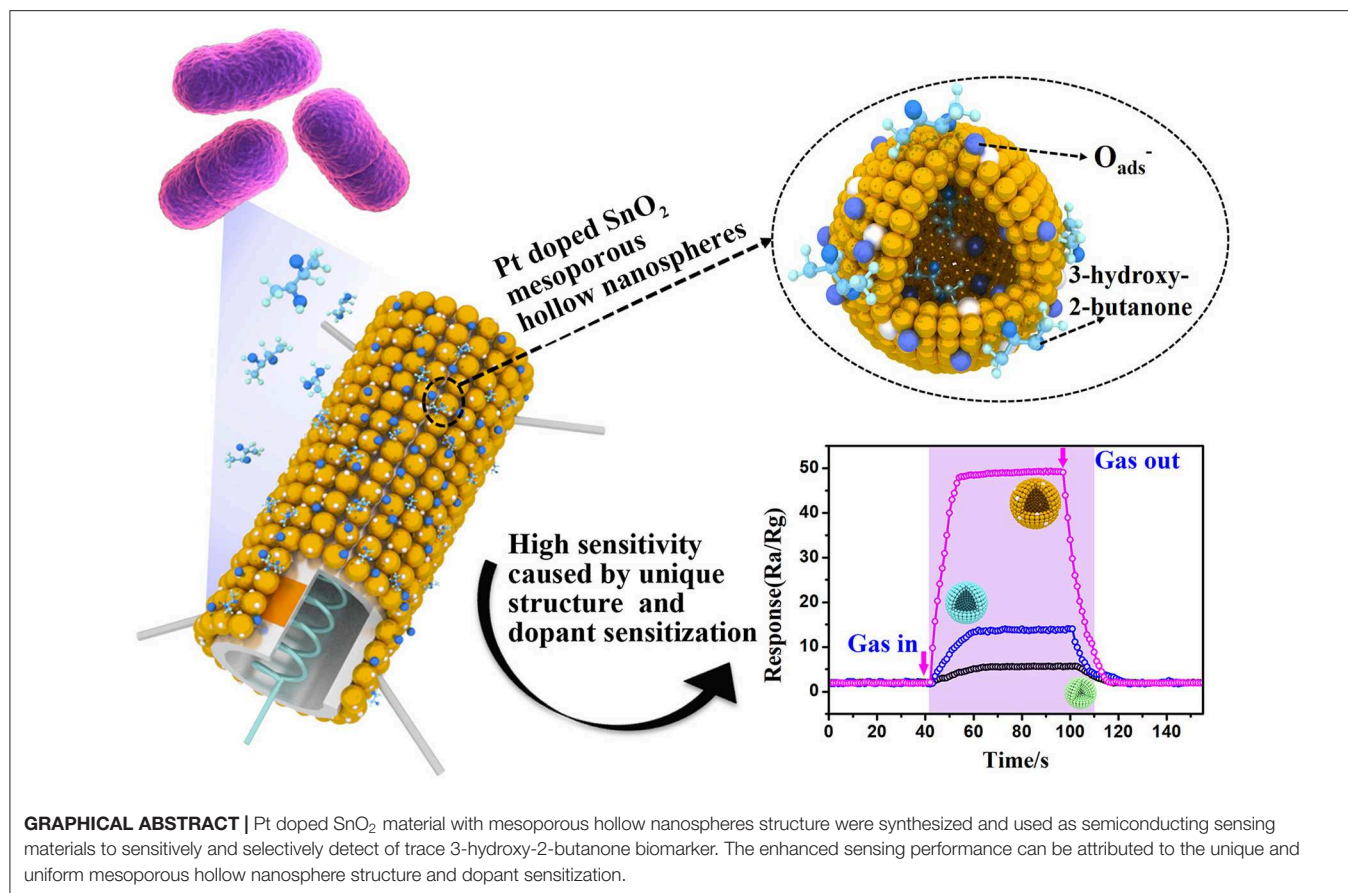
Published: 04 December 2019

Citation:

Cai H, Liu H, Ni T, Pan Y, Zhao Y and Zhu Y (2019) Controlled Synthesis of Pt Doped SnO₂ Mesoporous Hollow Nanospheres for Highly Selective and Rapidly Detection of 3-Hydroxy-2-Butanone Biomarker. *Front. Chem.* 7:843. doi: 10.3389/fchem.2019.00843

Listeria monocytogenes (*L. monocytogenes*) has been recognized as one of the extremely hazardous and potentially life-threatening food-borne pathogens, its real-time monitoring is of great importance to human health. Herein, a simple and effective method based on platinum sensitized tin dioxide semiconductor gas sensors has been proposed for selective and rapid detection of *L. monocytogenes*. Pt doped SnO₂ nanospheres with particular mesoporous hollow structure have been synthesized successfully through a robust and template-free approach and used for the detection of 3-hydroxy-2-butanone biomarker of *L. monocytogenes*. The steady crystal structure, unique micromorphology, good monodispersity, and large specific surface area of the obtained materials have been confirmed by X-ray diffraction (XRD), Raman spectroscopy, Scanning Electron Microscopy (SEM), Transmission Electron Microscopy (TEM), X-ray Photoelectron Spectroscopy (XPS), Brunauer-Emmett-Teller (BET), and Photoluminescence spectra (PL). Pt doped SnO₂ mesoporous hollow nanosphere sensors reach the maximum response of 3-hydroxy-2-butanone at 250°C. Remarkably, sensors based on SnO₂ mesoporous hollow nanospheres with 0.16 wt% Pt dopant exhibit excellent sensitivity ($R_{air}/R_{gas} = 48.69$) and short response/recovery time (11/20 s, respectively) to 10 ppm 3-hydroxy-2-butanone at the optimum working temperature. Moreover, 0.16 wt% Pt doped SnO₂ gas sensors also present particularly low limit of detection (LOD = 0.5 ppm), superb long-term stability and prominent selectivity to 3-hydroxy-2-butanone. Such a gas sensor with high sensing performance foresees its tremendous application prospects for accurate and efficient detection of foodborne pathogens for the food security and public health.

Keywords: 3-hydroxy-2-butanone, gas sensor, Pt doped SnO₂ nanomaterial, mesoporous hollow nanosphere, controlled synthesis



INTRODUCTION

Bacterial foodborne pathogens are widely spread and cause millions of cases of human illness every year around the world (Carlson et al., 2018). *Listeria monocytogenes* is a zoonotic pathogen with strong adaptability and can survive in the temperature between 3 and 45°C (Ciesielski et al., 1987) and pH varying from 4.4 to 9.6 (Farber et al., 1992), it frequently associated with outbreaks of foodborne illness via intaking contaminated foods (Radoshevich and Cossart, 2018). People infected by *L. monocytogenes* may suffer from serious diseases such as meningitis, septicemia and hyperthermia gastroenteritis, especially in susceptible populations, the mortality rate is as high as 30% (Cheng et al., 2014). Great efforts have been made in detecting *L. monocytogenes*. Conventional methods such as biochemical tests and cell culture, are standard monitoring methods, but they are time-consuming and laborious in detection (Välimaa et al., 2015). In the contrast, smart detection of *L. monocytogenes*, such as immunological assay and molecular analysis, can significantly improve the detection efficiency, however, these methods suffer from either requiring professional technicians or complicated and expensive facilities (Zhao et al., 2018; Zhang Z. et al., 2019). Consequently, advances in rapid and facile examination techniques is of great significance to the economy and real-time monitoring of bacterial foodborne pathogens.

Gas sensor based on metal oxide semiconductor is deemed as a desirable tool for on-site inspection of gases by virtue of the advantages of simplicity, portability, cost-effective, easy-operation, and fast response to target gas molecules (Panahi et al., 2018). The wide variety of microbial volatile organic compounds that produced the proliferation of *L. monocytogenes* (Audrain et al., 2015; Wang Y. et al., 2016a) make it possible for metal oxide semiconductors gas sensors to be widely used in timely examination of biological hazards in food. Among these exhaled gases, 3-hydroxy-2-butanone is considered as a biomarker and can be used to indirectly identify and detect *L. monocytogenes* (Yu et al., 2015; Chen et al., 2017). Our previous research creatively used mesoporous WO₃-based gas sensors to detect food-borne pathogens (Zhu et al., 2017). Later, Chen, Zhu et al. made new attempts in this direction and made further breakthroughs (Zhu et al., 2018; Chen et al., 2019). However, few studies have been conducted on the detection of *L. monocytogenes* by gas sensors based on metal sensitized nanomaterials. Accordingly, efforts are still needed to develop more sensitive and stable gas-sensitive nanomaterials for tracing *L. monocytogenes* in real time.

Tin dioxide (SnO₂), a representative wide bandgap (3.6 eV) n-type semiconductor, offers great advantages in gas sensing owing to its quick response and good stability (Li Z. et al., 2016). However, the pure SnO₂ based sensors are suffering from poor selectivity and harsh working temperature in gas detection. Two main promising approaches have been manifested

to be most efficacious to address these issues: (1) controlling synthesis of novel and complex unique nanostructures; (2) doping or decorating with noble metals or metal oxide. In terms of structural control, the homogeneous mesoporous hollow nanostructure with large surface area and pore size can provide vast reaction sites for gasses access and effective pathways for rapid electronic transport, thus improving the sensitivity of gas sensors (Chen et al., 2011; Chen and Lou, 2013). As for element doping or decorating aspect, metal oxide semiconductors always fabricated and functionalized with noble metals like Pd, Au, and Rh (McFarland and Metiu, 2013; Hua et al., 2018), especially Pt (Wang et al., 2013, 2014), to improve the gas sensing performances. Xue's research group reported the synthesis of Pt doped SnO₂ nanoflowers for highly sensitive gas sensor (Xue et al., 2019). Wang L. et al. (2016) synthesized hierarchical 3D SnO₂ nanocomposites functionalized by Pt nanoparticles for sensitive and selective detection of ethanol. D'Arienzo et al. (2010) discussed the influence of catalytic activity on the response of Pt-Doped SnO₂ gas sensors to reducing gas. Gas sensors based on Pt doped SnO₂ enable high gas sensing performance, especially selectivity, due to the sensitization activity of the metals in improving the surface properties and adjusting the band structure (Li et al., 2014; Yao et al., 2014).

In this study, we present a low-cost and easy-to-use Pt doped SnO₂ mesoporous hollow nanospheres based gas sensor for selective and rapid determination of 3-hydroxy-2-butanone biomarker. Firstly, the SnO₂ mesoporous hollow nanospheres were controlled synthesized through a simple one-step templateless method, based on a classical inside-out Ostwald ripening mechanism. Then, Pt doped SnO₂ compounds were obtained through a simple and novel approach possess by using dopamine as the adsorbent and reductant, and finally used to form the 3-hydroxy-2-butanone sensors. Compared to pure SnO₂ mesoporous hollow nanospheres, the Pt doped SnO₂ gas sensors achieve remarkably improved sensing performance toward 3-hydroxy-2-butanone vapor. Particularly, the 0.16 wt% Pt doped SnO₂ mesoporous hollow nanospheres sensor display the highest sensitivity, reaching 48.69 ($R_{\text{air}}/R_{\text{gas}}$) toward 10 ppm 3-hydroxy-2-butanone at 250°C, while that of gas sensor assembled with pure SnO₂ hollow nanospheres is only about 14.37 ($R_{\text{air}}/R_{\text{gas}}$). Moreover, this kind of gas sensor based on 0.16 wt% Pt sensitized metal oxide semiconductor presents fast response/recovery time (11/20 s, respectively), particularly low limit of detection (LOD = 0.5 ppm), excellent selectivity and long-term stability, showing greater advantages for rapid and ultrasensitive detection of *L. monocytogenes* in food, environment, clinical, and communal samples.

MATERIALS AND METHODS

Chemical and Reagents

Ethanol solution (100%) and urea of AR grade were purchased from SinoPharm Chemical Reagent Co. Ltd. (Shanghai, China). Potassium stannate trihydrate (K₂SnO₃·3H₂O, AR), dopamine hydrochloride, Tris-buffer (99.5%) and chloroplatinic acid (H₂PtCl₆·6H₂O) were purchased from Sigma-Aldrich (St. Louis, MO, USA).

Synthesis of SnO₂ Mesoporous Hollow Nanospheres

According to the previous work (Lou et al., 2006), a robust and template-free approach has been taken for the controlled synthesis of SnO₂ mesoporous hollow nanospheres. Typically, 1.15 mmol of K₂SnO₃·3H₂O was dissolved into 60 mL of 37.5% ethanol-water bi-component solvent. After magnetic stirring for at least 5 min, a translucent solution with slightly white color was obtained. Thirty millimolars of urea was added into the solution before it was transferred to a 60 mL Teflon-lined autoclave. After reacting at 150°C for 24 h, the system was cooled down spontaneously. Finally, the white products were collected and washed with ethanol and deionized water for more than five times, then dried at 50°C overnight for further application.

Doping of SnO₂ Mesoporous Hollow Nanospheres With Pt Nanoparticles

Pt doped SnO₂ mesoporous hollow spheres were fabricated through an *in-situ* reduction of the H₂PtCl₆·6H₂O by using dopamine as the adsorbent and deoxidizer. One hundred milligrams of SnO₂ mesoporous hollow nanospheres was evenly dispersed into the solution of 50 mg dopamine hydrochloride dissolved in 25 ml Tris-buffer (10 mM, pH 8.5). After stirring 12 h at room temperature, the gray product dopamine coated SnO₂ mesoporous hollow nanospheres were washed with ethanol and water in turn and laid aside at 50°C overnight. Then, appropriate obtained product was added to 30 ml H₂PtCl₆·6H₂O solution to reach the Pt dosage of 0.08 wt%, and keep stirring at normal temperature for 12 h. Afterwards, the white powder was obtained and then washed with ethanol and water and dried at 50°C overnight. Finally, the organic dopamine coating of Pt doped SnO₂ mesoporous hollow nanospheres were removed by annealing at 500°C in air for 5 h, with an up/down ramp rate of 5°C/min. In addition to adjusting the concentration of tin sources, the above processes were repeated for preparation of others Pt doped SnO₂ mesoporous hollow nanospheres at 0.12, 0.16, 0.24, and 0.48 wt% Pt loading.

Materials Characterization

The morphology and crystalline structure of as-prepared gas sensing materials were explored by the followed methodologies. The structural characteristics were recorded by X-ray diffraction (XRD; Bruker, D8 Advance, Germany) with Cu-K α radiation ($\lambda = 0.15418$ nm) in the range from 10° to 80° at normal temperature. The doping process of Pt metal after heat treatment was confirmed by Raman Spectrograph (Horiba, LabRAM HR Evolution, France) with an excitation wavelength of 532 nm. The microtopography of the materials was recorded with Scanning Electron Microscopy (SEM, FEI, Quanta FEG 450, USA) and Transmission Electron Microscope (TEM, FEI, Tecnai G220S-Twin, USA). The decorated Pt nanoparticles and their oxidized state were explored by X-ray Photoelectron Spectroscopy (XPS, Thermo Scientific, EscaLab 250Xi spectrometer). The specific surface areas of the particular mesoporous hollow nanostructures were calculated by Brunauer-Emmett-Teller (BET) method, using nitrogen as the adsorbate. Photoluminescence spectra

(PL) of the Pt doped metal oxide have been acquired from a fluorescence spectrometer (Shimadzu International Trade Company, RF5301, Japan).

Gas Sensor Fabrication and Measurement

The obtained nanomaterials were fully grounded with deionized water (4:1) to form a paste. The obtained homogeneous mixture was then carefully painted onto the ceramic tube welded with two gold electrodes and four platinum wires, which finally followed by sintering at 300°C for 2 h to remove the adhesive and get more closely combined gas sensor. Finally, a Ni-Cr heating resistance was plugged into the tube and then aged for 1 week under test conditions at 250°C to enhance the stability.

Gas sensing tests were performed on a commercial WS-30B Gas Sensing Measurement System developed and manufactured by Weisheng Instruments Co. (Zhengzhou, China). The test system comes with an 18 L test chamber. The gas sensing properties of the fabricated gas sensors to 3-hydroxy-2-butanone have been measured by recording the electrical resistance variation of the gas sensitive element and calculated according to the definition. The response value of the sensor is defined as the ratio of the resistances under target air and gas ($S = R_{\text{air}}/R_{\text{gas}}$), and the response and recovery time are defined as the time the sensor reaches 90% of the final equilibrium value after injection or release of the target gas.

RESULT AND DISCUSSION

Structural, Morphology, and Composition of the Samples

Figure 1 illustrates the scheme of the controlled synthesis of SnO₂ mesoporous hollow nanospheres doped with Pt metal. According to the Ostwald ripening mechanism, the controlled synthesis of SnO₂ mesoporous hollow nanospheres was accomplished in the aqueous alcohol solution taking K₂SnO₃·3H₂O as the precursor. Then, dopamine was used to form thin and surface-adherent polydopamine films on SnO₂ hollow nanospheres. As shown in **Figure 1**, the bio-inspired dopamine molecule could spontaneously polymerize to the outer surface and interior of the SnO₂ mesoporous hollow nanospheres. Subsequently, chloroplatinate adsorbed onto the positively charged amine groups of dopamine where they were reduced to platinum nanoparticles by dopamine (Bernsmann et al., 2011; Nda-Umar et al., 2018). Finally, Pt doped SnO₂ mesoporous hollow nanospheres with good monodispersity, stable crystals and large BET surface area were obtained by calcination in air. Most of the platinum nanoparticles were oxidized to PtO₂ during the calcination process. The use of dopamine as adhesive is not only simple and quick, but also inexpensive and “green” (Lee et al., 2007; Zhu et al., 2013). There is no need for any additional reducing agent, and is easily to remove the dopamine coating from the synthetic material through a calcination process in air.

The crystal structures of the one-fold SnO₂ and metal doped nano-sized mesoporous hollow spherical semiconductor materials were investigated by XRD analysis. The observed patterns in **Figure 2A** show that the three intense diffractions

peaks at $2\theta = 26.4^\circ$, 33.9° , and 51.8° correspond to (110), (101), and (211) planes of SnO₂, respectively. Other diffraction peaks in **Figure 2A** are matched with the (200), (111), (220), (002), (310), (112), (301), (202), and (321) planes of SnO₂. All of these emerged diffraction peaks are perfectly indexed to the JCPDS card No. 41-1445, confirming the tetragonal rutile crystal phase of the synthesized SnO₂ nanomaterials. Meanwhile, no Pt nanoparticle peak of Pt doped SnO₂ sample is observed, which is probably due to extremely small doses of added Pt (Ma et al., 2018). Since material synthesis is always carried out in a high temperature, the effect of temperature on the crystal structure is also worthy of attention (Wang et al., 2014). Therefore, the SnO₂ were prepared at calcination temperatures varying from 350 to 550°C, and their XRD patterns were presented in **Figure 2B**. Obviously, every sample exhibit all of the characteristic diffraction peaks of SnO₂, indicating the brilliant stable crystals of SnO₂ mesoporous hollow nanospheres.

Raman spectra of pristine SnO₂, pure dopamine, Pt-DPA-SnO₂ and Pt doped SnO₂ are shown in **Figure 3**. The three strong peaks locate at 475 cm⁻¹, 632 cm⁻¹ and 775 cm⁻¹ are attributed to E_g, A_{1g}, and B_{2g} vibrations of SnO₂, respectively. As for intermediate products, two new fitted peaks appeared at 1,340 and 1,590 cm⁻¹, representing the presence of dopamine. After calcining at 500°C for 5 h, no fingerprint peaks of dopamine in Pt doped SnO₂ were observed, demonstrating the exhaustive removal of dopamine in the final product. Notably, none of the reflection peaks was related to Pt due to the extremely small size of well-dispersed Pt (Oh and Jeong, 2014).

Figure 4 presents the morphological structure of Pt doped SnO₂ nanomaterials. Apparently, the products consist of spherical hollow sphere with particle diameter of 400–500 nm and a shell thickness of ~30 nm. SEM micrographs (**Figures 4A,B**) display the spherical morphology of the nanomaterials with similar size distribution. The inset SEM image of **Figure 4A** and bright contour in TEM images (**Figures 4D,E**) clearly located in the center of the particle present the corresponding mesoporous hollow structure of the as-prepared Pt doped SnO₂ nanomaterials. **Figure 4D** and the inset HRTEM image of **Figure 4E** reveal that the stable Pt doped SnO₂ mesoporous hollow nanosphere as synthesized is composed of multiple layers of tin dioxide nanoparticles. The mesoporous hollow nanostructures stacked by multiple layers of SnO₂ nanosphere have a highly usable alternating and stable structure (Wang Y. et al., 2016b), which is favorable for the diffusion of gases and then effectively improve the gas sensing performance. No phases of anchored Pt nanoparticles were observed in both SEM and HRTEM micrographs, possibly due to small amount of Pt catalyst (Bulemo et al., 2018). TEM mapping of Pt doped SnO₂ nanomaterial was also conducted (**Figure 4G**), which notarize the existence and equidistributional of only Sn, O, and Pt component. Noting that the Sn and O are originated from the SnO₂ hollow nanospheres, whereas Pt are exogenous doped.

The surface chemical state of the semiconductor plays a non-negligible part in sensing properties. Therefore, the chemical states of the respective elements present in the singlet and Pt doped SnO₂ mesoporous hollow nanospheres were analyzed by XPS. The complete spectra of the samples were displayed in

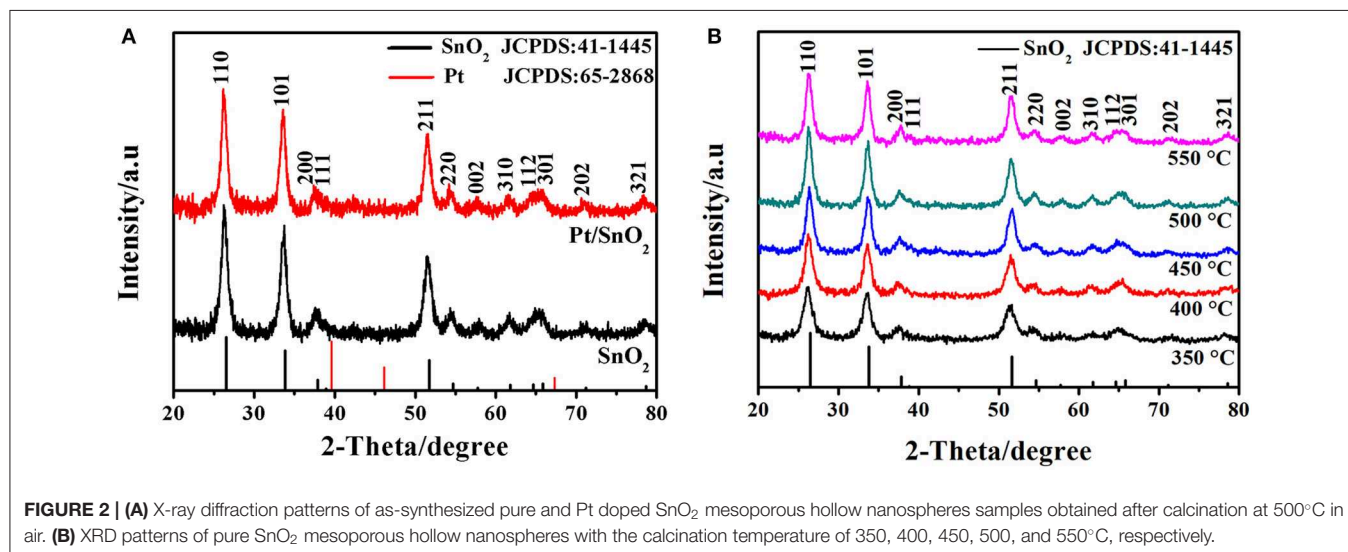
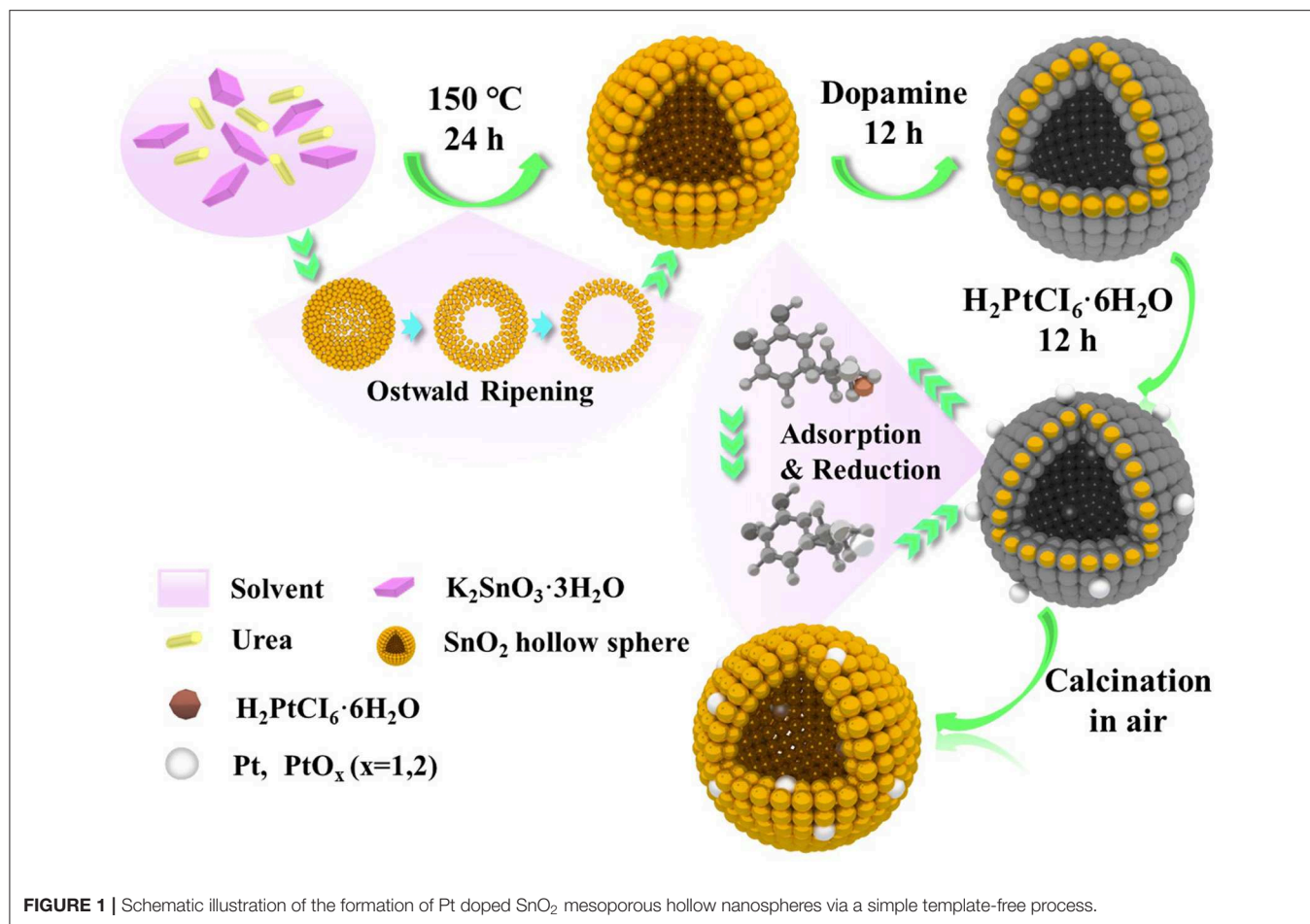


Figure 5A. Apart from the C 1s calibration peak at 284.78 eV, only peaks fitted to Sn, O, and Pt are observed in Pt doped SnO₂ samples, indicating the good monodispersity of the as-prepared Pt doped SnO₂ samples. The signal decomposed into Sn 3d_{5/2}

and Sn 3d_{3/2} (**Figure 5B**) two portions with peak located at 486.5 and 495.0 eV, respectively, which are typical characteristics of Sn⁴⁺ in tetragonal SnO₂. No shifts of the Sn 3d peaks between the singular SnO₂ and Pt doped SnO₂ nanomaterials were observed

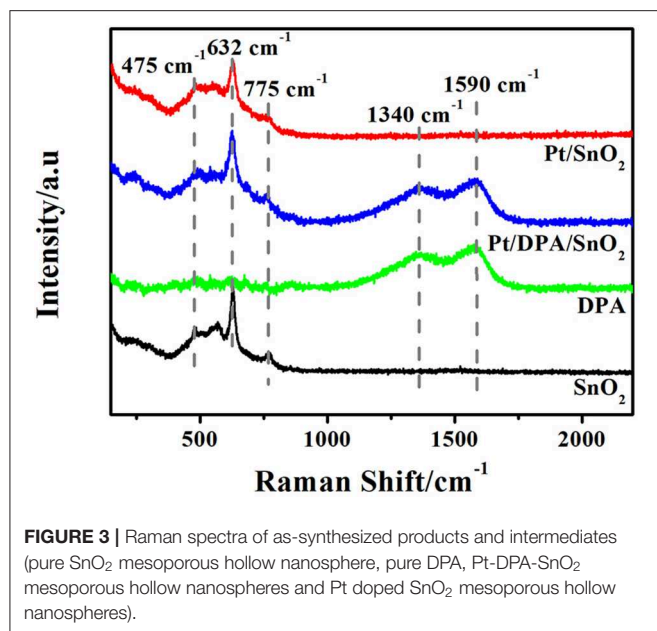


FIGURE 3 | Raman spectra of as-synthesized products and intermediates (pure SnO₂ mesoporous hollow nanosphere, pure DPA, Pt-DPA-SnO₂ mesoporous hollow nanospheres and Pt doped SnO₂ mesoporous hollow nanospheres).

mainly due to the low Pt dosage (Murata et al., 2013). The high-resolution XPS spectra of O 1s (**Figure 5C**) presents three peaks with binding energy at 530.2, 531.0, and 532.0 eV, which could be assigned to different chemical states of oxygen in the system: lattice oxygen (O²⁻) and absorbed oxygens (O⁻ and O₂⁻), respectively (Jeong et al., 2018b). Usually, lattice oxygens are pretty stable and have no benefit in improving sensitivity, in the meantime, the absorbed oxygens are very active, which play a key role in gas sensitivity (Liu et al., 2015). As **Figure 5D** shows, Pt peaks were not detected in the pure SnO₂ nanospheres. In contrast, five peaks were spited from XPS spectrum of Pt doped SnO₂ samples (Jang et al., 2015; Bulemo et al., 2018). Two main peaks observed at 75.00 and 78.35 eV fitted to PtO₂ (Kamble and Umarji, 2016), with a spin-orbit coupling energy between PtO₂ 4f_{7/2} and PtO₂ 4f_{5/2} of 3.35 eV. The peaks centered at 72.70 eV is suggested as assignable to PtO 4f_{7/2}. The two peaks at 71.50 and 74.80 eV correspond to Pt 4f_{7/2} and Pt 4f_{5/2} (Kim et al., 2016). A large proportion of Pt nanoparticles were oxidized to form PtO₂ at the annealing temperature ~500°C (Jang et al., 2015), caused the strong peaks of Pt⁴⁺, weak peaks of Pt and Pt²⁺.

To clearly investigate the surface adsorption properties of commercial, singular and Pt doped SnO₂ mesoporous hollow nanospheres, we carried out BET test (**Figure 6A**) and Barrett-Joyner-Halenda (BJH) analysis (**Table 1**). Nitrogen adsorption-desorption isotherms of the pure and Pt doped SnO₂ hollow nanospheres samples show typical type-IV curves with a hysteresis loop, demonstrating the uniform and large mesoporous structure of SnO₂ hollow nanospheres. In the contrast, commercial SnO₂ nanoparticles shows typical type-II curves. BET surface area of pure SnO₂ mesoporous hollow nanospheres (28.2 m²/g STP) is nearly four-folds larger than commercial SnO₂ (7.6 m²/g STP). Meanwhile, SnO₂ mesoporous hollow nanospheres with different Pt doped dosages how different surface area and pore size. 0.08 wt% Pt doped SnO₂

hollow nanospheres have the largest surface area (35.7 m²/g STP), while 0.16 wt% Pt doped SnO₂ hollow nanosphere shows a little lower surface area of 31.5 m²/g STP but has the biggest pore volume (0.12 cm³/g) and pore size (15.4 nm) (**Table 1**). These pores with large size are conducive to the facilitating diffusion of gaseous molecules (Zhou et al., 2015), and the big pore volume can provide high-density of active surface locations (Zhang et al., 2016).

Photoluminescence spectroscopy is a convenient and fast technique, which provides information about the types of oxygen vacancies in nanomaterials. PL emission spectra of the pure SnO₂ present three strong peaks at 425, 450, and 477 nm, and five weak peaks at 433, 490, 505, 529, and 561 nm at an excitation wavelength of 385 nm (**Figure 6B**). According to the literatures, the purple luminescence peak (425 nm) can be attributed to the luminescence center formed by the tin gap or dangling bond (Arik et al., 2011), the PL peaks at 433, 450, and 477 nm can be ascribed to crystal defects in SnO₂ matrix, the PL peaks appears at 490, 505, 529, and 561 nm which corresponds to green luminescence, and can be consider as singly charged oxygen vacancies in the material (Jean and Her, 2009). It is worth noting that the fluorescence intensity of Pt doped SnO₂ is lower than pure SnO₂, and the fluorescence intensity decreases gradually as the increases of platinum content, which can be attributed to the interaction of Pt metal and SnO₂. Owing to the stronger ability to capture electronics of Pt than SnO₂, the doped Pt can lead to reduction of donor type oxygen vacancies (Rani et al., 2007), thereby reducing the radiative recombination centers. Thus, the appearance of Pt and PtO₂ not only occupy material voids, reduce pore volume and pore size (shown by BET results), but also decrease in the number of oxygen vacancies.

Gas-Sensing Characteristics

Encouraged by the excellent structure of the synthesized SnO₂ and Pt doped SnO₂ nanomaterials, we further fabricated gas sensors based on commercial SnO₂ (S₁), pure SnO₂ mesoporous hollow spheres (S₂) and SnO₂ mesoporous hollow nanospheres with different Pt doped content (S₃–S₇), respectively, to systematically explore their application prospect in the detection of *L. monocytogenes*. Commercial non-mesoporous SnO₂ is employed as the reference for comparison. As previous studies investigated, the gas sensing characteristics depend upon the catalyst loading and dispersion. The insufficient loading of catalysts cannot reach the optimal catalytic effect, while, the excessive loading of catalysts on SnO₂ mesoporous hollow spheres causes saturation and aggregation of catalysts, leading to a poor sensing performance. Hence, we carefully varied the dosages range of catalysts (S₃: 0.08 wt%, S₄: 0.12 wt%, S₅: 0.16 wt%, S₆: 0.24 wt%, S₇: 0.48 wt%) to find the optimized dosage of catalysts.

Basically, working temperature affects the adsorption and desorption characteristics of target analytes and the charge transport features on the surface of semiconductors, thus affects the gas sensing properties (Li et al., 2019). Therefore, the operating temperature tests of sensors based on commercial SnO₂ particles, SnO₂ mesoporous hollow spheres and Pt doped SnO₂ mesoporous hollow spheres samples were firstly

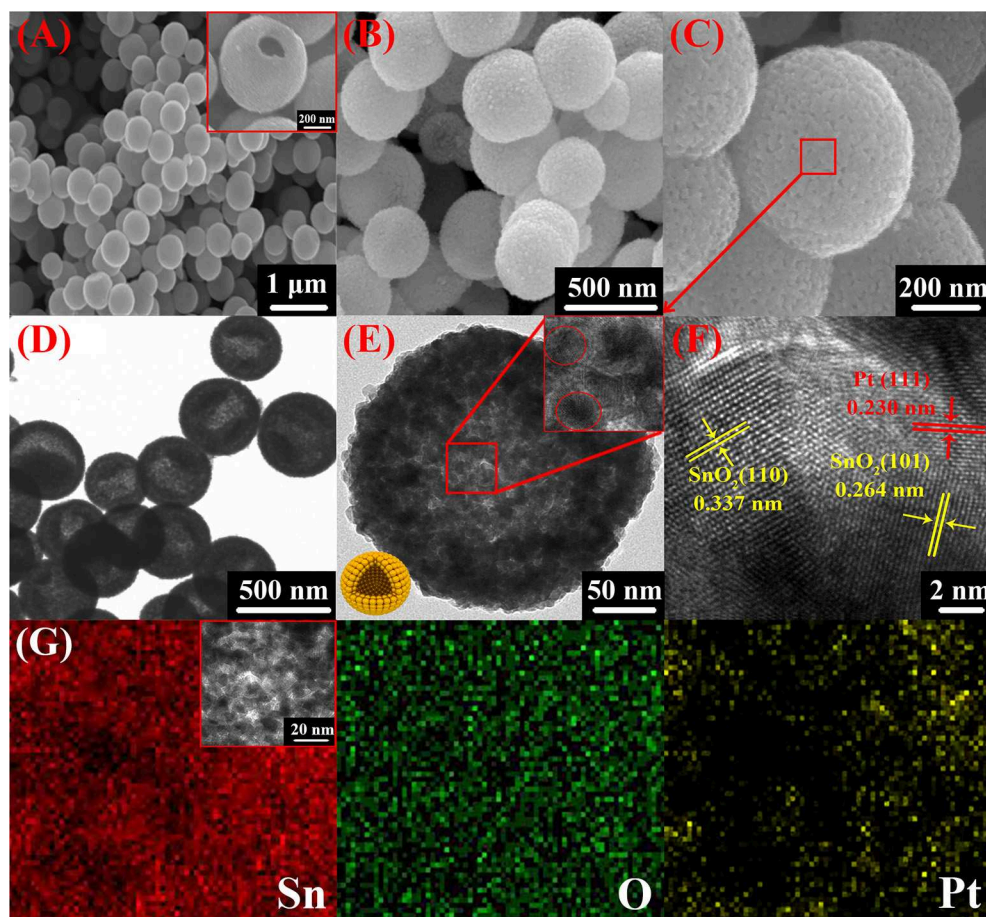


FIGURE 4 | SEM (A–C), TEM (D), and HRTEM (E,F) of 0.16 wt% Pt doped SnO₂ mesoporous hollow nanospheres; (G) elemental mappings of 0.16 wt% Pt doped SnO₂ mesoporous hollow nanospheres for Sn, O, and Pt.

carried out in 10 ppm 3-hydroxy-2-butanone over temperatures ranging from 200 to 400°C (**Figure 7A**). The gas response gradually increases as the working temperature increase from 200 to 250°C, then decreases as the further elevation in operating temperature. Hence, 250°C is considered as the optimum working temperature for further sensing observations. At the same time, it is obvious that the Pt doped samples possess much higher sensitivity, especially sensor S₅ based on 0.16 wt% Pt doped SnO₂ mesoporous hollow nanospheres. The gas response toward 10 ppm 3-hydroxy-2-butanone is greatly enhanced from 14.37 to 48.69 by the decoration of Pt.

The dynamic gas sensor response of different pure and Pt loading amount SnO₂ toward different concentrations of 3-hydroxy-2-butanone (0.5–20 ppm) at an operating temperature of 250°C were then measured and shown in **Figure 7B**. The gas sensing results of all the fabricated gas sensors show increasing continuously with the increment of 3-hydroxy-2-butanone concentration while decrease as the concentration fall from 20 to 0.5 ppm, indicate the excellent reversibility and repeatability. The results of S₂ sensor based on pure SnO₂ ($R_{\text{air}}/R_{\text{gas}} = 14.37$)

to 10 ppm of 3-hydroxy-2-butanone is almost 3 times higher than S₁ sensor based on commercial SnO₂ ($R_{\text{air}}/R_{\text{gas}} = 5.04$). Moreover, the gas sensor still has obvious response at 0.5 ppm 3-hydroxy-2-butanone concentration. Notably, the sensitivity can be increased by doping platinum. Among Pt decorated SnO₂ sensors, the S₅ sensor shows the best performance ($R_{\text{air}}/R_{\text{gas}} = 48.69$, 10 ppm) and excellent linearity with the 3-hydroxy-2-butanone concentration (**Figure 7C**). According to the results of BET and PL tests, the highest response is mainly attributed to effect of platinum particles: the incorporation of Pt and Pt oxide inhibited the agglomeration of SnO₂ particles and increased the specific surface area of the material then improves the sensitivity, however, excess Pt occupied the mesoporous space and even caused the decrease in oxygen vacancies, thereby reduced the response value (Singh and Singh, 2019). The response and recovery properties of sensors upon exposure to 10 ppm 3-hydroxy-2-butanone were also calculated from the sensing transients and the results were given in **Figure 7D**. The S₅ sensor based on 0.16 wt% Pt sensitized SnO₂ nanomaterials shows very low response (11 s) and recovery (20 s) times upon exposure to 3-hydroxy-2-butanone in those of commercial

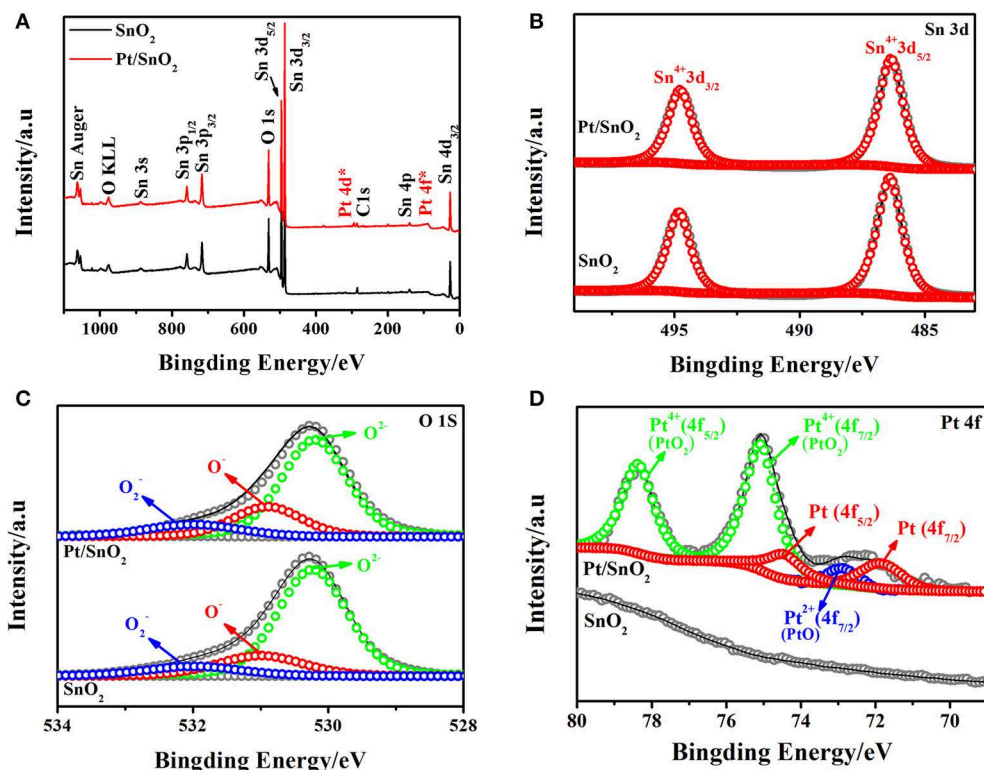


FIGURE 5 | (A) Survey, (B) Sn 3d high resolution XPS spectrum of as-synthesized pure and Pt doped SnO₂ mesoporous hollow nanospheres samples, (C) O 1s, (D) Pt 4f.

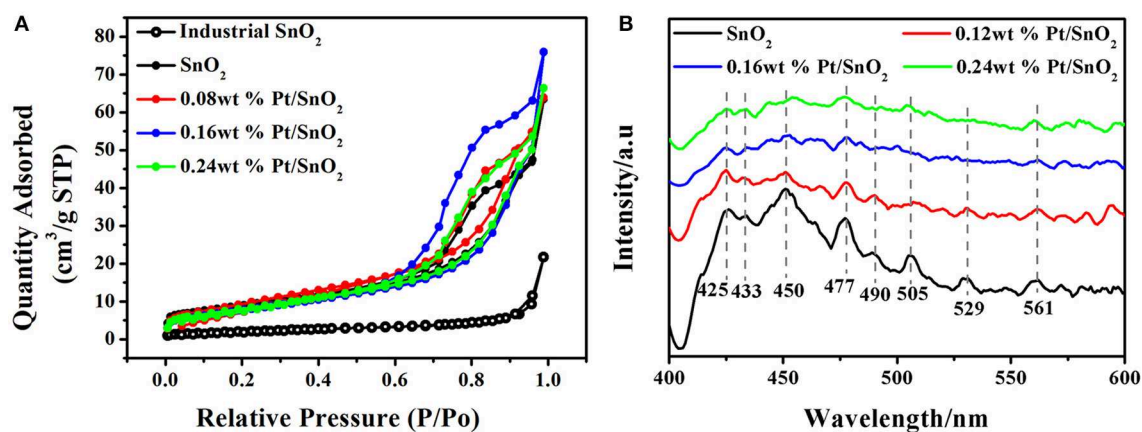


FIGURE 6 | (A) N₂ adsorption/desorption isotherms of commercial, pure SnO₂ mesoporous hollow nanospheres and Pt doped SnO₂ mesoporous hollow nanospheres. (B) PL spectra of as-synthesized pure SnO₂ mesoporous hollow nanospheres and Pt doped SnO₂ mesoporous hollow nanospheres.

SnO₂ (response/recovery: 22 s/21 s) and mesoporous hollow nanospheres (response/recovery: 18 s/20 s). The mesoporous hollow structure of SnO₂ nanosphere with a high specific surface and large pore size can offer substantial active reaction sites for sensing test (Li Y. et al., 2016; Chen et al., 2018) and facilitate the quick and easy diffusion of gas molecules within the mesoporous structure in S₅, resulting in the minimum

response-recovery duration of S₅ toward the target gas under the same conditions.

Practically, the sensor with high sensitivity and fast response speed cannot satisfy the requirement of accurate and efficient detection of 3-hydroxy-2-butanone in complex gas environment. Therefore, we investigated the sensitivities of commercial, pure and 0.16 wt% Pt doped SnO₂ mesoporous hollow nanospheres

based sensors. The response of S₁, S₂, and S₅ sensor in the presence of some common volatile organic compounds with a concentration of 10 ppm at 250°C, including acetone, ethanol, methanol, formaldehyde and ammonia, were shown in **Figure 8**. Obviously, sensor S₅ based on 0.16 wt% Pt doped SnO₂ mesoporous hollow nanospheres shows excellent selectivity to 3-hydroxy-2-butanone and less affected by other gases. Furthermore, four typical gases in exhaled *L. monocytogenes* breath, 2,3-butanedione, 3-methylbutanal, 2,5-dimethyl-pyrazine and benzaldehyde were also selected as interfering gases. The gas response of S₅ toward 3-hydroxy-2-butanone is roughly 10.5, 6.8, 6.5, and 3.5 times higher than that toward benzaldehyde, 2,3-butanedione, 2,5-dimethyl-pyrazine and 3-methylbutanal, respectively. These results clearly show that the S₅ sensor has

a good selectivity to the exhaled 3-hydroxy-2-butanone of *L. monocytogenes*. The highly selective properties of sensor are mainly attribute to the sensitization effect of Pt. The formation of p-n junction caused by Pt element can effectively increase the amount of electron transfer and thus increase the response (Jang et al., 2015). Meanwhile, the Pt element are capable of dissociating hydroxyl group and keto group, leading to selective detection of 3-hydroxy-2-butanone (Wu et al., 2011; Jeong et al., 2018b). All results shown above demonstrate that the S₅ gas sensor is suitable for the selective detection of the 3-hydroxy-2-butanone molecules in complex atmosphere.

Excellent repeatability and long-term stability are also requisite in actual detection. The repeatability of the S₅ sensor was recorded by exposing to 10 ppm of 3-hydroxy-2-butanone five times under the same conditions, and the response and recovery curves are shown in **Figure 9A**. The response level and response-recovery time in every test show no distinct difference, indicate that the as-fabricated 3-hydroxy-2-butanone sensor based on 0.16 wt% Pt doped SnO₂ hollow nanospheres has good repeatability. The results of stability test on the S₅ sensor to 10 ppm of 3-hydroxy-2-butanone show a neglectable change during the 5-week testing process (**Figure 9B**), reflecting the good long-term stability of 0.16 wt% Pt activated SnO₂ sensors.

TABLE 1 | BET Surface Area of as-synthesized pure and Pt doped SnO₂ mesoporous hollow nanospheres.

Sample	Commercial SnO ₂		0.08 wt% Pt-SnO ₂	0.16 wt% Pt-SnO ₂	0.24 wt% Pt-SnO ₂
BET surface area (m ² /g)	7.6	28.2	35.7	31.5	29.7
Pore volume (cm ³ /g)	0.03	0.07	0.09	0.12	0.10
Pore size (nm)	18.1	9.4	10.2	15.4	12.7

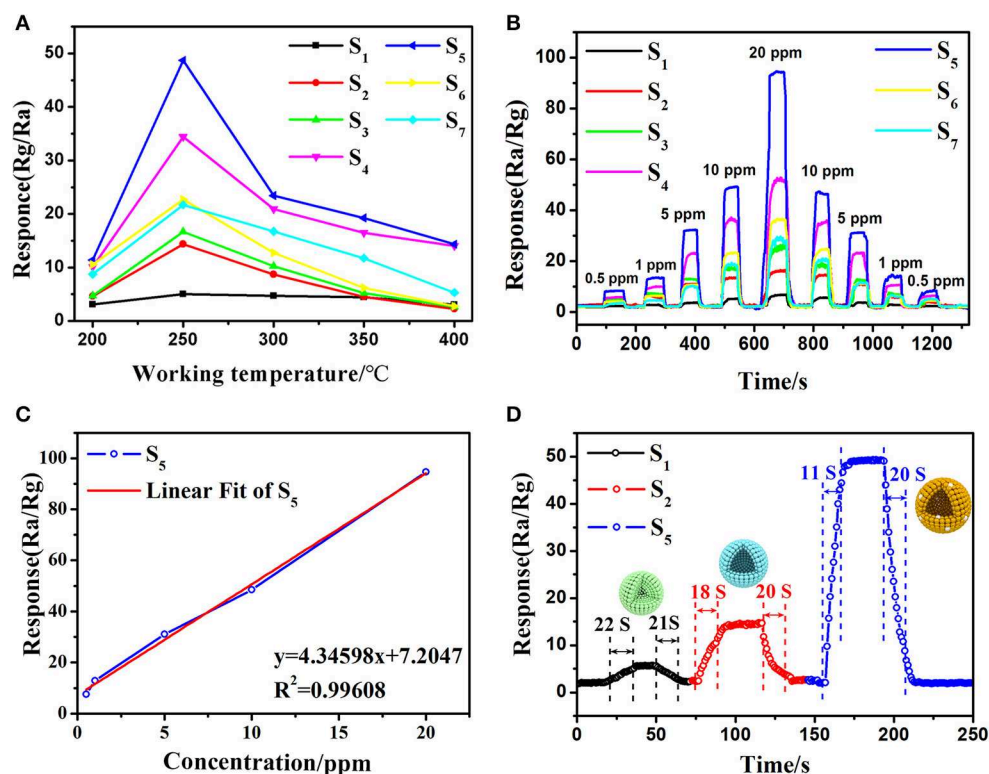
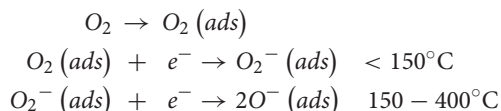


FIGURE 7 | Typical response curve and variations of the sensors base on different samples: **(A)** response of the gas sensors S₁–S₇ versus different operating temperature (200–400°C) to 10 ppm 3-hydroxy-2-butanone, **(B)** dynamic 3-hydroxy-2-butanone (0.5–20 ppm) sensing transients of the gas sensors S₁–S₇, **(C)** the relationship between gas sensor S₅ and concentration of 3-hydroxy-2-butanone gas and **(D)** response/recovery curves of gas sensor S₅ (gas sensor S₁ and S₂ based on commercial SnO₂ particles and as-synthesized pure SnO₂ mesoporous hollow nanospheres, gas sensor S₃–S₇ based on 0.08, 0.12, 0.16, 0.24, 0.48 wt% Pt doped SnO₂ mesoporous hollow nanospheres, respectively).

Sensitization Mechanism of 3-Hydroxy-2-Butanone Sensing

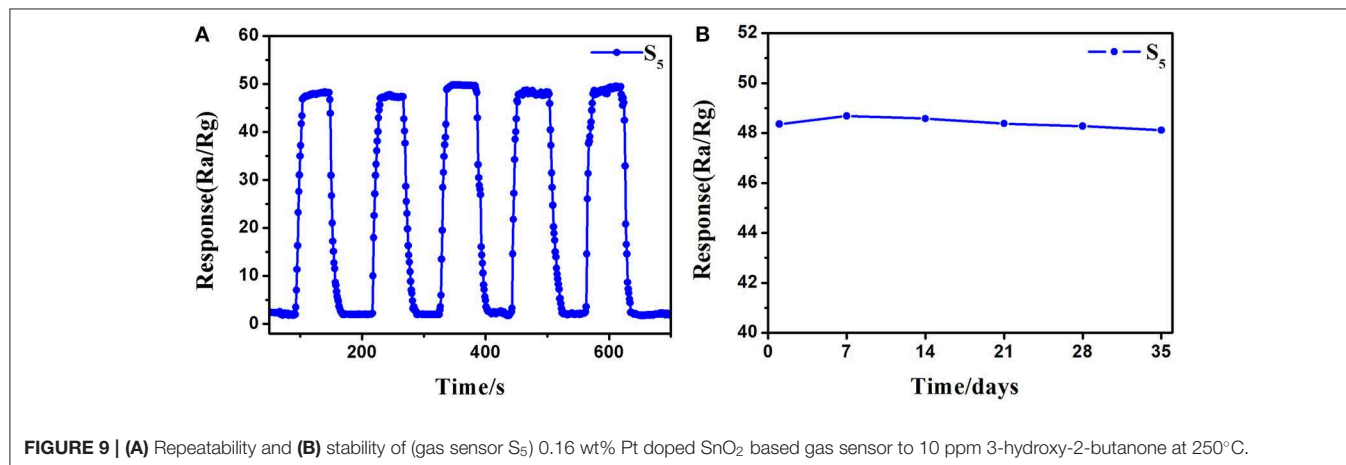
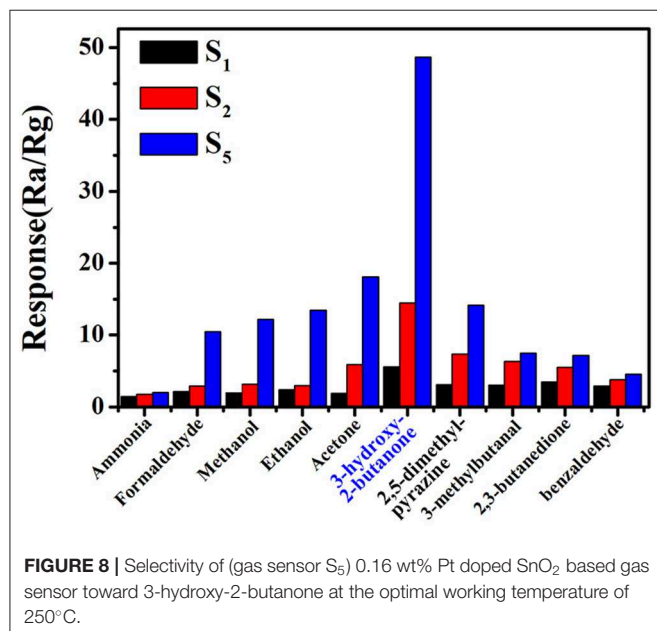
On the basis of comprehensive analyses of experimental results, the enhanced sensing performances may be attributed to the unique mesoporous hollow nanosphere structure and the doped of Pt nanoparticles. The detection mechanism of the as-fabricated 3-hydroxy-2-butanone sensor is on account of the change in conductance of the semiconductor metal oxide nanomaterial when reacted with the target gas adsorbed on the sensing layer, which belongs to the surface-controlled mode (Wang L. et al., 2016). As shown in **Figure 10**, the schematic illustration presents the sensing mechanism and energy band levels of the pure and Pt doped SnO₂ sensors. When the gas sensors are exposed to the air (left part of **Figure 10**), oxygen molecules are adsorbed on the SnO₂ mesoporous hollow nanosphere and generate adsorbed oxygen ions (O₂⁻ and O⁻) by trapping electrons from the

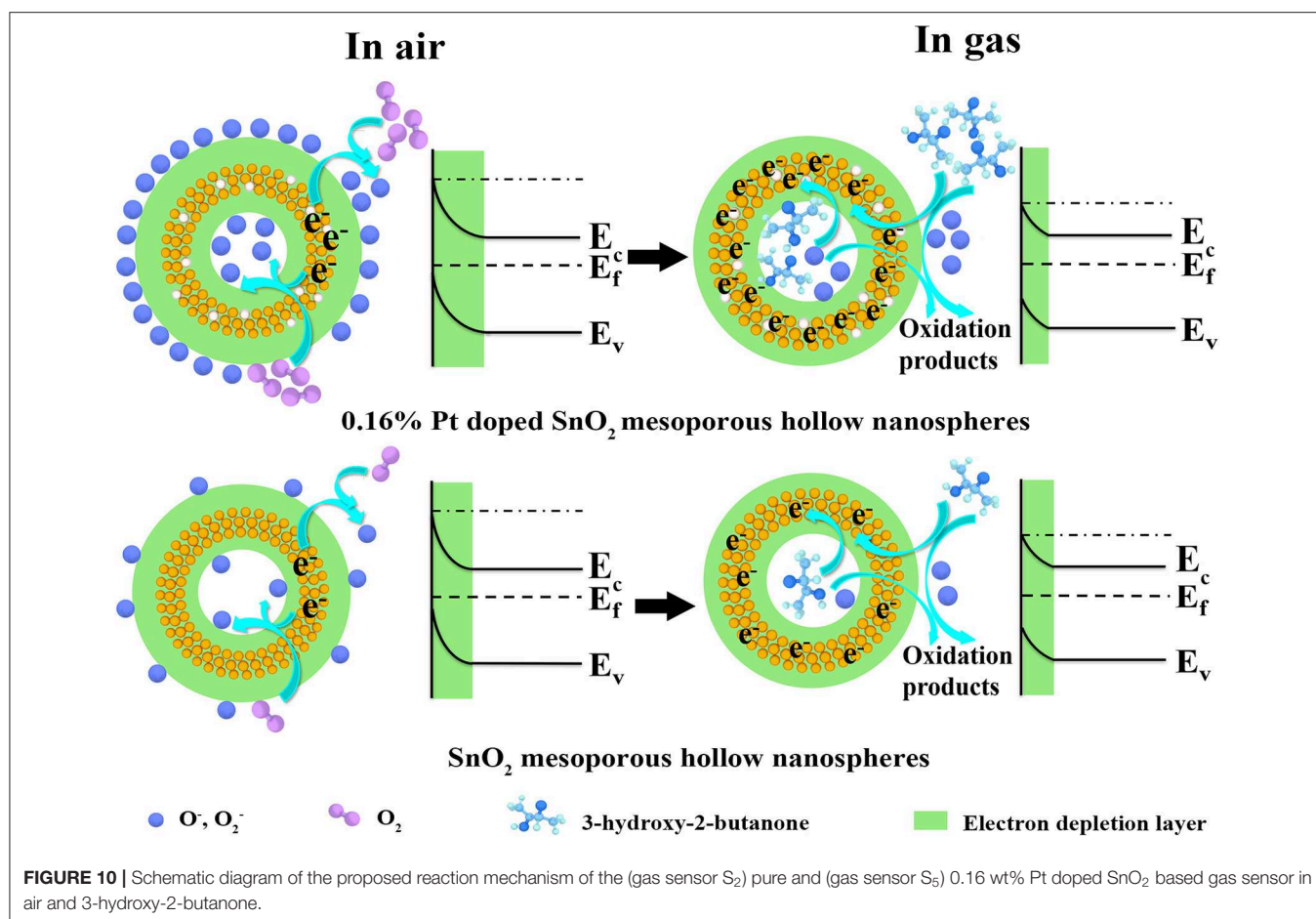
conduction band of SnO₂ semiconductor, causing the formation of a thick electron depletion layer and low conductance of the sensor (Zhang D. et al., 2019). The chemical reactions involved in this process can be summarized as follows:



As shown in the right part of **Figure 10**, once the target gas is injected, adsorbed oxygens react with the 3-hydroxy-2-butanone molecules immediately and oxidize such reductive molecules to oxidation products. As a result, adsorbed oxygens release electrons back to Pt doped SnO₂ hollow nanospheres, leading to reduction of electron depletion layer and a low conductance (Yang et al., 2018).

On the basis of above theories, the improved sensing performance of the Pt doped SnO₂ sensing materials can be concluded in two following aspects: (1) From the morphology structure aspect, the 0.16 wt% Pt doped SnO₂ mesoporous hollow nanosphere with high specific surface area provides a mass of active sites both on the surface for oxygen molecules adsorb as well as sensitization agent to decorate and show their function (Hu et al., 2018). (2) As for Pt doping aspect, previous studies have shown that Pt nanocatalysts exist as oxidized forms (PtO₂) at the annealing temperature ~500°C (Jang et al., 2015) which are p-type material, leading to the formation of p-n junction at the interface of SnO₂ and PtO₂ (Jeong et al., 2018a; Qiu et al., 2018). Therefore, this interaction between PtO₂ and SnO₂ play a significant role when the Pt doped SnO₂ nanomaterials are exposed to 3-hydroxy-2-butanone, which expands the electron depletion region on SnO₂ (**Figure 10**) and cause an increase in conductivity (Shao et al., 2016). Moreover, owing to the “spillover effect” of Pt element (Liu et al., 2017), oxygen molecules will be more easily absorbed on the surface of Pt and PtO₂ compare with pristine SnO₂ (Peng et al., 2018), leading to the promotion of sensing reaction between the tested gas molecules and adsorbed surface oxygen species. Under the above synergy between Pt dopant and SnO₂, the conductivity of the Pt doped





SnO₂ gas sensor changes more greatly as the 3-hydroxy-2-butanone gases are in or out, leading to a higher response than the pristine SnO₂. From all the above, the Pt doped SnO₂ mesoporous hollow nanosphere sensor shows excellent 3-hydroxy-2-butanone sensing property.

CONCLUSIONS

In summary, well-crystalline SnO₂ mesoporous hollow spheres nanomaterials have been synthesized via a simple one-step template-free and robust method by using K₂SnO₃·3H₂O as a precursor in the presence of precipitant urea, followed by doping with Pt by using H₂PtCl₆·6H₂O as Pt source in the presence of reducing agent dopamine. The obtained 0.16 wt% Pt doped SnO₂ mesoporous hollow nanospheres have high specific surface areas (31.5 m²/g) and large aperture of 15.3 nm. As a result of the doping of Pt element and the uniform mesoporous hollow structure with high surface areas, 0.16 wt% Pt doped SnO₂ based sensors exhibit superior sensitivity, excellent long-term stability and highly selective detection to 3-hydroxy-2-butanone, at a wide range concentration. Specifically, it displays rapid response (response/recovery: 11 s/20 s), superior sensitivity ($R_{\text{air}}/R_{\text{gas}} = 48.69$) toward low concentration of 3-hydroxy-2-butanone (10 ppm) at a working temperature of 250°C. Detailed analysis

demonstrates that the improved 3-hydroxy-2-butanone sensing characteristics are possibly due to the “sensitization effect” driven by Pt nanoparticles platinum tungsten oxide. This 0.16 wt% Pt doped SnO₂ mesoporous hollow nanosphere based gas sensor with superior 3-hydroxy-2-butanone sensitivity provide a great commitment for developing a novel, simple, accurate and rapid volatile organic compound portable sensor for the supervision of foodborne bacteria in food, environment, clinical, and communal samples.

DATA AVAILABILITY STATEMENT

All datasets generated for this study are included in the article/supplementary material.

AUTHOR CONTRIBUTIONS

YZhu and HC contributed to the experimental design. YP and YZha contributed to the data analysis and interpretation, manuscript writing, and manuscript revision. TN and HL contributed to the material synthesis and characterizations, and data acquisition. All authors reviewed the manuscript and approved the final version.

FUNDING

This work was financially supported by the National Natural Science Foundation of China (31701678), the Key Project of Shanghai Agriculture Prosperity through

Science and Technology (2019-02-08-00-15-F01147), the Key Science and Technology Project of Henan (No. 172102310586), China Postdoctoral Science Foundation (2018T110338). The authors sincerely thank all the panelists for experimental support.

REFERENCES

- Arik, K., Simanta, K., and Amitava, P. (2011). Surface defect-related luminescence properties of SnO₂ nanorods and nanoparticles. *J. Phys. Chem. C* 115, 118–124. doi: 10.1021/jp110313b
- Audrain, B., Farag, M. A., Ryu, C. M., and Ghigo, J. M. (2015). Role of bacterial volatile compounds in bacterial biology. *FEMS Microbiol. Rev.* 39, 222–233. doi: 10.1093/femsre/fuu013
- Bernsmann, F., Ball, V., Addiego, F., Ponche, A., Michel, M., Gracio, J. J., et al. (2011). Dopamine-melanin film deposition depends on the used oxidant and buffer solution. *Langmuir* 27, 2819–2825. doi: 10.1021/la104981s
- Bulemo, P. M., Cho, H. J., Kim, D. H., and Kim, I. D. (2018). Facile synthesis of pt-functionalized Meso/Macroporous SnO₂ hollow spheres through in situ templating with SiO₂ for H₂S sensors. *ACS Appl. Mater. Interfaces* 10, 18183–18191. doi: 10.1021/acsami.8b00901
- Carlson, K., Misra, M., and Mohanty, S. (2018). Developments in micro- and nanotechnology for foodborne pathogen detection. *Foodborne Pathog. Dis.* 15, 16–25. doi: 10.1089/fpd.2017.2309
- Chen, J., Archer, L. A., and Lou, X. (2011). SnO₂ hollow structures and TiO₂ nanosheets for lithium-ion batteries. *J. Mater. Chem.* 21, 9912–9933. doi: 10.1039/c0jm04163g
- Chen, J., and Lou, X. (2013). SnO₂-based nanomaterials: synthesis and application in lithium-ion batteries. *Small* 9, 1877–1893. doi: 10.1002/sml.201202601
- Chen, J., Tang, J., Shi, H., Tang, C., and Zhang, R. (2017). Characteristics of volatile organic compounds produced from five pathogenic bacteria by headspace-solid phase micro-extraction/gas chromatography-mass spectrometry. *J. Basic Microbiol.* 57, 228–237. doi: 10.1002/jobm.201600505
- Chen, M., Lu, Q., Jiang, S., Huang, C., Wang, X., Wu, B., et al. (2018). MnO₂ nanosheets grown on the internal/external surface of N-doped hollow porous carbon nanospheres as the sulfur host of advanced lithium-sulfur batteries. *Chem. Eng. J.* 335, 831–842. doi: 10.1016/j.cej.2017.11.039
- Chen, Z., Hu, K., Yang, P., Fu, X., Wang, Z., Yang, S., et al. (2019). Hydrogen sensors based on Pt-decorated SnO₂ nanorods with fast and sensitive room-temperature sensing performance. *J. Alloys Compd.* 811:152086. doi: 10.1016/j.jallcom.2019.152086
- Cheng, C., Peng, Y., Bai, J., Zhang, X., Liu, Y., Fan, X., et al. (2014). Rapid detection of *Listeria monocytogenes* in milk by self-assembled electrochemical immunosensor. *Sensors Actuat. B Chem.* 190, 900–906. doi: 10.1016/j.snb.2013.09.041
- Ciesielski, C. A., Swaminathan, B., and Broome, C. V. (1987). *Listeria monocytogenes*—a foodborne pathogen. *Clin. Microbiol. Newsl.* 9, 149–156. doi: 10.1016/0196-4399(87)90051-1
- D'Arienzo, M., Armelao, L., Cacciamani, A., Mari, C. M., Polizzi, S., Ruffo, R., et al. (2010). One-step preparation of SnO₂ and Pt-Doped SnO₂ as inverse opal thin films for gas sensing. *Chem. Mater.* 22, 4083–4089. doi: 10.1021/cm100866g
- Farber, J. M., Coates, F., and Dale, E. (1992). Minimum water activity requirements for the growth of *Listeria monocytogenes*. *Lett. Appl. Microbiol.* 15, 103–105. doi: 10.1111/j.1472-765X.1992.tb00737.x
- Hu, W., Wan, L., Jian, Y., Ren, C., Jin, K., Su, X., et al. (2018). Electronic noses: from advanced materials to sensors aided with data processing. *Adv. Mater. Technol.* 4:1800488. doi: 10.1002/admt.201800488
- Hua, Z., Tian, C., Huang, D., Yuan, W., Zhang, C., Tian, X., et al. (2018). Power-law response of metal oxide semiconductor gas sensors to oxygen in presence of reducing gases. *Sensors Actuat. B: Chem.* 267, 510–518. doi: 10.1016/j.snb.2018.04.002
- Jang, J. S., Kim, S. J., Choi, S. J., Kim, N. H., Hakim, M., Rothschild, A., et al. (2015). Thin-walled SnO(2) nanotubes functionalized with Pt and Au catalysts via the protein templating route and their selective detection of acetone and hydrogen sulfide molecules. *Nanoscale* 7, 16417–16426. doi: 10.1039/C5NR04487A
- Jean, S. T., and Her, Y. C. (2009). Synthesis of Sb-additivated SnO₂ nanostructures and dependence of photoluminescence properties on Sb addition concentration. *J. Appl. Phys.* 105:024310. doi: 10.1063/1.3068487
- Jeong, Y. J., Koo, W. T., Jang, J. S., Kim, D. H., Cho, H. J., and Kim, I. D. (2018a). Chitosan-templated Pt nanocatalyst loaded mesoporous SnO₂ nanofibers: a superior chemiresistor toward acetone molecules. *Nanoscale* 10, 13713–13721. doi: 10.1039/C8NR03242D
- Jeong, Y. J., Koo, W. T., Jang, J. S., Kim, D. H., and Kim, M. H. (2018b). Nanoscale PtO₂ catalysts-loaded SnO₂ multichannel nanofibers toward highly sensitive acetone sensor. *ACS Appl. Mater. Interfaces* 10, 2016–2025. doi: 10.1021/acsami.7b16258
- Kamble, V. B., and Umarji, A. M. (2016). Achieving selectivity from the synergistic effect of Cr and Pt activated SnO₂ thin film gas sensors. *Sensors Actuat. B Chem.* 236, 208–217. doi: 10.1016/j.snb.2016.05.119
- Kim, B. Y., Cho, J. S., Yoon, J. W., Na, C. W., Lee, C. S., Ahn, J. H., et al. (2016). Extremely sensitive ethanol sensor using Pt-doped SnO₂ hollow nanospheres prepared by Kirkendall diffusion. *Sensors Actuat. B Chem.* 234, 353–360. doi: 10.1016/j.snb.2016.05.002
- Lee, H., Dellatore, S. M., Miller, W. M., and Messersmith, P. B. (2007). Mussel-inspired surface chemistry for multifunctional coatings. *Science* 318, 426–430. doi: 10.1126/science.1147241
- Li, G., Cheng, Z., Xiang, Q., Yan, L., Wang, X., and Xu, J. (2019). Bimetal PdAu decorated SnO₂ nanosheets based gas sensor with temperature-dependent dual selectivity for detecting formaldehyde and acetone. *Sensors Actuat. B Chem.* 283, 590–601. doi: 10.1016/j.snb.2018.09.117
- Li, S., Lu, Z., Yang, Z., and Chu, X. (2014). The sensing mechanism of Pt-doped SnO₂ surface toward CO: A first-principle study. *Sensors Actuat. B Chem.* 202, 83–92. doi: 10.1016/j.snb.2014.05.071
- Li, Y., Deng, D., Chen, N., Xing, X., Xiao, X., and Wang, Y. (2016). Enhanced methanol sensing properties of SnO₂ microspheres in a composite with Pt nanoparticles. *RSC Adv.* 6, 83870–83879. doi: 10.1039/C6RA16636A
- Li, Z., Zhang, J., Guan, B., Wang, D., Liu, L., and Lou, X. (2016). A sulfur host based on titanium monoxide@carbon hollow spheres for advanced lithium-sulfur batteries. *Nat. Commun.* 7:13065. doi: 10.1038/ncomms13065
- Liu, X., Chen, N., Han, B., Xiao, X., Chen, G., Djerdj, I., et al. (2015). Nanoparticle cluster gas sensor: Pt activated SnO₂ nanoparticles for NH₃ detection with ultrahigh sensitivity. *Nanoscale* 7, 14872–14880. doi: 10.1039/C5NR03585F
- Liu, Y., Huang, J., Yang, J., and Wang, S. (2017). Pt nanoparticles functionalized 3D SnO₂ nanoflowers for gas sensor application. *Solid State Electron.* 130, 20–27. doi: 10.1016/j.sse.2017.01.005
- Lou, X., Wang, Y., Yuan, C., Lee, J., and Archer, L. A. (2006). Template-free synthesis of SnO₂ hollow nanostructures with high lithium storage capacity. *Adv. Mater.* 18, 2325–2329. doi: 10.1002/adma.200600733
- Ma, J., Ren, Y., Zhou, X., Liu, L., Zhu, Y., Cheng, X., et al. (2018). Pt nanoparticles sensitized ordered mesoporous WO₃ semiconductor: gas sensing performance and mechanism study. *Adv. Funct. Mater.* 28:1705268. doi: 10.1002/adfm.201705268
- McFarland, E. W., and Metiu, H. (2013). Catalysis by Doped Oxides. *Chem. Rev.* 113, 4391–4427. doi: 10.1021/cr300418s
- Murata, N., Suzuki, T., Kobayashi, M., Togoh, F., and Asakura, K. (2013). Characterization of Pt-doped SnO₂ catalyst for a high-performance micro gas sensor. *Phys. Chem. Chem. Phys.* 15, 17938–17946. doi: 10.1039/c3cp52490f
- Nda-Umar, U., Ramli, I., Taufiq-Yap, Y., and Muhamad, E. (2018). An overview of recent research in the conversion of glycerol into biofuels, fuel additives and other bio-based chemicals. *Catalysts* 9:15. doi: 10.3390/catal9010015
- Oh, Y. J., and Jeong, K. H. (2014). Optofluidic SERS chip with plasmonic nanoprobes self-aligned along microfluidic channels. *Lab Chip* 14, 865–868. doi: 10.1039/c3lc51257f

- Panahi, Y., Mellatyar, H., Farshbaf, M., Sabet, Z., Fattahi, T., and Akbarzadehe, A. (2018). Biotechnological applications of nanomaterials for air pollution and water/wastewater treatment. *Mater. Tdy Proc.* 5, 15550–15558. doi: 10.1016/j.matpr.2018.04.162
- Peng, R., Chen, J., Nie, X., Li, D., Si, P., Feng, J., et al. (2018). Reduced graphene oxide decorated Pt activated SnO₂ nanoparticles for enhancing methanol sensing performance. *J. Alloys Compd.* 762, 8–15. doi: 10.1016/j.jallcom.2018.05.177
- Qiu, Z., Hua, Z., Li, Y., Wang, M., Huang, D., Tian, C., et al. (2018). Acetone sensing properties and mechanism of Rh-Loaded WO₃ nanosheets. *Front Chem.* 6:385. doi: 10.3389/fchem.2018.00385
- Radoshevich, L., and Cossart, P. (2018). *Listeria monocytogenes*: towards a complete picture of its physiology and pathogenesis. *Nat. Rev. Microbiol.* 16, 32–46. doi: 10.1038/nrmicro.2017.126
- Rani, S., Roy, S. C., Karar, N., and Bhatnagar, M. C. (2007). Structure, microstructure and photoluminescence properties of Fe doped SnO₂ thin films. *Solid State Commun.* 141, 214–218. doi: 10.1016/j.ssc.2006.10.036
- Shao, S., Wu, H., Jiang, F., Wang, S., Wu, T., Lei, Y., et al. (2016). Regulable switching from p- to n-type behavior of ordered nanoporous Pt-SnO₂ thin films with enhanced room temperature toluene sensing performance. *RSC Adv.* 6, 22878–22888. doi: 10.1039/C5RA24736E
- Singh, G., and Singh, R. C. (2019). Synthesis, characterization and gas sensing properties of ga-doped SnO₂ nanostructures. *J. Electron. Mater.* 48, 4478–4490. doi: 10.1007/s11664-019-07231-5
- Välimäa, A. L., Tilsala-Timisjärvi, A., and Virtanen, E. (2015). Rapid detection and identification methods for *Listeria monocytogenes* in the food chain—a review. *Food Control* 55, 103–114. doi: 10.1016/j.foodcont.2015.02.037
- Wang, D., Niu, W., Tan, M., Wu, M., Zheng, X., Li, Y., et al. (2014). Pt nanocatalysts supported on reduced graphene oxide for selective conversion of cellulose or cellobiose to sorbitol. *Chem. Sustain. Chem.* 7, 1398–1406. doi: 10.1002/cssc.201301123
- Wang, K., Zhao, T., Lian, G., Yu, Q., Luan, C., Wang, Q., et al. (2013). Room temperature CO sensor fabricated from Pt-loaded SnO₂ porous nanosolid. *Sensors Actuatur. B Chem.* 184, 33–39. doi: 10.1016/j.snb.2013.04.054
- Wang, L., Wang, Y., Yu, K., Wang, S., Zhang, Y., and Wei, C. (2016). A novel low temperature gas sensor based on Pt-decorated hierarchical 3D SnO₂ nanocomposites. *Sensors Actuatur. B: Chem.* 232, 91–101. doi: 10.1016/j.snb.2016.02.135
- Wang, Y., Li, Y., Yang, J., Ruan, J., and Sun, C. (2016a). Microbial volatile organic compounds and their application in microorganism identification in foodstuff. *Trends in Anal. Chem.* 78, 1–16. doi: 10.1016/j.trac.2015.08.010
- Wang, Y., Yu, L., and Lou, X. (2016b). Synthesis of highly uniform molybdenum-glycerate spheres and their conversion into hierarchical MoS₂ hollow nanospheres for lithium-ion batteries. *Angew. Chem. Int. Ed Engl.* 55, 7423–7426. doi: 10.1002/anie.201601673
- Wu, Y., Chen, K., Pan, D., Zhu, J., Wu, B., and Shen, Y. (2011). Liquid-liquid equilibria of water+3-hydroxy-2-butanone+ethyl ethanoate. *Fluid Phase Equilib.* 305, 101–105. doi: 10.1016/j.fluid.2011.03.004
- Xue, D., Wang, P., Zhang, Z., and Wang, Y. (2019). Enhanced methane sensing property of flower-like SnO₂ doped by Pt nanoparticles: a combined experimental and first-principle study. *Sensors Actuatur. B Chem.* 296. doi: 10.1016/j.snb.2019.126710
- Yang, L., Wang, Z., Zhou, X., Wu, X., Han, N., and Chen, Y. (2018). Synthesis of Pd-loaded mesoporous SnO₂ hollow spheres for highly sensitive and stable methane gas sensors. *RSC Adv.* 8, 24268–24275. doi: 10.1039/C8RA03242D
- Yao, M., Ding, F., Cao, Y., Hu, P., Fan, J., Lu, C., et al. (2014). Sn doped ZnO layered porous nanocrystals with hierarchical structures and modified surfaces for gas sensors. *Sensors Actuatur. B Chem.* 201, 255–265. doi: 10.1016/j.snb.2014.04.078
- Yu, Y., Sun, X., Liu, Y., Pan, Y., and Zhao, Y. (2015). Odor fingerprinting of *Listeria monocytogenes* recognized by SPME-GC-MS and E-nose. *Can. J. Microbiol.* 61, 367–372. doi: 10.1139/cjm-2014-0652
- Zhang, D., Fan, Y., Li, G., Ma, Z., Wang, X., Cheng, Z., et al. (2019). Highly sensitive BTEX sensors based on hexagonal WO₃ nanosheets. *Sensors Actuatur. B Chem.* 293, 23–30. doi: 10.1016/j.snb.2019.04.110
- Zhang, H., Noonan, O., Huang, X., Yang, Y., Xu, C., Zhou, L., et al. (2016). Surfactant-free assembly of mesoporous carbon hollow spheres with large tunable pore sizes. *ACS Nano.* 10, 4579–4586. doi: 10.1021/acsnano.6b00723
- Zhang, Z., Zhou, J., and Du, X. (2019). Electrochemical biosensors for detection of foodborne pathogens. *Micromachines* 10:222. doi: 10.3390/mi10040222
- Zhao, X., Li, M., and Xu, Z. (2018). Detection of foodborne pathogens by surface enhanced raman spectroscopy. *Front. Microbiol.* 9:1236. doi: 10.3389/fmicb.2018.01236
- Zhou, D., Yang, L., Yu, L., Kong, J., Yao, X., Liu, W., et al. (2015). Fe/N/C hollow nanospheres by Fe (III)-dopamine complexation-assisted one-pot doping as nonprecious-metal electrocatalysts for oxygen reduction. *Nanoscale* 7, 1501–1509. doi: 10.1039/C4NR06366J
- Zhu, Y., Wang, D., Zhang, L., Sun, F., Xu, J., Jiang, S., et al. (2013). In situ-controlled growth of well-dispersed Au nanoparticles inside the channels of SBA-15 using a simple, bio-inspired method for surface-enhanced Raman spectroscopy. *RSC Adv.* 3, 10154–10157. doi: 10.1039/c3ra41338a
- Zhu, Y., Zhao, Y., Ma, J., Cheng, X., Xie, J., Xu, P., et al. (2017). Mesoporous tungsten oxides with crystalline framework for highly sensitive and selective detection of foodborne pathogens. *J. Am. Chem. Soc.* 139, 10365–10373. doi: 10.1021/jacs.7b04221
- Zhu, Z., Zheng, L., Zheng, S., Chen, J., Liang, M., Tian, Y., et al. (2018). Cr doped WO₃ nanofibers enriched with surface oxygen vacancies for highly sensitive detection of the 3-hydroxy-2-butanone biomarker. *J. Mater. Chem. A* 6, 21419–21427. doi: 10.1039/C8TA08670B

Conflict of Interest: The authors declare that the research was conducted in the absence of any commercial or financial relationships that could be construed as a potential conflict of interest.

Copyright © 2019 Cai, Liu, Ni, Pan, Zhao and Zhu. This is an open-access article distributed under the terms of the Creative Commons Attribution License (CC BY). The use, distribution or reproduction in other forums is permitted, provided the original author(s) and the copyright owner(s) are credited and that the original publication in this journal is cited, in accordance with accepted academic practice. No use, distribution or reproduction is permitted which does not comply with these terms.



Exonuclease III-Regulated Target Cyclic Amplification-Based Single Nucleotide Polymorphism Detection Using Ultrathin Ternary Chalcogenide Nanosheets

Yanling Hu^{1,2†}, Chaoliang Tan^{3†}, Xin Lin⁴, Zhuangchai Lai³, Xiao Zhang³, Qipeng Lu³, Ning Feng², Dongliang Yang^{2,5*} and Lixing Weng^{2*}

¹ School of Electrical and Control Engineering, Nanjing Polytechnic Institute, Nanjing, China, ² Jiangsu Key Laboratory for Biosensors, Institute of Advanced Materials (IAM), Nanjing University of Posts and Telecommunications, Nanjing, China, ³ School of Materials Science and Engineering, Nanyang Technological University, Singapore, Singapore, ⁴ School of Ophthalmology and Optometry, Eye Hospital, Wenzhou Medical University, Wenzhou, China, ⁵ School of Physical and Mathematical Sciences, Nanjing Tech University (NanjingTech), Nanjing, China

OPEN ACCESS

Edited by:

Mingshui Yao,
Kyoto University, Japan

Reviewed by:

Dianping Tang,
Fuzhou University, China
Hui Xu,
Ludong University, China

*Correspondence:

Dongliang Yang
yangdl1023@njtech.edu.cn
Lixing Weng
lxweng@njupt.edu.cn

[†]These authors have contributed
equally to this work

Specialty section:

This article was submitted to
Nanoscience,
a section of the journal
Frontiers in Chemistry

Received: 16 October 2019

Accepted: 19 November 2019

Published: 06 December 2019

Citation:

Hu Y, Tan C, Lin X, Lai Z, Zhang X,
Lu Q, Feng N, Yang D and Weng L
(2019) Exonuclease III-Regulated
Target Cyclic Amplification-Based
Single Nucleotide Polymorphism
Detection Using Ultrathin Ternary
Chalcogenide Nanosheets.
Front. Chem. 7:844.
doi: 10.3389/fchem.2019.00844

Herein, we report that the ternary chalcogenide nanosheet exhibits different affinity toward oligonucleotides with different lengths and efficiently quenches the fluorescence of dye-labeled DNA probes. Based on these findings, as a proof-of-concept application, the ternary chalcogenide nanosheet is used as a target cyclic amplification biosensor, showing high specificity in discriminating single-base mismatch. This simple strategy is fast and sensitive for the single nucleotide polymorphism detection. Ultralow detection limit of unlabeled target (250 fM) and high discrimination ratio (5%) in the mixture of perfect match (mutant-type) and single-base mismatch (wild-type) target are achieved. This sensing method is extensively compatible for the single nucleotide polymorphism detection in clinical samples, making it a promising tool for the mutation-based clinical diagnostic and genomic research.

Keywords: ternary chalcogenide nanosheets, single nucleotide polymorphisms, two-dimensional nanomaterials, fluorescent detection, sensor

INTRODUCTION

Single nucleotide polymorphisms (SNPs) are agents of various diseases such as cancers, Alzheimer disease, and diabetes (Martin et al., 2000; Syvanen, 2001; Unoki et al., 2008). Therefore, methods to discriminate SNPs are of significant importance as the first step for the disease prediction and clinical diagnosis. In the past two decades, several approaches have been developed for the SNP detection, such as ligation chain reaction, molecule beacons, and surface-enhanced Raman scattering (Chen et al., 2013, 2019; Li et al., 2019; Li Y. et al., 2019). However, the small thermodynamic energy difference between the perfect match and single-base mismatch makes it difficult to achieve both good sensitivity and high SNP discrimination (Zhang et al., 2013; Wu et al., 2015). Although many efforts have been made to develop analysis technologies and detection platforms for improving the sensitivity and specificity, such as polymerase chain reaction (PCR) technique and enzyme-assisted methods, sophisticated biological systems are designed to distinguish such mismatch due to allele-specific oligonucleotides hybridization and enzyme

recognition (Mhlanga and Malmberg, 2001; Doerks et al., 2002). Especially, high cost, complicated primer design, and specific enzyme recognition sites restrict their practical applications (Mhlanga and Malmberg, 2001; Nazarenko et al., 2002; Li et al., 2008; Gerasimova and Kolpashchikov, 2014; Chang et al., 2015; Huang et al., 2019). Over the past decades, nanomaterials have been greatly explored as biosensing platforms (Yang et al., 2016; Cai et al., 2018; Qiu et al., 2019; Zeng et al., 2019). As a new class of nanomaterials, single- and few-layered transition metal dichalcogenide (TMD) nanosheets have attracted tremendous attention (Chhowalla et al., 2013; Tan et al., 2017; Chen et al., 2018). Owing to their unique electronic, optical, chemical properties, and low toxicity (Zhang et al., 2018; Su et al., 2019), TMD nanosheets exhibit great potential in various applications including catalysis (Woods et al., 2016; Tang et al., 2019), electronic devices (Zhu W. et al., 2019), energy storage (Yun et al., 2019), and sensors (Chen et al., 2015; Li et al., 2015; Hu et al., 2017; Xu et al., 2019). Owing to their high-efficiency electron transfer, high surface/volume ratio, and easy dispersibility in water, TMD nanosheets have been chosen as competitive candidates for biosensing (Bolotsky et al., 2019). For example, our group previously reported that the MoS₂ nanosheet can serve as a platform to construct a fluorescent sensor for detection of DNA and small molecules due to its fluorescence quenching ability and adsorption of dye-labeled single-stranded (ss) DNA (Zhu C. et al., 2013). This strategy has been extended to other TMD nanosheets, such as WS₂, TaS₂, and TiS₂ (Ge et al., 2014; Zhang et al., 2015; Zhu D. et al., 2019). Recently, the ternary chalcogenide nanosheet, i.e., Ta₂NiS₅, also exhibited the similar ability for DNA detection and show better performance than that of MoS₂ (Tan et al., 2015). Therefore, efforts can be made in the exploration of applications of Ta₂NiS₅ nanosheets with good sensitivity and specificity, so that the sensing platform can be used in clinical diagnose especially genetic-variation-related diseases.

Here, the ternary chalcogenide nanosheet, i.e., Ta₂NiS₅, is used as a target cyclic amplification biosensor for the SNP detection, showing high sensitivity and good specificity. A dye-labeled DNA is used as probe (P) for the detection of mutant-type target (MT). Wild-type target (WT) is used to evaluate the SNP discrimination.

MATERIALS AND METHODS

Materials

DNA sequences were synthesized and purified by Sangon Biotechnology Co., Ltd. (Shanghai, China). Exonuclease III (Exo III), NEBuffer 1, and loading buffer were purchased from New England Biolabs (Singapore). DNA ladder was purchased from Takara Biotechnology Co. Ltd. (Dalian, China). Tris-acetate-ethylenediaminetetraacetic acid buffer (50×) was purchased from Axil Scientific Pte Ltd. Acrylamide/bis mixed solution [30% (w/v) (29:1)] was purchased from Nacalai Tesque, Inc. Ammonium persulfate and tetramethylethylenediamine were purchased from Biorad. All these chemicals were used without further purification. The Milli-Q water was obtained through a Milli-Q system (Millipore) and was used in all the experiments.

Preparation of Single-Layer Ta₂NiS₅ Nanosheets

The single-layer Ta₂NiS₅ nanosheets were synthesized based on the lithium-intercalation method developed by our group (Zeng et al., 2011). The obtained suspension was then centrifuged and washed with water for four times. The final product was collected for further experiments.

Characterization

Transmission electron microscopy (TEM) images were taken by a JEOL JEM-2100F transmission electron microscope. Atomic force microscopy (AFM) images were recorded by a Dimension 3100 AFM (Veeco, Fremont, CA, USA) in tapping mode. Fluorescence measurements were performed on a Shimadzu RF-5301 PC fluorophotometer.

Single-Nucleotide Polymorphism Detection

In a typical hybridization and digestion process, 5 μl of probe (P, 10 μM) was hybridized with a series of MT at increasing concentrations (5 μl, 0–1 μM) premixed with 5 μl of Exo III (2.5 U μl⁻¹) in 330 μl of NEBuffer 1 work solution for 30 min at 37°C. Two microliters of Ta₂NiS₅ nanosheets (0.125 mg ml⁻¹) was added to the mixture and incubated for 5 min. Then, the fluorescence measurements were carried out with the final concentration of MT (0–100 nM). The excitation and emission wavelengths were 590 and 610 nm, respectively.

Gel Electrophoresis Analysis

Gel electrophoresis analysis was performed using 12% polyacrylamide gel. The electrophoresis was carried out at 84 V for 100 min in 1× Tris-acetate-ethylenediaminetetraacetic acid with a load of 20 μl of sample containing 2 μl of loading buffer. Then, the gel was stained with ethidium bromide for 10 min. The gel images were obtained by a charge-coupled device under UV lamp illumination.

Cell Culture, Cellular Extracts Preparation, and Human Genomic Sample Analysis

Lung cancer cell lines (A549) and induced pluripotent stem cells were purchased from the American Type Culture Collection. The cells were cultured in Dulbecco's modified Eagle's medium supplemented with 10% fetal bovine serum, 100 μg ml⁻¹ streptomycin, and 100 U ml⁻¹ penicillin. All cells were maintained in a humidified incubator at 37°C containing 5% CO₂.

DNA was extracted from A549 cells and induced pluripotent stem cells with TRIzol following the manufacturer's protocol, respectively. Briefly, approximately 1 × 10⁷ cells were harvested and washed once with phosphate-buffered saline (pH 7.4, containing 137 mM NaCl, 2.7 mM KCl, 10 mM Na₂HPO₄, and 2.0 mM KH₂PO₄). Then, the total DNA was isolated according to the manufacturer's instruction and quantified using a NanoDrop 1000 Spectrophotometer (Thermo Scientific).

Target DNA amplification was performed in 100 μl of reaction mixture with 200 μM deoxyribonucleoside triphosphates, 1.5 mM MgCl₂, 1 μM forward and reverse primers, 0.02 U μl⁻¹ KOD Enzyme, 10 μl buffer (10× buffer for KOD Hot

Start DNA Polymerase) and genomic DNA (lung cancer DNA, 1.1 ng; normal DNA, 1.2 ng). The sequences of primers used in the experiment are listed in **Table S1**. After an initial denaturation at 95°C for 1 min, the amplification was achieved by 29 cycles of thermal cycling at 95°C for 20 s, 52°C for 10 s, and 70°C for 1 min to get 359 bp PCR products. The PCR products were used for subsequent experiments after purification with E.Z.N.A.[®] Cycle Pure Kit (Omega Bio-Tek Inc., Doraville, GA, USA) following the manufacturer's protocol. DNA sequencing was carried out by DNA Sequencing Facility (Institute of Molecular and Cell Biology, Singapore).

RESULTS AND DISCUSSION

Sensing Mechanism

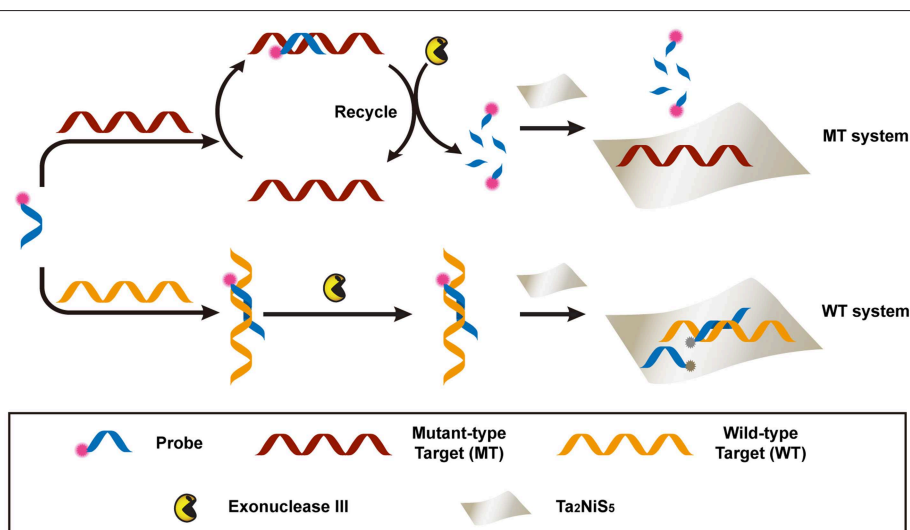
The proposed detection process is shown in **Scheme 1**. Briefly, the dye-labeled DNA probe (P) and MT were incubated together to form perfectly matched double-stranded (ds) DNA, used as the substrate of exonuclease III (Exo III) digestion. For the perfectly match system, Exo III could digest one strand of a duplex from the recessed 3' termini, so P was cleaved to shorter oligonucleotides. Meanwhile, MT was released and able to hybridize with other P in solution. This facilitated a new round of hybridization, digestion, and release process. Owing to the weak affinity between the Ta₂NiS₅ nanosheet and short oligonucleotides, the fluorescence of P would partially remain (Wu et al., 2011). In addition, the recycled process prompted an amplification of fluorescence signal. This is in contrast to the WT system, in which WT could form single-base mismatched duplex with P at 3' termini. The mismatched base prevented Exo III from digesting P, resulting in the fluorescence quenching after addition of Ta₂NiS₅ nanosheets. The DNA sequences used in this experiment are listed in **Table S1**.

Characterization of Ta₂NiS₅ Nanosheet

The Ta₂NiS₅ nanosheet was prepared through the electrochemical lithium-intercalation method according to our previous method (Zeng et al., 2011; Tan et al., 2015). AFM measurement revealed that the average thickness of Ta₂NiS₅ nanosheet is ~1.1 nm, indicating that the Ta₂NiS₅ nanosheet is single layer in thickness (**Figure 1A**) (Tan et al., 2015). The TEM and high-resolution TEM images of the Ta₂NiS₅ nanosheet are shown in **Figure 1B**. The measured lattice spacing from the high-resolution TEM is 0.26 nm, corresponding to the (006) planes of Ta₂NiS₅ (Tan et al., 2015). Previous studies indicate that the oligonucleotides can be absorbed to two-dimensional nanomaterials, and the fluorescence of dye-labeled oligonucleotides can be quenched due to the photo-induced electron transfer happening between the aromatic fluorescent dyes and two-dimensional nanomaterials (Ramakrishna Matte et al., 2011). After preparation of Ta₂NiS₅ nanosheets, their fluorescence quenching ability toward ssDNA with different lengths was studied. As shown in **Figure S1**, the Ta₂NiS₅ nanosheet exhibits the fluorescence quenching efficiency up to 50, 85, 99, and 99% toward ssDNA with 5, 10, 15, and 20 bases, demonstrating that for ssDNA with <15 bases, the affinity between ssDNA and Ta₂NiS₅ nanosheet increases along with the length of ssDNA, resulting in higher fluorescence quenching efficiency.

Feasibility Analysis

To investigate the feasibility of our designed method for the single-base mismatch discrimination, fluorescent spectra of P were carried out under different conditions of assays, as shown in **Figure 2A**. When P (1 μM) was incubated with MT (100 nM) with the addition of Ta₂NiS₅ nanosheet (5.0 μg ml⁻¹), only weak fluorescence can be observed [pink curve (P/MT + Ta₂NiS₅) in **Figure 2A**]. The fluorescence spectrum of P/WT in the presence of Ta₂NiS₅ also showed weak fluorescence intensity [green curve



SCHEME 1 | Schematic illustration of the Ta₂NiS₅ nanosheet-based fluorescent sensor for the single nucleotide polymorphism (SNP) detection.

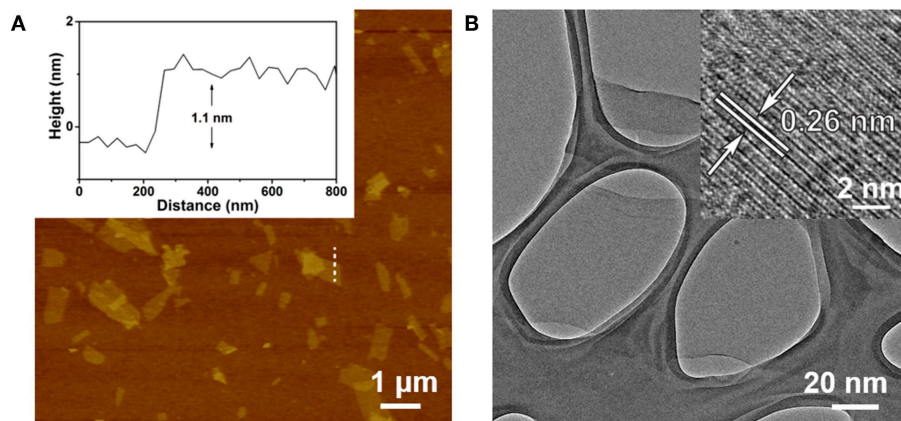


FIGURE 1 | (A) Atomic force microscopy (AFM) height image of Ta₂NiS₅ nanosheets with average height of 1.1 nm. **(B)** Transmission electron microscopy (TEM) image of Ta₂NiS₅ nanosheets. Inset: the corresponding high-resolution TEM (HRTEM) image.

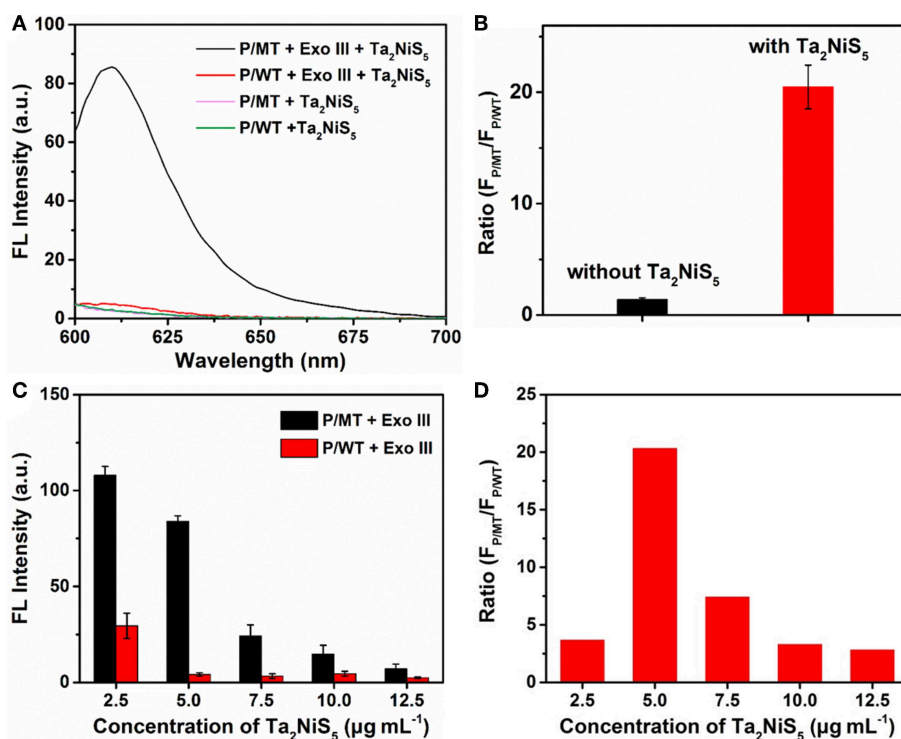


FIGURE 2 | (A) Fluorescence spectra of P/MT + Exo III + Ta₂NiS₅ (black), P/WT + Exo III + Ta₂NiS₅ (red), P/MT + Ta₂NiS₅ (pink), and P/WT + Ta₂NiS₅ (green). **(B)** The fluorescence intensity ratio ($F_{P/MT}/F_{P/WT}$) at 610 nm for P/MT + Exo III and P/WT + Exo III in the absence (black) and presence (red) of Ta₂NiS₅ nanosheets. **(C)** Fluorescence intensity of P/MT + Exo III (black) and P/WT + Exo III (red) in the presence of Ta₂NiS₅ nanosheets with different final concentrations of 2.5, 5.0, 7.5, 10.0, and 12.5 $\mu\text{g mL}^{-1}$ ($P = 1 \mu\text{M}$; $MT = 100 \text{ nM}$; $WT = 100 \text{ nM}$; $\text{Exo III} = 0.25 \text{ U } \mu\text{L}^{-1}$). **(D)** The fluorescence intensity ratio ($F_{P/MT}/F_{P/WT}$) at 610 nm in the presence of Ta₂NiS₅ nanosheets with different final concentrations of 2.5, 5.0, 7.5, 10.0, and 12.5 $\mu\text{g mL}^{-1}$ ($P = 1 \mu\text{M}$; $MT = 100 \text{ nM}$; $WT = 100 \text{ nM}$; $\text{Exo III} = 0.25 \text{ U } \mu\text{L}^{-1}$). The excitation wavelength is 590 nm.

(P/WT + Ta₂NiS₅) in **Figure 2A**]. When Exo III was employed in the aforementioned system, the fluorescence intensity retained for the perfect match system of P and MT [black curve (P/MT + Exo III + Ta₂NiS₅) in **Figure 2A**], indicating that P was digested by Exo III. As a result of the weak interaction between fluorophore and Ta₂NiS₅ nanosheet, the fluorescence

signal could be partially recovered. However, for the single-base mismatch system, no significant fluorescence increase was observed [red curve (P/WT + Exo III + Ta₂NiS₅) in **Figure 2A**], suggesting that the fluorophore was adsorbed on the surface of Ta₂NiS₅ nanosheet. Moreover, the discrimination ratio of P/MT + Exo III to P/WT + Exo III, referred to as $F_{P/MT}/F_{P/WT}$,

where $F_{P/MT}$ and $F_{P/WT}$ are the fluorescence signals of MT and WT systems, respectively, was 1.5 and 20.5 in the absence and presence of Ta₂NiS₅ nanosheet, respectively (Figure 2B). It suggests that the introduction of Ta₂NiS₅ nanosheets results in the effective discrimination of SNP. The digestion process has also been confirmed through the gel electrophoresis (Figure S2). These results demonstrated that the single-base mismatch at 3' terminus can weaken the digestion ability of Exo III (Figure S3), and the Ta₂NiS₅ nanosheet plays an important role in improving the single-base mismatch discrimination.

Optimization of Detection Conditions

To achieve better assay performance, we optimized the digestion and sensing conditions, including the concentration and digestion time of Exo III in the digestion process and the amount of Ta₂NiS₅ nanosheets. As shown in Figure S4, after using Exo III digestion for 30 min, fluorescence intensity of P/MT almost reaches the maximum value. Therefore, the reaction time of biosensor was chosen at 30 min. To optimize the concentration of Exo III, $F_{P/MT}/F_{P/WT}$ was used as the criterion. The dependence of $F_{P/MT}/F_{P/WT}$ on the concentration of Exo III is illustrated in Figure S5, showing maximum value at 0.25 U μl^{-1} of Exo III. Therefore, 0.25 U μl^{-1} was chosen for the concentration of Exo III and used throughout the subsequent assays. Besides the concentration of Exo III, the concentration of

Ta₂NiS₅ nanosheets should also affect the fluorescence response. As shown in Figure 2C, the fluorescence intensity changes of P/MT + Exo III and P/WT + Exo III were carried out in the presence of different concentrations of Ta₂NiS₅ nanosheets. Both $F_{P/MT}$ and $F_{P/WT}$ decreased along with the increasing concentration in Ta₂NiS₅ nanosheet, while $F_{P/MT}$ was always higher than $F_{P/WT}$. Figure 2D displayed the dependence of $F_{P/MT}/F_{P/WT}$ on the concentration of Ta₂NiS₅ nanosheets. $F_{P/MT}/F_{P/WT}$ increased with an increasing concentration of Ta₂NiS₅ nanosheets with maximum value at the final Ta₂NiS₅ nanosheet concentration of 5.0 $\mu\text{g ml}^{-1}$. Then, $F_{P/MT}/F_{P/WT}$ decreased with further increasing concentration of Ta₂NiS₅ nanosheets, resulting from the adsorption of short dye-labeled oligonucleotides with excess Ta₂NiS₅ nanosheets. Thus, the concentration of Ta₂NiS₅ nanosheet was optimized to be 5.0 $\mu\text{g ml}^{-1}$ for further experiments.

Sensitivity and Specificity Analysis

The sensitivity of the Ta₂NiS₅ nanosheet-based biosensor was examined under the optimal conditions. Different concentrations of MT from 0 to 100 nM were incubated with P (1 μM) in the presence of Exo III (0.25 U μl^{-1}) for 30 min and then mixed with the Ta₂NiS₅ nanosheets (5.0 $\mu\text{g ml}^{-1}$). The fluorescence intensity increases along with the increase in the MT concentration (Figure 3A). As shown in Figure 3B, the fluorescence intensity

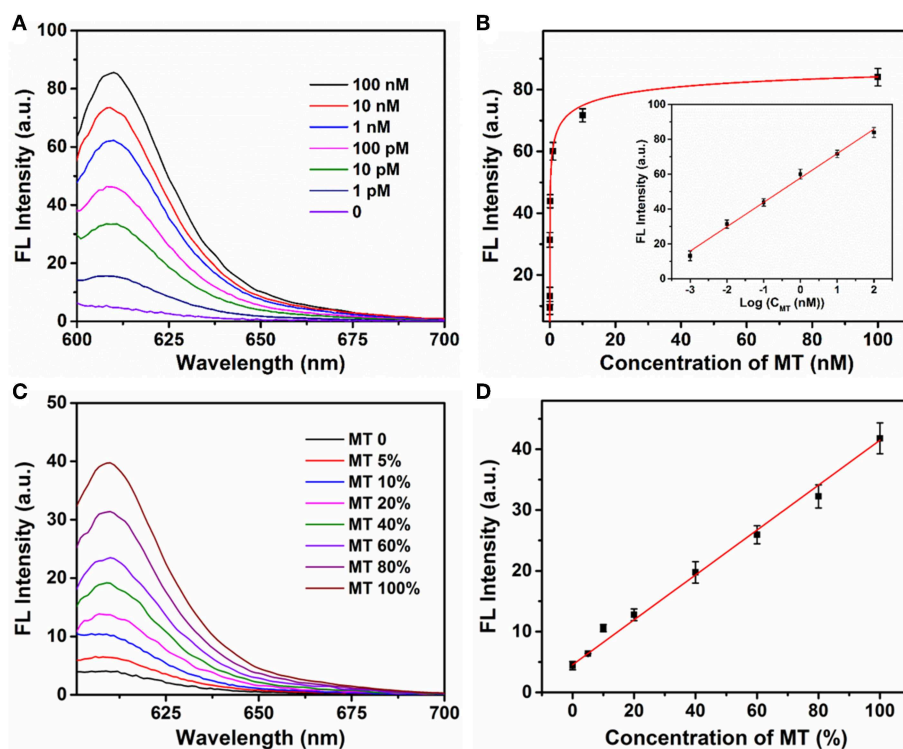


FIGURE 3 | (A) The fluorescence spectra of P (1 μM) in the presence of different concentrations of mutant-type target (0, 0.001, 0.01, 0.1, 1, 10, and 100 nM) and Exo III (0.25 U μl^{-1}) with addition of Ta₂NiS₅ nanosheets (5.0 $\mu\text{g ml}^{-1}$). **(B)** Relationship between fluorescence intensity at 610 nm and the concentrations of mutant-type target. Inset: Calibration curve for detection of mutant-type target. **(C)** Fluorescence spectra of different percentage of mutant-type target in mixed DNA samples (MT/(MT + WT) was 0, 5, 10, 20, 40, 60, 80, and 100%). **(D)** Fluorescence intensity at 610 nm as a function of allele frequency. The total concentration of the mutant and wild-type target is 100 pM. The excitation wavelength is 590 nm.

showed a linear correlation vs. a series of MT concentrations in logarithmic scale in the range from 1 pM to 100 nM. The calibration equation was $Y = 57.46 + 13.97 \lg X$ ($R^2 = 0.9952$), where Y stands for the fluorescence intensity and X is the concentration of MT. According to the 3σ rule, the limit of detection was calculated to be 250 fM (Hu et al., 2018). The comparison of Ta₂NiS₅ nanosheet-based biosensor with the conventional reported SNP biosensor based on Ti₃C₂ nanosheet, GO nanosheet, MoS₂@Au NPs, and Au NPs is presented in **Table S2**; the Ta₂NiS₅ nanosheet-based exhibits high sensitivity for SNP detection.

Different ratios of MT and WT were mixed and used as DNA samples for the analysis of allele sequence. Detection results were carried out for mixtures with various ratios of MT (0, 5, 10, 20, 40, 60, 80, and 100%). The total concentration of MT and WT was 100 pM. **Figure 3C** showed the fluorescence spectra of P with a series ratio of MT in the presence of Exo III (0.25 U μ l⁻¹) and Ta₂NiS₅ nanosheet (5.0 μ g ml⁻¹). The statistic curve of the relationship between fluorescence intensity and the percentage of MT in the tested samples is shown in **Figure 3D**. The increasing amount of MT in DNA mixtures led to an increase in fluorescence intensity at 610 nm. Moreover, MT, as low as 5%, could be detected. These results indicated that this strategy afforded high specificity as well as good sensitivity for SNP detection due to the quenching ability of Ta₂NiS₅ nanosheet and low detection background together with signal amplification of target cyclic amplification reaction. Based on this, the proposed method can be considered a potential candidate for mutant detection in practical cancer research.

The applicability of the proposed single nucleotide discrimination method was further validated by the PCR product of human genomic samples with a point mutant (C > T) in the CHRNA3 gene (rs1051730) (Han et al., 2015). Previous researches confirm that rs1051730 polymorphism have a significant correlation with lung cancer in the East Asia countries (Han et al., 2015). Therefore, rs1051730 polymorphism detection was performed. The 359-bp amplicons were obtained by PCR from four DNA samples (samples 1 and 2: mutant-type samples; samples 3 and 4: wild-type samples). Agarose gel analysis was performed to confirm the PCR amplicons (**Figure S6**). Then, the PCR amplicons were used for the mutation detection through the proposed method (**Figure S7**). It was observed that the fluorescence signals of samples 1 and 2 were much higher than those of samples 3 and 4, indicating that samples 1 and 2 were mutant type and could be distinguished from wild-type samples. These results were consistent with the DNA sequence data, indicating the potential application of the developed method for SNP detection of real samples.

REFERENCES

Bolotsky, A., Butler, D., Dong, C., Gerace, K., Glavin, N. R., Muratore, C. J., et al. (2019). Two-dimensional materials in biosensing and healthcare: from

CONCLUSIONS

In summary, we reported a ternary chalcogenide nanosheet-based biosensor combined with target cyclic amplification as a mean of SNP detection, with a discrimination of ~ 20.5 . This strategy is based on the high quenching ability of the Ta₂NiS₅ nanosheet and different affinity between the Ta₂NiS₅ nanosheet and oligonucleotides. The proposed sensing method is a label-free approach for detection of DNA concentrations from 1 pM to 100 nM, and high sensitivity with a detection limit of 250 fM was achieved. Perfectly matched base pairs can be efficiently discriminated from single-base mismatched pairs. Compared with conventional SNP analytical methods such as droplet digital PCR and DNA sequencing, the single-layer Ta₂NiS₅ nanosheet-based biosensor displays the advantages of low cost and simplicity. Significantly, this biosensor platform shows better performance compared to previously reported nanomaterial-based SNP sensors (e.g., Ti₃C₂ nanosheet and MoS₂@Au NPs) with broader detection range and a low detection limit. Furthermore, this method shows application potential for multiplexed assays by utilizing different DNA probes with diverse fluorophores. We anticipate that the proposed strategy can be used for clinical diagnostic and genomic research with great potential.

DATA AVAILABILITY STATEMENT

All datasets generated for this study are included in the article/**Supplementary Material**.

AUTHOR CONTRIBUTIONS

YH, LW, and CT conceived the project. YH, CT, and DY performed the experiments and wrote the manuscript. YH, ZL, XZ, NF, XL, and QL were involved in data analysis. All authors revised the manuscript and approved it for publication.

FUNDING

This research was funded by the National Key Basic Research Program of China (2017YFA0205301), the Natural Science Foundation of the Jiangsu Higher Education Institutions (19KJB150030, 19KJB150031), and the open research fund of Jiangsu Key Laboratory for Biosensors (51204080).

SUPPLEMENTARY MATERIAL

The Supplementary Material for this article can be found online at: <https://www.frontiersin.org/articles/10.3389/fchem.2019.00844/full#supplementary-material>

in vitro diagnostics to optogenetics and beyond. *ACS Nano*. 13, 9781–9810. doi: 10.1021/acsnano.9b03632

Cai, G., Yu, Z., Ren, R., and Tang, D. (2018). Exciton-plasmon interaction between AuNPs/graphene nanohybrids and CdS quantum dots/TiO₂ for

- photoelectrochemical aptasensing of prostate-specific antigen. *ACS Sens.* 3, 632–639. doi: 10.1021/acssensors.7b00899
- Chang, K., Deng, S., and Chen, M. (2015). Novel biosensing methodologies for improving the detection of single nucleotide polymorphism. *Biosens. Bioelectron.* 66, 297–307. doi: 10.1016/j.bios.2014.11.041
- Chen, J., Wu, Y., Fu, C., Cao, H., Tan, X., Shi, W., et al. (2019). Ratiometric SERS biosensor for sensitive and reproducible detection of microRNA based on mismatched catalytic hairpin assembly. *Biosens. Bioelectron.* 143:111619. doi: 10.1016/j.bios.2019.111619
- Chen, S. X., Zhang, D. Y., and Seelig, G. (2013). Conditionally fluorescent molecular probes for detecting single base changes in double-stranded DNA. *Nat. Chem.* 5, 782–789. doi: 10.1038/nchem.1713
- Chen, Y., Fan, Z., Zhang, Z., Niu, W., Li, C., Yang, N., et al. (2018). Two-dimensional metal nanomaterials: synthesis, properties, and applications. *Chem. Rev.* 118, 6409–6455. doi: 10.1021/acs.chemrev.7b00727
- Chen, Y., Tan, C., Zhang, H., and Wang, L. (2015). Two-dimensional graphene analogues for biomedical applications. *Chem. Soc. Rev.* 44, 2681–2701. doi: 10.1039/C4CS00300D
- Chhowalla, M., Shin, H. S., Eda, G., Li, L. J., Loh, K. P., and Zhang, H. (2013). The chemistry of two-dimensional layered transition metal dichalcogenide nanosheets. *Nat. Chem.* 5, 263–275. doi: 10.1038/nchem.1589
- Doerks, T., Copley, R. R., Schultz, J., Ponting, C. P., and Bork, P. (2002). Systematic identification of novel protein domain families associated with nuclear functions. *Genome Res.* 12, 47–56. doi: 10.1101/gr.203201
- Ge, J., Tang, L. J., Xi, Q., Li, X. P., Yu, R. Q., Jiang, J. H., et al. (2014). A WS₂ nanosheet based sensing platform for highly sensitive detection of T4 polynucleotide kinase and its inhibitors. *Nanoscale* 6, 6866–6872. doi: 10.1039/C4NR00944D
- Gerasimova, Y. V., and Koldashchikov, D. M. (2014). Enzyme-assisted target recycling (EATR) for nucleic acid detection. *Chem. Soc. Rev.* 43, 6405–6438. doi: 10.1039/C4CS00083H
- Han, Z., Jiang, Q., Zhang, T., Wu, X., Ma, R., Wang, J., et al. (2015). Analyzing large-scale samples confirms the association between the rs1051730 polymorphism and lung cancer susceptibility. *Sci. Rep.* 5:15642. doi: 10.1038/srep15642
- Hu, Y., Huang, Y., Tan, C., Zhang, X., Lu, Q., Sindoro, M., et al. (2017). Two-dimensional transition metal dichalcogenide nanomaterials for biosensing applications. *Mater. Chem. Front.* 1, 24–36. doi: 10.1039/C6QM00195E
- Hu, Y., Yang, D., Yang, C., Feng, N., Shao, Z., Zhang, L., et al. (2018). A novel “Off-On” fluorescent probe based on carbon nitride nanoribbons for the detection of citrate anion and Live cell imaging. *Sensors* 18:1163. doi: 10.3390/s18041163
- Huang, J., Shanguan, J., Guo, Q., Ma, W., Wang, H., Jia, R., et al. (2019). Colorimetric and fluorescent dual-mode detection of microRNA based on duplex-specific nuclease assisted gold nanoparticle amplification. *Analyst.* 144, 4917–4924. doi: 10.1039/C9AN01013K
- Li, B. L., Zou, H. L., Lu, L., Yang, Y., Lei, J. L., Luo, H. Q., et al. (2015). Size-dependent optical absorption of layered MoS₂ and DNA oligonucleotides induced dispersion behavior for label-free detection of single-nucleotide polymorphism. *Adv. Funct. Mater.* 25, 3541–3550. doi: 10.1002/adfm.201500180
- Li, J., Wang, L., Mamon, H., Kulke, M. H., Berbeco, R., and Makrigiorgos, G. M. (2008). Replacing PCR with COLD-PCR enriches variant DNA sequences and redefines the sensitivity of genetic testing. *Nat. Med.* 14, 579–584. doi: 10.1038/nm1708
- Li, X.-H., Zhang, X.-L., Wu, J., Lin, N., Sun, W.-M., Chen, M., et al. (2019). Hyperbranched rolling circle amplification (HRC)-based fluorescence biosensor for ultrasensitive and specific detection of single-nucleotide polymorphism genotyping associated with the therapy of chronic hepatitis B virus infection. *Talanta.* 191, 277–282. doi: 10.1016/j.talanta.2018.08.064
- Li, Y., Gao, T., Xu, G., Xiang, X., Zhao, B., Han, X. X., et al. (2019). Direct approach toward label-free DNA detection by surface-enhanced Raman spectroscopy: discrimination of a single-base mutation in 50 base-paired double helices. *Anal. Chem.* 91, 7980–7984. doi: 10.1021/acs.analchem.9b01887
- Martin, E. R., Lai, E. H., Gilbert, J. R., Rogala, A. R., Afshari, A. J., Riley, J., et al. (2000). SNPing away at complex diseases: analysis of single-nucleotide polymorphisms around APOE in Alzheimer disease. *Am. J. Hum. Genet.* 67, 383–394. doi: 10.1086/303003
- Mhlanga, M. M., and Malmberg, L. (2001). Using molecular beacons to detect single-nucleotide polymorphisms with real-time PCR. *Methods* 25, 463–471. doi: 10.1006/meth.2001.1269
- Nazarenko, I., Lowe, B., Darfler, M., Ikonomi, P., Schuster, D., and Rashtchian, A. (2002). Multiplex quantitative PCR using self-quenched primers labeled with a single fluorophore. *Nucleic Acids Res.* 30:e37. doi: 10.1093/nar/30.9.e37
- Qiu, Z., Shu, J., Liu, J., and Tang, D. (2019). Dual-channel photoelectrochemical ratiometric aptasensor with up-converting nanocrystals using spatial-resolved technique on homemade 3D printed device. *Anal. Chem.* 91, 1260–1268. doi: 10.1021/acs.analchem.8b05455
- Ramakrishna Matte, H. S. S., Subrahmanyam, K. S., Venkata Rao, K., George, S. J., and Rao, C. N. R. (2011). Quenching of fluorescence of aromatic molecules by graphene due to electron transfer. *Chem. Phys. Lett.* 506, 260–264. doi: 10.1016/j.cplett.2011.03.031
- Su, S., Sun, Q., Gu, X., Xu, Y., Shen, J., Zhu, D., et al. (2019). Two-dimensional nanomaterials for biosensing applications. *TRAC-Trends Anal. Chem.* 119:115610. doi: 10.1016/j.trac.2019.07.021
- Syvanen, A. C. (2001). Accessing genetic variation: genotyping single nucleotide polymorphisms. *Nat. Rev. Genet.* 2, 930–942. doi: 10.1038/35103535
- Tan, C., Cao, X., Wu, X., He, Q., Yang, J., Zhang, X., et al. (2017). Recent advances in ultrathin two-dimensional nanomaterials. *Chem. Rev.* 117, 6225–6331. doi: 10.1021/acs.chemrev.6b00558
- Tan, C., Yu, P., Hu, Y., Chen, J., Huang, Y., Cai, Y., et al. (2015). High-yield exfoliation of ultrathin two-dimensional ternary chalcogenide nanosheets for highly sensitive and selective fluorescence DNA sensors. *J. Am. Chem. Soc.* 137, 10430–10436. doi: 10.1021/jacs.5b06982
- Tang, W., Fan, W., Zhang, W., Yang, Z., Li, L., Wang, Z., et al. (2019). Wet/sono-chemical synthesis of enzymatic two-dimensional MnO₂ nanosheets for synergistic catalysis-enhanced phototheranostics. *Adv. Mater.* 31:1900401. doi: 10.1002/adma.201900401
- Unoki, H., Takahashi, A., Kawaguchi, T., Hara, K., Horikoshi, M., Andersen, G., et al. (2008). SNPs in KCNQ1 are associated with susceptibility to type 2 diabetes in East Asian and European populations. *Nat. Genet.* 40, 1098–1102. doi: 10.1038/ng.208
- Woods, J. M., Jung, Y., Xie, Y., Liu, W., Liu, Y., Wang, H., et al. (2016). One-step synthesis of MoS₂/WS₂ layered heterostructures and catalytic activity of defective transition metal dichalcogenide films. *ACS Nano.* 10, 2004–2009. doi: 10.1021/acsnano.5b06126
- Wu, M., Kempaiah, R., Huang, P. J., Maheshwari, V., and Liu, J. (2011). Adsorption and desorption of DNA on graphene oxide studied by fluorescently labeled oligonucleotides. *Langmuir.* 27, 2731–2738. doi: 10.1021/la1037926
- Wu, T., Xiao, X., Zhang, Z., and Zhao, M. (2015). Enzyme-mediated single-nucleotide variation detection at room temperature with high discrimination factor. *Chem. Sci.* 6, 1206–1211. doi: 10.1039/C4SC03375B
- Xu, Y., Ang, Y. S., Wu, L., and Ang, L. K. (2019). High sensitivity surface plasmon resonance sensor based on two-dimensional MXene and transition metal dichalcogenide: a theoretical study. *Nanomaterials* 9:165. doi: 10.3390/nano9020165
- Yang, D., Li, F., Hu, Y., Luo, Z., Bao, B., Hu, Y., et al. (2016). Conjugated polymer nanoparticles with aggregation induced emission characteristics for intracellular Fe³⁺ sensing. *J. Polym. Sci. Pol. Chem.* 54, 1686–1693. doi: 10.1002/pola.28024
- Yun, Q., Li, L., Hu, Z., Lu, Q., Chen, B., and Zhang, H. (2019). Layered transition metal dichalcogenide-based nanomaterials for electrochemical energy storage. *Adv. Mater.* 1903826. doi: 10.1002/adma.201903826
- Zeng, R., Luo, Z., Su, L., Zhang, L., Tang, D., Niessner, R., et al. (2019). Palindromic molecular beacon based Z-scheme BiOCl-Au-CdS photoelectrochemical biodetection. *Anal. Chem.* 91, 2447–2454. doi: 10.1021/acs.analchem.8b05265
- Zeng, Z., Yin, Z., Huang, X., Li, H., He, Q., Lu, G., et al. (2011). Single-layer semiconducting nanosheets: high-yield preparation and device fabrication. *Angew. Chem., Int. Ed.* 50, 11093–11097. doi: 10.1002/anie.201106004
- Zhang, X., Lai, Z., Ma, Q., and Zhang, H. (2018). Novel structured transition metal dichalcogenide nanosheets. *Chem. Soc. Rev.* 47, 3301–3338. doi: 10.1039/C8CS00094H
- Zhang, Y., Guo, Y., Quirke, P., and Zhou, D. (2013). Ultrasensitive single-nucleotide polymorphism detection using target-recycled ligation, strand displacement and enzymatic amplification. *Nanoscale* 5, 5027–5035. doi: 10.1039/c3nr01010d

- Zhang, Y., Zheng, B., Zhu, C., Zhang, X., Tan, C., Li, H., et al. (2015). Single-layer transition metal dichalcogenide nanosheet-based nanosensors for rapid, sensitive, and multiplexed detection of DNA. *Adv Mater.* 27, 935–939. doi: 10.1002/adma.201404568
- Zhu, C., Zeng, Z., Li, H., Li, F., Fan, C., and Zhang, H. (2013). Single-layer MoS₂-based nanoprobe for homogeneous detection of biomolecules. *J. Am. Chem. Soc.* 135, 5998–6001. doi: 10.1021/ja4019572
- Zhu, D., Huang, J., Lu, B., Zhu, Y., Wei, Y., Zhang, Q., et al. (2019). Intracellular microRNA imaging with MoS₂-supported nonenzymatic catalytic assembly of DNA hairpins. *ACS Appl Mater Interfaces*. 11, 20725–20733. doi: 10.1021/acsami.9b04883
- Zhu, W., Low, T., Wang, H., Ye, P., and Duan, X. (2019). Nanoscale electronic devices based on transition metal dichalcogenides. *2D Materials* 6:032004. doi: 10.1088/2053-1583/ab1ed9
- Conflict of Interest:** The authors declare that the research was conducted in the absence of any commercial or financial relationships that could be construed as a potential conflict of interest.
- Copyright © 2019 Hu, Tan, Lin, Lai, Zhang, Lu, Feng, Yang and Weng. This is an open-access article distributed under the terms of the Creative Commons Attribution License (CC BY). The use, distribution or reproduction in other forums is permitted, provided the original author(s) and the copyright owner(s) are credited and that the original publication in this journal is cited, in accordance with accepted academic practice. No use, distribution or reproduction is permitted which does not comply with these terms.



Current Applications of Gas Sensor Based on 2-D Nanomaterial: A Mini Review

Liang Ge¹, Xiaolin Mu¹, Guiyun Tian^{2*}, Qi Huang¹, Junaid Ahmed³ and Ze Hu¹

¹ Electrical and Mechanical Engineering Department, Southwest Petroleum University, Chengdu, China, ² Department of Engineering, Newcastle University, Newcastle upon Tyne, United Kingdom, ³ Electrical Department, Sukkur Institute of Business Administration, Sukkur, Pakistan

Gas sensor, as one of the most important devices to detect noxious gases, provides a vital way to monitor the concentration and environmental information of gas in order to guarantee the safety of production. Therefore, researches on high sensitivity, high selectivity, and high stability have become hot issues. Since the discovery of the nanomaterial, it has been increasingly applied to the gas sensor for its distinguishing surface performances. However, 0-D and 1-D nanomaterials, with limited electronic confinement effect and surface effect, cannot reach the requirement for the production of gas sensors. This paper gives an introduction about the current researching progress and development trend of 2-D nanomaterials, analyzes the common forms of 2-D nanoscale structure, and summarizes the mechanism of gas sensing. Then, widely concerned factors including morphological properties and crystalline structure of 2-D nanomaterial, impact of doped metal on the sensibility of gas sensors, impact of symmetry, and working temperature on the selectivity of gas sensors have been demonstrated in detail. In all, the detailed analysis above has pointed out a way for the development of new 2-D nanomaterial and enhancing the sensibility of gas sensors.

Keywords: 2-D nanomaterial, gas sensor, performance improvement, current application, development trend

OPEN ACCESS

Edited by:

Wen Zeng,
Chongqing University, China

Reviewed by:

Lihui Wang,
China Conservatory, China
Fengyun Huang,
Wuhan University of
Technology, China

*Correspondence:

Guiyun Tian
g.y.tian@ncl.ac.uk

Specialty section:

This article was submitted to
Nanoscience,
a section of the journal
Frontiers in Chemistry

Received: 25 August 2019

Accepted: 18 November 2019

Published: 10 December 2019

Citation:

Ge L, Mu X, Tian G, Huang Q,
Ahmed J and Hu Z (2019) Current
Applications of Gas Sensor Based on
2-D Nanomaterial: A Mini Review.
Front. Chem. 7:839.
doi: 10.3389/fchem.2019.00839

INTRODUCTION

Nanotechnology, a newly developed technology based on quantum mechanics, molecular biology, material science, microelectronics, and computer technology, is a scientific way to synthesize new materials on nanoscales. Prof. Tanggulachi firstly defined this newly emerged subject as nanotechnology in 1974 and clarified that the research on the characteristics and applications of nanomaterial should be restricted to the scale of 0.1–100 nm (Zhu et al., 2010; Huang et al., 2014). Nanomaterial has dramatic advantages over traditional material. Those advantages include distinguishing surface effect (Zhang, 2011) and quantum size effect (Xu et al., 2019). Factors like tiny particles, large surface areas, and high surface energy will enhance the performances of nanomaterial tremendously (Wang, 2013).

Gas sensor (You et al., 2012) converts the components and concentrations of various gases into standard electrical signals by using specific physical and chemical effects. It has been widely used in the detection of noxious and harmful gases and natural gas leakage. It has been improved greatly since the 1970s, with nanomaterials changed from single metallic oxide to combined metal oxide. Large progress has also been made on the sensing performances like sensitivity, accuracy, and stability when detecting specific variety of gas (Gonullu et al., 2012; Trung et al., 2012; Xu et al., 2012).

In recent years, the development of electronic devices is more about integration, miniaturization, and even microminiaturization. Nanomaterial plays an increasingly important role in the improvement of gas sensors. Based on the gas-sensing properties of 2-D nanomaterials such as response speed, selectivity, and stability, this paper gives a review of the factors that influence the performance of 2-D nanomaterial gas sensors and proposes the future development trend of the improvement of these sensors' parameters.

DEVELOPMENT OF RESEARCH ON 2-D NANOMATERIAL

Since the successful extraction of graphene (a 2-D nanoscale graphite with single atomic layer) by the Geim Group (Geim and Novoselov, 2007; Geim, 2009; Perreault et al., 2015; Varghese et al., 2015) from Manchester University, UK, in 2004, more and more researchers have been attracted to the study of 2-D nanomaterial. According to numerous researches, nanomaterials are sorted into four categories by their number of nanoscale

dimension. Each nanomaterial has different gas sensitivities due to electronics confinement effect, surface effect, etc. Generally speaking, three dimensions of 0-D nanomaterial are all in the scale of nanometers. Those 0-D nanomaterials include nanoscale particles, metallic cluster, etc. 1-D nanomaterial has two dimensions in nanoscale, with the other one of non-nanoscale size, such as the organic chain structures of nanoscale tube (Ma et al., 2014), nanoscale line (Tao et al., 2011), nanoscale band (Sun et al., 2003), nanoscale rod (Zhang et al., 2003), etc. 2-D nanomaterial only has one dimension of nanoscale, such as nanoscale membrane, 2-D single layer structure (Li et al., 2009), and nanoscale sheets (Liu et al., 2016). 3-D nanomaterial, such as nanoscale flowers (Wang and Rogach, 2014), etc. can be sorted into organic and inorganic nanomaterials according to its components.

In 2000, Kong et al. proved that a 1-D carbon nanoscale tube (CNTs) can detect the existence of NH_3 and NO_2 at low concentration under room temperature. CNTs have high absorption efficiency with rich adsorption structures and adsorption points, and they also have great value when it comes to application (Kong et al., 2000). In 2009, based on

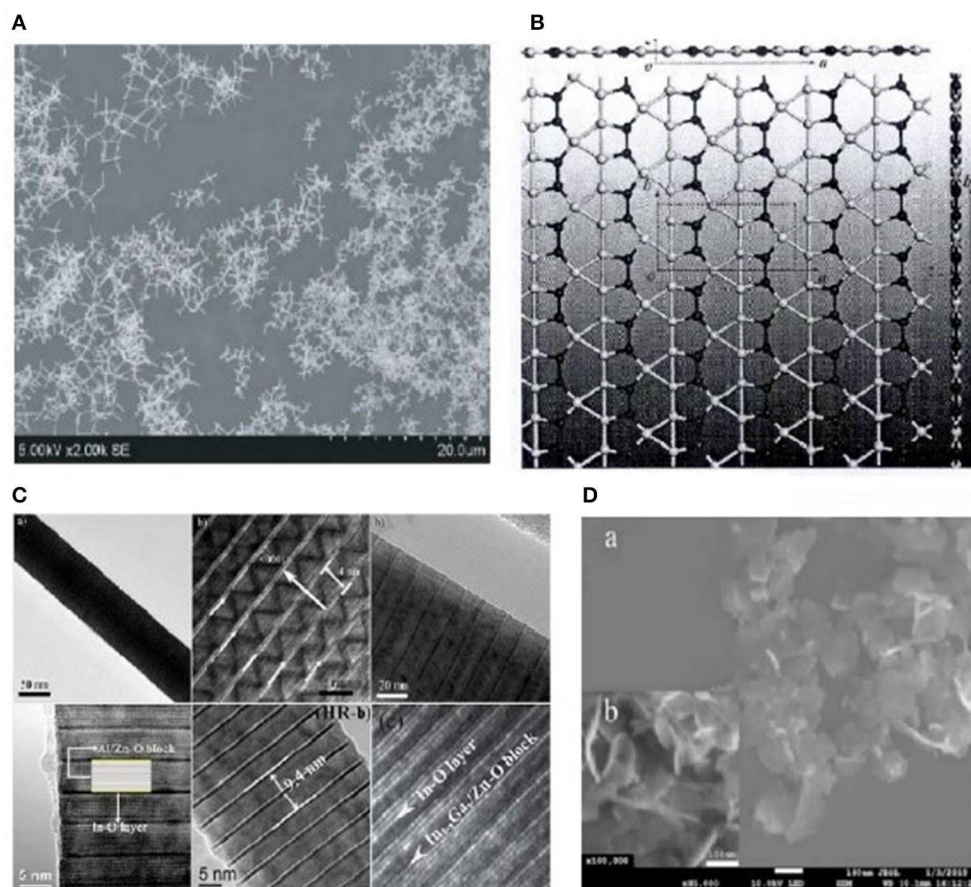


FIGURE 1 | Electron microscopic images of partial 2-D nanomaterials. **(A)** ZnO nanoscale membrane (adapted from Shen et al., 2018 with permission from Shen). **(B)** 2-D B₃N₂ single-layer structure (adapted from Sun et al., 2016 with permission from Sun). **(C)** InMO₃(ZnO)_m superlattice (adapted from Wang, 2018 with permission from Wang). **(D)** New SnO₂ nanoscale sheets (adapted from Yue and Yu, 2019 with permission from Yue).

2-D nanomaterial, Zhang et al. developed the SnO_2 hollow microsphere, which was used for NO_2 sensor. The results showed that SnO_2 hollow sphere sensors can respond to NO_2 at ppm level under 160°C and distinguishing selectivity (Zhang et al., 2009). In 2013, Sharm et al. produced a WO_3 cluster/tin oxide heterostructure that can detect NO_2 with low concentration of 10 ppm under 100°C (Sharma et al., 2013). In 2014, Rumyantsev et al. synthesized 2-D thin-film transistor MoS_2 as well as figured out the CV graph of it. Comparing this MoS_2 with ethanol, hexanenitrile, toluene, chloroform, and methanol on a time-current graph, a conclusion can be drawn that this material had better selectivity to alcohols (Shur et al., 2014). By using MoS_2 layers of different thicknesses, photodetection of gas could be achieved (Wen et al., 2018). In 2016, Pang et al. used CNTs doped with nanoscale SnO_2 particles to produce formic acid gas sensors, with their sensitivity reaching 13.49 (Pang et al., 2016). Also, this material lowered the working temperature by 120°C and shortened the response time by 4 s. Sun et al. constructed a graphene-like single-layered nanoscale structure (shown in **Figure 1B**). Though this material was a non-magnetic conductor, it had metallic characteristics. It could be a new research material in the nanotechnology field (Sun et al., 2016). In 2017, Tao et al. used ultrasonic spray pyrolysis with electrostatic enhancement to produce 2-DMWCNTs/ SnO_2 nanocomposite. When the deposition temperature was 300°C with MWCNTs' doping amount reaching 10 mg/ml, the performances of gas-sensitive material have improved greatly (Tao, 2017). In 2017, Yuan obtained 2-D PS/ WO_3 hollow nanoscale gas sensor with thick membrane by spin coating WO_3 hollow nanoscale structure on the surface of PS. The experiment showed that this material had high sensitivity and distinguishing response characteristics when facing ppb level of NO_2 (Yuan, 2017). In 2018, in order to cope with the problems that pure phase $\alpha - \text{MoO}_3$ had (excessively high working temperature, low stability, and long response time), Yu synthesized 2- $\text{DTiO}_2/\alpha - \text{MoO}_3$ nanosheet, $\alpha - \text{MoO}_3 - \text{PANI}$ p - n heterojunction, $\text{Au}/\alpha - \text{MoO}_3$ composite nanosheet, etc., which improved its sensitivity and stability greatly and shortened the response time (Yu, 2018). Shen et al. applied chemical vapor deposition (CVD) to synthesize ZnO nanofilm on the glass substrate, with the material having the best sensitivity to ethanol at room temperature (shown in **Figure 1A**) (Shen et al., 2018). Wang et al. composed Zn-Sn-O superlattice nanoscale particle (shown in **Figure 1C**), which had good selectivity and extremely high sensitivity to H_2S (Wang, 2018). In 2019, Yu et al. made a new SnO_2 nanoscale sheet structure (shown in **Figure 1D**), with the sensitivity of 12.14 at its best working temperature of 175°C and concentration of 100 ppm. This nanomaterial showed a tremendous improvement of sensitivity to gas like ethanol and formaldehyde (Yue and Yu, 2019). Kou's group systematically demonstrated the electronic, structure, and transport characters of monolayer BP with the adsorption of several typical gas molecules, CO , NH_3 , CO , NO_2 , and NO (Liu and Zhou, 2019). In 2018, Qiu et al. used ultraviolet rays and ozone method to *in-situ* synthesize oxide graphene membrane. The gas sensor of high performance can be made by combining oxide graphene membrane and two-terminal electrical devices. This sensor has higher sensitivity

to NH_3 , and better selectivity to NH_3 compared with acetone and absolute ethanol (Qiu et al., 2018). In 2019, Yang's study for dissertation proved this conclusion (Yang, 2019). Guo developed graphene/polyaniline material and analyzed its gas-sensing performances to multiple gases including NH_3 , CO , NO , H_2 , etc. The results showed that this material is characterized by higher selectivity to NH_3 because of higher sensitivity and stronger adsorption to it (Guo, 2018).

GAS-SENSING PERFORMANCE OF GAS SENSOR BASED ON 2-D NANOMATERIAL

Gas-Sensing Mechanism Based on 2-D Nanomaterial

The detecting principle of gas sensor is that gas molecules are adsorbed on the surface of the substrate nanomaterial. Then, charge transfer occurs between the gas molecule and the substrate material, which changes the resistivity of the substrate nanomaterial. By testing the resistivity of the substrate nanomaterial, characteristics of gas such as properties and concentration can be known. When it comes to substrate nanomaterial, process of choosing from 0-D quantum dot, 1-D quantum wire, to 2-D quantum surface is experienced. A large number of studies have shown that 2-D nanomaterial has larger surface compared with 0-D and 1-D nanomaterials. Special membranous or lamellar structure has stronger capability to absorb gas molecules. Meanwhile the gas sensitivity can be improved by metal doping to pure nanomaterial (Dai and Yuan, 2010; Beheshtian et al., 2012a,b; Zhang et al., 2012; Rastegar et al., 2013; Ahmad et al., 2019; Choi et al., 2019; Kim et al., 2019). Take graphene for instance. Pure graphene absorbs common gas molecules physically, which has a large limitation on gas sensitivity (Feng et al., 2012; Meng et al., 2013; Abideen et al., 2018; Mirzaei et al., 2019; Mourya et al., 2019). The performance of graphene can be changed by metal doping. Arsenene 2-D semiconductor structure (Fleurence et al., 2012), antimony-vinyl folded honeycomb 2-D structure, and telluriene structure can be produced by imitating the graphene's structure (Liu, 2017). In conclusion, 2-D nanomaterial has higher sensitivity and selectivity when compared with other materials on gas-sensing mechanism.

Effect of 2-D Nanomaterial on Gas-Sensing Performance

Gas-sensitive materials have many properties, such as sensitivity, selectivity, stability, response time, etc., which are directly related to the surface characteristics of material. Surface characteristics are decided by the particle size of material. When the scale of the material reaches nano size, its surface area and surface activity will increase. Nanomaterials can be designed into different shapes, which will greatly increase the capability of absorbing specific gases. Therefore, gas sensors made by those nanomaterials will have their performances enhanced dramatically. Take SnO_2 as an example; the porous hollow rod SnO_2 composed of 1-D nanoscale rod provides more paths for gaseous diffusion, due to massive petal shape

TABLE 1 | Relationship between microstructure, preparation, and gas sensitivity in 2-D nanomaterial (WO₃, ZnO).

Gas-sensitive material	Operation temperature (°C)	Target gas	Detection range (ppm)	The dynamic responses R		Response time (s)	References
				R = Ra/Rg	Concentration (ppm)		
WO ₃ nanoscale sheet	150	NO ₂	1–20	107.3	5.00	–	Qin et al., 2010
WO ₃ hollow half tube	300	H ₂ S	0.12–2	1.2	0.12	35	Choi et al., 2012
ZnO nanoscale sheet	350	Ethanol	1–500	20.0	100.00	12	Alenezi et al., 2013
WO ₃ hollow crystal sheet	340	Ethanol	10–500	2.5	10.00	–	Su et al., 2010
WO ₃ hollow microsphere	75	NO ₂	0.04–1	16.0	0.04	10	You et al., 2012
WO ₃ nanoscale cluster	320	Acetone	1–400	17.5	100.00	2	Huang et al., 2011
ZnO flower structure	370	Ethanol	5–500	31.0	100.00	12	Chen et al., 2013
ZnO nest	420	Acetone	5–1,000	17.4	100.00	7	Wang et al., 2012

nanosheets and pores. The conversion of sphere-like structures into petal-like ones and successful synthesis of 1-D nanoscale rod and cones when composing flower-like SnO₂ improves the gas sensitivity and shortens the response time. In order to avoid the performance degradation caused by accumulation of nanostructure, the porous flower-like SnO₂ structure composed by 2-D nanosheets not only enlarges the surface area of the structure but also increases the internal hole channels as well, which will promote gas diffusion. Finally, flake-like layered SnO₂ structure composed by numerous thin nanosheets marks further improvement on the material's surface activity and shows excellent gas selectivity and sensitivity in the test (shown in Table 1).

Effect of 2-D Nanomaterial on Gas Sensor's Sensitivity

Improving the response sensitivity of nanomaterial gas sensor is crucial in practical engineering applications. Response sensitivity can be improved by (1) changing the surface of the 2-D nanomaterial (generally metallic oxide) to enhance the sensibility of the reaction 1-D nanofiber formed by nanoparticles will provide more route for the electron to move rapidly and bigger specific surface area to improve its sensibility; Cho et al. produced hemispherical N_iO nanomaterial, which had a sensitivity of 1.5 to ethanol vapor (Cho et al., 2011); Song et al. produced nanotube N_iO nanomaterial, with a sensitivity of 3 to ethanol vapor; the particle size and touching area are also the important factors on the sensitivity (Song et al., 2011), (2) changing the morphology of the nanomaterial Szilagyi et al. sintered ammonium tungstate compounds to produce hexagonal phase h-WO₃, which was sensitive to H₂S and monoclinic γ - WO₃, CH₄, H₂, and CO (Szilagyi et al., 2010); Gao et al. used hydrothermal method to synthesize triclinic δ - WO₃ square nanosheet, which had higher gas response sensitivity to cyclohexene (Gao et al., 2013), and (3) doping of transition metal to improve the sensitivity

of nanomaterial Wang et al. doped Cr to produce ferroelectric monoclinic ϵ - WO₃, which had better selectivity to acetone (Wang et al., 2008); Kim et al. prepared N_iO doped with Fe³⁺ to make a gas sensor with the response value of 100 ppm ethanol improved from 5.5 to 172.5, which showed tremendous improvement of nanomaterial sensitivity by metallic doping (Kim, 2012).

Effect of 2-D Nanomaterial on Gas Sensor Selectivity

Something interesting will be found when we combine special microstructure of nanomaterial with specific structure of different gases. This interesting finding will be the nanomaterial's specific selectivity to gases in macroscopic. Selectivity of 2-D nanomaterial is an important factor to measure the effect of materials. The lower symmetry of structure indicates the better selectivity of gas sensors. Take WO₃ nanocrystal with exocentric structure as an example. The symmetry of triclinic WO₃ crystal is lower than that of monoclinic and hexagonal WO₃ crystals. So, the triclinic WO₃ crystal has higher sensitivity and selectivity on acetone molecules with larger dipole moments (Bai, 2014). The influence of working temperature on the selectivity of materials is also an important factor to consider. Triclinic WO₃ nanomaterial has better selectivity and sensitivity to acetone at higher temperature and better selectivity to NO₂ at lower temperature (Zhao et al., 2013).

DEVELOPMENT TREND OF GAS SENSOR BASED ON 2-D NANOMATERIAL

Throughout the development of nanotechnology, gas sensor based on nanomaterial is always an extremely important research field. It has deep and wide influence on life and production. However, 2-D nanomaterial research is still full of problems in the

aspects ranging from imperfect sensitive materials and immature preparation technology to disability on scaled production. Gas sensor materials will be developed from single metallic oxide to composite oxide. Morphology of nanomaterial can be changed to improve the sensing performances; particle size can be reduced to improve the surface activity of the material; new structure can be designed to absorb more specific gases; selectivity of the sensors can be improved by reducing the asymmetry of 2-D nanomaterial structure and improving its working temperature.

2-D nanomaterial plays an increasingly important role in the further improvement of the gas sensor's performance. In recent years, the development trend of various electronic components tends to be more integrated, miniaturized, and even microminiaturized. Gas sensor will also consume less power, be multi-functional, and have higher performance. The material of gas sensor will be changed from simple gas-sensitive materials to complex composite materials. The structure of gas sensor will be changed from monolayer to multilayer and from simple morphology to special morphology. Also, it will be widely used in chemical production, gas transportation, and other toxic and harmful gas detection. In 2019, Tian et al. prepared ternary complex of graphene/WO₃ nanorod/polythiophene (3D-r GO/WO₃/PTh), and studied its gas sensitivity to H₂S. The study results showed that under low temperature of 75°C, this material has fast response and distinguishing selectivity to H₂S (Tian et al., 2019). Therefore, it can be found that the study of multiple element compound is a very popular research issue for the development of new gas sensor materials with better performance.

CONCLUSION

In this paper, gas-sensing properties of the 2-D nanomaterial are reviewed. Firstly, the classification of nanomaterials

on the number of dimensions is briefly introduced, and the latest research progress and development trend of 2-D nanomaterial are summarized. Secondly, the gas-sensing mechanism of 2-D nanomaterial is summarized by comparing the characteristics of existing 2-D nanomaterials. The effects of particle size and morphology property of 2-D nanomaterial on the performance of gas sensors are discussed. Then, the enhancement related to morphology property, phase structure, and metal doping of 2-D nanomaterial on the sensitivity of gas sensors is analyzed. Also, the effect of symmetry structure of 2-D nanomaterial on the selectivity of gas sensors is concluded. Finally, the development trend of 2-D nanomaterials for gas sensors is proposed, and references for the next development of 2-D nanomaterial are provided.

AUTHOR CONTRIBUTIONS

XM and LG conceived and designed the experiments. ZH and GT performed the experiments. XM and JA analyzed the data. XM and QH wrote the manuscript with input from all authors. All authors read and approved the manuscript.

FUNDING

This work was supported by the international science and technology cooperation and exchange research project of Sichuan province (18GJHZ0195), downhole Intelligent Measurement and Control Science and technology innovation team of Southwest Petroleum University (2018CXTD04), and the National Natural Science Foundation (51974273 and 51874255).

REFERENCES

- Abideen, Z., Kim, J.-H., Mirzaei, A., Kim, W. H., and Kim, S. S. (2018). Sensing behavior to ppm-level gases and synergistic sensing mechanism in metal-functionalized rGO-loaded ZnO nanofibers. *Sens. Actuat. B Chem.* 255, 1884–1896. doi: 10.1016/j.snb.2017.08.210
- Ahmad, R., Majhi, S. M., Zhang, X., Swager, T. M., and Salama, K. N. (2019). Recent progress and perspectives of gas sensors based on vertically oriented ZnO nanomaterials. *Adv. Colloid Interface Sci.* 270, 1–27. doi: 10.1016/j.cis.2019.05.006
- Alenezi, M. R., Alshammari, A. S., and Jayawardena, K. I. (2013). Role of the exposed polar facets in the performance of thermally and UV activated ZnO nanostructured gas sensors. *J. Phys. Chem. C* 117, 17850–17858. doi: 10.1021/jp4061895
- Bai, X. (2014). *Microscopic morphology, phase and surface structure control and gas sensing properties of WO₃ nanocrystals* (master's thesis). Tianjin University, Tianjin, China.
- Beheshtian, J., Peyghan, A. A., and Bagheri, Z. (2012a). Selective function of Al₁₂N₁₂ nano-cage towards NO and CO molecules. *Comput. Mater. Sci.* 62, 71–74. doi: 10.1016/j.commatsci.2012.05.041
- Beheshtian, J., Peyghan, A. A., Bagheri, Z., and Kamfirooz, M. (2012b). Interaction of small molecules (NO, H₂, N₂, and CH₄) with BN nanocluster surface. *Struct. Chem.* 23, 1567–1572. doi: 10.1007/s11224-012-9970-9
- Chen, X., Liu, J., and Jing, X. (2013). Self-assembly of ZnO nanosheets into flower-like architectures and their gas sensing properties. *Mater. Lett.* 112, 23–25. doi: 10.1016/j.matlet.2013.08.118
- Cho, N. G., Hwang, I.-S., Kim, H.-G., Lee, J. H., and Kim, I. D. (2011). Gas sensing properties of p-type hollow NiO hemispheres prepared by polymeric colloidal templating method. *Sens. Actuat. B Chem.* 155, 366–371. doi: 10.1016/j.snb.2010.12.031
- Choi, M. S., Bang, J. H., Mirzaei, A., Na, H. G., Jin, C., Oum, W., et al. (2019). Exploration of the use of p-TeO₂-branch/n-SnO₂ core nanowires nanocomposites for gas sensing. *Appl. Surf. Sci.* 484, 1102–1110. doi: 10.1016/j.apsusc.2019.04.122
- Choi, S. J., Lee, I., Jang, B. H., Youn, D. Y., Ryu, W. H., Park, C. O. et al. (2012). Selective diagnosis of diabetes using Pt-functionalized WO₃ hemitube networks as a sensing layer of acetone in exhaled breath. *Anal. Chem.* 85, 1792–1796. doi: 10.1021/ac303148a
- Dai, J., and Yuan, J. (2010). Adsorption of molecular oxygen on doped graphene: atomic, electronic, and magnetic properties. *Phys. Rev. B* 81:165414. doi: 10.1103/PhysRevB.81.165414
- Feng, B., Ding, Z., Meng, S., Yao, Y., He, X., Cheng, P., et al. (2012). Evidence of silicene in honeycomb structures of silicon on Ag (111). *Nano Lett.* 12, 3507–3511. doi: 10.1021/nl301047g
- Fleurence, A., Friedlein, R., Ozaki, T., Kawai, H., Wang, Y., and Yamada-Takamura, Y. (2012). Experimental evidence for epitaxial silicene on diboride thin films. *Phys. Rev. Lett.* 108:245501. doi: 10.1103/PhysRevLett.108.245501

- Gao, X., Su, X., Yang, C., Xiao, F., Wang, J., Cao, X., et al. (2013). Hydrothermal synthesis of WO₃ nanoplates as highly sensitive cyclohexene sensor and high-efficiency MB photocatalyst. *Sens. Actuat. B Chem.* 181, 537–543. doi: 10.1016/j.snb.2013.02.031
- Geim, A. K. (2009). Graphene: status and prospects. *Science* 324, 1530–1534. doi: 10.1126/science.1158877
- Geim, A. K., and Novoselov, K. S. (2007). The rise of graphene. *Nat. Mater.* 6, 183–191. doi: 10.1038/nmat1849
- Gonullu, Y., Rodriguez, G. C. M., Saruhan, B., and Ürgen, M. (2012). Improvement of gas sensing performance of TiO₂ towards NO₂ by nano~tubular structuring. *Sens. Actuat. B Chem.* 169, 151–160. doi: 10.1016/j.snb.2012.04.050
- Guo, Z. (2018). *Research on gas sensitivity of graphene/polyaniline composite material based on multiscale analysis[D]*. University of Wenzhou.
- Huang, J., Xu, X., and Gu, C. (2011). Large-scale synthesis of hydrated tungsten oxide 3D architectures by a simple chemical solution route and their gas-sensing properties. *J. Mater. Chem.* 21, 13283–13289. doi: 10.1039/c1jm11292a
- Huang, X., Tan, C. L., Yin, Z. Y., and Zhang, H. (2014). 25th anniversary article: hybrid nanostructures based on two-dimensional nanomaterials. *Adv. Mater.* 26, 2185–2204. doi: 10.1002/adma.201304964
- Kim, J.-H., Mirzaei, A., Kim, H. W., and Kim, S. S. (2019). Combination of Pd loading and electron beam irradiation for superior hydrogen sensing of electrospun ZnO nanofibers. *Sens. Actuat. B Chem.* 284, 628–637. doi: 10.1016/j.snb.2018.12.120
- Kim, K.-M., et al. (2012). Highly sensitive C₂H₅OH sensors using Fe-doped NiO hollow spheres. *Sens. Actuat. B Chem.* 171–172, 1029–1037. doi: 10.1016/j.snb.2012.06.029
- Kong, J., Franklin, N. R., Zhou, C., Chapline, M. G., Peng, S., Cho, K., et al. (2000). Nanotube molecular wires as chemical sensors. *Science* 287, 622–625. doi: 10.1126/science.287.5453.622
- Li, Y., Guo, Y., Tan, R., Cui, P., Li, Y., and Song, W. (2009). Synthesis of SnO₂ nano-sheets by a template-free hydrothermal method. *Mater. Lett.* 63, 2085–2088. doi: 10.1016/j.matlet.2009.06.060
- Liu, B., and Zhou, K. (2019). Recent progress on graphene-analogous 2D nanomaterials: properties, modeling and applications. *Prog. Mater. Sci.* 100, 99–169. doi: 10.1016/j.pmatsci.2018.09.004
- Liu, C. (2017). *Gas sensing properties based on 2-D nanomaterials* (Master's thesis). Nanjing University of Posts and Telecommunications, Nanjing, China.
- Liu, J. X., Cao, H., Jiang, B., Xue, Y., and Fu, L. (2016). Application of emerging 2-D materials in flexible energy storage and conversion. *Sci. China Mater.* 59, 459–474. doi: 10.1007/s40843-016-5055-5
- Ma, R., Hu, J., Cai, Z., and Ju, H. (2014). Highly selective enrichment of phosphopeptides with high-index facets exposed octahedral tin dioxide nanoparticles for mass spectrometric analysis. *Talanta* 119, 452–457. doi: 10.1016/j.talanta.2013.11.049
- Meng, L., Wang, Y., Zhang, L., Du, S., Wu, R., Li, L., et al. (2013). Buckled silicene formation on Ir (111). *Nano Lett.* 13, 685–690. doi: 10.1021/nl304347w
- Mirzaei, A., Yousefi, H. R., Falsafi, F., Bonyani, M., Lee, J.-H., Kim, J.-H., et al. (2019). An overview on how Pd on resistive-based nanomaterial gas sensors can enhance response toward hydrogen gas. *Int. J. Hydrogen Energy* 44, 20552–20571. doi: 10.1016/j.ijhydene.2019.05.180
- Mourya, S., Kumar, A., Jaiswal, J., Malik, G., Kumar, B., Chandra, R., et al. (2019). Development of Pd-Pt functionalized high performance H₂ gas sensor based on silicon carbide coated porous silicon for extreme environment applications. *Sens. Actuat. B Chem.* 283, 373–383. doi: 10.1016/j.snb.2018.12.042
- Pang, J. H., Tan, Q. L., and Liu, W. Y. (2016). Preparation of CNT-SnO₂ composites and study on formaldehyde gas sensitivity. *Sci. Technol. Eng.* 16, 53–57. doi: 10.3969/j.issn.1671-1815.2016.01.009
- Perreault, F., de Faria, A. F., and Elimelech, M. (2015). Environmental applications of graphene-based nanomaterials. *Chem. Soc. Rev.* 44, 5861–5896. doi: 10.1039/C5CS00021A
- Qin, Y., Hu, M., and Zhang, J. (2010). Microstructure characterization and NO₂-sensing properties of tungsten oxide nanostructures. *Sens. Actuat. B Chem.* 150, 339–345. doi: 10.1016/j.snb.2010.06.063
- Qiu, H. F., Zhao, D., Teng, J. Q., Jia, T. H., Lei, S. C., Wang, C., et al. (2018). A construction method and gas sensitive characteristics of graphene oxide sensors. *J. Xi'an Jiaotong University* 52, 95–101. doi: 10.7652/xjtubx201810013
- Rastegar, S. F., Peyghan, A. A., Ghenaatian, H. R., and Hadipour, N. L. (2013). NO₂ detection by nanosized AlN sheet in the presence of NH₃: DFT studies. *Appl. Surf. Sci.* 274, 217–220. doi: 10.1016/j.apsusc.2013.03.019
- Sharma, A., Tomar, M., and Gupta, V. (2013). WO₃ nanoclusters-SnO₂ film gas sensor heterostructure with enhanced response for NO₂. *Sens. Actuat. B Chem.* 176, 675–684. doi: 10.1016/j.snb.2012.09.094
- Shen, Z. D., Hu, J. J., Li, Z. Z., Zhao, W. L., Qu, J., and Fan, H. (2018). Study on the gas sensitivity of ZnO Nano-film materials to ethanol at room temperature. *J. Hebei Inst. Architect. Eng.* 36, 130–134. doi: 10.3969/j.issn.1008-4185.2018.04.028
- Shur, M. S., Rumyantsev, S. L., Jiang, C., Samnakay, R., Renteria, J., and Balandin, A. A. (2014). Selective gas sensing with MoS₂ thin film transistors. *Sensors* 2014, 55–57. doi: 10.1109/ICSENS.2014.6984931
- Song, X., Gao, L., and Mathur, S. (2011). Synthesis, characterization, and gas sensing properties of porous nickel oxide nanotubes. *J. Phys. Chem. C* 115, 21730–21735. doi: 10.1021/jp208093s
- Su, X., Li, Y., and Jian, J. (2010). *In situ* etching WO₃ nanoplates: hydrothermal synthesis, photoluminescence and gas sensor properties. *Mater. Res. Bull.* 45, 1960–1963. doi: 10.1016/j.materresbull.2010.08.011
- Sun, N. N., Liu, Y., Li, Y., Ji, Q. C., Wang, L., and Zhang, Y. M. (2016). Study on electronic properties and stability of 2-D B₃N₂ monolayer structure. *J. Hebei Tech. Coll.* 4, 25–29. doi: 10.16046/j.cnki.issn1008-3782.2016.04.007
- Sun, S. H., Meng, G. W., Zhang, G. X., Gao, T., Geng, B. Y., Zhang, L. D., et al. (2003). Raman scattering study of rutile SnO₂ nanobelts synthesized by thermal evaporation of Sn powders. *Chem. Phys. Lett.* 376, 103–107. doi: 10.1016/S0009-2614(03)00965-5
- Szilagyi, I. M., Saukko, S., and Mizsei, J. (2010). Gas sensing selectivity of hexagonal and monoclinic WO₃ to H₂S. *Solid State Sci.* 12, 1857–1860. doi: 10.1016/j.solidstatesciences.2010.01.019
- Tao, Q. (2017). *Fabrication and characterization of carbon nanotube/SnO₂ flexible gas sensor* (Master's thesis). Tianjin University of Technology, Tianjin, China.
- Tao, T., Chen, Q., Hu, H., and Chen, Y. (2011). Tree-like SnO₂ nanowires and optical properties. *Mater. Chem. Phys.* 126, 128–132. doi: 10.1016/j.matchemphys.2010.11.052
- Tian, J. F., Yi, Z. G., and Han, G. L. (2019). Preparation of three-dimensional of Graphene/WO₃ nanorod/polythiophene Composites and their gas sensing properties at low temperature. *Sci. Technol. Eng.* 19, 94–98.
- Trung, D. D., Toan, N. V., Tong, P. V., Duy, N. V., Hoa, N. D., Van Hieu, N. (2012). Synthesis of single-crystal SnO₂ nanowires for NO_x gas sensors application. *Ceram. Int.* 38, 6557–6563. doi: 10.1016/j.ceramint.2012.05.039
- Varghese, S. S., Varghese, S. H., Swaminathan, S., Singh, K. K., and Mittal, V. (2015). Two-dimensional materials for sensing: graphene and beyond. *Electronics* 4, 651–687. doi: 10.3390/electronics4030651
- Wang, H., and Rogach, A. L. (2014). Hierarchical SnO₂ nanostructures: recent advances in design, synthesis, and applications. *Chem. Mater.* 26, 123–133. doi: 10.1021/cm4018248
- Wang, J. (2013). *Synthesis, characterization and regulation of nanoparticles in ion implanted transparent insulating materials* (Master's thesis). University of Tianjin, Tianjin, China.
- Wang, L., Teleki, A., and Pratsinis, S. (2008). Ferroelectric WO₃ nanoparticles for acetone selective detection. *Chem. Mater.* 20, 4794–4796. doi: 10.1021/cm800761e
- Wang, Q. G. (2018). *Preparation and gas sensitivity of new Zn-Sn-O superlattice nanoparticles* (Master's thesis). Southwest Jiaotong University, Chengdu, China.
- Wang, X., Liu, W., Liu, J., Wang, F., Kong, J., Qiu, S., et al. (2012). Synthesis of nestlike ZnO hierarchically porous structures and analysis of their gas sensing properties. *ACS Appl. Mater. Interfaces* 4, 817–825. doi: 10.1021/am201476b
- Wen, W., Song, Y., Yan, X., Zhu, C., Du, D., Wang, S., et al. (2018). Recent advances in emerging 2D nanomaterials for biosensing and bioimaging applications. *Mater. Today* 21, 164–177. doi: 10.1016/j.mattod.2017.09.001
- Xu, T., Wang, S., Li, L., and Liu, X. (2019). Dual templated synthesis of tri-modal porous SrTiO₃/TiO₂@carbon composites with enhanced photocatalytic activity. *Appl. Catal. A* 575, 132–141. doi: 10.1016/j.apcata.2019.02.017
- Xu, X. M., Wang, D. M., Wang, W., Sun, P., Ma, J., Liang, X., et al. (2012). Porous hierarchical In₂O₃ nanostructures: Hydrothermal preparation

- and gas sensing properties. *Sens. Actuat. B Chem.* 171, 1066–1072. doi: 10.1016/j.snb.2012.06.035
- Yang, J. Z. (2019). *Preparation of graphene oxide gas sensitive material and its application in the detection of harmful and toxic gases[D]*. Southwest University of Science and Technology, Mianyang, China.
- You, L., He, X., Wang, D., Sun, P., Sun, Y. F., Liang, X. S., et al. (2012). Ultrasensitive and low operating temperature NO₂ gas sensor using nanosheets assembled hierarchical WO₃ hollow microspheres. *Sens. Actuat. Chem. B.* 173, 426–432. doi: 10.1016/j.snb.2012.07.029
- Yu, H. Q. (2018). *Direct fabrication and properties of 2-D alpha-MoO₃ nano-material gas sensors* (Master's thesis). Jinan University, Guangzhou, China.
- Yuan, L. (2017). *Research on porous silicon-based nano-tungsten oxide multi-level structure material gas sensor* (Master's thesis). Tianjin University, Tianjin, China.
- Yue, Y., and Yu, H. (2019). Study on gas sensitivity of new SnO₂ nanosheets. *Enterprise Sci. Technol. Dev.* 6, 90–91. doi: 10.3969/j.issn.1674-0688.2019.06.040
- Zhang, D., Sun, L., Yin, J., and Yan, C. (2003). Low-temperature fabrication of highly crystalline SnO₂ nanorods. *Adv. Mater.* 15, 1022–1025. doi: 10.1002/adma.200304899
- Zhang, J., Wang, S., Wang, Y., Wang, Y., Zhu, B., Xia, H., et al. (2009). NO₂ sensing performance of SnO₂ hollow-sphere sensor. *Sens. Actuat. B Chem.* 135, 610–617. doi: 10.1016/j.snb.2008.09.026
- Zhang, T., Xue, Q., Shan, M., Jiao, Z., Zhou, X., Ling, C., et al. (2012). Adsorption and catalytic activation of O₂ molecule on the surface of Au-doped graphene under an external electric field. *J. Phys. Chem. C* 116, 19918–19924. doi: 10.1021/jp3073359
- Zhang, X. Z. (2011). Research progress of metal oxide semiconductor nanometer gas sensitive materials. *Sci. Technol. Western China* 10, 5–6. doi: 10.3969/j.issn.1671-6396.2011.32.003
- Zhao, L., Tian, F. H., Wang, X., Zhao, W., Fu, A., Shen, Y., et al. (2013). Mechanism of CO adsorption on hexagonal WO₃ (001) surface for gas sensing: a DFT study. *Comput. Mater. Sci.* 79, 691–697. doi: 10.1016/j.commatsci.2013.07.046
- Zhu, S. D., Zhu, G. S., Cai, R., Han, Y., and Tian, W. (2010). Research progress of nanomaterials at home and abroad, structure, I., Specific effect and properties of nanomaterials. *Therm. Process Technol.* 31, 1–5. doi: 10.19382/j.cnki.1673-4971.2010.03.001

Conflict of Interest: The authors declare that the research was conducted in the absence of any commercial or financial relationships that could be construed as a potential conflict of interest.

Copyright © 2019 Ge, Mu, Tian, Huang, Ahmed and Hu. This is an open-access article distributed under the terms of the Creative Commons Attribution License (CC BY). The use, distribution or reproduction in other forums is permitted, provided the original author(s) and the copyright owner(s) are credited and that the original publication in this journal is cited, in accordance with accepted academic practice. No use, distribution or reproduction is permitted which does not comply with these terms.



NO₂ Sensing Properties of Cr₂WO₆ Gas Sensor in Air and N₂ Atmospheres

Yi Wu^{1*}, Meng Yan¹, Chen Tian¹, Yuhang Liu² and Zhongqiu Hua¹

¹ Tianjin Key Laboratory of Electronic Materials and Devices, School of Electronics and Information Engineering, Hebei University of Technology, Tianjin, China, ² Institute of Polymer Materials, Beijing Institute of Machine and Equipment, Beijing, China

Gas sensors were fabricated from Cr₂WO₆ nanoparticles for NO₂ detection. Low dimensional materials Cr₂WO₆ were prepared by a wet chemistry method followed by hydrothermal treatment. The morphology of the nanoparticles and their sensing properties to NO₂ were investigated in both dry and humid conditions. Additionally, the sensing response was also characterized in a non-oxygen condition. It was concluded that the sensor responses in N₂ conditions were higher than that in air conditions at 200°C. Moreover, the sensing characteristics were inhibited by water vapor at 200°C. The oxygen adsorption behavior was also investigated to verify the basic sensing mechanism of Cr₂WO₆ in the absence and presence of NO₂ and water vapor separately. Based on the power law response, it was indicated that both NO₂ and water vapor have a strong adsorption ability than oxygen ions of Cr₂WO₆ sensors.

OPEN ACCESS

Edited by:

Mingshui Yao,
Kyoto University, Japan

Reviewed by:

Le-Xi Zhang,
Tianjin University of Technology, China
Liwei Wang,
Guangxi University, China

*Correspondence:

Yi Wu
wuyi@hebut.edu.cn

Specialty section:

This article was submitted to
Nanoscience,
a section of the journal
Frontiers in Chemistry

Received: 04 November 2019

Accepted: 16 December 2019

Published: 23 January 2020

Citation:

Wu Y, Yan M, Tian C, Liu Y and Hua Z
(2020) NO₂ Sensing Properties of
Cr₂WO₆ Gas Sensor in Air and N₂
Atmospheres. *Front. Chem.* 7:907.
doi: 10.3389/fchem.2019.00907

Keywords: nitrogen dioxide, Cr₂WO₆, low dimensional material, gas sensors, humidity

INTRODUCTION

National nitrogen oxide (NO_x) emissions were 20.6 million metric tons (Mt) in 2015, with annual growth rates of 5.9% since 1949 in China (Richter et al., 2005; Sun et al., 2018). Among them, owing to its toxic effects to animals and plants, NO₂ is irritant and corrosive even at ppm level with serious harm to the respiratory tract and causticity particularly in children and elderly (Ling and Leach, 2004; Kida et al., 2009). Thus, determination of NO_x emissions is vital to regional and global ozone air pollution, acid deposition, and climate change (Jaegle et al., 2005). There have been great demands for cheap, reliable, and effective methods of real-time monitoring of NO₂ level in the environment (Stănoiu et al., 2012). To date, gas sensors based on metal oxide semiconductors (MOS) have been extensively investigated and successfully commercialized for NO_x detection due to their superior properties, simple structure, and low cost (Afzal et al., 2012). Among them, WO₃ based sensors show an excellent property to NO₂ in respect of sensitivity (Choi et al., 2004; Hua et al., 2018d). It was reported that WO₃ sensors fabricated through a wet process were sensitive to ppb levels of NO₂ with a low temperature due to a strong adsorption ability of NO₂ onto tungsten atoms compared with the weak adsorption of oxygen (Choi et al., 2004). Recently, gas sensors based on P-type MOS materials have been reported to have a sensitive and selective response to NO₂ with a low cross-sensitivity to humidity (Nguyen and El-Safty, 2011; Stănoiu et al., 2012). It was reported that the NO₂ sensors based on Cr₂O₃ showed a selectivity relative to CO and low cross-sensitivity to humidity, which was due to the higher surface reactivity toward NO₂ than CO through the electrical resistance and work function changes both in dry and humid air (Stănoiu et al., 2012). Gas sensors based on NiO nanosheets were fabricated by a hydrothermal method, which

showed high sensitivity and selectivity to NO₂ (Nguyen and El-Safty, 2011). That may be due to NO₂ having higher electron affinity than the pre-adsorbed oxygen (Hoa et al., 2009). In this paper, chromium tungstate (Cr₂WO₆) was prepared by a wet chemistry method followed by hydrothermal treatment. The sensing properties to NO₂ in oxygen and non-oxygen atmosphere were investigated under dry and humid conditions, respectively. It was found that sensors based on P-type Cr₂WO₆ were very sensitive to NO₂ even with a high humid condition. In addition, the sensing mechanism was verified by the oxygen adsorption behavior in different conditions. Eventually, the fundamental sensing mechanism to NO₂ was explained.

EXPERIMENTAL

Chromium(III) nitrate nonahydrate (99.95%) and sodium tungstate dehydrate (ACS 99.0–101.0%) were provided by Shanghai Aladdin Biochemical Technology Co., Ltd. Chromium tungstate (Cr₂WO₆) nanoparticles were synthesized by a hydrothermal assisted process as described in **Supplementary Materials A** (Zhou et al., 2015). Subsequently, the powders were annealed at 1,000°C in air for 2 h. The samples were characterized using X-ray diffraction (XRD; D8 FOCUS, Bruker, Germany) in CuK α radiation with corresponding wavelengths of 1.54 Å and a filament current and voltage of 15 mA and 40 kV and a field-emission scanning electron microscope (FE-SEM; Nova Nano SEM 450, FEI). The surface morphology of the material was analyzed by transmission electron microscopy (TEM; Tecnai-F20, FEI, USA) with an accelerating voltage of 200 kV. The sample powders were mixed with glycerin to form a homogeneous paste and then was screen-printed on the alumina substrate. In order to obtain good stability, all sensors were aged at 400°C for 24 h. The gas sensing performance was measured by DC resistance with a homemade apparatus equipped with a dynamic gas distribution system as shown schematically in **Figure 1**. Target gases were supplied by gas cylinders with appropriate concentrations balanced

with the carrier gases (air or nitrogen). The humidity and oxygen concentrations were calibrated using a humidity sensor (SHT31-ARP, Sensirion, Switzerland) and oxygen analyzer (SST, England), respectively. Keithley multimeter (Keithley 2000, USA) was used to record all data in real time. The sensor response was defined as $S = R_a/R_g$, where R_a and R_g were the resistances in the presence of air/N₂ and oxidizing gases, respectively.

RESULTS AND DISCUSSION

In order to obtain a high purity of Cr₂WO₆ phase, a high sintering temperature of 1,000°C was used and the crystal structure was characterized by XRD. **Figure S3** shows the XRD patterns of prepared Cr₂WO₆ powders. Obviously, XRD patterns exhibit very narrow peaks indicating a good crystal quality and the patterns could be well-fit with the tetragonal phase (JCPDS 35-0791) indicating a high purity of the prepared Cr₂WO₆. The morphology of Cr₂WO₆ powders was characterized by SEM and TEM. **Figures 2A,B** show SEM images of Cr₂WO₆ powders, which consisted of huge number of particles in a grain shape with a large size. According to the insert SEM images the grain shape is estimated around 300 nm by counting. TEM images in **Figure 2C** show that the grain size is consistent with the SEM images. Additionally, HRTEM images in **Figure 2D** also suggest a good crystalline quality of Cr₂WO₆ nanoparticles and the lattice spacing of 0.323 nm and 0.248 nm is in good accordance with (110) and (103) planes of tetragonal Cr₂WO₆ (JCPDS 35-0791) and results of XRD (Zhou et al., 2015).

The sensing properties were characterized with NO₂ ranging from 0.2 to 5 ppm balanced with syntheses with an operation temperature of 200–350°C. According to previous reports, chemiresistive type sensors with a low concentration of carriers, i.e., holes in the present case, have a strong transduction ability with high cost of resistance (Bârsan et al., 2010; Hua et al., 2018a). It is worth noting that two identical sensor devices fabricated

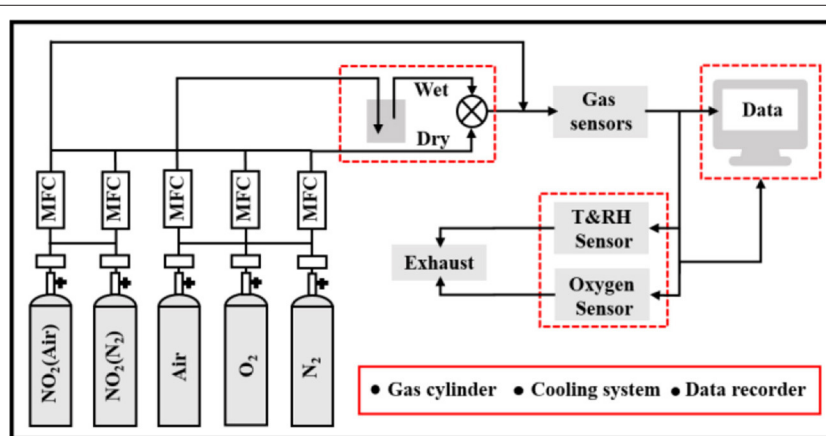


FIGURE 1 | Experimental system for the sensing characteristics of sensor devices.

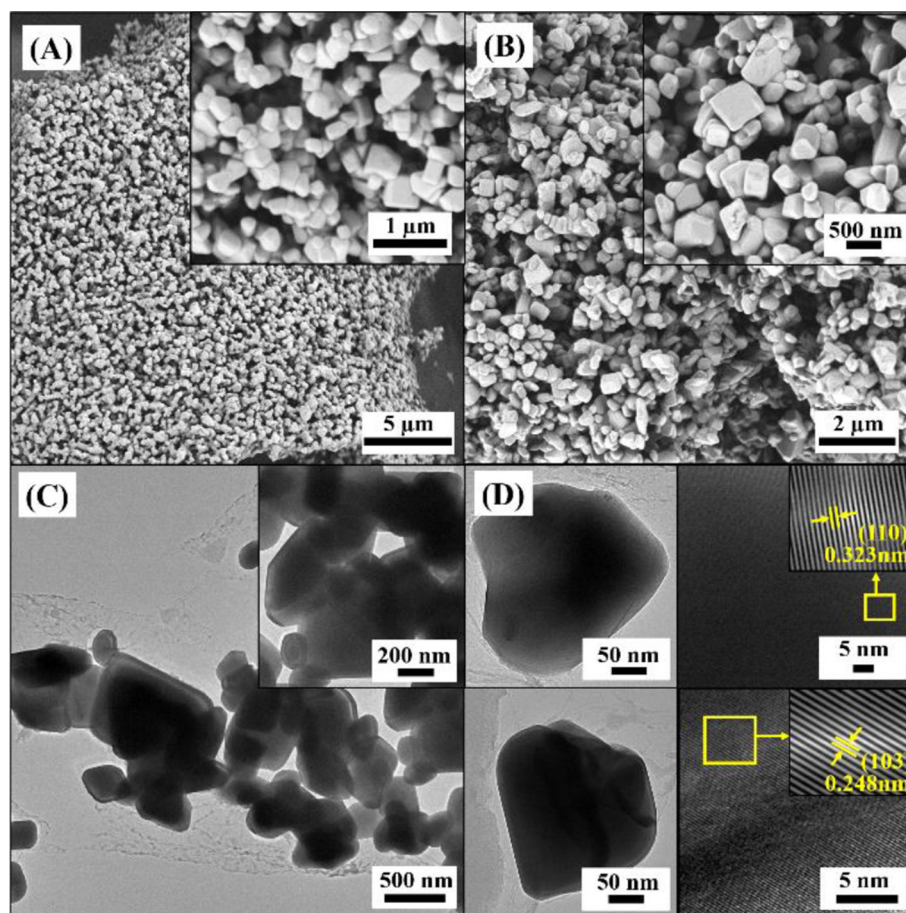
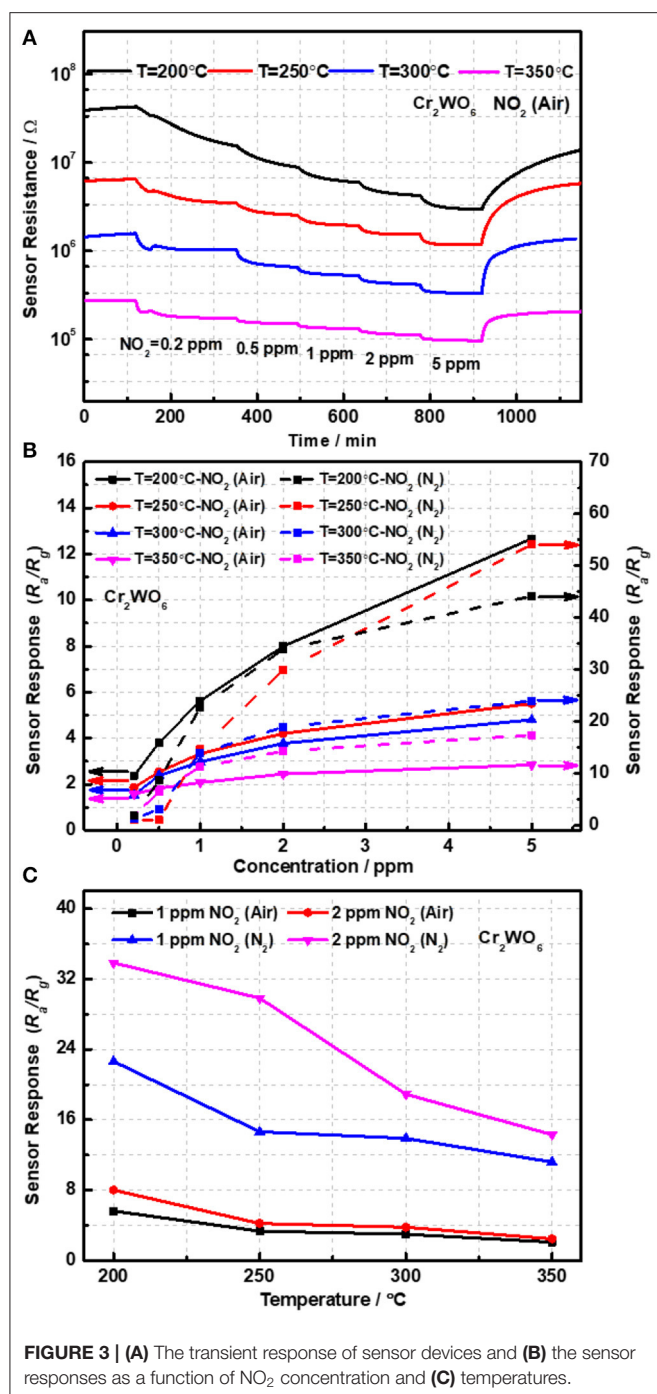


FIGURE 2 | The morphology analysis of powders (A,B) SEM images, (C) TEM images, and (D) HRTEM micrograph with lattice diffraction pattern of nanoparticles.

from the same materials were measured; however, only one sensor's data was presented for simplicity. The other one was used as a reference and not shown. **Figure 3A** presented the time and temperature dependence of sensor resistance. It was found that sensor resistance significantly increased with reduction in operation temperatures. When the temperature decreased from 250 to 200°C, sensor resistance was almost increased by 3 times. However, when the temperature was lower than 200°C, sensors gave an extremely high resistance reaching to $10^8 \Omega$ and over the range of measurement (Keithley 2000), which is also very difficult for practical applications. Thus, sensing response was only characterized from 200 to 350°C. One can note that sensor resistance is significantly reduced when exposed to NO₂, suggesting a P-type response of Cr₂WO₆. Moreover, the sensor responses were found to be highly temperature-dependent and increased with reduction in temperatures (Bodneva et al., 2019). When the working temperature increased to 350°C, the responses of 5 ppm NO₂ were reduced by 4.5 times.

Detection of NO₂ in the non-oxygen atmosphere was highly required and could be applied to some specific scenes, such as the fuel leaks in aerospace systems. The sensor responses to NO₂ balanced with N₂ were investigated from 200 to 350°C

in the absence of oxygen. Owing to its p-type conduction, the baseline resistance in N₂ was largely enhanced caused by the increase in electrons released by adsorbed oxygens on the surface. Consequently, the sensor responses were greatly increased to NO₂ higher than 1 ppm and much higher than in air atmosphere as shown in **Figure 3B**. It was shown that the responses in N₂ conditions were 4 times as much as that in air conditions at 200°C as shown in **Figure 3C**. It was well-known that in the presence of oxygen there could be a competitive adsorption between oxygen and NO₂, and therefore, that may give a reason for the clear difference of sensing responses in the presence and absence of oxygen (Hua et al., 2018d). What's more, the competitive relation between NO₂ and oxygen will be analyzed by the oxygen adsorption behavior in the following. In addition, it was indicated that the sensing responses in N₂ atmosphere were highly dependent on the working temperatures similar to that in the air atmosphere. When the temperature decreased from 350 to 200°C, sensor resistance was almost promoted by 2 orders and sensor responses were enhanced by almost 4 times. As shown in **Figure S4**, it seems that the sensors gave a relatively poor response to NO₂ below 1 ppm, almost no response in a dry condition. In other words, the



limit of detection (LOD) of NO₂ for Cr₂WO₆ nanoparticles is better than 1 ppm. This is very similar to a typical n-type MOS gas sensor when exposed to reducing gases such as H₂ and CO (Hua et al., 2018c). A small concentration of gas could be shielded by adsorption of oxygen due to the release of free electrons by the reaction of adsorbed oxygens with reducing gases. Thus, small concentration of reducing gases could not be detected (Hua et al., 2018d). However, in the present case, it is believed that the shielding effect of NO₂

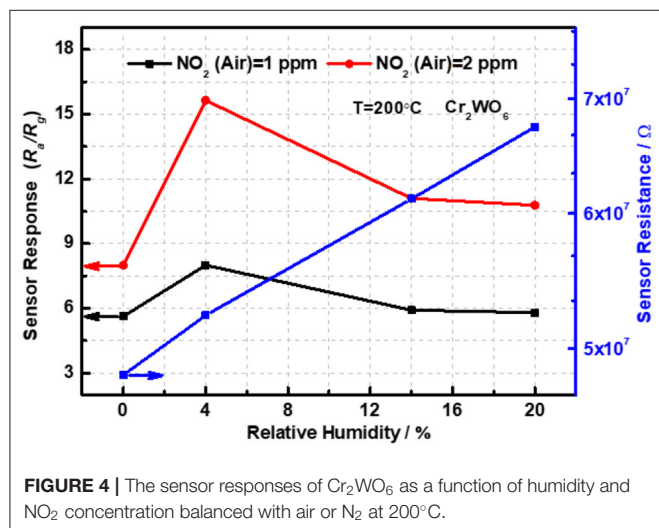
could be caused by a competitive adsorption of oxygen and NO₂ on the surface of Cr₂WO₆. When NO₂ adsorbed onto the surface and shared the same sites with oxygen adsorption leading to desorption of oxygen, there was no electron charge transfer. As NO₂ molecular trap the electrons, which released from desorption of O₂, the surface density will not generate a net increase. As a result, there was no resistive response, which was known as a chemical shielding effect for MOS gas sensors (Hua et al., 2018d). Finally, a comparison of MOS sensors to NO₂, including various n-type and p-type materials, was given in Table 1 (Ling and Leach, 2004; Hoa et al., 2009; Nguyen and El-Safty, 2011; Vyas et al., 2013; Marichy et al., 2015). In conclusion, the Cr₂WO₆ sensors have great sensitivity and lower operation temperatures to NO₂ compared with the n-type materials including SnO₂/WO₃ and ZnO both in air and N₂ atmospheres. Furthermore, some typical p-type materials were listed in Table 1, and the Cr₂WO₆ sensors displayed high sensitivity, which had great potential to be applied to some specific scenes. The stability of sensors have been also investigated in Figure S7 of Supplementary Material E.

Moreover, the sensing properties to NO₂ balanced with air in the presence of humidity were also investigated at 200°C and the transient responses were shown in Figure S5 of Supplementary Materials C. It was clear that all sensor resistances were a direct proportion to the relative humidity at 25°C (RH at 25°C) compared with that in dry conditions as revealed in Figure 4. The phenomenon can be explained by water vapor competing for adsorption sites of NO₂ on the surface of Cr₂WO₆ nanoparticles. When the humidity reached 4% RH at 25°C, sensor resistance was promoted by ~2 times and the sensor responses were enhanced in the humid conditions in Figure 4. The sensor response was increased by almost 2 times to 2 ppm NO₂ in the presence of 4% RH at 25°C. In the sensing processes, NO₂ acted as the acceptor, meanwhile the water vapor was the donor. Moreover, the water vapor gave an inhibition to the oxygen adsorption on the material surface. Interestingly, the sensor responses were reduced when the humidity increased to 14 and 20% RH at 25°C. That may owe to the chemical adsorption of water vapor, which occupies the adsorption sites of NO₂. However, the responses were still higher than that in dry conditions. Moreover, the sensing properties balanced with N₂ in humid atmosphere were also analyzed by Keithley multimeter; nevertheless, the water vapor gave a promotion to sensor resistance compared with that in dry conditions. Therefore, we cannot evaluate the performance of the sensor devices based on the existing equipment in the laboratory.

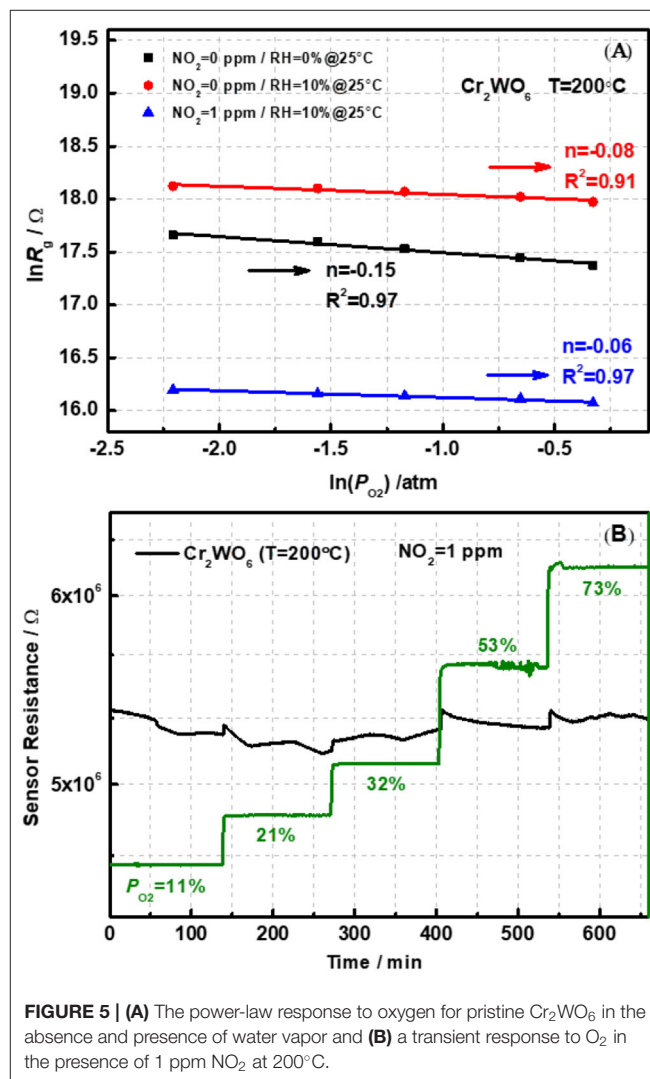
According to our previous reports, oxygen adsorption, and reaction play a basic role in the sensing process with the formation of O₂⁻, O⁻, or O²⁻ on the surface of metal oxides (Hua et al., 2018a,b,c). The oxygen adsorption behavior could be analyzed by the relationship between sensor resistance (R_g) and partial pressure of oxygen (P_{O_2}) in different atmospheres, i.e., power-law response. Figure 5 shows the linear plot of R_g on the P_{O_2} ranging from 0.1 to 0.7 atm (1 atm = 100% in volume) in a double logarithm-scale at an operation temperature of 200°C. It was obvious that the R_g decreased with increasing

TABLE 1 | The response to NO_x compared with other MOS sensors.

MOS sensors	Target gases	Detection concentration (ppm)	Response	Temperature (°C)	Conduction characteristic	References
SnO ₂ /WO ₃	NO ₂ /Air	2	6.5	300	n-type	Ling and Leach, 2004
Cr ₂ O ₃	NO ₂ /Air	3	2	200	p-type	Stănoiu et al., 2012
NiO	NO ₂ /Air	1	13	250	p-type	Nguyen and El-Safty, 2011
SnO ₂ – SWNT	NO _x /Air	60	2,300%	200	n-type	Hoa et al., 2009
TiO ₂ /CNT700	NO ₂ /Air	8	10	150	p-type	Marichy et al., 2015
ZnO	NO ₂ /N ₂	20	1.2	300	n-type	Vyas et al., 2013
Cr ₂ WO ₆	NO ₂ /Air	2	8	200	p-type	This work
Cr ₂ WO ₆	NO ₂ /N ₂	2	33.9	200	p-type	This work



P_{O_2} , indicating the presence of oxygen adsorption on the surface of Cr₂WO₆ nanoparticles. Adsorption of oxygen on the surface traps electrons and releases holes resulting in a reduction in sensor resistance. Moreover, **Figure 5A** presents the power-law response to oxygen, and the fitting slope (n) was -0.15 at 200°C. However, for p-type materials, the receptor and transducer functions have not been built yet. Thus, the fitting power-law exponent could not be well-clarified. However, it was quite clear that oxygen adsorption served as the receptor function for Cr₂WO₆ without difference with typical n-type WO₃ or p-type Cr₂O₃ (Hua et al., 2018a,b,c). As mentioned before, water vapor forms chemical adsorption on surface leading to a block on oxygen adsorption as shown in **Figure 5A**. With humidity increasing from 0 to 10% RH at 25°C, R_g was promoted at all P_{O_2} and the absolute value of n was decreased, suggesting a strong electronic interaction of oxygen with the Cr₂WO₆ surface. This may be caused by the competitive adsorption between oxygen and water molecules (Hua et al., 2018c). With the presence of NO₂, the power-law response to oxygen was also investigated to clarify the role of oxygen on the sensing process of NO₂ (Hua et al., 2018d). When exposed to NO₂ of 1 ppm, the sensor resistance greatly decreased. According to **Figure 5B**, the power-law response to oxygen is not linear, suggesting that



the adsorption of oxygen is influenced by NO₂ adsorption. More specifically, the electronic interaction of oxygen with the Cr₂WO₆ surface was significantly inhibited by NO₂, i.e., shielded by NO₂. This could be due to a competitive adsorption of NO₂, which may share the same adsorption sites, in case of

typical MOS, are metal atoms and oxygen vacancies. When exposed to humidity in the presence of NO₂ (1 ppm balanced with N₂), sensor resistance was almost independent of P_{O_2} , and the power-law exponent was merely 0.06, which is much smaller than that in a dry condition. The corresponding transient responses of power law response were shown in **Figure S6 of Supplementary Material D**. In addition, it was noted that the absolute value of the power-law exponent, n became much smaller compared with that in the absence of NO₂. In other words, humidity not only promotes the sensing response but also changes the basic mechanism of p-type Cr₂WO₆ to NO₂ according to the power-law response. It is possible that in the presence of humidity oxygen adsorption may take place with a competitive adsorption with water, which forms a weak adsorption on the surface of Cr₂WO₆. This causes a weak adsorption.

CONCLUSION

A new sensing material Cr₂WO₆ was prepared and its sensing properties to NO₂ were investigated in both dry and humid conditions. The basic sensing mechanism was also analyzed by surface oxygen adsorption behavior in different atmospheres. Here are the conclusions:

- Sensors based on Cr₂WO₆ nanoparticles showed great response to NO₂ based on air atmosphere down to 0.2 ppm. The sensor responses in N₂ conditions were higher than in air conditions over 1 ppm of NO₂.
- Sensor resistances were raised up with the relative humidity increasing. However, sensor responses to all gases were enhanced by water vapor over the range of 0–20% RH at 25°C.

REFERENCES

- Afzal, A., Cioffi, N., Sabbatini, L., and Torsi, L. (2012). NO_x sensors based on semiconducting metal oxide nanostructures: Progress and perspectives. *Sens. Actuators B Chem.* 171, 25–42. doi: 10.1016/j.snb.2012.05.026
- Bărsan, N., Simion, C., Heine, T., Pokhrel, S., and Weimar, U. (2010). Modeling of sensing and transduction for p-type semiconducting metal oxide based gas sensors. *J. Electroceram.* 25, 11–19. doi: 10.1007/s10832-009-9583-x
- Bodнева, V., Ilegbusi, O., Kozhushner, M., Kurmangaleev, K., Posvyanskii, V., and Trakhtenberg, L. (2019). Modeling of sensor properties for reducing gases and charge distribution in nanostructured oxides: a comparison of theory with experimental data. *Sens. Actuators B Chem.* 287, 218–224. doi: 10.1016/j.snb.2019.02.034
- Choi, Y., Sakai, G., Shimanoe, K., and Yamazoe, N. (2004). Wet process-based fabrication of WO₃ thin film for NO₂ detection. *Sens. Actuators B Chem.* 101, 107–111. doi: 10.1016/j.snb.2004.02.031
- Hoa, N., Quy, N., and Kim, D. (2009). Nanowire structured SnO_x-SWNT composites: high performance sensor for NO_x detection. *Sens. Actuators B Chem.* 142, 253–259. doi: 10.1016/j.snb.2009.07.053
- Hua, Z., Li, Y., Zeng, Y., and Wu, Y. (2018a). A theoretical investigation of the power-law response of metal oxide semiconductor gas sensors I: Schottky barrier control. *Sens. Actuators B Chem.* 255, 1911–1919. doi: 10.1016/j.snb.2017.08.206
- Hua, Z., Qiu, Z., Li, Y., Zeng, Y., Wu, Y., Tian, X., et al. (2018b). A theoretical investigation of the power-law response of metal oxide semiconductor gas sensors II: Size and shape effects. *Sens. Actuators B Chem.* 255, 3541–3549. doi: 10.1016/j.snb.2017.09.189
- Hua, Z., Tian, C., Huang, D., Yuan, W., Zhang, C., Tian, X., et al. (2018c). Power-law response of metal oxide semiconductor gas sensors to oxygen in presence of reducing gases. *Sens. Actuators B Chem.* 267, 510–518. doi: 10.1016/j.snb.2018.04.002
- Hua, Z., Tian, C., Qiu, Z., Li, Y., Tian, X., Wang, M., et al. (2018d). An investigation on NO₂ sensing mechanism and shielding behavior of WO₃ nanosheets. *Sens. Actuators B Chem.* 259, 250–257. doi: 10.1016/j.snb.2017.12.016
- Jaegle, L., Steinberger, L., Martin, R., and Chance, K. (2005). Global partitioning of NO_x sources using satellite observations: relative roles of fossil fuel combustion, biomass burning and soil emissions. *Faraday Discuss.* 130, 407–423. doi: 10.1039/b502128f
- Kida, T., Nishiyama, A., Yuasa, M., Shimanoe, K., and Yamazoe, N. (2009). Highly sensitive NO₂ sensors using lamellar-structured WO₃ particles prepared by an acidification method. *Sens. Actuators B Chem.* 135, 568–574. doi: 10.1016/j.snb.2008.09.056
- Ling, Z., and Leach, C. (2004). The effect of relative humidity on the NO₂ sensitivity of a SnO₂/WO₃ heterojunction gas sensor. *Sens. Actuators B Chem.* 102, 102–106. doi: 10.1016/j.snb.2004.02.017
- Marichy, C., Donato, N., Latino, M., Georg Willinger, M., Tessonnier, J.-P., Neri, G., et al. (2015). Gas sensing properties and p-type response

- The oxygen adsorption played a vital basic role in the sensing process. However, the oxygen adsorption behavior was inhibited by the presence of water vapor and NO₂.

In conclusion, sensing material Cr₂WO₆ shows a great response to detect NO₂ in dry and humid conditions.

DATA AVAILABILITY STATEMENT

All datasets generated for this study are included in the article/Supplementary Material.

AUTHOR CONTRIBUTIONS

MY and CT performed the experiments and analyzed the data with the help from YW, YL, and ZH. YW and ZH conceived and modified the manuscript based on experimental data.

FUNDING

This study was supported by the National Natural Science Foundation of China (Grant Nos. 51977059 and 51777056). The characterization results were supported by Beijing Zhongkebaice Technology Service Co., Ltd, and we acknowledge critical and quantity of testing work supported by Beijing Zhongkebaice Technology Service Co., Ltd.

SUPPLEMENTARY MATERIAL

The Supplementary Material for this article can be found online at: <https://www.frontiersin.org/article/10.3389/fchem.2019.00907/full#supplementary-material>

- of ALD TiO₂ coated carbon nanotubes. *Nanotechnology* 26:024004. doi: 10.1088/0957-4484/26/2/024004
- Nguyen, D., and El-Safty, S. (2011). Synthesis of mesoporous NiO nanosheets for the detection of toxic NO₂ gas. *Chem. Eur. J.* 17, 12896–12901. doi: 10.1002/chem.201101122
- Richter, A., Burrows, J., Nüß, H., Granier, C., and Niemeier, U. (2005). Increase in tropospheric nitrogen dioxide over China observed from space. *Nature* 437, 129–132. doi: 10.1038/nature04092
- Stănoiu, A., Simion, C., Diamandescu, L., Tărăbășanu-Mihăilă, D., and Feder, M. (2012). NO₂ sensing properties of Cr₂O₃ highlighted by work function investigations. *Thin Solid Films* 522, 395–400. doi: 10.1016/j.tsf.2012.09.003
- Sun, W., Shao, M., Granier, C., Liu, Y., Ye, C., and Zheng, J. (2018). Long-term trends of anthropogenic SO₂, NO_x, CO, and NMVOCs emissions in China. *Earths Future* 6, 1112–1133. doi: 10.1029/2018EF000822
- Vyas, R., Sharma, S., Gupta, P., Prasad, A. K., Dhara, S., Tyagi, A. K., et al. (2013). Nitrogen dioxide induced conductivity switching in ZnO thin film. *J. Alloys Comp.* 571, 6–11. doi: 10.1016/j.jallcom.2013.03.217
- Zhou, W., Huang, J., Li, J., Xu, Z., Cao, L., Yao, C., et al. (2015). Cr₂WO₆ nanoparticles prepared by hydrothermal assisted method with selective adsorption properties for methylene blue in water. *Mater. Sci. Semicond. Process.* 34, 170–174. doi: 10.1016/j.mssp.2015.02.010

Conflict of Interest: YL was employed by the Beijing Institute of Mechanical Equipment that is a government-owned non-profit organization.

The remaining authors declare that the research was conducted in the absence of any commercial or financial relationships that could be construed as a potential conflict of interest.

Copyright © 2020 Wu, Yan, Tian, Liu and Hua. This is an open-access article distributed under the terms of the Creative Commons Attribution License (CC BY). The use, distribution or reproduction in other forums is permitted, provided the original author(s) and the copyright owner(s) are credited and that the original publication in this journal is cited, in accordance with accepted academic practice. No use, distribution or reproduction is permitted which does not comply with these terms.



Qualitative Detection Toward Military and Improvised Explosive Vapors by a Facile TiO₂ Nanosheet-Based Chemiresistive Sensor Array

Yushu Li^{1,2†}, Wenyi Zhou^{1,2,3†}, Baiyi Zu^{1,2} and Xincun Dou^{1,2,3*}

¹ Xinjiang Key Laboratory of Explosives Safety Science, Xinjiang Technical Institute of Physics & Chemistry, Urumqi, China,

² Key Laboratory of Functional Materials and Devices for Special Environments, Chinese Academy of Sciences,

Urumqi, China, ³ Center of Materials Science and Optoelectronics Engineering, University of Chinese Academy of Sciences, Beijing, China

OPEN ACCESS

Edited by:

Mingshui Yao,
Kyoto University, Japan

Reviewed by:

Jun Zhang,
Qingdao University, China
Jianxin Yi,
University of Science and Technology
of China, China

*Correspondence:

Xincun Dou
xcdou@ms.xjb.ac.cn

[†]These authors have contributed
equally to this work

Specialty section:

This article was submitted to
Nanoscience,
a section of the journal
Frontiers in Chemistry

Received: 14 November 2019

Accepted: 09 January 2020

Published: 31 January 2020

Citation:

Li Y, Zhou W, Zu B and Dou X (2020)
Qualitative Detection Toward Military
and Improvised Explosive Vapors by a
Facile TiO₂ Nanosheet-Based
Chemiresistive Sensor Array.
Front. Chem. 8:29.
doi: 10.3389/fchem.2020.00029

A facile TiO₂ nanosheets-based chemiresistive gas sensor array was prepared to identify 11 kinds of military and improvised explosive vapors at room temperature. The morphology of TiO₂ nanosheets was well-controlled by adjusting the concentration of HF applied during the preparation. Owing to the morphology difference, the TiO₂ nanosheet-based sensors show different response values toward 11 kinds of explosives, which is the basis of the successful discriminative identification. This method owes lots of advantages over other detection techniques, such as the facile preparation procedure, high response value (115.6% for TNT and 830% for PNT) at room temperature, rapid identifying properties (within 30 s for 9 explosives), simple operation, high anti-interference property, and low probability of misinforming, and consequently has a huge potential application in the qualitative detection of explosives.

Keywords: TiO₂, chemiresistive sensor array, military explosives, improvised explosives, vapor detection

INTRODUCTION

Rapid and accurate detection of explosives has been a hot issue of global concern due to the deepening terrorism crisis (Chen et al., 2010; Lichtenstein et al., 2014; Yang et al., 2015; Guo et al., 2017; Bastatas et al., 2018; Liu et al., 2019). The illegal blast induced by terrorists applied not only the powerful military explosives, but also the less powerful improvised explosives made of commercial available chemicals. Military explosives, mainly referred to nitro-explosives, such as 2,4,6-trinitrotoluene (TNT), dinitrotoluene (DNT), hexogen (RDX), and so on. The sensitive, selective, and rapid detection of nitro-explosive vapors is still a challenge owing to their low vapor pressures at room temperature. For instance, the room temperature saturated vapor pressures of TNT, DNT, para-nitro toluene (PNT), picric acid (PA), RDX are 9 ppb (part per billion), 180 ppb, 647 ppb, 0.97 ppb, and 4.9 ppt (part per trillion), respectively (Ewing et al., 2013). During the past decade, several techniques have been applied for the detection of military explosive vapors, such as fluorescence (Andrew and Swager, 2007; He et al., 2009; Olley et al., 2010; Zhu et al., 2011), surface enhanced Raman scattering (SERS) (Yang et al., 2010; Wang et al., 2014), ion mobility spectrometer (IMS) (Zhou et al., 2015), and chemiresistive sensors (Che et al., 2010; Chen et al., 2010; Engel et al., 2010; Wang et al., 2011a; Aluri et al., 2013). However, most of the previous reports were unable to realize the identification of different kinds of military explosives

(Andrew and Swager, 2007; He et al., 2009; Che et al., 2010; Chen et al., 2010; Engel et al., 2010; Olley et al., 2010; Wang et al., 2011a; Zhu et al., 2011; Aluri et al., 2013; Zhou et al., 2015). Moreover, some of the reported techniques suffer from the extremely low response at room temperature (Chen et al., 2010; Aluri et al., 2013) and time consuming problem (Hutchinson et al., 2007; Zhu et al., 2011), inhabiting their application in the rapid on-the-spot detection of military explosives.

Different from the relative mature development of military explosive vapors detection, the detection of improvised explosives barely got any attention due to their ultra-low vapor pressure even at the typical maximum desorber temperature (Steinfeld and Wormhoudt, 1998; Mäkinen et al., 2011; Najarro et al., 2012; Peng et al., 2014). Improvised explosives are generally made of non-explosive compounds including KClO₃, KNO₃, KMnO₄, S, NH₄NO₃, and urea (Kuila et al., 2006; Peters et al., 2015), *via* simple reaction or just blending, and are extensively used in terrorist attacks owing to their readily availability and low cost. Some techniques have been utilized for the detection of improvised explosives, such as capillary electrophoresis (CE) (Hutchinson et al., 2007; Blanco et al., 2011), ion chromatography (IC) (Dicinoski et al., 2006; Meng et al., 2008), and electrospray ionization mass spectrometry (ESIMS) (Zhao and Yinon, 2002; Flanigan et al., 2011). However, their drawbacks limited their application in the rapid identification of improvised explosives. For example, CE and IC need about 10 min to identify various kinds of anions and cations (Hutchinson et al., 2007; Johns et al., 2008), while ESIMS requires large equipment and therefore results in high testing expense and difficulties in on-the-spot application. Ionization mass spectrometry (IMS) has been proved to be an efficient technique for on-the-spot detection of trace improvised explosives such as KNO₃, KClO₃, and KClO₄ within 5 s (Peng et al., 2014). However, it involves a time-consuming pretreatment procedure including sample swap and acidification. Therefore, a method to identify improvised explosives in a simple, fast, and low energy consuming manner is urgently needed.

Nanomaterial-based chemiresistive-gas sensor is an important explosives detection method due to the small device size, low energy consumption, high and rapid response (Senesac and Thundat, 2008; Che et al., 2010; Chen et al., 2010; Engel et al., 2010; Zu et al., 2013; Guo et al., 2014). For the detection of the military explosives, such as TNT, DNT, and RDX, several nanostructures have been explored as the sensing components, including TiO₂(B) nanowires (Wang et al., 2011a), GaN/TiO₂ heterostructure (Aluri et al., 2013), organic nanoribbons (Che et al., 2010), carbon nanotubes and ZnO nanowires (Chen et al., 2010). Moreover, nanostructured materials, such as Mn²⁺-doped ZnS nanocrystal, Fe-doped ZnO nanomaterial, and Aphen-doped TiO₂ nanocrystal, have also been proved to be efficient for the gas sensing of improvised explosives (Qu et al., 2016; Wu et al., 2016; Xie and Liu, 2019). However, these chemiresistors can only detect a few explosive vapors, and the response values are as low as 5% at room-temperature (Chen et al., 2010; Aluri et al., 2013), leading to the increased possibility of misinforming.

In order to avoid the interference of other similar gases and decrease the misinformation, the chemically modified single-walled carbon nanotube (SWCNT)-based (Schnorr et al., 2013; Liu et al., 2015) and Si nanowire-based (Lichtenstein et al., 2014) nanosensor array were prepared to discriminatively identify different vapors. However, it is confirmed that the covalent functionalization of the SWCNTs can disrupt the extended electronic states and thus increase the base resistance, which may lower the sensitivity (Schnorr et al., 2013). Although quality sensors can be obtained by modest degree of functionalization, the experiment procedure is rather complicated (Bekyarova et al., 2010; Schnorr et al., 2013). In addition, the chemically modified selectors may increase the contact distance due to the existence of the functionalized molecular chains between analytes and the sensing materials, which may lower the sensor sensitivity. Nanostructured TiO₂ is proved to be an efficient sensing material toward nitro-explosives detection (Wang et al., 2011a,b, 2013; Aluri et al., 2013; Tao et al., 2013; Yang et al., 2015). While doping with Apen, the TiO₂ nanocrystal is applied for the detection of limited number of military and improvised explosives under UV-light illustration, including TNT, DNT, PA, S, AN, and TATP (Xie and Liu, 2019). However, the application of undoped TiO₂ nanomaterials in the detection of improvised explosives remains unexplored. To the best of our knowledge, the morphology of nanomaterials has significant impact on their gas sensing performance since the geometric morphology difference can cause different specific surface area and the change in electron depletion layer (Gurlo, 2011; Cho et al., 2013). Hence, gas sensory array based on MoS₂/RGO composites with various morphologies has been constructed for the recognitive detection of Triacetone Triperoxide (TATP) precursors (Sun et al., 2019). Furthermore, utilizing the fluorine as the capping agent for exposure facets stabilization, the morphology of TiO₂ nanomaterials with treatment could be well tailored by modulating the synthesis parameters, including F sources, the concentration of the source, reaction temperature and time, and so on (Lee et al., 2016; Yan et al., 2017; Zhao et al., 2017). However, there is no attempt on the construction of gas sensor array based on nanostructured TiO₂ with different morphologies to realize the discrimination of various explosives.

In this work, a series of TiO₂ nanosheets with different morphologies were successfully prepared via the hydrothermal reaction with the help of F⁻. The gas sensor array with these TiO₂ nanosheets as the sensing components can identify the 5 nitro-explosive vapors (TNT, DNT, PNT, RDX, PA) and 6 improvised explosive vapors (including KNO₃, KClO₃, KMnO₄, S, NH₄NO₃, urea) successfully.

MATERIALS AND METHODS

Chemicals

Tetrabutyl orthotitanate (TBOT), concentrated sulfuric acid (H₂SO₄, 98%), hydrofluoric acid (HF, 40%), 2,4-dinitrotoluene (DNT), *p*-nitrotoluene (PNT), picric acid (PA), potassium nitrate (KNO₃), potassium chloride (KClO₃), potassium permagnate (KMnO₄), sulfur (S), ammonium nitrate (NH₄NO₃), and urea were purchased from Sigma-Aldrich. 2,4,6-trinitrotoluene (TNT)

and hexogen (RDX) were obtained from the National Security Department of China. Except for TNT was recrystallized with ethanol before use, all other chemicals were of analytical grade and used without further purification.

Caution

TNT and other nitro-explosives used in the present study are highly explosive and should be handled only in small quantities.

Preparation of TiO₂ Nanosheets

The TiO₂ nanosheets were prepared via a hydrothermal method. In a typical procedure, different amounts of HF (0–1 ml) were added to the mixture of 12.5 ml TBOT and 1.5 ml H₂SO₄ with vigorous stirring, followed by the addition of certain amount of H₂O to maintain the total volume of the reaction mixture as 15 ml. The mixture was then transferred to Teflon lined autoclave and kept at 180 °C for 24 h. After completion of the reaction, the white precipitate was filtered and washed with ethanol several times and then dried in air at 60 °C.

Characterization

X-ray diffraction (XRD) measurement was conducted using powder XRD (Bruker D8 Advance, with Cu-K_α radiation operating at 40 kV and 40 mA, scanning from 2θ = 10 to 90°). Field-emission scanning electron microscopy (FESEM, ZEISS SUPRA 55VP), and transmission electron microscope (JEM-2011 TEM, 200 kV) were used to characterize the morphology and the detailed structure of the samples.

Sensor Array Fabrication and Gas Sensing Performance Testing

The obtained TiO₂ nanosheets were mixed with deionized water in a weight ratio of 4:1 and ground in a mortar for 10 min to form a uniform paste. The paste was then coated on a ceramic substrate, on which silver interdigitated electrodes with both finger-width and inter-finger spacing of about 200 μm was previously printed, by a thin brush to construct a gas sensor. The thickness of the film was controlled by the brushed cycles. The sample was dried naturally in air overnight and aged at 10 V in air to ensure the good stability. Five gas sensors from TiO₂ with different morphologies were fabricated together to construct the sensor array. The room temperature-saturated explosive vapor was obtained by putting solid explosive powder (1 g) at the bottom of a conical flask (50 mL) before it was sealed for 48 h. All tests were performed at consistent operating temperature (room temperature, 25 ± 2 °C) and relative humidity (30 ± 3%) to avoid undesired signal fluctuate. For gas sensing test, the sensor was inserted into the saturated vapor of an explosive. After the sensor resistance reached a new constant value, the sensor was then inserted into a same size conical flask full of air to recover. The electric signal (current) of the sensor was recorded by electrochemical workstation (CIMPS-2, ZAHNER). The essential gas sensing characteristics, namely the corresponding response value, response time and recovery time, can be obtained from the response curves. The response value is the steady-state value

of the response with exposure toward explosive vapors, and is defined as,

$$\text{Response} = \frac{I_g - I_a}{I_a} * 100\% \quad (1)$$

where I_g and I_a are the current value of the gas sensor measured in explosive vapor and in air at room temperature, respectively. The response time is defined as the period it takes to cause 90% of the current changes upon exposure to the explosive vapor, while the recovery time is defined as the period it takes to cause 90% of the current changes after the explosive vapor is removed.

RESULTS AND DISCUSSION

Morphology Tailoring of TiO₂ Nanosheets

X-ray diffraction (XRD) analysis was performed to investigate the crystal phase of the TiO₂ nanosheets prepared by adjusting the amounts of HF solution (0–1.0 ml) applied in the hydrothermal reaction. As shown in **Figure 1A**, it is obvious that all the diffraction peaks of TiO₂ nanosheets prepared via this method can be well-indexed as the anatase TiO₂ phase (JCPDS NO. 21-1272), demonstrating that the phase of the TiO₂ nanosheets would not be affected by the concentrations of HF solution within this range during the preparation. The morphology of the TiO₂ nanosheets was investigated by transmission electron microscopy (TEM) and field emission scanning electron microscopy (FESEM), as shown in **Figures 1B–F**. It is found that the morphologies are different with the increasing amount of HF applied from 0 to 1.0 ml. With the absence of HF, the TiO₂ nanoparticles grew randomly and form the irregular shape with size ranging from 5 to 20 nm, and there is no continuous growth of large nanosheets (**Figure 1B**). With the amount of HF increasing to 0.25 ml, it is observed that the TiO₂ crystals grew larger to form rectangular-shaped nanosheets, which consist of the smaller ones with size of 15–25 nm as major and limited number of larger nanosheets over 40 nm (**Figure 1C**). With the amount of HF continuously increasing to 0.50 ml, the number of relatively larger sized TiO₂ nanosheets (45 nm in average) increased, however, the smaller nanosheets (20 nm in average) are still the major component due to the restricted HF amount (**Figure 1D**). Meanwhile, it is also observed that extra-large nanosheets with size about 100 nm start to form. With the amount of HF continuously increasing to 0.75 ml, although there are still smaller nanosheets (20 nm) and larger sized TiO₂ nanosheets (45 nm in average) existing, the extra-large nanosheets with size around 100 nm are distinctively observed (**Figure 1E**). When the amount of HF further increases to 1.0 ml, the overgrowth of TiO₂ nanosheets occurred leading to the sheet-like structures with size of several microns (**Figure 1F**). Hence, with the amount of HF increasing from 0 to 1 ml, the size of TiO₂ nanosheets grew from a dozen nanometers to several microns. High resolution transmission electron microscopy (HRTEM) was adopted to obtain the detailed crystal structure (insets in **Figures 1B–F**), clear lattice fringes with the lattice spacing corresponding to the (101) plane of anatase TiO₂ were shown, indicating the

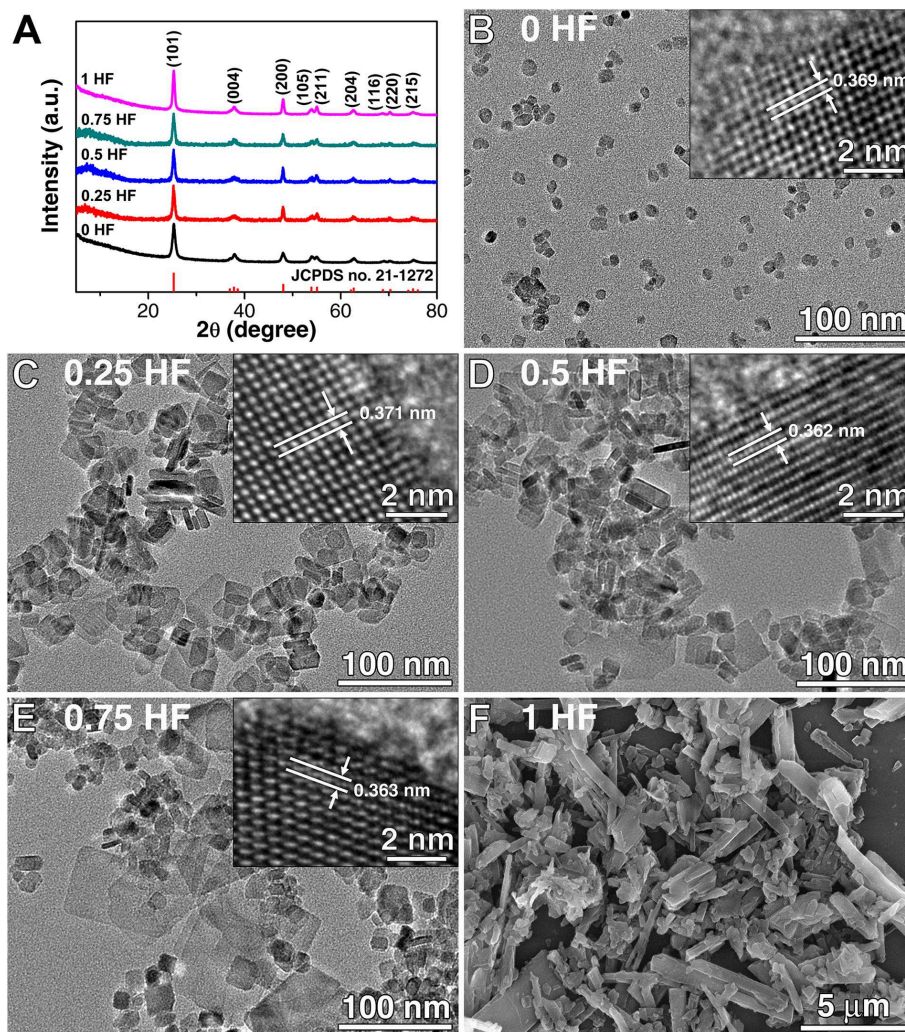


FIGURE 1 | (A) XRD patterns of five kinds of TiO₂ nanosheets, TEM, and SEM images of the TiO₂ nanosheets prepared with different amounts of HF (B) 0 ml, (C) 0.25 ml, (D) 0.5 ml, (E) 0.75 ml, and (F) 1 ml (insets are HRTEM images).

good crystallinity of the samples. As a whole, the increased HF content in the original reaction mixture promotes the growth of the anatase TiO₂ nanosheets with more reactive facets beneficial for sensing due to the enlarged capping effect. This phenomenon is in good agreement with the previously reported results, in which the growth behavior of TiO₂ with various contents of F⁻ is systematically studied (Lee et al., 2016). Therefore, the introduction of F⁻ ion during the preparation is a reasonable choice to control the growth, tailor the morphology, and thus adjust the sensing performance of anatase TiO₂ nanosheets.

Varying Sensing Performance Toward Military and Improvised Explosive Vapors

The as-prepared TiO₂ nanosheets with different morphologies were fabricated on ceramic substrate with comb-like electrodes, respectively, to construct a chemiresistive gas sensor array, as schematically shown in **Figure 2A**. The obtained sensor array

was exposed to five saturated military explosive vapors (TNT, DNT, PNT, RDX, PA) and six saturated improvised explosive vapors (KNO₃, KClO₃, KMnO₄, S, NH₄NO₃, urea) at room-temperature for evaluation of the sensing properties (**Figure 2B**). The room-temperature saturated vapor pressures of all these analytes are extremely low, such as 9 ppb for TNT, 411 ppb for DNT, 647 ppb for PNT, 0.97 ppb for PA, 4.9 ppt for RDX, 2 ppb for S, 9 ppt for urea, and 14.7 ppb for NH₄NO₃ (Lyons, 2011; Ewing et al., 2013). Meanwhile, the other three explosives, KNO₃, KClO₃, and KMnO₄, owing to their ionic crystal nature, are non-volatile and hard to decompose at room temperature indicating that neither the vapor of themselves nor their decomposition products is responsible for the gas sensing signal (**Supplementary Table 1**). However, it has been discovered that microparticulates could be separated from non-volatile solids and suspended in air (Clark and Shirley, 1973; Samet et al., 2004; Li et al., 2018; Yao et al., 2018). Therefore, we believe that the microparticulates suspended in the vapor

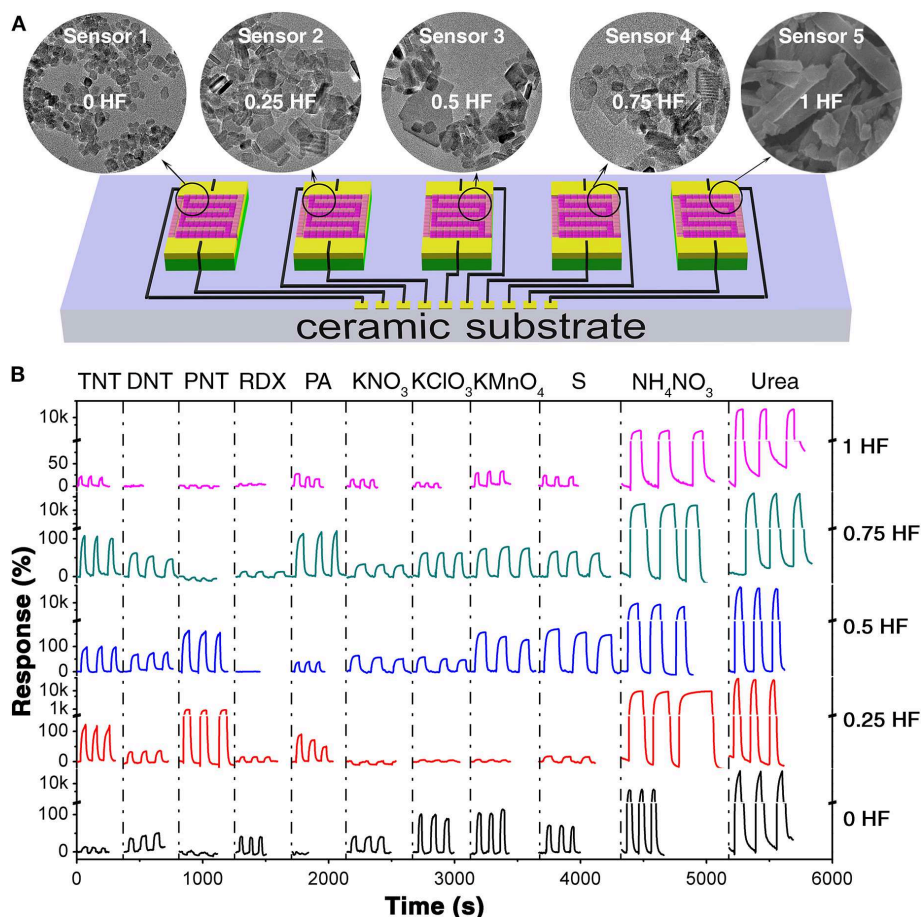
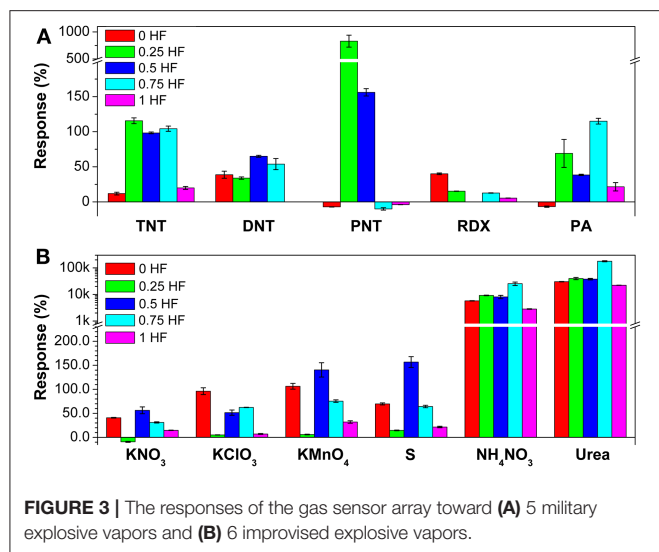


FIGURE 2 | (A) The schematic diagram of the gas sensor array based on TiO₂ nanosheets. **(B)** The corresponding response curves toward 11 explosive vapors (TNT, DNT, PNT, RDX, PA, KNO₃, KClO₃, KMnO₄, S, NH₄NO₃, and urea).

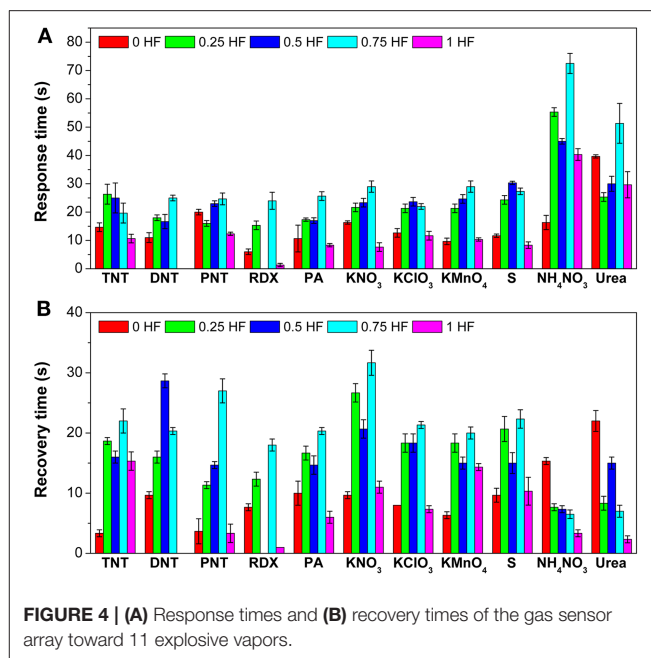
of these explosives, which could interact with the surface of sensing materials and hence are responsible for the electric signal changes of the sensors in the array. The response curves are generated from the current change traces of the sensors toward explosive vapors at an applied voltage of 10 V. From the current change behaviors (**Supplementary Figures 1–10**), it is obvious that with the immersing of the sensor array into explosive vapors, the resistances change immediately, and then with the immersing of the sensor array into air, the resistance change back to its initial value rapidly, indicating the good repeatability of the sensor array toward each explosive vapor. It is also observed that each sensor in the array shows different resistance change with exposure to different kinds of explosive vapors. While with immersion into the same explosive vapor, the sensors in the array show different resistance change as well. It is believed that the resistance change of the TiO₂ nanosheets sensing materials was caused by the change of the charge depletion layer depth. For a single sensor in the array exposed to various explosive vapors, the different gas molecules adsorbed on the surface of TiO₂ nanosheets would lead to different surface potential barrier, which depends on

the charge density established upon interaction between the adsorbed target gas and active sites on the surface of the sensing layer. Thus, different charge depletion layer depth would be resulted and hence the difference in resistance was observed. Furthermore, the differences in response among all sensors in the array toward the same explosive vapor are caused by the different charge depletion layer depth introduced by morphology tailoring. The modulation of sensing performance by morphology tailoring could be attribute to the capping effect of F[−] ion. It is observed that the response of the TiO₂ nanosheets toward certain explosive vapor generally increased first and then decrease with the increasing amount of F[−] ion. On one hand, since the F[−] ion serves as the capping agent for stabilizing reactive facets (Lee et al., 2016), with the increasing amount of F[−] ion, more reactive facets are exposed for sensing, resulting in the enhanced sensing performance. While on the other hand, with the increasing amount of F[−] ion, the TiO₂ nanosheet crystals grow larger, leading to a reduced charge depletion layer depth which is hindering the sensing performance enhancement. However, due to the extreme complicated gas sensing response process, the responses could be affected by



many factors, including the interaction between the analyte and the sensing material, decomposition products, the humidity change caused by the analyte and the floating tiny clusters of the analyte (**Supplementary Table 1**), and hence they are not strictly in line with the changing trend. Therefore, the sensing performance of TiO₂ nanosheets toward explosive vapors could be modulated by morphology tailoring.

The response values of the sensor array toward 5 kinds of military explosive vapors and 6 kinds of improvised explosive vapors are summarized from the response curves (**Figure 3**). It is clearly shown that all 5 gas sensors consisted in the array can detect 11 kinds of explosive vapors yielding different response values. For military explosives detection (**Figure 3A**), such as, toward TNT and PNT vapors, sensor 2 (0.25 HF) shows the largest responses of 115.6 and 830.0%, respectively. Sensor 3 (0.5 HF) shows the largest response value (65.0%) toward DNT. Toward RDX, sensor 1 (0 HF) shows the largest response of 40.0%. Sensor 4 (0.75 HF) shows the largest response value of 115.0% toward PA. Toward improvised explosives, the TiO₂ nanosheet-based gas sensor array also show excellent gas sensing performance (**Figure 3B**). Sensor 3 (0.5 HF) exhibits the largest responses toward KNO₃, KMnO₄ and S, while the corresponding values are 56.3, 140.5, and 156.8%, respectively. Sensor 1 (0 HF) exhibits the largest response of 96.2% toward KClO₃. Toward NH₄NO₃ and urea, all sensors show strikingly large responses, and sensor 4 (0.75 HF) exhibits the largest responses of 255.6 and 1783.1 times, respectively. To sum up, TiO₂ nanosheets with different morphologies show different response values toward nitro- and improvised explosive vapors, which further indicates that the sensing performance of TiO₂ nanosheets can be well-regulated to achieve the response differences by simply controlling the morphology. Furthermore, it should be noted that the TiO₂ nanosheet-based sensor array can work in a very large response range, from zero to a few thousands, which would enhance the practical application of the array.



Besides the response values, response time and recovery time of the gas sensor array toward 11 explosive vapors are also summarized (**Figure 4**). Toward TNT, PNT, RDX, PA, KNO₃, KClO₃, and S, sensor 5 (1 HF) shows the fastest response with response times of 10.7, 12.3, 1.3, 8.3, 7.7, 11.7, and 8.3 s, respectively (**Figure 4A**). Meanwhile, toward DNT, KMnO₄, and NH₄NO₃, sensor 1 (0 HF) shows the fastest response, and the corresponding response times are 11.0, 9.7, and 16.3 s, respectively. It should be noted that the response time of sensor 2 (0.25 HF) toward urea is only 25.3 s although the response value is as high as 399.5. The response time periods are within 30 s for most of the explosive vapors.

Similar as the response time, the recovery time of sensors in the array are also different resulting from the morphology differences of TiO₂ nanosheets (**Figure 4B**). Toward TNT, DNT, PNT, KNO₃, KClO₃, KMnO₄, and S, sensor 1 (0 HF) shows the fastest recovery, and the corresponding recovery times are 3.3, 9.7, 3.7, 9.7, 8.0, 6.3, and 9.7 s, respectively. Toward RDX, PA, NH₄NO₃, and urea, sensor 5 (1 HF) shows the fastest recovery with recovery times of 1.0, 6.0, 3.3, and 2.3 s, respectively. As a whole, the TiO₂ nanosheet-based gas sensor array can recover to its initial state within 35 s in atmosphere, indicating that it can be employed for the next detection cycle rapidly.

The anti-interfering performance of the sensor array is evaluated by exposing the sensor array to common interfering gases, namely ethanol (EtOH), NO₂, and NH₃, with concentration of 1 ppm (**Figure 5; Supplementary Figures 11–15**). All 5 gas sensors in the array exhibit positive response toward EtOH and NO₂ gases and negative response toward NH₃ (**Figure 5A**), which is in good agreement with results discussed above. It is worth to notice that the currents of the TiO₂ nanosheets based sensors increase in typical electron withdrawing target vapors, such as TNT,

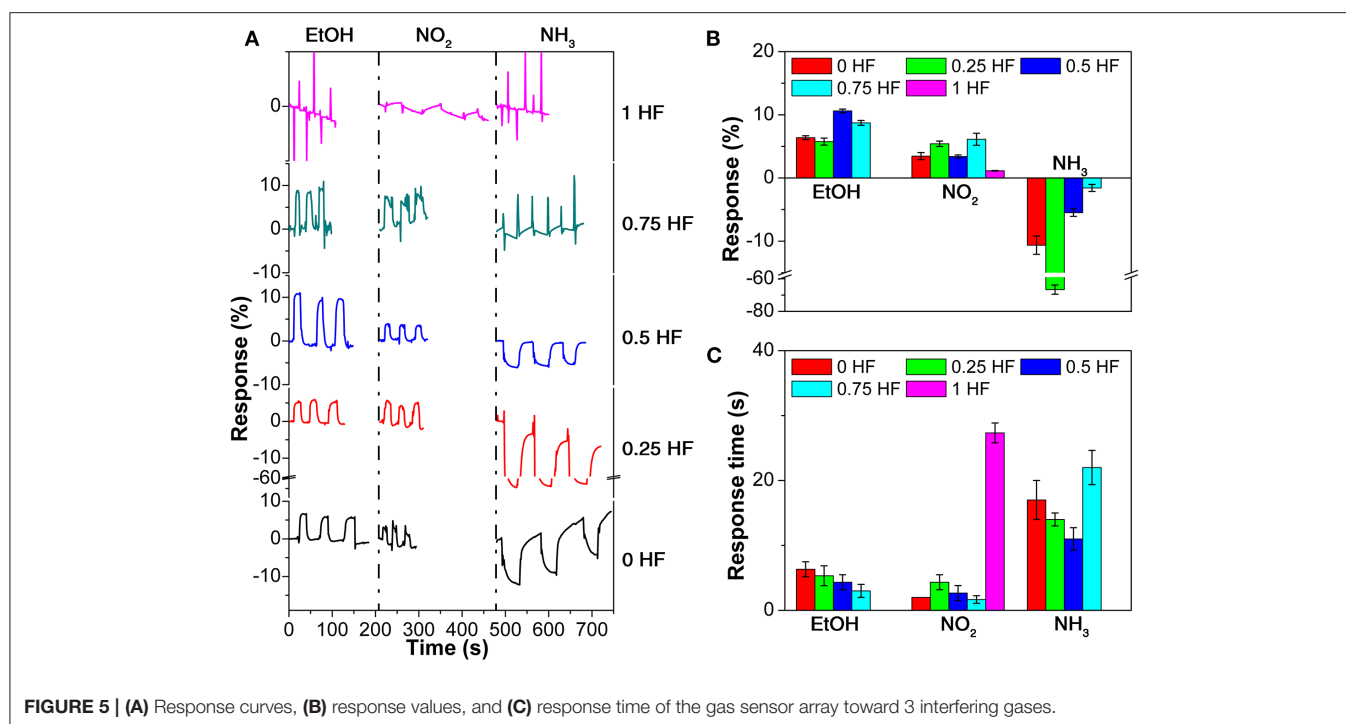


FIGURE 5 | (A) Response curves, **(B)** response values, and **(C)** response time of the gas sensor array toward 3 interfering gases.

DNT, and NO₂, which is rare and under further exploration. The response values toward EtOH and NO₂ are much smaller compared with that of explosive vapors. For instance, sensor 3 (0.5 HF) shows the largest response of 10.6% toward EtOH, while sensor 4 (0.75 HF) shows the largest response of 6.1% toward NO₂ (Figure 5B). Meanwhile, in the case of NH₃, the sensors in the array all show negative response values with a largest response of -66.7%, which is relatively large but in the opposite direction compared with that of explosive vapors. The response time toward these interfering gases are all <30 s which are comparable with that of the explosive vapors (Figure 5C). Considering the fact that the room temperature vapor pressures of the explosives are much lower than 1 ppm, it can be concluded that the common interfering gases in real-world have limited influence on the sensing performance of the sensor array toward explosive vapors.

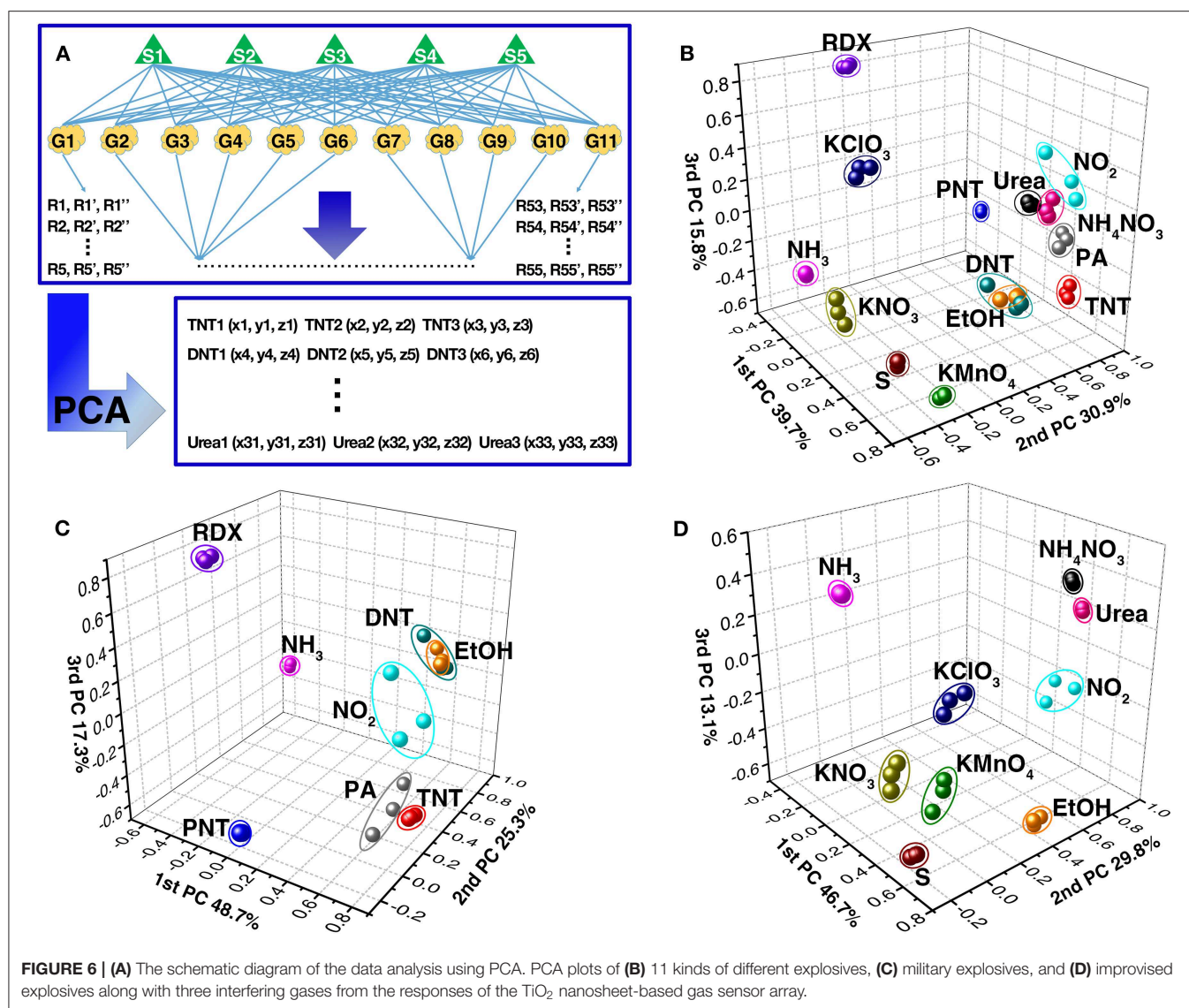
Discriminative Recognition of Explosive Vapors

The methodology of principal component analysis (PCA), which could extract the selective feature of original data depending on variance criteria and visualize the extracted feature, was used to discriminatively recognize explosives. Its analysis procedure is schematically shown in Figure 6A. All responses data from the gas sensor array were subjected to PCA, and were transformed to a new coordinate system. Afterwards, each kind of explosive vapor can be represented as a point in the new three-dimensional space, such as TNT1 (x1, y1, z1). Thus, different explosives and the interfering gases appear at different positions in the new coordinate system, as shown in Figures 6B–D.

Based on the response difference induced by morphology difference between TiO₂ nanosheets, all 11 kinds of explosives

and 3 interfering gases can be discriminatively identified except for DNT and EtOH, which are overlapping, and urea and NH₄NO₃, which are very close to each other (Figure 6B). If only the family of military explosives and the interfering gases are considered, the clusters of organic explosives and some of the interfering gases are scattered further from each other with the exception of DNT and EtOH (Figure 6C). Similarly, if only the family of improvised explosives and the interfering gases are of interest, the clusters of improvised explosives are also scattered further from each other, such as KNO₃, KClO₃, KMnO₄, S, NH₃, NO₂, and EtOH from NH₄NO₃ and urea (Figure 6D). However, it should be noted that although the PCA analysis of responses is powerful enough to discriminate 10 explosives and 2 interfering gases, it is difficult to discriminate DNT from EtOH and urea from NH₄NO₃ using PCA analytical method based only on the response values.

During the gas sensing procedure, the response value as a steady state parameter is associated with the thermodynamic interaction between the explosive species and the TiO₂ nanosheets, while the response time and recovery time are associated with the kinetic interaction between them. However, response time is a more meaningful kinetic parameter for explosives recognition in practical detecting situation since fast responding is essential to achieve early alarming. Therefore, by combining the rapid mathematical analysis of the thermodynamic and kinetic interactions, namely the response value and response time, a visible fingerprinting method is utilized to realize the discriminative identification of explosives. This fingerprinting method is suitable for discriminative identification as the shape of the fingerprinting pattern is independent with the analyte concentration (Lichtenstein et al., 2014). Figure 7 shows the fingerprinting radar plot patterns of



all explosive vapors and 3 interfering gases generated from the response values and response times of the sensors in the array. It is obvious that each analyte has its unique fingerprinting pattern, which can be used to distinguish from each other and thus to realize the discriminative identification of all the analytes including not only the explosives but also the interfering gases (Figures 7A–G). For instance, TNT, DNT, and PNT exhibit different patterns although they have similar molecular structures. Meanwhile, although KNO₃ and KClO₃ are both potassium salts, their radar plot patterns distinguish from each other. This distinction should be ascribed to the different interactions between different explosive vapors and TiO₂ nanosheets with different morphologies. In the case of NH₄NO₃ and urea, which are hard to be discriminated using PCA method, they can be differentiated from each other easily owing to their remarkably different radar plot patterns. While for DNT and EtOH, which are unable to be distinguished in the PCA

plot, the radar plot patterns are of great difference and thus it is also easy to discriminate them from each other using this method. Therefore, with straightforward data analysis, the chemiresistive sensor array from TiO₂ nanosheets with different morphologies is capable of discriminatively identifying 11 types of explosive vapors and 3 common interfering gases.

Furthermore, the present chemiresistive gas sensor array has lots of advantages for practical application. Compared with other vapor electrical sensors (Che et al., 2010; Chen et al., 2010; Wang et al., 2011a; Aluri et al., 2013; Schnorr et al., 2013; Liu et al., 2015; Yang et al., 2015), it shows a higher sensitivity toward TNT, DNT, and PNT, and can detect RDX vapor at ppt level (Supplementary Table 2). Compared with other military explosive detecting techniques (Andrew and Swager, 2007; He et al., 2009; Olley et al., 2010; Zhu et al., 2011; Wang et al., 2014; Zhou et al., 2015), it can identify 5 military explosives within 30 s and avoid (1) the interference induced by other

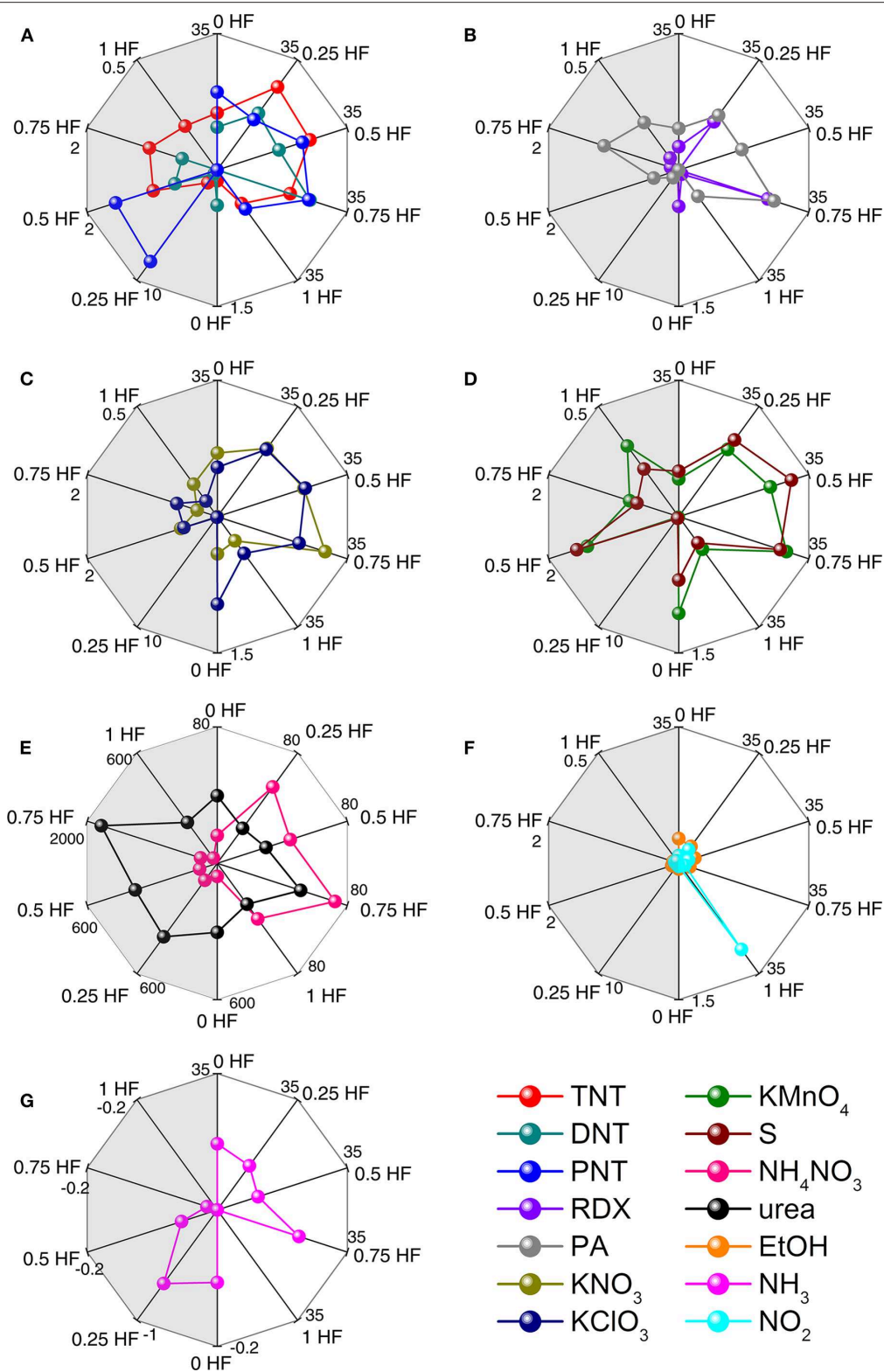


FIGURE 7 | Radar plots of response values and response times of 11 explosives and 3 interfering gases: **(A)** TNT, DNT, and PNT; **(B)** RDX and PA; **(C)** KNO₃ and KClO₃; **(D)** KMnO₄ and S; **(E)** NH₄NO₃ and urea; **(F)** EtOH and NH₃; **(G)** NO₂. Left side response value represents the thermodynamically derived results for each analyte, and the right side response time represents the kinetically derived results for each analyte.

substances, (2) the large and expensive instrumentation, and (3) complicated operating procedure, which might be problematic for fluorescence, SERS, and IMS (**Supplementary Table 3**). In the case of detection of improvised explosives, the present gas sensor array can discriminatively identify 6 improvised explosive vapors within 75 s, which is much more efficient compared with CE and IC (**Supplementary Table 4**; Hutchinson et al., 2007; Peng et al., 2014). Moreover, it can avoid complicated operation which is essential in IMS technique (Johns et al., 2008). Therefore, the present TiO₂ nanosheet-based chemiresistive gas sensor array shows high sensitivity, short testing time, handy operation, and the ability to avoid interference, which are beneficial for practical application in rapid identification of military and improvised explosives.

CONCLUSIONS

A series of TiO₂ nanosheets with well-tailored morphologies were successfully prepared via a simple hydrothermal method. HF was utilized as morphology modulation agent in the reaction. The size of the TiO₂ nanosheets grew larger with the increase of the amount of HF. The morphological difference of TiO₂ nanosheets leads to the dissimilarity of the specific surface area and the charge depletion layer depth, and hence different responses toward explosive vapors. The gas sensor array based on the series of TiO₂ nanosheets can rapidly and discriminatively identify the vapors of 5 nitro-explosives (TNT, DNT, PNT, RDX, PA) and 6 improvised explosives (KNO₃, KClO₃, KMnO₄, S, NH₄NO₃, urea) along with 3 common interfering gases (EtOH, NO₂, NH₃) successfully under room-temperature condition with the help of PCA and fingerprinting pattern recognition method. It has a huge potential for practical application owing to its obviously superior advantages compared with other detection techniques. Thus, this work presents an

efficient method to achieve the response differences simply by the morphology tailoring, and consequently to realize the identification of nitro- and improvised explosives, which is an important attempt for the development of quality sensor array for explosive detection.

DATA AVAILABILITY STATEMENT

The raw data supporting the conclusions of this article will be made available by the authors, without undue reservation, to any qualified researcher.

AUTHOR CONTRIBUTIONS

All authors listed have made a substantial, direct and intellectual contribution to the work, and approved it for publication.

FUNDING

This work was supported by the West Light Foundation of the Chinese Academy of Sciences (2017-XBQNXZ-B-003), the National Natural Science Foundation of China (51572292, U1903306), National High-level Talents Special Support Plan of China for Young Talents, the Xinjiang Program of Introducing High Level Talents, the Key Research and Development Program of Xinjiang (2017B03021-1), and Tianshan Innovation Team Plan (2018D14007).

SUPPLEMENTARY MATERIAL

The Supplementary Material for this article can be found online at: <https://www.frontiersin.org/articles/10.3389/fchem.2020.00029/full#supplementary-material>

REFERENCES

- Aluri, G. S., Motayed, A., Davydov, A. V., Oleshko, V. P., Bertness, K. A., and Rao, M. V. (2013). Nitro-aromatic explosive sensing using GaN nanowire-titania nanocluster hybrids. *IEEE Sens. J.* 13, 1883–1888. doi: 10.1109/JSEN.2013.2241423
- Andrew, T. L., and Swager, T. M. (2007). A fluorescence turn-on mechanism to detect high explosives RDX and PETN. *J. Am. Chem. Soc.* 129, 7254–7255. doi: 10.1021/ja071911c
- Bastatas, L. D., Echeverria-Mora, E., Wagle, P., Mainali, P., Austin, A., and McIlroy, D. N. (2018). Emergent electrical properties of ensembles of 1D nanostructures and their impact on room temperature electrical sensing of ammonium nitrate vapor. *ACS Sensors* 3, 2367–2374. doi: 10.1021/acssensors.8b00746
- Bekyarova, E., Kalinina, I., Sun, X., Shastry, T., Worsley, K., Chi, X., et al. (2010). Chemically engineered single-walled carbon nanotube materials for the electronic detection of hydrogen chloride. *Adv. Mater.* 22, 848–852. doi: 10.1002/adma.200903427
- Blanco, G. A., Nai, Y. H., Hilder, E. F., Shellie, R. A., Dicinoski, G. W., Haddad, P. R., et al. (2011). Identification of inorganic improvised explosive devices using sequential injection capillary electrophoresis and contactless conductivity detection. *Anal. Chem.* 83, 9068–9075. doi: 10.1021/ac2020195
- Che, Y., Yang, X., Liu, G., Yu, C., Ji, H., Zuo, J., et al. (2010). Ultrathin n-type organic nanoribbons with high photoconductivity and application in optoelectronic vapor sensing of explosives. *J. Am. Chem. Soc.* 132, 5743–5750. doi: 10.1021/ja909797q
- Chen, P. C., Sukcharoenchoke, S., Ryu, K., Gomez de Arco, L., Badmaev, A., Wang, C., et al. (2010). 2,4,6-Trinitrotoluene (TNT) chemical sensing based on aligned single-walled carbon nanotubes and ZnO nanowires. *Adv. Mater.* 22, 1900–1904. doi: 10.1002/adma.200904005
- Cho, S., Kwon, O. S., You, S. A., and Jang, J. (2013). Shape-controlled polyaniline chemiresistors for high-performance DMMP sensors: effect of morphologies and charge-transport properties. *J. Mater. Chem. A* 1, 5679–5688. doi: 10.1039/c3ta01427d
- Clark, R. P., and Shirley, S. G. (1973). Identification of skin in airborne particulate matter. *Nature* 246, 39–40. doi: 10.1038/246039a0
- Dicinoski, G. W., Shellie, R. A., and Haddad, P. R. (2006). Forensic identification of inorganic explosives by ion chromatography. *Anal. Lett.* 39, 639–657. doi: 10.1080/00032710600609735
- Engel, Y., Elnathan, R., Pevzner, A., Davidi, G., Flaxer, E., and Patolsky, F. (2010). Supersensitive detection of explosives by silicon nanowire arrays. *Angew. Chem. Int. Edn.* 49, 6830–6835. doi: 10.1002/anie.201000847
- Ewing, R. G., Waltman, M. J., Atkinson, D. A., Grate, J. W., and Hotchkiss, P. J. (2013). The vapor pressures of explosives. *Trac-Trend Anal. Chem.* 42, 35–48. doi: 10.1016/j.trac.2012.09.010

- Flanigan, I. V. P. M., Brady, J. J., Judge, E. J., and Levis, R. J. (2011). Determination of inorganic improvised explosive device signatures using laser electrospray mass spectrometry detection with offline classification. *Anal. Chem.* 83, 7115–7122. doi: 10.1021/ac2014299
- Guo, L., Yang, Z., and Dou, X. (2017). Artificial olfactory system for trace identification of explosive vapors realized by optoelectronic schottky *Sensing* 29:1604528. doi: 10.1002/adma.201604528
- Guo, L., Zu, B., Yang, Z., Cao, H., Zheng, X., and Dou, X. (2014). APTS and rGO co-functionalized pyrenated fluorescent nanonets for representative vapor phase nitroaromatic explosive detection. *Nanoscale* 6, 1467–1473. doi: 10.1039/C3NR04960D
- Gurlo, A. (2011). Nanosensors: towards morphological control of gas sensing activity. SnO₂, In₂O₃, ZnO and WO₃ case studies. *Nanoscale* 3, 154–165. doi: 10.1039/C0NR00560F
- He, G., Zhang, G., Lü, F., and Fang, Y. (2009). Fluorescent film sensor for vapor-phase nitroaromatic explosives via monolayer assembly of oligo (diphenylsilane) on glass plate surfaces. *Chem. Mater.* 21, 1494–1499. doi: 10.1021/cm900013f
- Hutchinson, J. P., Evenhuis, C. J., Johns, C., Kazarian, A. A., Breadmore, M. C., Macka, M., et al. (2007). Identification of inorganic improvised explosive devices by analysis of postblast residues using portable capillary electrophoresis instrumentation and indirect photometric detection with a light-emitting diode. *Anal. Chem.* 79, 7005–7013. doi: 10.1021/ac0708792
- Johns, C., Shellie, R. A., Potter, O. G., O'Reilly, J. W., Hutchinson, J. P., Guijt, R. M., et al. (2008). Identification of homemade inorganic explosives by ion chromatographic analysis of post-blast residues. *J. Chromatogr. A* 1182, 205–214. doi: 10.1016/j.chroma.2008.01.014
- Kuila, D., Chakraborty, A., Sharma, S., and Lahiri, S. (2006). Composition profile of low explosives from cases in India. *Forensic Sci. Int.* 159, 127–131. doi: 10.1016/j.forsci.2005.06.012
- Lee, S. M., Park, G. C., Seo, T. Y., Jung, S. B., Lee, J. H., Kim, Y. D., et al. (2016). Facet-controlled anatase TiO₂ nanoparticles through various fluorine sources for superior photocatalytic activity. *Nanotechnology* 27:395604. doi: 10.1088/0957-4484/27/39/395604
- Li, H., Zhong, J., Vehkamäki, H., Kurtén, T., Wang, W., Ge, M., et al. (2018). Self-catalytic reaction of SO₃ and NH₃ to produce sulfamic acid and its implication to atmospheric particle formation. *J. Am. Chem. Soc.* 140, 11020–11028. doi: 10.1021/jacs.8b04928
- Lichtenstein, A., Havivi, E., Shacham, R., Hahamy, E., Leibovich, R., Pevzner, A., et al. (2014). Supersensitive fingerprinting of explosives by chemically modified nanosensors arrays. *Nat. Commun.* 5:4195. doi: 10.1038/ncomm54195
- Liu, R., Li, Z., Huang, Z., Li, K., and Lv, Y. (2019). Biosensors for explosives: state of art and future trends. *TrAC Trends Anal. Chem.* 118, 123–137. doi: 10.1016/j.trac.2019.05.034
- Liu, S. F., Moh, L. C., and Swager, T. M. (2015). Single-walled carbon nanotube-metalloporphyrin chemiresistive gas sensor arrays for volatile organic compounds. *Chem. Mater.* 27, 3560–3563. doi: 10.1021/acs.chemmater.5b00153
- Lyons, J. R. (2011). An estimate of the equilibrium speciation of sulfur vapor over solid sulfur and implications for planetary atmospheres. *J. Sulfur Chem.* 29, 269–279. doi: 10.1080/17415990802195615
- Mäkinen, M., Nousiainen, M., and Sillanpää, M. (2011). Ion spectrometric detection technologies for ultra-traces of explosives: a review. *Mass Spectrom. Rev.* 30, 940–973. doi: 10.1002/mas.20308
- Meng, H.-B., Wang, T.-R., Guo, B.-Y., Hashi, Y., Guo, C.-X., and Lin, J.-M. (2008). Simultaneous determination of inorganic anions and cations in explosive residues by ion chromatography. *Talanta* 76, 241–245. doi: 10.1016/j.talanta.2008.01.054
- Najarro, M., Morris, M. E. D., Staymates, M. E., Fletcher, R., and Gillen, G. (2012). Optimized thermal desorption for improved sensitivity in trace explosives detection by ion mobility spectrometry. *Analyst* 137, 2614–2622. doi: 10.1039/c2an16145a
- Olley, D. A., Wren, E. J., Vamvounis, G., Fernee, M. J., Wang, X., Burn, P. L., et al. (2010). Explosive sensing with fluorescent dendrimers: the role of collisional quenching[†]. *Chem. Mater.* 23, 789–794. doi: 10.1021/cm1020355
- Peng, L., Hua, L., Wang, W., Zhou, Q., and Li, H. (2014). On-site rapid detection of trace non-volatile inorganic explosives by stand-alone ion mobility spectrometry via acid-enhanced evaporation. *Sci. Rep.* 4:6631. doi: 10.1038/srep06631
- Peters, K. L., Corbin, I., Kaufman, L. M., Zreibe, K., Blanes, L., and McCord, B. R. (2015). Simultaneous colorimetric detection of improvised explosive compounds using microfluidic paper-based analytical devices (μPADs). *Anal. Methods* 7, 63–70. doi: 10.1039/C4AY01677G
- Qu, J., Ge, Y. R., Zu, B. Y., Li, Y. X., and Dou, X. C. (2016). Transition-metal-doped p-Type ZnO nanoparticle-based sensory array for instant discrimination of explosive vapors. *Small* 12, 1369–1377. doi: 10.1002/smll.201503131
- Samet, J. M., Demarini, D. M., and Malling, H. V. (2004). Do airborne particles induce heritable mutations? *Science* 304, 971–972. doi: 10.1126/science.1097441
- Schnorr, J. M., van der Zwaag, D., Walish, J. J., Weizmann, Y., and Swager, T. M. (2013). Sensory arrays of covalently functionalized single-walled carbon nanotubes for explosive detection. *Adv. Funct. Mater.* 23, 5285–5291. doi: 10.1002/adfm.201300131
- Senesac, L., and Thundat, T. G. (2008). Nanosensors for trace explosive detection. *Mater. Today* 11, 28–36. doi: 10.1016/S1369-7021(08)70017-8
- Steinfeld, J. I., and Wormhoudt, J. (1998). Explosives detection: a challenge for physical chemistry. *Annu. Rev. Phys. Chem.* 49, 203–232. doi: 10.1146/annurev.physchem.49.1.203
- Sun, Q., Wu, Z., Duan, H., and Jia, D. (2019). Detection of Triacetone Triperoxide (TATP) Precursors with an array of sensors based on MoS₂/RGO composites. *Sensors* 19:1281. doi: 10.3390/s19061281
- Tao, J., Cuan, Q., Halpegamage, S., Addou, R., Gong, X.-Q., and Batzill, M. (2013). Combined surface science and DFT study of the adsorption of Dinitrotoluene (2,4-DNT) on rutile TiO₂ (110): molecular scale insight into sensing of explosives. *J. Phys. Chem. C* 117, 16468–16476. doi: 10.1021/jp405050a
- Wang, D., Chen, A., Jang, S.-H., Yip, H.-L., and Jen, A. K.-Y. (2011a). Sensitivity of titania (B) nanowires to nitroaromatic and nitroamino explosives at room temperature via surface hydroxyl groups. *J. Mater. Chem.* 21, 7269–7273. doi: 10.1039/c1jm10124b
- Wang, D., Chen, A., and Jen, A. K.-Y. (2013). Reducing cross-sensitivity of TiO₂-(B) nanowires to humidity using ultraviolet illumination for trace explosive detection. *Phys. Chem. Chem. Phys.* 15, 5017–5021. doi: 10.1039/c3cp43454k
- Wang, D., Chen, A., Zhang, Q., and Cao, G. (2011b). Room-temperature chemiresistive effect of nanowires to nitroaromatic and nitroamine explosives. *IEEE Sens. J.* 11, 1352–1358. doi: 10.1109/JSEN.2010.2089618
- Wang, J., Yang, L., Liu, B., Jiang, H., Liu, R., Yang, J., et al. (2014). Inkjet-printed silver nanoparticle paper detects airborne species from crystalline explosives and their ultratrace residues in open environment. *Anal. Chem.* 86, 3338–3345. doi: 10.1021/ac403409q
- Wu, Z. F., Zhou, C. Y., Zu, B. Y., Li, Y. S., and Dou, X. C. (2016). Contactless and rapid discrimination of improvised explosives realized by Mn²⁺ doping tailored ZnS nanocrystals. *Adv. Funct. Mater.* 26, 4578–4586. doi: 10.1002/adfm.201600592
- Xie, G. S., and Liu, B. X. (2019). Fingerprinting of nitroaromatic explosives realized by aphe-functionalized titanium dioxide. *Sensors* 19:2407. doi: 10.3390/s19102407
- Yan, W., Zou, Y., Zhou, H., Wang, L., and Meng, X. J. J. (2017). Synergistic effect of sodium ions and fluoride ions on synthesis of pure-phase TiO₂(B) nanorings. *J. Nanoparticle Res.* 19:192. doi: 10.1007/s11051-017-3889-4
- Yang, L., Ma, L., Chen, G., Liu, J., and Tian, Z. Q. (2010). Ultrasensitive SERS detection of TNT by imprinting molecular recognition using a new type of stable substrate. *Chem. Eur. J.* 16, 12683–12693. doi: 10.1002/chem.201001053
- Yang, Z., Dou, X., Zhang, S., Guo, L., Zu, B., Wu, Z., et al. (2015). A High-performance nitro-explosives schottky sensor boosted by interface modulation. *Adv. Funct. Mater.* 25, 4039–4048. doi: 10.1002/adfm.201501120
- Yao, L., Garmash, O., Bianchi, F., Zheng, J., Yan, C., Kontkanen, J., et al. (2018). Atmospheric new particle formation from sulfuric acid and amines in a Chinese megacity. *Science* 361, 278–281. doi: 10.1126/science.aao4839

- Zhao, J. X., Li, W. T., Li, X., and Zhang, X. K. (2017). Low temperature synthesis of water dispersible F-doped TiO₂ nanorods with enhanced photocatalytic activity. *RSC Adv.* 7, 21547–21555. doi: 10.1039/C7RA00850C
- Zhao, X., and Yinon, J. (2002). Forensic identification of explosive oxidizers by electrospray ionization mass spectrometry. *Rapid Commun. Mass Spectrom.* 16, 1137–1146. doi: 10.1002/rcm.692
- Zhou, Q., Peng, L., Jiang, D., Wang, X., Wang, H., and Li, H. (2015). Detection of nitro-based and peroxide-based explosives by fast polarity-switchable ion mobility spectrometer with ion focusing in vicinity of faraday detector. *Sci. Rep.* 5:10659. doi: 10.1038/srep10659
- Zhu, D., He, Q., Chen, Q., Fu, Y., He, C., Shi, L., et al. (2011). Sensitivity gains in chemosensing by optical and structural modulation of ordered assembly arrays of ZnO nanorods. *ACS Nano* 5, 4293–4299. doi: 10.1021/nn103211d
- Zu, B., Guo, Y., and Dou, X. (2013). Nanostructure-based optoelectronic sensing of vapor phase explosives—a promising but challenging method. *Nanoscale* 5, 10693–10701. doi: 10.1039/c3nr03792d
- Conflict of Interest:** The authors declare that the research was conducted in the absence of any commercial or financial relationships that could be construed as a potential conflict of interest.
- Copyright © 2020 Li, Zhou, Zu and Dou. This is an open-access article distributed under the terms of the Creative Commons Attribution License (CC BY). The use, distribution or reproduction in other forums is permitted, provided the original author(s) and the copyright owner(s) are credited and that the original publication in this journal is cited, in accordance with accepted academic practice. No use, distribution or reproduction is permitted which does not comply with these terms.



Gas-Sensing Performances of Metal Oxide Nanostructures for Detecting Dissolved Gases: A Mini Review

Wei Guan^{1,2}, Na Tang³, Kuang He^{1,2}, Xiaoying Hu^{1,2}, Mingshan Li^{1,2*} and Kaiming Li^{1,2}

¹ South China Institute of Environmental Sciences, Ministry of Ecological Environment, Guangzhou, China, ² The Key Laboratory of Water and Air Pollution Control of Guangdong Province, South China Institute of Environmental Sciences, Ministry of Environmental Protection (MEP), Guangzhou, China, ³ Chongqing Solid Wastes Management Center, Chongqing, China

OPEN ACCESS

Edited by:

Wen Zeng,
Chongqing University, China

Reviewed by:

Juanjuan Zhang,
Key Laboratory of Drinking Water
Science and Technology, Research
Center for Eco-Environmental
Sciences (CAS), China
Yanbin Wang,
Henan Normal University, China

*Correspondence:

Mingshan Li
limingshan@scies.org

Specialty section:

This article was submitted to
Nanoscience,
a section of the journal
Frontiers in Chemistry

Received: 06 December 2019

Accepted: 23 January 2020

Published: 21 February 2020

Citation:

Guan W, Tang N, He K, Hu X, Li M
and Li K (2020) Gas-Sensing
Performances of Metal Oxide
Nanostructures for Detecting
Dissolved Gases: A Mini Review.
Front. Chem. 8:76.
doi: 10.3389/fchem.2020.00076

Gas sensors have been widely used in various fields related to people's lives. Gas sensor materials were the core factors that affected the performances of various gas sensors, and these have attracted much attention from scientific researchers due to their high sensitivity, high selectivity, adjustable reliability, low cost, and other advantages. The preparation of nanostructures with a highly specific surface area was a useful method to improve the gas-sensing performance of a metal oxide semiconductor. Meanwhile, lots of research has focused on preparing nanostructures with a highly specific surface area. This paper has explored some fabricated sensors with high sensitivity, good selectivity, and long-term stability, which has also made them promising candidates for toxic gas detection. Besides, this paper has reviewed the development status of metal oxides used as gas sensors.

Keywords: metal oxides nanostructures, gas sensors, gas sensing mechanism, gas sensing performance, modification methods

INTRODUCTION

Gas sensors depend on converting gas into electrical signal output through chemical and physical effects in order to detect the composition and concentration of gas. Gas sensors are widely used in the fields of flammable detection, explosive detection, toxic and harmful gases detection, and environmental control (Zhou et al., 2019).

Recently, most of the gas sensors have been surface-controlled resistance sensors in which the sensitive materials of semiconductor resistance gas sensors are mainly concentrated in metal oxide semiconductors (Jeong et al., 2019). Due to a large number of free electrons in the conduction band and oxygen vacancies on the surface of the metal semiconductors, the material surface has strong adsorption characteristics and high reactivity and is changed under the action of surface gas. Therefore, the measurements can be made based on the electrical parameters (Rabee et al., 2019). Metal oxide materials have outstanding physical and chemical properties, are of low cost to produce, and have simple preparation methods (Wang et al., 2019). Therefore, they have been increasingly used in gas sensing.

Song et al. prepared hollow porous core-shell NiO nanotubes using a hydrothermal method. There were many micropores on the wall of a single nanotube with a specific surface area of 97.3 m² g⁻¹ (Song et al., 2011). Due to the large specific surface area, the sensitivity of the NiO gas sensor to 50 ppm ethanol gas was very high. It was believed that the hollow porous core-shell structure enabled ethanol molecules to diffuse and transport rapidly into the interior of the sensor, and so the material showed an excellent gas-sensing performance.

Ma et al. prepared hollow microtubules of In_2O_3 with degreased cotton as a soft biological template (Ma et al., 2019). The length of the hollow microtubule was 50–70 μm , the width was 5–6 μm , and the wall thickness was about 1 μm . The $R_{\text{gas}}/R_{\text{air}}$ value to 10 ppm Cl_2 gas was 1,051 for the hollow microtubule sensor of In_2O_3 , which was 25 times higher than that of In_2O_3 particles at 200°C. The existence of the hollow morphology of In_2O_3 with a highly specific surface area, rich oxygen vacancy, and narrow band gap were the reasons for the improving gas-sensing performance.

Wanit et al. prepared the ZnO nano-trees with a multistage branching structure through a hydrothermal growth method where numerous nano trees with dense distribution formed a vast nano forest (Wanit et al., 2012). This nano forest structure was suitable for dye-sensitized solar cells; it was similar to the role of the actual forest, which was used to convert solar energy into electricity. Obviously, this kind of nano forest structure had a very large specific surface area, which could be used significantly improve the gas-sensing performance of materials. Besides, the experiments indicated that this structure could greatly improve the light conversion efficiency and the overall light conversion efficiency was five times higher than that of dye-sensitized solar cells constructed by vertical ZnO nanowires. The improvement of light conversion efficiency was due to the large increase of specific surface area, which made

the photosensitive dye adhesion area more extensive and could capture more sunlight. Moreover, the multi-level branch of the “nano tree” provided a direct conduction path for the charge and reduced the neutralization of the charge in the transmission process.

RESEARCH STATUS OF METAL OXIDES FOR GAS SENSORS

Gas sensors mainly include semiconductor gas sensors, electrochemical gas sensors, and contact combustion gas sensors, among which the most promising ones are the semiconductor gas sensors. With the application of a series of oxide semiconductors, including NiO , ZnO , SnO_2 , and CdO , the research into metal oxide for gas sensing is popular. The oxidation semiconductor refers to the one whose conductivity increases with the oxidation atmosphere, which belongs to the p-type semiconductor. The reduction semiconductor refers to the one whose conductivity increases with the reduction atmosphere, which belongs to the n-type semiconductor. The amphoteric semiconducting refers to the one whose conductivity type forms the p-type or n-type semiconductor with the oxygen partial pressure in the atmosphere. There are some methods to improve the gas-sensing performance, such as surface modification with organic molecules, perpetration of inorganic heterojunction

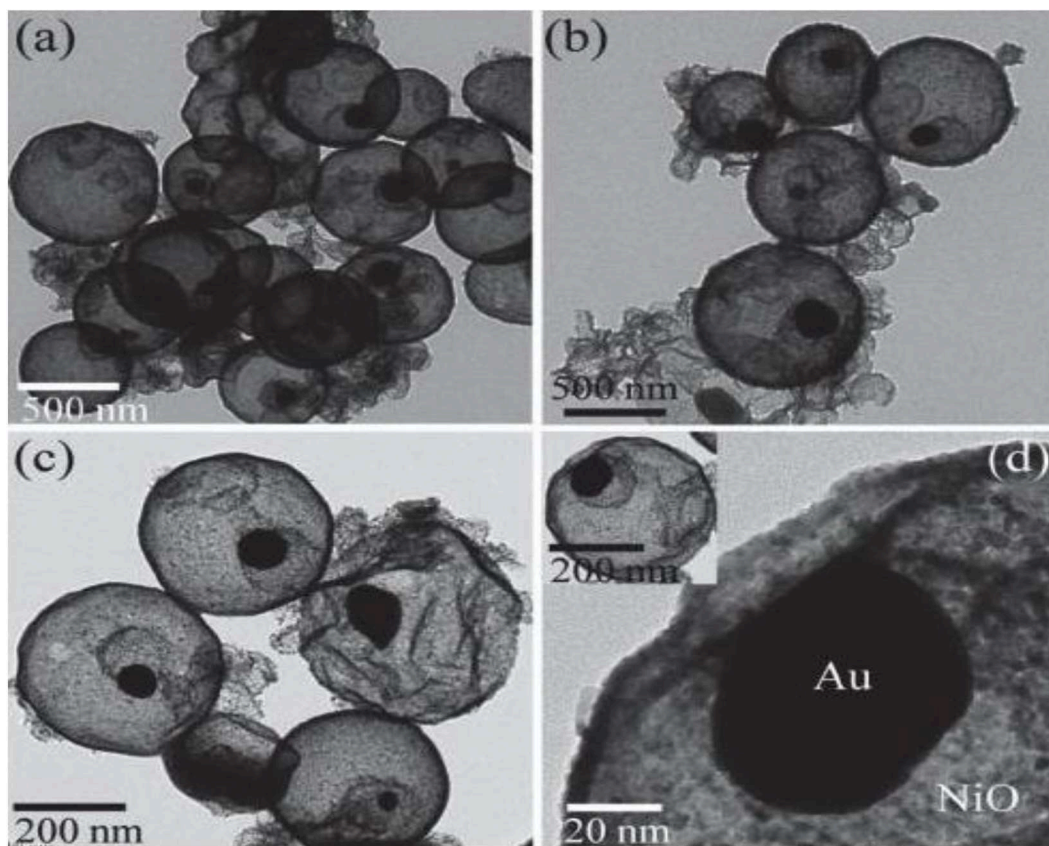


FIGURE 1 | (a–d) TEM images of the Au/NiO core-shell structure. Reprinted with permission from Rai et al. (2014). Copyright (2014) Elsevier Science BV.

sensitization, generation of hybrid structures with 1D or 2D materials, and oxygen vacancy modification (Zhang et al., 2019).

Adding a small amount of precious metals to semiconductor materials is an effective way to improve the gas-sensitive properties of materials. Shaver first found that the noble metal Pt had a significant enhancement for improving the sensitivity and selectivity of gas sensors, and that it also shortened the response time for WO_3 oxide semiconductor gas sensors. In addition, adding a certain amount of rare earth metals to the material was also an effective way to improve the sensitivity and selectivity of the material.

Wang et al. prepared a series of polyaniline- TiO_2 nanocomposites on the TiO_2 surface by *in-situ* chemical oxidation polymerization of aniline (Wang et al., 2017). It was found that the polyaniline chain formed by TiO_2 and polyaniline could increase the CO adsorption, which led to much more electrons transfer from CO to polyaniline. Following from polyaniline to TiO_2 through a hydrogen bond, this resulted in promoting the photocatalytic oxidation of CO on the

composite film sensor. This study provided a method for the development of a gas-sensitive material with organic-inorganic hybrid nanocomposites.

Nulhakim et al. prepared highly Ga-doped ZnO polycrystalline thin films deposited by radio-frequency magnetron sputtering for hydrogen gas sensing (Nulhakim et al., 2017). The relationship between the microstructure of preferred *c*-axis-oriented thin films and the hydrogen gas-sensing performance was introduced. It is found that the sensitivity of the sample to hydrogen increased slightly with the decrease of the microcrystalline size under the working temperature of 330°C . Moreover, the sensitivity was significantly improved by increasing the preferred orientation distribution. It was concluded that the *c*-axis orientation had a great influence on the sensitivity of the hydrogen gas sensor.

Amani et al. prepared a WO_3 semiconductor gas sensor by electron beam evaporation technology, and the gas-sensing characteristics of the WO_3 nano film activated by Pt and Au were studied (Amani et al., 2017). The results indicated that the

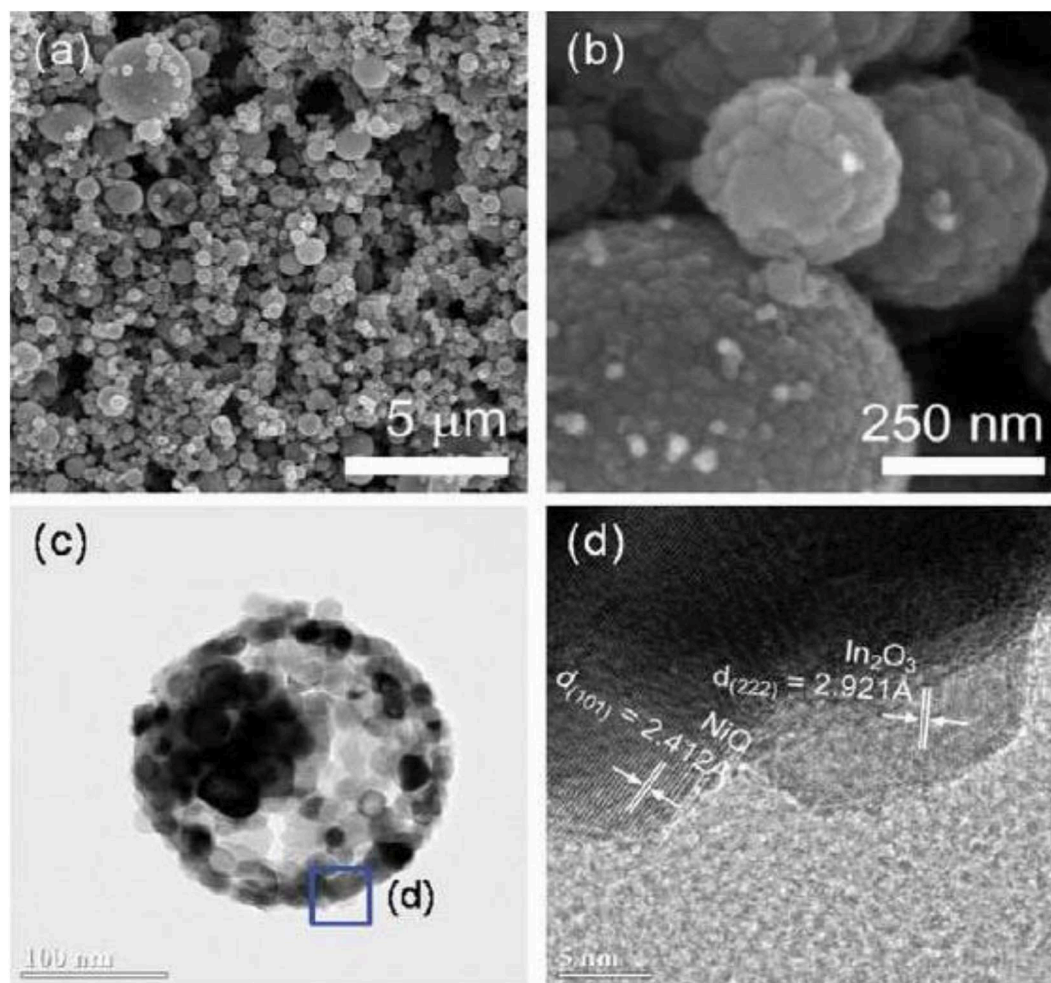


FIGURE 2 | (a,b) SEM image of In_2O_3 -Decorated NiO hollow nanostructures. (c,d) TEM image of In_2O_3 -Decorated NiO hollow nanostructures. Reprinted with permission from Kim et al. (2014) Copyright 2014 American Chemical Society.

existence of a Pt and Cu layer reduced the working temperature of the WO_3 sensor; the WO_3 nano thin film activation by the Pt layer significantly reduced the working temperature of the sensor.

Yang et al. synthesized ultralong MoO_3 nanobelts with an average length of $200\text{ }\mu\text{m}$ and width of $200\text{--}400\text{ nm}$ by simple hydrothermal technology (Yang et al., 2016). The results indicated that the gas sensor prepared by an ultralong MoO_3 nanobelt had a good gas-sensing performance for trimethylamine under the temperature of 240°C . The selectivity test of different reducing gases showed that the gas sensor had a better response to TMA than other gases, such as ethanol, ammonia, toluene, methanol, and acetone.

Zolghadr et al. conducted research on the effect of annealing temperatures at 600°C and 800°C on the gas-sensing properties of $\alpha\text{-Fe}_2\text{O}_3$ (Zolghadr et al., 2016). The results showed that the gas sensitivity of $\alpha\text{-Fe}_2\text{O}_3$ film annealed at 800°C was more stable, and the gas sensitivity of $\alpha\text{-Fe}_2\text{O}_3$ to NO_2 gas was higher than that of other gases.

Liu et al. prepared SnO_2 thin films for gas sensors by ultrasonic spray pyrolysis technology and showed the effect of Cu doping amount on the gas-sensing performance (Liu et al., 2017). The results indicated that Cu doping could improve the gas sensitivity of SnO_2 films, which was incorporated at the Cu/Sn ratio of 0–1.

Rai et al. synthesized the Au/NiO core-shell structure with uniform dispersion by two-step hydrothermal method (Rai et al., 2014). As shown in **Figure 1**, Au existing alone in the NiO spherical shell showed an excellent gas-sensing performance for hydrogen sulfide gas. A wonderful rotten egg connection of gas-sensing material and gas was generated. The results indicated that the sensitivity to H_2S gas for the NiO core-shell structure with Au as the core was nearly four times higher than that of the NiO sphere. Moreover, the sulfurization layer formed on the surface of Au particles adsorbed H_2S gas; this reduced the reaction potential energy and made it easier for electrons to transfer from Au particles to the NiO shell and increased the resistance value.

Kim et al. also synthesized the NiO hollow sphere nanostructure and used In_2O_3 to modify the NiO hollow sphere (Kim et al., 2014). The results indicated that the sensitivity to ethanol gas for In_2O_3 -Decorated NiO hollow nanostructures was nearly five times higher than that of NiO sphere. The existence

of n-type semiconductor of In_2O_3 reduced the accumulation of holes on the surface of NiO shell, as shown in **Figure 2**, which greatly reduced time for response and recovery to ethanol gas.

Finally, the gas-sensing mechanisms for metal oxides are the change in electrical signal caused by the gas. Gas-sensing mechanisms are included in two parts. One part explains the changes in electrical properties from a relatively microscopic perspective and includes mechanisms. The other part is relatively macroscopic, and it focus on the relationship between materials and gases (Ji et al., 2019).

CONCLUSION

The research included some metal oxides used for gas sensing; some modification methods, such as metal oxide doping, metal/oxide heterojunction, metal oxide/metal oxide heterojunction, and metal oxide/conductive polymer heterojunction were introduced. The theoretical qualitative models of gas sensing include an atomic valence control model, double electric layer model, and grain boundary barrier model. Many researchers also put forward reasonable explanations based on the actual performance of the samples according to their specific research situation. The preparation of nanostructures with highly specific surface areas was a useful method to improve the gas-sensing performance.

AUTHOR CONTRIBUTIONS

WG and ML wrote the manuscript. All the authors read and approved the manuscript.

FUNDING

This work was supported by the China Postdoctoral Science Foundation (No. 2019M652948); the Science and Technology Planning Project of Guangdong Province (2017A050506032); the Science and Technology Planning Project of Guangzhou (201804010204); and the South China Institute of Environmental Sciences Central Public-Interest Scientific Institution Basal Research Fund (PM-zx703-201904-135 and PM-zx703-201904-101).

REFERENCES

- Amani, E., Khojier, K., and Zoriatian, S. (2017). Improving the hydrogen gas sensitivity of WO_3 thin films by modifying the deposition angle and thickness of different promoter layers. *Int. J. Hydrog. Energy* 42, 29620–29628. doi: 10.1016/j.ijhydene.2017.10.027
- Jeong, H. I., Park, S., Yang, H. I., and Choi, W. (2019). Electrical properties of MoSe_2 metal-oxide-semiconductor capacitors. *Mater. Lett.* 253, 209–212. doi: 10.1016/j.matlet.2019.06.072
- Ji, H. C., Zeng, W., and Li, Y. Q. (2019). Gas sensing mechanisms of metal oxide semiconductors: a focus review. *Nanoscale* 11, 22664–22684. doi: 10.1039/C9NR07699A
- Kim, H. J., Jeong, H. M., Kim, T. H., Chung, J. H., Kang, Y. C., and Lee, J. H. (2014). Enhanced ethanol sensing characteristics of In_2O_3 -decorated NiO hollow nanostructures via modulation of hole accumulation layers. *ACS Appl. Mater. Interfaces* 6, 18197–18204. doi: 10.1021/am5051923
- Liu, J. Q., Lu, Y. T., Cui, X., Geng, Y. C., Jin, G. H., and Zhai, Z. X. (2017). Gas-sensing properties and sensitivity promoting mechanism of Cu-added SnO_2 thin films deposited by ultrasonic spray pyrolysis. *Sens. Actuat. B Chem.* 248, 862–867. doi: 10.1016/j.snb.2017.01.057
- Ma, J. W., Fan, H. Q., Zhao, N., Zhang, W. M., Ren, X. H., Wang, C., et al. (2019). Synthesis of In_2O_3 hollow microspheres for chlorine gas sensing using yeast as bio-template. *Ceram. Int.* 45, 9225–9230. doi: 10.1016/j.ceramint.2019.01.268
- Nullhakim, L., Makino, H., Kishimoto, S., Nomoto, J., and Yamamoto, T. (2017). Enhancement of the hydrogen gas sensitivity by large distribution of c-axis preferred orientation in highly Ga-doped ZnO polycrystalline thin films. *Mat. Sci. Semicon. Proc.* 68, 322–326. doi: 10.1016/j.mssp.2017.06.045

- Rabee, A. S. H., Hameed, M. F. O., Heikal, A. M., and Obayya, S. S. A. (2019). Highly sensitive photonic crystal fiber gas sensor. *Optik* 188, 78–86. doi: 10.1016/j.ijleo.2019.05.044
- Rai, P., Yoon, J. W., Jeong, H. M., Hwang, S. J., Kwaka, C. H., and Lee, J. H. (2014). Design of highly sensitive and selective Au@NiO yolk-shell nanoreactors for gas sensor applications. *Nanoscale* 6, 8292–8299. doi: 10.1039/C4NR01906G
- Song, X. F., Gao, L., and Mathur, S. (2011). Synthesis, characterization, and gas sensing properties of porous nickel oxide nanotubes. *J. Phys. Chem. C* 115, 21730–21735. doi: 10.1021/jp208093s
- Wang, Y. R., Ma, S. H., Wang, L. F., and Jiao, Z. Y. (2019). A novel highly selective and sensitive NH₃ gas sensor based on monolayer Hf₂CO₂. *Appl. Surf. Sci.* 492, 116–124. doi: 10.1016/j.apsusc.2019.06.212
- Wang, Z. M., Peng, X. Y., Huang, C. Y., Chen, X., Dai, W. X., and Fu, X. Z. (2017). CO gas sensitivity and its oxidation over TiO₂ modified by PANI under UV irradiation at room temperature. *Appl. Catal. B Environ.* 219, 379–390. doi: 10.1016/j.apcatb.2017.07.080
- Wanit, M., Yeo, J., Hong, S. J., Suh, Y. D., Ko, S. H., Lee, D., et al. (2012). ZnO nano-tree growth study for high efficiency solar cell. *Energy Proced.* 14, 1093–1098. doi: 10.1016/j.egypro.2011.12.1060
- Yang, S., Liu, Y. L., Chen, W., Jin, W., Zhou, J., Zhang, H., et al. (2016). High sensitivity and good selectivity of ultralong MoO₃ nanobelts for trimethylamine gas. *Sens. Actuat. B Chem.* 226, 478–485. doi: 10.1016/j.snb.2015.12.005
- Zhang, C., Luo, Y. F., Xu, J. Q., and Debliquy, M. (2019). Room temperature conductive type metal oxide semiconductor gas sensors for NO₂ detection. *Sens. Actuat. A Phys.* 289, 118–133. doi: 10.1016/j.sna.2019.02.027
- Zhou, Q., Zeng, W., Chen, W. G., Xu, L. N., Kumar, R., and Umar, A. (2019). High sensitive and low-concentration sulfur dioxide (SO₂) gas sensor application of heterostructure NiO-ZnO nanodisks. *Sens. Actuat. B Chem.* 298, 126870–126876. doi: 10.1016/j.snb.2019.126870
- Zolghadr, S., Khojier, K., and Kimiagar, S. (2016). Study of sensitivity and selectivity of α -Fe₂O₃ thin films for different toxic gases and alcohols. *Mat. Sci. Semicon. Proc.* 54, 6–13. doi: 10.1016/j.mssp.2016.06.016

Conflict of Interest: The authors declare that the research was conducted in the absence of any commercial or financial relationships that could be construed as a potential conflict of interest.

Copyright © 2020 Guan, Tang, He, Hu, Li and Li. This is an open-access article distributed under the terms of the Creative Commons Attribution License (CC BY). The use, distribution or reproduction in other forums is permitted, provided the original author(s) and the copyright owner(s) are credited and that the original publication in this journal is cited, in accordance with accepted academic practice. No use, distribution or reproduction is permitted which does not comply with these terms.



Simultaneously Optimize the Response Speed and Sensitivity of Low Dimension Conductive Polymers for Epidermal Temperature Sensing Applications

Cheng Zhou, Ning Tang, Xiaoshuang Zhang, Ye Fang, Yang Jiang, Hainan Zhang and Xuexin Duan*

State Key Laboratory of Precision Measuring Technology & Instruments, Tianjin University, Tianjin, China

OPEN ACCESS

Edited by:

Weiwei Wu,
Xidian University, China

Reviewed by:

Soong Ju Oh,
Korea University, South Korea
Han Jin,
Shanghai Jiao Tong University, China

*Correspondence:

Xuexin Duan
xduan@tju.edu.cn

Specialty section:

This article was submitted to
Nanoscience,
a section of the journal
Frontiers in Chemistry

Received: 27 September 2019

Accepted: 02 March 2020

Published: 19 March 2020

Citation:

Zhou C, Tang N, Zhang X, Fang Y, Jiang Y, Zhang H and Duan X (2020) Simultaneously Optimize the Response Speed and Sensitivity of Low Dimension Conductive Polymers for Epidermal Temperature Sensing Applications. *Front. Chem.* 8:194. doi: 10.3389/fchem.2020.00194

Low dimension poly(3,4-ethylenedioxythiophene) poly (styrenesulfonate) (PEDOT: PSS) has been applied as resistor-type devices for temperature sensing applications. However, their response speed and thermal sensitivity is still not good enough for practical application. In this work, we proposed a new strategy to improve the thermal sensing performance of PEDOT: PSS by combined micro/nano confinement and materials doping. The dimension effect is carefully studied by fabricating different sized micro/nanowires through a low-cost printing approach. It was found that response speed can be regulated by adjusting the surface/volume (S/V) ratio of PEDOT: PSS. The fastest response (<3.5 s) was achieved by using nanowires with a maximum S/V ratio. Besides, by doping PEDOT: PSS nanowires with Graphene oxide (GO), its thermo-sensitivity can be maximized at specific doping ratio. The optimized nanowires-based temperature sensor was further integrated as a flexible epidermal electronic system (FEES) by connecting with wireless communication components. Benefited by its flexibility, fast and sensitive response, the FEES was demonstrated as a facile tool for different mobile healthcare applications.

Keywords: temperature sensor, nanowires, fast response, healthcare, tumor, smartphone

INTRODUCTION

Real-time and continuous measurement of human body local epidermal temperature enables a better tracking of personal health status such as local wounds infection (Celeste et al., 2013), subcutaneous tumor (Sudharsan et al., 1999), as well as monitoring of body activities, since many diseases and physiological behaviors will cause local changes in body epidermal temperature (Deng and Liu, 2004; Helmy and Rizkalla, 2008; Ng, 2009; Li et al., 2017). Recently, wearable epidermal electronic systems (EESs) based on flexible devices have opened new frontiers in the measurement of body local temperature (Gao et al., 2014; Takei et al., 2015). Due to their soft and flexible nature, they can be directly attached to the human skin and conform to the body, local temperature can

be detected anytime and anywhere (Webb et al., 2013; Zhang et al., 2016). Besides, the use of soft substrate enables high mechanical durability in different bending conditions, thus their responses will not be influenced by the movement of the body (Wu and Haick, 2018; Chang et al., 2019). However, due to the materials limitation, current EESs based thermal meters still suffer from the issues of responding slowly or not sensitive enough to body temperature change, which in fact cannot provide real-time precise temperature tracking. Hence the development of fast and sensitive response wearable temperature sensors which can track personal health status is still required.

Among all EES temperature sensor, PEDOT: PSS based resistor-type electronics have been largely applied since the PEDOT: PSS itself is very sensitive to temperature changes (Culebras et al., 2016) and the soft nature of such organic electronics ensures its excellent performance as flexible sensors (Lipomi et al., 2012). The thermosensitive mechanism of PEDOT: PSS can be explained by the structural change of PEDOT: PSS induced by the temperature change which eventually alters the conductivity of PEDOT: PSS (Takano et al., 2012; Zhou et al., 2014; Vuorinen et al., 2016). Previous studies on PEDOT: PSS based temperature sensors were focused on doping the PEDOT: PSS with other materials to enhance the device's response to temperature (Honda et al., 2014; Oh et al., 2018). However, understanding the control parameters regarding their response time to temperature change is less covered.

In this work, in order to simultaneously optimize the response speed and sensitivity of conductive polymers for epidermal temperature sensing applications such as quick temperature detecting or real-time precise temperature tracking, we proposed a strategy to combine the micro/nano confinement with the materials doping to simultaneously optimize the response time and sensitivity of PEDOT: PSS based resistor-type temperature sensor. Low dimension PEDOT: PSS wires from a few micrometers down to sub-100 nm in diameters were fabricated using a low-cost micro/nanoscale printing approach (Gates et al., 2005; Massi et al., 2006; Duan et al., 2010; Tang et al., 2019). Their sensitivity and response time to temperature were compared (Scheme 1). Then, graphene oxide (GO) was selected to dope the PEDOT: PSS and the doping ratios were carefully optimized to enhance their temperature sensing performance. Hence the fabricated sensor under such strategy is responding both fast and sensitive enough to detect minute temperature change and track temperature in real-time. The sensor shows ultra-fast response and sensitive to body temperature change. Furthermore, the sensor is also used to achieve temperature monitoring of subcutaneous tumors in mice and by detecting the minute change of body temperature in mice to test the effect of drugs. Given the prominent mechanical and sensing properties, a homemade wearable system based on the temperature sensor was further developed to achieve a live and wireless transmission of the signals to a smartphone using Bluetooth assisted communication. These results demonstrate that this fast response skin-attachable nanowires-based temperature sensor has great potential as a wearable bioelectronic for application in medical diagnosis and mobile healthcare.

EXPERIMENTAL METHODS

Reagents and Materials

mr-I T85 was purchased from Micro-Resist. PEDOT: PSS aqueous suspension (~ 1.3 wt%) with a conductivity of 1 S cm^{-1} was purchased from Sigma-Aldrich. GO was purchased from Chengdu Organic Chemical company and further sonicated for 30 min to form a uniform and stable dispersion with a concentration of 7 mg/ml. The compound solution was obtained by stirring PEDOT: PSS aqueous suspension and GO aqueous suspension for 10 min. Polydimethylsiloxane (PDMS) was purchased from Dow corning.

Fabrication of Flat PDMS Molds With Micro/Nano Grooves

First, casting the liquid prepolymer of PDMS base and the curing agent in a 10:1 (w/w) ratio onto a silicon wafer with two kinds of silicon micro-ridges ($3 \mu\text{m}$ in width and $1 \mu\text{m}$ in height and spacing $5 \mu\text{m}$, $5 \mu\text{m}$ in width and $1 \mu\text{m}$ in height and spacing $10 \mu\text{m}$, respectively). After the bubbles generated during the stirring process disappear, the wafer with the uncured PDMS was put into hot oven. After curing at 80°C for 40 min, the PDMS with microgrooves was cooled to room temperature and peeled off from the silicon wafer. Then, the PDMS with microgrooves was cut into pieces with the boundary of the microgrooves. The fabrication of the molds with nanogroove can be seen on previous case articles performed in our lab (Tang et al., 2019).

Formation of Micro/Nano Channels

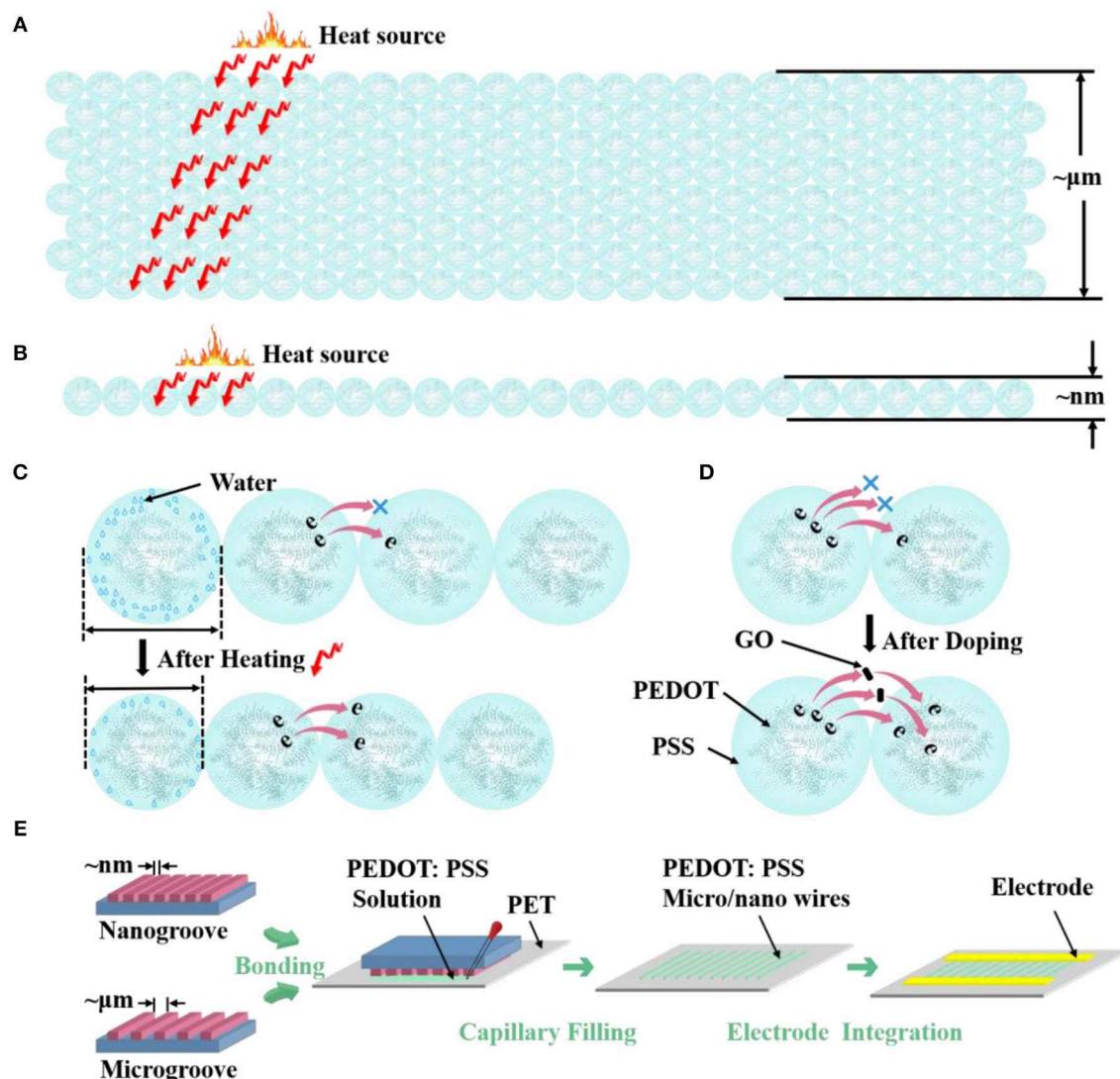
The molds with micro/nano groove were first treated with oxygen plasma (10 mTorr; 10 sccm O_2 ; 10 W; 15 s) to facilitate the contact between the molds and PET substrates. The molds were then bonded to the PET substrates which were also treated with oxygen plasma (20 mTorr; 20 sccm O_2 ; 20 W; 15 s). The molds can conformal contact with the PET substrates because of the oxygen plasma treated procedure and soft properties of the molds and PET substrates. Hence the micro/nano grooves changed into micro/nano channels after contacting.

Electrodes Fabrication

The Au electrodes were then prepared by thermal evaporation on the PET substrate with nanowires under self-made copper shadow masks to promote the electrical connection. The electrodes were with pad length in 7 mm, width in $300 \mu\text{m}$ and spacing in $300 \mu\text{m}$. The electrodes of microwires-based devices were silver paste at an interval of 3 mm approximately. Silver paste and silver wires were used to have further electrical contacts.

Measurements

Atomic force microscope (AFM), Scanning electron microscope (SEM) and the confocal laser scanning microscope (CLSM) images were carried out with Dimension Icon (Bruker), FEI FP 2031/12 Inspect F50 and OLYMPUS OLS5000, respectively. Electrical measurements with a constant voltage of +1 V were performed with a semiconductor analyzer (Agilent Technologies, B1500A).



SCHEME 1 | Morphological model shows the different S/V ratio of PEDOT: PSS (A) microwires and (B) nanowire. Morphological model of the (C) thermosensitive and (D) doping mechanism of PEDOT: PSS. (E) Carton shows the fabrication process of micro/nanowires.

Animal Tumor Model

Liver cancer tumor cells was injected into KM mice to establish an animal tumor model.

Temperature Monitoring Based on Smartphone

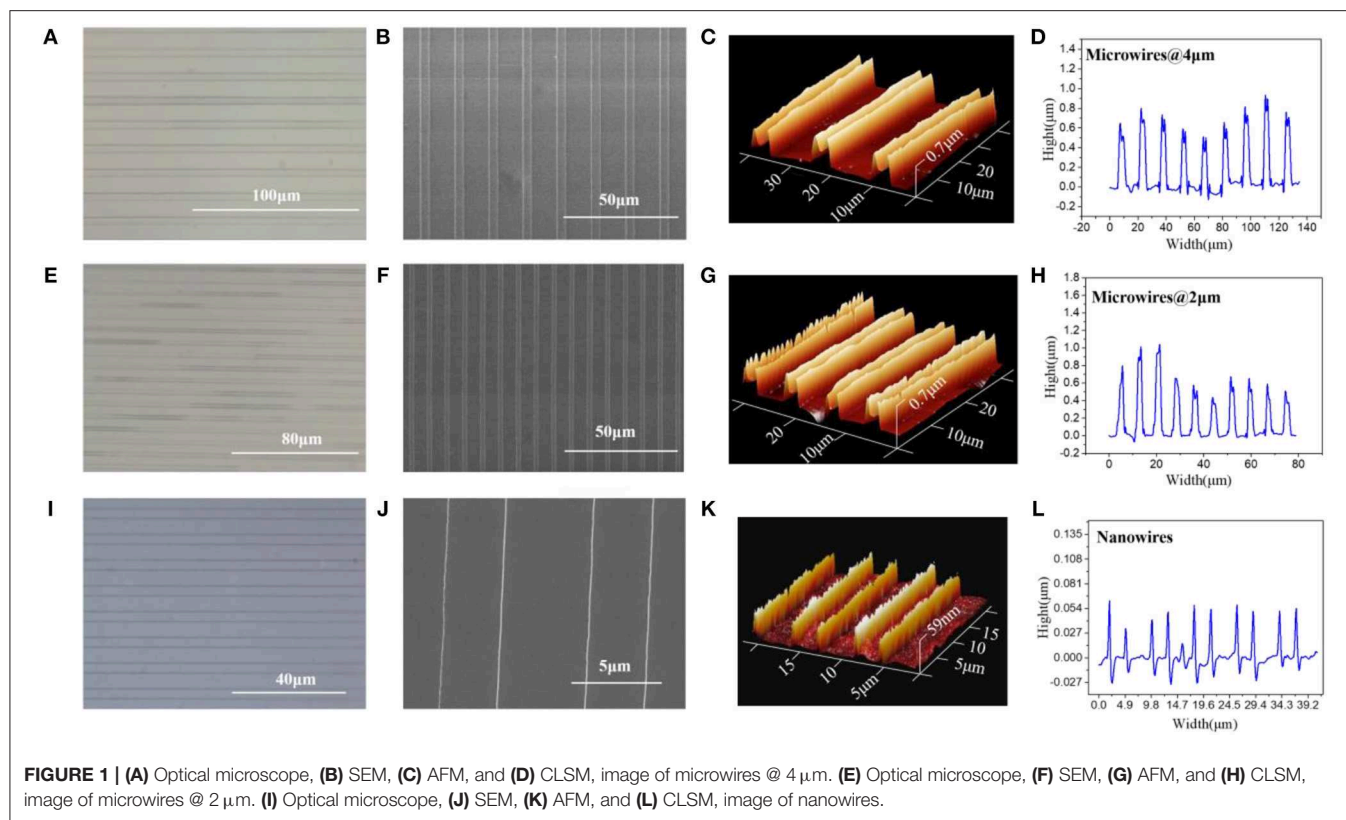
The homemade wearable watch-type system was fabricated by integrating the AD5933/STM32/HC-05 and their peripheral circuits on a flexible circuit board. AD5933/STM32/HC-05 control resistance measurement, communication, and data transmission, respectively. An Android application program was developed on the smartphone to receive real-time data from the wearable watch-type system and plot the responses on the screen. Comparing the response change to its resistance

calibration at standard temperature, the temperature was successfully measured.

RESULTS AND DISCUSSION

Micro/nanowires Fabrication and Characterization

To study the structure effects on the thermal sensing performance of PEDOT: PSS, here we design three different sized PEDOT: PSS wires, where their widths vary from $4\mu\text{m}$ to 70nm (Scheme 1). Hence different S/V ratios are achieved. The micro/nanowires were fabricated by an adapted soft lithography which does not require any cleanroom facilities (Gates et al., 2005; Massi et al., 2006; Duan et al., 2010; Tang et al., 2019). Scheme 1E shows the schematic of fabricating procedure



of micro/nanowires. After the micro/nanochannels (The preparation process is shown in the Experimental Methods) have completely formed, the PEDOT: PSS aqueous solution were dropped to the margins of channels. The solution filled the channels spontaneously by traction of the Laplace pressure. After the solvent has completely evaporated, removed the mold from PET and leaved the micro/nanowires on the PET substrate. Then, metal electrodes were fabricated on the side of the micro/nanowires through evaporation as the contact electrodes, thus resistor-type sensors have been achieved. The comparison between our method and current available methods for fabricating nanowires in the format of a table is shown in **Supplementary Information**.

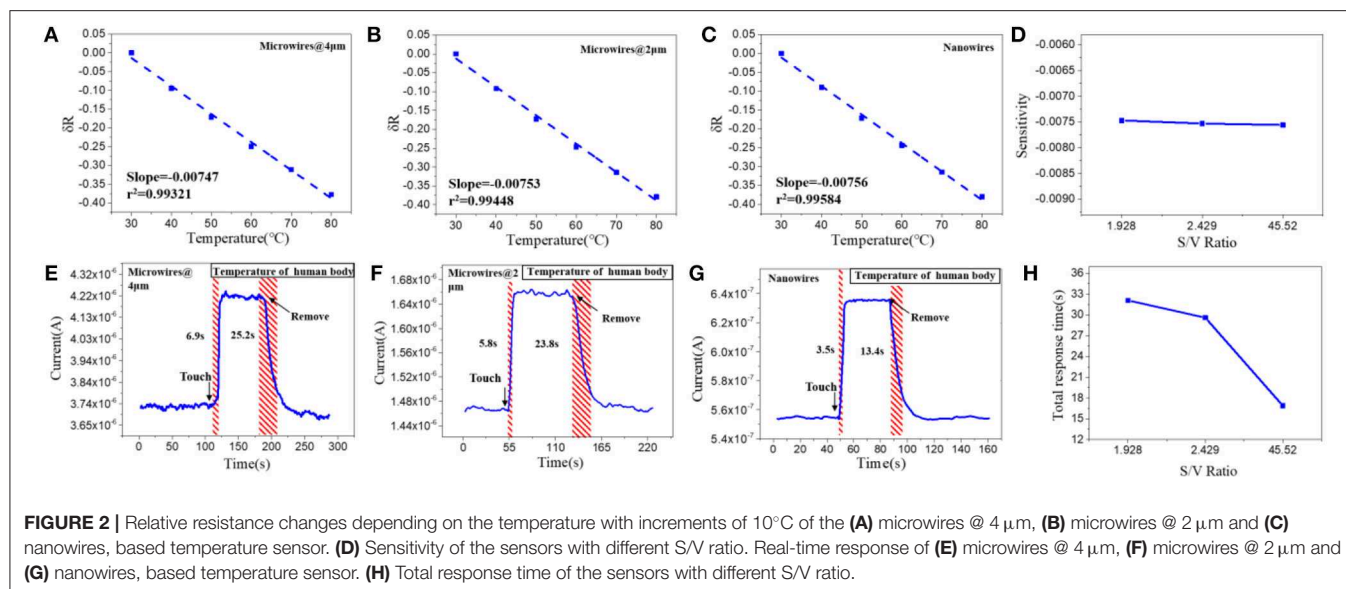
Figure 1 shows the optical microscope, Scanning Electron Microscope (SEM), Atomic Force Microscope (AFM) and Confocal Laser Scanning Microscope (CLSM) images of the micro/nanowires with different sizes, respectively. These results show that the microwires have the same height ($\sim 0.7 \mu\text{m}$) but with different width (4 μm , 2 μm). The nanowires have an average width of 70 nm and an average height of 59 nm. Thus, the S/V ratio of microwires @ 4 μm , microwires @ 2 μm and nanowires can be calculated as follow: 1.928, 2.429, and 45.52. As can be seen in the AFM images, the height of the microwires sides are higher than the middle part, which is due to the microchannels are treated with O_2 plasma hence are more hydrophilic, thus the aqueous solution tends to stick to the wall before evaporates, which resulting in this phenomenon.

Temperature Sensing

To study the structure effects on their temperature sensing behavior, we compared the response value and response speed of the three PEDOT: PSS based resistor-type temperature sensors with different S/V ratio. Their resistance were measured under a temperature range from 30 to 80°C with an interval of 10°C (**Figures 2A–C**). The response value is defined as:

$$\delta R = ((R - R_0)/R_0)$$

where R_0 and R are the resistance values at 30°C and the set temperature. And TCR is defined as $\text{TCR} = ((R - R_0)/R_0)/\Delta T = \delta R/\Delta T$. The results show that the resistance of the three devices decrease linearly as the temperature rises and their sensitivity (slope of the liner fitting) are rather similar (**Figure 2D**). The δR of PEDOT: PSS microwires @ 4 μm , microwires @ 2 μm and nanowires-based temperature sensor between 30 and 80°C (303 and 353 K) are -0.377 , -0.378 , and -0.379 , so the TCR of them can be calculated as -0.007545 , -0.007579 , and -0.007599 K^{-1} . We then tested their response speed to temperature change by attaching or removing these devices to human arm which has a constant temperature. As shown in **Figures 2E–G**, the currents show increase or decrease after touching or removing the devices from the human skin. Compare with their thermal sensitivity, very differently, the devices with different S/V ratio show quite different temperature response speed (defined as the



time required to reach 90% of the zenith response). The response and recovery time of the microwires @ 4 μm, microwires @ 2 μm and nanowires-based temperature sensor were 6.9 and 25.2 s, 5.8 and 23.8 s, 3.5 and 13.4 s, respectively. As compared in **Figure 2H**, a clear trend can be observed that the response speed increases with the increase of the S/V ratio, especially the nanowires with a maximum S/V ratio shows an ultra-fast response speed. This behavior can be explained by the electron transportation and thermal sensing mechanism of PEDOT: PSS which is very related to its microstructure. As shown in **Scheme 1C**, PEDOT: PSS has a typical core-shell structure in which the core is PEDOT nanocrystal and surrounded by PSS-rich shell. The insulating PSS boundaries with a strong hygroscopic ability have a major effect to the overall conductance of the PEDOT: PSS (Takano et al., 2012; Zhou et al., 2014). When temperature rising, the water molecules absorbed in the PSS boundaries will be partially released, which leads to the shrinkage of PSS boundaries and results in a decrease of the distance between adjacent PEDOT (**Scheme 1C**). This will facilitate the electron transportation between the PEDOT domains and results the decrease of the resistance of PEDOT: PSS (Zhou et al., 2014; Vuorinen et al., 2016). The response of PEDOT: PSS film are shown in **Figure S1** in Supplementary Information. By confining the PEDOT: PSS from 2D thin film to 1D nanowire (increase of its S/V ratio), PSS boundaries can be fully exposed to the external environment, thus increase its thermal conduction and facilitates the water evaporation, which will increase its response speed to temperature change. Besides, the electron transport efficiency within the 1D nanowire is improved as well. Other nanomaterials-based resistive temperature sensors also have showed such advantages of nanomaterials in temperature detecting (Joh et al., 2018; Sehwat et al., 2018; Bang et al., 2019; Cui et al., 2019). However, reducing the materials dimension will not influence the deformation ratio of the PSS boundaries, which is related to the amount of the water absorbed, thus the

change of S/V ratio will not influence the thermal sensitivity of PEDOT: PSS.

Doping Effect

As discussed above, nanoscale confinement strategy can enhance the response speed of the PEDOT: PSS to temperature and PEDOT: PSS nanowires with the highest S/V ratio show the fastest response to temperature change which is rather important to develop as temperature sensor. Next, we focus on improving its thermal sensitivity. As reported before, doping of PEDOT: PSS with other temperature-sensitive materials such as graphene (Trung et al., 2014, 2016, 2018) can further increase its response to temperature (Honda et al., 2014; Oh et al., 2018). Here, we applied the graphene doping strategy to further adjust the temperature sensitivity of PEDOT: PSS nanowires. Since the mixtures are required to be dispersed in aqueous solution for capillary filling, the oxidation form of graphene (GO) was used, which contains many oxygen-containing functional groups, such as hydroxyl, epoxide and carboxyl groups and ensures its good solubility in aqueous solution (Wang et al., 2009; Chen and Li, 2012; Lee et al., 2012; Dwandaru et al., 2019). The doped mixtures were characterized by FT-IR (**Figure S2** in Supporting Information), the mixtures have the same characteristics as PEDOT: PSS and contain the specific bands of GO, which proves that the two materials have been fully mixed and the chemical structures of PEDOT: PSS and GO are well-maintained. We then optimized the GO doping ratio to understand its thermal sensing effect. I-V curves of the nanowires constructed by mixtures with different mixing ratios (PEDOT: PSS/GO, V/V) were measured under temperature range from 30 to 80°C with an interval of 10°C. As shown in **Figure 3A**, the GO doping has a conspicuous influence on the thermal sensitivity of the PEDOT: PSS. The nanowire device with mixing ratio of 13:1 shows the highest temperature response. This can be explained by the fact that GO is a kind of relatively hydrophilic material, thus GO should be

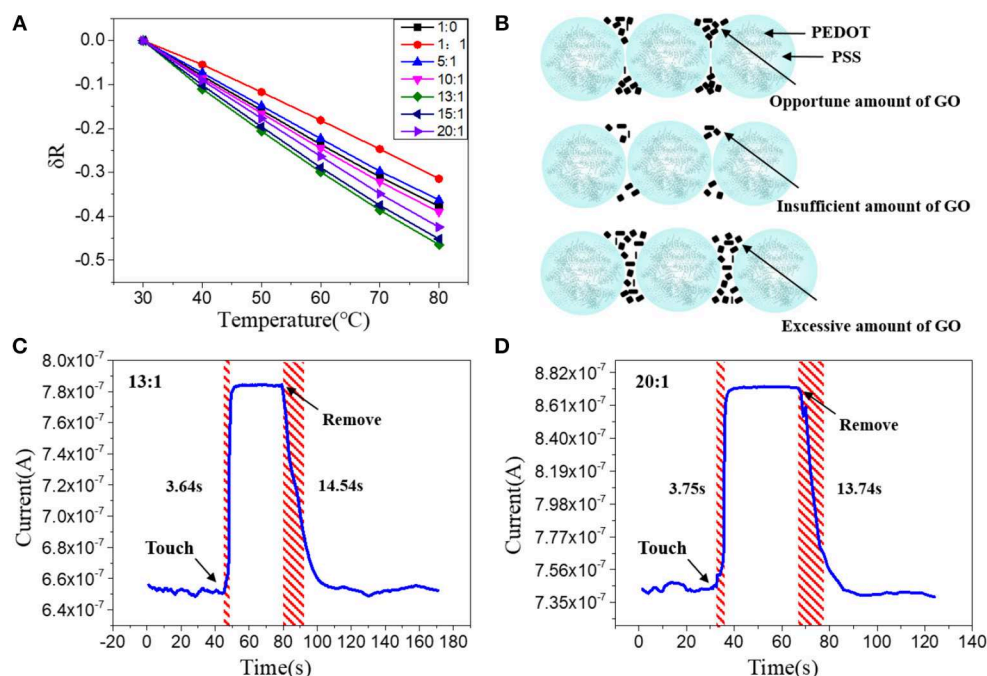


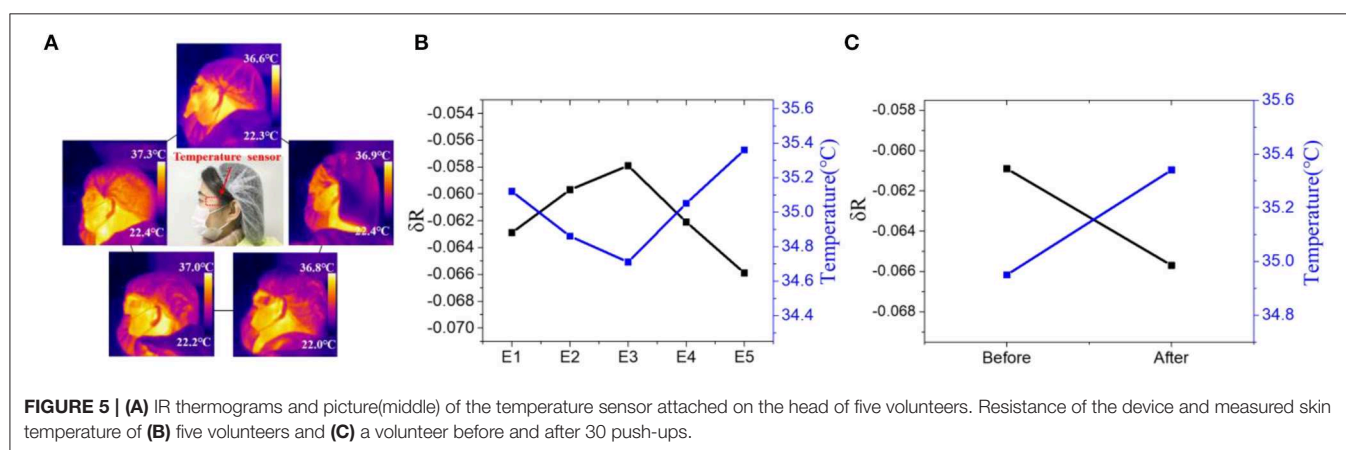
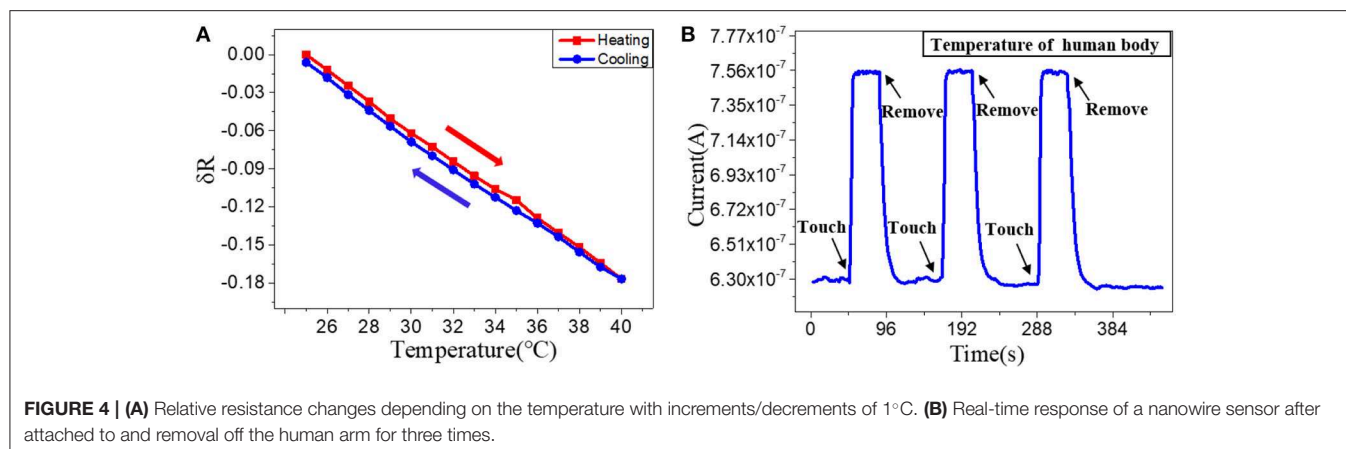
FIGURE 3 | (A) Relative resistance changes of the sensors with different mixing ratios at different temperatures. **(B)** Schematic diagram of PEDOT: PSS nanowires doped with opportune, insufficient and excessive amount of GO; Real-time response of the nanowire sensors with a mixing ratio of **(C)** 13:1 and **(D)** 20:1, after attached to and removal off the human arm.

mostly adsorbed on the hydrophilic PSS when it is mixed with PEDOT: PSS. Hence a little bit of GO will not affect the overall conductivity of PEDOT: PSS due to PSS does not participate in conductivity of PEDOT: PSS. However, GO has excellent thermal conductivity (Teng et al., 2011; Yao et al., 2016), hence doping GO can affect the thermal sensitivity of PEDOT: PSS. When the mixing ratio is 13:1 (The upper schematic of Figure 3B), the GO flakes are fully filled in the PSS and the gap between the adjacent PEDOT: PSS nanoparticles. Such composite materials show higher temperature sensitivity compared to the less, more or no GO filling. If the mixing ratio is higher than 13:1, such as 15:1, which means the amount of GO flakes is less than that of 13:1, hence the GO flakes are not adequately filled in the PSS and the gap between adjacent PEDOT: PSS nanoparticles (The middle schematic of Figure 3B), leading to the temperature sensitivity of this ratio lower than that of 13:1 but higher than non-doped pure PEDOT: PSS. If the mixing ratio is lower than 13:1, such as 10:1, under such mixing ratio, the amount of GO is larger than that of 13:1, hence the connection between adjacent PEDOT: PSS nanoparticles will be affected (The bottom schematic of Figure 3B), leading to the response of this ratio lower than that of 13:1. Furthermore, when the ratio is further reduced, such as 1:1, which means the proportion of GO is far more than that of 13:1, hence the connection between the PEDOT: PSS nanoparticles will be affected severely, leading to the response of this ratio is even lower than that of non-doped pure PEDOT: PSS. We also explored whether the GO doping would affect the response speed of PEDOT: PSS nanowires. As shown in Figures 3C,D,

compared with the pure PEDOT: PSS nanowires (Figure 2E), the response time and recovery time of these GO doped nanowires have no obvious difference. It proves that the GO doping did not affect the response speed of PEDOT: PSS nanowires but only enhance the thermal sensitivity. Thus, by combining the nanoconfinement and GO doping strategy, the response speed and thermal sensitivity can be simultaneously optimized. The 13:1 GO doped nanowires are used to prepare the temperature sensor for rest of the applications.

Repeatability and Stability

After optimization the structure and the materials, we then fabricated the optimized Go doped PEDOT: PSS nanowires on a flexible PET substrate to facilitate their epidermal sensing applications. The repeatability and stability of the nanoscale flexible sensors were tested, especially for their hysteretic behavior (Han et al., 2018). Figure 4A shows the hysteresis of the nanowires response to temperature with a heating and cooling cycle, which indicates a very minor hysteresis (~ 0.0046). Next, we evaluated the repeatability of the nanowires-based sensor by applying the sensor for multiple tests of touch to and removal from the skin (Figure 4B). The stable performance demonstrates that the devices have good repeatability and stability. The sensors were then kept under ambient air for 1 months and their response to temperature change were measured again. The results in Figure S3 in the Supporting Information show that their temperature response after 1 months is slightly changed



in comparison with the as-fabricated sensors, which prove the long-term stability of the PEDOT: PSS nanowires in ambient air.

Skin Temperature Detection

We then tested the nanowires-based temperature sensor for skin temperature detection. Five volunteers were chosen to use the sensors for monitoring their local skin temperature by attaching these devices on their heads (**Figure 5A**). The good mechanical property and ultra-thin size of the flexible sensor facilitate its attachment to human skin and hence ensure the reliable temperature measurement. According to the results of the previous fitting, the corresponding skin temperature of five volunteers can be calculated. As shown in **Figure 5B**, the skin temperature of the five volunteers is 35.12°C, 34.86°C, 34.71°C, 35.05°C, 35.36°C, respectively. The results are consistent with the results obtained by thermocouple which proves the accuracy of the device (35.1°C, 34.7°C, 34.7°C, 35.0°C, 35.2°C). Since the skin temperature will change during strenuous or long-term exercise, we apply the temperature sensor to track the volunteer exercise status. The sensor was attached to the head of a volunteer to monitor the subtle temperature changes during exercise. The normal skin temperature of the volunteer's temple was measured to be approximately 34.93°C. It increased to approximately

35.37°C after doing 30 push-ups (see **Figure 5C**). These results demonstrate that the nanowire-based temperature sensors can be effectively applied for rapidly and accurately tracking of human skin temperature.

Mobile Healthcare Based on Nanoscale Fees

Many diseases and physiological behaviors will cause local changes in body epidermal temperature, hence real-time and continuous measurement of the local skin temperature could enable a better tracking of personal health status (Deng and Liu, 2004; Helmy and Rizkalla, 2008; Ng, 2009; Li et al., 2017). Based on the nanoscale flexible temperature sensor, a wearable FEES was further developed by integrating the nanowires with commercial electronic components to enable the wireless communication. An Android application program was further developed and installed on a smartphone to directly receive and process the sensing signals in real-time. As shown in **Figure S4**, the FEES can be worn on the wrist for continuously monitoring the skin temperature. **Figure 6A** shows the screenshot of the smartphone interacting with the FEES system by touching or removing the system from the skin, which demonstrates their rapid response to

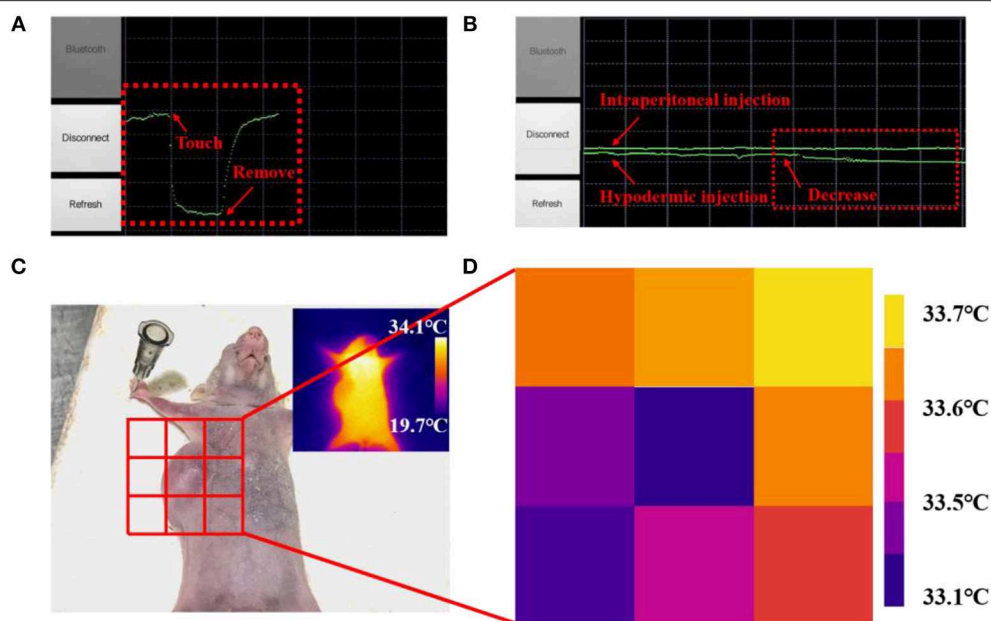


FIGURE 6 | A screenshot of the smartphone when the sensor was attached on (A) a human arm, (B) a mouse after intraperitoneal injection of adrenaline and a mouse after hypodermic injection of adrenaline. (C) Picture of the mouse with a subcutaneous tumor. (D) Skin temperature distribution of subcutaneous tumor and eight points near it measured by the nanowires-based EES.

human skin temperature. The system was further applied to compare the administration route of drugs by monitoring the subtle skin temperature changes after intraperitoneal and hypodermic injection of adrenaline to a mouse (**Figure 6B**). It clearly shows that after intraperitoneal injection of adrenaline, the resistance of the device did not change significantly, indicating that body temperature of the mouse was constant. While after hypodermic injection, the resistance of the sensor was slowly and continuously decreased, indicating that body temperature of the mouse was slowly increasing, which are consistent with the existing studies (Maling et al., 1979). These results demonstrate the feasibility of the FEES system in real temperature monitoring applications.

Subcutaneous tumors, as a kind of common tumor, will change the metabolic activity of the lesion area and in turn change the normal temperature distribution on the skin surface (Sudharsan et al., 1999). Benefited by the fast response and high thermal sensitivity, the EES could provide a neat tool to monitoring skin temperature outside the subcutaneous tumors in a new way. **Figure 6D** shows the skin temperature distribution around the tumor area detected by attaching the FEES on different place of the skin (**Figure 6C**). The results indicate that the temperature in the tumor area is significantly lower than the surrounding area, which is consistent with the results of existing studies (Konerding and Steinberg, 1988). Meanwhile, the results detected by the FEES are more accurate than IR thermograms (inset in **Figure 6C**), and this method provides the possibility of real-time monitoring. It also shows that the sensor has great potential to be made into temperature sensor

arrays, which can detect spatial mapping of skin temperature so that the arrays could provide a feasible method to judge the diffusion area and monitor the deterioration status of the subcutaneous tumors efficiently and conveniently. All these results demonstrate that this EES has great potential as a wearable bioelectronic for mobile medical diagnosis and healthcare applications.

CONCLUSION

In this work, we developed a strategy by combining the micro/nano confinement with materials doping to enable simultaneous optimization of the response speed and sensitivity of low dimension conductive polymers. By confining the PEDOT:PSS into nanowires and doping with GO at optimized doping ratio, ultra-fast response to temperature change (<3.5 s) and maximized thermal-sensitivity is achieved. Well-defined sub-100 nm nanowires were fabricated on flexible substrates using a low-cost nanoscale printing approach which were further integrated as a functional skin-attachable flexible epidermal electronic system (FEES) to enable a live and wireless temperature sensing. The developed FEES were applied for different physiological behaviors and diseases monitoring by recording the real-time skin temperature changes.

DATA AVAILABILITY STATEMENT

All datasets generated for this study are included in the article/**Supplementary Material**.

ETHICS STATEMENT

The animal study was reviewed and approved by the ethics committee of the Institute of Radiation Medicine Chinese Academy of Medical Sciences.

AUTHOR CONTRIBUTIONS

CZ developed the ideas of the study, carried out most of the experiments, and also wrote most parts of the manuscript. NT and XZ also developed some ideas of the study and participated in some experiments, and also reviewed the manuscript. YF, YJ, and HZ participated in some experiments of the study and reviewed the manuscript. XD developed some ideas and improved the ideas other authors developed and also wrote parts of the manuscript. All authors read and approved the final manuscript.

REFERENCES

- Bang, J., Lee, W. S., Park, B., Joh, H., Woo, H. K., Jeon, S., et al. (2019). Highly sensitive temperature sensor: ligand-treated ag nanocrystal thin films on PDMS with thermal expansion strategy. *Adv. Functional Mater.* 29:1903047. doi: 10.1002/adfm.201903047
- Celeste, C. J., Deschesne, K., Riley, C. B., and Theoret, C. L. (2013). Skin temperature during cutaneous wound healing an equine model of cutaneous fibroproliferative disorder: kinetics and anatomic-site differences. *Vet. Surg.* 42, 147–153. doi: 10.1111/j.1532-950X.2012.00966.x
- Chang, Y., Zuo, J., Zhang, H., and Duan, X. (2019). State-of-the-art and recent developments in micro/nanoscale pressure sensors for smart wearable devices and health monitoring systems. *Nanotechnol. Eng.* 3, 43–52. doi: 10.1016/j.npe.2019.12.006
- Chen, F., and Li, J. H. (2012). Graphene oxide: preparation, functionalization, and electrochemical applications. *Chem. Rev.* 112, 6027–6053. doi: 10.1021/cr300115g
- Cui, Z., Poblete, F. R., and Zhu, Y. (2019). Tailoring the temperature coefficient of resistance of silver nanowire nanocomposites and their application as stretchable temperature sensors. *ACS Appl. Mater. Interface* 11, 17836–17842. doi: 10.1021/acsami.9b04045
- Culebras, M., López, A. M., Gómez, C. M., and Cantarero, A. (2016). Thermal sensor based on a polymer nanofilm. *Sens. Actuators A Phys.* 239, 161–165. doi: 10.1016/j.sna.2016.01.010
- Deng, Z. S., and Liu, J. (2004). Mathematical modeling of temperature mapping over skin surface and its implementation in thermal disease diagnostics. *Comput. Biol. Med.* 34, 495–521. doi: 10.1016/S0010-4825(03)00086-6
- Duan, X., Zhao, Y., Berenschot, E., Tas, N. R., Reinhoudt, D. N., and Huskens, J. (2010). Large-area nanoscale patterning of functional materials by nanomolding in capillaries. *Adv. Funct. Mater.* 20, 2519–2526. doi: 10.1002/adfm.201000492
- Dwandar, W. S. B., Parwati, L. D., and Wisnuwijaya, R. I. (2019). Formation of graphene oxide from carbon rods of zinc-carbon battery wastes by audiosonic sonication assisted by commercial detergent. *Nanotechnol. Eng.* 2, 89–94. doi: 10.1016/j.npe.2019.03.001
- Gao, L., Zhang, Y. H., Malyarchuk, V., Jia, L., Jang, K. I., Webb, R. C., et al. (2014). Epidermal photonic devices for quantitative imaging of temperature and thermal transport characteristics of the skin. *Nat. Commun.* 5:4938. doi: 10.1038/ncomms5938
- Gates, B. D., Xu, Q., Stewart, M., Ryan, D., Willson, C. G., and Whitesides, G. M. (2005). New approaches to nanofabrication: molding, printing, and other techniques. *Chem. Rev.* 105, 1171–1196. doi: 10.1021/cr030076o
- Han, S., Liu, Q., Han, X., Dai, W., and Yang, J. (2018). An E-type temperature sensor for upper air meteorology. *Nanotechnol. Eng.* 1, 145–149. doi: 10.13494/j.npe.20170016

FUNDING

This work was supported by National Natural Science Foundation of China (NSFC Nos. 61674114, 91743110, 21861132001), National Key R&D Program of China (2017YFF0204604, 2018YFE0118700), Tianjin Applied Basic Research and Advanced Technology (17JCJC43600), the Foundation for Talent Scientists of Nanchang Institute for Microtechnology of Tianjin University, and the 111 Project (B07014).

SUPPLEMENTARY MATERIAL

The Supplementary Material for this article can be found online at: <https://www.frontiersin.org/articles/10.3389/fchem.2020.00194/full#supplementary-material>

- Helmy, H., and Rizkalla, M. (2008). Application of thermography for non-invasive diagnosis of thyroid gland disease. *IEEE Trans. Biomed. Eng.* 55, 1168–1175. doi: 10.1109/TBME.2008.915731
- Honda, W., Harada, S., Arie, T., Akita, S., and Takei, K. (2014). Printed wearable temperature sensor for health monitoring. *IEEE Sens. Proc.* 2014, 2227–2229. doi: 10.1109/ICSENS.2014.6985483
- Joh, H., Lee, W. S., Kang, M. S., Seong, M., Kim, H., Bang, J., et al. (2018). Surface design of nanocrystals for high-performance multifunctional sensors in wearable and attachable electronics. *Chem. Mater.* 31, 436–444. doi: 10.1021/acs.chemmater.8b03914
- Konerding, M. A., and Steinberg, F. (1988). Computerized infrared thermography and ultrastructural studies of xenotransplanted human tumors on nude mice. *Thermology* 3, 7–14.
- Lee, K. D., You, J. M., Kim, S. K., and Yun, M., Jeon, S. (2012). Electrocatalytic oxidation of hydrazine and hydroxylamine by graphene oxide-Pd nanoparticle-modified glassy carbon electrode. *J. Nanosci. Nanotechnol.* 12, 8886–8892. doi: 10.1166/jnn.2012.6792
- Li, Q. L., Zhang, N. X., Tao, M., and Ding, X. (2017). Review of flexible temperature sensing networks for wearable physiological monitoring. *Adv. Healthcare Mater.* 6, 1–23. doi: 10.1002/adhm.201601371
- Lipomi, D. J., Lee, J. A., Vosgueritchian, M., Tee, B. C. K., Bolander, J. A., and Bao, Z. (2012). Electronic properties of transparent conductive films of PEDOT:PSS on stretchable substrates. *Chem. Mater.* 24, 373–382. doi: 10.1021/cm203216m
- Maling, H. M., Williams, M. A., and Koppányi, T. (1979). Salivation in mice as an index of adrenergic activity. Salivation, I., and temperature responses to d-amphetamine and other sialogogues and the effects of adrenergic blocking agents. *Arch. Int. Pharmacodyn. Ther.* 199, 318–332.
- Massi, M., Albonetti, C., Facchini, M., Cavallini, M., and Biscarini, F. (2006). Toward amorphous conductors: enhanced conductivity of doped polyaniline via interchain crosslinking promoted by acid-functionalized aluminum quinolines. *Adv. Mater.* 18, 2739–2742. doi: 10.1002/adma.200600465
- Ng, E. Y. K. (2009). A review of thermography as promising non-invasive detection modality for breast tumor. *Int. J. Therm. Sci.* 48, 849–859. doi: 10.1016/j.ijthermalsci.2008.06.015
- Oh, J. H., Hong, S. Y., Park, H., Jin, S. W., Jeong, Y. R., Oh, S. Y., et al. (2018). Fabrication of high-sensitivity skin-attachable temperature sensors with bioinspired microstructured adhesive. *ACS Appl. Mater. Interfaces* 10, 7263–7270. doi: 10.1021/acsami.7b17727
- Sehrawat, P., Islam, S. S., and Mishra, P. (2018). Reduced graphene oxide based temperature sensor: extraordinary performance governed by lattice dynamics assisted carrier transport. *Sens. Actuators B Chem.* 258, 424–435. doi: 10.1016/j.snb.2017.11.112
- Sudharsan, N. M., Ng, E. Y. K., and Teh, S. L. (1999). Surface temperature distribution of a breast with and without tumour. *Comput. Methods Biomech. Biomed. Eng.* 2, 187–199. doi: 10.1080/10255849908907987

- Takano, T., Masunaga, H., Fujiwara, A., Okuzaki, H., and Sasaki, T. (2012). PEDOT nanocrystal in highly conductive PEDOT: PSS polymer films. *Macromolecules* 45, 3859–3865. doi: 10.1021/ma300120g
- Takei, K., Honda, W., Harada, S., Arie, T., and Akita, S. (2015). Toward flexible and wearable human-interactive health-monitoring devices. *Adv. Healthcare Mater.* 4, 487–500. doi: 10.1002/adhm.201400546
- Tang, N., Zhou, C., Xu, L., Jiang, Y., Qu, H., and Duan, X. (2019). A fully integrated wireless flexible ammonia sensor fabricated by soft nano-lithography. *ACS Sens.* 4, 726–732. doi: 10.1021/acssensors.8b01690
- Teng, C. C., Ma, C. M., Lu, C. H., Yang, S. Y., Lee, S. H., Hsiao, M. C., et al. (2011). Thermal conductivity and structure of non-covalent functionalized graphene/epoxy composites. *Carbon* 49, 5107–5116. doi: 10.1016/j.carbon.2011.06.095
- Trung, T. Q., Le, H. S., Dang, T. M. L., Ju, S., Park, S. Y., and Lee, N. E. (2018). Freestanding, fiber-based, wearable temperature sensor with tunable thermal index for healthcare monitoring. *Adv. Healthc. Mater.* 7, 1–9. doi: 10.1002/adhm.201800074
- Trung, T. Q., Ramasundaram, S., Hong, S. W., and Lee, N. E. (2014). Flexible and transparent nanocomposite of reduced graphene oxide and P(VDF-TrFE) copolymer for high thermal responsivity in a field-effect transistor. *Adv. Funct. Mater.* 24, 3438–3445. doi: 10.1002/adfm.201304224
- Trung, T. Q., Ramasundaram, S., Hwang, B. U., and Lee, N. E. (2016). An all-elastomeric transparent and stretchable temperature sensor for body-attachable wearable electronics. *Adv. Mater.* 28, 502–509. doi: 10.1002/adma.201504441
- Vuorinen, T., Niittynen, J., Kankkunen, T., Kraft, T. M., and Mäntysalo, M. (2016). Inkjet-printed graphene/PEDOT: PSS temperature sensors on a skin-conformable polyurethane substrate. *Sci. Rep.* 6, 1–8. doi: 10.1038/srep35289
- Wang, Y., Li, Y., Tang, L., Lu, J., and Li, J. (2009). Application of graphene-modified electrode for selective detection of dopamine. *Electrochem. Commun.* 11, 889–892. doi: 10.1016/j.elecom.2009.02.013
- Webb, R. C., Bonifas, A. P., Behnaz, A., Zhang, Y., Yu, K. J., Cheng, H., et al. (2013). Ultrathin conformal devices for precise and continuous thermal characterization of human skin. *Nat. Mater.* 12, 938–944. doi: 10.1038/nmat3755
- Wu, W., and Haick, H. (2018). Materials and wearable devices for autonomous monitoring of physiological markers. *Adv. Mater.* 30:1705024. doi: 10.1002/adma.201705024
- Yao, Y., Zeng, X., Wang, F., Sun, R., Xu, J. B., and Wong, C. P. (2016). Significant enhancement of thermal conductivity in bioinspired freestanding boron nitride papers filled with graphene oxide. *Chem. Mater.* 28, 1049–1057. doi: 10.1021/acs.chemmater.5b04187
- Zhang, Y. H., Webb, R. C., Luo, H. Y., Xue, Y. G., Kurniawan, J., Cho, N. H., et al. (2016). Theoretical and experimental studies of epidermal heat flux sensors for measurements of core body temperature. *Adv. Healthcare Mater.* 5, 119–127. doi: 10.1002/adhm.201500110
- Zhou, J., Anjum, D. H., Chen, L., Xu, X., Ventura, I. A., Jiang, L., et al. (2014). The temperature-dependent microstructure of PEDOT/PSS films: insights from morphological, mechanical and electrical analyses. *J. Mater. Chem. C* 2, 9903–9910. doi: 10.1039/C4TC01593B

Conflict of Interest: The authors declare that the research was conducted in the absence of any commercial or financial relationships that could be construed as a potential conflict of interest.

Copyright © 2020 Zhou, Tang, Zhang, Fang, Jiang, Zhang and Duan. This is an open-access article distributed under the terms of the Creative Commons Attribution License (CC BY). The use, distribution or reproduction in other forums is permitted, provided the original author(s) and the copyright owner(s) are credited and that the original publication in this journal is cited, in accordance with accepted academic practice. No use, distribution or reproduction is permitted which does not comply with these terms.



Application of WO₃ Hierarchical Structures for the Detection of Dissolved Gases in Transformer Oil: A Mini Review

Zhijie Wei¹, Lingna Xu^{1*}, Shudi Peng² and Qu Zhou^{1*}

¹ College of Engineering and Technology, Southwest University, Chongqing, China, ² Chongqing Electric Power Research Institute, State Grid Chongqing Electric Power Company, Chongqing, China

OPEN ACCESS

Edited by:

Mingshui Yao,
Kyoto University, Japan

Reviewed by:

Yanqiong Li,
Chongqing University of Arts and
Sciences, China
Ruixian Luo,
Beijing University of Chemical
Technology, China

*Correspondence:

Lingna Xu
lingnaxu@swu.edu.cn
Qu Zhou
zhouqu@swu.edu.cn

Specialty section:

This article was submitted to
Nanoscience,
a section of the journal
Frontiers in Chemistry

Received: 11 January 2020

Accepted: 28 February 2020

Published: 07 April 2020

Citation:

Wei Z, Xu L, Peng S and Zhou Q
(2020) Application of WO₃ Hierarchical
Structures for the Detection of
Dissolved Gases in Transformer Oil: A
Mini Review. *Front. Chem.* 8:188.
doi: 10.3389/fchem.2020.00188

Oil-immersed power transformers are considered to be one of the most crucial and expensive devices used in power systems. Hence, high-performance gas sensors have been extensively explored and are widely used for detecting fault characteristic gases dissolved in transformer oil which can be used to evaluate the working state of transformers and thus ensure the reliable operation of power grids. Hitherto, as a typical n-type metal-oxide semiconductor, tungsten trioxide (WO₃) has received considerable attention due to its unique structure. Also, the requirements for high quality gas detectors were given. Based on this, considerable efforts have been made to design and fabricate more prominent WO₃ based sensors with higher responses and more outstanding properties. Lots of research has focused on the synthesis of WO₃ nanomaterials with different effective and controllable strategies. Meanwhile, the various morphologies of currently synthesized nanostructures from 0-D to 3-D are discussed, along with their respective beneficial characteristics. Additionally, this paper focused on the gas sensing properties and mechanisms of the WO₃ based sensors, especially for the detection of fault characteristic gases. In all, the detailed analysis has contributed some beneficial guidance to the exploration on the surface morphology and special hierarchical structure of WO₃ for highly sensitive detection of fault characteristic gases in oil-immersed transformers.

Keywords: WO₃, gas sensors, hierarchical structure, oil-immersed transformer, fault characteristic gas, mechanism

INTRODUCTION

The safe and reliable operation of transformers is of vital importance for a stable and continuous power supply to the power grid (Lu et al., 2018; Zhang D. Z. et al., 2018; Zhang Q. Y. et al., 2018; Cui et al., 2019; Yang et al., 2019a,b). To date, the number of oil-immersed transformers accounts for more than 90% of the total number of power transformers, and the operating state of these power transformers will directly affect the condition of power systems (Zhou et al., 2016; Zhang X. X. et al., 2019). For a long-running transformer, partial overheating and partial discharge will lead to the decomposition of transformer oil into a variety of fault gases, namely hydrogen (H₂), carbon monoxide (CO), carbon dioxide (CO₂), methane (CH₄), acetylene (C₂H₂), ethylene (C₂H₄), and ethane (C₂H₆) (Jin et al., 2017; Gao et al., 2019; Park et al., 2019; Wang J. X. et al., 2019). Hence, the detection of these fault

characteristic gases has been extensively applied to diagnose early latent faults and evaluate the operation quality of oil-immersed transformers (Zhang et al., 2018a; Cui et al., 2019; Gui et al., 2019). In this respect, metal oxide semiconductor (MOS) gas sensors have attracted considerable attention due to their high-performance capability and wide range of applications for the detection of these fault characteristic gases in transformer oil (Zhou et al., 2013; Zhang Y. Z. et al., 2019).

Given this, various metal oxides have been investigated via different synthesis routes (Ge et al., 2017; Zhou et al., 2018a,b; Wei et al., 2019a). Of all the oxides, as a typical n-type metal-oxide semiconductor, WO₃ has attracted a large amount interest due to its excellent physicochemical properties (Miao et al., 2015; Xu et al., 2019). To improve the performance of the gas sensors, sustainable efforts have been made to synthesize various nanostructures such as nanoparticles, nanorods, nanosheets, and nanoflowers (Wei et al., 2019b). Additionally, previous researchers have confirmed that these unique structures are closely related to its gas sensing properties (Yu et al., 2016). Therefore, the morphology controllable synthesis of different hierarchical WO₃ nanostructures and the enhanced gas sensing performances thereof are of great importance to explore and discuss. In this review, we focus on the morphology controllable synthesis of hierarchical WO₃ nanostructures including 0-dimensional (0-D), 1-dimensional (1-D), 2-dimensional (2-D), and 3-dimensional (3-D). In addition, the enhanced gas sensing performance and related mechanisms, especially the detection of the dissolved gases in transformer oil, have been introduced.

SYNTHESIS, SENSOR FABRICATION AND MEASUREMENT

Synthesis of WO₃ Materials With Different Strategies

Up to now, various effective strategies have been proposed for preparing special surface morphologies and then fabricating WO₃ based sensors with an enhanced gas sensing performance. Among these synthesis routes the template route, hydrothermal process, electrospinning method, and chemical deposition have all been widely used. Wang M. D. et al. (2019) synthesized three-dimensionally porous WO₃ materials with different pore sizes via the template route, and they proposed a relationship between the pore size and the enhanced gas sensing performance. Gibot et al. (2011) reported the template synthesis of a highly specific surface area WO₃ nanoparticle and discussed the surface properties, morphology and crystallographic structure in detail. Jin et al. (2019) developed different types of WO₃ nanoparticles through a facile hydrothermal process and proposed the morphology controllable route of changing the proportion of the reagents. Cao and Chen (2017) used a facile CTAB (Hexadecyl trimethyl ammonium bromide)-assisted hydrothermal method to synthesize an urchin-like WO₃ nanostructure, and a sensor based on this possessed an excellent gas sensing performance due to its special microstructure. Giancaterini et al. (2016) investigated the influence of thermal- and visible light-activation

on the response of WO₃ nanofibers via an electrospinning method. Jaroenapibal et al. (2018) presented the electrospinning synthesis of Ag-doped WO₃ nanofibers and demonstrated an enhanced gas sensing mechanism.

Sensor Fabrication and Measurement

To investigate the gas sensing performances of the different morphologies of WO₃ materials, the prepared samples are used to fabricate side-heated structures, the most common versions of which are known as planar and tubular configurations. As depicted in **Figure 1A**, both of the structures were composed of four parts: sensing materials, wires, electrodes, and substrate. The sensing materials in the sensor structure are prepared by dissolving the obtained WO₃ powders into a water-ethanol mixed solution. After forming a homogeneous slurry, the paste is coated onto an alumina ceramic substrate evenly to obtain a sensing film (Zhou et al., 2019a,b). The wires are used to connect the whole measuring circuit and the electrodes are used to measure the change in sensor resistance which directly reflects the performance of the fabricated sensor (Zhou et al., 2018a). The substrate is usually made of aluminum, which can provide reliable support for sensing materials (Zhou et al., 2018c,d).

The gas sensing properties of fabricated WO₃ based sensors are investigated using a static intelligent gas sensing analysis platform. **Figure 1B** presents an example gas sensor experimental process. In this set up the background gas and target gas are alternately introduced into the gas chamber to measure the characteristic dynamic response and response-recovery rate of the prepared device. The flow controller is used to adjust the flux and speed of gases in order to control their concentrations. The fabricated sensors are installed in the testing chamber and the gas sensitivity data will be directly transmitted to the central computer for processing (Wei et al., 2019c).

MORPHOLOGY CONTROL FROM 0-D TO 3-D

In general, the change in sensor resistance caused by the redox reaction between oxygen molecules and test gas molecules is used to explain the basic operating principle of gas sensors. The surface morphology and special hierarchical microstructures have a crucial effect on the performance of gas sensors. In this respect, various morphologies from 0-D to 3-D with unique physical and chemical properties have been successfully synthesized and extensively explored via different effective strategies (Guo et al., 2015; Yao et al., 2015). Additionally, the controllable synthesis routes of WO₃ nanostructures have been proposed to allow further investigation into how surface morphology affects gas sensing properties. As shown in **Figure 1C**, the four typical kinds of nanostructures, from 0-D to 3-D, can be controllably synthesized with different effective strategies. Given this, to further optimize the performance of WO₃ based sensors for practical application, the exploration of surface morphology and special hierarchical structure is still a challenging but meaningful work.

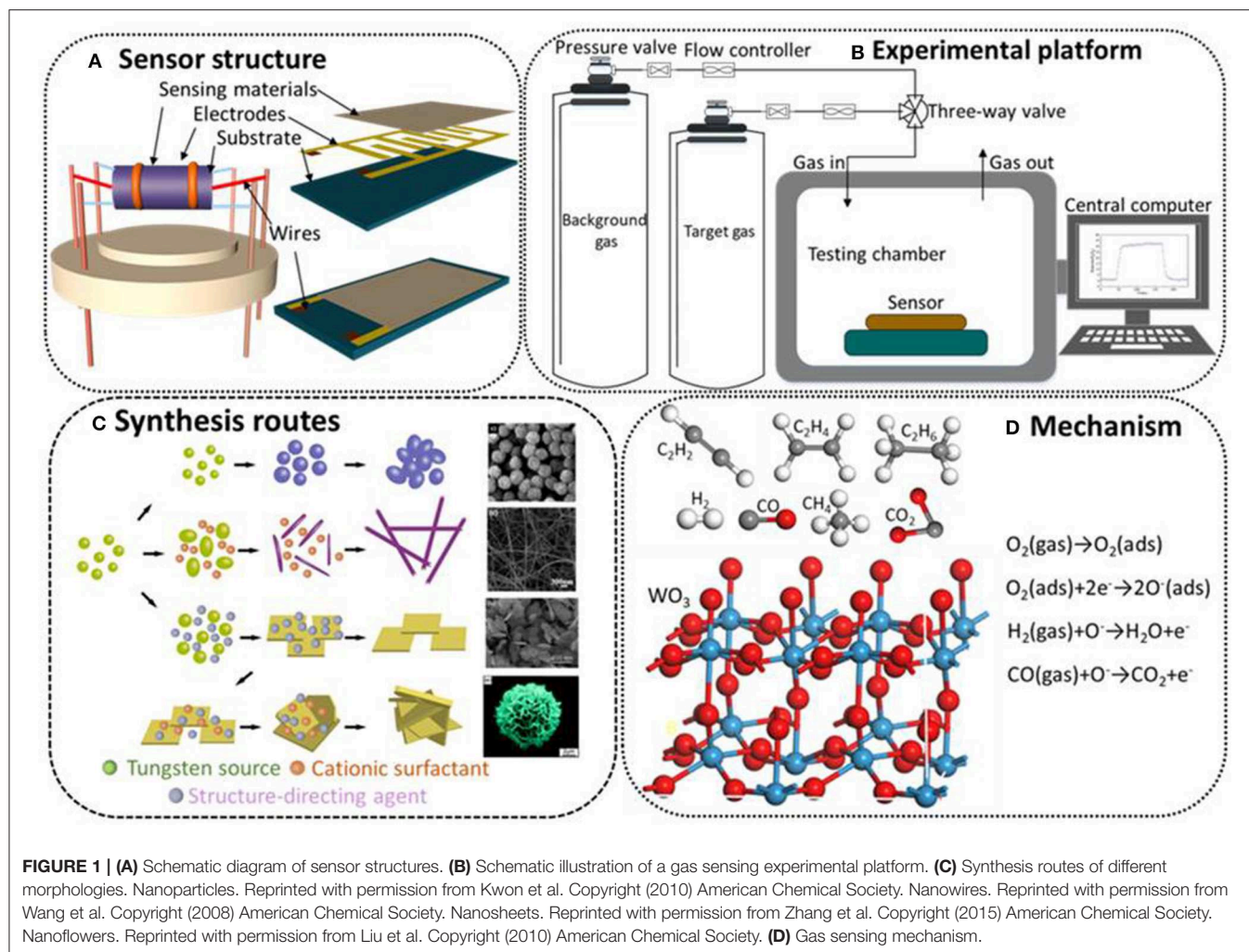


FIGURE 1 | (A) Schematic diagram of sensor structures. **(B)** Schematic illustration of a gas sensing experimental platform. **(C)** Synthesis routes of different morphologies. Nanoparticles. Reprinted with permission from Kwon et al. Copyright (2010) American Chemical Society. Nanowires. Reprinted with permission from Wang et al. Copyright (2008) American Chemical Society. Nanosheets. Reprinted with permission from Zhang et al. Copyright (2015) American Chemical Society. Nanoflowers. Reprinted with permission from Liu et al. Copyright (2010) American Chemical Society. **(D)** Gas sensing mechanism.

0-Dimensional (0-D) WO₃

As the lowest dimensional structure, 0-D WO₃ has been investigated less as it is limited by its low specific surface area and insufficient porous structure. These disadvantages limit the diffusion and adsorption of target gas molecules during the sensing process, leading to unsatisfactory performances. Additionally, during the preparation of 0-D WO₃ nanoparticles and the operation of the fabricated sensor, the coarsening and agglomeration of the nanoparticles might decrease the response of the device. However, various WO₃ nanoparticles have been rationally designed and synthesized. Based on the defects mentioned above, WO₃ nanoparticles with high dispersivity and ultra-small diameters might improve the performance of nanoparticle based sensors. In this respect, Li et al. (2019) synthesized highly dispersible WO₃ nanoparticles with sizes ranging from 10 to 50 nm and they found the fabricated sensor exhibited an excellent gas sensing performance due to the highly effective surface area and sufficient oxygen vacancies.

1-Dimensional (1-D) WO₃

1-D WO₃ structures, for instance, nanorods, nanofibers, nanotubes, and nanowires, are considered to be beneficial

nanostructures with improved special surface areas compared to. Also, the typical morphology has been applied to the detection the fault characteristic gases dissolved in transformer oil. Wisitsoorat et al. (2013) developed 1-D WO₃ nanorods via a magnetron sputtering method, an H₂ sensor based on which possessed prominent properties including a high response and fast response-recovery time. To further enhance the performance of 1-D WO₃, the doping of metal ions and the introduction of surfactants have been confirmed to be effective strategies to improve the redox reaction and the orientation of special structures. Atomic platinum (Pt) is considered to be an effective doping element which can optimize the sensing properties and this strategy can be explained by the spillover effect of oxygen species and the enhancement of adsorption and desorption (Park et al., 2012).

2-Dimensional (2-D) WO₃

Compared with low dimensional structures, 2-D structures possess a larger special surface area for the target gas molecules and therefore higher gas responses (Dral and ten Elshof, 2018). In comparison to the bulk 3-D structure, freestanding 2-D structures such as nanosheets, nanoplates, and thin

films can provide better optimization routes including the modulation of the materials activity, surface polarization and rich oxygen vacancies. Additionally, the hierarchical microstructure assembled by rigid 2-D nanosheets possesses an open and well-defined structure which can promote the diffusion of target gas molecules (Nasir and Pumera, 2019). Especially in the field of the detection of fault characteristic gases in oil-immersed transformers, 2-D WO₃ based sensors have been confirmed to be promising candidates with excellent gas sensing performances. Huang et al. (2020) synthesized Ru-loaded WO₃ nanosheets via a facile impregnation method and they believed that the higher activity of surface lattice oxygens in WO₃ nanosheets was activated by the introduction of Ru. Ou et al. (2012) fabricated H₂ sensors based on WO₃ nanoplates at different calcination temperatures and proved that the 2-D structure possesses a higher surface to volume ratio which clearly increased the number of surface interactive areas that could interact with H₂ molecules.

3-Dimensional (3-D) WO₃

Hierarchical 3-D structures are always assembled from diverse lower dimension fundamental blocks such nanoparticles, nanorods, and nanosheets. These various assembly routes make the hierarchical microstructures present different special morphologies, for instance, microspheres, microflowers, mesoporous structures, and other irregular structures. The well-defined structures always possess a larger special surface area and more unique microstructures, leading to better gas sensing performances including higher response times, more prominent selectivity, stability, and repeatability (Zhang et al., 2013). To detect fault characteristic gases, Zhang Y. X. et al. (2019) prepared a sea-urchin-like hexagonal WO₃ structure created by the capping effect of potassium sulfate (which can prompt the anisotropic growth of WO₃) and the H₂ sensing performance was confirmed to benefit from the special hierarchical 3-D microstructure. Wei et al. (2017) synthesized hollow cauliflower-like WO₃ by a facile hydrothermal process and found that the higher and faster response to CO might benefit from the hollow porous microstructure.

GAS SENSING PROPERTIES AND MECHANISM

To improve the performances of the detection of fault characteristic gases in oil-immersed transformers, WO₃ based sensors with different hierarchical structures have been confirmed to be promising candidates for on-line monitoring of oil-immersed power transformers due to their excellent gas sensing properties. In this section, we summarize the related works based on the recently published investigations (Table 1) and propose a plausible gas sensing mechanism.

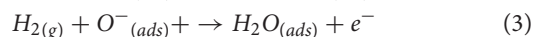
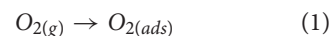
The gas sensing mechanism of the WO₃ based sensors can be demonstrated as the change in sensor resistance caused by the redox reaction between the oxygen species (mainly O²⁻) and test gas molecules on the surface of synthesized materials, as shown in Figure 1D. For typical n-type WO₃ based sensing materials,

TABLE 1 | Summary of recent researches on WO₃ based sensors for sensing of fault characteristic gases dissolved in transformer oil.

Gas	Sensing material	Concentration	Temp.	Response	Referenecees
H ₂	WO ₃ nanoparticles	200 ppm	200°C	20	Boudiba et al., 2013
	WO ₃ nanoparticles	0.5 vol%	R.T.	27.3	Xiao et al., 2018
	Pd-doped mesoporous WO ₃	5000 ppm	R.T.	11.78	Wu et al., 2019
	PdO-WO ₃ nanohybrids	40 ppm	100°C	23.5	Geng et al., 2017
	WO ₃ nanosheets	1%	250°C	80%	Rahmani et al., 2017
CO	Pt doped mesoporous WO ₃	100 ppm	125°C	10.1	Ma et al., 2018
	Cauliflower-like WO ₃	50 ppm	270°C	16.6	Wei et al., 2017
	Pt-modified WO ₃ films	20 ppm	150°C	114	Lei et al., 2016
	Pt-WO ₃ nanorods	30 ppm	300°C	4.82	Park et al., 2012
CH ₄	SnO ₂ -WO ₃ nanosheets	500 ppm	90°C	1.5	Xue et al., 2019a
	Rh-modified WO ₃ films	5 ppm	350°C	63.1	Tan and Lei, 2019
	Au-WO ₃ nanowire	100 ppm	250°C	37%	Vuong et al., 2015
	SnO ₂ -WO ₃ nanoplates	500 ppm	110°C	2.85	Xue et al., 2019b
C ₂ H ₂	Porous WO ₃ networks	200 ppm	300°C	58	Zhang et al., 2018b
	WO ₃ nanoflowers	50 ppm	275°C	20.95	Wei et al., 2019b
	rGO-WO ₃ nanocomposite	50 ppm	150°C	15	Jiang et al., 2018

R.T., room temperature.

the oxygen molecules in the testing environment will be reduced and adsorbed on the surface of the materials by capturing the electrons from the conduction band, and the target gas molecules will react with the oxygen ions and release the electrons back to the conduction band. The involved reactions can be described as follows (H₂ and CO gas are taken as examples):



CONCLUSION

In this mini review, we focus on the synthesis strategies, morphology control, sensing experimental procedures, and gas sensing performances of hierarchical WO₃ structures from 0-D to 3-D. The gas sensing properties of various high-performance WO₃ based sensors are summarized and discussed, especially in regards to the detection of fault characteristic gases dissolved in transformer oil. With an increasing requirement for high quality gas sensors with high responses, prominent selectivity, outstanding stability, and excellent repeatability, considerable

efforts have been made to propose more effective synthesis routes, more beneficial morphology control and more accurate experiment processes. It can be foreseen that more and more hierarchical WO₃ structures will be rationally designed and prepared due to their complicated microstructures with high special surface areas, broad internal contact area, and well-defined structures. These special hierarchical structures will provide more diffusion paths, reactive sites, and micro reaction spaces for target gas molecules adsorption, retention, and reaction. Although some achievements have been made by unremitting efforts, the further enhancement of the gas sensing properties of WO₃ based sensors for practical applications is still a challenging but meaningful work. We hope that our work can contribute some beneficial guidance to the exploration of the surface morphology and special hierarchical structures of WO₃. Additionally, much effort should be made to fabricate high-performance WO₃ based sensors with

predictably complicated hierarchical structures for detecting various gases, especially the fault characteristic gases dissolved in transformer oil.

AUTHOR CONTRIBUTIONS

All authors listed have made a substantial, direct and intellectual contribution to the work, and approved it for publication.

FUNDING

This work has been supported in part by the National Natural Science Foundation of China (No. 51507144), Fundamental Research Funds for the Central Universities (No. XDJK2019B021), the Chongqing Science and Technology Commission (CSTC) (No. cstc2016jcyjA0400) and the project of China Scholarship Council (CSC).

REFERENCES

- Boudiba, A., Roussel, P., Zhang, C., Olivier, M. G., Snyders, R., and Debliquy, M. (2013). Sensing mechanism of hydrogen sensors based on palladium-loaded tungsten oxide (Pd-WO₃). *Sensor. Actuator. B Chem.* 187, 84–93. doi: 10.1016/j.snb.2012.09.063
- Cao, S. X., and Chen, H. (2017). Nanorods assembled hierarchical urchin-like WO₃ nanostructures: hydrothermal synthesis, characterization, and their gas sensing properties. *J. Alloy Compo.* 702, 644–648. doi: 10.1016/j.jallcom.2017.01.232
- Cui, H., Zhang, X. X., Zhang, G. Z., and Tang, J. (2019). Pd-doped MoS₂ monolayer: a promising candidate for DGA in transformer oil based on DFT method. *Appl. Surf. Sci.* 470, 1035–1042. doi: 10.1016/j.apsusc.2018.11.230
- Dral, A. P., and ten Elshof, J. E. (2018). 2D metal oxide nanoflakes for sensing applications: review and perspective. *Sensor Actuator B Chem.* 272, 369–392. doi: 10.1016/j.snb.2018.05.157
- Gao, X., Zhou, Q., Lu, Z. R., Xu, L. N., Zhang, Q. Y., and Zeng, W. (2019). Synthesis of Cr₂O₃ nanoparticle-coated SnO₂ nanofibers and C₂H₂ sensing properties. *Front. Mater.* 6:163. doi: 10.3389/fmats.2019.00163
- Ge, Q., Ma, S. Y., Xu, Y. B., Xu, X. L., Chen, H., Qiang, Z., et al. (2017). Preparation, characterization and gas sensing properties of Pr-doped ZnO/SnO₂ nanoflowers. *Mater. Lett.* 191, 5–9. doi: 10.1016/j.matlet.2016.12.116
- Geng, X., Luo, Y. F., Zheng, B. B., and Zhang, C. (2017). Photon assisted room-temperature hydrogen sensors using PdO loaded WO₃ nanohybrids. *Int. J. Hydrogen Energ.* 42, 6425–6343. doi: 10.1016/j.ijhydene.2016.12.117
- Giancaterini, L., Emamjomeh, S. M., De Marcellis, A., Palange, E., Resmini, A., Anselmi-Tamburini, U., et al. (2016). The influence of thermal and visible light activation modes on the NO₂ response of WO₃ nanofibers prepared by electrospinning. *Sensor Actuator B Chem.* 229, 387–395. doi: 10.1016/j.snb.2016.02.007
- Gibot, P., Comet, M., Vidal, L., Moitrier, F., Lacroix, F., Suma, Y., et al. (2011). Synthesis of WO₃ nanoparticles for superthermites by the template method from silica spheres. *Solid State Sci.* 13, 908–914. doi: 10.1016/j.solidstatesciences.2011.02.018
- Gui, Y. G., Li, T., He, X., Ding, Z. Y., and Yang, P. G. (2019). Pt cluster modified h-BN for gas sensing and adsorption of dissolved gases in transformer oil: a Density Functional Theory Study. *Nanomaterials* 9:1746. doi: 10.3390/nano9121746
- Guo, T., Yao, M. S., Lin, Y. H., and Nan, C. W. (2015). A comprehensive review on synthesis methods for transition-metal oxide nanostructures. *CrystEngComm* 17, 3551–3585. doi: 10.1039/C5CE00034C
- Huang, D., Yuan, W. J., Fan, S. R., Tian, C., Hua, Z. Q., Tian, X. M., et al. (2020). Hydrogen sensing mechanism of Ru-loaded WO₃ nanosheets. *Sensor Actuator B Chem.* 304:127339. doi: 10.1016/j.snb.2019.127339
- Jaroenapibal, P., Boonma, P., Saksilaporn, N., Horprathum, M., Amornkitbamrung, V., and Triroj, N. (2018). Improved NO₂ sensing performance of electrospun WO₃ nanofibers with silver doping. *Sensor Actuator B Chem.* 255, 1831–1840. doi: 10.1016/j.snb.2017.08.199
- Jiang, Z. K., Chen, W. G., Jin, L. F., Cui, F., Song, Z. H., and Zhu, C. Z. (2018). High performance acetylene sensor with heterostructure based on WO₃ nanolamellae/reduced graphene oxide (rGO) nanosheets operating at low temperature. *Nanomaterials* 8. doi: 10.3390/nano8110909
- Jin, L. F., Chen, W. G., Zhang, H., Xiao, G. W., Yu, C. T., and Zhou, Q. (2017). Characterization of reduced graphene oxide (rGO)-loaded SnO₂ nanocomposite and applications in C₂H₂ gas detection. *Appl. Sci. Basel* 7:19. doi: 10.3390/app7010019
- Jin, Z. W., Hu, P. F., Xu, W., Zhou, J., Guo, W. W., Chen, Y., et al. (2019). Hydrothermal synthesis and gas sensing properties of hybrid WO₃ nano-materials using octadecylamine. *J. Alloy. Compo.* 785, 1047–1055. doi: 10.1016/j.jallcom.2019.01.248
- Lei, T., Deng, Q., Zhang, S. P., Cai, S. Z., and Xie, C. S. (2016). Fast identification of CO by using single Pt-modified WO₃ sensing film based on optical modulation. *Sensor Actuator B Chem.* 232, 506–513. doi: 10.1016/j.snb.2016.04.001
- Li, T. T., Shen, Y. B., Zhao, S. K., Zhong, X. X., Zhang, W., Han, C., et al. (2019). Sub-ppm level NO₂ sensing properties of polyethyleneimine-mediated WO₃ nanoparticles synthesized by a one-pot hydrothermal method. *J. Alloy. Compo.* 783, 103–112. doi: 10.1016/j.jallcom.2018.12.287
- Lu, Z. R., Zhou, Q., Xu, L. N., Gui, Y. G., Zhao, Z. Y., Tang, C., et al. (2018). Synthesis and characterization of highly sensitive hydrogen (H₂) sensing device based on Ag doped SnO₂ nanospheres. *Materials* 11:492. doi: 10.3390/ma11040492
- Ma, J. H., Ren, Y., Zhou, X. R., Liu, L. L., Zhu, Y. H., Cheng, X. W., et al. (2018). Pt Nanoparticles sensitized ordered mesoporous WO₃ semiconductor: gas sensing performance and mechanism study. *Adv. Funct. Mater.* 28:1705268. doi: 10.1002/adfm.201705268
- Miao, B., Zeng, W., Mu, Y. J., Yu, W. J., Hussain, S., Xu, S. B., et al. (2015). Controlled synthesis of monodisperse WO₃•H₂O square nanoplates and their gas sensing properties. *Appl. Surf. Sci.* 349, 380–386. doi: 10.1016/j.apsusc.2015.04.226
- Nasir, M. Z. M., and Pumera, M. (2019). Emerging mono-elemental 2D nanomaterials for electrochemical sensing applications: from borophene to bismuthene. *Trac Trend. Anal. Chem.* 121:115696. doi: 10.1016/j.trac.2019.115696
- Ou, J. Z., Yaacob, M. H., Campbell, J. L., Breedon, M., Kalantar-zadeh, K., and Wlodarski, W. (2012). H₂ sensing performance of optical fiber coated with nano-platelet WO₃ film. *Sensor Actuator B Chem.* 166, 1–6. doi: 10.1016/j.snb.2011.01.033
- Park, M. S., Lee, J. H., Park, Y., Yoo, R., Park, S., Jung, H., et al. (2019). Doping effects of ZnO quantum dots on the sensitive and selective detection of acetylene for dissolved-gas analysis applications of transformer oil. *Sensor Actuator B Chem.* 299:126992. doi: 10.1016/j.snb.2019.126992
- Park, S., Kim, H., Jin, C., Choi, S. W., Kim, S. S., and Lee, C. (2012). Enhanced CO gas sensing properties of Pt-functionalized WO₃ nanorods. *Thermochim. Acta* 542, 69–73. doi: 10.1016/j.tca.2011.12.002

- Rahmani, M. B., Yaacob, M. H., and Sabri, Y. M. (2017). Hydrogen sensors based on 2D WO₃ nanosheets prepared by anodization. *Sensor Actuator B Chem.* 251, 57–64. doi: 10.1016/j.snb.2017.05.029
- Tan, Y., and Lei, Y. (2019). Atomic layer deposition of Rh nanoparticles on WO₃ thin film for CH₄ gas sensing with enhanced detection characteristics. *Ceram. Inter.* 46, 9936–9942. doi: 10.1016/j.ceramint.2019.12.094
- Vuong, N. M., Kim, D., and Kim, H. (2015). Porous Au-embedded WO₃ nanowire structure for efficient detection of CH₄ and H₂S. *Sci. Rep.* 5:11040. doi: 10.1038/srep11040
- Wang, J. X., Zhou, Q., Lu, Z. R., Wei, Z. J., and Zeng, W. (2019). A Gas sensing performances and mechanism at atomic level of Au-MoS₂ microspheres. *Appl. Surf. Sci.* 490, 124–136. doi: 10.1016/j.apsusc.2019.06.075
- Wang, M. D., Li, Y. Y., Yao, B. H., Zhai, K. H., Li, Z. J., and Yao, H. C. (2019). Synthesis of three-dimensionally ordered macro/mesoporous C-doped WO₃ materials: effect of template sizes on gas sensing properties. *Sensor Actuator B Chem.* 288, 656–666. doi: 10.1016/j.snb.2019.03.051
- Wei, S. H., Han, L. X., Wang, M. Y., Zhang, H. H., Du, W. M., and Zhou, M. H. (2017). Hollow cauliflower-like WO₃ nano structures: Hydrothermal synthesis and their CO sensing properties. *Mater. Lett.* 186, 259–262. doi: 10.1016/j.matlet.2016.10.016
- Wei, Z. J., Zhou, Q., Lu, Z. R., Xu, L. N., Gui, Y. G., and Tang, C. (2019b). Morphology controllable synthesis of hierarchical WO₃ nanostructures and C₂H₂ sensing properties. *Phys. E* 109, 253–260. doi: 10.1016/j.physe.2019.01.006
- Wei, Z. J., Zhou, Q., Wang, J. X., Gui, Y. G., and Zeng, W. (2019a). A novel porous NiO nanosheet and its H₂ sensing performance. *Mater. Lett.* 245, 166–169. doi: 10.1016/j.matlet.2019.03.013
- Wei, Z. J., Zhou, Q., Wang, J. X., Lu, Z. R., Xu, L. N., and Zeng, W. (2019c). Hydrothermal synthesis of SnO₂ nanoneedle-anchored NiO microsphere and its gas sensing performances. *Nanomaterials* 9:1015. doi: 10.3390/nano9071015
- Wisitsoorat, A., Ahmad, M. Z., Yaacob, M. H., Horpratum, M., Phakaratkul, D., Lomas, T., et al. (2013). Optical H₂ sensing properties of vertically aligned Pd/WO₃ nanorods thin films deposited by glancing angle rf magnetron sputtering. *Sensor Actuator B Chem.* 182, 795–801. doi: 10.1016/j.snb.2013.03.091
- Wu, C. H., Zhu, Z., Huang, S. Y., and Wu, R. J. (2019). Preparation of palladium-doped mesoporous WO₃ for hydrogen gas sensors. *J. Alloy Compo.* 776, 965–973. doi: 10.1016/j.jallcom.2018.10.372
- Xiao, S. H., Liu, B., Zhou, R., Liu, Z. W., Li, Q. H., and Wang, T. H. (2018). Room-temperature H₂ sensing interfered by CO based on interfacial effects in palladium-tungsten oxide nanoparticles. *Sensor Actuator B Chem.* 254, 966–972. doi: 10.1016/j.snb.2017.07.169
- Xu, Y., Zeng, W., and Li, Y. Q. (2019). A novel seawave-like hierarchical WO₃ nanocomposite and its ammonia gas properties. *Mater. Lett.* 248, 86–88. doi: 10.1016/j.matlet.2019.04.010
- Xue, D. P., Wang, J. J., Wang, Y., Sun, G., Cao, J. L., Bala, H., et al. (2019a). Enhanced methane sensing properties of WO₃ nanosheets with dominant exposed (200) facet via loading of SnO₂ nanoparticles. *Nanomaterials* 9:351. doi: 10.3390/nano9030351
- Xue, D. P., Wang, Y., Cao, J. L., Sun, G., and Zhang, Z. Y. (2019b). Improving methane gas sensing performance of flower-like SnO₂ decorated by WO₃ nanoplates. *Talanta* 199, 603–611. doi: 10.1016/j.talanta.2019.03.014
- Yang, Z., Zhou, Q., Wu, X. D., and Zhao, Z. Y. (2019b). A novel measuring method of interfacial tension of transformer oil combined PSO optimized SVM and multi frequency ultrasonic technology. *IEEE Access* 7, 182624–182631. doi: 10.1109/ACCESS.2019.2954899
- Yang, Z., Zhou, Q., Wu, X. D., Zhao, Z. Y., Tang, C., and Chen, W. G. (2019a). Detection of water content in transformer oil using multi frequency ultrasonic with PCA-GA-BPNN. *Energies* 12:1379. doi: 10.3390/en12071379
- Yao, M. S., Li, Q. H., Hou, G. L., Lu, C., Cheng, B. L., Wu, K. C., et al. (2015). Dopant-controlled morphology evolution of WO₃ polyhedra synthesized by RF thermal plasma and their sensing properties. *ACS Appl. Mater. Inter.* 7, 2856–2866. doi: 10.1021/am5081277
- Yu, Y. C., Zeng, W., Xu, M. X., and Peng, X. H. (2016). Hydrothermal synthesis of WO₃•H₂O with different nanostructures from 0D to 3D and their gas sensing properties. *Phys. E* 79, 127–132. doi: 10.1016/j.physe.2015.12.023
- Zhang, D. Z., Jiang, C. X., and Wu, J. F. (2018). Layer-by-layer assembled In₂O₃ nanocubes/flower-like MoS₂ nanofilm for room temperature formaldehyde sensing. *Sensor Actuator B Chem.* 273, 176–184. doi: 10.1016/j.snb.2018.06.044
- Zhang, H., Chen, W. G., Jin, L. F., and Cui, F. (2018b). Hierarchically porous WO₃ microstructures with networks for acetylene sensing application. *Mater. Lett.* 214, 198–201. doi: 10.1016/j.matlet.2017.11.122
- Zhang, H., Chen, W. G., Li, Y. Q., Jin, L. F., Cui, F., and Song, Z. H. (2018a). 3D Flower-like NiO hierarchical structures assembled with size-controllable 1D blocking units: gas sensing performances towards acetylene. *Front. Chem.* 6:472. doi: 10.3389/fchem.2018.00472
- Zhang, H. B., Yao, M. S., Bai, L. Y., Xiang, W. C., Jin, H. C., Li, J. L., et al. (2013). Synthesis of uniform octahedral tungsten trioxide by RF induction thermal plasma and its application in gas sensing. *CrystEngComm* 15, 1432–1438. doi: 10.1039/c2ce26514a
- Zhang, Q. Y., Zhou, Q., Lu, Z. R., Wei, Z. J., Xu, L. N., and Gui, Y. G. (2018). Recent advances of SnO₂-based sensors for detecting fault characteristic gases extracted from power transformer oil. *Front. Chem.* 6:364. doi: 10.3389/fchem.2018.00364
- Zhang, X. X., Fang, R. X., Chen, D. C., and Zhang, G. Z. (2019). Using Pd-doped gamma-graphyne to detect dissolved gases in transformer oil: a density functional theory investigation. *Nanomaterials* 9:1490. doi: 10.3390/nano9101490
- Zhang, Y. Z., Zeng, W., and Li, Y. Q. (2019). NO₂ and H₂ sensing properties for urchin-like hexagonal WO₃ based on experimental and first-principle investigations. *Ceram. Inter.* 45, 6043–6050. doi: 10.1016/j.ceramint.2018.12.075
- Zhang, Y. X., Sun, X., Tan, S., Liu, T., and Cui, H. (2019). Adsorption characteristic of Rh-doped MoSe₂ monolayer towards H₂ and C₂H₂ for DGA in transformer oil based on DFT method. *Appl. Surf. Sci.* 487, 930–937. doi: 10.1016/j.apsusc.2019.05.108
- Zhou, Q., Chen, W. G., Xu, L. N., Kumar, R., Gui, Y. G., Zhao, Z. Y., et al. (2018c). Highly sensitive carbon monoxide (CO) gas sensors based on Ni and Zn doped SnO₂ nanomaterials. *Ceram. Inter.* 44, 4392–4399. doi: 10.1016/j.ceramint.2017.12.038
- Zhou, Q., Chen, W. G., Xu, L. N., and Peng, S. D. (2013). Hydrothermal synthesis of various hierarchical ZnO nanostructures and their methane sensing properties. *Sensors* 13, 6171–6182. doi: 10.3390/s130506171
- Zhou, Q., Hong, C. X., Yao, Y., Hussain, S., Xu, L. N., Zhang, Q. Y., et al. (2018d). Hierarchically MoS₂ nanospheres assembled from nanosheets for superior CO gas-sensing properties. *Mater. Res. Bull.* 101, 132–139. doi: 10.1016/j.materresbull.2018.01.030
- Zhou, Q., Lu, Z. R., Wei, Z. J., Xu, L. N., Gui, Y. G., and Chen, W. G. (2019b). Hydrothermal synthesis of hierarchical ultrathin NiO nanoflakes for high-performance CH₄ sensing. *Front. Chem.* 6:194. doi: 10.3389/fchem.2018.00194
- Zhou, Q., Tang, C., Zhu, S. P., Chen, W. G., and Li, J. (2016). Synthesis, characterisation and sensing properties of Sm₂O₃ doped SnO₂ nanorods to C₂H₂ gas extracted from power transformer oil. *Mater. Technol.* 31, 364–370. doi: 10.1179/1753555715Y.0000000069
- Zhou, Q., Umar, A., Sodki, E., Amine, A., Xu, L. N., Gui, Y. G., et al. (2018a). Fabrication and characterization of highly sensitive and selective sensors based on porous NiO nanodisks. *Sensor Actuator B Chem.* 259, 604–615. doi: 10.1016/j.snb.2017.12.050
- Zhou, Q., Xu, L. N., Umar, A., Chen, W. G., and Kumar, R. (2018b). Pt nanoparticles decorated SnO₂ nanoneedles for efficient CO gas sensing applications. *Sensor Actuator B Chem.* 256, 656–664. doi: 10.1016/j.snb.2017.09.206
- Zhou, Q., Zeng, W., Chen, W. G., Xu, L. N., Kumar, R., and Umar, A. (2019a). High sensitive and low-concentration sulfur dioxide (SO₂) gas sensor application of heterostructure NiO-ZnO nanodisks. *Sensor Actuator B Chem.* 298:126870. doi: 10.1016/j.snb.2019.126870

Conflict of Interest: The authors declare that the research was conducted in the absence of any commercial or financial relationships that could be construed as a potential conflict of interest.

Copyright © 2020 Wei, Xu, Peng and Zhou. This is an open-access article distributed under the terms of the Creative Commons Attribution License (CC BY). The use, distribution or reproduction in other forums is permitted, provided the original author(s) and the copyright owner(s) are credited and that the original publication in this journal is cited, in accordance with accepted academic practice. No use, distribution or reproduction is permitted which does not comply with these terms.



The Functionalized Single-Walled Carbon Nanotubes Gas Sensor With Pd Nanoparticles for Hydrogen Detection in the High-Voltage Transformers

Sirui Tang¹, Weigen Chen^{1*}, He Zhang¹, Zihao Song¹, Yanqiong Li² and Yu Wang^{3*}

¹ State Key Laboratory of Power Transmission Equipment and System Security and New Technology, Chongqing University, Chongqing, China, ² School of Electronic and Electrical Engineering, Chongqing University of Arts and Sciences, Chongqing, China, ³ Shanghai Urban Construction Vocational College, Shanghai, China

OPEN ACCESS

Edited by:

Weiwei Wu,
Xidian University, China

Reviewed by:

Zhongchang Wang,
International Iberian Nanotechnology
Laboratory (INL), Portugal
Ming-Guo Ma,
Beijing Forestry University, China
Keng Xu,
Jiangxi Normal University, China

*Correspondence:

Weigen Chen
weigench@cqu.edu.cn
Yu Wang
wangyu@succ.edu.cn

Specialty section:

This article was submitted to
Nanoscience,
a section of the journal
Frontiers in Chemistry

Received: 31 December 2019

Accepted: 26 February 2020

Published: 07 April 2020

Citation:

Tang S, Chen W, Zhang H, Song Z,
Li Y and Wang Y (2020) The
Functionalized Single-Walled Carbon
Nanotubes Gas Sensor With Pd
Nanoparticles for Hydrogen Detection
in the High-Voltage Transformers.
Front. Chem. 8:174.
doi: 10.3389/fchem.2020.00174

Single-walled carbon nanotubes (SWCNTs) have been widely discussed and applied as novel gas sensing nanomaterials. Hydrogen is one of the remarkable fault characteristic gases in high-voltage oil-paper insulated transformers. In this paper, 3.07 wt% Pd nanoparticles (NPs) were used to decorate SWCNTs. The unloaded, the carboxylated, and the Pd-doped SWCNTs were fabricated into three planar gas sensors, and their gas sensing properties to hydrogen were studied. Gas sensing mechanism was analyzed. Results show that the optimal operating temperature of a Pd-doped SWCNTs-based gas sensor is 125°C lower than that of the unloaded SWCNTs-based gas sensor, and it shows the highest gas sensing response value. This is attributed to the decreasing work function of Pd, which reduces the hole carries in the nanotubes.

Keywords: single-walled carbon nanotubes, Pd-doped, hydrogen detection, gas sensing properties, high-voltage transformers

INTRODUCTION

Novel gas sensing materials were discovered and have been studied over the past five decades. A number of works on the improvement of microstructures, structures, and sensing properties of gas sensing materials have been done by researchers. Nanomaterials, such as nanofibers, nanowires, carbon nanotubes (CNTs), and nanoparticles, are the main focus of this research. In a study by Zhou et al. (2017a,b), the highly porous NiO nanodisks (NiO-NDs) and its synthesis, characterization, and sensing applications to alcohol were analyzed. In the reference (Zhou et al., 2018), the 1D hierarchical p-n heterostructured Mn₃O₄/SnO₄ hybrid materials (HMs) was synthesized by Zhou et al., and the sensing results to acetone indicates the perfect gas sensing performance of hybrid materials.

Due to CNTs fullerene structure and its large surface area, and the excellent electrical, mechanical, and thermal properties they have, CNTs have been one of the most widely studied gas sensing materials in the past two decades (Chen et al., 2001; Rana et al., 2017; Zaporotskova et al., 2017). Single-walled carbon nanotubes (SWCNTs) and multi-walled carbon nanotubes (MWCNTs) are the two main types of CNTs. The microstructure of SWCNTs and MWCNTs are somehow the same, that is, they consist of a rolled-up single sheet of a layer of graphene. However, MWCNTs are

composed of concentric tubes of graphene fitted inside each other (Pitroda et al., 2016; Beitollahi et al., 2018; Han et al., 2019). It is confirmed that adsorption of electron withdrawing (e.g., NO_2 , O_2) or donating (like NH_3) molecules on SWCNTs will cause the charge transfer between the nanotubes and molecules (Kong et al., 2001). Compared with other gas sensing materials, like MOS, CNTs—especially single-walled carbon nanotubes—have remarkable properties. For example, they have the highest Young's modulus, highest thermal conductivity, ballistic electron transport, and a high aspect ratio structure. What's more, CNTs are a more stable electrode material than other gas sensing materials due to its lower probability to be reduced or oxidized during a substantial range of potentials (Robertson, 2004). In the reference (Naje et al., 2016), the detection of NO_2 using SWCNTs and MWCNTs on porous silicon wafers was done by Naje et al. The NO_2 gas sensing performance of SWCNTs and MWCNTs vary at temperatures ranging from 25 to 250°C , and it shows that equal sensitivity can be reached with a higher temperature

for SWCNTs compared to MWCNTs, while the highest response of SWCNTs (79.8%) is higher than MWCNTs (59.6%) at their optimum temperature (150°C for SWCNTs, 200°C for MWCNTs). The trace level detection of NH_3 and NO_2 at room temperature via randomly oriented SWCNTs, which is grown by PECVD technique at 650°C , were realized by Lone et al. (2018). Results show the quick response and recovery characteristics of both NH_3 and NO_2 . Additionally, the gas sensing abilities of unloaded SWCNTs to N_2O_4 (Dai et al., 1999), O_2 (Kong et al., 1998), CO_2 (Yoon et al., 2018), and CH_4 (Poonia et al., 2015) are widely discussed.

High-voltage oil-paper insulated transformers play an essential role in power transmission, but during the long-term operation, due to oxidation, pollution, and excessive inner temperature, the transformer insulation oil will be degraded and decomposed, producing traces of characteristic gases dissolving in the oil. Hydrogen is one of the main characteristic gases reflecting overheat fault and discharge

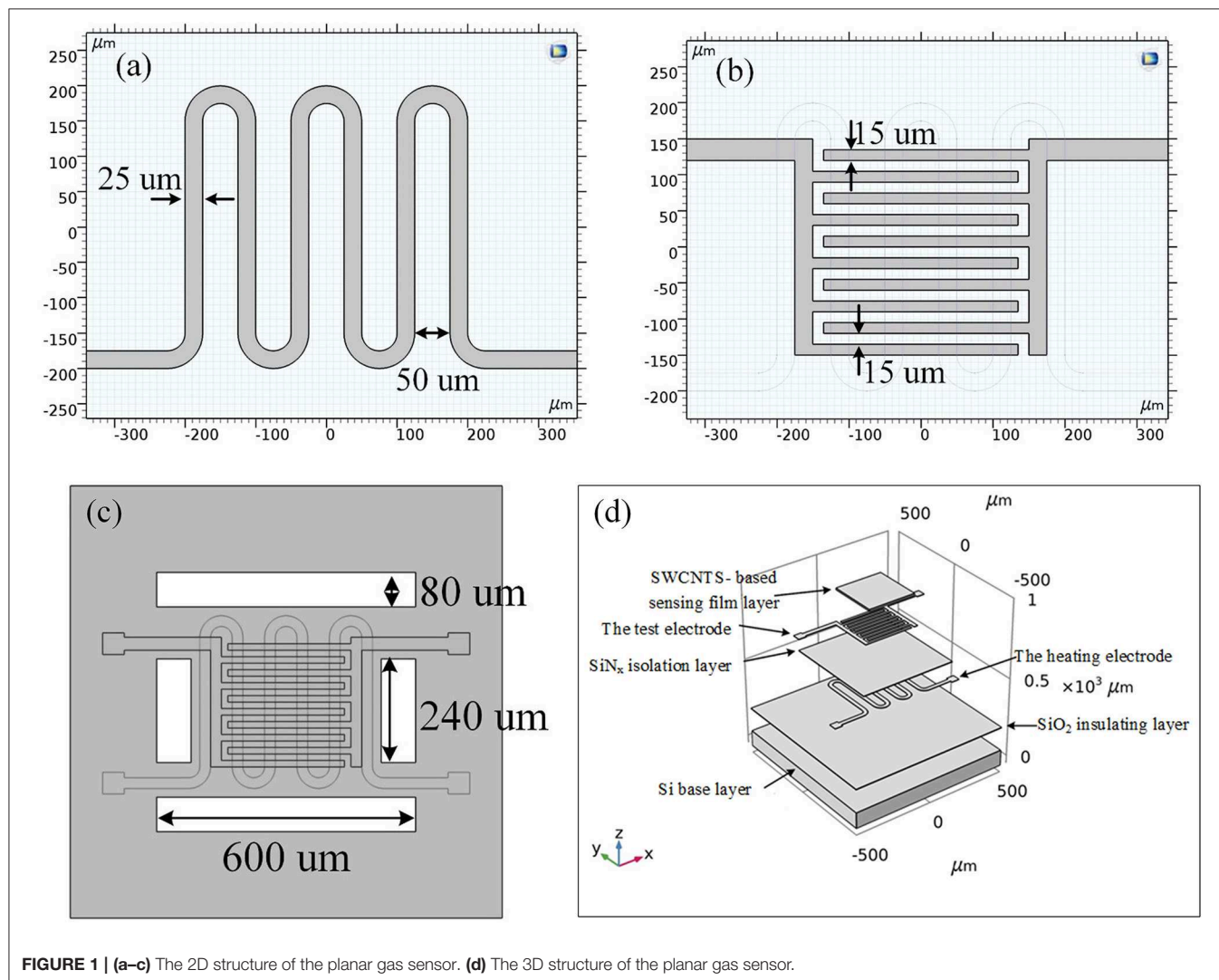


FIGURE 1 | (a–c) The 2D structure of the planar gas sensor. **(d)** The 3D structure of the planar gas sensor.

fault in the oil-immersed transformer (International Standard IEC 60599: 2015, 2015). Gas sensing nanomaterials such as SnO_2 , ZnO , WO_3 , and MoS_2 , as well as their functionalized derivatives, have been applied in studies on characteristic gases detecting of high-voltage transformers (Tang et al., 2017; Zhou et al., 2018; Wang et al., 2019; Wei et al., 2019). More importantly, Zhang et al. found that CNTs are well-performed gas sensing materials for gas detection of high-voltage electrical equipment (Zhang et al., 2017). However, it was reported in the study Kong et al. (2001) that nanotubes show a poor sensing response to some gas molecules. Instead, geometrical optimizations of SWCNTs with and without doped metals and their gas adsorption structures were studied based on computational methodology by applying restricted density functional theory (DFT) by Tabtimtsai et al. (2011). Calculation and simulation indicated that decorating SWCNTs with Pd nanoparticles can effectively enhance the gas sensing performance to NO_2 , NH_3 , H_2O , and H_2 . The hydrogen atoms dissociated from the hydrogen molecules have smaller adsorption energy and dissociation energy on the Pd cluster. As an electron donor, Pd clusters can quickly dissociate hydrogen atoms, electron acceptors, and accelerate electron transfer in gas-sensitive materials.

In this paper, the carboxylated and 3.07 wt% Pd-doped SWCNTs-based nanomaterials were synthesized based on the unloaded SWCNTs-based nanomaterials. Three SWCNTs-based nanomaterials (the unloaded, the carboxylated, and the Pd-doped) were fabricated into corresponding planar gas sensors. Gas sensing properties including the temperature characteristics, the concentration characteristics, the linearity, detecting limitation, and the response and recovery time characteristics of three SWCNTs-based gas sensors to hydrogen were studied. Gas sensing mechanisms

were analyzed. In the results, Pd-doped SWCNTs-base gas sensor presents the best gas sensing performance to hydrogen. This study can provide a novel solution to the issue of characteristic gases detection in high-voltage oil-paper insulated transformers.

MATERIALS AND METHODS

Preparation of SWCNTs-Based Nanomaterials

The unloaded SWCNTs-based nanomaterials were made by Timesnano of Chengdu Organic Chemicals Co. Ltd., Chinese Academy of Sciences. The outer Diameter (OD) of the unloaded SWCNTs-based gas sensing nanomaterials is 1–3 nm, and the purity is all higher than 90 wt%. The length of nanomaterials is about 50 microns. Concentrated hydrochloric acid, concentrated sulfuric acid, concentrated nitric acid, isopropanol, and ammonia used in the preparation process were purchased from Chongqing Chuandong Chemical Co., Ltd. (China), and all were of analytical grade. Palladium chloride (PdCl_2) provided a source of palladium. Deionized water was also used.

The processes of preparation of SWCNTs-based nanomaterials are classified into three steps:

(1) Purification of the unloaded SWCNTs

Six hundred milligram of unloaded SWCNTs were added to 300 ml of concentrated hydrochloric acid and ultrasonically cleaned for 30 min. Five hundred milligram of deionized water was used to ultrasonically clean the mixture for another 30 min. The cleaned mixture was placed in a drying box and dried at 150°C for 10 h. Purified unloaded SWCNTs were obtained.

(2) Acidification of the purified SWCNTs

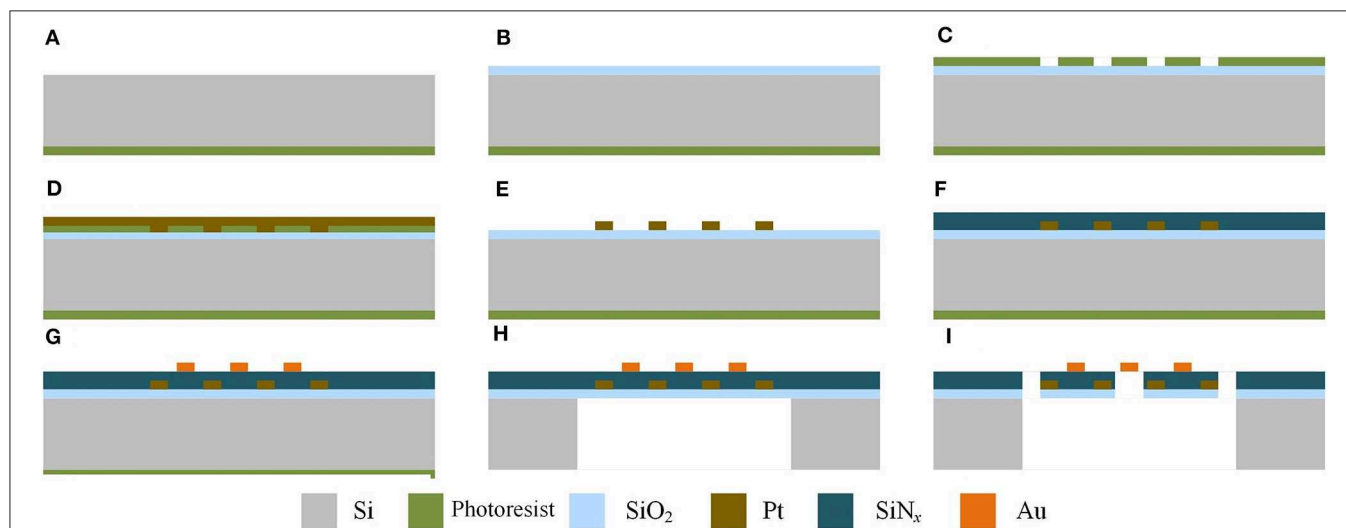


FIGURE 2 | Steps of processing of the planar gas sensor in sectional view. **(A)** The productive layer of Si base layer productive. **(B)** SiO_2 insulating layer is produced by thermal oxidation. **(C)** Photolithography on the heating electrode. **(D)** Sputter the Pt electrode. **(E)** Remove the metal-attached photoresist by stripping. **(F)** Deposition of SiN_x isolation layer on the heating electrode. **(G)** Photolithography, sputtering and stripping of Au electrode. **(H)** Corrosion of Si base layer. **(I)** Etching of SiO_2 insulating layer and SiN_x isolation layer.

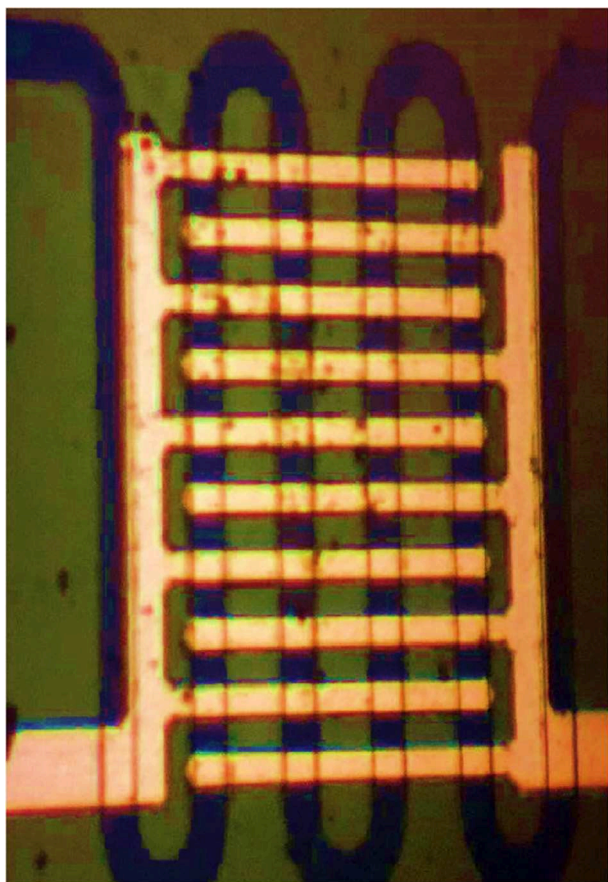


FIGURE 3 | The planar gas sensor.

Four hundred milligram of purified unloaded SWCNTs were added to 50 ml of concentrated sulfuric acid and 20 ml of concentrated nitric acid, and heated and stirred at 80°C for 4 h. After the mixture was cooled down, it was diluted with 60 ml deionized water. The mixture was filtered through a microporous membrane with a pore diameter of 0.45 microns, and washed repeatedly with deionized water until pH = 7. After drying at 80°C for 12 h, acidified SWCNTs were obtained.

(3) Functionalization of the acidified SWCNTs

Two hundred milligram of SWCNT was dissolved in 50 ml of isopropanol and sonicated for 20 min to improve the dispersibility of SWCNTs. 10.31 mg of PdCl₂ was dissolved in 3 ml of ammonia water. PdCl₂ solution was added to the SWCNTs/isopropanol mixed solution drop by drop, and stirred at a high speed for 2 h. The obtained suspension was put in a drying box and dried at 80°C for 2 h. The obtained powder was put in a calciner at 600°C for 2 h. 3.07 wt% Pd-doped SWCNTs-based nanomaterials were synthesized successfully.

The microstructure of the nanomaterials was characterized by Scanning Electron Microscopy (SEM) (SU8020, HITACHI, Japan) and Transmission Electron Microscopy (TEM) (JEM-2000EX, JEOL, Japan).

Fabricated of SWCNTs-Based Gas Sensors

Planar gas sensors are applied in this paper. The structure of planar gas sensors is shown in **Figure 1**. The planar gas sensor is mainly composed of a Pt heating electrode, a Si base layer, an Au gas sensing electrode, and a SWCNTs-based sensing film layer. The size of the testing area is 300 μm × 300 μm. The hardware structure of the gas sensor is fabricated by Zhengzhou Winsen Electronics Technology CO., Ltd by processes mainly including oxidation, photolithography, sputtering, stripping, deposition, and etching, which are presented in **Figure 2**.

The planar sensor array is shown in **Figure 3**. The n-type (110) crystal face double polished silicon wafer (thickness is about 300 μm, and conductivity is 0.001–0.1 S/m) is used. In this paper, three SWCNTs-based sensing nanomaterials are coated by the droplet guiding method. After fully grinding the appropriate number of SWCNTs-based nanomaterials, it was dissolved in absolute ethanol for 1 h to obtain the corresponding dispersion, which was then dried at 400°C to get ultrafine powder. The deionized water droplets were applied to the sensor unit testing area using a micro syringe, and the SWCNTs-based nanomaterial powder was carefully applied to the droplets. After drying for 8 h, the powder was closely attached to the testing area, and three SWCNTs-based planar gas sensors were fabricated successfully.

Gas Sensing Test Methods

The experimental platform consists of air source, RSC2000-A automatic gas mixing system (Beijing JS Co.), and CGS-8 intelligent gas sensitivity analysis system (Beijing Elite Tech Co., China), which is presented in **Figure 4**. The detection of the electrical signals of the gas sensor is mainly realized by the classical resistor divider principle, and the test circuit is shown in **Figure 5**, where R_L is the adjustable load resistance and R_S is the resistance at both ends of the test electrode. R_H is the resistance of the heating electrode of the sensing unit. V_H and V_S is the heating voltage and test voltage, respectively. During the test, R_S will vary with the change of condition and can be calculated by the principle of voltage division.

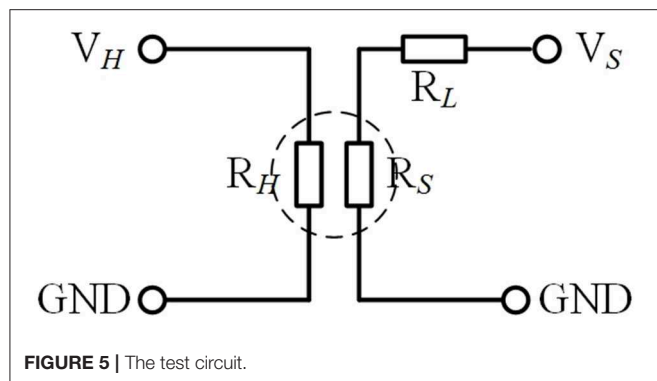
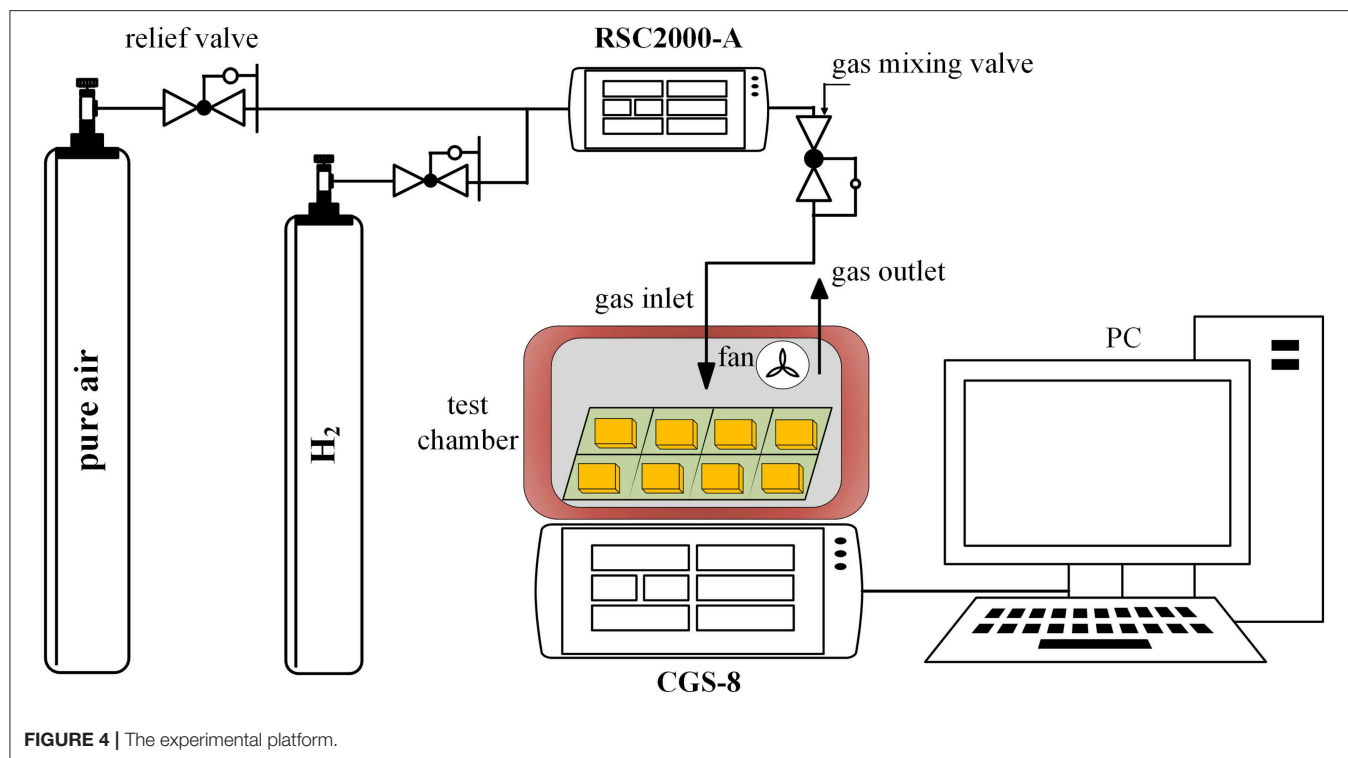
The sensor response values defined here are as follows (Wang et al., 2010):

$$R_s = (R_{gas} - R_{air})/R_{air}$$

Specific steps are as follows:

1. The gas sensor is placed in a closed air chamber filled with pure air (20 L), and the sensing signal (R_s) is recorded by CGS-8 system during the test.
2. The determined concentrations of hydrogen are injected by RSC2000-A system (gas flow: 250 sccm). The resistance value is recorded after the signal is stable.
3. The air chamber is opened through the fume hood and the resistance made to return to the initial value R_{air} .
4. Step (2) and step (3) are repeated.
5. The recorded data is saved and further experiments can be proceeded with.

Experiments were all carried out at a temperature of 28°C and at 60% humidity.



RESULTS AND DISCUSSIONS

Morphology

Figure 6 shows the SEM and TEM images of the unloaded, the carboxylated, and the Pd-doped SWCNTs. From the SEM images, the three kinds of SWCNTs are all intertwined and woven into a mesh, and the morphology of the SWCNTs after functioning has not changed much. However, in **Figures 6b,c**, the carboxylated and the Pd-doped SWCNTs are shorter in length and more distributed compared to the unloaded SWCNTs in **Figure 6a**. In the TEM images, all three SWCNTs are curved and tubular, and the basic structure has not been functionally damaged.

After acidification treatment, SWCNTs were oxidized under the action of concentrated sulfuric acid and concentrated nitric acid. Oxygen atoms released by concentrated nitric acid attacked carbon nanotubes, especially the defects at the ends and on the tube walls. Because carbon atoms are not stable six-membered

rings in SWCNTs and are in a metastable state, SWCNTs will break in places where the nanotube curvature is large. Thus, the length of nanotubes becomes shorter, and nanotubes gradually disperse.

Gas Sensing Properties

The temperature characteristics, concentration characteristics (including linearity and detecting limitation), response and recovery time characteristics of the unloaded, the carboxylated, and the Pd-doped SWCNTs-based gas sensors were studied in the hydrogen atmosphere.

In **Figure 7**, the temperature characteristics of three SWCNTs-based gas sensors are illustrated among 150–400°C to 100 $\mu\text{L/L}$ hydrogen. On the one hand, three different SWCNTs-based gas sensors present the same trend of temperature characteristics: curves climb at first with the increase of the temperature and decrease after reaching the optimal operating temperature. This might be because when heated to a certain temperature, the surface of SWCNTs nanomaterials is occupied by oxygen atoms released from the air, which increases the surface conductance of the materials and, thus, shows a decrease in resistance. On the other hand, after modifying SWCNTs-based nanomaterials with Pd nanoparticles, the optimal operating temperature dropped sharply by 125°C, and the peak response of Pd-doped SWCNTs-based gas sensor is 10.1 and 3.2 times higher than that of the unloaded and carboxylated SWCNTs-based gas sensors under the respective optimal operating temperature, respectively.

Concentration characteristics were tested in 0–500 $\mu\text{L/L}$ hydrogen at 275°C, as shown in **Figure 8**. As the gas concentration rises, the growth rate of the response value of all three gas sensors slows down and gradually becomes

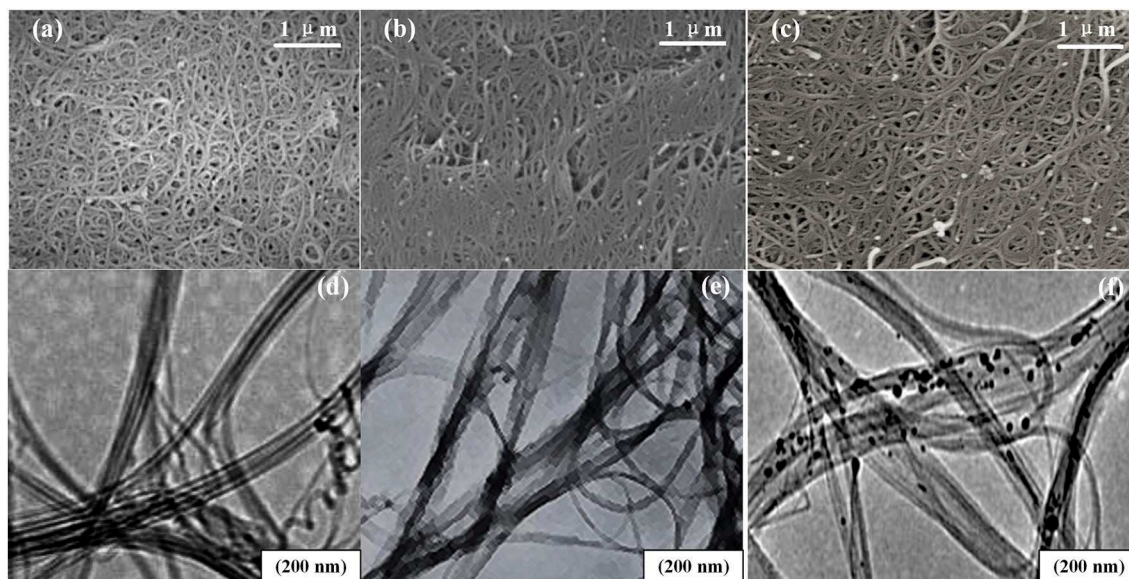


FIGURE 6 | The morphology of nanomaterials. (a–c) The SEM images of the unloaded, the carboxylated, and the Pd-doped SWCNTs. (d–f) The TEM images of the unloaded, the carboxylated, and the Pd-doped SWCNTs.

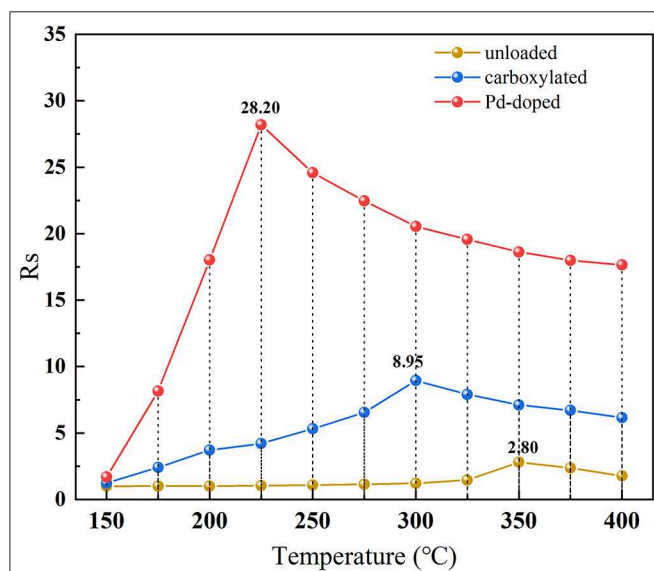


FIGURE 7 | The temperature characteristics of the unloaded, carboxylated, and 3.07 wt% Pd-doped SWCNTs-based gas sensors.

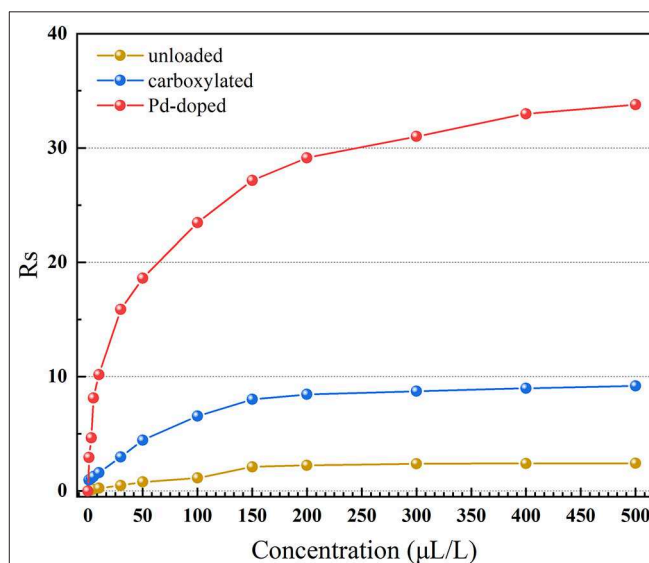


FIGURE 8 | The concentration characteristics of the unloaded, carboxylated, and 3.07 wt% Pd-doped SWCNTs-based gas sensors.

saturated. However, 3.07 wt% Pd-doped SWCNT-based gas sensor has better gas sensing performance in an extreme high gas concentration atmosphere. When the concentration of hydrogen is 500 $\mu\text{L/L}$, the gas sensing response of Pd-doped SWCNTs-based gas sensor is about 33.79, which is almost 14 and 3.7 times higher than the gas sensing response of the unloaded and the carboxylated SWCNTs-based gas sensors, respectively.

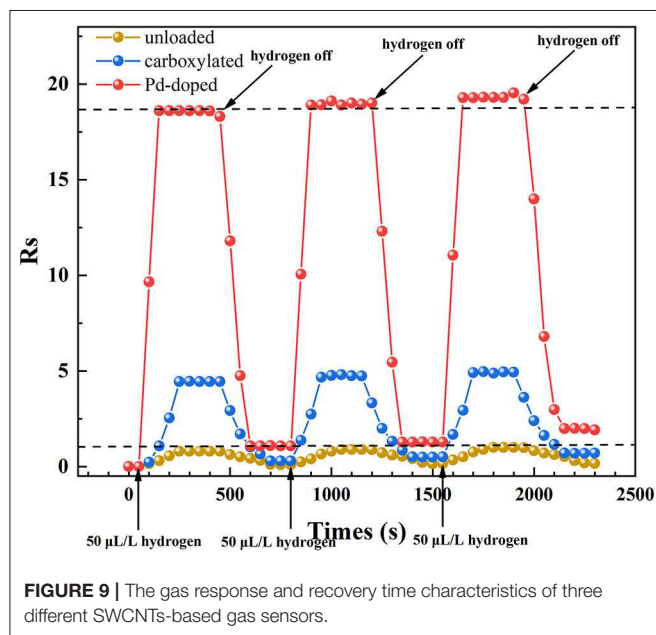
In **Figure 8**, R_s is linearly related to the concentration in the respective low concentration ranges (1–30 $\mu\text{L/L}$), and the fitting function and corresponding R^2 (linearity) is shown in **Table 1**. Assuming that when hydrogen is 1 $\mu\text{L/L}$, the gas sensing response

is not lower than 1, the corresponding gas sensor is able to reach the detecting limitation (International Standard IEC 60599: 2015, 2015; Tang et al., 2017). Results are shown in **Table 1**. SWCNTs-based gas sensors with or without functionalization all show perfect linearity, while only the Pd-doped SWCNTs-based gas sensor can meet the requirement of detecting limitation.

Figure 9 presents the response and recovery time characteristics of three gas sensors which were tested at 275°C to 50 $\mu\text{L/L}$ hydrogen. The experiment was repeated three times: 50 $\mu\text{L/L}$ hydrogen was injected at 50, 800, and 1,550 s, and was exhausted at 450, 1,200, and 1,950 s. It is obvious that

TABLE 1 | The fitting function, linearity and detecting limitation of three SWCNTs-based gas sensors to hydrogen.

Sensor units	The fitting function	R ²	Detection limit
Unloaded	$y = 0.0148x + 0.0574$	0.994	×
Carboxylated	$y = 0.0706x + 0.8921$	0.9999	×
Pd-doped	$y = 1.2757x + 0.9729$	0.9697	✓

**FIGURE 9** | The gas response and recovery time characteristics of three different SWCNTs-based gas sensors.

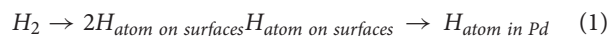
both response and recovery time of Pd-doped SWCNTs-based gas sensor are shorter than the other two. The response time and recovery time of Pd-doped SWCNTs-based gas sensor are about 100 and 150 s. What's more, the gas sensing response value of the three gas sensors is slightly increased after the third time test, which might be because of the incomplete exhaust each time, resulting in the presence of more hydrogen than expected in the final gas chamber. The recovery process of gas sensing materials is a dynamic process of adsorption and desorption between the molecules of the test gas, hydrogen, and nanotubes. If the hydrogen molecules in the gas chamber are not exhausted cleanly, a small amount of hydrogen molecules will still be adsorbed with the active sites on the surface of the nanotube at high temperatures, shown as the hydrogen atoms, so that there will still be less electron exchange in the gas sensing material nanotubes.

Gas Sensing Mechanism

Obviously, after decorating SWCNTs with Pd nanoparticles, the gas sensing performance to hydrogen was remarkably enhanced. This is attributed to the enhanced electrical property toward molecular hydrogen compared with the undecorated SWCNTs. The gas sensing reaction is the interactions between H₂, Pd, and the nanotubes. After heating, hydrogen molecules dissociate faster into atomic hydrogen on Pd surface, resulting in the dissolution of atomic hydrogen in Pd with high solubility,

consequently decreasing the work function of Pd, that is shown in the formula (1). The lowering of the work function of Pd leads to faster and easier electron transfer from Pd to SWCNTs, reducing the number of hole-carriers in the p-type nanotubes and the value of conductance.

When the Pd-doped SWCNTs-based gas sensor was in a low hydrogen atmosphere, the reason why it can reverse and auto recover is because of the oxygen in the air and on the surfaces, which is represented as the formulas (2) and (3) (Mandelis et al., 1993; Collins, 2000; Kong, 2000).



CONCLUSION

In this paper, we prepared the carboxylated and 3.07 wt% Pd-doped SWCNTs-based nanomaterials based on the unloaded SWCNTs, and three different SWCNTs-based planar gas sensors were fabricated and tested in hydrogen to study their gas sensing properties. Results show that functionalized SWCNTs-based gas sensor with Pd nanoparticles present the best gas sensing performance, and has the lowest optimal operating temperature (225°C) and the highest gas sensing response to 500 μL/L hydrogen at 275°C ($R_s \cong 33.79$). The gas response and recovery time of Pd-doped SWCNTs-based gas sensor are both 50 s shorter than those of the unloaded and carboxylated SWCNTs-based gas sensors. This was because the Pd doping lowers the work function and enhances the electrical property toward molecular hydrogen. Results could assist the development of novel SWCNTs-based gas sensors for fault characteristic gases detection in the high-voltage electrical transformers.

DATA AVAILABILITY STATEMENT

The datasets generated for this study are available on request to the corresponding author.

AUTHOR CONTRIBUTIONS

ST designed the experiment, finished the experiment, data collected and analyzed, and wrote the paper. WC helped correct the paper. HZ helped design and finished the experiment. ZS helped collect the data. YL helped correct the paper. YW helped correct the paper.

FUNDING

This work was supported by the National Science Foundation of China (Grant No. U1766217), Fundamental Research Funds for the Central University (No. 2019CDJGFCL001), and State Grid Corporation of China Science and Technology Project (52110418000Q).

REFERENCES

- Beitollahi, H., Movahedifar, F., Tajik, S., and Jahani, S. (2018). A review on the effects of introducing CNTs in the modification process of electrochemical sensors. *Electroanalysis* 31, 1195–1203. doi: 10.1002/elan.201800370
- Chen, R., Franklin, N., Kong, J., Cao, J., Tomblor, T., Zhang, Y., et al. (2001). Molecular photodesorption from single-walled carbon nanotubes. *Appl. Phys. Lett.* 79, 2258–2260. doi: 10.1063/1.1408274
- Collins, P. G. (2000). Extreme oxygen sensitivity of electronic properties of carbon nanotubes. *Science* 287, 1801–1804. doi: 10.1126/science.287.5459.1801
- Dai, H., Kong, J., Zhou, C., Franklin, N., Tomblor, T., Cassell, A., et al. (1999). Controlled chemical routes to nanotube architectures, physics, and devices. *J. Phys. Chem. B* 103, 11246–11255. doi: 10.1021/jp992328o
- Han, T., Nag, A., Mukhopadhyay, S. C., and Xu, Y. (2019). Carbon nanotubes and its gas-sensing applications: a review. *Sens. Actuators A Phys.* 291, 107–143. doi: 10.1016/j.sna.2019.03.053
- International Standard IEC 60599: 2015 (2015). *Mineral Oil-Filled Electrical Equipment in Service-Guide on the Interpretation of Dissolved and Free Gases Analysis*. International Electrotechnical Commission.
- Kong, J. (2000). Nanotube molecular wires as chemical sensors. *Science* 287, 622–625. doi: 10.1126/science.287.5453.622
- Kong, J., Chapline, M. G., and Dai, H. (2001). Functionalized carbon nanotubes for molecular hydrogen sensors. *Adv. Mater.* 13, 1384–1386. doi: 10.1002/1521-4095(200109)13:18<1384::AID-ADMA1384>3.0.CO;2-8
- Kong, J., Soh, H., Cassell, A., Quate, C., and Dai, H. (1998). Synthesis of single single-walled carbon nanotubes on patterned silicon wafers. *Nature* 395, 878–881. doi: 10.1038/27632
- Lone, M., Kumar, A., Husain, S., Singh, R. C., Zulfequar, M., and Husain, M. (2018). Fabrication of sensitive SWCNT sensor for trace level detection of reducing and oxidizing gases (NH₃ and NO₂) at room temperature. *Phys. E Low Dimens. Syst. Nanostruct.* 108, 206–214. doi: 10.1016/j.physe.2018.11.020
- Mandelis, A., Christofides, C., and Winefordner, J. D. (1993). *Physics, Chemistry and Technology of Solid State Gas Sensor Devices*. New York, NY: Wiley.
- Naje, A., Ibraheem, R., and Ibrahim, F. (2016). Parametric analysis of NO₂ gas sensor based on carbon nanotubes. *Photonic Sens.* 6, 153–157. doi: 10.1007/s13320-016-0304-1
- Pitroda, J., Jethwa, B., and Dave, S. K. (2016). A critical review on carbon nanotubes. *Int. J. Construct. Res. Civil Eng.* 2, 36–42. doi: 10.20431/2454-8693.0205007
- Poonia, M., Manjuladevi, V., Gupta, R., Gupta, S. K., Singh, J., Agarwal, P., et al. (2015). Ultrathin films of single-walled carbon nanotubes: a potential methane gas sensor. *Sci. Adv. Mater.* 7, 455–462. doi: 10.1166/sam.2015.1989
- Rana, M., Dauda, S., Mohd, R., Mohd, A., Jarin, S., and Tomal, A. (2017). A review on recent advances of CNTs as gas sensors. *Sens. Rev.* 37, 127–136. doi: 10.1108/SR-10-2016-0230
- Robertson, J. (2004). Realistic applications of CNTs. *Mater. Today* 7, 46–52. doi: 10.1016/S1369-7021(04)00448-1
- Tabtimsai, C., Keawwangchai, S., Wanno, B., and Ruangpornvisuti, V. (2011). Gas adsorption on the Zn-, Pd- and Os-doped armchair (5,5) single-walled carbon nanotubes. *J. Mol. Model.* 18, 351–358. doi: 10.1007/s00894-011-1047-y
- Tang, S., Chen, W., Xu, L., and Gao, T. (2017). Fabrication of Ag-doped ZnO nanoparticle gas sensor and its application in detection of CO. *Nanosci. Nanotechnol. Lett.* 9, 214–219. doi: 10.1166/nnl.2017.2313
- Wang, C., Yin, L., Zhang, L., Xiang, D., and Gao, R. (2010). Metal oxide gas sensors: Sensitivity and influencing factors. *Sensors* 10, 2088–2106. doi: 10.3390/s100302088
- Wang, J., Zhou, Q., Lu, Z., Wei, Z., and Zeng, W. (2019). Gas sensing performances and mechanism at atomic level of Au-MoS₂ microspheres. *Appl. Surf. Sci.* 490, 124–136. doi: 10.1016/j.apsusc.2019.06.075
- Wei, Z., Zhou, Q., Lu, Z., Xu, L., Gui, Y., and Tang, C. (2019). Morphology controllable synthesis of hierarchical WO₃ nanostructures and C₂H₂ sensing properties. *Phys. E Low Dimens. Syst. Nanostruct.* 109, 253–260. doi: 10.1016/j.physe.2019.01.006
- Yoon, B., Choi, S.-J., Swager, T., and Walsh, G. (2018). Switchable single-walled carbon nanotube-polymer composites for CO₂ sensing. *ACS Appl. Mater. Interf.* 10, 33373–33379. doi: 10.1021/acsami.8b11689
- Zaporotskova, I., Boroznina, N., Parkhomenko, Y., and Kozhitov, L. (2017). Carbon nanotubes: sensor properties. A review. *Modern Electr. Mater.* 2, 95–105. doi: 10.1016/j.moem.2017.02.002
- Zhang, X., Cui, H., Gui, Y., and Tang, J. (2017). Mechanism and application of carbon nanotube sensors in SF₆ decomposed production detection: a review. *Nanoscale Res. Lett.* 12:177. doi: 10.1186/s11671-017-1945-8
- Zhou, Q., Umar, A., Sodki, E., Amine, A., Xu, L., Gui, Y., et al. (2017a). Fabrication and characterization of highly sensitive and selective sensors based on porous NiO nanodisks. *Sens. Actuators B Chem.* 259, 604–615. doi: 10.1016/j.snb.2017.12.050
- Zhou, Q., Xu, L., Umar, A., Chen, W., and Kumar, R. (2017b). Pt nanoparticles decorated SnO₂ nanoneedles for efficient CO gas sensing applications. *Sensors and Actuators B Chem.* 256, 656–664. doi: 10.1016/j.snb.2017.09.206
- Zhou, T., Liu, X., Zhang, R., Wang, L., and Zhang, T. (2018). Constructing hierarchical heterostructured Mn₃O₄/Zn₂SnO₄ materials for efficient gas sensing reaction. *Adv. Mater. Interf.* 5:1800115. doi: 10.1002/admi.201800115

Conflict of Interest: The authors declare that the research was conducted in the absence of any commercial or financial relationships that could be construed as a potential conflict of interest.

Copyright © 2020 Tang, Chen, Zhang, Song, Li and Wang. This is an open-access article distributed under the terms of the Creative Commons Attribution License (CC BY). The use, distribution or reproduction in other forums is permitted, provided the original author(s) and the copyright owner(s) are credited and that the original publication in this journal is cited, in accordance with accepted academic practice. No use, distribution or reproduction is permitted which does not comply with these terms.



Study on Interaction Between TATA-Box Binding Protein (TBP), TATA-Box and Multiprotein Bridging Factor 1(MBF1) in *Beauveria bassiana* by Graphene-Based Electrochemical Biosensors

OPEN ACCESS

Edited by:

Mingshui Yao,
Kyoto University, Japan

Reviewed by:

Dianping Tang,
Fuzhou University, China
Jie Wang,
South China Agricultural
University, China
Lingfang Wang,
University of Electronic Science and
Technology of China, China

*Correspondence:

Xiaogang Lin
xglin@cqu.edu.cn

Specialty section:

This article was submitted to
Nanoscience,
a section of the journal
Frontiers in Chemistry

Received: 29 January 2020

Accepted: 23 March 2020

Published: 15 April 2020

Citation:

Song C, Peng Z, Lin X, Luo H,
Song M, Jin L, Xiao X and Ji H (2020)
Study on Interaction Between
TATA-Box Binding Protein (TBP),
TATA-Box and Multiprotein Bridging
Factor 1(MBF1) in *Beauveria bassiana*
by Graphene-Based Electrochemical
Biosensors. *Front. Chem.* 8:278.
doi: 10.3389/fchem.2020.00278

Chi Song¹, Zhijia Peng², Xiaogang Lin^{2*}, Haoyue Luo², Min Song², Lifeng Jin²,
Xiangyue Xiao¹ and Hong Ji¹

¹ Department of Life Science and Technology, Changshu Institute of Technology, Changshu, China, ² Key Laboratory of Optoelectronic Technology and Systems of Ministry of Education of China, Chongqing University, Chongqing, China

The regulation of transcription level is an important step in gene expression process. *Beauveria bassiana* is a broad-spectrum insecticidal fungi widely used in the biologic control of arthropod. The regulation of its transcription level is a multilevel complex process. Multiprotein bridging factor 1(MBF1) is a transcriptional co-activator that bridges sequence-specific activators and the TATA-box binding protein(TBP). Little is known about the interaction between MBF1, TBP, and TBP binding to DNA(TATA-sequences)in filamentous fungi of *Beauveria bassiana*. The binding of TBP to TATA-box and TBP to MBF1 was investigated via electrochemical biosensor. Graphene oxide has an electronic mobility that is unattainable for any metal, so it will be highly sensitive as a test electrode. Hence, we developed a simple, sensitive and specific sensor based on an TBP probe and graphene oxide that successfully detected the interaction of TBP and TATA-box or MBF1. From the electrochemical impedance spectroscopy (EIS), we find that the radius will increase when adding TATA-box or MBF1 buffer to the modified TBP protein electrode. When adding no TATA-box or no MBF1, the radius is relatively unchanged. The interaction between TBP and TATA-box or MBF1 was proved based on the results. These data confirmed the specificity of the interactions, (1) our developed graphene-based electrochemical biosensor can be used for monitoring the interaction between TBP and TATA-box or MBF1, (2) TBP can bind to TATA-box, (3) TBP can bind to MBF1, and (4) TBP mediates the interactions of MBF1 to DNA. Therefore, this work provided a label-free, low-cost and simple detection method for the complex process of eukaryotic gene transcription regulation.

Keywords: *Beauveria bassiana*, TATA-box binding protein (TBP), multiprotein bridging factor 1(MBF1), graphene oxide, electrochemical impedance spectroscopy (EIS)

INTRODUCTION

Transcription factors are a major group of important protein factors in cell life activities. They are active in the nucleus and regulate the expression of genetic genes, thus affecting all aspects of life. Transcription is a complex process of synthesis of RNA catalyzed by RNA polymerase, in which DNA is used as template and ATP, CTP, GTP, and UTP are used as raw materials. The transcription of eukaryotic cells can be divided into three categories according to different RNA polymerases: (1) RNA polymerase I transcription rRNA; (2) RNA polymerase II transcription mRNA; (3) RNA polymerase III transcription tRNA and other small RNA.

The TATA-box binding protein (TBP) is a key protein in transcription initiation of eukaryotic cells. And it is a universal transcription factor with 30 kD. At the same time, it is required for transcription initiation of RNA polymerase and the only universal transcription factor that can specifically bind to DNA (Lee and Young, 2000). In most eukaryotes, the TBP protein binds to a conserved sequence called TATA-box at about 25 bp on the promoter (Kornberg, 2007). TBP is an important component of transcription factor IID (TFIID). It, together with other transcription factors, constitutes TATA binding protein-related factors involved in transcription initiation and regulation of transcription activity (Tang et al., 1996).

At present, studies have found that nearly 30 species of protein can interact with TBP to form TATA binding protein-related factors (Davidson, 2003). Binding of TBP to the transcription coactivator MBF1 (Takemaru et al., 1997) *in vivo* and *in vitro* has been reported in humans, arabidopsis, and yeasts (Mariotti et al., 2000; Brendel et al., 2002; Liu, 2003).

In this work, in order to study the binding of TBP with TATA-box or MBF1 in filamentous fungus, we attempted to establish a biosensor based on electrochemical impedance spectroscopy to carry out the study. Graphene or graphene oxide (GO) has carrier mobility inaccessible to any metal and as a test electrode that is high sensitive to changes in electrochemical parameters (Shu et al., 2018; Zeng et al., 2018). The unique capacity of graphene or graphene oxide (GO) in adsorbing biomolecules such as nucleic acids and proteins will make graphene biosensor more sensitive and target-specific than other detection methods, such as chromatography, colorimetry, and fluorescence analysis (Hu et al., 2011, 2012; Wang et al., 2011; Pei et al., 2012; Xing et al., 2012). In addition, Electrochemical Impedance spectrum (EIS) use a small amplitude sine wave voltage (or current) as the disturbance signal and make the response of the electrode system to produce the approximate linear relationship (Newman, 1989). It is a kind of measuring method of frequency domain, so it can get more dynamic information and electrode interface structure information than conventional Electrochemical methods (Newman, 1989). At present, most biosensors based on electrochemical impedance spectroscopy focus on the interaction between antibodies and antigens (Katz et al., 2004; Hou et al., 2014). The impedance change on the electrode surface was measured by the electrochemical system to reflect the binding effects of the antigens and antibodies (Hou et al., 2013). Based on the principle, we adopt a more

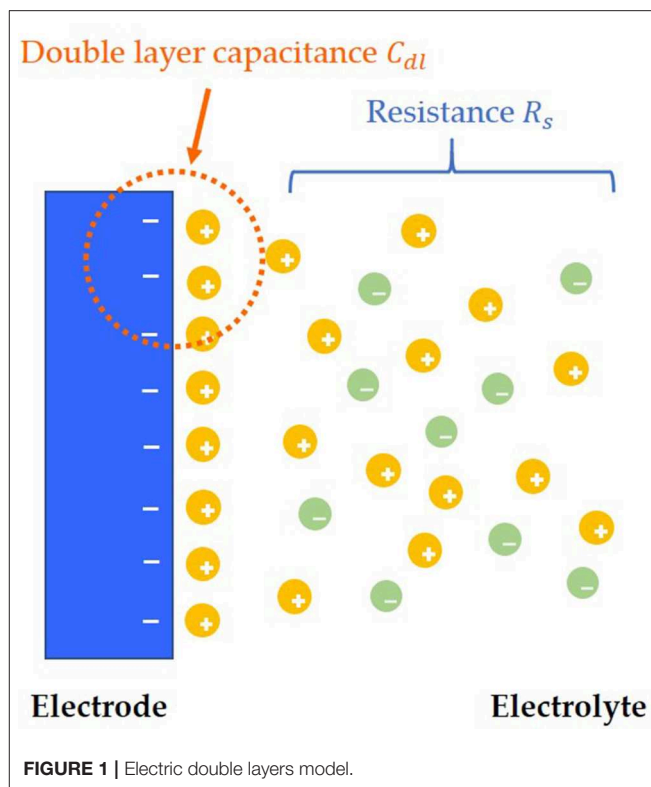


FIGURE 1 | Electric double layers model.

intuitive Nyquist diagram to reflect the binding effect of TBP and TATA-box or MBF1 in filamentous fungus (Hu et al., 2011). The variation of the semicircle radius in the Nyquist diagram reflects the impedance change at the electrode interface, so as to verify the binding effect of TBP and TATA-box or MBF1 in filamentous fungus.

MECHANISM OF EXPERIMENT

After adding solution to the surface of the electrode, the charges near the interface between the electrode and the solution will be redistributed, and the opposite charges will be equally distributed on both sides of the interface, thus forming the simplest electric double layers model, which is also called the Helmholtz electric double layers model (Helmholtz, 1879; Christine et al., 2001). However, there is a flaw in the Helmholtz model, which assumes that the capacitance C_{dl} of electric double layers is a constant value. However, in the experiment, C_{dl} is a variable, which can be influenced by relative potential and the concentration of electrolyte. According to the concept of Helmholtz model, the improved model of electrode and solution interface distribution is shown in Figure 1 (Helmholtz, 1879).

Both charge transfer and diffusion control the process. The Nyquist plots are made up of a semicircle in the high frequency region and a straight line with a dip angle of 45° in the low frequency region. The high frequency area is controlled by charge transfer, while the low frequency area is controlled by diffusion of solution. In an ideal situation, the typical EIS diagram obtained

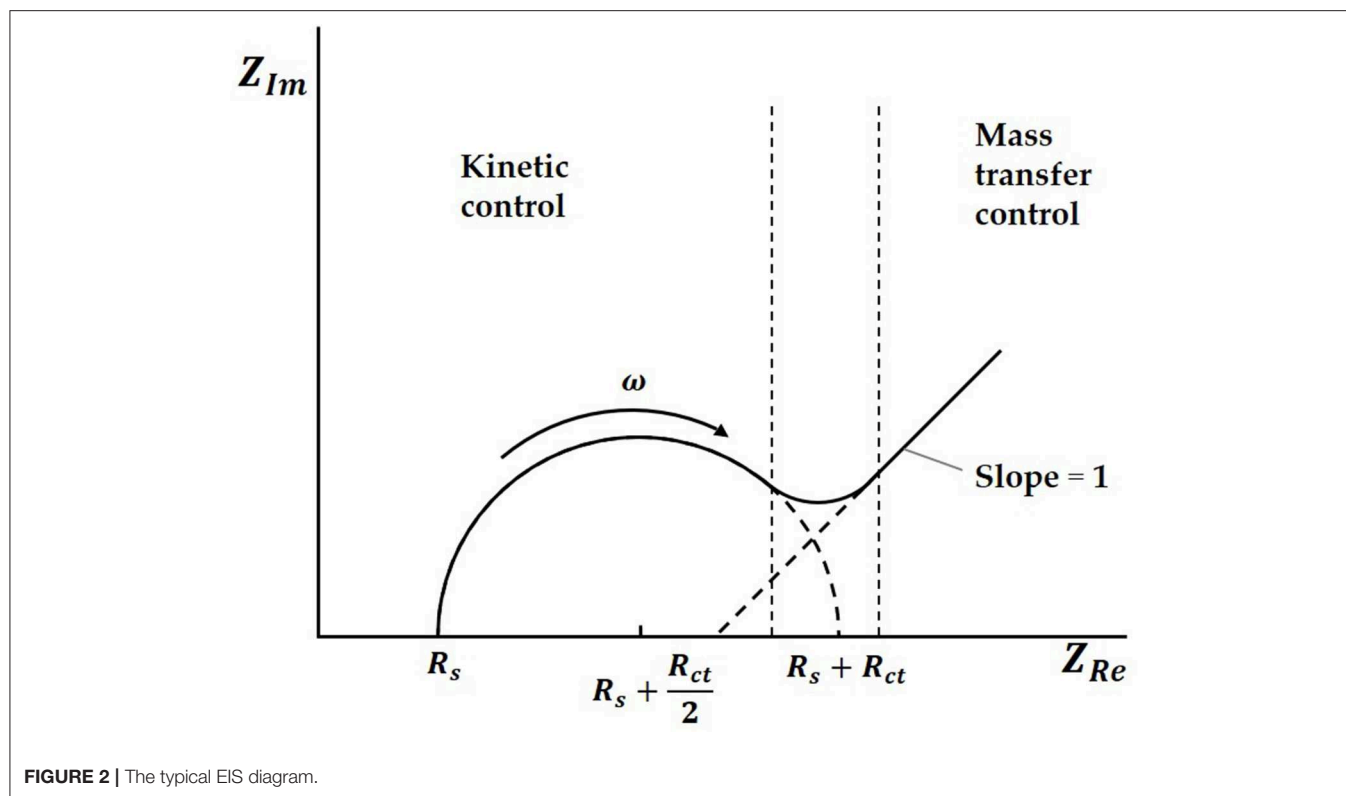


FIGURE 2 | The typical EIS diagram.

is a curve with a semicircle and tail, as shown in **Figure 2** (Prodromidis, 2010; Lu et al., 2011; Asadi et al., 2016).

In the Nyquist plots, we can calculate electrode resistance via the diameter of the semicircle. The larger the resistance, the larger the radius of the semicircle, which can directly reflect the changes in the electrode interface. In this work, when the solution was added to the electrode surface, the specific interaction between TBP protein and TATA-box, as well as the binding between TBP protein and BbMBF1 protein, will lead to the increase in the thickness of the electric double layers, resulting in the reduction of C_{dl} , as shown in **Figure 3** (Helmholtz, 1879). According to the equation (1) shows that when the electric double-layer capacitance C_{dl} decreases, the impedance Z of the equivalent circuit will increase, the corresponding radius of Nyquist plots will also increase.

$$Z = R_s + \frac{1}{j\omega C_{dl} + \frac{1}{R_{ct} + \sigma w^{\frac{1}{2}}(1-j)}} \quad (1)$$

Where R_s is the ohm internal resistance, R_{ct} is the charge transfer resistance, C_{dl} is the electric double-layers capacitance, σ is the diffused coefficient, ω is the angular frequency, j is the imaginary unit.

MATERIALS AND METHODS

Materials and Reagents

Beauveria bassiana ARSEF2860 was purchased from RW Holley Center for Agriculture and Health, Ithaca, NY, USA. Expression

carrier: pET-28-a (+) contains six histidine labels and was gained from Novagen (USA). T4DNA ligase was acquired from New England BioLabs. *Escherichia coli* Rosetta DE3 cells were purchased from Novagen (USA) and used for heterologous expression of proteins. *Escherichia coli* TOP10 were applied to vector transformation and plasmid amplification and purchased from Invitrogen (USA).

Methods

Heterologous Expression and Purification of BbTBP and BbMBF1

Before heterogenous expression and purification of TBP and MBF1, expression carriers of TBP and MBF1 were constructed. In order to build pET-28a-BbTBP and pET-28a-BbTBP recombinant vector, we applied T4DNA ligase to connect the target gene to the vector. The recombinant carrier was transformed into *E. coli* TOP 10 for transformation and extraction, thus obtaining the recombinant plasmid. The recombinant plasmids pET-28a-BbTBP and pET-28a-BbMBF1 were transformed into *E. coli* Rosetta DE3 cells of protein-expressing. According to the characteristics of host bacteria, different inducers were added to induce protein expression. The expression levels of BbTBP and BbMBF1 proteins were optimized based on induction time and temperature. Optimal conditions for large-scale expression of BbTBP and BbMBF1 were selected. The protein was purified according to the label of recombinant protein, then concentrated and dialyzed to obtain BbTBP and BbMBF1 proteins. This process of expression and purification is described in more detail in article (Chi et al., 2015). Among them,

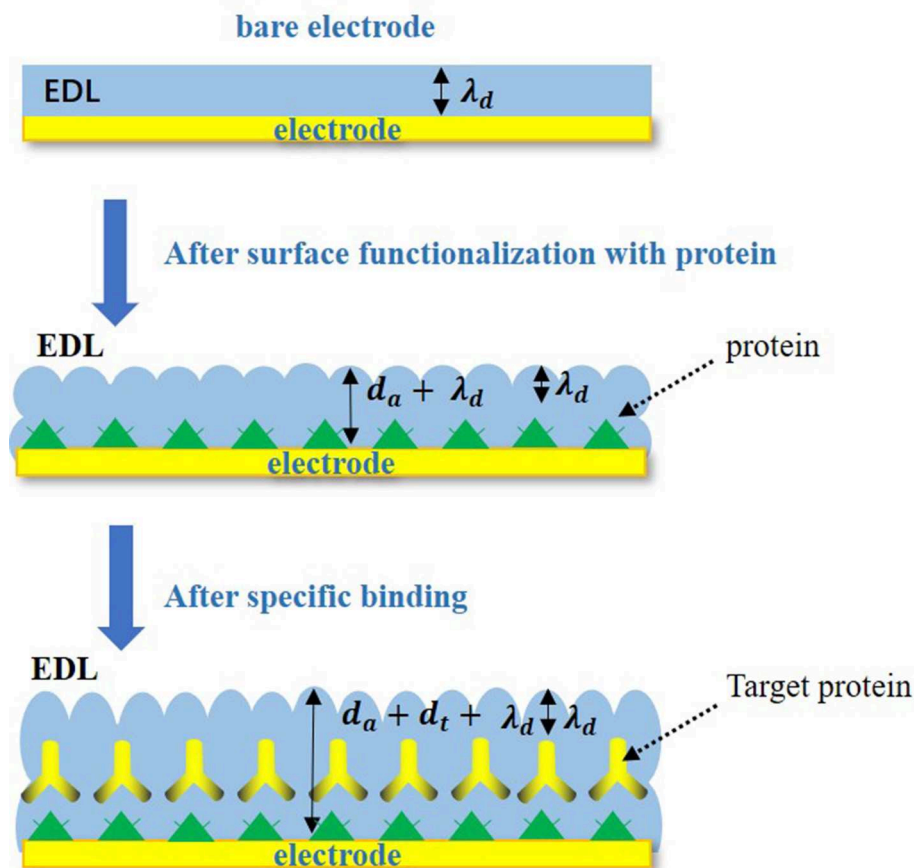


FIGURE 3 | Specific binding changes on electrode surface.

the concentration induced by BbTBP heterologous expression of IPTG was 0.3 mM, the induction temperature was 18°C and induction time was 12 h. BbMBF1 induce expression of IPTG at a concentration of 0.5 mM, and the induction condition was 30°C for 4 h.

Methods

An e-corder impedance analyzer (EDAQ Instruments, USA) was applied in this work. The specific electrode is a three-electrode system, the test electrode is a graphene electrode, the reference electrode is a platinum wire, and the connection electrode is an Ag/AgCl (saturated KCl) electrode. The three electrodes were placed in the potassium iron hydride electrolyte to keep distance from each other to prevent short circuit. Before testing the sample, the electrode assembly was verified by cyclic voltammetry and impedance method. And the cyclic voltammetry has a working potential of 0 ~ 0.65 V and a sweep speed of 0.1 V/S.

As shown in **Figure 4**, 2 μ l of the BbTBP protein sample contains a 6 \times His label was added dropwise to the graphene electrode for functionalization. After the sample was dried, the graphene electrode surface was detected impedance value. Then add the BbMBF1 protein or the nucleic acid sequence TATA-box to be tested to the middle of the electrode, and after drying, measure the change in the surface impedance of the graphene

electrode, and obtain the Nyquist plot. Using the impedance meter's own software ZMAN 2.2 to analyze the spectrum and obtain the impedance value of the electrode surface. In this work, BbTBP protein was firstly dropped onto the surface of graphene electrode and the changes of impedance on the electrode surface were measured. The Nyquist plot was acquired through measuring the current changes on the electrode surface via an electrochemical system, which could present the physical changes on the surface in a numerical way.

RESULTS AND DISCUSSIONS

EIS Analysis of BbTBP and TATA-Box Probes

The sensitivity and linear relationship of BbTBP protein binding test electrode were tested firstly. Two microliter BbTBP protein (0.26, 0.51, 1.02, 2.04, 3.06, 4.08, and 5.1 μ g) of different concentrations were dropped onto the electrode surface, and then the impedances of electrode surface were measured, respectively. In the **Figure 5A**, the radius of the semicircle increased with the increasing of concentration. Where the starting point of the semicircles were almost equal, the R_s resistance was almost unchanged. The increase of the radius represented the increase

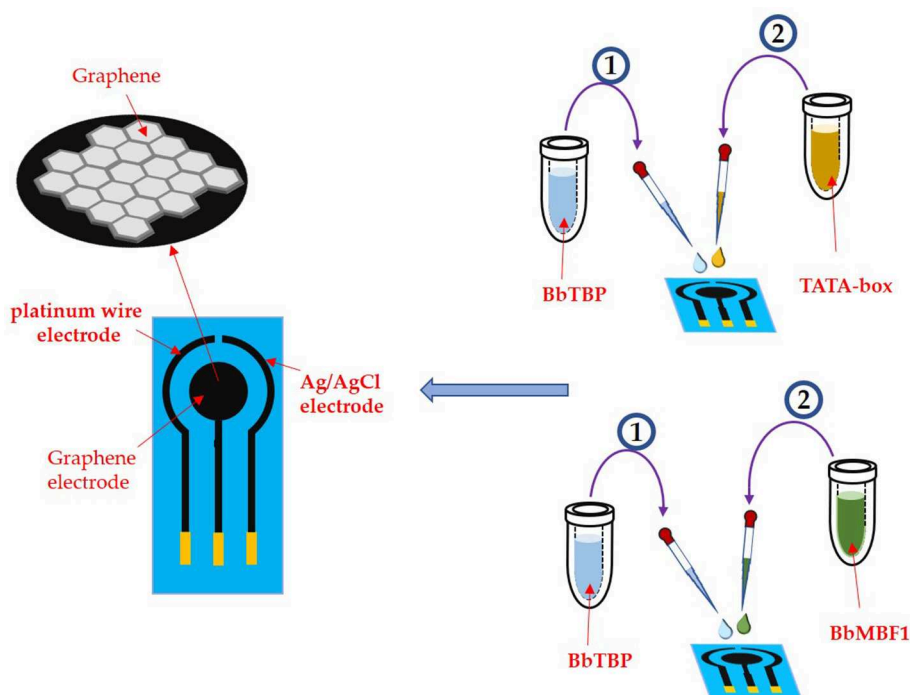


FIGURE 4 | Experimental process.

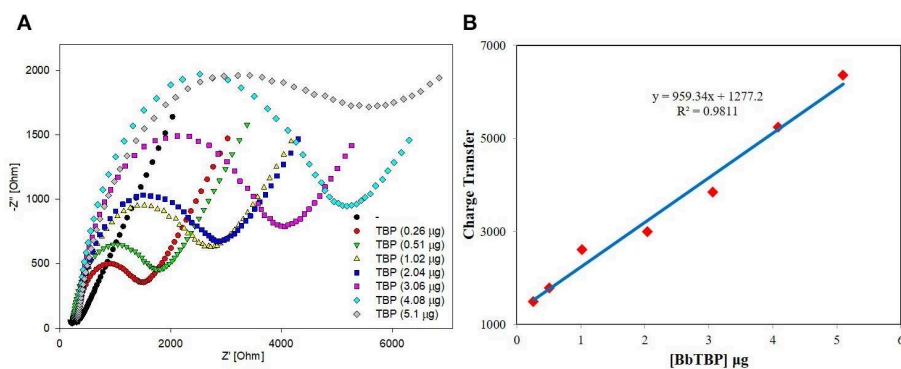


FIGURE 5 | Sensitivity and linearity of different concentration of BbTBP protein detected with test electrode. **(A)** The EIS diagram of different concentration of BbTBP. **(B)** The impedance of the sensor increased proportionally to the concentration of BbTBP.

of the transfer resistance R_{ct} , which reflected the strength of charge transfer at the interface. The stronger the charge transfer was, the larger the transfer resistance R_{ct} was, the smaller the interface capacitance C_{dl} was, and the impedance value on the corresponding electrode surface increased. This also indicated that with the increase of BbTBP protein concentration, more and more proteins adsorbed on the electrode surface, resulting in the increase in the thickness of the electric double layer and enhanced charge transfer, which increased R_{ct} and decreased C_{dl} . And the impedance of the equivalent circuit was also increased. From **Figure 5B**, we could see that the impedance of the electrode surface increased with the change

TABLE 1 | The nucleic sequences of TATA-box and no-TATA-box.

Name	Nucleic sequences
TATA-box	CAGTAAAGCTTGGTAGTATTT TATAT CTTCTCTCTTTAC
No TATA-box	CAGTAAAGCTTGGTAGTATTTCTTCTCTCTTTAC

of BbTBP protein concentration, showing a certain linear relationship ($R^2 = 0.9811$).

According to the experiment and detection principle of the BbTBP protein binding test electrode, a low concentration of

BbTBP protein (0.26 μg) was selected to detect its binding effect on TATA-box. Firstly, 2 μL , 0.26 μg of BbTBP protein was dropped onto the test electrode surface, and then 4, 8, 12, 18, and 20 ng TATA-box 1 nucleic acid sequences were sequentially added dropwise to the test electrode surface. The concentrations of TATA-box 1 is 80, 160, 240, 360, 400 nM. In order to evaluate the specificity of BbTBP and TATA-box, the concentrations 360 nM of TATA-box and no-TATA-box were kept as controls. At the concentration and same volume (2 μL), TATA-box 1 nucleic acid (24843Da) mass is 18 ng, and no-TATA-box nucleic acid (24073Da) mass is 17.4 ng. The nucleic sequences of tata-box and no-tata-box are shown in **Table 1**, the bold part is the TATA core sequence, and their masses are calculated by formula 2. Simultaneous detection of impedance changes on the test electrode surface. The results were shown in **Figure 6A**. It could be seen that the adsorptive behavior of TBP and controls were very different. But for control group, the Nyquist plots of the electrode surface without BbTBP protein were very similar. For TBP and TBP+no TATA DNA

(360 nM), the Nyquist plots of the electrode surface were very similar. And for TBP and TBP+ TATA DNA (360 nM), the Nyquist plots of the electrode surface were very different. It could be seen from the figure that the radius of Nyquist plot of the electrode surface with BbTBP protein increased with the addition of TATA-box 1 at different concentrations, indicating that the impedance of the electrode surface increased after the addition of TATA-box 1, which further proved that BbTBP protein and TATA-box 1 had binding effect on the electrode surface. **Figure 6B** was the impedance corresponding to the Nyquist diagram.

$$M = C \times V \times M_r \quad (2)$$

Where M is the mass, C is the concentration (mM), V is the volume (ml), M_r is the molecular weight (g/mol).

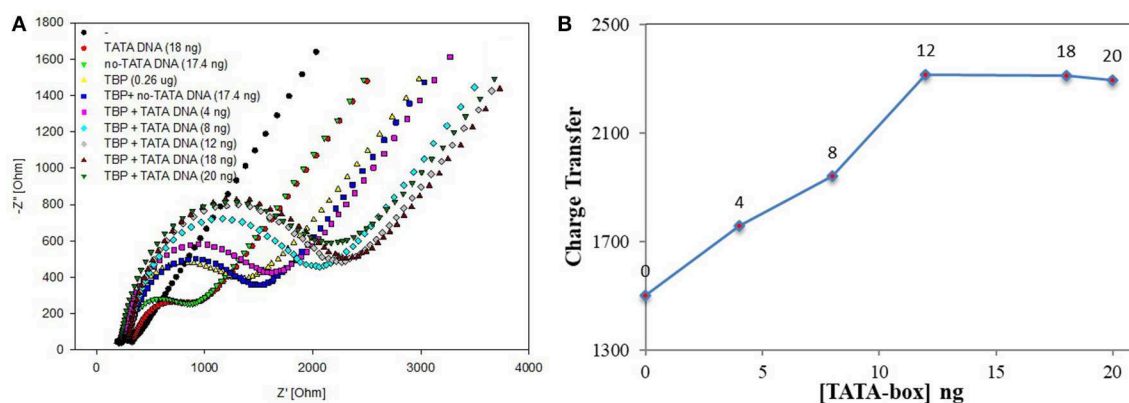


FIGURE 6 | EIS analyzed BbTBP with different concentration of TATA-box 1. **(A)** The EIS diagram of BbTBP changed with the addition of TATA-box 1 at different concentrations. **(B)** The impedance of the sensor changed with different concentration of TATA-box 1.

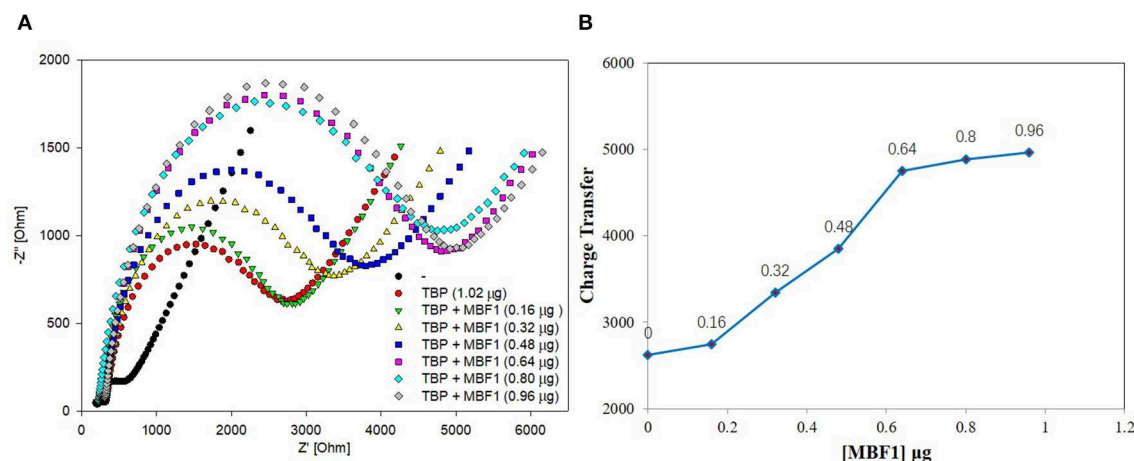


FIGURE 7 | EIS analyzed BbTBP with different concentration of BbMBF1. **(A)** The EIS diagram of BbTBP changed with the addition of BbMBF1 at different concentrations. **(B)** The impedance of the sensor changed with different concentration of BbMBF1.

EIS Analysis of the Interaction Between BbTBP and BbMBF1

The results of BbTBP protein and TATA-box electrochemical experiments showed that the electrochemical impedance spectroscopy could be used for the interaction between protein and nucleic acid. Similarly, the electrochemical system was also used to try to detect the possibility of protein-protein interactions. Firstly, the His-tag of the BbMBF1 protein was removed, we used the thrombin cleavage site on the expression vector pET28a to remove the BbMBF1 protein. Then, the digested protein was dropped onto the surface of the test electrode, and the impedance of the electrode surface was detected to verify the effect of the enzyme digestion. The enzyme digestion conditions of His-tag were determined by comparing the impedance of the blank electrode. The results were shown in **Figure 7**. Compared with the blank electrode, the enzyme-digested BbMBF1 protein was less adsorbed on

the electrode surface with the same impedance level as the negative control. This shows that the BbMBF1 protein His-tag was completely excised.

BbTBP containing His-tag of 1.02 μg was dropped onto the surface of the test electrode, and then the BbMBF1 protein containing His-tag of different concentrations were removed successively (0.16, 0.32, 0.48, 0.64, 0.8, and 0.96 μg). The impedance changes on the surface of the test electrode were detected by electrochemical system. As shown in **Figure 7**, it was obvious from **Figure 7A** that the semicircle radius increased with the increase of concentration of BbMBF1, which also reflected the binding effect between the BbTBP protein and BbMBF1 protein on the electrode surface. And with the increase of BbMBF1 protein concentration, the binding effect was enhanced, and binding was basically saturated at a certain concentration (0.64 μg). **Figure 7B** showed the impedance on the electrode surface with the increase of BbMBF1 protein concentration. It could

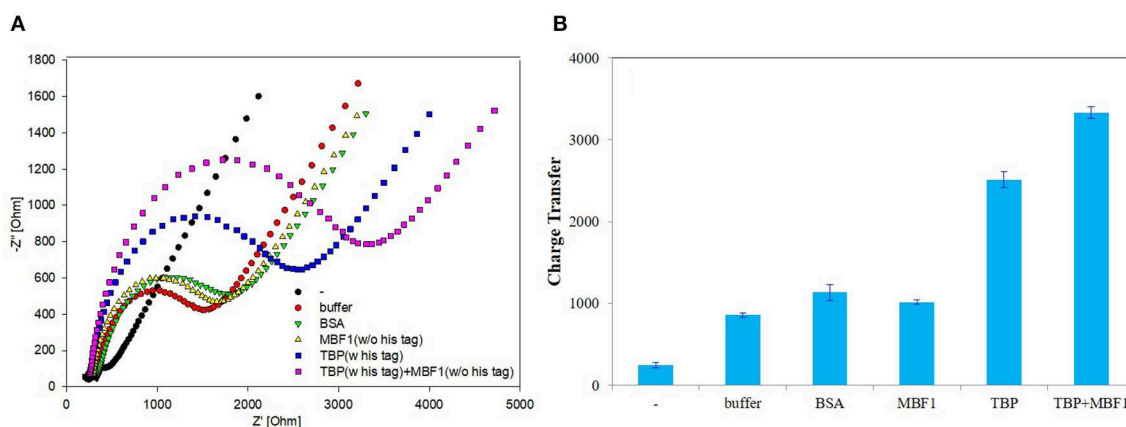


FIGURE 8 | Control 1 of EIS analyzed BbTBP with different concentration of BbMBF1. **(A)** The EIS diagram of BSA, buffer, BbMBF1, and BbTBP + BbMBF1. **(B)** The impedance of the sensor changed with BSA, buffer, BbMBF1, and BbTBP + BbMBF1.

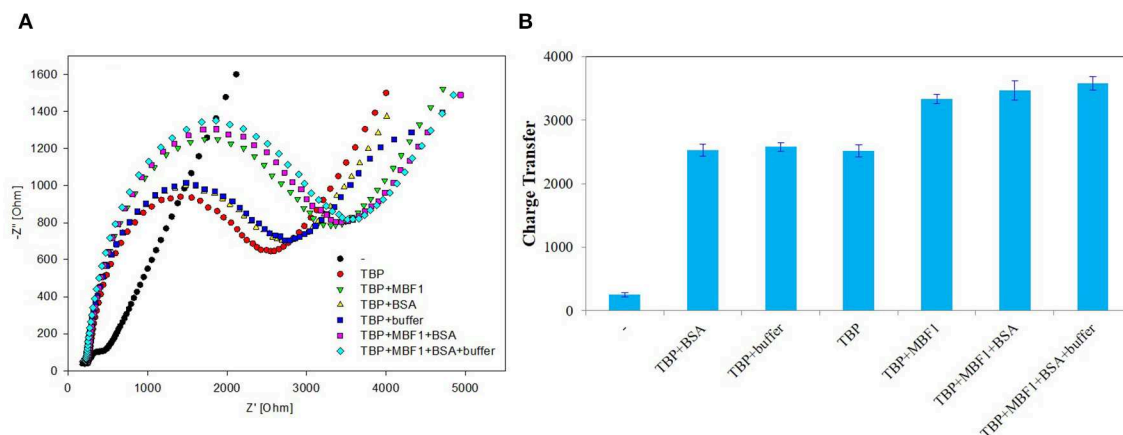


FIGURE 9 | Control 2 of EIS analyzed BbTBP with different concentration of BbMBF1. **(A)** The EIS diagram of BbTBP, BbTBP + BbMBF1, BbTBP + BSA, BbTBP + buffer, BbTBP + BbMBF1 + BSA, and BbTBP + BbMBF1 + BSA + buffer. **(B)** The impedance of the sensor changed with BbTBP, BbTBP + BbMBF1, BbTBP + BSA, BbTBP + buffer, BbTBP + BbMBF1 + BSA, and BbTBP + BbMBF1 + BSA + buffer.

be more intuitively seen from the figure that the changes of impedance on the electrode surface. This experiment showed that electrochemical impedance spectroscopy could also be used to detect protein-protein interactions.

In order to further determine the accuracy of the experiment, a detailed control experiment was conducted, as was shown in **Figures 8, 9**. The 1.02 μg BbTBP protein and 0.48 μg BbMBF1 protein were selected for electrochemical detection of the interaction. BSA and buffer were added as controls. **Figure 8** showed that the impedance on the surface of the BbMBF1 protein test electrode with only BSA, buffer and His-tag removed was only slightly higher than the blank electrode. After BbTBP was dropped, the impedance on the surface of the electrode was significantly higher. This indicated that the binding of BbTBP protein to the electrode was not disturbed by other factors. In addition, the effects of BbTBP protein and BbMBF1 protein were also unaffected by other factors.

DISCUSSION

To verify the interaction between BbTBP and TATA-box, this work tried a graphene biosensor based on electrochemical impedance spectroscopy. Firstly, BbTBP containing a histidine tag was combined with test electrode, which can specifically recognize TATA-box. By measuring the impedance changes of electrode surface to detect binding of BbTBP with TATA-box is effective and practical. Secondly, the interaction signal between BbTBP and BbMBF1 was acquired by the graphene-based electrochemical biosensors. The interaction between BbTBP and BbMBF1 was proved based on the results. Compared with gel migration experiment (Chi et al., 2015), DNase

footprinting method and chromatin immunoprecipitation, the method has label-free, simple operation, and low-cost. In addition, the use of the target-specific probe DNA imparts extraordinarily high selectivity to the sensor, so it provides a simple detection method for the complex process of eukaryotic gene transcription regulation.

DATA AVAILABILITY STATEMENT

All datasets generated for this study are included in the article/supplementary material.

AUTHOR CONTRIBUTIONS

CS, ZP, and HL: methodology, formal analysis, investigation, data curation, writing—original draft. XL: conceptualization, validation, writing—review and editing, supervision, project administration, funding acquisition. MS, LJ, XX, and HJ: resources, writing—original draft.

FUNDING

This work was supported by the Fundamental Research Funds for the Central Universities (Project No. 2019CDYGZD006), the Postgraduate education and teaching reform research project of Chongqing University (Project No. cqyjg18323), Venture & Innovation Support Program for Chongqing Overseas Returnees (cx2018017), Basic research on agricultural applications in Suzhou city (No. SNG201616) and Fundamental Research Funds for the Central Universities (No. 10611CDJXZ238826).

REFERENCES

- Asadi, M., Kim, K., Liu, C., Addepalli, A. V., Abbasi, P., Yasaei, P., et al. (2016). Nanostructured transition metal dichalcogenide electrocatalysts for CO₂ reduction in ionic liquid. *Science* 353, 467–470. doi: 10.1126/science.aaf4767
- Brendel, C., Gelman, L., and Auwerx, J. (2002). Multiprotein bridging factor-1 (MBF-1) is a cofactor for nuclear receptors that regulate lipid metabolism. *Mol. Endocrinol.* 16, 1367–1377. doi: 10.1210/mend.16.6.0843
- Chi, S., Almudena, O. U., Sheng-Hua, Y., Zhang, J. X., and Keyhani, O. (2015). Interaction between TATA-binding protein (TBP) and multiprotein bridging factor-1 (MBF1) from the filamentous insect pathogenic fungus *Beauveria bassiana*. *PLoS ONE* 10:e0140538. doi: 10.1371/journal.pone.0140538
- Christine, B., Bjarnason, B., and Johansson, G. (2001). Capacitive biosensors. *Electroanalysis* 13, 173–180. doi: 10.1002/1521-4109(200103)13:3<173::AID-ELAN173>3.0.CO;2-B
- Davidson, I. (2003). The genetics of TBP and TBP-related factors. *Trends Biochem. Sci.* 28, 391–398. doi: 10.1016/S0968-0004(03)00117-8
- Helmholtz (1879). Wise. Abhandl. physik. tech. *Reichsanstalt I*, 925.
- Hou, L., Cui, Y., Xu, M., Gao, Z., Huang, J., and Tang, D. (2013). Graphene oxide-labeled sandwich-type impedimetric immunoassay with sensitive enhancement based on enzymatic 4-chloro-1-naphthol oxidation. *Biosens. Bioelectron.* 47, 149–156. doi: 10.1016/j.bios.2013.02.035
- Hou, L., Gao, Z., Xu, M., Cao, X., Wu, X., Chen, G., et al. (2014). DNAzyme-functionalized gold-palladium hybrid nanostructures for triple signal amplification of impedimetric immunosensor. *Biosens. Bioelectron.* 54, 365–371. doi: 10.1016/j.bios.2013.11.014
- Hu, Y., Li, F., Bai, X., Li, D., Hua, S., Wang, K., et al. (2011). Label-free electrochemical impedance sensing of DNA hybridization based on functionalized graphene sheets. *Chem. Commun.* 47, 1743–1745. doi: 10.1039/C0CC04514D
- Hu, Y., Wang, K., Zhang, Q., Li, F., Wu, T., Niu, L., et al. (2012). Decorated graphene sheets for label-free DNA impedance biosensing. *Biomaterials* 33, 1097–1106. doi: 10.1016/j.biomaterials.2011.10.045
- Katz, E., Willner, I., and Wang, J. (2004). Electroanalytical and bioelectroanalytical systems based on metal and semiconductor nanoparticles. *Electroanalysis* 16, 19–44. doi: 10.1002/elan.200302930
- Kornberg, R. (2007). The molecular basis of eukaryotic transcription. *Proc. Natl. Acad. Sci. U.S.A.* 104, 12955–12961. doi: 10.1073/pnas.0704138104
- Lee, T. I., and Young, R. A. (2000). Transcription of eukaryotic protein-coding genes. *Annual Rev. Genet.* 34, 77–137. doi: 10.1146/annurev.genet.34.1.77
- Liu, Q.-X. (2003). Drosophila MBF1 is a co-activator for Tracheae defective and contributes to the formation of tracheal and nervous systems. *Development* 130, 719–728. doi: 10.1242/dev.00297
- Lu, C. H., Li, J., Zhang, X. L., Zheng, A. X., Yang, H. H., Chen, X., et al. (2011). General approach for monitoring peptide-protein interactions based on graphene-peptide complex. *Analyt. Chem.* 83, 7276–7282. doi: 10.1021/ac200617k
- Mariotti, M., De Benedictis, L., Avon, E., and Maier, J. A. M. (2000). Interaction between Endothelial Differentiation-related Factor-1 and Calmodulin *in vitro* and *in vivo*. *J. Biol. Chem.* 275, 24047–24051. doi: 10.1074/jbc.M001928200
- Newman, A. (1989). Biological binding system. *Google Patents*. 25, 1–12.

- Pei, H., Li, J., Lv, M., Wang, J., Gao, J., Lu, J., et al. (2012). A graphene-based sensor array for high-precision and adaptive target identification with ensemble aptamers. *J. Am. Chem. Soc.* 134, 13843–13849. doi: 10.1021/ja305814u
- Prodromidis, M. I. (2010). Impedimetric immunosensors—A review. *Electrochim. Acta* 55, 4227–4233. doi: 10.1016/j.electacta.2009.01.081
- Shu, J., Qiu, Z., and Tang, D. (2018). Self-referenced smartphone imaging for visual screening of H₂S using Cu x O-polypyrrole conductive aerogel doped with graphene oxide framework. *Analyt. Chem.* 90, 9691–9694. doi: 10.1021/acs.analchem.8b03011
- Takamaru, K. I., Li, F.-Q., Ueda, H., and Hirose, S. (1997). Multiprotein bridging factor 1 (MBF1) is an evolutionarily conserved transcriptional coactivator that connects a regulatory factor and TATA element-binding protein. *Proc. Natl. Acad. Sci. U.S.A.* 94, 7251–7256. doi: 10.1073/pnas.94.14.7251
- Tang, H., Sun, X., Reinberg, D., and Ebright, R. H. (1996). Protein-protein interactions in eukaryotic transcription initiation: structure of the preinitiation complex. *Proc. Natl. Acad. Sci. U.S.A.* 93, 1119–1124. doi: 10.1073/pnas.93.3.1119
- Wang, H., Zhang, Q., Chu, X., Chen, T., Ge, J., and Yu, R. (2011). Graphene oxide-peptide conjugate as an intracellular protease sensor for caspase-3 activation imaging in live cells. *Angew. Chem. Int. Edn.* 50, 7065–7069. doi: 10.1002/anie.201101351
- Xing, X. J., Liu, X. G., Yue-He, Luo, Q. Y., Tang, H. W., Pang, D. W., et al. (2012). Graphene oxide based fluorescent aptasensor for adenosine deaminase detection using adenosine as the substrate. *Biosens. Bioelectron.* 37, 61–67. doi: 10.1016/j.bios.2012.04.037
- Zeng, R., Luo, Z., Zhang, L., and Tang, D. (2018). Platinum nanozyme-catalyzed gas generation for pressure-based bioassay using polyaniline nanowires-functionalized graphene oxide framework. *Analyt. Chem.* 90, 12299–12306. doi: 10.1021/acs.analchem.8b03889

Conflict of Interest: The authors declare that the research was conducted in the absence of any commercial or financial relationships that could be construed as a potential conflict of interest.

Copyright © 2020 Song, Peng, Lin, Luo, Song, Jin, Xiao and Ji. This is an open-access article distributed under the terms of the Creative Commons Attribution License (CC BY). The use, distribution or reproduction in other forums is permitted, provided the original author(s) and the copyright owner(s) are credited and that the original publication in this journal is cited, in accordance with accepted academic practice. No use, distribution or reproduction is permitted which does not comply with these terms.



Application of Zero-Dimensional Nanomaterials in Biosensing

Zhengdi Wang, Tingting Hu, Ruizheng Liang* and Min Wei*

State Key Laboratory of Chemical Resource Engineering, Beijing Advanced Innovation Center for Soft Matter Science and Engineering, Beijing University of Chemical Technology, Beijing, China

OPEN ACCESS

Edited by:

Weiwei Wu,
Xidian University, China

Reviewed by:

Youbin Zheng,
Technion Israel Institute of
Technology, Israel
Cheng Zhou,
Tianjin University, China

*Correspondence:

Ruizheng Liang
liangruizheng2000@163.com
Min Wei
weimin@mail.buct.edu.cn

Specialty section:

This article was submitted to
Nanoscience,
a section of the journal
Frontiers in Chemistry

Received: 27 February 2020

Accepted: 30 March 2020

Published: 17 April 2020

Citation:

Wang Z, Hu T, Liang R and Wei M
(2020) Application of
Zero-Dimensional Nanomaterials in
Biosensing. *Front. Chem.* 8:320.
doi: 10.3389/fchem.2020.00320

Zero-dimensional (0D) nanomaterials, including graphene quantum dots (GQDs), carbon quantum dots (CQDs), fullerenes, inorganic quantum dots (QDs), magnetic nanoparticles (MNPs), noble metal nanoparticles, upconversion nanoparticles (UCNPs) and polymer dots (Pdots), have attracted extensive research interest in the field of biosensing in recent years. Benefiting from the ultra-small size, quantum confinement effect, excellent physical and chemical properties and good biocompatibility, 0D nanomaterials have shown great potential in ion detection, biomolecular recognition, disease diagnosis and pathogen detection. Here we first introduce the structures and properties of different 0D nanomaterials. On this basis, recent progress and application examples of 0D nanomaterials in the field of biosensing are discussed. In the last part, we summarize the research status of 0D nanomaterials in the field of biosensing and anticipate the development prospects and future challenges in this field.

Keywords: 0D nanomaterials, biosensing, ion detection, disease diagnosis, pathogen detection

INTRODUCTION

Nanotechnology has been a fast-growing field in the past few decades. By changing the chemical composition, atomic arrangement, or dimension of nanomaterials, many nanomaterials with alterations in physical and physicochemical properties are produced (Carneiro et al., 2019; Raja et al., 2019; Vikrant et al., 2019). Since the term “nano” was coined by Norio Taniguchi in 1974, zero-dimensional (0D) nanomaterials have been hailed as the forerunner of nanotechnology. Due to the inherent structural properties of 0D nanomaterials, such as ultra-small sizes and high surface-to-volume ratios, they have more active edge sites per unit mass. The edge and quantum confinement effects of 0D nanomaterials endow them with more improved or novel properties such as high photoluminescence (PL) quantum efficiency and chemiluminescence (Jiang and Tian, 2018; Chen J. B. et al., 2019; Farzin et al., 2019; Pirzada and Altintas, 2019). Up to now, various 0D nanomaterials have been extensively explored. For instance, graphene quantum dots (GQDs) (Qian et al., 2014; Lu et al., 2018; Yan et al., 2019), carbon quantum dots (CQDs) (Zheng et al., 2015; Li et al., 2018b; Pandit et al., 2019), fullerenes (Barberis et al., 2015; Zhang C. et al., 2018), inorganic quantum dots (QDs) (Freeman et al., 2012; Li et al., 2018a; Robidillo et al., 2019), magnetic nanoparticles (MNPs) (Yu et al., 2017; Bragina et al., 2019), noble metal nanoparticles (Yang C. T. et al., 2016; Jain and Chauhan, 2017; Bagheri et al., 2018), upconversion nanoparticles (UCNPs) (Cheng Z. H. et al., 2019; Gu et al., 2019) and polymer dots (Pdots) (Ou et al., 2019; Zhang H. et al., 2019) are all representative 0D nanomaterials with potential applications in materials science (Zhang X. et al., 2014), photovoltaic science (Guo et al., 2010), catalysis (Xu et al., 2015), energy (Guldi and Sgobba, 2011), sensing (Ramanathan et al., 2019), biomedicine (Yao et al., 2018) and nanodevices (Zhang Y. et al., 2014).

By changing the size of nanomaterials and converting them to zero-dimensional structures, the newly fabricated structure can be given novel properties that differ from those of higher-dimensional materials (Liang et al., 2014a). Compared with bulk high-dimensional nanomaterials, 0D nanomaterials are mostly spherical or quasi-spherical nanoparticles with a diameter of less than 100 nm (Liu J. N. et al., 2017; Chen J. B. et al., 2019; Sondhi et al., 2020). With such novel properties as optical stability, wavelength-dependent photoluminescence, chemical inertness, cellular permeability and biocompatibility, 0D nanomaterials offer great adaptability to biomedical applications such as nanomedicine, cosmetics, bioelectronics, biosensor and biochip (Koh and Josephson, 2009; Yao et al., 2018). Biosensor is considered as a reliable and usually portable tool for the rapid and cost-effective determination of analytes including biomolecules, antigens, proteins, biotoxins, DNA, viruses, bacteria and others. One of the main challenges in the field of biosensor is to develop highly sensitive biosensors by increasing the active surface area, electrochemical activity and conductivity or optical performance of biosensors (Pirzada and Altintas, 2019; Dhenadhyalan et al., 2020). Therefore, 0D nanomaterials as a powerful sensing material are utilized as an important probe to increase the sensitivity of biosensors and thus enhance their analytical performance due to their conductive properties and special optical properties (Carneiro et al., 2019; Sondhi et al., 2020).

Over the past few years, an increasing number of studies on 0D nanomaterials regarding their application in biosensors have been reported (Jiang and Tian, 2018; Chen J. B. et al., 2019), but few have provided a comprehensive overview of this application, which possesses great significance to the biosensing development of 0D nanomaterials. Therefore, this review intends to present an overview of the most frequently used 0D nanomaterials in the development of biosensing. Firstly, the structures and properties of these 0D nanomaterials are introduced. Subsequently, their application in ion, biomolecule and pathogen detection and disease diagnosis are discussed in detail for a comprehensive understanding of biosensors based on 0D nanomaterials. In the end, we summarize the research status of 0D nanomaterials in the field of biosensing, and anticipate the development prospects and future challenges in this field.

0D CARBON-BASED NANOMATERIALS

Carbon-based nanomaterials are one of the most widely studied materials in the field of nanotechnology due to their low cost of mass production, low intrinsic toxicity and multifunctional surface functionalization (Panwar et al., 2019). Because of these excellent properties, carbon-based nanomaterials have become promising alternatives to other nanomaterials in a variety of biological applications, such as imaging, sensing and drug delivery (Xu Q. et al., 2019). Among all these carbon-based nanomaterials, 0D carbon-based nanomaterials have inimitable electrical, optical properties, low toxicity and high quantum yield; therefore can be used to produce micro-sensors with superior performance and low power consumption (Shi et al., 2019; Zhou et al., 2019). In this section, we will give a detailed introduction

to the latest progress in the application of 0D carbon-based nanomaterials in the field of biosensing.

Graphene Quantum Dots

Graphene quantum dots (GQDs) are a new type of 0D graphene nanomaterials characterized by atom-thin graphitized planes (usually 1 or 2 layers, not exceeding 2 nanometers in thickness) and small transverse dimensions (<10 nanometers in general) (Chung et al., 2019; Li et al., 2019). One of the outstanding features of GQDs is PL. A large number of studies have demonstrated that the PL excitation and emission wavelength of GQDs can be changed by adjusting their dimension, morphology or dopant. The tunable PL property enables GQDs' use in bioimaging and biosensing. In addition, there are plenty of oxygen-rich functional groups at the edge of GQDs, which contributes to their good water solubility and biocompatibility (Sun et al., 2013). Furthermore, due to such advantages as anti-bleaching, luminescence stability and good conductivity, the application of GQDs in the field of biosensing has been further expanded (Zhu et al., 2015). Now, GQDs-based sensors are widely used in the detection of various ions and biomarkers as well as the diagnosis of major diseases.

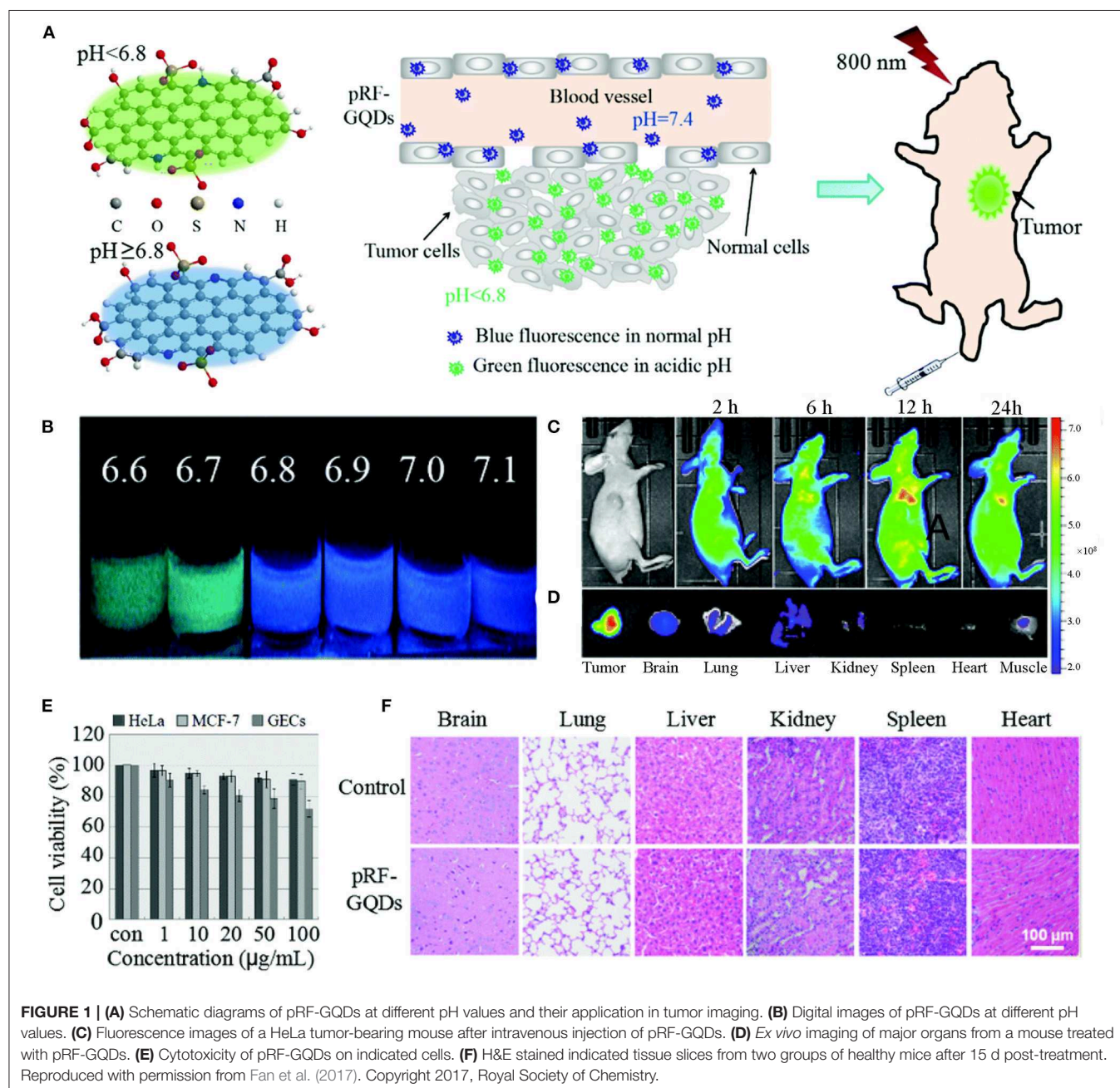
By virtue of their PL properties, GQDs have been used in the manufacture of many optical biosensors to detect various metal ions (Chung et al., 2019). For example, Pathan et al. constructed an aggregation-induced enhanced PL sensing system based on magnetic graphene oxide quantum dots (Fe-GQDs) to sensitively and selectively detect arsenic ions in contaminated water. The detection limit of Fe-GQDs for As^{3+} was 5.1 ppb, which is lower than the WHO allowable limit for arsenic in drinking water (10 $\mu\text{g/L}$) (Pathan et al., 2019). In another work, Qian et al. synthesized a fluorescent sensor based on GQDs–aptamer probe and graphene oxide (GO) to detect Pb^{2+} . The GQDs–aptamer served as the fluorophore for the detection of Pb^{2+} , and the unique electron transfer between GQDs and GO was used to achieve the efficient detection of Pb^{2+} . This nanosensor possessed a linear range of 400.0 nM and a detection limit as low as 0.6 nM. Due to the excellent biocompatibility of GQDs and GO, this sensing system was expected to be used for the detection of Pb^{2+} *in vivo* and *in vitro* (Qian et al., 2015).

In addition, GQDs-based biosensors play a significant role in the detection of biomarkers, such as ascorbic acid (AA), dopamine, DNA and amino acid. In a recent study, a sensitive and rapid fluorescence turn-on nanosensor based on orange emission GQDs was developed for the detection of AA. AA could consume hydroxyl radicals and recover the fluorescence of GQDs quenched by o-benzoquinone. Such a fluorescence switch mode provided the sensor with such advantages as universality and high selectivity. Besides, no heavy metal element was added to the system and thus avoided heavy metal contamination. According to the experimental results, the detection limit of this GQDs-based biosensor on AA was 0.32 μM , which was lower than that of other fluorescence biosensors. Glutathione (GSH) monitoring has received considerable attention for its vital role in human diseases (Liu H. et al., 2017). Yan et al. designed a fluorescence “turn-off-on” biosensor based on GQDs– MnO_2 nanosheets for the ultrasensitive detection of GSH in living

cells. The fluorescence intensity of GQDs was quenched by the fluorescence resonance energy transfer between MnO_2 and GQDs. After the nanometer sensor entered the cell, GSH could reduce MnO_2 nanosheets to Mn^{2+} cation so as to release GQDs and sufficiently recover the fluorescence signal. This sensing platform displayed a sensitive response to GSH with an ultralow detection limit of 150 nM (Yan et al., 2016).

Apart from the detection of small molecules, GQDs-based biosensors can also be used as tools to diagnose cancer (Xi et al., 2016). Because tumors can produce lactic acid and conduct adenosine triphosphate hydrolysis under anaerobic and energy-deficient conditions, their pH values are lower than those of

healthy tissues. This characteristic has been clinically exploited for efficient cancer diagnosis. A pH-responsive fluorescent sulfur-nitrogen-doped GQDs probe (pRF-GQDs) was constructed to distinguish tumors from normal tissues (Figure 1). The pRF-GQDs showed green PL in pH below 6.8 and transited into blue PL in pH overtop 6.8, a value matching the acidic extracellular microenvironment in solid tumors. The fluorescence switch was reversible and the fluorescence intensity was related to the degree of acidosis. The prepared pRF-GQDs showed excellent stability. The fluorescence intensity remained unchanged after continuous irradiation for 24 h. After the injection of pRF-GQDs, the tumor sites of tumor-bearing mice showed a strong green PL signal (Fan



et al., 2017). This GQDs-based biosensor has great potential to be used as a universal fluorescent probe to tumor diagnosis.

Carbon Quantum Dots

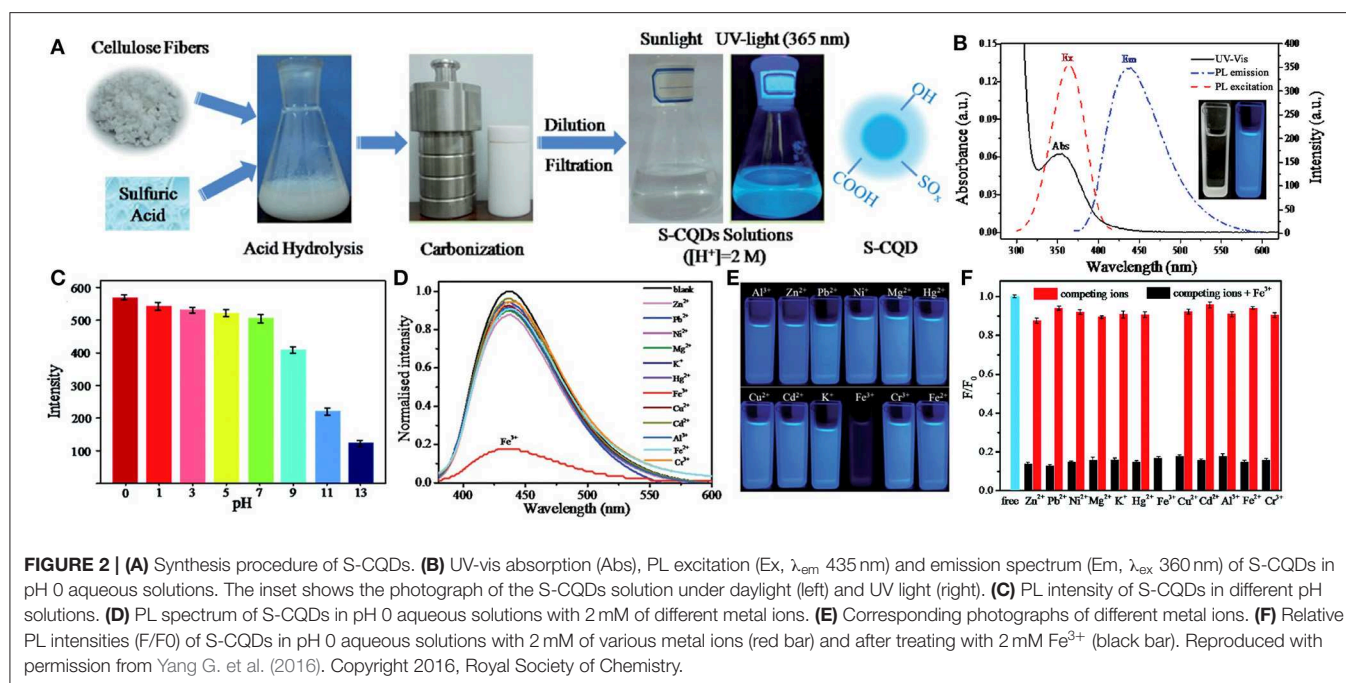
Carbon quantum dots (CQDs), commonly known as carbon dots (CDs), are quasi-spherical fluorescent particles with sizes <10 nm. Compared with GQDs, CQDs have poorer crystallinity, which is due to the lower content of crystalline sp^2 carbon and more surface defects (Pirzada and Altintas, 2019). CQDs possess excellent optical properties in fluorescence, chemiluminescence (CL) and electrochemiluminescence (ECL); therefore are widely used in fields of bioimaging, drug delivery and biosensing (Atabaev, 2018; Molaei, 2019b). Similar to GQDs, CQDs can be synthesized and functionalized quickly and easily. The doping or surface functionalization can further improve the topical chemical properties, optical properties, surface reaction activity and biocompatibility of CQDs, so as to improve their sensitivity as biosensors (Molaei, 2019a). In this part, recent advances of CQDs in ion detection and disease diagnosis are reviewed in detail.

The use of CQDs in metal ion sensing has been developing rapidly, and a large number of CQDs-based electrochemical and fluorescent sensors have been reported. For instance, Fan et al. constructed a functionalized CQDs-modified gating electrode for Cu^{2+} detection based on solution-gated graphene transistors. The combination of CQDs and Cu^{2+} led to the change of the capacitance of the double electrical layer near the gate electrode, which further led to the change of channel current. Since Cu^{2+} bounded with CQDs very well, the detection limit of Cu^{2+} in the CQDs-modified sensor was as low as 1×10^{-14} M (Fan et al., 2020). Another example of ion detection is the application of CQDs in the rapid quantitative detection of heavy metal contamination in water. Yang et al. synthesized a novel S-doped

CQDs (S-CQDs) with excellent selectivity and sensitivity for the detection of Fe^{3+} in pH 0 solutions (Figure 2). These S-CQDs exhibited strong acidophilia, high luminescence and high quantum yield (up to 32%) in strong acid solutions, and the detection limit for Fe^{3+} was as low as $0.96 \mu M$. S-CQDs also had robust stability. After 8 cycles, these pH-switch PL properties of S-CQDs were not significantly affected. These results showed that doped CQDs have a promising prospect in the detection of heavy metal pollutants in strong acid environments (Yang G. et al., 2016).

In addition, CQDs can also be utilized to detect intracellular biomolecules (Loo et al., 2016; Liu T. et al., 2017; Zhang Q. Q. et al., 2018). Selenoproteins are involved in a variety of cellular functions and are associated with various human diseases such as cancer and cardiovascular diseases. Wang et al. prepared a CQDs-based novel fluorescent nanoprobe for the fluorescence imaging of selenol *in vitro*. After selenocysteine treatment, the 2,4-dinitrobenzenesulfonyl chloride fragment of CQDs was split easily by selenolate to form yellow-green fluorescence CQDs. The prepared nanoprobe was highly sensitive and selective to selenol and could achieve the fluorescence imaging of exogenous and endogenous selenol in living cells. By adding different identifying elements, the functionalized CQDs were expected to be used to detect other biological analytes (Wang et al., 2017).

Besides, CQDs have been successfully used in cancer diagnosis. Lu et al. developed an ultra-sensitive fluorescent sensor platform based on nitrogen-doped CQDs (N-CQDs) for the detection of tumor invasive biomarker β -glucuronidase (GLU). In this sensor platform, N-CQDs with green PL were used as the fluorophore, and 4-nitrophenyl-catalyzed d-glucuronide served as the GLU substrate. The GLU catalytic product (p-nitrophenol) acted as a robust absorber to turn off the fluorescence of



N-CQDs. Therefore, the activity of GLU could be reflected by the fluorescence intensity of N-CQDs. The as-prepared sensor could detect GLU with high sensitivity and the detection limit was 0.3 U/L. This sensing strategy avoided complex modification of fluorophores or covalent bond connections between receptors and fluorophores; therefore provided a new idea for the development of sensitive sensors to detect tumor biomarkers by fluorescent CQDs (Lu et al., 2016).

Fullerenes

Fullerene is a molecular allotrope of carbon discovered in 1985 by Kroto et al. C₆₀, the most common fullerene, consists of five to six sp² hybrid carbon rings, forming a truncated icosahedron (Carneiro et al., 2019; Pirzada and Altintas, 2019). Fullerenes exhibit high electron affinity, large surface volume ratios and structural stability (Sun et al., 2018). With these characteristics, fullerenes are used in a diverse range of applications, including electronics, biology and medicine. In addition, fullerenes also possess good biocompatibility and inertia, and have good affinity with various organic molecules; therefore can be used to construct various biosensors (Winkler et al., 2006; Afreen et al., 2015). As a nanomaterial for amplifying detection signals, fullerenes are also used in the ultra-sensitive detection of analytes in different chemical and biological materials, such as amino acids, DNA and biomarkers for early-stage cancer diagnosis (Miyazawa, 2015).

Because of their large electroactive surface area, fullerenes are often used to construct electrochemical biosensors to detect amino acids. As an example, Jaiswal et al. produced a C₆₀-based electrochemical sensor to quantitatively distinguish D- from L- serine, which was essential to the function of central nervous system. This sensor demonstrated a very good analytical performance, showing a detection limit of 0.24 ng/mL for both isomerides. The experimental results showed that the C₆₀-based electrochemical sensor could maintain the original performance without current deviation, and was durable in water samples for up to 3 weeks. In view of this, this sensor had higher detection sensitivity, stability and repeatability than previously reported sensors. It could be a promising tool for the diagnosis of schizophrenia in clinical patients (Jaiswal et al., 2019).

In another study, a photoelectrochemical (PEC) biosensor based on fullerenes was prepared to detect DNA. Wang et al. synthesized a smart PEC biosensor based on Co₃O₄-fullerene to realize ultrasensitive DNA detection, in which p-n-sensitized heterostructure Co₃O₄-fullerene as an efficient sensitizer improved the photoelectric conversion efficiency greatly, making it 6 times higher than that of the fullerene alone (Figure 3). As reported, the Co₃O₄-fullerene biosensing structure was successfully used in the ultrasensitive investigation of model DNA (a fragment of the p53 gene) with a detection limit of 20 aM and a wide linear range from 60 to 1 × 10⁵ aM (Wang H. H. et al., 2019). This study opens a fascinating avenue to construct sensitized photoconductive candidates with excellent PEC performance

and exhibits significant application foreground in the detection of biomolecules.

Like QDs and CQDs, fullerenes also have their use in cancer diagnosis. For example, Yuan et al. constructed a sandwich-type electrochemical biosensor based on 4-MPBA@n-C₆₀-PdPt to detect tumor biomarkers α2,3-sialylated glycans. Maackia amurensis lectin (MAL) was fixed on Au-poly (Au-PMB) to form a specific recognition tool for α2,3-sial-Gs. Amino-functionalized fullerene (n-C₆₀) was introduced to the surface of PdPt bimetallic alloy to further improve the load capacity and conductivity of the sensor. The n-C₆₀ nanomaterial had a good electron transferability, which could accelerate the electron transfer rate and improve the sensitivity of the biosensor. The detection limit was observed to be as low as 3 fg/mL (S/N = 3). Moreover, this sensing platform exhibited good recovery and stability, indicating its potential application in clinical research (Yuan et al., 2018).

In conclusion, we have discussed three kinds of 0D carbon-based nanomaterials used in different sensors such as PL sensor, electronic sensor, electrochemical sensor and electrochemiluminescence sensor that can be applied to ion detection, biomolecular recognition and disease diagnosis (Sun et al., 2013; Raja et al., 2019; Dhenadhayalan et al., 2020). Although 0D carbon-based nanomaterials have been noticed by a lot of researchers, research on them is still in the initial stage. Current synthesis methods cannot control the structure of materials at the atomic level. Moreover, the fluorescence quenching mechanism of 0D carbon nanomaterials has not been well-explained. In the future, the synthesis accuracy and optical and electrical properties of 0D carbon-based nanomaterials should be studied, so as to prepare biosensors with more clinical application value.

QUANTUM DOTS

As fluorescent semiconductor nanocrystals, quantum dots (QDs) are generally prepared with atoms from group II-VI or III-V in the periodic table. The most common QDs, such as CdTe, CdSe, and InP, have potential applications in various biomedicine fields, including bioimaging, biosensing, and therapy (Wegner and Hildebrandt, 2015; Xiao et al., 2019). Because of the toxicity of heavy metals, the biocompatibility of inorganic QDs is generally questioned. To some extent, this problem is solved by the synthesis of QDs in aqueous solution, which improves not only the biocompatibility but also the water solubility and stability. Emerging heavy metal-free QDs such as SiQDs can also be an ideal alternative to commercially available cytotoxic CdTe and CdSe QDs (Keshavarz et al., 2018). QDs have been used to develop a variety of fluorescence, chemiluminescence and bioluminescence sensors due to their unique optical properties such as enhanced brightness, resistance to photobleaching, large absorption coefficient, narrow emission spectrum and size-tunable light emission (Liang et al., 2014b; Ma et al., 2019). In this section, we will focus on the application of QDs in biosensing in recent years.

Owning to their unique photochemical stability and high PL quantum yields, QDs have been widely employed in

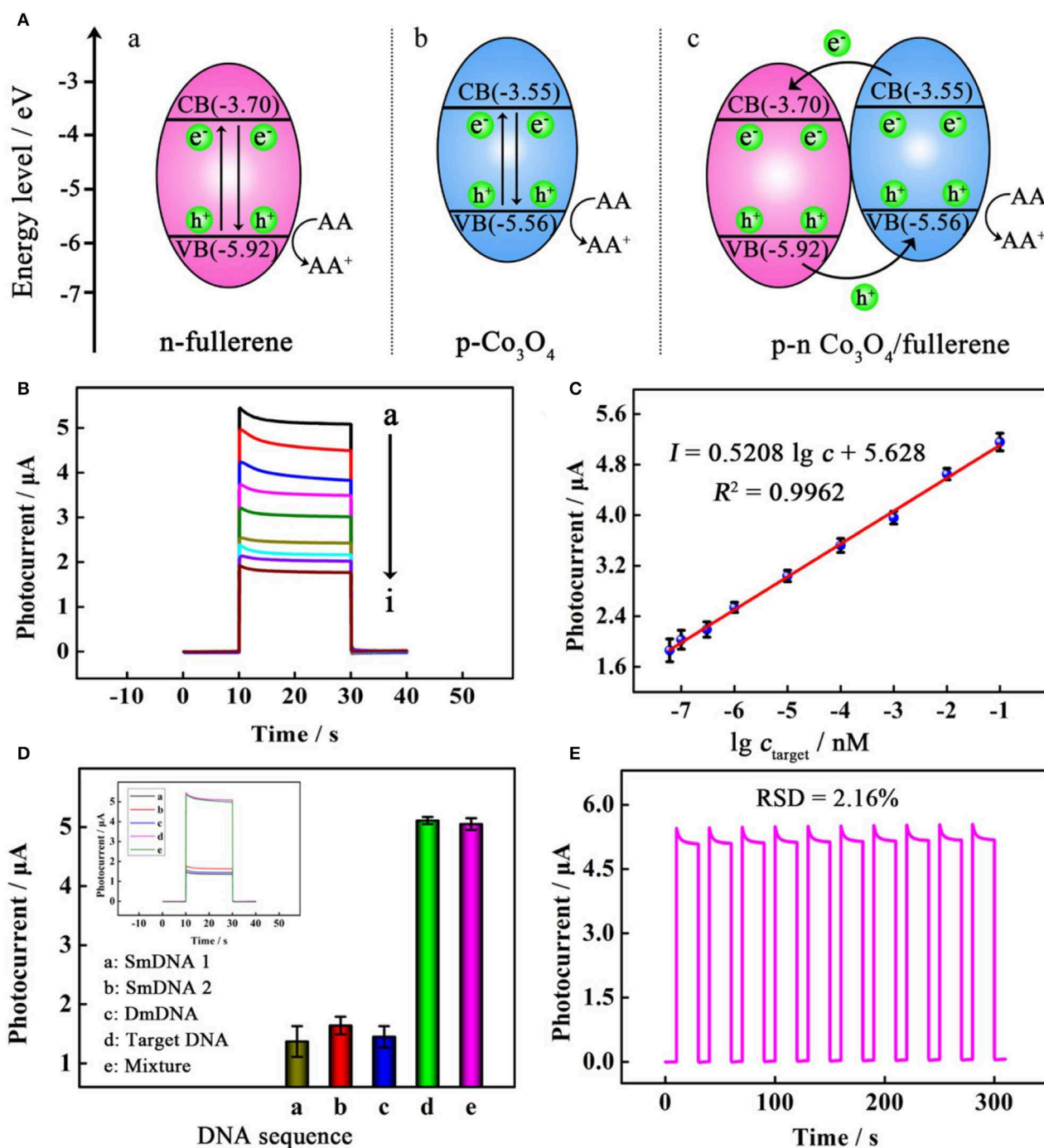


FIGURE 3 | (A) Schematic illustration of the proposed mechanism for the photocurrent responses of (a) n-fullerene, (b) p-Co₃O₄, and (c) p-n Co₃O₄/fullerene. (B) Photocurrent responses of the PEC biosensor toward a target at different concentrations (from top to bottom): (a) 100 pM, (b) 10 pM, (c) 1 pM, (d) 100 fM, (e) 10 fM, (f) 1 fM, (g) 0.3 fM, (h) 0.1 fM, and (i) 0.06 fM. (C) linear relationship between photocurrent responses and the logarithm of the target concentration. (D) selectivity with photocurrent responses in the inset for incubating different samples; and (E) stability of the PEC biosensor. Reproduced with permission from Wang H. H. et al. (2019). Copyright 2019, American Chemical Society.

pathogen detection. For example, Zhang et al. functionalized an integrated microfluidic chip with high-luminance QDs and magnetic nanoparticles for the detection and subtyping of

multiple influenza viruses (H9N2, H3N2, H1N1) simultaneously. By conducting superparamagnetic beads and QDs-assisted multiple DNA hybridization detection on microfluidic chips

with controlled micro-magnetic fields, H9N2, H3N2, and H1N1 cDNAs could be simultaneously detected within 80 min with a very low sample and reagent consumption (only 3 μ L). This was a convenient, time-saving, cost-effective, and highly sensitive way; therefore could be a powerful technology platform for the rapid detection of multiple influenza viruses (Zhang R. Q. et al., 2018).

In addition, water-soluble and low toxic QDs can be used for cell detection and dynamic evaluation. As a paradigm, Li et al. constructed a novel PEC biosensing platform combining near-infrared (NIR) Ag_2S QDs with AuNPs for the non-destructive analysis of living cells. The water-dispersed Ag_2S QDs were photoelectrochemically active species with excellent PEC properties under NIR. Under NIR light of 810 nm, the linear range in this strategy was 1×10^2 to 1×10^7 cells/mL, and the detection limit was 100 cells/mL (Li et al., 2018c). All these experimental results show that NIR QDs have a good application prospect in the construction of novel PEC platforms for the detection of biomolecules.

Moreover, QDs-based biosensors can be employed as universal tools to detect biomarkers of cancer and brain diseases. For instance, Li et al. designed a new kind of ECL biosensor based on CdSe@ZnS QDs that combined target

recovery amplification with a double-output conversion strategy to achieve the ultrasensitive detection of microRNA in human prostate cancer cells. Experimental results showed that the ECL biosensor could quantitatively detect miRNA-141 in a wide range from 100 aM to 10 pM with a detection limit of 33 aM (Li et al., 2017). In another work, Li et al. prepared a $\text{V\&A@Ag}_2\text{S}$ QDs fluorescent nanoprobe in the second near-infrared (NIR-II) window for the real-time *in vivo* imaging of early biomarkers of traumatic brain injury (TBI) (Figure 4). The fluorescence of Ag_2S was turned off due to the energy transfer from Ag_2S to A1094 chromophore. After intravenous injection, A1094 was bleached by the TBI precursor biomarker peroxynitrite (ONOO^-), achieving rapid recovery of Ag_2S QDs fluorescence. This NIR-II *in vivo* turn-on sensing and imaging strategy indicated a broad prospect of QDs fluorescence imaging in clinical applications (Li et al., 2020).

SiQDs are a new type of heavy metal-free QDs developed in recent years. They have the advantages of aqueous solubility, low cost, high quantum yield and strong resistance to photobleaching. Because of these interesting properties and good biocompatibility, SiQDs are widely used as fluorescent probes to detect small molecules, ions and biological macromolecules.

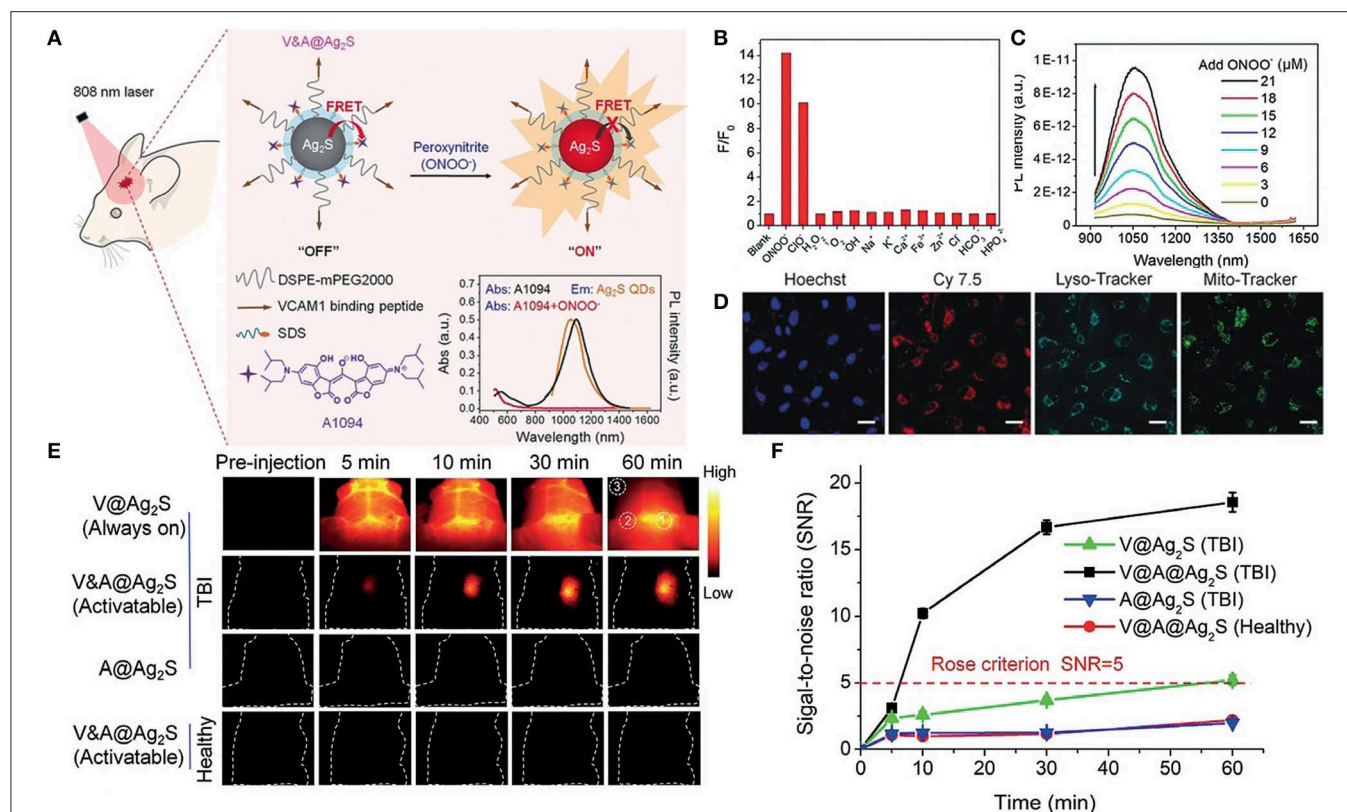


FIGURE 4 | (A) Schematic diagrams of the synthesis procedure of the $\text{V\&A@Ag}_2\text{S}$ probe and detection of ONOO^- *in vivo*. **(B)** NIR-II fluorescence intensity changes of $\text{V\&A@Ag}_2\text{S}$ upon the addition of various ROS/RNS analytes and ions. **(C)** Photoluminescence recovery of $\text{V\&A@Ag}_2\text{S}$ in aqueous solutions as a function of ONOO^- concentration. **(D)** Confocal fluorescence images of inflamed endothelial cells. The cells were incubated with Cy7.5-modified $\text{V\&A@Ag}_2\text{S}$ first and then further incubated with LysoTracker, MitoTracker, and Hoechst. **(E)** The timespan of NIR-II fluorescence in brain vascular injury and healthy mice at different time points after injection of $\text{V@Ag}_2\text{S}$, $\text{V\&A@Ag}_2\text{S}$, and $\text{A@Ag}_2\text{S}$. **(F)** Time-dependent signal-to-noise ratio (SNR) changes determined by the NIR-II fluorescence imaging of mice after various treatments. Reproduced with permission from Li et al. (2020). Copyright 2020, Wiley-VCH.

Li et al. prepared SiQDs through a one-pot approach by using 3-(aminopropyl)-trimethoxysilane (APTMS) as precursors. The incorporation of salicylaldehyde effectively inhibited SiQDs emission through nucleophilic reaction. In addition, the addition of Zn^{2+} led to the evolution of emission peak. The green band at 500 nm gradually shifted to the blue direction at 455 nm, and corresponding changes in the ratiometric signal (I_{455} / I_{500}) could accurately reflect the concentration of Zn^{2+} , with a detection limit of $0.17 \mu\text{M}$ (Li et al., 2018d). These fluorescence emission changes based on SiQDs would provide a new idea for the development of nanoscale functional sensors.

In general, we have introduced various biosensing applications of QDs in this part, which greatly improves the comprehension of QDs as potential biomaterials for biosensing applications (Wegner and Hildebrandt, 2015; Ma et al., 2019). QDs have a good affinity for biomolecules and their chemical and optical properties enable their use as optical sensors to detect various biomolecules (Yao et al., 2018). It is expected that more QDs-based research in fields of pathogen detection, non-destructive analysis of living cells and disease diagnosis will be conducted.

MAGNETIC NANOPARTICLES

0D magnetic nanoparticles (MNPs), with a size range of 1–100 nanometers, are composed of materials with high saturation magnetization, such as pure metals (Fe, Co, Ni), alloys (FeCo, permalloy, alnico) and oxides (Fe_3O_4 , CoFe_2O_4) (Lin et al., 2017; Gloag et al., 2019). MNPs have attracted extensive attention in hyperthermia treatment, biosensing and drug delivery due to their high saturation magnetization and superparamagnetism (Nabaei et al., 2018). Biosensors with 0D MNPs are important in the field of sensing because they provide viable solutions to the long-term challenge of low detection limits and non-specific effects (Morón et al., 2015). Modulation of the size, composition and magnetic properties of MNPs benefits their application in the ultralow detection of proteins, disease biomarkers and pathogens (Chen Y. et al., 2018; Knežević et al., 2019).

MNPs can be used for protein capture after combined with specific recognition molecules. For example, Chuah et al. synthesized anti-prostate-specific antigen (PSA)-labeled MNPs to selectively capture protein analyte PSA (Figure 5). In the external magnetic field, the (anti-PSA)-MNPs captured PSA and rapidly carried them into nanopores. After (anti-PSA)-MNPs captured PSA, they would form a sandwich complex with the anti-PSA antibodies in the nanopore. The magnetic field was then reversed to remove the (anti-PSA)-MNPs that did not capture PSA to avoid miscounting. The detection limit of this nanopore sensor was 0.8 fM, which was nearly an order of magnitude higher than that of the previous nanopore sensors. This MNPs nanopore blockade concept could be further expanded to other proteins with suitable antibodies (Chuah et al., 2019).

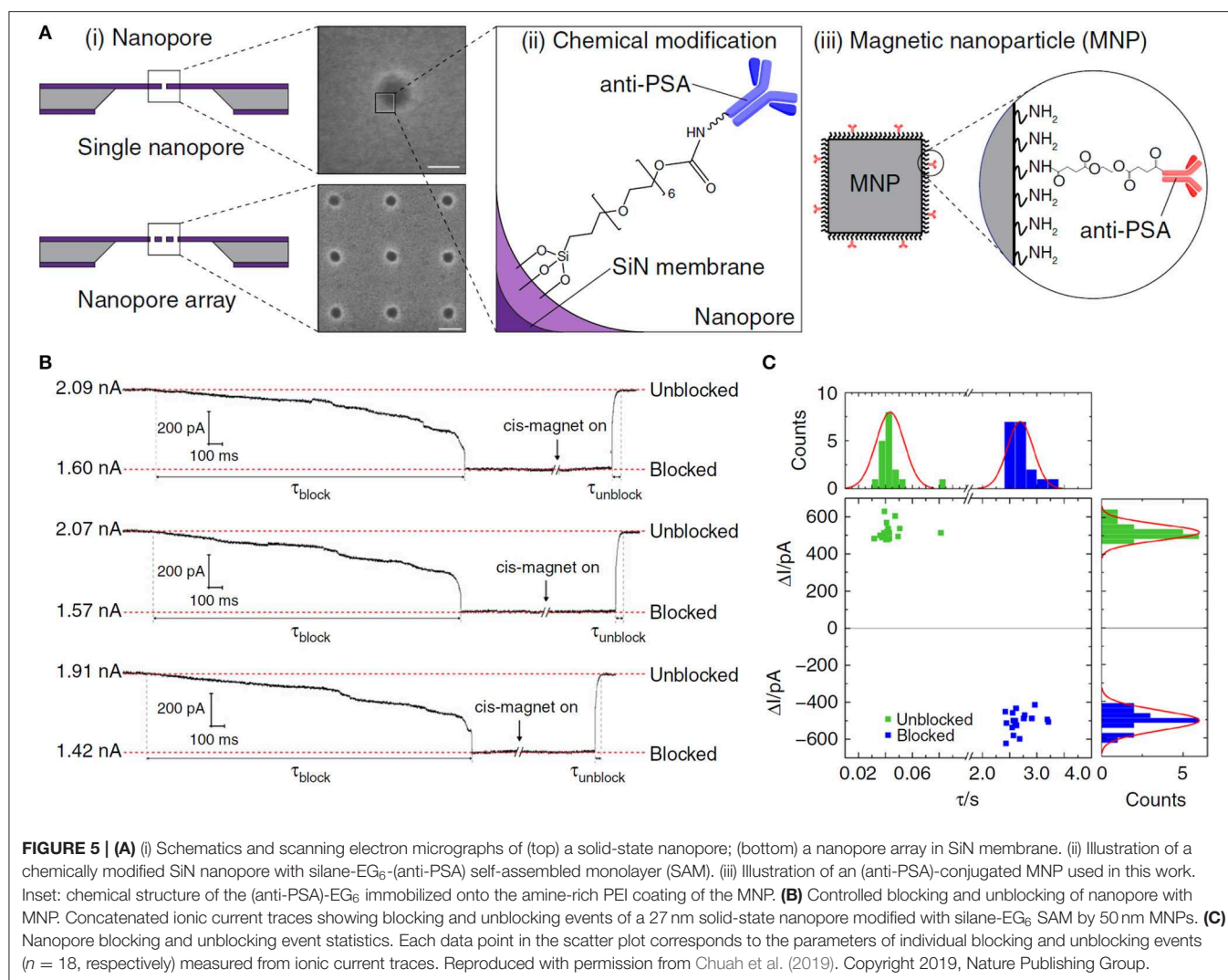
MNPs have exhibited tremendous potential in early-stage cancer diagnosis. The ability of biosensors to detect ultralow levels of circulating microRNAs in the blood is significant for

the development of liquid biopsies to monitor the progression of diseases. Tavallaie et al. synthesized a network of gold-coated MNPs modified by probe DNA (DNA Au@MNPs) to directly analyze nucleic acids in whole blood. The sensor for the first time detected the concentration of microRNA in untreated blood samples (10 aM to 1 nM). *In vivo* experiments showed that it could monitor the small changes in microRNA concentration in the blood of tumor-growing mice. The use of electrically reconfigurable DNA Au@MNPs network to supersensitively and directly detect microRNAs made the device a promising tool for cancer diagnosis (Tavallaie et al., 2018). In another study, Pal et al. designed an MNPs-Abs-based fluorescence spectroscopic platform to analyze ovarian cancer biomarkers [cancer antigen 125 (CA-125), β_2 -microglobulin (β_2 -M), and Apolipoprotein A1 (ApoA1)]. A sandwich method was established with the help of polyclonal antibodies. Sandwich particles were extracted from the sensing medium by magnetic force, and fluorescence changes at standard concentrations were monitored in real time. The detection limits were 7.7 ng/mL, 0.55 ng/mL and 0.26 U/mL respectively. The sensor also successfully distinguished ovarian cancer patients from healthy individuals with a sensitivity of 94% and a specificity of 98% (Pal et al., 2015).

MNPs-based biosensors have also been studied for the diagnosis of other diseases. Lee et al. constructed functionalized Au@ Fe_3O_4 core-shell structures to detect asthma biomarker eosinophil cationic protein (ECP). The core-shell magnetic nanostructures modified by cysteamine-tagged heparin (Hep) amplified the differences in electrochemical signals, thus increasing the sensitivity of the biosensor. This method provided a wide linear range of 1–1000 nM for the logarithmic analysis of ECP concentrations, with a determination coefficient of 0.992 and a detection limit of 0.30 nM. It could be applied to the sensitive detection of other analytes by replacing the Hep/ECP pair with a relevant probe/target combination (Lee et al., 2018).

The unique optical properties and magnetism of MNPs can be used to construct biosensors for pathogen detection. Alhogan et al. fabricated a low-cost colorimetric biosensor based on MNPs for the rapid clinical detection of *Pseudomonas aeruginosa*. The detection limit was as low as 10^2 cfu/mL within one min. This biosensor is expected to be a rapid medical device to diagnose *Pseudomonas aeruginosa*-related infections (Alhogan et al., 2019). As we know, Norovirus (NoV) can cause infectious diarrhea which is highly contagious and can spread quickly. Takemura et al. developed an AuNP/MNP hybrid nanocomposite for the hypersensitive detection of NoV. The high localized surface plasmon resonance (LSPR) effect was achieved by combining the AuNP/MNP hybrid nanocomposite with CdSeS QDs using anti-norovirus genome II antibody (Ab). This sensor system could be applied to norovirus detection in fecal samples with a detection limit of 0.48 pg/mL (Takemura et al., 2019).

To sum up, remarkable progress has been made in the application of MNPs to single-molecule detection, disease diagnosis as well as pathogen detection. In biosensing devices, MNPs can be assembled onto the sensor surface or used as labels (Weddemann et al., 2010; Chen Y. et al., 2018). In addition to the structure and composition of MNPs, the selection of surface functional groups and target molecules is also crucial to the



expansion of MNPs to a variety of biosensor applications (Chen et al., 2017; Avval et al., 2019). Moreover, the stability of MNPs is particularly important in biological systems where there are many oxidizing and reducing substances. A stable coating of the functionalized MNPs is essential to ensure that the MNPs do not accumulate or cause changes in their finely controlled magnetic properties. Therefore, adjusting the composition of MNPs and immobilizing appropriate functional groups on the surface play important roles in significantly improving the sensitivity and stability of biosensor pieces.

NOBLE METAL NANOPARTICLES

Noble metal nanoparticles are a kind of nanoscale ultrafine particles with totally different properties from macroscopic metals. They have attracted more and more attention due to their small sizes, good biocompatibility and excellent photophysical properties. In the presence of light, nanoparticles can generate electron resonance; therefore the scattering and absorption of

light can be easily enhanced (Chen J. B. et al., 2019; Zhao X. et al., 2019). Noble metal (gold, silver, etc.) nanoparticles as fluorescent probes have a broad application prospect in biomedical fields (Kim et al., 2017; Wang H. et al., 2019; Zhao Y. et al., 2019). Traditional organic fluorescent dyes often have the disadvantages of fast photobleaching rate, short fluorescence life and high biotoxicity, which can be overcome by the unique optical thermoelectricity and biocompatibility of noble metal nanoparticles (Koo Lee et al., 2009). In this section, we will focus on the application of noble metal nanoparticles as biosensors in biomolecular detection and disease diagnosis.

Gold Nanoparticles

Gold nanoparticles (AuNPs) are conductive materials with a large surface area and unique optical properties (Kurochkina et al., 2018). In AuNPs, the surface plasma was constrained to produce high LSPR (Pirzada and Altintas, 2019). By adjusting the size, shape and polymerization of AuNPs, it is possible to develop multifunctional AuNPs that can be used as optical and electrical biosensors (de la Escosura-Muñoz et al., 2016; Tian et al., 2016;

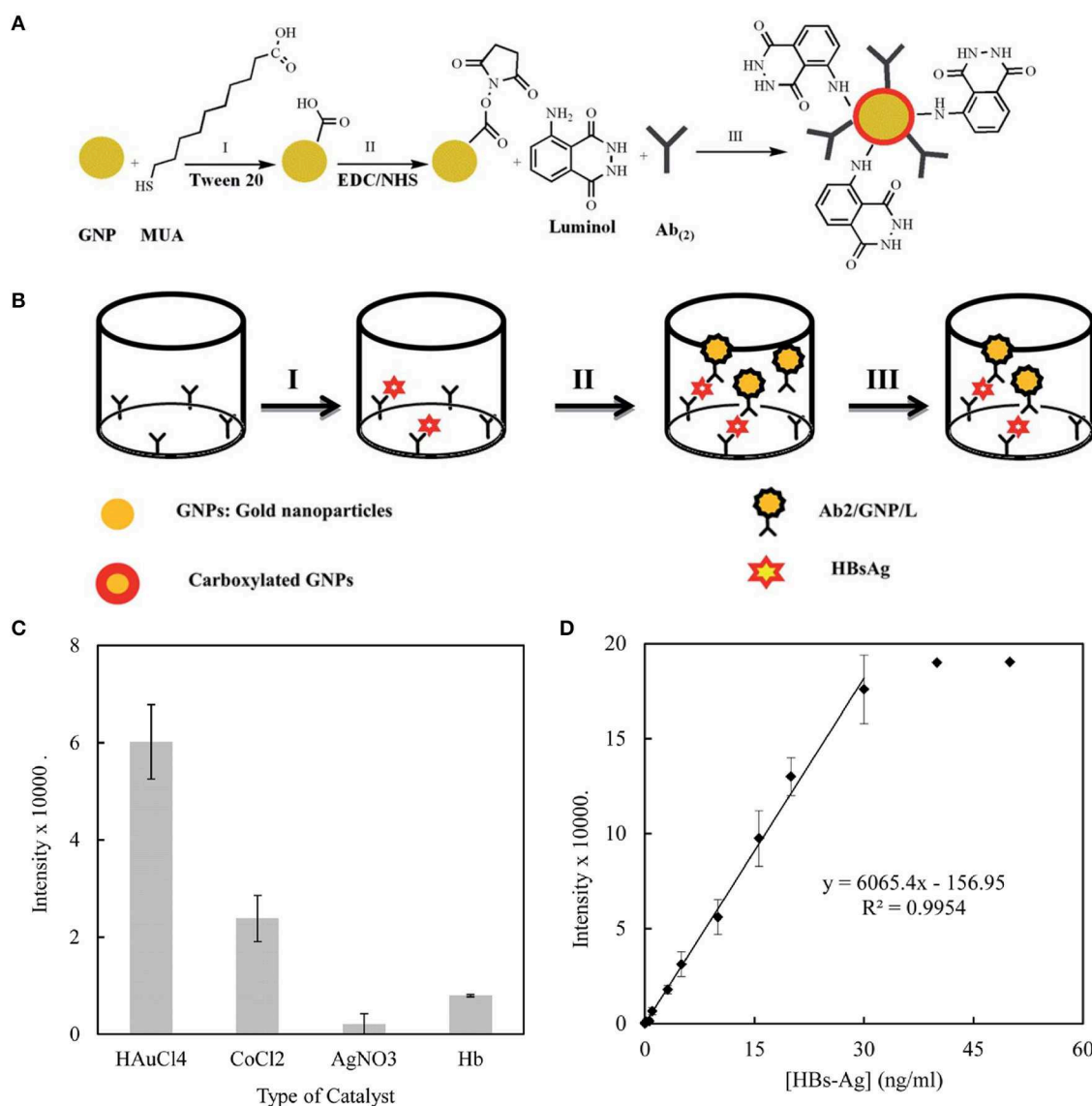


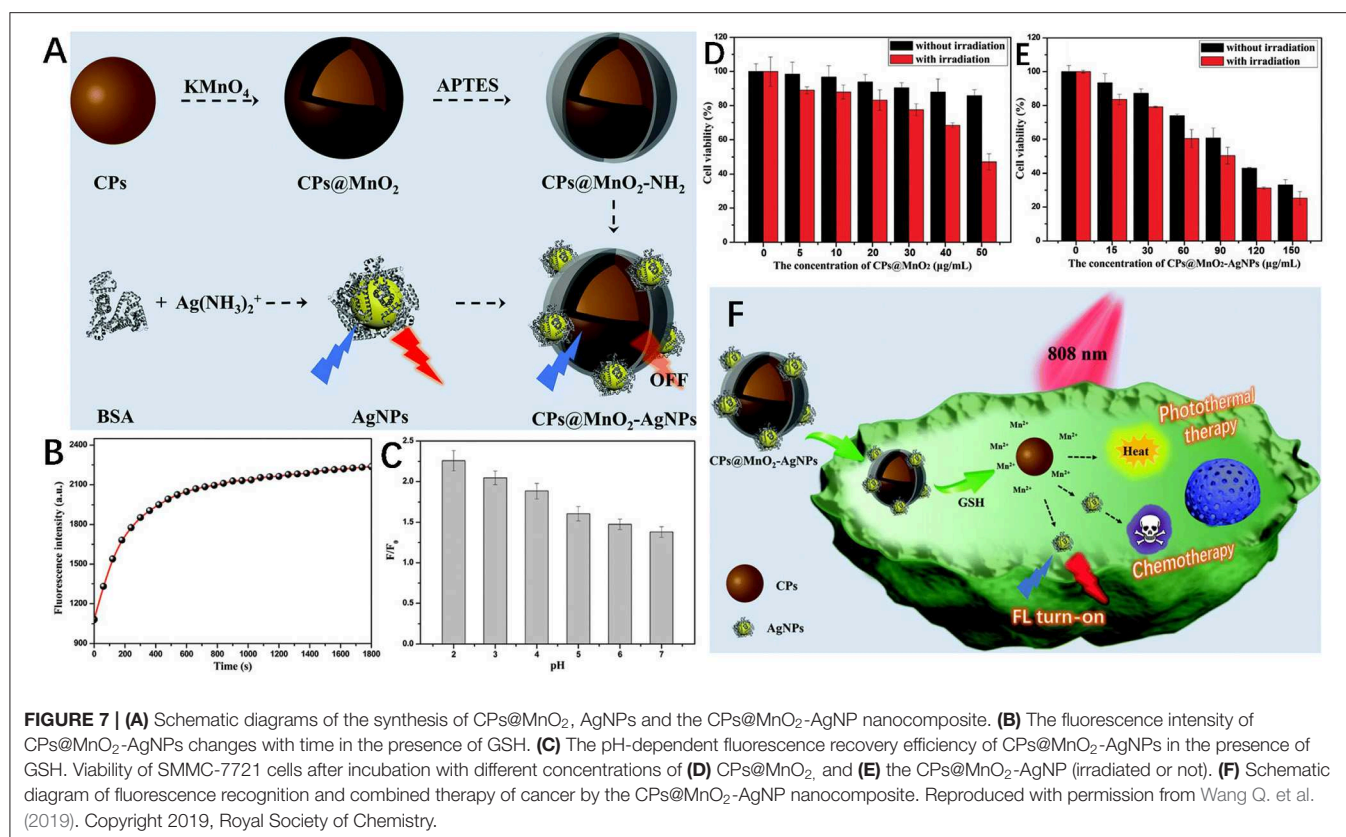
FIGURE 6 | (A) The process for the functionalization of the gold nanoparticles. **(B)** The process for the immune sandwich formation and chemiluminescence measurement. **(C)** A comparison of the effects of different catalysts on the immunoassay. The chemiluminescence intensity of the sandwich containing HBsAg (10 ng/mL) was recorded in the presence of H₂O₂ (10⁻³ M) and different catalysts at their optimized concentration: AgNO₃ 10⁻⁵ M, CoCl₂ 0.01 M, HAuCl₄ 0.1% w/v, Hb (150 mg/mL) in SCB (100 mM, pH 9). **(D)** The calibration curve of the immunosensor toward HBsAg. Reproduced with permission from Sabouri et al. (2014). Copyright 2014, Royal Society of Chemistry.

Mei et al., 2018). Currently, functional AuNPs used for detecting biomarkers for cancer, neurological diseases, proteins, nucleic acids, and various pathogens are extensively studied.

The excellent electrical conductivity of AuNPs can enhance the electron transfer between the redox center and the electrode surface, providing abundant active sites for the highly sensitive detection of cancer biomarkers by the biosensor electrode (Altintas et al., 2014; Yan et al., 2015; Jia et al., 2017). For instance, Tran et al. used AuNPs to develop a bimetallic nanocrystal platform for the highly sensitive detection of carcinoembryonic antigen (CEA). Since the combination of Au and Cu enhanced

the active surface area of Au and enhanced the interaction between these two components, this nanohybrid-based biosensor showed excellent electrochemical sensitivity to CEA detection with a very low detection limit (0.5 pg/mL), proving that the AuNPs-based sensor had potential application in the diagnosis of tumors (Tran et al., 2018).

Various clinically relevant compounds, including neurotransmitters and antigen, have been detected using AuNPs. Parkinson's disease (PD) is a common neurodegenerative disease whose standard treatment is levodopa supplementation. However, excess accumulation of levodopa can lead to



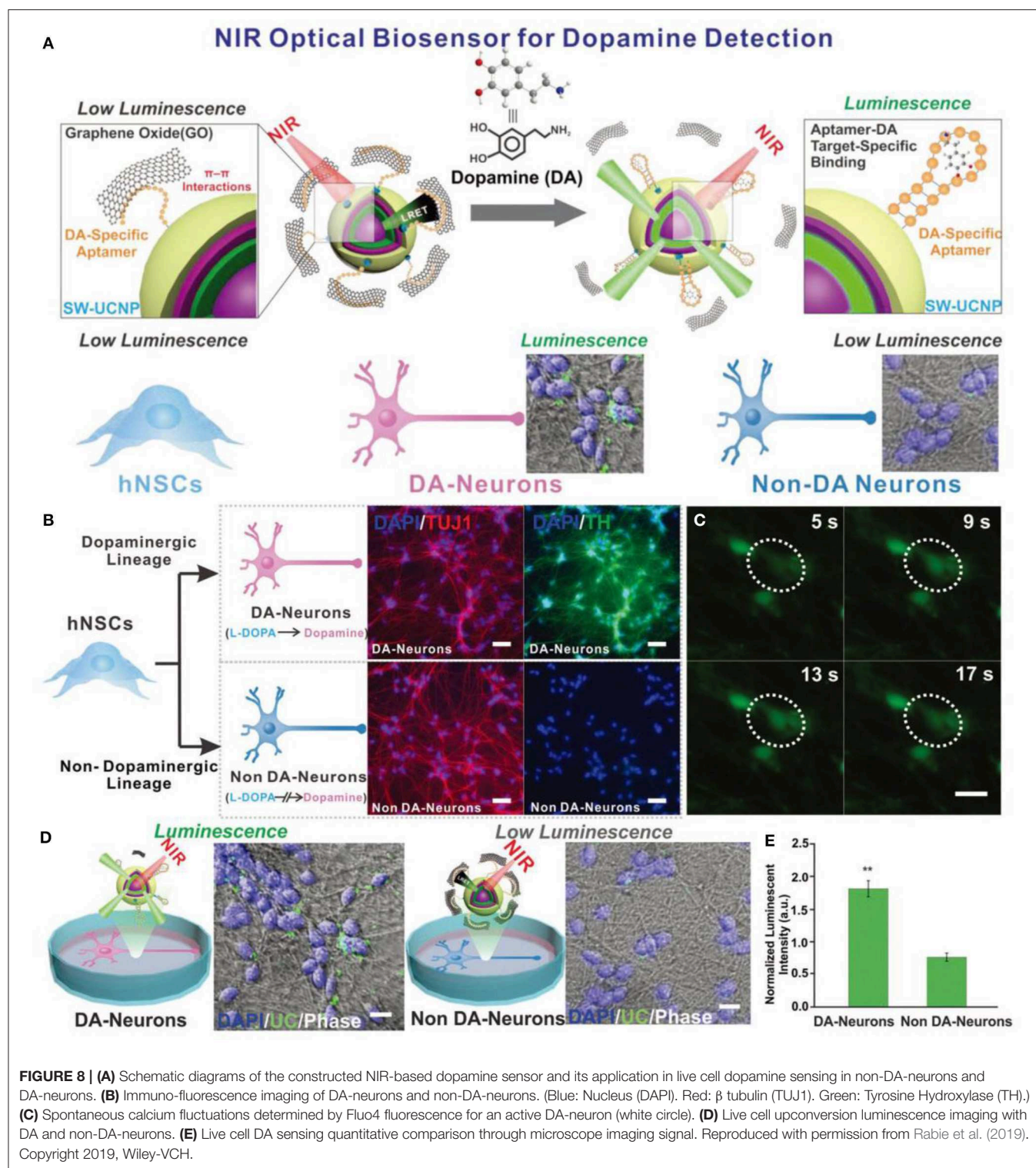
dyskinesia and emotional incontinence. Therefore, Ji et al. developed an AuNPs-based electrochemical detection system to monitor levodopa concentration in real time. In this system, AuNPs were used to modify the electrode to improve the electrical conductivity and electrocatalytic performance so as to increase the sensitivity of the sensor. This sensor could detect levodopa at concentration as low as 0.5 μ M in human serum (Ji et al., 2019). In another study, AuNPs were used to detect hepatitis B surface antigen. Sabouri et al. designed a gold nanoparticle-based immunosensor to detect HBsAg with a linear concentration range of 0.12 \sim 30 ng/mL and a detection limit of 14 pg/mL (Figure 6). The prepared immunosensor possessed the advantages of low cost, easy-to-operate and time-saving, and was expected to be used in clinical immunoassay (Sabouri et al., 2014).

AuNPs are also frequently used in pathogen detection (Altintas et al., 2018; Savas et al., 2018; Zhang X. et al., 2019). Outbreaks of zika virus (ZIKV) in the tropics have posed major challenges to global health in recent years. Steinmetz et al. constructed a novel impedance DNA biosensor based on an oxidized glassy carbon electrode. Due to the high surface area and high conductivity of AuNPs, the payload of the DNA probe increased obviously and the electrochemical response sensitivity of the developed biosensor was significantly improved. The detection limit of the device was determined to be 0.82 pM by electrochemical impedance spectroscopy (EIS). After 90 days of evaluation with EIS, the response of the sensor was about 98.0% of the initial response, indicating the good stability of

the biosensor. This the device was expected to be used as a commercially viable diagnostic tool for ZIKV (Steinmetz et al., 2019). Furthermore, AuNPs can be used to construct fluorescent sensors for pathogen detection due to their unique optical properties. Lee et al. used gold nanoparticle-decorated carbon nanotubes to construct a plasmon-assisted fluoro-immunoassay platform to detect influenza viruses. The minimum detection limit for the influenza virus was 0.1 pg/mL. This fluorescence immunoassay system also had good selectivity to influenza virus, which was 100 times higher than that of commercial diagnostic kits (Lee et al., 2015).

Silver Nanoparticles

Silver nanoparticles (AgNPs) have similar physical and chemical properties to gold nanoparticles and are commonly used in medical diagnosis. Due to the LSPR absorption, the optical properties of AgNPs are also influenced by their shape, size and degree of aggregation (Chen J. B. et al., 2019; Xu H. V. et al., 2019). However, AgNPs have fewer applications than AuNPs due to the concern about cytotoxicity. Nevertheless, the use of AgNPs in biomedical research is increasingly encouraged because of their antifungal and antibacterial properties (Malekzad et al., 2017; Pirzada and Altintas, 2019). In addition, AgNPs have attractive electrical properties. Compared with AuNPs of the same dimension, they have higher extinction coefficient and are more prone to electrochemical oxidation (Bahrami et al., 2016). In the field of biosensing, AgNPs have been widely used in



SERS-based biosensors to improve their performance due to their strong plasmon resonance characteristics.

AgNPs-based nanocomposites have excellent recognition ability and specific response in tumor microenvironment; therefore can be used for the biomolecular sensing of cancer

cells and cancer treatment. A notable feature of tumor microenvironment is that the GSH level is significantly higher than that of normal tissues (Gao et al., 2018; Peng et al., 2018). Wang et al. constructed a multifunctional nanosensor of carbon nanoparticles (CPs)@MnO₂-AgNPs for GSH sensing and cancer

TABLE 1 | Summary of 0D nanomaterial-based biosensors for disease diagnosis.

Sensor platform/label	Analyte	Experimental subject	Detection range	LOD	References
afGQDs	cTnl	Blood serum	0.001–1000 ng/mL	0.192 pg/mL	Bhatnagar et al., 2016
pRF-GQDs	Solid tumors	Mice	-	-	Fan et al., 2017
N-CQDs	GLU	Blood serum	1–60 U/L	0.3 U/L	Lu et al., 2016
nano-C ₆₀ /CdTe QDs	Thrombin (TB)	Blood serum	1 fM–10 nM	0.3 fM	Li M. et al., 2016
SnS ₂ QDs	anti-CMV pp65	Blood serum	1 fM–100 nM	0.33 fM	Lei et al., 2018
CdSe@ZnS QDs	miRNA-141	Cancer cells	100 aM–10 pM	33 aM	Li et al., 2017
V&A@Ag ₂ S QDs	ONOO ⁻	Mice	-	0.06 μM	Li et al., 2020
MNPs-Abs	CA-125, β2M, ApoA1	Blood serum	-	0.26 U/mL, 0.55 ng/mL, 7.7 ng/mL	Pal et al., 2015
rGO/Au	L-Cysteine	Cancer cells	-	0.51 nM	Thirumalraj et al., 2018
CPs@MnO ₂ -AgNPs	GSH	Cancer cells	0.8–80 μM	0.55 μM	Wang Q. et al., 2019
UCNP@SiO ₂ @Cy5-pep	Caspase-9	Mice	0.5–100 U/mL	0.068 U/mL	Liu L. et al., 2019

diagnosis (**Figure 7**). In this sensor, the AgNPs fluorescence was quenched by MnO₂ through internal filter effect and static quenching effect, and then recovered by GSH due to MnO₂ decomposition. The detection limit of GSH was as low as 0.55 μM. In addition, due to the photothermal activity of CPs and the chemotherapy effect of AgNPs as anti-proliferators, the prepared multifunctional nanocomposite could be used for cancer fluorescence identification and combination therapy (Wang Q. et al., 2019).

AgNPs have also been used to test various drugs and monitor their effects on human body. Recently, a sensitive biosensor based on AgNPs and electrochemical reduced graphene oxide nanocomposites (AgNPs: ErGO/PG) was developed to determine the effect of caffeine (CAF) on estradiol (EST) concentration in women of childbearing age (18–35 years). According to the analysis of EST and CAF in serum and urine samples of 5 women of child-bearing age, the detection limits of EST and CAF were 0.046 and 0.54 nM, respectively (Raj and Goyal, 2019). Mao et al. synthesized Au@Ag core-shell nanoparticles for the SERS detection of methylamphetamine (MAMP). Compared with AuNPs, SERS with a core-shell structure had better performance. By adjusting the concentration of MAMP adaptor modified on the surface of the sensing platform, the highly sensitive detection of MAMP was realized. The MAMP sensor had a wide dynamic range of 0.5 ppb to 40 ppb and a detection limit of 0.16 ppb. All these results indicated that AgNPs could be used for the rapid screening of abused illegal drugs and the detection of drug content *in vivo* (Mao et al., 2018).

AgNPs are one of the most widely used antibacterial nanomaterials. Apart from their use as antimicrobial agents, AgNPs are also broadly used in the construction of electrical analysis platforms due to their unique functions such as enhanced electron transfer and controlled electrode microenvironment (Zheng et al., 2018; Hussain et al., 2019). Yang et al. prepared vancomycin-functionalized AgNPs/3D-ZnO nanorod arrays for the detection and clearance of pathogenic bacteria. Based on Van's specific identification of gram-positive bacteria, the

constructed electrochemical platform was highly sensitive to the detection of staphylococcus aureus with a detection limit of 330 cfu/mL. Furthermore, the platform had a high antibacterial activity (99.99%) due to the synergistic bactericidal effect of AgNPs and Van (Yang et al., 2017).

In this section, the recent development of AuNPs and AgNPs in biosensing fields including the detection of cancer markers, pathogens and drug analytes has been summarized and discussed. Despite the remarkable progress, the clinical application of noble metal nanoparticles still faces great challenges. In order to prepare multifunctional noble metal nanoparticles with excellent optical and electrical properties, their synthesis and modification methods need to be optimized (Guo and Wang, 2011; Zhao X. et al., 2019). To improve sensor specificity, the discovery of functional molecules is very crucial. The selectivity of noble metal nanoparticles can be effectively improved through functionalization (Chen J. B. et al., 2019; Pirzada and Altintas, 2019; Wang H. et al., 2019). In addition, the correlations between the composition, structure and performance of noble metal nanoparticles sensors needs to be further studied.

OTHER TYPES OF 0D NANOMATERIALS

In addition to the above 0D nanomaterials, UCNPs and Pdts also have their application in biosensing. UCNPs have attracted extensive attention for their highly efficient up-conversion PL and photobleaching resistance, and their cytotoxicity is much lower than that of other nanoparticles (Park et al., 2015). As a type of fluorescent nanoparticles, Pdts have attracted much interest because of their good photostability, high brightness, and facile surface functionalization of fluorescence (Cheng X. et al., 2019). In the following part, the biosensing application of these three 0D nanomaterials will be introduced.

TABLE 2 | Summary of advantages and disadvantages of different 0D nanomaterial-based biosensors.

0D nanomaterials	Advantages	Disadvantages
GQDs	The tunable PL; high photostability against photobleaching and blinking; excellent aqueous solubility; low toxicity.	The confusing relationship between the surface chemistry and physicochemical properties; the unclear transmission mechanism.
CQDs	High chemical stability; simple and low-cost synthesis process; fast and easy functionalization; highly resistant to photobleaching; high aqueous stability.	The ambiguous of exact origin of fluorescence; the unclear role of doped ions; the unknown location of doped ions in CQDs.
Fullerenes	Broad light absorption in the UV-vis region; the ability to accommodate multiple electrons and endohedral metal atoms; high electron affinities; charge separation acceleration; good adsorption abilities to organic molecules.	High-cost synthesis; weak fluorescent emission; lack of proper chemical modification and bio-conjugation.
QDs	Low costs; facile preparation; size tunable light emission; high PL quantum yield; large Stokes shifts.	Potential toxic effects.
MNPs	Low toxicity; high saturation magnetization; stable magnetic and surface properties; rapid collection of the analyte; rapid response time for sensors; highly sensitive detection.	Easy aggregation.
AuNPs	Easy operation; simplicity of construction; easy functionalization; easy to absorb and capture of target analyte; readily enhance scattering and absorption of light; low toxicity.	Unoptimized synthesis conditions.
AgNPs	Similar physicochemical properties to AuNPs; more affordable than AuNPs; antifungal and antibacterial properties; strong plasmon resonance.	Potential toxic effects.
UCNPs	Efficient upconversion PL; resistance to photoblinking and photobleaching; minimal background autofluorescence; deep tissue penetration; low toxicity.	Low emission intensities; relatively poor upconversion efficiencies.
Pdots	Excellent biocompatibility; easy surface functionalization; high fluorescence quantum yield; high photo stability; low cytotoxicity.	Difficult to change the emission spectrum.

Upconversion Nanoparticles

UCNPs are a special class of lanthanide-doped nanoparticles capable of converting NIR light into multicolor and high-energy ultraviolet/visible light. As an efficient fluorescence resonance energy transfer (FRET) donor, UCNPs can be used to construct FRET sensor platforms for the detection of various biomolecules (Liu C. et al., 2019; Wang F. et al., 2019). For example, Liu et al. synthesized a FRET sensing platform based on peptide-functionalized UCNPs for the specific detection of apoptosis-associated caspase-9 activity *in vitro* and *in vivo*. Examination

of caspase-9 activity *in vitro* showed that the UCNPs-based sensing platform could identify cisplatin mediated changes in intracellular caspase-9 activity with a detection limit of 0.068 U/mL. Moreover, due to its excellent FRET performance, low cytotoxicity and good colloidal stability, this UCNPs-based sensing platform was successfully used *in vivo* to visualize caspase-9 activity. Such a UCNPs-based biosensor could serve as a powerful sensing platform to monitor the apoptotic process and evaluate anti-cancer drug efficacy (Liu L. et al., 2019).

In addition, like GQDs and AuNPs, UCNPs can also be used for neurotransmitter sensing. Rabie et al. developed a Yb@Er@Yb sandwich UCNPs sensing platform with a wide detection range from 1 pM to 10 pM to detect dopaminergic neurons (DA) in stem cell-derived neural interface (**Figure 8**). The as-prepared UCNPs-based sensor platform overcame the disadvantage of low emission intensity of traditional UCNPs, and generated bright visible light emissions in response to low power density NIR excitation. The highly efficient upconversion process of UCNPs greatly improved the detection sensitivity to DA. Therefore, this UCNPs-based biosensor could be used to detect neurotransmitters in stem cell-derived neural interface, showing great potential in the neuroscience and stem cell biology fields (Rabie et al., 2019).

Polymer Dots

As advanced nanomaterials, Pdots generally possess high fluorescence brightness and high photostability (Alizadeh and Salimi, 2019; Kim et al., 2020). In recent years, Pdots have emerged as interesting fluorescent probes in biosensors and are widely used in biomolecular detection. Luo et al. designed a coreactant-free dual amplified ECL sensing platform with conjugated Pdots as luminophores for the hypersensitive detection of miRNA. Conjugated Pdots with high carrier mobility could obtain a super-strong ECL signal without adding any coreactant, thus improving the sensitivity of the sensor. As a result, this sensing platform showed a minimum detection limit of 3.3 aM for RNA. These conjugated Pdots provided a good platform for the construction of coreactant-free ECL biosensors and expand the application of Pdots in the clinical analysis (Luo et al., 2019).

In general, the above mentioned emerging 0D nanomaterials (UCNPs, Pdots, SiQDs) have made important contributions to ion detection and biomolecular detection in the field of biosensing. However, experimental studies on their application in disease diagnosis remain rare, and there is also short of studies on their metabolism, biodegradation and long-term toxicology. What's more, emphasis should be attached to the innovation of synthesis methods and realization of large-scale preparation. It is also worth noting that the functional modification can also benefit the application of these 0D nanomaterials in the field of biosensing.

CONCLUSIONS AND PERSPECTIVES

0D nanomaterials are characterized by small volume, high surface-to-volume ratio, edge and quantum constraint effect and good biocompatibility. Due to the unique structures and

properties, the application of 0D nanomaterials in the field of biosensing is expanding rapidly. In this short review, we have highlighted recent progress in 0D nanomaterials regarding their structures, properties and biosensing applications. Carbon-based nanomaterials (GQDs, CQDs, fullerenes), inorganic QDs, MNPs and noble metal nanoparticles (AuNPs, AgNPs) remain to be the research focuses in the biosensing field. The recently studied UCNPs, Pdots, and SiQDs exhibit promising application prospects. However, the research of all these nanomaterials in biosensing is still at the immature stage. In order to advance this field and promote further clinical application, several challenges need to be addressed.

Although the emergence of various fabrication methods has made the synthesis of intricately tuned 0D nanomaterials possible, no specific atomic precise structure has been reported, which limits the in-depth study of the relationship between the structure and performance, the precise control of performance and the sensing mechanism. For instance, a great deal of research has been conducted on the sensing of metal ions. Most of them involve the fluorescence quenching of 0D nanomaterials, but how such quenching is carried out and to what extent the selectivity is achieved have not been figured out at present. Studies on the relationship between these structures and properties will broaden and deepen the applications of 0D nanomaterials.

0D nanomaterial-based biosensors play an important role in the *in vivo* bioassay. However, their application is limited due to the complexity of the *in vivo* environment. The non-specific components in the biological body affect the accuracy of detection. Furthermore, currently, most of the 0D nanomaterial-based biosensors can only be used for *in vitro* testing and laboratory experiments. As **Table 1** shows, a large number of studies on disease diagnosis have been conducted, but most of them are limited to human serum, cells and animal models (mice). The lack of long-term biotoxicity evaluation and biodegradation of these materials further limit their clinical application.

Despite the remarkable achievements of 0D nanomaterials in the field of biosensors, there are still some disadvantages. In **Table 2**, we summarize in detail the advantages and disadvantages of different 0D nanomaterials in biosensing applications. Moreover, compared with other low-dimensional nanomaterials (Li B. L. et al., 2016; Jiang et al., 2018; Chen X.

et al., 2019), 0D nanomaterials have higher PL quantum yield due to the quantum confinement effect. Thus, 0D nanomaterials play a more important role in many fluorescence sensing systems. In addition, *in vivo* applications, the size advantage of 0D nanomaterials is extremely useful for cell uptake and downstream cell processing. However, soft and scalable electronic devices based on one-dimensional nanomaterials have gained rapidly increasing attention in recent years because they can perform real-time non-invasive continuous monitoring (Araki et al., 2019; Tang et al., 2019; Zhai et al., 2019; Zhou et al., 2020). Research into the manufacture of scalable biomedical sensors using 0D nanomaterials is still scarce. Furthermore, due to their ultra-small sizes, 0D nanomaterials are more difficult to regulate in the synthesis process than other low-dimensional materials.

All in all, 0D nanomaterials have an excellent affinity with biomolecules and can promote the fixation of enzyme, antibody, proteins, nucleic acid and many other clinically relevant substances, providing the possibility for the development of a variety of biosensor platforms. 0D structures provide nanomaterials with different physical and chemical properties such as high surface-to-volume ratios, tunable optical properties, and excellent binding ability with biomolecules. As discussed in this review, the extensive application of 0D nanomaterials demonstrates their ability to increase the sensitivity and adjustability of biomolecular detection methods. There is no doubt that 0D nanomaterials will expand the field of biosensing, and enter the clinical research and application stage in the near future.

AUTHOR CONTRIBUTIONS

RL and MW conceived the review topic and modified the manuscript. ZW wrote the manuscript in consultation with all the other authors. TH arranged all the figures. All authors contributed to the final manuscript.

FUNDING

This work was supported by the National Natural Science Foundation of China (NSFC: 21521005, 21971007, 21671013, and 21601010) and the Fundamental Research Funds for the Central Universities (buctylkxj01, XK1806-2, and XK1803-05).

REFERENCES

- Afreen, S., Muthoosamy, K., Manickam, S., and Hashim, U. (2015). Functionalized fullerene (C₆₀) as a potential nanomediator in the fabrication of highly sensitive biosensors. *Biosens. Bioelectron.* 63, 354–364. doi: 10.1016/j.bios.2014.07.044
- Alhagail, S., Suaifan, G. A., Bikker, F. J., Kaman, W. E., Weber, K., Cialla-May, D., et al. (2019). Rapid colorimetric detection of *Pseudomonas aeruginosa* in clinical isolates using a magnetic nanoparticle biosensor. *ACS Omega* 4, 21684–21688. doi: 10.1021/acsomega.9b02080
- Alizadeh, N., and Salimi, A. (2019). Polymer dots as a novel probe for fluorescence sensing of dopamine and imaging in single living cell using droplet microfluidic platform. *Anal. Chim. Acta* 1091, 40–49. doi: 10.1016/j.aca.2019.08.036
- Altintas, Z., Akgun, M., Kokturk, G., and Uludag, Y. (2018). A fully automated microfluidic-based electrochemical sensor for real-time bacteria detection. *Biosens. Bioelectron.* 100, 541–548. doi: 10.1016/j.bios.2017.09.046
- Altintas, Z., Kallemudi, S. S., and Gurbuz, Y. (2014). Gold nanoparticle modified capacitive sensor platform for multiple marker detection. *Talanta* 118, 270–276. doi: 10.1016/j.talanta.2013.10.030
- Araki, T., Uemura, T., Yoshimoto, S., Takemoto, A., Noda, Y., Izumi, S., et al. (2019). Wireless monitoring using a stretchable and transparent sensor sheet containing metal nanowires. *Adv. Mater.* 1902684. doi: 10.1002/adma.201902684
- Atabaev, T. S. (2018). Doped carbon dots for sensing and bioimaging applications: a minireview. *Nanomaterials* 8:342. doi: 10.3390/nano8050342
- Avval, Z. M., Malekpour, L., Raeisi, F., Babapoor, A., Mousavi, S. M., Hashemi, S. A., et al. (2019). Introduction of magnetic and supermagnetic nanoparticles in

- new approach of targeting drug delivery and cancer therapy application. *Drug Metab. Rev.* 52, 157–184. doi: 10.1080/03602532.2019.1697282
- Bagheri, N., Khataee, A., Habibi, B., and Hassanzadeh, J. (2018). Mimetic Ag nanoparticle/Zn-based MOF nanocomposite (AgNPs@ ZnMOF) capped with molecularly imprinted polymer for the selective detection of patulin. *Talanta* 179, 710–718. doi: 10.1016/j.talanta.2017.12.009
- Bahrami, S., Abbasi, A. R., Roushani, M., Derikvand, Z., and Azadbakht, A. (2016). An electrochemical dopamine aptasensor incorporating silver nanoparticle, functionalized carbon nanotubes and graphene oxide for signal amplification. *Talanta* 159, 307–316. doi: 10.1016/j.talanta.2016.05.060
- Barberis, A., Spissu, Y., Fadda, A., Azara, E., Bazzu, G., Marceddu, S., et al. (2015). Simultaneous amperometric detection of ascorbic acid and antioxidant capacity in orange, blueberry and kiwi juice, by a telemetric system coupled with a fullerene- or nanotubes-modified ascorbate subtractive biosensor. *Biosens. Bioelectron.* 67, 214–223. doi: 10.1016/j.bios.2014.08.019
- Bhatnagar, D., Kumar, V., Kumar, A., and Kaur, I. (2016). Graphene quantum dots FRET based sensor for early detection of heart attack in human. *Biosens. Bioelectron.* 79, 495–499. doi: 10.1016/j.bios.2015.12.083
- Bragina, V. A., Znoyko, S. L., Orlov, A. V., Pushkarev, A. V., Nikitin, M. P., and Nikitin, P. I. (2019). Analytical platform with selectable assay parameters based on three functions of magnetic nanoparticles: demonstration of highly sensitive rapid quantitation of staphylococcal enterotoxin B in food. *Anal. Chem.* 91, 9852–9857. doi: 10.1021/acs.analchem.9b01519
- Carneiro, P., Morais, S., and Pereira, M. C. (2019). Nanomaterials towards biosensing of Alzheimer's disease biomarkers. *Nanomaterials* 9:1663. doi: 10.3390/nano9121663
- Chen, J. B., Yousefi, H., Nemr, C. R., Gomis, S., Atwal, R., Labib, M., et al. (2019). Nanostructured architectures for biomolecular detection inside and outside the cell. *Adv. Funct. Mater.* 1907701. doi: 10.1002/adfm.201907701
- Chen, X., Shen, Y., Zhou, P., Zhong, X., Li, G., Han, C., et al. (2019). Bimetallic Au/Pd nanoparticles decorated ZnO nanowires for NO₂ detection. *Sens. Actuators B Chem.* 289, 160–168. doi: 10.1016/j.snb.2019.03.095
- Chen, Y., Ding, X., Zhang, Y., Natalia, A., Sun, X., Wang, Z., et al. (2018). Design and synthesis of magnetic nanoparticles for biomedical diagnostics. *Quant. Imaging. Med. Surg.* 8, 957–970. doi: 10.21037/qims.2018.10.07
- Chen, Y. T., Kolhatkar, A. G., Zenasni, O., Xu, S., and Lee, T. R. (2017). Biosensing using magnetic particle detection techniques. *Sensors* 17:2300. doi: 10.3390/s17102300
- Cheng, X., Huang, Y., Li, D., Yuan, C., Li, Z. L., Sun, L., et al. (2019). A sensitive polymer dots fluorescent sensor for determination of α -L-fucosidase activity in human serum. *Sens. Actuators B Chem.* 288, 38–43. doi: 10.1016/j.snb.2019.02.076
- Cheng, Z. H., Liu, X., Zhang, S. Q., Yang, T., Chen, M. L., and Wang, J. H. (2019). Placeholder strategy with upconversion nanoparticles–eriochrome black T conjugate for a colorimetric assay of an anthrax biomarker. *Anal. Chem.* 91, 12094–12099. doi: 10.1021/acs.analchem.9b03342
- Chuah, K., Wu, Y., Vivekchand, S. R. C., Gaus, K., Reece, P. J., Micolich, A. P., et al. (2019). Nanopore blockade sensors for ultrasensitive detection of proteins in complex biological samples. *Nat. Commun.* 10:2109. doi: 10.1038/s41467-019-10147-7
- Chung, S., Revia, R. A., and Zhang, M. (2019). Graphene quantum dots and their applications in bioimaging, biosensing, and therapy. *Adv. Mater.* 1904362. doi: 10.1002/adma.201904362
- de la Escosura-Muñiz, A., Baptista-Pires, L., Serrano, L., Altet, L., Francino, O., Sánchez, A., et al. (2016). Magnetic bead/gold nanoparticle double-labeled primers for electrochemical detection of isothermal amplified leishmania DNA. *Small* 12, 205–213. doi: 10.1002/smll.201502350
- Dhenadhayalan, N., Lin, K. C., and Saleh, T. A. (2020). Recent advances in functionalized carbon dots toward the design of efficient materials for sensing and catalysis applications. *Small* 16:1905767. doi: 10.1002/smll.201905767
- Fan, Q., Li, J., Zhu, Y., Yang, Z., Shen, T., Guo, Y., et al. (2020). Functional carbon quantum dots towards highly sensitive graphene transistors for Cu²⁺ ion detection. *ACS Appl. Mater. Interfaces* 12, 4797–4803. doi: 10.1021/acsami.9b20785
- Fan, Z., Zhou, S., Garcia, C., Fan, L., and Zhou, J. (2017). pH-Responsive fluorescent graphene quantum dots for fluorescence-guided cancer surgery and diagnosis. *Nanoscale* 9, 4928–4933. doi: 10.1039/C7NR00888K
- Farzin, L., Shamsipur, M., Samandari, L., and Sheibani, S. (2019). HIV biosensors for early diagnosis of infection: the intertwine of nanotechnology with sensing strategies. *Talanta* 206:120201. doi: 10.1016/j.talanta.2019.120201
- Freeman, R., Finder, T., Bahshi, L., Gill, R., and Willner, I. (2012). Functionalized CdSe/ZnS QDs for the detection of nitroaromatic or RDX explosives. *Adv. Mater.* 24, 6416–6421. doi: 10.1002/adma.201202793
- Gao, R., Mei, X., Yan, D., Liang, R., and Wei, M. (2018). Nano-photosensitizer based on layered double hydroxide and isophthalic acid for singlet oxygenation and photodynamic therapy. *Nat. Commun.* 9:2789. doi: 10.1038/s41467-018-05223-3
- Gloag, L., Mehdipour, M., Chen, D., Tilley, R. D., and Gooding, J. J. (2019). Advances in the application of magnetic nanoparticles for sensing. *Adv. Mater.* 31:1904385. doi: 10.1002/adma.201904385
- Gu, Y., Wang, J., Shi, H., Pan, M., Liu, B., Fang, G., et al. (2019). Electrochemiluminescence sensor based on upconversion nanoparticles and oligoaniline-crosslinked gold nanoparticles imprinting recognition sites for the determination of dopamine. *Biosens. Bioelectron.* 128, 129–136. doi: 10.1016/j.bios.2018.12.043
- Guldi, D. M., and Sgobba, V. (2011). Carbon nanostructures for solar energy conversion schemes. *Chem. Commun.* 47, 606–610. doi: 10.1039/C0CC02411B
- Guo, C. X., Yang, H. B., Sheng, Z. M., Lu, Z. S., Song, Q. L., and Li, C. M. (2010). Layered graphene/quantum dots for photovoltaic devices. *Angew. Chem. Int. Ed.* 49, 3014–3017. doi: 10.1002/anie.200906291
- Guo, S., and Wang, E. (2011). Noble metal nanomaterials: controllable synthesis and application in fuel cells and analytical sensors. *Nano Today* 6, 240–264. doi: 10.1016/j.nantod.2011.04.007
- Hussain, M., Nafady, A., Avci, A., Pehlivan, E., Nisar, J., Sherazi, S. T. H., et al. (2019). Biogenic silver nanoparticles for trace colorimetric sensing of enzyme disrupter fungicide vinclozolin. *Nanomaterials* 9:1604. doi: 10.3390/nano9111604
- Jain, U., and Chauhan, N. (2017). Glycated hemoglobin detection with electrochemical sensing amplified by gold nanoparticles embedded N-doped graphene nanosheet. *Biosens. Bioelectron.* 89, 578–584. doi: 10.1016/j.bios.2016.02.033
- Jaiswal, S., Singh, R., Singh, K., Fatma, S., and Prasad, B. B. (2019). Enantioselective analysis of D- and L-Serine on a layer-by-layer imprinted electrochemical sensor. *Biosens. Bioelectron.* 124, 176–183. doi: 10.1016/j.bios.2018.09.090
- Ji, D., Xu, N., Liu, Z., Shi, Z., Low, S. S., Liu, J., et al. (2019). Smartphone-based differential pulse amperometry system for real-time monitoring of levodopa with carbon nanotubes and gold nanoparticles modified screen-printing electrodes. *Biosens. Bioelectron.* 129, 216–223. doi: 10.1016/j.bios.2018.09.082
- Jia, X., Song, T., Liu, Y., Meng, L., and Mao, X. (2017). An immunochromatographic assay for carcinoembryonic antigen on cotton thread using a composite of carbon nanotubes and gold nanoparticles as reporters. *Anal. Chim. Acta* 969, 57–62. doi: 10.1016/j.aca.2017.02.040
- Jiang, Y., Tang, N., Zhou, C., Han, Z., Qu, H., and Duan, X. (2018). A chemiresistive sensor array from conductive polymer nanowires fabricated by nanoscale soft lithography. *Nanoscale* 10, 20578–20586. doi: 10.1039/C8NR04198A
- Jiang, Y., and Tian, B. (2018). Inorganic semiconductor biointerfaces. *Nat. Rev. Mater.* 3, 473–490. doi: 10.1038/s41578-018-0062-3
- Keshavarz, M., Tan, B., and Venkatakrishnan, K. (2018). Label-free SERS quantum semiconductor probe for molecular-level and in vitro cellular detection: a Noble-metal-free methodology. *ACS Appl. Mater. Interfaces* 10, 34886–34904. doi: 10.1021/acsami.8b10590
- Kim, D., Lee, Y. D., Jo, S., Kim, S., and Lee, T. S. (2020). Detection and imaging of cathepsin L in cancer cells using the aggregation of conjugated polymer dots and magnetic nanoparticles. *Sens. Actuators B Chem.* 307:127641. doi: 10.1016/j.snb.2019.127641
- Kim, S. J., Choi, S. J., Jang, J. S., Cho, H. J., and Kim, I. D. (2017). Innovative nanosensor for disease diagnosis. *Acc. Chem. Res.* 50, 1587–1596. doi: 10.1021/acs.accounts.7b00047
- Knežević, N. Ž., Gadžanski, I., and Durand, J. O. (2019). Magnetic nanoarchitectures for cancer sensing, imaging and therapy. *J. Mater. Chem. B* 7, 9–23. doi: 10.1039/C8TB02741B
- Koh, I., and Josephson, L. (2009). Magnetic nanoparticle sensors. *Sensors* 9, 8130–8145. doi: 10.3390/s91008130

- Koo Lee, Y. E., Smith, R., and Kopelman, R. (2009). Nanoparticle PEBBLE sensors in live cells and *in vivo*. *Annu. Rev. Anal. Chem.* 2, 57–76. doi: 10.1146/annurev.anchem.1.031207.112823
- Kurochkina, M., Konshina, E., Oseev, A., and Hirsch, S. (2018). Hybrid structures based on gold nanoparticles and semiconductor quantum dots for biosensor applications. *Nanotechnol. Sci. Appl.* 11, 15–21. doi: 10.2147/NSA.S155045
- Lee, C. Y., Wu, L. P., Chou, T. T., and Hsieh, Y. Z. (2018). Functional magnetic nanoparticles-assisted electrochemical biosensor for eosinophil cationic protein in cell culture. *Sens. Actuators B Chem.* 257, 672–677. doi: 10.1016/j.snb.2017.11.033
- Lee, J., Ahmed, S. R., Oh, S., Kim, J., Suzuki, T., Parmar, K., et al. (2015). A plasmon-assisted fluoro-immunoassay using gold nanoparticle-decorated carbon nanotubes for monitoring the influenza virus. *Biosens. Bioelectron.* 64, 311–317. doi: 10.1016/j.bios.2014.09.021
- Lei, Y. M., Zhou, J., Chai, Y. Q., Zhuo, Y., and Yuan, R. (2018). SnS₂ quantum dots as new emitters with strong electrochemiluminescence for ultrasensitive antibody detection. *Anal. Chem.* 90, 12270–12277. doi: 10.1021/acs.analchem.8b03623
- Li, B. L., Wang, J., Zou, H. L., Garaj, S., Lim, C. T., Xie, J., et al. (2016). Low-dimensional transition metal dichalcogenide nanostructures based sensors. *Adv. Funct. Mater.* 26, 7034–7056. doi: 10.1002/adfm.201602136
- Li, C., Li, W., Liu, H., Zhang, Y., Chen, G., Li, Z., et al. (2020). An activatable NIR-II nanoprobes for *in vivo* early real-time diagnosis of traumatic brain injury. *Angew. Chem. Int. Ed.* 59, 247–252. doi: 10.1002/anie.201911803
- Li, H., Xu, Q., Wang, X., and Liu, W. (2018a). Ultrasensitive surface-enhanced raman spectroscopy detection based on amorphous molybdenum oxide quantum dots. *Small* 14, 1801523. doi: 10.1002/smll.201801523
- Li, H., Yan, X., Qiao, S., Lu, G., and Su, X. (2018b). Yellow-emissive carbon dot-based optical sensing platforms: cell imaging and analytical applications for biocatalytic reactions. *ACS Appl. Mater. Interfaces* 10, 7737–7744. doi: 10.1021/acsami.7b17619
- Li, M., Chen, T., Gooding, J. J., and Liu, J. (2019). Review of carbon and graphene quantum dots for sensing. *ACS Sens.* 4, 1732–1748. doi: 10.1021/acssensors.9b00514
- Li, M., Zheng, Y., Liang, W., Yuan, Y., Chai, Y., and Yuan, R. (2016). An ultrasensitive “on-off-on” photoelectrochemical aptasensor based on signal amplification of a fullerene/CdTe quantum dots sensitized structure and efficient quenching by manganese porphyrin. *Chem. Commun.* 52, 8138–8141. doi: 10.1039/C6CC02791A
- Li, R., Tu, W., Wang, H., and Dai, Z. (2018c). Near-infrared light excited and localized surface plasmon resonance-enhanced photoelectrochemical biosensing platform for cell analysis. *Anal. Chem.* 90, 9403–9409. doi: 10.1021/acs.analchem.8b02047
- Li, X., Zhou, Z., Zhang, C. C., Zheng, Y., Gao, J., and Wang, Q. (2018d). Ratiometric fluorescence platform based on modified silicon quantum dots and its logic gate performance. *Inorg. Chem.* 57, 8866–8873. doi: 10.1021/acs.inorgchem.8b00788
- Li, Z., Lin, Z., Wu, X., Chen, H., Chai, Y., and Yuan, R. (2017). Highly efficient electrochemiluminescence resonance energy transfer system in one nanostructure: its application for ultrasensitive detection of MicroRNA in cancer cells. *Anal. Chem.* 89, 6029–6035. doi: 10.1021/acs.analchem.7b00616
- Liang, R., Wei, M., Evans, D. G., and Duan, X. (2014a). Inorganic nanomaterials for bioimaging, targeted drug delivery and therapeutics. *Chem. Commun.* 50, 14071–14081. doi: 10.1039/C4CC03118K
- Liang, R., Yan, D., Tian, R., Yu, X., Shi, W., Li, C., et al. (2014b). Quantum dots-based flexible films and their application as the phosphor in white light-emitting diodes. *Chem. Mater.* 26, 2595–2600. doi: 10.1021/cm404218y
- Lin, G., Makarov, D., and Schmidt, O. G. (2017). Magnetic sensing platform technologies for biomedical applications. *Lab Chip* 17, 1884–1912. doi: 10.1039/C7LC00026j
- Liu, C., Yu, Y., Chen, D., Zhao, J., Yu, Y., Li, L., et al. (2019). Cupredoxin engineered upconversion nanoparticles for ratiometric luminescence sensing of Cu²⁺. *Nanoscale Adv.* 1, 2580–2585. doi: 10.1039/C9NA00168A
- Liu, H., Na, W., Liu, Z., Chen, X., and Su, X. (2017). A novel turn-on fluorescent strategy for sensing ascorbic acid using graphene quantum dots as fluorescent probe. *Biosens. Bioelectron.* 92, 229–233. doi: 10.1016/j.bios.2017.02.005
- Liu, J. N., Bu, W., and Shi, J. (2017). Chemical design and synthesis of functionalized probes for imaging and treating tumor hypoxia. *Chem. Rev.* 117, 6160–6224. doi: 10.1021/acs.chemrev.6b00525
- Liu, L., Zhang, H., Wang, Z., and Song, D. (2019). Peptide-functionalized upconversion nanoparticles-based FRET sensing platform for Caspase-9 activity detection *in vitro* and *in vivo*. *Biosens. Bioelectron.* 141:111403. doi: 10.1016/j.bios.2019.111403
- Liu, T., Li, N., Dong, J. X., Zhang, Y., Fan, Y. Z., Lin, S. M., et al. (2017). A colorimetric and fluorometric dual-signal sensor for arginine detection by inhibiting the growth of gold nanoparticles/carbon quantum dots composite. *Biosens. Bioelectron.* 87, 772–778. doi: 10.1016/j.bios.2016.08.098
- Loo, A. H., Sofer, Z., Bouša, D., Ulbrich, P., Bonanni, A. and Pumera, M. (2016). Carboxylic carbon quantum dots as a fluorescent sensing platform for DNA detection. *ACS Appl. Mater. Interfaces* 8, 1951–1957. doi: 10.1021/acsami.5b10160
- Lu, L., Zhou, L., Chen, J., Yan, F., Liu, J., Dong, X., et al. (2018). Nanochannel-confined graphene quantum dots for ultrasensitive electrochemical analysis of complex samples. *ACS Nano* 12, 12673–12681. doi: 10.1021/acsnano.8b07564
- Lu, S., Li, G., Lv, Z., Qiu, N., Kong, W., Gong, P., et al. (2016). Facile and ultrasensitive fluorescence sensor platform for tumor invasive biomarker β -glucuronidase detection and inhibitor evaluation with carbon quantum dots based on inner-filter effect. *Biosens. Bioelectron.* 85, 358–362. doi: 10.1016/j.bios.2016.05.021
- Luo, J. H., Li, Q., Chen, S. H., and Yuan, R. (2019). Coreactant-free dual amplified electrochemiluminescent biosensor based on conjugated polymer dots for the ultrasensitive detection of microRNA. *ACS Appl. Mater. Interfaces* 11, 27363–27370. doi: 10.1021/acsami.9b09339
- Ma, Y., Zhang, Y., and William, W. Y. (2019). Near infrared emitting quantum dots: synthesis, luminescence properties and applications. *J. Mater. Chem. C* 7, 13662–13679. doi: 10.1039/C9TC04065J
- Malekzad, H., Zangabad, P. S., Mirshekari, H., Karimi, M., and Hamblin, M. R. (2017). Noble metal nanoparticles in biosensors: recent studies and applications. *Nanotechnol. Rev.* 6, 301–329. doi: 10.1515/ntrev-2016-0014
- Mao, K., Zhou, Z., Han, S., Zhou, X., Hu, J., Li, X., et al. (2018). A novel biosensor based on Au@Ag core-shell nanoparticles for sensitive detection of methylamphetamine with surface enhanced Raman scattering. *Talanta* 190, 263–268. doi: 10.1016/j.talanta.2018.07.071
- Mei, X., Wang, W., Yan, L., Hu, T., Liang, R., Yan, D., et al. (2018). Hydrothermal monolayer toward high performance synergistic dual-modal imaging and cancer therapy. *Biomaterials* 165, 14–24. doi: 10.1016/j.biomaterials.2018.02.032
- Miyazawa, K. I. (2015). Synthesis of fullerene nanowhiskers using the liquid-liquid interfacial precipitation method and their mechanical, electrical and superconducting properties. *Sci. Technol. Adv. Mater.* 16:013502. doi: 10.1088/1468-6996/16/1/013502
- Molaei, M. J. (2019a). A review on nanostructured carbon quantum dots and their applications in biotechnology, sensors, and chemiluminescence. *Talanta* 196, 456–478. doi: 10.1016/j.talanta.2018.12.042
- Molaei, M. J. (2019b). Carbon quantum dots and their biomedical and therapeutic applications: a review. *RSC Adv.* 9, 6460–6481. doi: 10.1039/C8RA08088G
- Morón, C., Cabrera, C., Morón, A., García, A., and González, M. (2015). Magnetic sensors based on amorphous ferromagnetic materials: a review. *Sensors* 15, 28340–28366. doi: 10.3390/s151128340
- Nabaei, V., Chandrawati, R., and Heidari, H. (2018). Magnetic biosensors: modelling and simulation. *Biosens. Bioelectron.* 103, 69–86. doi: 10.1016/j.bios.2017.12.023
- Ou, J., Tan, H., Chen, Z., and Chen, X. (2019). FRET-based semiconducting polymer dots for pH sensing. *Sensors* 19, 1455. doi: 10.3390/s19061455
- Pal, M. K., Rashid, M., and Bisht, M. (2015). Multiplexed magnetic nanoparticle-antibody conjugates (MNPs-ABS) based prognostic detection of ovarian cancer biomarkers, CA-125, β -2M and ApoA1 using fluorescence spectroscopy with comparison of surface plasmon resonance (SPR) analysis. *Biosens. Bioelectron.* 73, 146–152. doi: 10.1016/j.bios.2015.05.051
- Pandit, S., Behera, P., Sahoo, J., and De, M. (2019). In situ synthesis of amino acid functionalized carbon dots with tunable properties and their biological applications. *ACS Appl. Bio. Mater.* 2, 3393–3403. doi: 10.1021/acsabm.9b00374

- Panwar, N., Soehartono, A. M., Chan, K. K., Zeng, S., Xu, G., Qu, J., et al. (2019). Nanocarbons for biology and medicine: sensing, imaging, and drug delivery. *Chem. Rev.* 119, 9559–9656. doi: 10.1021/acs.chemrev.9b00099
- Park, Y. I., Lee, K. T., Suh, Y. D., and Hyeon, T. (2015). Upconverting nanoparticles: a versatile platform for wide-field two-photon microscopy and multi-modal *in vivo* imaging. *Chem. Soc. Rev.* 44, 1302–1317. doi: 10.1039/C4CS00173G
- Pathan, S., Jalal, M., Prasad, S., and Bose, S. (2019). Aggregation-induced enhanced photoluminescence in magnetic graphene oxide quantum dots as a fluorescence probe for As (III) sensing. *J. Mater. Chem. A* 7, 8510–8520. doi: 10.1039/C8TA11358K
- Peng, L., Mei, X., He, J., Xu, J., Zhang, W., Liang, R., et al. (2018). Monolayer nanosheets with an extremely high drug loading toward controlled delivery and cancer theranostics. *Adv. Mater.* 30:1707389. doi: 10.1002/adma.201707389
- Pirzada, M., and Altintas, Z. (2019). Nanomaterials for healthcare biosensing applications. *Sensors* 19:5311. doi: 10.3390/s19235311
- Qian, Z. S., Shan, X. Y., Chai, L. J., Chen, J. R., and Feng, H. (2015). A fluorescent nanosensor based on graphene quantum dots–aptamer probe and graphene oxide platform for detection of lead (II) ion. *Biosens. Bioelectron.* 68, 225–231. doi: 10.1016/j.bios.2014.12.057
- Qian, Z. S., Shan, X. Y., Chai, L. J., Ma, J. J., Chen, J. R., and Feng, H. (2014). DNA nanosensor based on biocompatible graphene quantum dots and carbon nanotubes. *Biosens. Bioelectron.* 60, 64–70. doi: 10.1016/j.bios.2014.04.006
- Rabie, H., Zhang, Y., Pasquale, N., Lagos, M. J., Batson, P. E., and Lee, K. B. (2019). NIR biosensing of neurotransmitters in stem cell-derived neural interface using advanced core-shell upconversion nanoparticles. *Adv. Mater.* 31:1806991. doi: 10.1002/adma.201806991
- Raj, M., and Goyal, R. N. (2019). Silver nanoparticles and electrochemically reduced graphene oxide nanocomposite based biosensor for determining the effect of caffeine on estradiol release in women of child-bearing age. *Sens. Actuators B Chem.* 284, 759–767. doi: 10.1016/j.snb.2019.01.018
- Raja, I. S., Song, S. J., Kang, M. S., Lee, Y. B., Kim, B., Hong, S. W., et al. (2019). Toxicity of zero- and one-dimensional carbon nanomaterials. *Nanomaterials* 9:1214. doi: 10.3390/nano9091214
- Ramanathan, S., Gopinath, S. C., Arshad, M. M., and Poopalan, P. (2019). Multidimensional (0D–3D) nanostructures for lung cancer biomarker analysis: Comprehensive assessment on current diagnostics. *Biosens. Bioelectron.* 141:111434. doi: 10.1016/j.bios.2019.111434
- Robidillo, C. J. T., Wandelt, S., Dalangin, R., Zhang, L., Yu, H., Meldrum, A., et al. (2019). Ratiometric detection of nerve agents by coupling complementary properties of silicon-based quantum dots and green fluorescent protein. *ACS Appl. Mater. Interfaces* 11, 33478–33488. doi: 10.1021/acsami.9b10996
- Sabouri, S., Ghourchian, H., Shourian, M., and Boutorabi, M. (2014). A gold nanoparticle-based immunosensor for the chemiluminescence detection of the hepatitis B surface antigen. *Anal. Methods* 6, 5059–5066. doi: 10.1039/C4AY00461B
- Savas, S., Ersoy, A., Gulmez, Y., Kilic, S., Levent, B., and Altintas, Z. (2018). Nanoparticle enhanced antibody and DNA biosensors for sensitive detection of salmonella. *Materials* 11:1541. doi: 10.3390/ma11091541
- Shi, X., Meng, H., Sun, Y., Qu, L., Lin, Y., Li, Z., et al. (2019). Far-red to near-infrared carbon dots: preparation and applications in biotechnology. *Small* 15:1901507. doi: 10.1002/smll.201901507
- Sondhi, P., Maruf, M. H. U., and Stine, K. J. (2020). Nanomaterials for biosensing lipopolysaccharide. *Biosensors* 10:2. doi: 10.3390/bios10010002
- Steinmetz, M., Lima, D., Viana, A. G., Fujiwara, S. T., Pessôa, C. A., Etto, R. M., et al. (2019). A sensitive label-free impedimetric DNA biosensor based on silsesquioxane-functionalized gold nanoparticles for Zika Virus detection. *Biosens. Bioelectron.* 141:111351. doi: 10.1016/j.bios.2019.111351
- Sun, H., Wu, L., Wei, W., and Qu, X. (2013). Recent advances in graphene quantum dots for sensing. *Mater. Today* 16, 433–442. doi: 10.1016/j.mattod.2013.10.020
- Sun, H., Zhou, Y., Ren, J., and Qu, X. (2018). Carbon nanozymes: enzymatic properties, catalytic mechanism, and applications. *Angew. Chem. Int. Ed.* 57, 9224–9237. doi: 10.1002/anie.201712469
- Takemura, K., Lee, J., Suzuki, T., Hara, T., Abe, F., and Park, E. Y. (2019). Ultrasensitive detection of norovirus using a magnetofluoroimmunoassay based on synergic properties of gold/magnetic nanoparticle hybrid nanocomposites and quantum dots. *Sens. Actuators B Chem.* 296:126672. doi: 10.1016/j.snb.2019.126672
- Tang, N., Zhou, C., Xu, L., Jiang, Y., Qu, H., and Duan, X. (2019). A fully integrated wireless flexible ammonia sensor fabricated by soft nano-lithography. *ACS Sens.* 4, 726–732. doi: 10.1021/acssensors.8b01690
- Tavallaie, R., McCarroll, J., Le Grand, M., Ariotti, N., Schuhmann, W., Bakker, E., et al. (2018). Nucleic acid hybridization on an electrically reconfigurable network of gold-coated magnetic nanoparticles enables microRNA detection in blood. *Nature Nanotech.* 13, 1066–1071. doi: 10.1038/s41565-018-0232-x
- Thirumalraj, B., Dhenadhyalan, N., Chen, S. M., Liu, Y. J., Chen, T. W., Liang, P. H., et al. (2018). Highly sensitive fluorogenic sensing of L-Cysteine in live cells using gelatin-stabilized gold nanoparticles decorated graphene nanosheets. *Sens. Actuators B Chem.* 259, 339–346. doi: 10.1016/j.snb.2017.12.028
- Tian, R., Yan, D., Li, C., Xu, S., Liang, R., Guo, L., et al. (2016). Surface-confined fluorescence enhancement of Au nanoclusters anchoring to a two-dimensional ultrathin nanosheet toward bioimaging. *Nanoscale* 8, 9815–9821. doi: 10.1039/C6NR01624C
- Tran, D. T., Kim, N. H., and Lee, J. H. (2018). Cu-Au nanocrystals functionalized carbon nanotube arrays vertically grown on carbon spheres for highly sensitive detecting cancer biomarker. *Biosens. Bioelectron.* 119, 134–140. doi: 10.1016/j.bios.2018.08.022
- Vikrant, K., Bhardwaj, N., Bhardwaj, S. K., Kim, K. H., and Deep, A. (2019). Nanomaterials as efficient platforms for sensing DNA. *Biomaterials* 214:119215. doi: 10.1016/j.biomaterials.2019.05.026
- Wang, F., Zhang, C., Qu, X., Cheng, S., and Xian, Y. (2019). Cationic cyanine chromophore-assembled upconversion nanoparticles for sensing and imaging H₂S in living cells and zebrafish. *Biosens. Bioelectron.* 126, 96–101. doi: 10.1016/j.bios.2018.10.056
- Wang, H., Rao, H., Luo, M., Xue, X., Xue, Z., and Lu, X. (2019). Noble metal nanoparticles growth-based colorimetric strategies: From monocolorimetric to multicolorimetric sensors. *Coord. Chem. Rev.* 398:113003. doi: 10.1016/j.ccr.2019.06.020
- Wang, H. H., Li, M. J., Wang, H. J., Chai, Y. Q., and Yuan, R. (2019). p–n-Sensitized heterostructure Co₃O₄/fullerene with highly efficient photoelectrochemical performance for ultrasensitive DNA detection. *ACS Appl. Mater. Interfaces* 11, 23765–23772. doi: 10.1021/acsami.9b05923
- Wang, Q., Wang, C., Wang, X., Zhang, Y., Wu, Y., Dong, C., et al. (2019). Construction of CPs@ MnO₂-AgNPs as a multifunctional nanosensor for glutathione sensing and cancer theranostics. *Nanoscale* 11, 18845–18853. doi: 10.1039/C9NR06443E
- Wang, Q., Zhang, S., Zhong, Y., Yang, X. F., Li, Z., and Li, H. (2017). Preparation of yellow-green-emissive carbon dots and their application in constructing a fluorescent turn-on nanoprobe for imaging of selenol in living cells. *Anal. Chem.* 89, 1734–1741. doi: 10.1021/acs.analchem.6b03983
- Weddemann, A., Albon, C., Auge, A., Wittbracht, F., Hedwig, P., Akemeier, D., et al. (2010). How to design magneto-based total analysis systems for biomedical applications. *Biosens. Bioelectron.* 26, 1152–1163. doi: 10.1016/j.bios.2010.06.031
- Wegner, K. D., and Hildebrandt, N. (2015). Quantum dots: bright and versatile *in vitro* and *in vivo* fluorescence imaging biosensors. *Chem. Soc. Rev.* 44, 4792–4834. doi: 10.1039/C4CS00532E
- Winkler, K., Balch, A. L., and Kutner, W. (2006). Electrochemically formed fullerene-based polymeric films. *J. Solid State Electrochem.* 10, 761–784. doi: 10.1007/s10008-006-0171-6
- Xi, J., Xie, C., Zhang, Y., Wang, L., Xiao, J., Duan, X., et al. (2016). Pd nanoparticles decorated N-doped graphene quantum dots@ N-doped carbon hollow nanospheres with high electrochemical sensing performance in cancer detection. *ACS Appl. Mater. Interfaces* 8, 22563–22573. doi: 10.1021/acsami.6b05561
- Xiao, M., Lai, W., Man, T., Chang, B., Li, L., Chandrasekaran, A. R., et al. (2019). Rationally engineered nucleic acid architectures for biosensing applications. *Chem. Rev.* 119, 11631–11717. doi: 10.1021/acs.chemrev.9b00121
- Xu, H. M., Wang, H. C., Shen, Y., Lin, Y. H., and Nan, C. W. (2015). Low-dimensional nanostructured photocatalysts. *J. Adv. Ceram.* 4, 159–182. doi: 10.1007/s40145-015-0159-8
- Xu, H. V., Zhao, Y., and Tan, Y. N. (2019). Nanodot-directed formation of plasmonic-fluorescent nanohybrids toward dual optical detection of glucose and cholesterol via hydrogen peroxide sensing. *ACS Appl. Mater. Interfaces* 11, 27233–27242. doi: 10.1021/acsami.9b08708

- Xu, Q., Li, W., Ding, L., Yang, W., Xiao, H., and Ong, W. J. (2019). Function-driven engineering of 1D carbon nanotubes and 0D carbon dots: mechanism, properties and applications. *Nanoscale* 11, 1475–1504. doi: 10.1039/C8NR08738E
- Yan, X., Song, Y., Zhu, C., Song, J., Du, D., Su, X., et al. (2016). Graphene quantum dot-MnO₂ nanosheet based optical sensing platform: a sensitive fluorescence “turn off-on” nanosensor for glutathione detection and intracellular imaging. *ACS Appl. Mater. Interfaces* 8, 21990–21996. doi: 10.1021/acsami.6b05465
- Yan, Y., Gong, J., Chen, J., Zeng, Z., Huang, W., Pu, K., et al. (2019). Recent advances on graphene quantum dots: from chemistry and physics to applications. *Adv. Mater.* 31:1808283. doi: 10.1002/adma.201808283
- Yan, Z., Yang, M., Wang, Z., Zhang, F., Xia, J., Shi, G., et al. (2015). A label-free immunosensor for detecting common acute lymphoblastic leukemia antigen (CD10) based on gold nanoparticles by quartz crystal microbalance. *Sens. Actuators B Chem.* 210, 248–253. doi: 10.1016/j.snb.2014.12.104
- Yang, C. T., Wu, L., Liu, X., Tran, N. T., Bai, P., Liedberg, B., et al. (2016). Exploiting surface-plasmon-enhanced light scattering for the design of ultrasensitive biosensing modality. *Anal. Chem.* 88, 11924–11930. doi: 10.1021/acs.analchem.6b03798
- Yang, G., Wan, X., Su, Y., Zeng, X., and Tang, J. (2016). Acidophilic S-doped carbon quantum dots derived from cellulose fibers and their fluorescence sensing performance for metal ions in an extremely strong acid environment. *J. Mater. Chem. A* 4, 12841–12849. doi: 10.1039/C6TA05943K
- Yang, Z., Wang, Y., and Zhang, D. (2017). A novel multifunctional electrochemical platform for simultaneous detection, elimination, and inactivation of pathogenic bacteria based on the vancomycin-functionalised AgNPs/3D-ZnO nanorod arrays. *Biosens. Bioelectron.* 98, 248–253. doi: 10.1016/j.bios.2017.06.058
- Yao, J., Li, P., Li, L., and Yang, M. (2018). Biochemistry and biomedicine of quantum dots: From biodetection to bioimaging, drug discovery, diagnostics, and therapy. *Acta biomaterialia* 74, 36–55. doi: 10.1016/j.actbio.2018.05.004
- Yu, E. Y., Chandrasekharan, P., Berzon, R., Tay, Z. W., Zhou, X. Y., Khandhar, A. P., et al. (2017). Magnetic particle imaging for highly sensitive, quantitative, and safe in vivo gut bleed detection in a murine model. *ACS nano* 11, 12067–12076. doi: 10.1021/acs.nano.7b04844
- Yuan, Q., He, J., Niu, Y., Chen, J., Zhao, Y., Zhang, Y., et al. (2018). Sandwich-type biosensor for the detection of α 2, 3-sialylated glycans based on fullerene-palladium-platinum alloy and 4-mercaptophenylboronic acid nanoparticle hybrids coupled with Au-methylene blue-MAL signal amplification. *Biosens. Bioelectron.* 102, 321–327. doi: 10.1016/j.bios.2017.11.043
- Zhai, Q., Gong, S., Wang, Y., Lyu, Q., Liu, Y., Ling, Y., et al. (2019). Enokitake mushroom-like standing gold nanowires toward wearable noninvasive bimodal glucose and strain sensing. *ACS Appl. Mater. Interfaces* 11, 9724–9729. doi: 10.1021/acsami.8b19383
- Zhang, C., He, J., Zhang, Y., Chen, J., Zhao, Y., Niu, Y., et al. (2018). Cerium dioxide-doped carboxyl fullerene as novel nanoprobe and catalyst in electrochemical biosensor for amperometric detection of the CYP2C19* 2 allele in human serum. *Biosens. Bioelectron.* 102, 94–100. doi: 10.1016/j.bios.2017.11.014
- Zhang, H., Dong, X., Wang, J., Guan, R., Cao, D., and Chen, Q. (2019). Fluorescence emission of polyethylenimine-derived polymer dots and its application to detect copper and hypochlorite ions. *ACS Appl. Mater. Interfaces* 11, 32489–32499. doi: 10.1021/acsami.9b09545
- Zhang, Q. Q., Chen, B. B., Zou, H. Y., Li, Y. F., and Huang, C. Z. (2018). Inner filter with carbon quantum dots: a selective sensing platform for detection of hematin in human red cells. *Biosens. Bioelectron.* 100, 148–154. doi: 10.1016/j.bios.2017.08.049
- Zhang, R. Q., Hong, S. L., Wen, C. Y., Pang, D. W., and Zhang, Z. L. (2018). Rapid detection and subtyping of multiple influenza viruses on a microfluidic chip integrated with controllable micro-magnetic field. *Biosens. Bioelectron.* 100, 348–354. doi: 10.1016/j.bios.2017.08.048
- Zhang, X., Rajaraman, B. R., Liu, H., and Ramakrishna, S. (2014). Graphene's potential in materials science and engineering. *RSC Adv.* 4, 28987–29011. doi: 10.1039/C4RA02817A
- Zhang, X., Xie, G., Gou, D., Luo, P., Yao, Y., and Chen, H. (2019). A novel enzyme-free electrochemical biosensor for rapid detection of pseudomonas aeruginosa based on high catalytic Cu-ZrMOF and conductive super P. *Biosens. Bioelectron.* 142:111486. doi: 10.1016/j.bios.2019.111486
- Zhang, Y., Duan, L. F., Zhang, Y., Wang, J., Geng, H., and Zhang, Q. (2014). Advances in conceptual electronic nanodevices based on 0D and 1D nanomaterials. *Nano-Micro Lett.* 6, 1–19. doi: 10.1007/BF03353763
- Zhao, X., Zhao, H., Yan, L., Li, N., Shi, J., and Jiang, C. (2019). Recent developments in detection using noble metal nanoparticles. *Crit. Rev. Anal. Chem.* 97–110. doi: 10.1080/10408347.2019.1576496
- Zhao, Y., Zhou, H., Zhang, S., and Xu, J. (2019). The synthesis of metal nanoclusters and their applications in bio-sensing and imaging. *Methods Appl. Fluoresc.* 8:012001. doi: 10.1088/2050-6120/ab57e7
- Zheng, L., Qi, P., and Zhang, D. (2018). A simple, rapid and cost-effective colorimetric assay based on the 4-mercaptophenylboronic acid functionalized silver nanoparticles for bacteria monitoring. *Sens. Actuators B Chem.* 260, 983–989. doi: 10.1016/j.snb.2018.01.115
- Zheng, M., Ruan, S., Liu, S., Sun, T., Qu, D., Zhao, H., et al. (2015). Self-targeting fluorescent carbon dots for diagnosis of brain cancer cells. *ACS Nano* 9, 11455–11461. doi: 10.1021/acs.nano.5b05575
- Zhou, B., Guo, Z., Lin, Z., Zhang, L., Jiang, B. P., and Shen, X. C. (2019). Recent insights into near-infrared light-responsive carbon dots for bioimaging and cancer phototherapy. *Inorg. Chem. Front.* 6, 1116–1128. doi: 10.1039/C9QI00201D
- Zhou, C., Zhang, X., Tang, N., Fang, Y., Zhang, H., and Duan, X. (2020). Rapid response flexible humidity sensor for respiration monitoring using nano-confined strategy. *Nanotechnology* 31:125302. doi: 10.1088/1361-6528/ab5cda
- Zhu, S., Song, Y., Zhao, X., Shao, J., Zhang, J., and Yang, B. (2015). The photoluminescence mechanism in carbon dots (graphene quantum dots, carbon nanodots, and polymer dots): current state and future perspective. *Nano Res.* 8, 355–381. doi: 10.1007/s12274-014-0644-3

Conflict of Interest: The authors declare that the research was conducted in the absence of any commercial or financial relationships that could be construed as a potential conflict of interest.

Copyright © 2020 Wang, Hu, Liang and Wei. This is an open-access article distributed under the terms of the Creative Commons Attribution License (CC BY). The use, distribution or reproduction in other forums is permitted, provided the original author(s) and the copyright owner(s) are credited and that the original publication in this journal is cited, in accordance with accepted academic practice. No use, distribution or reproduction is permitted which does not comply with these terms.



A Fast and Highly Selective Nitrite Sensor Based on Interdigital Electrodes Modified With Nanogold Film and Chrome-Black T

Haoyue Luo¹, Xiaogang Lin^{1*}, Zhijia Peng¹, Yong Zhou¹, Shibin Xu¹, Ming Song¹, Lifeng Jin¹ and Xiaodong Zheng^{2*}

¹ Key Laboratory of Optoelectronic Technology and Systems of Ministry of Education of China, Chongqing University, Chongqing, China, ² Chongqing University Cancer Hospital, Chongqing University, Chongqing, China

OPEN ACCESS

Edited by:

Weiwei Wu,
Xidian University, China

Reviewed by:

Ming Lei,
Beijing University of Posts and
Telecommunications (BUPT), China
Cheng Zhou,
Tianjin University, China

*Correspondence:

Xiaogang Lin
xglin@cqu.edu.cn
Xiaodong Zheng
zxd0052005@163.com

Specialty section:

This article was submitted to
Nanoscience,
a section of the journal
Frontiers in Chemistry

Received: 11 January 2020

Accepted: 08 April 2020

Published: 29 April 2020

Citation:

Luo H, Lin X, Peng Z, Zhou Y, Xu S,
Song M, Jin L and Zheng X (2020) A
Fast and Highly Selective Nitrite
Sensor Based on Interdigital
Electrodes Modified With Nanogold
Film and Chrome-Black T.
Front. Chem. 8:366.
doi: 10.3389/fchem.2020.00366

Nitrite is a toxic substance, when excessive nitrite enters the human body, it will be seriously harmful to human. At present, the detection methods of nitrite are complicated to operate and require expensive detection instruments. Therefore, an effective, fast and highly selective nanogold film interdigital electrode sensors that can detect nitrite easily and quickly is developed in the work. Firstly, the variation of the sensitivity of nanogold film nitrite sensors with concentrations (1 mol/L, 10^{-1} mol/L, 10^{-2} mol/L, 10^{-3} mol/L, 10^{-4} mol/L, and 10^{-5} mol/L) was measured by experiments. Then, Chrome-black T was modified to the surface of the nanogold film interdigital electrodes by electrochemical polymerization, and the film of chrome-black T had affinity for nitrite ions, so nitrite ions were enriched on the sensor surface. The change law of the impedance signal of the modified nanogold film nitrite sensors after being added to different concentrations of sodium nitrite solution were also concluded. The study demonstrates that the larger the concentration of sodium nitrite solution is added to the modified interdigital electrodes, the smaller impedance and resistance of the modified interdigital electrodes are reflected. Finally, specificity of the modified interdigital electrode sensors has been demonstrated. The novel interdigital electrode sensors can detect the concentration of nitrite solution conveniently and quickly with only 30 s. Therefore, the prospect of applying the novel nanogold film interdigital electrode sensors to the detection of nitrite in blood, body fluid, food and drinking water is promising.

Keywords: interdigital electrode sensors, nanogold film, detection of nitrite, impedance, capacitance

INTRODUCTION

Nitrite is a food preservative and therefore commonly used as a food preservative. So humans are ubiquitously exposed to nitrite. It will destroy the function of red blood cells when excessive nitrite enters the human body. What's worse, it may result in death. In addition, Nitrite is also able to react with other compounds to produce carcinogens under specific conditions.

A highly sensitive, simple, and rapid method to detect nitrite in foods and water is essential for us. At present, there are several methods to detect nitrite. The detection of nitrite by spectroscopic

method is one of the most basic and common methods, but it is easy to be interfered by impurities with low accuracy and sensitivity. A surface-enhanced Raman spectroscopy (SERS) method coupled with a commercially available gold nano substrate was evaluated for the detection of nitrate and nitrite in water by Gajaraj et al. (2013). Chromatographic method has the advantages of simple operation and wide linear range. But toxic agents and the expensive instruments should be used in the detection, which has impeded its development. Akio Tanaka used an electron capture detector to analyze nitrite in meat and cheese by gas-liquid chromatography (Tanaka et al., 1982). A method was developed for determination of inorganic anions, including nitrite (NO_2^-) and nitrate (NO_3^-) in seawater by ion chromatography (Ito et al., 2012). In recent years, electrochemical sensors are widely used to measure the content of nitrite in water and food. It has the advantages of easy operation, high sensitivity and good stability. The development of an electrode system for the determination of nitrite was presented. The approach was based upon the deposition of a macroporous copper deposit which showed marked specificity for nitrite ion under mildly acidic conditions (pH 3) with a linear range extending from 10 to 200 $\mu\text{mol/L}$ nitrate (Davis et al., 2000). Xu et al. used a glassy carbon electrode modified by combining bovine hemoglobin with nanometer gold-reduced graphene oxide to detect nitrite, they found that the modified electrode had good specificity and sensitivity, and had wide linear range of detection: 0.5–100 $\mu\text{mol/L}$, the minimum detection limit

of 0.1 $\mu\text{mol/L}$ (Xu et al., 2015). A paper test-strip technology, used in conjunction with a modern hand-held reflectometer was tested to permit fine spatial and temporal resolution analysis of nitrite breakthrough in a large undisturbed soil block. The techniques proved cost effective and had the added benefit of stopping locally generated toxic waste (Holden and Scholefield, 2008; Jiang et al., 2018). However, some of these methods have low accuracy and sensitivity, some of them are time-consuming and require expensive apparatuses which are also operated by highly expert experimenter.

In order to develop a highly sensitive, simple, and rapid method, we used nanogold film interdigital electrode sensors to detect nitrite in this study. The advantages of the nanogold film interdigital electrode sensors are convenient, economical, and high throughput capacity. Purified water was used as the background solution in experiments. We detected the frequency sweep curve and the alternating voltage sweep curve of the nanogold film interdigital electrode sensors to find the changes of their impedance. But the nanogold film interdigital electrode sensors didn't own good specificity and stability. Therefore, Chrome-black T was modified to the surface of the interdigitated electrode by electrochemical polymerization, and the film of chrome-black T have affinity for nitrite ions. The change law of the impedance, capacitance, and resistance signals of the modified nanogold film nitrite sensors were further concluded. Finally, we have also demonstrated the specificity of the modified interdigital electrode sensors in the work.

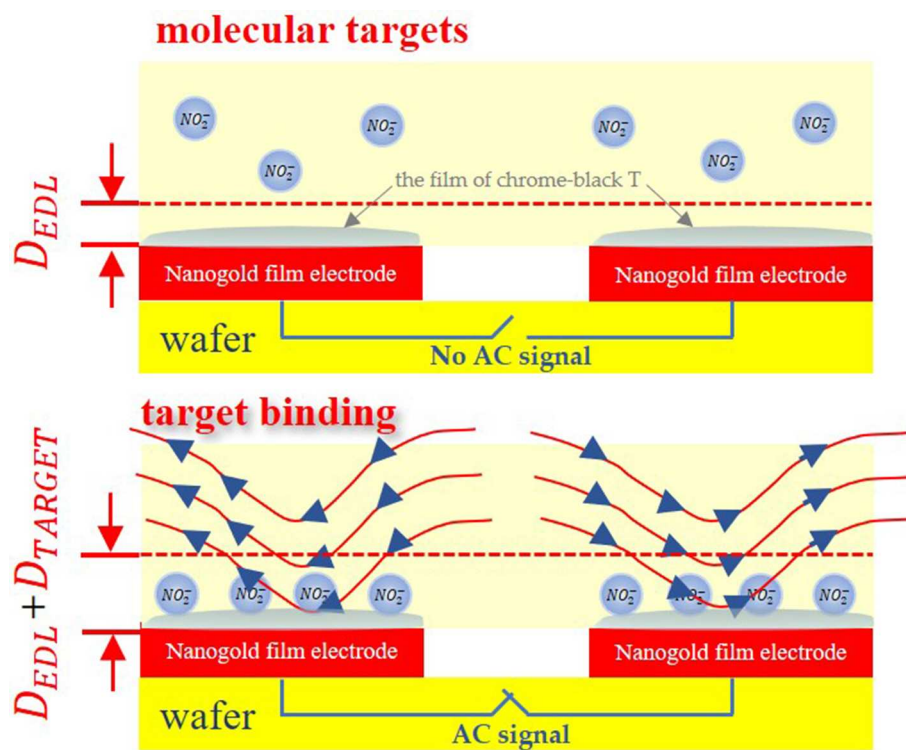


FIGURE 1 | Mechanism of capacitive sensing.

MATERIALS AND METHODS

Materials

The sodium nitrite was purchased from Tansoole (China). The sodium nitrite was firstly dissolved in purified water to make a 1 mol/L stock solution and stored at room temperature. Then the stock solution was further diluted in purified water to make the working solution at 10^{-1} mol/L, 10^{-2} mol/L, 10^{-3} mol/L, 10^{-4} mol/L, and 10^{-5} mol/L for testing. At the same time, the purified water was used as the background solution. Chrome-black T and Sodium hydroxide were also purchased from Tansoole (China). Chrome-black T and Sodium hydroxide were dissolved in purified water to make the solution which included 1 mmol/L Chrome-black T and 10 mmol/L Sodium hydroxide for modifying. All other reagents were of analytical grade (Lin et al., 2019a,b). At the same time, the sodium nitrite mixture solution was also prepared with the concentration of 10^{-1} mol/L, in which the concentration of carbonate ion was 0.1 mol/L, the concentration of chloride ion was 0.1 mol/L, the concentration of nitrate ion was 0.1 mol/L, the concentration of magnesium ion was 0.05 mol/L, and the concentration of potassium ion was 0.3 mol/L. Then the sodium nitrite mixture solution was further diluted in purified water to make the sodium nitrite mixture solution at 10^{-1} mol/L, 10^{-2} mol/L, 10^{-3} mol/L, 10^{-4} mol/L, and 10^{-5} mol/L for specificity testing. And the mixture solution without the sodium nitrite was also prepared for testing.

Detection Mechanisms

In this study, we utilized nanogold film interdigital electrodes as the sensors. The interdigital microelectrodes are finger-shaped in its surface. At the same time, the tiny size of the interdigital microelectrodes is able to achieve microminiaturization. When nanogold film interdigital microelectrodes are immersed in solution, the electrodes impedance can be approximated as a network of resistors and capacitors, as conceptually shown in **Figure 1**. Electrical double layer (EDL) is a structure that appears on the surface of nanogold film when it is exposed to a fluid. And EDL can be modeled as a capacitor. When sodium nitrite molecules are adsorbed onto the nanogold film surface, the interfacial capacitance C_{int} will change due to the change in the thickness and surface area of C_{int} , which can then be used to indicate the deposition of sodium nitrite molecules on the nanogold film (Li et al., 2015; Lin et al., 2017).

Before the affinity assay, the electrode surface is immobilized with the film of chrome-black T to achieve selectivity for the targeted particles. The interfacial capacitance can be approximated by following equation.

$$C_{int} = \frac{A}{\frac{1}{\epsilon_s} D_{edl} + \frac{1}{\epsilon_p} D_{target}} \quad (1)$$

Where ϵ_s and ϵ_p are permittivity of the sample and target molecules, A is the surface area and D_{edl} , D_{target} are electric double layer, target thickness respectively.

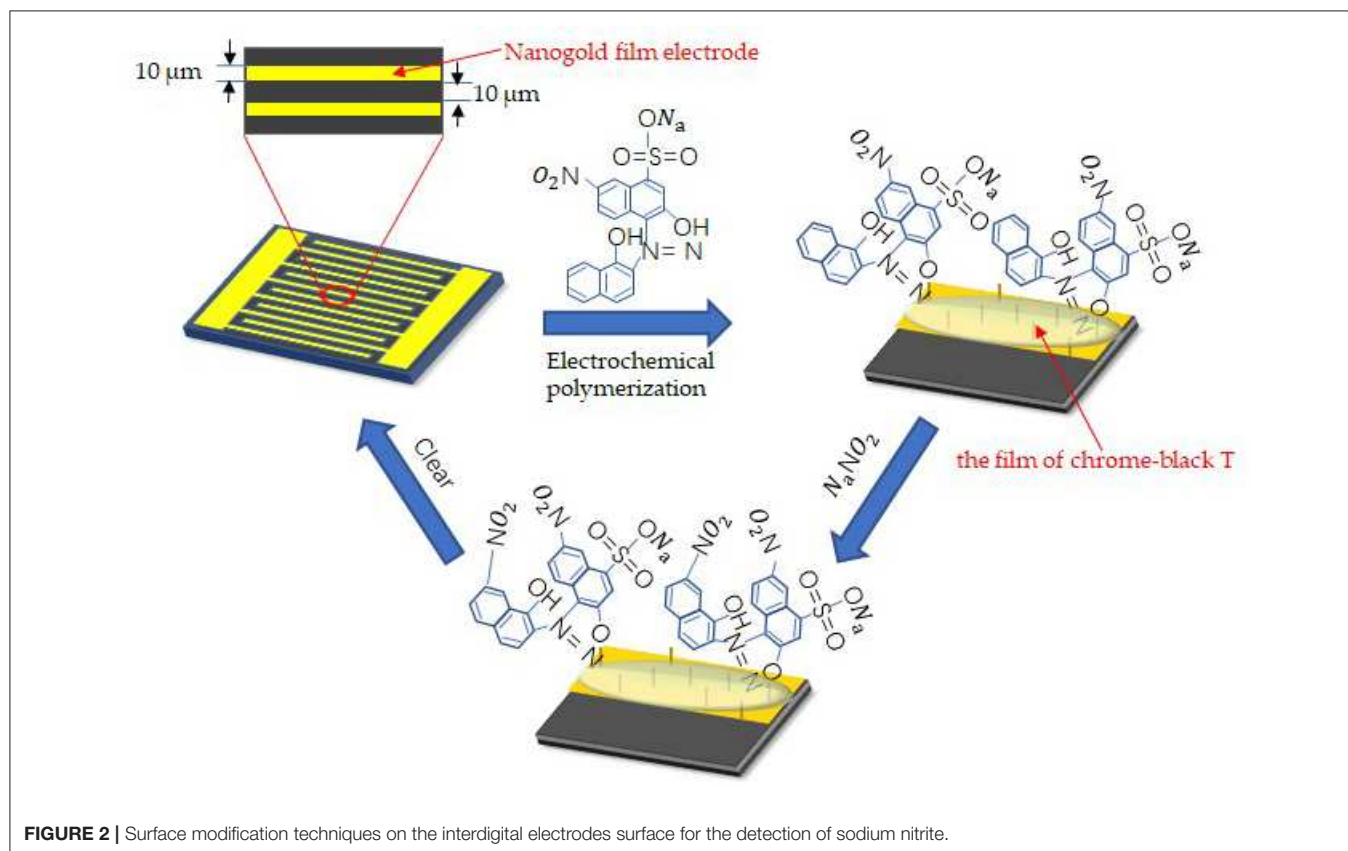


FIGURE 2 | Surface modification techniques on the interdigital electrodes surface for the detection of sodium nitrite.

What's more, when AC signals are applied to the interdigital electrodes, an AC electric field is able to generate microflows through AC electroosmosis (Wu et al., 2005; Mirzajani et al., 2016) or AC electrothermal (Hart et al., 2010) effect. And these mechanisms can accelerate detection. This method has been used to detect small molecules, proteins, virus particles, and nuclei acids (Cui et al., 2015; Liu et al., 2016; Cheng et al., 2017a,b). In this work, the sample solutions were added to the interdigital electrodes, which could alter electrodes' impedance, so the law of changes of the impedance was used to demonstrate the concentration of sample solution.

Preparation of Nanogold Film Interdigital Microelectrodes

In this work, the nanogold film interdigital microelectrodes were fabricated on silicon wafers. And there were four kinds of microelectrodes. We test all of them in order to select the optimal one. At last, we used the nanogold film interdigital microelectrodes which had interdigitated arrays with widths of 10 μm separated by 10 μm gaps to accomplish the test work.

Before the detection, the nanogold film interdigital microelectrodes should be cleaned with the following steps: immersed in acetone for 4 min with ultrasonic cleaning; rinsed in absolute ethyl alcohol for 3 min with ultrasonic cleaning; rinsed in deionized water for 3 min with ultrasonic cleaning; dried with drying oven. After pretreatment, Chrome-black T was modified to the surface of the electrode by electrochemical polymerization. In order to form the film of chrome-black T, 10 μL of solution which included 1 mmol/L Chrome-black T and 10 mmol/L Sodium hydroxide was added to the nanogold film interdigital microelectrodes. At the same time, alternating voltage that differed from 0.01 to 0.9 V were applied to the microelectrodes with a settled frequency (10 kHz). And the number of times of alternating voltage sweep were 25. **Figure 2** shows the process of surface modification on the nanogold film interdigital microelectrodes and the affinity for nitrite ions. Here, we get the nanogold film nitrite sensors.

Apparatus and Methods

Firstly, an impedance analyzer of model IM3536 (HIOKI, Japan) was used to obtain the impedance datum of the bare nanogold film interdigital electrodes with different concentrations of sodium nitrite solutions. In the first stage, the frequency that differed from 100 Hz to 100 kHz were applied to the microelectrodes when they were under a settled alternating voltage. In the fact, we conducted frequency scanning on the bare interdigital microelectrodes. At the same time, we set the alternating voltage as nine equal voltage gradients which differed from 10 to 90 mV. Ten microliter of different concentrations of sodium nitrite solutions were added to the bare nanogold film interdigital microelectrodes. Then the impedance of the bare interdigital microelectrodes was detected. In the second stage, continuous alternating voltage which differed from 10 to 90 mV were applied to the bare interdigital microelectrodes when they were under a fixed

frequency. In the same way, the impedance of the bare interdigital microelectrodes was detected when 10 μL of different concentrations of sodium nitrite solutions were added to them.

The impedance of nanogold film interdigital microelectrodes was reflected in the frequency sweep curve when different concentrations of sodium nitrite solution were added to them. Furthermore, the impedance of bare interdigital microelectrodes was also reflected in the alternating voltage sweep curve when

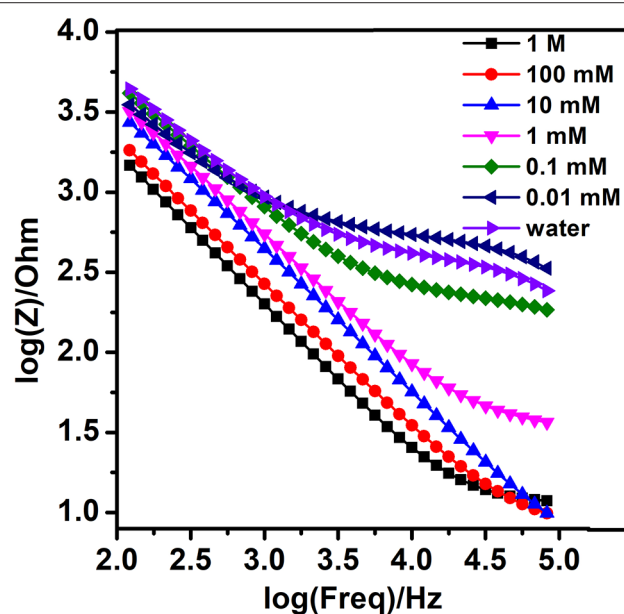


FIGURE 3 | Bode diagram of different concentrations of nitrite with AC signal of 10 mV.

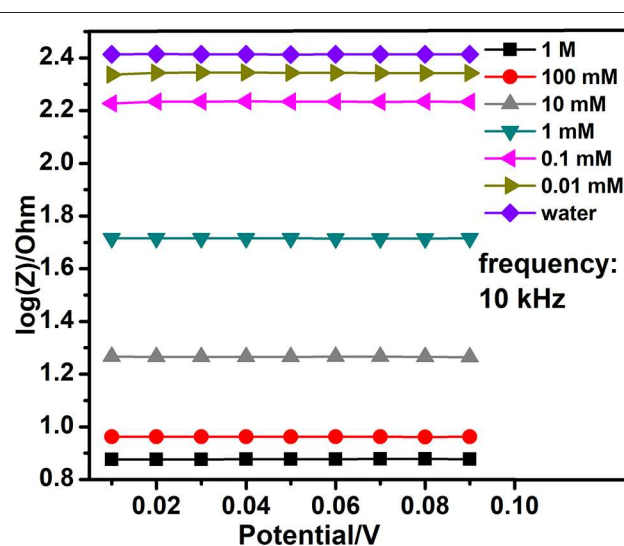


FIGURE 4 | The voltage sweep of different concentrations of nitrite with AC signal of 10 kHz.

different concentrations of sodium nitrite solution were added to them.

Secondly, in order to demonstrate the specificity of the modified nanogold film interdigital electrode sensors, the impedance analyzer of model IM3536 (HIOKI, Japan) was used to obtain the impedance, capacitance, resistance signals of the modified nanogold film nitrite sensors. A 10 kHz AC

signal of 10 mV was used for pumping signal. And the voltage used in the experiments is rms. Ten microliter of different concentrations of working solutions were added to the sensors. Then the impedance, capacitance and resistance signals of the modified nanogold film interdigital electrodes were continuously measured at the AC signal for 30 s. We tested three times for each experimental datum. And we used the average of the

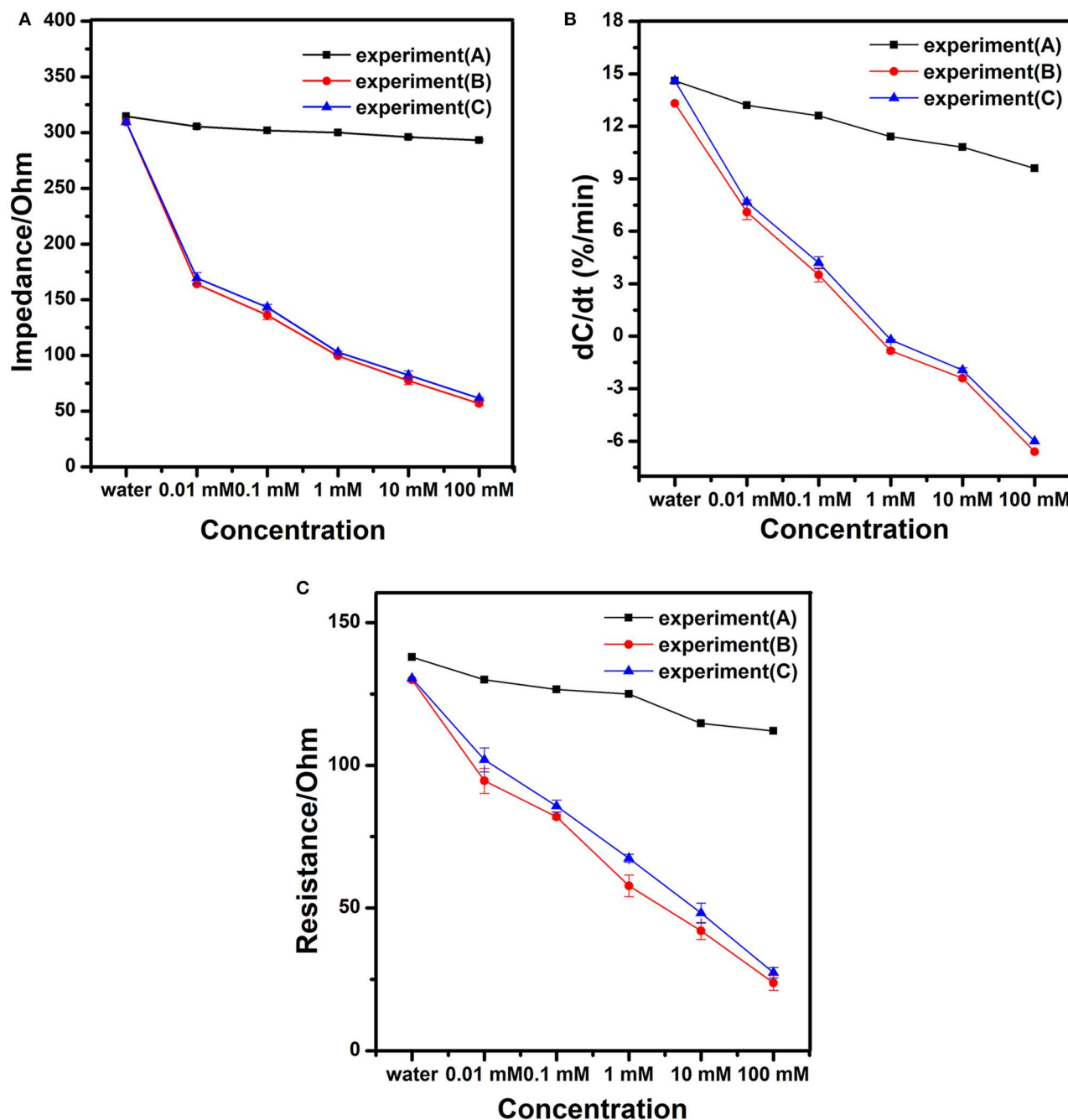


FIGURE 5 | Diagrams of (A) the impedance, (B) the change rate of normalized capacitance, and (C) the resistance of the modified interdigital electrode sensor after being added different concentrations of working solutions.

experimental datum to analyze (Tang et al., 2019). The change rate of normalized capacitance was then calculated to indicate the binding level of sodium nitrite, which is shown as the slope of normalized capacitance vs. time (%/min), found by a least square linear fitting method. The normalized capacitance was calculated as C_t/C_0 , where C_t and C_0 are the capacitance values at time t and time zero, respectively. The capacitance of each biosensor may be quite different. But the normalized capacitance can reduce the errors caused by the difference of each biosensor. So it can reduce the influence on the results.

RESULTS AND DISCUSSION

Detection in Fixed Alternating Voltage

In the first stage, in order to evaluate the performance of the bare nanogold film interdigital electrodes, the optimal interdigital electrode ($10\ \mu\text{m}$ widths, $10\ \mu\text{m}$ gaps) was tested with different concentrations of the sodium nitrite solutions in fixed alternating voltages (Zhou et al., 2019). And the frequency that differed from 100 Hz to 100 kHz and a fixed alternating voltage were set well. The detections were repeated three times. At last, 10 mV was selected from various fixed alternating voltages. At the fixed alternating voltage, the Bode diagram demonstrated the relationship between concentrations of the sodium nitrite solutions and the impedance of interdigital microelectrodes which were added to these working solutions. As is shown in **Figure 3**, the larger concentration of sodium nitrite solution is added to the bare nanogold film interdigital electrodes, the faster reduction rate of the bare nanogold film interdigital electrodes' impedance presents. At the same time, the change rate of the sodium nitrite solution at $10^{-5}\ \text{mol/L}$ is approximately consistent with that of purified water.

Detection in Fixed Frequency

On the base of the previous work, we tested the optimal interdigital electrode again with different concentrations of the sodium nitrite solutions in fixed frequencies. In the second stage, the alternating voltage that differed from 10 to 90 mV and a fixed frequency were set well. The detections were repeated three times. At last, 10 kHz was selected from various fixed frequencies. At the fixed frequency, the alternating voltage sweep curve demonstrated the relationship between concentrations of the sodium nitrite solutions and the impedance of interdigital microelectrodes which were added to these working solutions. The **Figure 4** evidently shows that the larger concentration of sodium nitrite solution is added to the bare nanogold film interdigital electrodes, the smaller impedance of the bare nanogold film interdigital electrodes presents.

Specificity Studies of the Modified Interdigital Electrode Sensors

Different concentrations of working solutions were tested to evaluate the performance of the modified nanogold film interdigital electrode sensors. Based on the 10 kHz and 10 mV AC excitation signal, we measured the impedance of the modified nanogold film interdigital electrode sensors for 30 s.

Three experiments were designed to verify the specificity of the sensor. The impedance of different concentrations of mixture solutions without sodium nitrite were measured in experiment (A). The impedance of different concentrations of sodium nitrite solutions were measured in experiment (B). The impedance of different concentrations of sodium nitrite mixture solutions were measured in experiment (C). The sodium nitrite mixture solution includes nitrite ion, carbonate ion, chloride ion, nitrate ion, magnesium ion and potassium ion. As is shown in **Figure 5A**, the larger concentration of sodium nitrite solution is added on the sensors, the smaller impedance of the sensors present. From **Figure 5B**, we can see a correlation between concentrations of sodium nitrite solutions and the change rate of normalized capacitance. And **Figure 5C** shows that the law of changes of the modified nanogold film interdigital electrode sensor's resistance is similar to the impedance after being added different concentrations of sodium nitrite solutions. The impedance, capacitance, and resistance are common electrical parameters of biosensor for detecting. At the same time, **Figure 5** shows an excellent specificity of the modified nanogold film interdigital electrode sensors. When different concentrations of sodium nitrite mixture solutions were tested, there was nearly no effect on the detection of the nitrite ions. While when different concentrations of mixture solutions without sodium nitrite were tested, the result was similar to that of purified water. Because of the AC electrokinetic effect, some other ions in the mixture solutions may be accelerated to deposit on the surface of the electrode. So the value of impedance, normalized capacitance and resistance decrease slightly when different concentrations of mixture solutions without sodium nitrite were added to the modified interdigital electrode sensors. However, the decreases don't have influences on the results. What's more, the results between mixture solutions without sodium nitrite and sodium nitrite solutions had obvious difference in **Figure 5**.

CONCLUSIONS

In this research, we developed an effective, rapid, and high specificity method for detection of nitrite in water. The larger concentration of sodium nitrite solution is dropped on the modified nanogold film interdigital electrode sensors, the smaller impedance of the modified nanogold film interdigital electrode sensors has. In this work, we selected the optimal dimension of the interdigital electrode sensors and the best experiment conditions for detection. The developed modified nanogold film interdigital electrode sensors have the high specificity to the nitrite ions when different concentrations of sodium nitrite mixture solutions were tested. And the nitrite biosensor can detect the concentration of nitrite solution quickly with only 30 s. At the same time, the limit of detection (LOD) of the developed sensors is nearly $10^{-5}\ \text{mol/L}$, which is more sensitive than those reported by current detection methods such as Phenol spectrophotometry (Lin and Ye, 2010) (LOD is nearly $8.84\ \text{mol/L}$) or gas chromatography (Walsh, 2001) (LOD is nearly $3.45 \times 10^{-3}\ \text{mol/L}$). However, there are also some problems and limitations in our studies. The method needs the

corresponding apparatus to accomplish the detection which is same as the other methods. Further development of the method may provide a more convenient and effective detection for nitrite in complex samples.

DATA AVAILABILITY STATEMENT

All datasets generated for this study are included in the article/supplementary material.

AUTHOR CONTRIBUTIONS

HL, ZP, and YZ: methodology, formal analysis, investigation, data curation, and writing—original draft. XL and XZ:

conceptualization, validation, writing—review and editing, supervision, project administration, and funding acquisition. SX, MS, and LJ: resources, writing—original draft.

FUNDING

This work was supported by the Fundamental Research Funds for the Central Universities (Project No. 2019CDYGZD006), National Natural Science Foundation of China (Project No. 6137 7001), the Postgraduate education and teaching reform research project of Chongqing University (Project No. cqyjg18323), and Venture & Innovation Support Program for Chongqing Overseas Returnees (Project No. cx2018017) and Fundamental Research Funds for the Central Universities (No. 10611CDJXZ238826).

REFERENCES

- Cheng, C., Cui, H., Wu, J., and Eda, S. (2017a). A PCR-free point-of-care capacitive immunoassay for influenza A virus. *Microchimica Acta* 184, 1649–1657. doi: 10.1007/s00604-017-2140-4
- Cheng, C., Oueslati, R., Wu, J., Chen, J., and Eda, S. (2017b). Capacitive DNA sensor for rapid and sensitive detection of whole genome human herpesvirus-1 dsDNA in serum. *Electrophoresis* 38, 1617–1623. doi: 10.1002/elps.201700043
- Cui, H., Wu, J. J., Eda, S., Chen, J., Chen, W., and Zheng, L. (2015). Rapid capacitive detection of femtomolar levels of bisphenol A using an aptamer-modified disposable microelectrode array. *Microchimica Acta* 182, 2361–2367. doi: 10.1007/s00604-015-1556-y
- Davis, J., Moorcroft, M. J., Wilkins, S. J., Compton, R. G., and Cardosi, M. F. (2000). Electrochemical detection of nitrate and nitrite at a copper modified electrode. *Analyst* 125, 737–742. doi: 10.1039/a909762g
- Gajjaraj, S., Fan, C., Lin, M., and Hu, Z. (2013). Quantitative detection of nitrate in water and wastewater by surface-enhanced Raman spectroscopy. *Environ. Monitor. Assess.* 185, 5673–5681. doi: 10.1007/s10661-012-2975-4
- Hart, R., Lec, R., and Noh, H. M. (2010). Enhancement of heterogeneous immunoassays using AC electroosmosis. *Sens. Actuators B Chem.* 147, 366–375. doi: 10.1016/j.snb.2010.02.027
- Holden, N. M., and Scholefield, D. (2008). Paper teststrips for rapid determination of nitrate tracer. *Commun. Soil Sci Plant Anal.* 26, 1885–1894. doi: 10.1080/00103629509369415
- Ito, K., Nomura, R., Fujii, T., Tanaka, M., Tsumura, T., Shibata, H., et al. (2012). Determination of nitrite, nitrate, bromide, and iodide in seawater by ion chromatography with UV detection using dilauryldimethylammonium-coated monolithic ODS columns and sodium chloride as an eluent. *Anal. Bioanal. Chem.* 404, 2513–2517. doi: 10.1007/s00216-012-6405-9
- Jiang, Y., Tang, N., Zhou, C., Han, Z., Qu, H., and Duan, X. (2018). A chemiresistive sensor array from conductive polymer nanowires fabricated by nanoscale soft lithography. *Nanoscale* 10, 20578–20586. doi: 10.1039/C8NR04198A
- Li, S., Ren, Y., Cui, H., Yuan, Q., Wu, J., Eda, S., et al. (2015). Alternating current electrokinetics enhanced *in situ* capacitive immunoassay. *Electrophoresis* 36, 471–474. doi: 10.1002/elps.201400284
- Lin, Q., and Ye, R. (2010). Determination of nitrate and nitrite in food by phenol-spectrophotometry. *J. Minjiang Uni.* 31, 111–114. doi: 10.3969/j.issn.1009-7821.2010.02.028
- Lin, S., Liu, J., Wang, Q., Zu, D., Wang, H., Wu, F., et al. (2019a). Highly robust, flexible, and large-scale 3D-metallized sponge for high-performance electromagnetic interference shielding. *Adv. Mater. Technol.* 5:1900761. doi: 10.1002/admt.201900761
- Lin, S., Wang, H., Wu, F., Wang, Q., Bai, X., Zu, D., et al. (2019b). Room-temperature production of silver-nanofiber film for large-area, transparent and flexible surface electromagnetic interference shielding. *NPJ Flexible Electron.* 3:6. doi: 10.1038/s41528-019-0050-8
- Lin, X., Cheng, C., Terry, P., Chen, J., Cui, H., Wu, J., et al. (2017). Rapid and sensitive detection of bisphenol A from serum matrix. *Biosens. Bioelectron.* 91, 104–109. doi: 10.1016/j.bios.2016.12.024
- Liu, X., Cheng, C., Wu, J., Eda, S., and Guo, Y. (2016). A low cost and palm-size analyzer for rapid and sensitive protein detection by AC electrokinetics capacitive sensing. *Biosens. Bioelectron.* 90, 83–90. doi: 10.1016/j.bios.2016.10.098
- Mirzajani, H., Cheng, C., Wu, J., Ivanoff, C. S., Aghdamb, E. N., Ghavifekr, H. B., et al. (2016). Design and characterization of a passive, disposable wireless AC-electroosmotic lab-on-a-film for particle and fluid manipulation. *Sens. Actuators B Chem.* 235, 330–342. doi: 10.1016/j.snb.2016.05.073
- Tanaka, A., Nose, N., and Iwasaki, H. (1982). Determination of nitrate in meat products and cheese by gas-liquid chromatography with electron-capture detection. *J. Chromatogr. A* 235, 173–185. doi: 10.1016/S0021-9673(00) 95798-4
- Tang, N., Zhou, C., Xu, L., Jiang, Y., Qu, H., and Duan, X. (2019). A fully integrated wireless flexible ammonia sensor fabricated by soft nano-lithography. *ACS Sens.* 4, 726–732. doi: 10.1021/acssensors.8b01690
- Walsh, M. E. (2001). Determination of nitroaromatic, nitramine, and nitrate ester explosives in soil by gas chromatography and an electron capture detector. *Talanta* 54, 427–438. doi: 10.1016/S0039-9140(00)00541-5
- Wu, J., Ben, Y., and Chang, H. C. (2005). Particle detection by electrical impedance spectroscopy with asymmetric-polarization AC electroosmotic trapping. *Microfluid. Nanofluidics* 1, 161–167. doi: 10.1007/s10404-004-0024-5
- Xu, H., Ding, S., Cao, X., Ye, Y., Ye, Y., and Sun, H. (2015). Rapid detection of nitrite in food using the electrode modified by hemoglobin/gold nanoparticle-reduced graphene oxide composite. *Modern Food Sci. Technol.* 31, 319–323. doi: 10.13982/j.mfst.1673-9078.2015.11.048
- Zhou, C., Zhang, X., Tang, N., Fang, Y., Zhang, H., and Duan, X. (2019). Rapid response flexible humidity sensor for respiration monitoring using nano-confined strategy. *Nanotechnology* 4, 726–732. doi: 10.1088/1361-6528/ab5cda

Conflict of Interest: The authors declare that the research was conducted in the absence of any commercial or financial relationships that could be construed as a potential conflict of interest.

Copyright © 2020 Luo, Lin, Peng, Zhou, Xu, Song, Jin and Zheng. This is an open-access article distributed under the terms of the Creative Commons Attribution License (CC BY). The use, distribution or reproduction in other forums is permitted, provided the original author(s) and the copyright owner(s) are credited and that the original publication in this journal is cited, in accordance with accepted academic practice. No use, distribution or reproduction is permitted which does not comply with these terms.



Study on AgInZnS-Graphene Oxide Non-toxic Quantum Dots for Biomedical Sensing

Chi Song¹, Haoyue Luo², Xiaogang Lin^{2*}, Zhijia Peng², Lingdong Weng², Xiaosheng Tang², Shibin Xu², Ming Song², Lifeng Jin² and Xiaodong Zheng^{3*}

¹ Department of Life Science and Technology, Changshu Institute of Technology, Changshu, China, ² Key Laboratory of Optoelectronic Technology and Systems of Ministry of Education of China, Chongqing University, Chongqing, China,

³ Chongqing University Cancer Hospital, Chongqing University, Chongqing, China

OPEN ACCESS

Edited by:

Weiwei Wu,
Xidian University, China

Reviewed by:

Ming Lei,
Beijing University of Posts and
Telecommunications (BUPT), China
Cheng Zhou,
Tianjin University, China

*Correspondence:

Xiaogang Lin
xglin@cqu.edu.cn
Xiaodong Zheng
zxd0052005@163.com

Specialty section:

This article was submitted to
Nanoscience,
a section of the journal
Frontiers in Chemistry

Received: 11 January 2020

Accepted: 31 March 2020

Published: 05 May 2020

Citation:

Song C, Luo H, Lin X, Peng Z,
Weng L, Tang X, Xu S, Song M, Jin L
and Zheng X (2020) Study on
AgInZnS-Graphene Oxide Non-toxic
Quantum Dots for Biomedical
Sensing. *Front. Chem.* 8:331.
doi: 10.3389/fchem.2020.00331

In recent years, non-toxic quantum dot has caught the attention of biomedical fields. However, the inherent cytotoxicity of QDs makes its biomedical application painful, and is a major drawback of this method. In this paper, a non-toxic and water-soluble quantum dot AgInZnS-GO using graphene oxide was synthesized. A simple model of state complex was also established, which is produced through a combination of quantum dots and protein. The interaction between AIZS-GO QDs and human serum albumin (HSA) has significant meaning *in vivo* biological application. Herein, the binding of AIZS-GO QDs and HSA were researched using fluorescence spectra, Uv-visible absorption spectra, FT-IR spectra, and circular dichroism (CD) spectra. The results of fluorescence spectra demonstrate that AIZS-GO QDs have an obvious fluorescence quenching effect on HSA. The quenching mechanism is static quenching, which implies that some type of complex was produced by the binding of QDs and HSA. These results were further proved by Uv-visible absorption spectroscopy. The Stern-Volmer quenching constant K_{SV} at various temperatures (298 K, 303 K, 308 K) were acquired from analyzing Stern-Volmer plots of the fluorescence quenching information. The Van't Hoff equation could describe the thermodynamic parameters, which demonstrated that the van der Waals and hydrogen bonds had an essential effect on the interaction. FT-IR spectra and CD spectra further indicate that AIZS-GO QDs can alter the structure of HSA. These spectral methods show that the quantum dot can combine well with HSA. The experimental results showed that AgInZn-GO water-soluble quantum dots have good biocompatibility, which can be combined with proteins to form new compounds which have no cytotoxicity and biological practicability. It provides an important basis for the combination of quantum dots and specific proteins as well as fluorescent labeling.

Keywords: quantum dots, AgInZnS-graphene oxide, non-toxic, interaction mechanism, human serum albumin, spectroscopy

INTRODUCTION

In recent years, researchers have devoted themselves to the development of various nanomaterials and their manufacturing methods, which have opened up new research directions for nano-biotechnology in the field of biomedicine. Due to its special optical and physical properties, quantum dots (QDs) have caught the attention of various research fields

(Alivisatos, 1996; Dabbousi et al., 1997; Niemeyer, 2001; Fu and Lakowicz, 2006; Jiang et al., 2018; Tang et al., 2019; Wang et al., 2019). Quantum dots can be used as fluorescent markers to detect proteins, DNA, and specific proteases qualitatively or quantitatively. In general, reactions will occur between QDs and proteins because of the diverse modified coating agents and elemental composition on the surface of QDs (Bruchez et al., 1998; Chan and Nie, 1998). However, the inherent cytotoxicity of QDs makes the biomedical application painful, a major drawback of the method. For instance, many studies reported the influence CdTe and CdSe quantum dots have on protein. The toxicity of Cd, Te, and Se elements remains a problem for practical application and makes its use non-negligible (Nirmal et al., 1994; Shiang et al., 1995; Ragab et al., 2014). In response to the above issues, some researches refer to the I-III-VI₂ type QDs (Allen and Bawendi, 2008) like AgInS₂ (Hamanaka et al., 2011), CuInS₂ (Cassette et al., 2010; Li et al., 2015) and ZnS-AgInS₂ (Torimoto et al., 2007).

In this paper, we focus on novelty AgInZnS (AIZS) non-toxic quantum dots. AIZS QDs are prevalent in diverse fields because of their optical and electrical characteristics, which include tunable-emission wavelength, high absorbance coefficient, and high quantum yield (Sheng et al., 2012). The as-prepared hydrophobic AIZS QDs should be converted into a hydrophilic polymer before reacting with the protein. Compared with other phase transfer agents, strong absorption ability was shown in graphene oxide (GO) (Gao et al., 2013; Shin et al., 2014; Farid et al., 2016). Due to its biocompatibility, non-toxicity, and excellent water solubility, GO is suitable to transfer the hydrophobic AIZS QDs in hydrophilic polymers and for further biological application (Zu et al., 2016).

HSA is broadly distributed in blood plasma. It has a significant effect on equilibrium osmotic pressure and transports various molecules in blood (Carter et al., 1989; Dong et al., 1990; Leckband, 2000; Lin et al., 2019a). Nanoparticles and drugs can bind with HSA for their exogenous ligand and is then transported into the body's circulatory system. Because there are some interactions between nanoparticles and the protein, it is necessary to analyze the influence of nanoparticles on HSA at the molecular level after it enters the human body. In many biophysical and biochemical studies, HSA has been diffusely utilized as a model protein because of its medicinal value and its unique ligand binding properties (Figge et al., 1991).

As far as we know, AIZS-GO QDs has enormous potential in biological research. At first, we wanted to establish a molecular model of interaction *in vitro* between quantum dots and proteins. In this paper, the specific biomedical research contents mainly include the following three aspects. First, the preparation of the water-soluble quantum dot AgInZnS-GO with high biocompatibility. The particle size and distribution of quantum dots were observed by transmission electron microscopy, and the carboxyl group was distributed according to the Fourier transform infrared spectroscopy. Second, the effects of the AgInZnS-GO quantum dot with HSA was studied using a multispectral technique. In this paper, the quenching mechanism of the quantum dot and protein interaction was analyzed by fluorescence spectrometry. The ultraviolet and visible absorption

spectra is used to determine whether a new ground state complex was generated. The structural changes of protein and the major chemical bond changes during the reaction were analyzed by the Fourier transform infrared spectra and the circular dichromatic spectrum. Third, the cytotoxicity of quantum dots was analyzed. The safe concentration and time range of quantum dots were analyzed from two perspectives: cell appreciation rate and cell morphology. Next, we will perform a binding study *in vivo* in animal models.

MATERIALS AND METHODS

Materials

HSA was purchased from Sigma-Aldrich (Sigma, St. Louis, MO, USA), and its purity was greater than 99.9%, containing very few fatty acids. HSA was dissolved in 0.058 M Tris-HCL buffer solution (pH 7.4) and kept at 4°C. Tris-HCL buffer was widely used as the solvent of the protein, which could prevent the dramatic fluctuation of pH, thus preventing the denaturation of the protein which could create an approximate physiological condition. The concentration was measured by Uv-visible absorption spectrum, to which the extinction coefficient at 280 nm of 36,600 L.mol⁻¹.cm⁻¹ was applied. AgInZnS nanoparticles were synthesized base on previous research. The oily AIZS QDs were transferred by graphene oxide into red-emission water soluble quantum dots. All the experiments used ultrapure water.

Synthesis of AIZS QDs

The synthesis of high quality water-soluble AIZS QDs is an important factor in the research, which enabled it to be further applied in biological detection. The main synthesis process was as follows. First, 0.1 mM indium acetate, 0.1 mM silver nitrate, 0.1 mM oleic acid, 2 mM double chlorobenzene trichloroethane, 40 ml trioctylphosphine, and 4 mM octadecene, respectively, were added to three neck flasks heated to 85°C for 30 min. Next, 0.1 mM sulfur was added into the ODE and oleic acid, after which they were gradually added into a three-neck flask. After 2 min, 0.1 mM zinc was dissolved in the ODE and oleic acid and gradually added into the reaction solution. At the same time, the solution was quickly heated to 130°C, and 10 drops of zinc stearate was then added, and the ODE mixture was annealed for 10 min. Lastly, the mixture left to cool to room temperature. Oil-soluble AIZS QDs are obtained by centrifugation after dropping ethanol. Based on the synthesis of oil-soluble AIZS QDs, the AIZS-GO QDs composite nanomaterials can be further synthesized by micro-emulsification. First, GO is modified with oleylamine as the emulsifier, and then GO-OAM is precipitated after cleaning. Finally, GO-OAM and oil-soluble AIZS QDs are mixed in chloroform, then the pure AIZS-GO QDs are obtained through a series of processes.

Fluorescence Spectroscopy

All fluorescence spectra were obtained by Cary Eclipse spectrofluorometer (Varian, USA), which was equipped with a 150 W xenon lamp and a thermostatic water bath. Quartz cells (1 cm path-length) were applied to all measurements. At various

temperatures (298 K, 303 K, 308 K), the fluorescence emission spectra were obtained with a wavelength range of 300–480 nm and excitation at 285 nm as titration of QDs was used in HSA. Excitation and emission slit widths were then set to 5.0 nm and 10.0 nm. The averages of the three scans were reflected in the spectra. To begin with, 2.8 ml of 1×10^{-6} mol/L HSA solution was added to a 10 mm quartz cell and 5 μ l AIZS-GO QDs of different concentrations was subsequently added to the HSA each time, which meant that a series of HSA concentrations were obtained to determine the quenching capacity.

Uv-Visible Absorption Spectroscopy

Uv-visible absorption spectrum was recorded by Cary 60 Uv-visible spectrophotometer (Varian, USA), which was equipped with 10 mm quartz cells. The recorded wavelength ranged from 220 to 440 nm at 298 K. The dissimilitude between AIZS-GO QDs-HSA and AIZS-GO QDs was acquired by the Uv-visible absorption spectrum of AIZS-GO QDs-HSA, which put AIZS-GO QDs as the reference.

CD Spectroscopy

CD spectrum was recorded by MOS-450 CD spectropolarimeter (Bio-Logic, France), which was equipped with 10 mm quartz cells. The CD spectrum ranged from 190 to 250 nm and the acquisition duration was set at 2 s. Each spectrum was corrected by 0.05 M Tris-HCl buffer solution. The results were the average of the three scans. As reported in the literature, the tris buffer system was widely used as the solvent of protein, which could prevent the dramatic fluctuation of PH, thus preventing the denaturation of protein, which could create an approximate physiological condition (Chuang and Otagiri, 2002; Hu et al., 2005; Zhang et al., 2008; Feroz et al., 2012; Lin et al., 2017, 2019b). So, we used the tris buffer system as the environment for the protein binding assay *in vitro*.

FT-IR Spectroscopy

Fourier transform infrared (FT-IR) spectrum was measured by Nicolet iS5 spectrometer (Thermo, USA). All FT-IR spectra were obtained in the range of $1,300\text{--}1,800\text{ cm}^{-1}$ with the resolution ratio of 4 cm^{-1} . Tris-HCl solution as the reference solution was used to ensure the spectra of HSA and AIZS-GO QDs has were not influenced.

RESULTS AND DISCUSSION

Characterization of AgInZnS-GO QDs

The typical Uv-visible absorption of AIZS QDs and AIZS-GO QDs can be seen in **Figure 1A**. Both had strong absorptivity but had no obvious absorption peak. AIZS-GO QDs had high water solubility while AIZS QDs had high oil solubility. From **Figure 1B**, we can see the fluorescence spectra of AgInZnS QDs and AgInZnS-GO QDs, which demonstrates that AIZS QDs and AIZS-GO QDs exhibit obvious and almost symmetrical emission spectrums with excitation wavelengths of 370 nm. The emission wavelength of AIZS QDs was about 570–750 nm, while

the emission wavelength of AIZS-GO QDs was about 500–780 nm. The spectrums were symmetric, indicating that they were homogenous.

Effects of Reaction Time

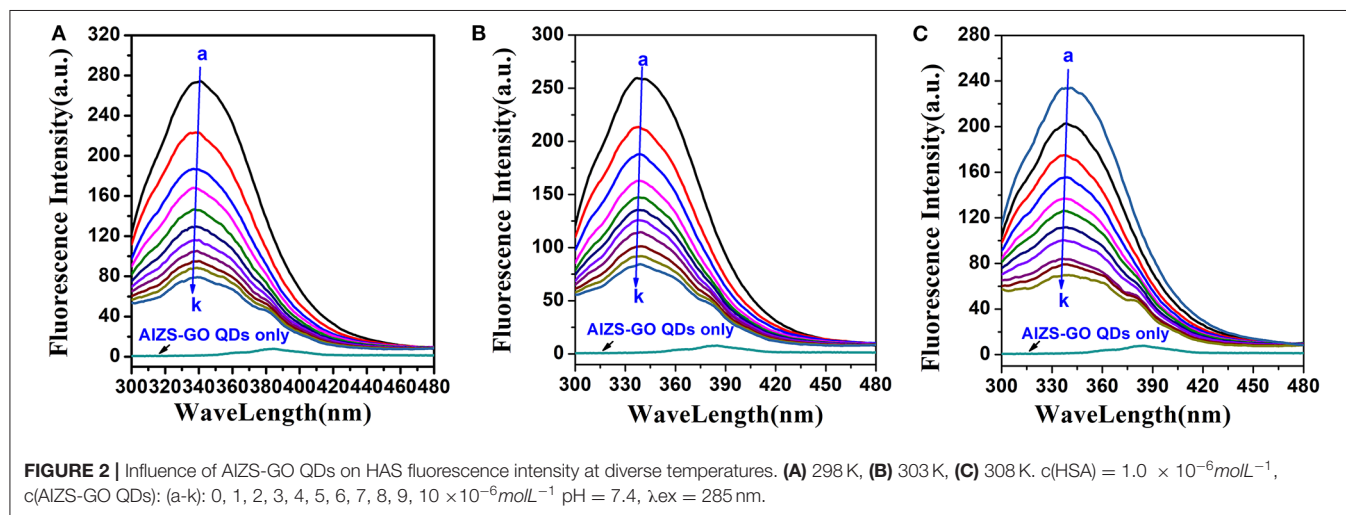
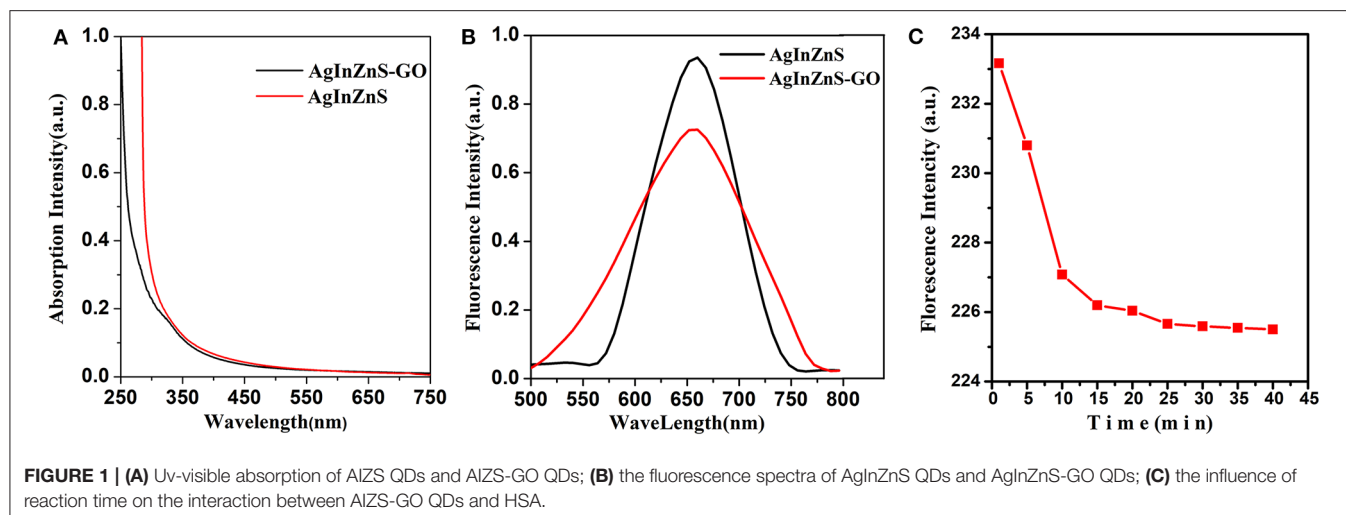
By observing the reaction time influence on the fluorescence intensity of the AIZS-GO QDs and HSA system, the extent of interaction in the system could be researched better. As shown in **Figure 1C**, in the first 20 min during the reaction process, the fluorescence intensity of the system reduced along with the time. That was because AIZS-GO QDs had an obvious fluorescence quenching effect on HSA and it was a static quenching. In the early stage of the static quenching, AIZS-GO QDs could combine with the fluorescent molecules which were in the ground state, so as to generate the new compound which had no fluorescence characteristics. That is to say, the photons were not emitted in the new compound, which resulted in the dramatic decline of the fluorescence intensity in the first 20 min. After 25 min, the number of new compounds formed by the combination between AIZS-GO QDs and HSA was stable, and the fluorescence intensity of the system was approximately unchanged. All experiment data should therefore be tested after 25 min, when the AIZS-GO solution titrated.

Fluorescence Quenching of HSA by QDs

AIZS-GO QDs are able to effectively quench the fluorescence intensity of HSA. **Figure 2** shows the influence of AIZS-GO QDs on HSA fluorescence intensity. It obviously illustrated that the fluorescence intensity decreased bit by bit when the concentration of AIZS-GO QDs increased at diverse temperatures (298 K, 303 K, 308 K). At the same time, **Figure 2** shows that AIZS-GO QDs had a weak fluorescence peak when the excitation wavelength was 285 nm, but the fluorescence peak did not appear at 340 nm where the fluorescence peak of AIZS-GO QDs and the HSA system appeared. Furthermore, the fluorescence peak value of AIZS-GO QDs was very low. Therefore, the fluorescence of AIZS-GO QDs will not affect the fluorescence spectrum of HSA. We did not therefore correct the fluorescence data for inner filter effect.

The fluorescence quenching mechanism could be distributed into dynamic quenching and static quenching. Quencher and fluorescence materials generated no fluorescing complex in static quenching, which could result in the decrease of the fluorescence intensity. Dynamic quenching was caused by quencher and fluoresce material molecules colliding at the excited state. Quenching mechanisms could be distinguished by quenching constants at various temperatures (Ghali, 2010; Lacerda et al., 2010). Higher temperatures lead to larger diffusion coefficients and larger masses of collisional quenching. As a result, higher temperatures could also increase the dynamic quenching constants. On the contrary, higher temperatures could not only bring about stability of decreased complexes, but also decreased the static quenching constants (Brown and Royer, 1997; Dzagli et al., 2010). The fluorescence quenching is able to be ordinarily determined by Stern-Volmer equation.

$$\frac{F_0}{F} = 1 + K_q \tau_0 [Q] = 1 + K_{SV} [Q] \quad (1)$$



where F_0 and F are steady-state of fluorescence intensities before and after adding quencher (AIZS-GO QDs solution), respectively. K_q is the quenching rate constant of bimolecular, K_{SV} is the Stern-Volmer quenching constant, $[Q]$ is the concentration of quenching agent.

Therefore, the above equation could determine K_{SV} by linear regression of a plot of F_0/F against $[Q]$. **Figure 3A** shows the graphs of Stern-Volmer equation at diverse temperatures. And the Stern-Volmer quenching constant K_{SV} values are listed in **Table 1**.

In order to determine whether it was dynamic quenching or static quenching, we explored the quenching mechanism of AIZS-GO QDs and HSA systems by studying fluorescence quenching under different temperatures. It was obvious that the Stern-Volmer quenching constant K_{SV} reduced when the temperature increased, which implied that the quenching mechanism was static quenching.

Moreover, the quenching information was further verified by the amendatory Stern-Volmer equation (Liang et al., 2008; Asha

Jhonsi et al., 2009; Sun et al., 2015).

$$\frac{F_0}{\Delta F} = \frac{F_0}{F_0 - F} = \frac{1}{f_a K_a} \frac{1}{[Q]} + \frac{1}{f_a} \quad (2)$$

where ΔF is a variation of fluorescence intensity, f_a is a proportion of accessible fluorescence. K_a is an effective quenching constant. The dependence of $F_0/\Delta F$ on the reciprocal value of the quenching agent concentration $[Q]^{-1}$ was linear with the slope, equaling the value of $(f_a K_a)^{-1}$ and the ordinate equaling the value of f_a^{-1} . **Figure 3B** shows the graphs of the amendatory Stern-Volmer equation at diverse temperatures.

We found that the effective quenching constant K_a reduced when temperature increased in **Table 1**. And it was same as the change of K_{SV} , which further implied the static quenching mechanism of AIZS-GO QDs and the HSA system.

Moreover, the K_a values varied slightly, indicating that the combination between AIZS-GO QDs and HSA is stronger, which is a result of the synergistic forces among ions. Meanwhile, these

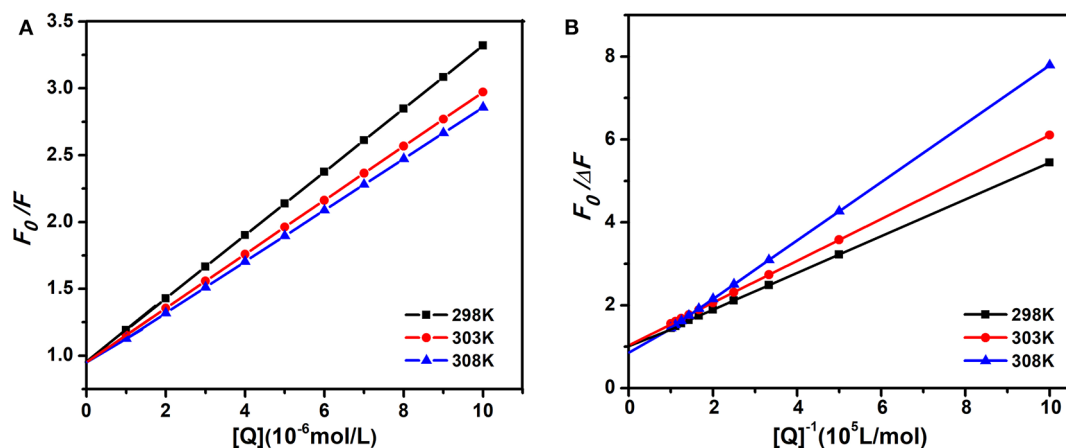


FIGURE 3 | The Stern-Volmer and amendatory Stern-Volmer curves of AIZS-GO QDs with HSA at diverse temperatures. **(A)** Stern-Volmer, **(B)** the amendatory Stern-Volmer.

TABLE 1 | Stern-Volmer quenching constant K_{SV} , amendatory Stern-Volmer effective quenching constant K_A and the correlation coefficient R for the interaction between AIZS-GO QDs and HSA at diverse temperatures.

T(K)	$K_{sv}(10^5 \text{ Lmol}^{-1})$	R	$K_a(10^5 \text{ Lmol}^{-1})$	R
298	2.230	0.9999	2.147	0.9993
303	1.922	0.9996	1.970	0.9995
308	1.829	0.9994	0.999	0.9998

demonstrate that QDs will stay in the blood plasma longer and will be more difficult clear away.

When quantum dots bind with HSA, molecules were in a state of partial equilibrium. This relationship can be calculated using the following equation (Huang et al., 2012; Tabassum et al., 2012).

$$\lg \frac{F_0 - F}{F} = \lg K_A + n \lg [Q] \quad (3)$$

where K_A is the binding constant and n is the number of binding points in the interaction between AIZS-GO QDs and HSA at diverse temperatures. **Figure 4** shows graphs of the double log equation at diverse temperatures. The binding constant K_A values and the number of binding points n are listed in **Table 2**. From the results, n was close to 1, which indicates that there was at least one binding point in the interaction between AIZS-GO QDs and HSA. The binding constant is importance to understand the distribution of AIZS-GO solution. The binding constant increased with rising temperatures, meaning that the complex produced in the reaction became more stable. From the above analysis, we could form a site binding model to judge the reaction degree of protein and quenching agent. That was why we studied the other temperatures condition in this study.

Combination Between QDs and HSA

The combination power between extraneous parts and HSA mainly involve hydrophobic, van der Waals, and hydrogen bonds (Sudlow et al., 1976). Based on plenty of experimental data

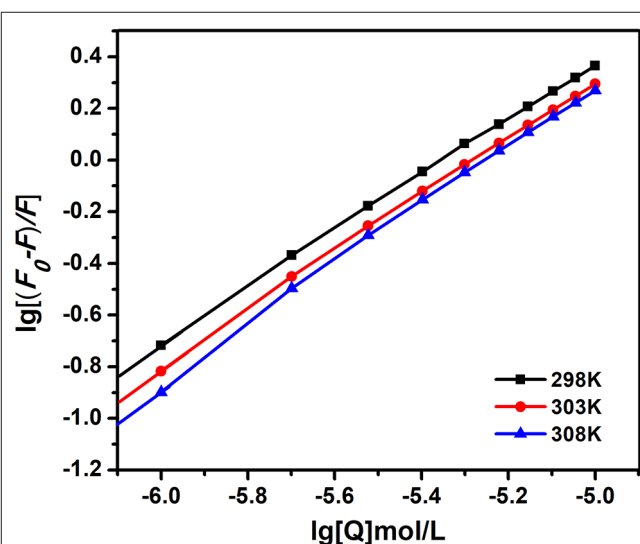


FIGURE 4 | The double log plot of AIZS-GO QDs with HSA at diverse temperatures.

and by analyzing results, Ross and Surbamanian concluded that the interaction forces were associated with a magnitude of thermodynamic parameters, containing enthalpy (ΔH) and entropy (ΔS). The thermodynamic parameters can be described by van't Hoff's equation (Koegler et al., 2012).

$$\ln K_A = -\frac{H}{RT} + \frac{S}{R} \quad (4)$$

$$G = -RT \ln K_A = H - TS \quad (5)$$

where K_A is the binding constant at settled temperature T , R is the gas constant, and ΔG is free energy. We could draw the linear fitting plot of $\ln K_A$ against $\frac{1}{RT}$. The values of ΔH and ΔS were acquired from the slope and intercept of the plot. The values are shown in **Table 3**. The values of ΔH and ΔS were both less than zero demonstrating that hydrogen bonds and van der Waals'

forces made great contributions to the interaction of AIZS-GO QDs and HSA. The values of ΔG were negative demonstrating that the interaction is a spontaneous process.

UV-Vis Absorption Spectra

Furthermore, the distinction of Uv-visible absorption spectrum could identify the fluorescence quenching mechanism. Dynamic quenching only affects excited states of molecules, and there was no distinction in the absorption spectrum. But the complex generation in the process of static quenching disturbed the absorption spectrum (Gelamo et al., 2002; Hu et al., 2010).

We could see that the Uv-visible absorption spectrum of HSA was significantly altered by adding different concentrations of AIZS-QDs in **Figure 5A**. **Figure 5B** shows that AIZS-GO QDs have strong absorptivity, and the absorption spectrum between the AIZS-GO QDs-HSA system and AIZS-GO illustrated that changes in the absorption spectrum of has, after instilling

TABLE 2 | The binding constant K_A , numbers of binding site n and the correlation coefficient R for the interaction between AIZS-GO QDs and HSA at diverse temperatures.

T(K)	$K_{sv}(10^5 Lmol^{-1})$	n	R
298	5.695	1.076	0.9992
303	6.490	1.101	0.9988
308	10.942	1.150	0.9973

TABLE 3 | The thermodynamic parameters of AIZS-GO QDs and HSA system at diverse temperatures.

T(K)	$\Delta H (KJmol^{-1})$	$\Delta G (KJmol^{-1})$	$\Delta S (Jmol^{-1}K^{-1})$
298		-30.723	
303	-66.417	-30.124	-119.78
308		-29.525	

AIZS-GO, was not influenced by the absorbency of quantum dots. This further confirmed the static quenching mechanism.

Conformation Alteration of HSA by QDs

FT-IR spectroscopy can effectively analyze the alteration of the structure of HSA (Ding et al., 2011; Hemmateenejad et al., 2015).

Figure 6A shows that HSA had two primary amide bands of about 1652 cm^{-1} (C=O stretch) and $1,544\text{ cm}^{-1}$ (C-N stretch, N-H bending mode). QDs had two primary absorption bands of about $1,634\text{ cm}^{-1}$ (C=O stretch) and $1,466\text{ cm}^{-1}$ (C-H stretch), too. Furthermore, the absorption spectrum of AIZS-GO QDs-HSA had a distinct wavelength movement (from $1,652\text{--}1,650$ to $1,544\text{--}1,537\text{ cm}^{-1}$) when it was compared with HSA's. These results demonstrate that QDs interact with groups on the surface of HSA that alter HSA's structure.

CD spectroscopy can research the conformation of HSA quantitatively (Nordén and Tjerneld, 1982; Venyaminov and Woody, 1999). **Figure 6B** shows that HSA had two negative absorption points of about 208, 220 nm. It implies that the α -helical structure existed in HSA. This phenomenon was owed to the $n \rightarrow \pi^*$ and $\pi \rightarrow \pi^*$ electron transfer to the peptide's bonds of the α -helica. Meanwhile, the diversity between the HSA and AIZS-GO QDs-HSA system demonstrates the cause of the conformational alteration of HSA. CD spectra can be described using following equation.

$$MRE_{208nm} = \frac{\text{ObservedCD (mdeg)}}{c \cdot n \cdot l \times 10} \quad (6)$$

$$\alpha - \text{helix (\%)} = \frac{-MRE_{208nm} - 4000}{33000 - 4000} \times 100 \quad (7)$$

Where MRE_{208nm} is the mean residue ellipticity at 208 nm, c is the concentration of HSA, n is the number of amino acid residues in HSA ($n = 585$) and l is the path length. It was calculated that approximately 54.52% of the α -helix existed in HSA, which implied that HSA remained α -helix structure. In addition, when AIZS-GO QDs exist, the α -helix would decrease to 50.35%, which

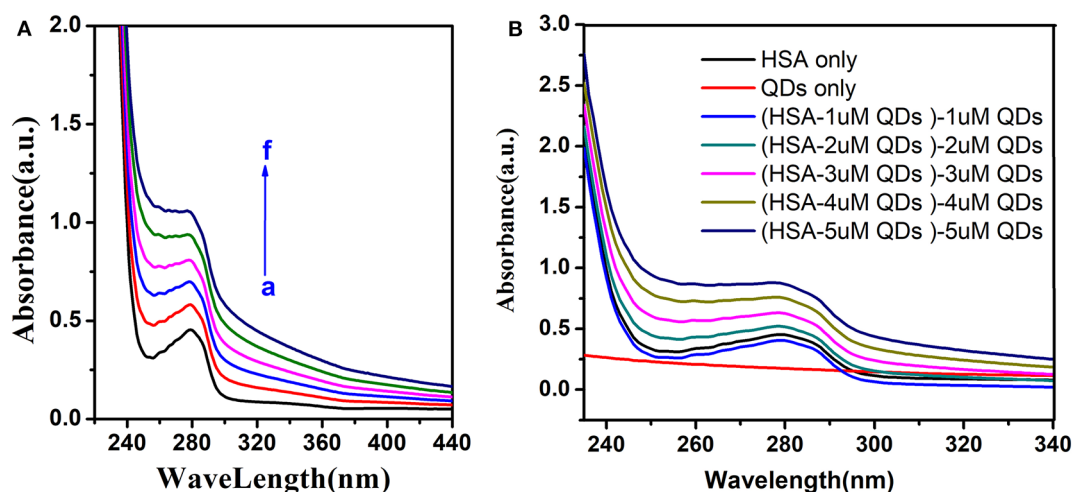


FIGURE 5 | (A) Uv-visible absorption spectra of HSA ($T = 298\text{ K}$) in different concentration of AIZS-GO QDs. $c(\text{HSA}) = 1.0 \times 10^{-6}\text{ mol/L}^{-1}$, $c(\text{AIZS-GO QDs})$: (a-f): 0, 1, 2, 3, 4, 5 $\times 10^{-6}\text{ mol/L}^{-1}$, $\text{pH} = 7.4$. **(B)** is the Uv-visible absorption spectra of QDs, HSA and the distinction of HSA-QD and QDs.

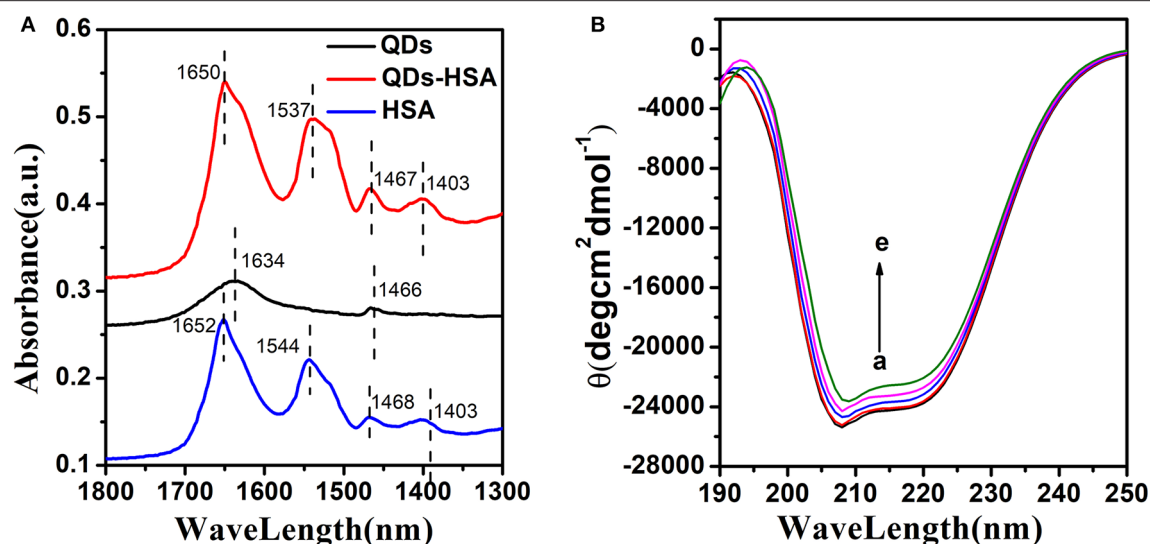


FIGURE 6 | (A) FT-IR spectra of HSA, AIZS-GO QDs, and AIZS-GO QDs-HSA system. **(B)** CD spectra of HSA with different concentration AIZS-GO QDs. $c(\text{HSA}) = 1.0 \times 10^{-6} \text{ mol/L}$, $c(\text{AIZS-GO QDs})$: (a-e): 0, 2, 4, 6, $8 \times 10^{-6} \text{ mol/L}$. pH = 7.4.

demonstrates more alterations in the structure and that surface coverage of HSA is reduced after interacting with AIZS-GO QDs. The α -helix content of HSA has an effect on the bioactivity of HSA.

All FT-IR spectra and CD spectra results demonstrate that AIZS-GO QDs bind stronger with HSA, which leads to major conformation alterations of HSA.

Cytotoxicity of QDs

The quantum dots in this work were nearly non-toxic. When AIZS-GO QDs are gradually applied to live experiments, their toxicity always needs to be further researched systematically. In order to use AIZS-GO QDs to label liver cancer cells, the cck-8 (Cell Counting Kit-8) analytical method was used to test the survival rate of hepatocellular carcinoma Hep-G2 cells and to determine the cytotoxicity of AIZS-GO QDs in the experiment. The results were the average of five tests. The cytotoxicity of AIZS-GO QDs was analyzed by using quantum dots with different concentrations (1, 10, 50, 100 $\mu\text{mol/L}$) and different action times (6, 12, 24 h). The cell survival rate is shown in Figure 7.

Figure 7 shows that the damage to cells was the greatest when the concentration of AIZS-GO QDs was 10^{-6} mol/L . After 24 h of culture, cell survival rate was only 53.87%. With the increased action time, the cell survival rate gradually decreased at different concentrations. When the concentration of AIZS-GO QDs was 10^{-8} mol/L and the action time was 24 h, the cell survival rate was still 78.15%, indicating that the effect of AIZS-GO QDs on cell activity was not significant at the appropriate concentration. The results also implied that AIZS-GO QDs could affect the cells' survival rate by cultivating with them for too long. Moreover, when the concentration of AIZS-GO QDs exceeded a certain range, the apoptosis rate of cells could increase.

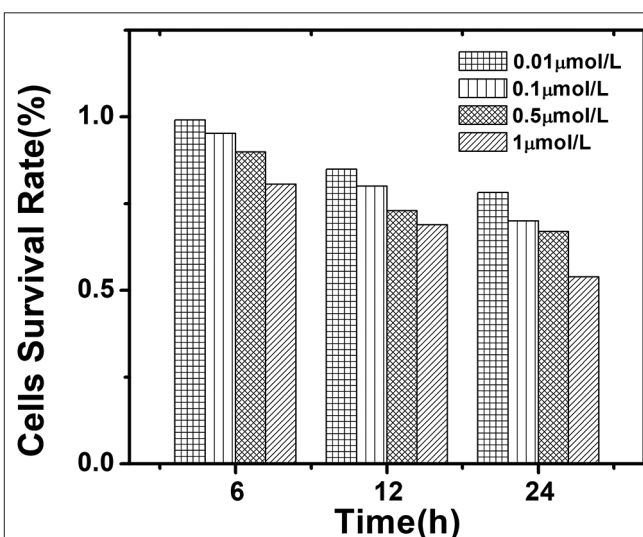


FIGURE 7 | The influence of different concentrations of AIZS-GO QDs and different incubation time on the survival rate of hepatocellular carcinoma Hep-G2 cells.

Table 4 shows the comparison in cytotoxicity of different quantum dots of the other reported work. It was shown that the synthesized AIZS-GO QDs had greatly lowered cytotoxicity than cadmium quantum dots which contained heavy metal ions. It is beneficial for us to study the cytotoxicity of AIZS-GO QDs in normal cells in the future.

CONCLUSIONS

In summary, the interaction between AIZS-GO QDs and HSA was researched by fluorescence spectra, Uv-visible absorption spectra, FT-IR spectra, and CD spectra. AIZS-GO QDs then

TABLE 4 | Cytotoxicity comparison of different quantum dots after 6 h.

Quantum dots	Concentration of QDs	Cells	Cells survival rate	Reference
NAC-CdTe QDs	20 nM	Hepatocytes	75.38%	Wang et al., 2019
CdSe QD-polymerNPs	10 nM	HaCaT cells	71.84%	Ando et al., 2016
AIZS-GO QDs	10 nM	Hep-G2 cells	99.15%	This work
AIZS-GO QDs	100 nM	Hep-G2 cells	95.23%	This work

closely bind to HSA and form a complex, and hydrogen bonds and van der Waals' forces have made major contributions to this binding process. The Stern-Volmer quenching constants and thermodynamic parameters were determined by fluorescence information. The results demonstrate that the fluorescence intensity of HSA can be quenched by AIZS-GO QDs. The FT-IR spectra and CD spectra further accounted for the structure alterations of HSA when AIZS-GO QDs existed. It means that AIZS-GO QDs can influence the bioactivity of HSA. All the results are conducive to understanding the interaction between AIZS-GO QDs and HSA. Besides HSA, we also found that AIZS - GO QDs could combine with the lysozyme which is a kind of protein in the blood. After AIZS - GO QDs combined with the lysozyme, however, the fluorescence characteristic, UV-visible absorption spectroscopy, and the conformation of the lysozyme were obviously distinct from the corresponding performance of HSA. It also implied that after AIZS - GO QDs combined with HSA, the performance of HSA had specificity. In the future, specific antibodies and antigens can be connected on the surface of quantum dots through this binding mechanism to make bioluminescence probes to detect and label corresponding proteins or tumor cells. It can also further promote the development of medical diagnostics and

medical research. Compared with the other substitutes, AIZS-GO QDs have high luminescence efficiency, low preparation costs, and strong fluorescence performance. Most importantly, the advantage is that AIZS-GO QDs are non-toxic because they do not contain heavy metal ions which are toxic. In other words, AIZS-GO QDs have more potential, than other substitutes, to be applied in biological fields for medical diagnosis and research. The experimental results show that AgInZn-GO water soluble quantum dots have good biocompatibility, which can be combined with proteins to form new compounds and have no cytotoxicity and biological practicability. It provides an important basis for the combination of quantum dots and specific proteins and fluorescent labeling (Zhou et al., 2019).

DATA AVAILABILITY STATEMENT

All datasets generated for this study are included in the article/supplementary material.

AUTHOR CONTRIBUTIONS

CS, HL, LW, and ZP: methodology, formal analysis, investigation, data curation, and writing—original draft. XL and XZ: conceptualization, validation, writing—review and editing, supervision, project administration, and funding acquisition. XT, SX, MS, and LJ resources and writing—original draft.

FUNDING

This work was supported by the Fundamental Research Funds for the Central Universities (Project No. 2019CDYGD006), the National Natural Science Foundation of China (Project no. 6137 7001), the Postgraduate education and teaching reform research project of Chongqing University (Project No. cqyjg18323), the Venture & Innovation Support Program for Chongqing Overseas Returnees (cx2018017), and the Fundamental Research Funds for the Central Universities (No. 10611CDJXZ238826).

REFERENCES

- Alivisatos, A. P. (1996). Semiconductor clusters, nanocrystals, and quantum dots. *Science* 271, 933–937. doi: 10.1126/science.271.5251.933
- Allen, P. M., and Bawendi, M. G. (2008). Ternary I-III-VI quantum dots luminescent in the red to near-infrared. *J. Am. Chem. Soc.* 130, 9240–9241. doi: 10.1021/ja8036349
- Ando, M., Horie, M., Akazawa-Ogawa, Y., Hagihara, Y., Murase, N., and Shigeri, Y. (2016). Cytotoxicity of CdSe-based quantum dots incorporated in glass nanoparticles evaluated using human keratinocyte HaCaT cells. *Biosci. Biotechnol. Biochem.* 80, 210–213. doi: 10.1080/09168451.2015.1069702
- Asha Jhonsi, M., Kathiravan, A., and Renganathan, R. (2009). Spectroscopic studies on the interaction of colloidal capped CdS nanoparticles with bovine serum albumin. *Colloids Surfaces B Biointerfaces* 72:167. doi: 10.1016/j.colsurfb.2009.03.030
- Brown, M. P., and Royer, C. (1997). Fluorescence spectroscopy as a tool to investigate protein interactions. *Curr. Opin. Biotechnol.* 8, 45–49. doi: 10.1016/S0958-1669(97)80156-5
- Bruchez, M., Moronne, M., Gin, P., Weiss, S., and Alivisatos, A. P. (1998). Semiconductor nanocrystals as fluorescent biological labels. *Science* 281:2013. doi: 10.1126/science.281.5385.2013
- Carter, D. C., He, X. M., Munson, S. H., Twigg, P. D., Gernert, K. M., Broom, M. B., et al. (1989). Three-dimensional structure of human serum albumin. *Science* 244, 1195–1198. doi: 10.1126/science.2727704
- Cassette, E., Pons, T., and Bouet, C. (2010). Synthesis and characterization of near-infrared CuInSe/ZnS Core/Shell quantum dots for *in vivo* imaging. *Chem. Mater.* 22, 6117–6124. doi: 10.1021/cm101881b
- Chan, W. C., and Nie, S. (1998). Quantum dot bioconjugates for ultrasensitive nonisotopic detection. *Science* 281, 2016–2018. doi: 10.1126/science.281.5385.2016
- Chuang, V. T., and Otagiri, M. (2002). How do fatty acids cause allosteric binding of drugs to human serum albumin? *Pharm. Res.* 19, 1458–1464. doi: 10.1023/A:1020496314081
- Dabbousi, B. O., Rodriguez-Viejo, J., Mikulec, F. V., Mattoussi, H., Ober, R., Jensen, K. F., et al. (1997). ChemInform abstract: (CdSe) ZnS core-shell quantum dots: synthesis and characterization of a size series of highly luminescent nanocrystallites. *Cheminform* 101, 9463–9475. doi: 10.1021/jp971091y
- Ding, L., Zhou, P. J., Li, S. Q., Shi, G. Y., Zhong, T., and Wu, M. (2011). Spectroscopic studies on the thermodynamics of L-cysteine capped

- CdSe/CdS quantum dots-BSA interactions. *J. Fluoresc.* 21, 17–24. doi: 10.1007/s10895-010-0685-2
- Dong, A., Huang, P., and Caughey, W. S. (1990). Protein secondary structures in water from second-derivative amide I infrared spectra. *Biochemistry* 29, 3303–3308. doi: 10.1021/bi00465a022
- Dzagli, M., Canpean, V., Iosin, M., Mohou, M. A., and Astilean, S. (2010). Study of the interaction between CdSe/ZnS core-shell quantum dots and bovine serum albumin by spectroscopic techniques. *J. Photochem. Photobiol. A Chem.* 215, 118–122. doi: 10.1016/j.jphotochem.2010.08.008
- Farid, M. M., Goudini, L., Piri, F., Zamani, A., and Saadati, F. (2016). Molecular imprinting method for fabricating novel glucose sensor: Polyvinyl acetate electrode reinforced by MnO₂/CuO loaded on graphene oxide nanoparticles. *Food Chem.* 194:61. doi: 10.1016/j.foodchem.2015.07.128
- Feroz, S. R., Mohamad, S. B., Bujang, N., Malek, S. N., and Tayyab, S. (2012). Multispectroscopic and molecular modeling approach to investigate the interaction of flavokawain B with human serum albumin. *J. Agri. Food Chem.* 60, 5899–5908. doi: 10.1021/jf301139h
- Figge, J., Rossing, T. H., and Fencel, V. (1991). The role of serum proteins in acid-base equilibria. *J. Lab. Clin. Med.* 117, 453–467.
- Fu, Y., and Lakowicz, J. R. (2006). Enhanced fluorescence of Cy5-labeled DNA tethered to silver island films: fluorescence images and time-resolved studies using single-molecule spectroscopy. *Analyt. Chem.* 78, 6238–6245. doi: 10.1021/ac060586t
- Gao, Y., Zou, X., Zhao, J. X., Li, Y., and Su, X. (2013). Graphene oxide-based magnetic fluorescent hybrids for drug delivery and cellular imaging. *Colloids Surfaces B Biointerfaces* 112, 128–133. doi: 10.1016/j.colsurfb.2013.07.020
- Gelamo, E. L., Silva, C. H., Imasato, H., and Tabak, M. (2002). Interaction of bovine (BSA) and human (HSA) serum albumins with ionic surfactants: spectroscopy and modelling. *Biochim. Biophys. Acta* 1594, 84–99. doi: 10.1016/S0167-4838(01)00287-4
- Ghali, M. (2010). Static quenching of bovine serum albumin conjugated with small size CdS nanocrystalline quantum dots. *J. Luminescence* 130, 1254–1257. doi: 10.1016/j.jlumin.2010.02.034
- Hamanaka, Y., Ogawa, T., and Tsuzuki, M. (2011). Photoluminescence properties and its origin of AgInS₂ quantum dots with chalcopyrite structure. *J. Phys. Chem. C* 115, 1786–1792. doi: 10.1021/jp110409q
- Hemmateenejad, B., Shamsipur, M., Samari, F., and Rajab, H. R. (2015). Study of the interaction between human serum albumin and Mn-doped ZnS quantum dots. *J. Iran. Chem. Soc.* 12, 1–10. doi: 10.1007/s13738-015-0647-3
- Hu, Y. J., Liu, Y., Pi, Z. B., and Qu, S. S. (2005). Interaction of cromolyn sodium with human serum albumin: a fluorescence quenching study. *Bioorg. Med. Chem.* 13, 6609–6614. doi: 10.1016/j.bmc.2005.07.039
- Hu, Y. J., Yu, O. Y., Bai, A. M., Li, W., and Liu, Y. (2010). Investigation of the interaction between ofloxacin and bovine serum albumin: spectroscopic approach. *J. Solut. Chem.* 39, 709–717. doi: 10.1007/s10953-010-9527-8
- Huang, S., Qiu, H., Lu, S., Zhu, F., and Xiao, Q. (2012). Study on the molecular interaction of graphene quantum dots with human serum albumin: combined spectroscopic and electrochemical approaches. *J. Hazard Mater.* 285, 18–26. doi: 10.1016/j.jhazmat.2014.11.019
- Jiang, Y., Tang, N., Zhou, C., Han, Z., Qu, H., and Duan, X. (2018). A chemiresistive sensor array from conductive polymer nanowires fabricated by nanoscale soft lithography. *Nanoscale* 10, 20578–20586. doi: 10.1039/C8NR04198A
- Koegler, P., Clayton, A., Thissen, H., Santos, G. N. C., and Kingshott, P. (2012). The influence of nanostructured materials on biointerfacial interactions. *Adv. Drug Deliv. Rev.* 64, 1820–1839. doi: 10.1016/j.addr.2012.06.001
- Lacerda, S. H., Park, J. J., Meuse, C., Pristinski, D., Becker, M. L., Karim, A., et al. (2010). Interaction of gold nanoparticles with common human blood proteins. *ACS Nano* 4, 365–379. doi: 10.1021/nn9011187
- Leckband, D. (2000). Measuring the forces that control protein interactions. *Ann. Rev. Biophys. Biomol. Struct.* 29, 1–26. doi: 10.1146/annurev.biophys.29.1.1
- Li, J., Parisi, J., and Kolny-Olesiak, J. (2015). Synthesis of CuInS₂-ZnS alloyed nanorods and hybrid nanostructures. *MRS Proc.* 1780:mrss15-2136281. doi: 10.1557/opl.2015.771
- Liang, J., Cheng, Y., and Han, H. (2008). Study on the interaction between bovine serum albumin and CdTe quantum dots with spectroscopic techniques. *J. Mol. Struct.* 892, 116–120. doi: 10.1016/j.molstruc.2008.05.005
- Lin, S., Bai, X., Wang, H., Wang, H., Song, J., Huang, K., et al. (2017). Roll-to-roll production of transparent silver-nanofiber-network electrodes for flexible electrochromic smart windows. *Adv. Mater.* 29:1703238. doi: 10.1002/adma.201703238
- Lin, S., Liu, J., Li, W., Wang, D., Huang, Y., Jia, C., et al. (2019a). A flexible, robust, and gel-free electroencephalogram electrode for noninvasive brain-computer interfaces. *Nano Lett.* 19, 6853–6861. doi: 10.1021/acs.nanolett.9b02019
- Lin, S., Wang, H., Zhang, X., Wang, D., Zu, D., Song, J., et al. (2019b). Direct spray-coating of highly robust and transparent Ag nanowires for energy saving windows. *Nano Energy* 62, 111–116. doi: 10.1016/j.nanoen.2019.04.071
- Niemeyer, C. M. (2001). Nanoparticles, proteins, and nucleic acids: biotechnology meets materials science. *Angew. Chem. Int. Ed.* 40, 4128–4158. doi: 10.1002/1521-3773(20011119)40:22<4128::AID-ANIE4128>3.0.CO;2-S
- Nirmal, M., Murray, C. B., and Bawendi, M. G. (1994). Fluorescence-line narrowing in CdSe quantum dots: Surface localization of the photogenerated exciton. *Phys. Rev. B Condensed Matter.* 50:2293. doi: 10.1103/PhysRevB.50.2293
- Nordén, B., and Tjernelid, F. (1982). Structure of methylene blue-DNA complexes studied by linear and circular dichroism spectroscopy. *Biopolymers* 21, 1713–1734. doi: 10.1002/bip.360210904
- Ragab, A. E., Gadallah, A. S., Mohamed, M. B., and Azzouz, I. M. (2014). Photoluminescence and upconversion on Ag/CdTe quantum dots. *Optics Laser Technol.* 63, 8–12. doi: 10.1016/j.optlastec.2014.03.006
- Sheng, Y., Tang, X., Peng, E., and Xue, J. (2012). Graphene oxide based fluorescent nanocomposites for cellular imaging. *J. Mater. Chem. B* 1, 512–521. doi: 10.1039/C2TB00123C
- Shiang, J. J., Kadavanich, A. V., Grubbs, R. K., and Alivisatos, A. P. (1995). Symmetry of annealed wurtzite CdSe nanocrystals: assignment to the C_{3v} point group. *J. Phys. Chem.* 100, 17417–17422. doi: 10.1021/j100048a017
- Shin, Y., Lee, J., Yang, J., Park, J., Lee, K., Kim, S., et al. (2014). Mass production of graphene quantum dots by one-pot synthesis directly from graphite in high yield. *Small* 10, 866–870. doi: 10.1002/smll.201302286
- Sudlow, G., Birkett, D. J., and Wade, D. N. (1976). Further characterization of specific drug binding sites on human serum albumin. *Mol. Pharmacol.* 12, 1052–1061.
- Sun, H., Yang, X., and Li, M. (2015). Insights into the effect of N-acetyl-L-cysteine-capped CdTe quantum dots on the structure and activity of human serum albumin by spectroscopic techniques. *J. Luminescenc* 167, 1–7. doi: 10.1016/j.jlumin.2015.06.005
- Tabassum, S., Al-Asbahy, W. M., Afzal, M., Arjmand, F., and Khan, R. H. (2012). Interaction and photo-induced cleavage studies of a copper based chemotherapeutic drug with human serum albumin: spectroscopic and molecular docking study. *Mol. Biosyst.* 8, 2424–2433. doi: 10.1039/c2mb25119a
- Tang, N., Zhou, C., Xu, L., Jiang, Y., Qu, H., and Duan, X. (2019). A fully integrated wireless flexible ammonia sensor fabricated by soft nano-lithography. *ACS Sensors* 4, 726–732. doi: 10.1021/acssensors.8b01690
- Torimoto, T., Adachi, T., Okazaki, K., Sakuraoka, M., Shibayama, T., Ohtani, B., et al. (2007). Facile synthesis of ZnS-AgInS₂ solid solution nanoparticles for a color-adjustable luminophore. *J. Am. Chem. Soc.* 129, 12388–12389. doi: 10.1021/ja0750470
- Venjaminov, S. Y., and Woody, R. W. (1999). Estimation of the number of [alpha]-helical and [beta]-strand, segments in proteins using circular dichroism spectroscopy. *Protein Sci. A Publi. Protein Soc.* 8, 370–380. doi: 10.1110/ps.8.2.370
- Wang, X., Cui, Y., Li, T., Lei, M., Li, J., and Wei, Z. (2019). Recent advances in the functional 2D photonic and optoelectronic devices. *Adv. Optical Mater.* 7:1801274. doi: 10.1002/adom.201801274

- Zhang, G., Que, Q., Pan, J., and Guo, J. (2008). Study of the interaction between icariin and human serum albumin by fluorescence spectroscopy. *J. Mol. Struct.* 881, 132–138. doi: 10.1016/j.molstruc.2007.09.002
- Zhou, C., Zhang, X., Tang, N., Fang, Y., Zhang, H., and Duan, X. (2019). Rapid response flexible humidity sensor for respiration monitoring using nano-confined strategy. *Nanotechnology* 31:125302. doi: 10.1088/1361-6528/ab5cda
- Zu, Z., Hu, W., Tang, X., Yang, P. H. W., Chen, W., Li, S., et al. (2016). A facile method for synthesizing AgInZnS/RGO nanocomposites and their photoelectric detection application. *Mater. Lett.* 182:240–243. doi: 10.1016/j.matlet.2016.07.001

Conflict of Interest: The authors declare that the research was conducted in the absence of any commercial or financial relationships that could be construed as a potential conflict of interest.

Copyright © 2020 Song, Luo, Lin, Peng, Weng, Tang, Xu, Song, Jin and Zheng. This is an open-access article distributed under the terms of the Creative Commons Attribution License (CC BY). The use, distribution or reproduction in other forums is permitted, provided the original author(s) and the copyright owner(s) are credited and that the original publication in this journal is cited, in accordance with accepted academic practice. No use, distribution or reproduction is permitted which does not comply with these terms.



Recent Advances of SnO₂-Based Sensors for Detecting Volatile Organic Compounds

Baoliang Li¹, Qu Zhou^{1*}, Shudi Peng² and Yiming Liao¹

¹ College of Engineering and Technology, Southwest University, Chongqing, China, ² Chongqing Electric Power Research Institute, State Grid Chongqing Electric Power Company, Chongqing, China

SnO₂ based sensors has received extensive attention in the field of toxic gas detection due to their excellent performances with high sensitivity, fast response, long-term stability. Volatile organic compounds (VOCs), originate from industrial production, fuel burning, detergent, adhesives, and painting, are poisonous gases with significant effects on air quality and human health. This mini-review focuses on significant improvement of SnO₂ based sensors in VOCs detection in recent years. In this review, the sensing mechanism of SnO₂-based sensors detecting VOCs are discussed. Furthermore, the improvement strategies of the SnO₂ sensor from the perspective of nanomaterials are presented. Finally, this paper summarizes the sensing performances of these SnO₂ nanomaterial sensors in VOCs detection, and the future development prospect and challenges is proposed.

OPEN ACCESS

Edited by:

Weiwei Wu,
Xidian University, China

Reviewed by:

Wei Luo,
Donghua University, China
Mingzai Wu,
Anhui University, China

*Correspondence:

Qu Zhou
zhouqu@swu.edu.cn

Specialty section:

This article was submitted to
Nanoscience,
a section of the journal
Frontiers in Chemistry

Received: 29 January 2020

Accepted: 30 March 2020

Published: 05 May 2020

Citation:

Li B, Zhou Q, Peng S and Liao Y
(2020) Recent Advances of
SnO₂-Based Sensors for Detecting
Volatile Organic Compounds.
Front. Chem. 8:321.
doi: 10.3389/fchem.2020.00321

Keywords: SnO₂ based sensor, gas detection, VOCs, nanomaterials, improvement strategies

INTRODUCTION

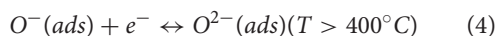
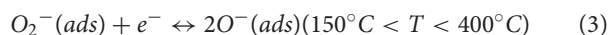
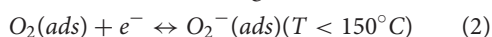
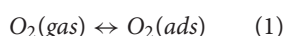
Volatile Organic Compounds (VOCs) are the most crucial cause of indoor air pollution and harm to human health, including a variety of toxic compounds and carcinogens (Shrubsole et al., 2019). For example, organic waste gases such as formaldehyde and polycyclic aromatic hydrocarbons have strong carcinogenicity, when the human body is in this environment for a long time, the possibility of carcinogenesis will greatly increase. There are also some organic waste gas shows a strong toxic effect, the human body in the excessive inhalation, will lead to coma or even death (Li G. et al., 2019). In addition, VOCs exhaust gas may also cause environmental problems such as acid rain, ozone layer damage, and atmospheric warming (Meng et al., 2018). Therefore, it is very essential to analyze the composition and concentration of VOCs in the air. Current methods for detecting VOCs include Gas Chromatography (GC), Gas Chromatography-mass spectrometry (GC-MS) and gas sensor detection (Vesely et al., 2003; Teixeira et al., 2004). GC determination of a single sample requires reference to known standards, and GC-MS requires a high time cost and complicated process. More importantly, both methods are offline and cannot detect the content and change of VOCs in real-time. In recent years, gas sensors has been widely noticed because of its fast detection speed, small volume, simple measurement and on-line monitoring.

Carbon materials and metal oxide semiconductor materials like SnO₂, ZnO, WO₃, and In₂O₃ have received scientific and technological importance and are widely used to detect VOCs gases (Luo et al., 2016; Lin et al., 2019; Zhao et al., 2019b). SnO₂ gas sensor has been extensively studied for its applications in air quality detection, flammable and explosive gas detection, and environmental monitoring (Zhang Q. Y. et al., 2018; Zhou et al., 2018c). Nanomaterials have

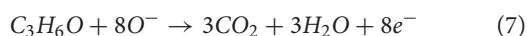
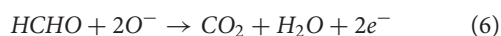
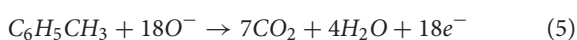
become the focus of the best sensing materials in recent years. Nanomaterials have many natural advantages such as large specific surface area, small size, and lightweight (Lu et al., 2018a; Zhou et al., 2018a). At present, there are many kinds of structures such as nanowires, nanofilaments, nanowires hollow spheres, nanofilaments flowers, and nanotubes (Mirzaei et al., 2016; Zhang Q. Y. et al., 2017). Different nanostructures and morphologies have different effects on the properties of materials. In order to change the nanostructure of a single material, there are other ways to improve the gas sensitivity of the sensor. This mini-review summarizes the gas-sensing performances of SnO₂ based sensor, which were influenced by the microstructure, doping, oxide composite and noble metal modification, toward toluene (C₆H₅CH₃), formaldehyde (HCHO), and acetone (C₃H₆O).

SENSING MECHANISM OF SNO₂ GAS SENSOR

SnO₂ sensor is a surface-controlled gas sensor. The gas-sensing reaction can only cause changes in parameters such as surface conductivity of the semiconductor (Ducere et al., 2012; Korotcenkov and Cho, 2017). When exposed to air, oxygen molecules would be adsorbed on the surface of the SnO₂ nanostructures and capture electrons from the conduction band of SnO₂ to generate chemisorbed oxygen species [O₂⁻, O⁻, and O²⁻, depending on temperatures; (Shahabuddin et al., 2017; Zhou et al., 2019)]. The chemical adsorption process can be explained by the following reactions:



When SnO₂ sensor contacts with the measured gas, its resistance will change according to the oxidation or reduction characteristics of the gas. Toluene, formaldehyde and acetone tested in this paper are reductive gases. When SnO₂ material surface comes into contact with a reducing gas, the reducing gas will react with oxygen anions to produce carbon dioxide and water, and the resulting electrons will return to the conduction band of the semiconductor. Therefore, this process will increase the carrier concentration on the surface of SnO₂ material, resulting in a decrease in the resistance value. When finally restored to the air environment, the sensor returns to its original state (Lu et al., 2018b; Al-Hashem et al., 2019; Mahajan and Jagtap, 2019). The sensing mechanism of the SnO₂ sensor reacting with these gases can be represented by the following path, where O⁻ is taken as an example (Lian et al., 2017; Zhu et al., 2019):



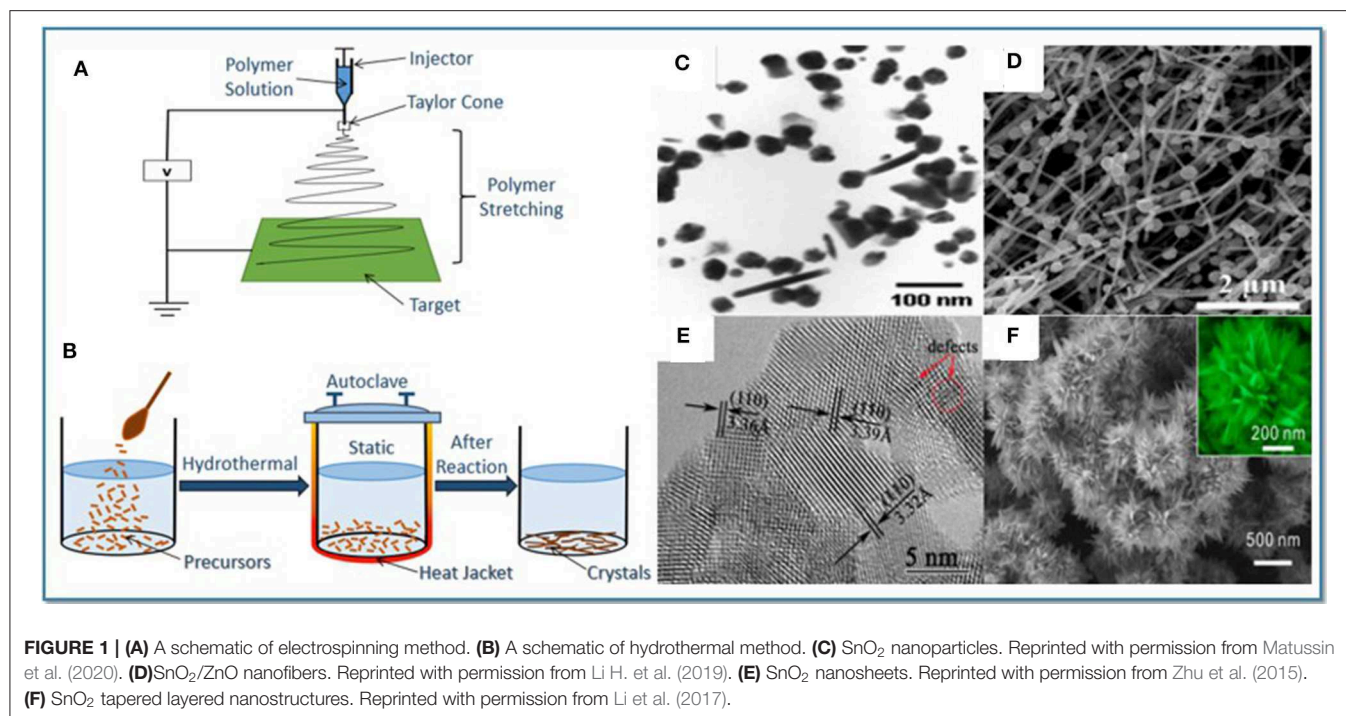
OPTIMIZATION OF SNO₂ GAS-SENSING MATERIALS

With the development of semiconductor gas-sensing materials, it has been the focus of research to enhance their gas-sensing properties for gas detection. The most common preparation methods of SnO₂ sensing materials include electrostatic spinning and hydrothermal methods, as shown in **Figures 1A,B**. Different preparation methods will change the structure and morphology of SnO₂ sensing materials and further enhance the gas sensitivity (Long et al., 2018; Zhang Y. J. et al., 2018; Zhou et al., 2018b). This section mainly reflects the changes in the gas-sensing properties of SnO₂ nanomaterials from the aspects of structure and morphology design, ion doping, oxide composite and noble metal modification (Chen et al., 2013; Das and Jayaraman, 2014).

Different nanostructures and morphologies cause various effects on the properties of materials. In this respect, various morphologies from 0-D to 3-D with unique physical and chemical properties have been successfully synthesized. High dispersivity, ultra-small diameter 0-D SnO₂ nanoparticles (**Figure 1C**) have highly effective surface areas and sufficient oxygen vacancies, which can improve the performance of nanoparticle based sensors (Matussin et al., 2020). 1-D SnO₂ structure, such as nanofibers (**Figure 1D**), has excellent sensitivity and stability due to its large specific surface area, high porosity and good permeability (Li H. et al., 2019). Compared with low dimensional structure, 2-D structure possesses larger special surface area. In comparison to the 3-D structure, freestanding 2-D structures such as SnO₂ nanosheets (**Figure 1E**) can provide better optimization including the modulation of the materials activity, surface polarization, and rich oxygen vacancies (Zhu et al., 2015). 3-D structures, such as microspheres, microflowers, and mesoporous structures, are assembled by diverse lower dimension fundamental blocks. Microstructured analyses suggest that the favorable gas sensitivity of SnO₂ tapered layered nanostructures (**Figure 1F**) are mainly ascribed to the formation of more active surface defects and mismatches (Li et al., 2017).

Ion doping can change the cell parameters of the material, the number of suspensions on the surface of the material and the richness of defects, thereby enhance the gas sensitivity of the sensor (Korotcenkov and Cho, 2014). The Y-doped SnO₂ three-dimensional flower-like nanostructure prepared by one-step hydrothermal method has a large number of rough nanoflakes, which increases the specific surface area and is more conducive to the adsorption and desorption of oxygen and formaldehyde gas. It is a highly sensitive formaldehyde detection material (Zhu et al., 2019). The doping of Ce ions into the SnO₂ lattice results in the smaller size of nanoparticles and the formation of a porous structure. Therefore, Ce ions can provide more active sites for the adsorption and reaction of acetone (Lian et al., 2017).

The combination of two metal oxides can improve the gas sensitivity of semiconductor materials. The dispersion of functional components is the key factor to realize good gas sensitivities (Wei et al., 2020). Moreover, the heterostructure formed by SnO₂ and another metal oxide can promote the transfer of carriers between materials and change the



conductivity and energy band structure of composite materials (Gusain et al., 2019; Wei et al., 2019). In a recent research, a facile solvent EIOC has been demonstrated for the synthesis of novel hierarchical branched mesoporous TiO₂-SnO₂ semiconducting heterojunctions. The uniform distribution of SnO₂ NCs in the pore walls of TiO₂ forms numerous n-n heterojunctions which are extremely useful for surface catalytic reaction. Owing to the rational combination of a hierarchical mesoporous structure, a high crystallinity, and well-defined n-n heterojunctions, the SHMT-based gas sensor shows an excellent sensing performance with a fast response and recovery dynamics, ultralow limit of detection and a superior selectivity (Zhao et al., 2019a). The cactus-like WO₃-SnO₂ nanocomposite was prepared by one-step hydrothermal method by attaching many tiny SnO₂ nanospheres to large WO₃ nanospheres, which provided many active sites for the acetone molecule and provided heterojunctions between WO₃ and SnO₂. The synergistic effect between them improves the sensing performance of the composite nanomaterial to acetone gas (Zhu et al., 2018).

Precious metal modification usually uses Au, Ag, Pt, and Pd or their oxides to improve the sensitivity and response speed of gas sensing materials and reduce the working temperature. Ag modified SnO₂ nanoparticles prepared by hydrothermal *in situ* reduction improved the sensor's ability to detect formaldehyde. This is due to the charge transfer between Ag and SnO₂, which increases the absorption band on the composite by 20 nm, thus improving the gas sensitivity (Liu et al., 2019). When the acetone is detected by Ag/SnO₂ porous tubular nanostructures prepared by electrospinning, the sensor resistance changed rapidly and significantly. On the one hand, the p-n hybrid interface of p-type Ag₂O and n-type SnO₂ causes the energy band of the

depletion layer to bend, increasing the initial resistance. On the other hand, the hollow nanostructure promotes the adsorption and electron transfer of acetone, which makes the resistance change rapidly (Xu et al., 2017). The bimetal PdAu modified SnO₂ nanosheet showed excellent selectivity and responsiveness to low concentrations of acetone, which is due to the chemical sensitization of Au, electronic sensitization of Pd and synergism of PdAu bimetal nanosheet (Li G. et al., 2019).

SENSING PERFORMANCE OF VOCs BASED ON SNO₂ NANOMATERIALS

For VOCs, this review mainly introduces toluene, formaldehyde and acetone. This section summarizes the gas-sensitive characteristics of SnO₂-based nanomaterials for the above gases, as shown in **Table 1**. In the detection of common VOCs, the lower detection limit, response value and detection temperature of SnO₂ based nanomaterials are different.

Toluene, a colorless volatile liquid, is one of the most widely used aromatic hydrocarbons and is considered as a biomarker of cancer. Occupational Safety and Health Administration (OSHA) stipulates that the permissible exposure limit for toluene is 100 ppm for 8 h (Sui et al., 2017). The Pd-doped SnO₂ hollow spheres prepared by hydrothermal method measured a response value of 52.9 for toluene at 20 ppm and a lower temperature of 230°C (Zhang K. et al., 2017). The Pd-loaded SnO₂ cubic nanocages are also an ideal choice for toluene detection, with a minimum detection concentration of 100 ppb, a response to 20 ppm of toluene of 41.4, and an optimal reaction temperature of 250°C (Qiao et al., 2017). Formaldehyde is a colorless and pungent gas.

TABLE 1 | Comparison of SnO₂ based nanomaterials for VOCs detection.

VOCs	Material	Synthesis method	Detection limit	Response	Temperature (°C)	References
Toluene	Pd-doped SnO ₂ hollow spheres	One-pot hydrothermal method	100 ppb	52.9 (20 ppm)	230	Zhang K. et al., 2017
	Micro-/mesoporous SnO ₂ spheres	Solvothermal method	10 m	20.2 (50 ppm)	400	Hermawan et al., 2019
	Pd-loaded SnO ₂ cubic nanocages	Multi-step route	100 ppb	41.4 (20 ppm)	250	Qiao et al., 2017
	Pd/SnO ₂ nanofibers	electrospinning and carbonization	0.5 ppm	24.6 (100 ppm)	250	Xie et al., 2018
Formaldehyde	Ag-SnO ₂ composites	Hydrothermal and <i>in situ</i> reduction method	10 ppm	14.4 (10 ppm)	125	Liu et al., 2019
	Ag doped Zn ₂ SnO ₄ /SnO ₂ hollow nanospheres	Hydrothermal method	5 ppm	62.2 (50 ppm)	140	Zhang et al., 2019
	Ni doping of SnO ₂ nanoparticles	Hydrothermal method	1 ppm	130 (100 ppm)	200	Hu et al., 2018
	Y-doped SnO ₂ flower-shaped nanostructures	Hydrothermal method	1 ppm	18 (50 ppm)	180	Zhu et al., 2019
	NiO-SnO ₂ heterojunction microflowers	Hydrothermal method	1 ppm	39.2 (100 ppm)	100	Meng et al., 2018
	Cedar-like SnO ₂ hierarchical micro-nanostructures	Low-temperature hydrothermal method	5 ppm	13.3 (100 ppm)	200	Yu et al., 2017
	GO/SnO ₂ nanocomposites	Electrospinning and calcination procedure	500 ppb	32 (100 ppm)	120	Wang et al., 2017
	SnO/SnO ₂ nano-flowers	Hydrothermal method	8.15 ppb	80.9 (50 ppm)	120	Li N. et al., 2019
	Cd-doped SnO ₂ nanofibers	Hydrothermal method	1 ppm	51.11 (100 ppm)	160	Zhao et al., 2020
Acetone	Ca ²⁺ /Au co-doped SnO ₂ nanofibers	Electrospinning and calcination procedure	10 ppm	62 (100 ppm)	180	Jiang et al., 2017
	La ₂ O ₃ -doped SnO ₂ nanoparticulate thick films	Flame-spray-made	100 ppb	3,626 (400 ppm)	350	Tammanoon et al., 2018
	Ce-doped SnO ₂ nanoparticles	Hydrothermal method	10 ppm	50.5 (50 ppm)	270	Lian et al., 2017
	Ag-decorated SnO ₂ hollow nanofibers	Electrospinning method	5 ppm	117 (200 ppm)	160	Xu et al., 2017
	Au@WO ₃ -SnO ₂ corrugated nanofibers	Hydrothermal treatment process	200 ppb	79.6 (0.5 ppm)	150	Shao et al., 2019
	PdAu decorated SnO ₂ nanosheets	<i>In situ</i> reduction method	45 ppb	109 (50 ppm)	250	Li G. et al., 2019
	Cactus-like WO ₃ -SnO ₂ nanocomposite	Hydrothermal method		26 (600 ppm)	360	Zhu et al., 2018

Due to the toxicity of formaldehyde, OSHA has established the Threshold Limit Value (TLV) as a concentration of 0.75 ppm for 8 h. The SnO/SnO₂ nano-flowers prepared by hydrothermal method have a minimum detection concentration of 8.15 for formaldehyde, an optimal response temperature of 120°C, and a response value of 80.9 at 50 ppm. It is an ideal material for formaldehyde detection (Li N. et al., 2019). The hydrothermal Ni doping of SnO₂ nanoparticles also had a good response value of 130–100 ppm of formaldehyde at 200°C (Hu et al., 2018). In addition, the Ag-doped Zn₂SnO₄/SnO₂ hollow nanospheres responded to 50 ppm of formaldehyde with a value of 62.2 and a lower detection temperature of 140°C (Zhang et al., 2019). Acetone is a colorless and irritant liquid. Long term exposure to acetone can stimulate human sensory organs and lead to inflammation. Therefore, the quantitative detection of acetone is of great significance (Cheng et al., 2015; Lian et al., 2017). PdAu decorated SnO₂ nanosheets sensor was able to detect acetone at 45 ppb and to respond to acetone at 50 ppm to 109 (Li G. et al., 2019). The detection limit of Au @ WO₃-SnO₂ corrugated nanofibers prepared by hydrothermal treatment was

200 ppb acetone, and the best response to 0.5 ppm acetone at 150°C was 79.6. The Au@WO₃-SnO₂ corrugated nanofibers is an ideal low concentration acetone gas sensor with low detection limit and high response (Shao et al., 2019). La₂O₃-doped SnO₂ nanoparticle thick films has an amazing response value of 3,626–400 ppm at 350°C, which is suitable for the detection of high concentration acetone (Tammanoon et al., 2018).

CONCLUSION AND PERSPECTIVE

This review discusses the performance improvements of SnO₂-based nanomaterials and the comparison of gas sensitivity in VOCs in recent years. SnO₂-based nanostructures provide a larger specific surface area and more active sites, which is conducive to VOCs adsorption. Ion doping can reduce the size of nanomaterials and make the surface of the material rougher, thereby increasing the specific surface area. Metal oxide composite can not only achieve functional dispersion, but also form heterojunctions to promote the movement of charge

carriers. Precious metals have excellent catalytic activity for SnO₂ nanomaterials. These optimization methods make SnO₂-based gas sensors operate at lower temperatures, higher sensitivity, and better stability. Despite great progress has been made in the application of SnO₂ nanomaterials, there is still much room for further development. First of all, cross sensitivity is a huge challenge for the preparation of high-performance sensors. In the future, SnO₂ gas sensor will be able to detect a single gas in the mixture. Secondly, most of the SnO₂ sensors currently used work at high temperature, which limits their wide application in detecting VOCs at room temperature. In addition, long-term stability is also one of the research hotspots of SnO₂ sensors in the future. Due to the influence of external environment and other factors, the stability of the sensor can not be guaranteed. Therefore, it is of great significance to develop more stable gas sensors. It has become a research hotspot to optimize the existing gas sensing materials by chemical modification and develop new gas sensing materials such as composite and hybrid semiconductor materials and polymer gas sensing materials. In addition, new sensors, such as optical waveguide gas sensor,

quartz resonant gas sensor and microbial gas sensor, developed with advanced processing technology and microstructure, can make the sensor more stable, and versatility. Finally, we hope our work will be helpful for the further exploration of metal oxide nanomaterials in the detection of VOCs.

AUTHOR CONTRIBUTIONS

All authors listed have made a substantial, direct and intellectual contribution to the work, and approved it for publication.

FUNDING

This work has been supported in part by the National Natural Science Foundation of China (No. 51507144), Fundamental Research Funds for the Central Universities (No. XDJK2019B021), the Chongqing Science and Technology Commission (CSTC) (No. cstc2016jcyjA0400), and the project of China Scholarship Council (CSC).

REFERENCES

- Al-Hashem, M., Akbar, S., and Morris, P. (2019). Role of oxygen vacancies in nanostructured metal-oxide gas sensors: a review. *Sensor. Actuat. B Chem.* 301:126845. doi: 10.1016/j.snb.2019.126845
- Chen, W. G., Zhou, Q., Gao, T. Y., Su, X. P., and Wan, F. (2013). Pd-doped SnO₂-based sensor detecting characteristic fault hydrocarbon gases in transformer oil. *J. Nanomater.* 2013:127345. doi: 10.1155/2013/127345
- Cheng, L., Ma, S. Y., Wang, T. T., and Luo, J. (2015). Synthesis and enhanced acetone sensing properties of 3D porous flower-like SnO₂ nanostructures. *Mater. Lett.* 143, 84–87. doi: 10.1016/j.matlet.2014.12.062
- Das, S., and Jayaraman, V. (2014). SnO₂: a comprehensive review on structures and gas sensors. *Prog. Mater. Sci.* 66, 112–255. doi: 10.1016/j.pmatsci.2014.06.003
- Ducere, J. M., Hemeryck, A., Esteve, A., Rouhani, M. D., Landa, G., Menini, P., et al. (2012). A computational chemist approach to gas sensors: modeling the response of SnO₂ to CO, O₂, and H₂O gases. *J. Comput. Chem.* 33, 247–258. doi: 10.1002/jcc.21959
- Gusain, R., Gupta, K., Joshi, P., and Khatri, O. P. (2019). Adsorptive removal and photocatalytic degradation of organic pollutants using metal oxides and their composites: a comprehensive review. *Adv. Colloid. Interface.* 272:102009. doi: 10.1016/j.cis.2019.102009
- Hermawan, A., Asakura, Y., Inada, M., and Yin, S. (2019). One-step synthesis of micro-/mesoporous SnO₂ spheres by solvothermal method for toluene gas sensor. *Ceram. Int.* 45, 15435–15444. doi: 10.1016/j.ceramint.2019.05.043
- Hu, J., Wang, T., Wang, Y., Huang, D., He, G., Han, Y., et al. (2018). Enhanced formaldehyde detection based on Ni doping of SnO₂ nanoparticles by one-step synthesis. *Sensor. Actuat. B Chem.* 263, 120–128. doi: 10.1016/j.snb.2018.02.035
- Jiang, Z., Yin, M., and Wang, C. (2017). Facile synthesis of Ca²⁺/Au co-doped SnO₂ nanofibers and their application in acetone sensor. *Mater. Lett.* 194, 209–212. doi: 10.1016/j.matlet.2017.02.031
- Korotcenkov, G., and Cho, B. K. (2014). Bulk doping influence on the response of conductometric SnO₂ gas sensors: understanding through cathodoluminescence study. *Sensor. Actuat. B Chem.* 196, 80–98. doi: 10.1016/j.snb.2014.01.108
- Korotcenkov, G., and Cho, B. K. (2017). Metal oxide composites in conductometric gas sensors: achievements and challenges. *Sensor. Actuat. B Chem.* 244, 182–210. doi: 10.1016/j.snb.2016.12.117
- Li, G., Cheng, Z., Xiang, Q., Yan, L., Wang, X., and Xu, J. (2019). Bimetal PdAu decorated SnO₂ nanosheets based gas sensor with temperature-dependent dual selectivity for detecting formaldehyde and acetone. *Sensor. Actuat. B Chem.* 283, 590–601. doi: 10.1016/j.snb.2018.09.117
- Li, H., Chu, S. S., Ma, Q., Li, H., Che, Q. D., Wang, J. P., et al. (2019). Multilevel effective heterojunctions based on SnO₂/ZnO 1D fibrous hierarchical structure with unique interface electronic effects. *ACS Appl. Mater. Inter.* 11, 31551–31561. doi: 10.1021/acsami.9b10410
- Li, N., Fan, Y., Shi, Y., Xiang, Q., Wang, X., and Xu, J. (2019). A low temperature formaldehyde gas sensor based on hierarchical SnO/SnO₂ nano-flowers assembled from ultrathin nanosheets: Synthesis, sensing performance and mechanism. *Sensor. Actuat. B Chem.* 294, 106–115. doi: 10.1016/j.snb.2019.04.061
- Li, Y. X., Guo, Z., Su, Y., Jin, X. B., Tang, X. H., Huang, J. R., et al. (2017). Hierarchical morphology-dependent gas-sensing performances of three-dimensional SnO₂ nanostructures. *ACS Sens.* 2, 102–110. doi: 10.1021/acssensors.6b00597
- Lian, X., Li, Y., Tong, X., Zou, Y., Liu, X., An, D., et al. (2017). Synthesis of Ce-doped SnO₂ nanoparticles and their acetone gas sensing properties. *Appl. Surf. Sci.* 407, 447–455. doi: 10.1016/j.apsusc.2017.02.228
- Lin, T., Lv, X., Hu, Z., Xu, A., and Feng, C. (2019). Semiconductor metal oxides as chemoresistive sensors for detecting volatile organic compounds. *Sensors Basel.* 19:233. doi: 10.3390/s19020233
- Liu, D., Pan, J., Tang, J., Liu, W., Bai, S., and Luo, R. (2019). Ag decorated SnO₂ nanoparticles to enhance formaldehyde sensing properties. *J. Phys. Chem. Solids.* 124, 36–43. doi: 10.1016/j.jpcs.2018.08.028
- Long, H., Zeng, W., Wang, H., Qian, M., Liang, Y., and Wang, Z. (2018). Self-assembled biomolecular 1D nanostructures for aqueous sodium-ion battery. *Adv. Sci.* 5:1700634. doi: 10.1002/adv.201700634
- Lu, Z. R., Zhou, Q., Wang, C. S., Wei, Z. J., Xu, L. N., and Gui, Y. G. (2018a). Electrospun ZnO-SnO₂ composite nanofibers and enhanced sensing properties to SF₆ decomposition byproduct H₂S. *Front. Chem.* 6:540. doi: 10.3389/fchem.2018.00540
- Lu, Z. R., Zhou, Q., Xu, L. N., Gui, Y. G., Zhao, Z. Y., Tang, C., et al. (2018b). Synthesis and characterization of highly sensitive hydrogen (H₂) sensing device based on Ag doped SnO₂ nanospheres. *Materials.* 11:492. doi: 10.3390/ma11040492
- Luo, W., Zhao, T., Li, Y. H., Wei, J., Xu, P. C., Li, X. X., et al. (2016). A micelle fusion-aggregation assembly approach to mesoporous carbon materials with rich active sites for ultra-sensitive ammonia. *Sensing. J. Am. Chem. Soc.* 138, 12586–12595. doi: 10.1021/jacs.6b07355
- Mahajan, S., and Jagtap, S. (2019). Metal-oxide semiconductors for carbon monoxide (CO) gas sensing: a review. *Appl. Mater. Today.* 18:100483. doi: 10.1016/j.apmt.2019.100483

- Matussin, S., Harunsani, M. H., Tan, A. L., and Khan, M. M. (2020). Plant-extract-mediated SnO₂ nanoparticles: synthesis and applications. *Acs. Sustain. Chem. Eng.* 8, 3040–3054. doi: 10.1021/acsschemeng.9b06398
- Meng, D., Liu, D., Wang, G., Shen, Y., San, X., Li, M., et al. (2018). Low-temperature formaldehyde gas sensors based on NiO-SnO₂ heterojunction microflowers assembled by thin porous nanosheets. *Sensor. Actuat. B Chem.* 273, 418–428. doi: 10.1016/j.snb.2018.06.030
- Mirzaei, A., Leonardi, S. G., and Neri, G. (2016). Detection of hazardous volatile organic compounds (VOCs) by metal oxide nanostructures-based gas sensors: a review. *Ceram. Int.* 42, 15119–15141. doi: 10.1016/j.ceramint.2016.06.145
- Qiao, L., Bing, Y., Wang, Y., Yu, S., Liang, Z., and Zeng, Y. (2017). Enhanced toluene sensing performances of Pd-loaded SnO₂ cubic nanocages with porous nanoparticle-assembled shells. *Sensor. Actuat. B Chem.* 241, 1121–1129. doi: 10.1016/j.snb.2016.10.024
- Shahabuddin, M., Umar, A., Tomar, M., and Gupta, V. (2017). Custom designed metal anchored SnO₂ sensor for H₂ detection. *Int. J. Hydrogen Energ.* 42, 4597–4609. doi: 10.1016/j.ijhydene.2016.12.054
- Shao, S., Chen, X., Chen, Y., Lai, M., and Che, L. (2019). Ultrasensitive and highly selective detection of acetone based on Au@WO₃-SnO₂ corrugated nanofibers. *Appl. Surf. Sci.* 473, 902–911. doi: 10.1016/j.apsusc.2018.12.208
- Shrubsole, C., Dimitroulopoulou, S., Foxall, K., Gadeberg, B., and Doutsis, A. (2019). IAQ guidelines for selected volatile organic compounds (VOCs) in the UK. *Build. Environ.* 165:106382. doi: 10.1016/j.buildenv.2019.106382
- Sui, L. L., Zhang, X. F., Cheng, X. L., Wang, P., Xu, Y. M., Gao, S., et al. (2017). Au-loaded hierarchical MoO₃ hollow spheres with enhanced gas-sensing performance for the detection of BTX (benzene, toluene, and xylene) and the sensing mechanism. *Acs. Appl. Mater. Inter.* 9, 1661–1670. doi: 10.1021/acsaami.6b11754
- Tammanoon, N., Wisitsoraat, A., Phokharatkul, D., Tuantranont, A., Phanichphant, S., Yordsri, V., et al. (2018). Highly sensitive acetone sensors based on flame-spray-made La₂O₃-doped SnO₂ nanoparticulate thick films. *Sensor. Actuat. B Chem.* 262, 245–262. doi: 10.1016/j.snb.2018.01.238
- Teixeira, L. S., Leao, E. S., Dantas, A. F., Pinheiro, H. L., Costa, A. C., and de Andrade, J. B. (2004). Determination of formaldehyde in Brazilian alcohol fuels by flow-injection solid phase spectrophotometry. *Talanta* 64, 711–715. doi: 10.1016/j.talanta.2004.03.047
- Vesely, P., Lusk, L., Basarova, G., Seabrooks, J., and Ryder, D. (2003). Analysis of aldehydes in beer using solid-phase microextraction with on-fiber derivatization and gas chromatography/mass spectrometry. *J. Agr. Food Chem.* 51, 6941–6944. doi: 10.1021/jf034410t
- Wang, D., Zhang, M., Chen, Z., Li, H., Chen, A., Wang, X., et al. (2017). Enhanced formaldehyde sensing properties of hollow SnO₂ nanofibers by graphene oxide. *Sensor. Actuat. B Chem.* 250, 533–542. doi: 10.1016/j.snb.2017.04.164
- Wei, Z. J., Zhou, Q., Wang, J. X., Lu, Z. R., Xu, L. N., and Zeng, W. (2019). Hydrothermal synthesis of SnO₂ nanoneedle-anchored NiO microsphere and its gas sensing performances. *Nanomaterials Basel* 9:1015. doi: 10.3390/nano9071015
- Wei, Z. J., Zhou, Q., and Zeng, W. (2020). Hierarchical WO₃-NiO microflower for high sensitivity detection of SF₆ decomposition byproduct H₂S. *Nanotechnology* 31:215701. doi: 10.1088/1361-6528/ab73bd
- Xie, N., Guo, L. L., Chen, F., Kou, X. Y., Wang, C., Ma, J., et al. (2018). Enhanced sensing properties of SnO₂ nanofibers with a novel structure by carbonization. *Sensor. Actuat. B Chem.* 271, 44–53. doi: 10.1016/j.snb.2018.05.039
- Xu, X., Chen, Y., Zhang, G., Ma, S., Lu, Y., Bian, H., et al. (2017). Highly sensitive VOCs-acetone sensor based on Ag-decorated SnO₂ hollow nanofibers. *J. Alloy. Compd.* 703, 572–579. doi: 10.1016/j.jallcom.2017.01.348
- Yu, H., Yang, T., Wang, Z., Li, Z., Xiao, B., Zhao, Q., et al. (2017). Facile synthesis cedar-like SnO₂ hierarchical micro-nanostructures with improved formaldehyde gas sensing characteristics. *J. Alloy. Compd.* 724, 121–129. doi: 10.1016/j.jallcom.2017.07.017
- Zhang, K., Yang, X., Wang, Y., Bing, Y., Qiao, L., Liang, Z., et al. (2017). Pd-loaded SnO₂ ultrathin nanorod-assembled hollow microspheres with the significant improvement for toluene detection. *Sensor. Actuat. B Chem.* 243, 465–474. doi: 10.1016/j.snb.2016.11.153
- Zhang, Q. Y., Zhou, Q., Lu, Z. R., Wei, Z. J., Xu, L. N., and Gui, Y. G. (2018). Recent advances of SnO₂-based sensors for detecting fault characteristic gases extracted from power transformer oil. *Front. Chem.* 6:364. doi: 10.3389/fchem.2018.00364
- Zhang, Q. Y., Zhou, Q., Yin, X. T., Liu, H. C., Xu, L. N., Tan, W. M., et al. (2017). The effect of PMMA pore-forming on hydrogen sensing properties of porous SnO₂ thick film sensor. *Adv. Sci.* 9, 1350–1355. doi: 10.1166/sam.2017.3111
- Zhang, R., Ma, S. Y., Zhang, Q. X., Zhu, K. M., Tie, Y., Pei, S. T., et al. (2019). Highly sensitive formaldehyde gas sensors based on Ag doped Zn₂SnO₄/SnO₂ hollow nanospheres. *Mater. Lett.* 254, 178–181. doi: 10.1016/j.matlet.2019.07.065
- Zhang, Y. J., Zeng, W., and Li, Y. Q. (2018). The hydrothermal synthesis of 3D hierarchical porous MoS₂ microspheres assembled by nanosheets with excellent gas sensing properties. *J. Alloy. Compd.* 749, 355–362. doi: 10.1016/j.jallcom.2018.03.307
- Zhao, R., Zhang, X., Peng, S., Hong, P., Zou, T., Wang, Z., et al. (2020). Shaddock peels as bio-templates synthesis of Cd-doped SnO₂ nanofibers: a high performance formaldehyde sensing material. *J. Alloy. Compd.* 813:152170. doi: 10.1016/j.jallcom.2019.152170
- Zhao, T., Qiu, P. P., Fan, Y. C., Yang, J. P., Jiang, W., Wang, L. J., et al. (2019a). Hierarchical branched mesoporous TiO₂-SnO₂ nanocomposites with well-defined n-n heterojunctions for highly efficient ethanol sensing. *Adv. Sci.* 6:1902008. doi: 10.1002/adv.201902008
- Zhao, T., Ren, Y., Jia, G. Y., Zhao, Y. Y., Fan, Y. C., Yang, J. P., et al. (2019b). Facile synthesis of mesoporous WO₃@graphene aerogel nanocomposites for low-temperature acetone sensing. *Chin. Chem. Lett.* 30, 2032–2038. doi: 10.1016/j.cclet.2019.05.006
- Zhou, Q., Chen, W. G., Xu, L. N., Kumar, R., Gui, Y. G., Zhao, Z. Y., et al. (2018a). Highly sensitive carbon monoxide (CO) gas sensors based on Ni and Zn doped SnO₂ nanomaterials. *Ceram. Int.* 44, 4392–4399. doi: 10.1016/j.ceramint.2017.12.038
- Zhou, Q., Umar, A., Sodki, E., Amine, A., Xu, L. N., Gui, Y. G., et al. (2018b). Fabrication and characterization of highly sensitive and selective sensors based on porous NiO nanodisks. *Sensor. Actuat. B Chem.* 259, 604–615. doi: 10.1016/j.snb.2017.12.050
- Zhou, Q., Xu, L. N., Umar, A., Chen, W. G., and Kumar, R. (2018c). Pt nanoparticles decorated SnO₂ nanoneedles for efficient CO gas sensing applications. *Sensor. Actuat. B Chem.* 256, 656–664. doi: 10.1016/j.snb.2017.09.206
- Zhou, Q., Zeng, W., Chen, W. G., Xu, L. N., Kumar, R., and Umar, A. (2019). High sensitive and low-concentration sulfur dioxide (SO₂) gas sensor application of heterostructure NiO-ZnO nanodisks. *Sensor. Actuat. B Chem.* 298:126870. doi: 10.1016/j.snb.2019.126870
- Zhu, K., Ma, S., Tie, Y., Zhang, Q., Wang, W., Pei, S., et al. (2019). Highly sensitive formaldehyde gas sensors based on Y-doped SnO₂ hierarchical flower-shaped nanostructures. *J. Alloy. Compd.* 792, 938–944. doi: 10.1016/j.jallcom.2019.04.102
- Zhu, L., Zeng, W., and Li, Y. (2018). A novel cactus-like WO₃-SnO₂ nanocomposite and its acetone gas sensing properties. *Mater. Lett.* 231, 5–7. doi: 10.1016/j.matlet.2018.08.007
- Zhu, Y. Q., Guo, H. Z., Zhai, H. Z., and Cao, C. B. (2015). Microwave-assisted and gram-scale synthesis of ultrathin SnO₂ nanosheets with enhanced lithium storage properties. *Acs. Appl. Mater. Inter.* 7, 2745–2753. doi: 10.1021/am507826d

Conflict of Interest: The authors declare that the research was conducted in the absence of any commercial or financial relationships that could be construed as a potential conflict of interest.

Copyright © 2020 Li, Zhou, Peng and Liao. This is an open-access article distributed under the terms of the Creative Commons Attribution License (CC BY). The use, distribution or reproduction in other forums is permitted, provided the original author(s) and the copyright owner(s) are credited and that the original publication in this journal is cited, in accordance with accepted academic practice. No use, distribution or reproduction is permitted which does not comply with these terms.



Asymptomatic Diagnosis of Huanglongbing Disease Using Metalloporphyrin Functionalized Single-Walled Carbon Nanotubes Sensor Arrays

Hui Wang^{1,2,3,5}, Pankaj Ramnani³, Tung Pham³, Claudia Chaves Villarreal⁴, Xuejun Yu³, Gang Liu^{1*} and Ashok Mulchandani^{3*}

OPEN ACCESS

Edited by:

Jiandong Pang,
Texas A&M University, United States

Reviewed by:

Yingmu Zhang,
University of Southern California,
United States
Suresh Kumar Kalangi,
Amity University Gurgaon, India

*Correspondence:

Ashok Mulchandani
adani@engr.ucr.edu
Gang Liu
pac@cau.edu.cn

Specialty section:

This article was submitted to
Nanoscience,
a section of the journal
Frontiers in Chemistry

Received: 05 December 2019

Accepted: 07 April 2020

Published: 12 May 2020

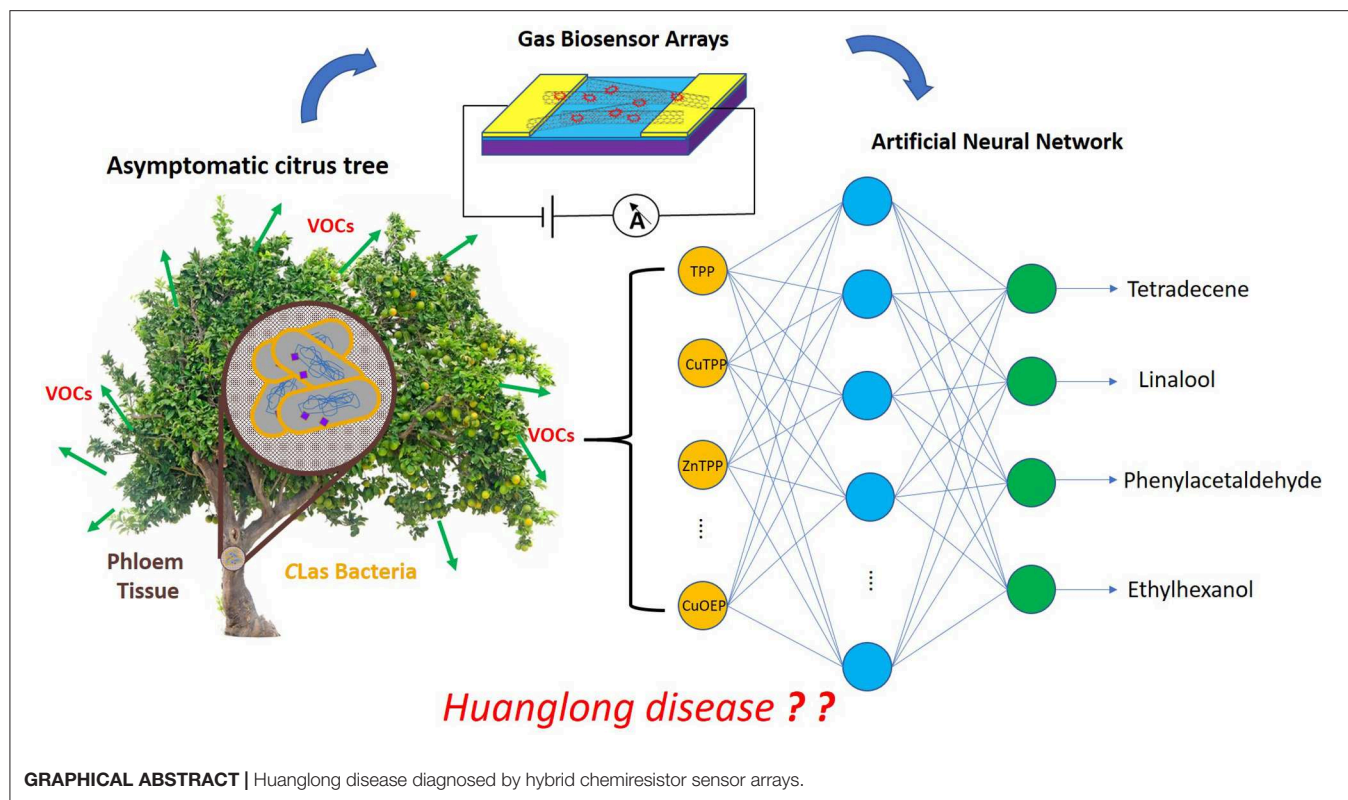
Citation:

Wang H, Ramnani P, Pham T, Villarreal CC, Yu X, Liu G and Mulchandani A (2020) Asymptomatic Diagnosis of Huanglongbing Disease Using Metalloporphyrin Functionalized Single-Walled Carbon Nanotubes Sensor Arrays. *Front. Chem.* 8:362. doi: 10.3389/fchem.2020.00362

¹ Key Laboratory of Modern Precision Agriculture System Integration Research, Ministry of Education and Key Laboratory of Agricultural Information Acquisition Technology, Ministry of Agriculture China Agricultural University, Beijing, China, ² State Key Laboratory of Animal Nutrition, Institute of Animal Science, Chinese Academy of Agricultural Sciences, Beijing, China, ³ Department of Chemical and Environmental Engineering and Materials Science and Engineering Program, University of California, Riverside, Riverside, CA, United States, ⁴ Escuela de Ciencia e Ingeniería de Materiales, Centro de Investigación y Extensión de Materiales, Instituto Tecnológico de Costa Rica, Cartago, Costa Rica, ⁵ Research Institute of Wood Industry, Chinese Academy of Forestry, Beijing, China

Porphyrins, with or without metal ions (MPs), have been explored and applied in optical and electrochemical sensor fields owing to their special physicochemical properties. The presence of four nitrogen atoms at the centers of porphyrins means that porphyrins chelate most metal ions, which changes the binding ability of MPs with gas molecules via non-specific binding. In this article, we report hybrid chemiresistor sensor arrays based on single-walled carbon nanotubes (SWNTs) non-covalently functionalized with six different MPs using the solvent casting technique. The characteristics of MP-SWNTs were investigated through various optical and electrochemical methods, including UV spectroscopy, Raman, atomic force microscopy, current-voltage (I-V), and field-effect transistor (FET) measurement. The proposed sensor arrays were employed to monitor the four VOCs (tetradecene, linalool, phenylacetaldehyde, and ethylhexanol) emitted by citrus trees infected with Huanglongbing (HLB), of which the contents changed dramatically at the asymptomatic stage. The sensitivity to VOCs could change significantly, exceeding the lower limits of the SWNT-based sensors. For qualitative and quantitative analysis of the four VOCs, the data collected by the sensor arrays were processed using different regression models including partial least squares (PLS) and an artificial neural network (ANN), which further offered a diagnostic basis for Huanglongbing disease at the asymptomatic stage.

Keywords: citrus greening disease, carbon nanotube, metalloporphyrin, chemiresistor, volatile organic compounds, artificial neural networks (ANN), gas sensor



INTRODUCTION

Porphyrins (Auwarter et al., 2015; Gutiérrez-Cerón et al., 2016), known as one of the critical types of biological ligands, are macromolecular heterocyclic compounds consisting of four modified pyrrole rings, which are connected together through a methine bridge so that the molecule takes the form of a large ring (Zahou et al., 2016). Each pyrrole ring is made from four carbons and one nitrogen. All of the nitrogen atoms located at the interior of the large ring form a central cavity that can coordinate with most metal ions to form metalloporphyrin complexes (MPs). Due to the coordinated metal ions of MPs being in an unsaturated state, MPs can bind with one or two additional ligands at the axial position. MPs can combine with gas molecules through Van der Waal forces, hydrogen bonding, or interaction with the central metal ion (Penza et al., 2010; Shirsat et al., 2012). The optical and electrical properties will change sharply when MPs interact with gas molecules. Therefore, sensors decorated with different MPs or MP hybrid materials are considered to be excellent gas-sensing devices at room temperature (Liu et al., 2010), of which the sensing performance has been investigated by several groups. Song and coworkers (Song et al., 2016) used 5, 10, 15, 20-tetrakis(4-aminophenyl)porphyrin zinc (ZnTAP) and nanoporous anodized aluminum oxide membrane to assemble highly ordered nanotubes of ZnTAP, which was applied to detect NO₂ at ambient temperature with high sensitivity and fast response-recovery time. Xie et al. developed a nitric oxide (NO) sensor based on a reduced graphene oxide field-effect transistor

functionalized with iron-porphyrin. This gas sensor for real-time monitoring of NO released from cultured human cells measured NO in living cells with high sensitivity and specificity (Xie et al., 2016).

Single-walled carbon nanotubes (SWNTs) (Peng et al., 2016), one-dimensional structures with a nanometer-range diameter, are seamless cylinders comprised of a layer of graphene. They have gained widespread use in electrochemical sensors due to their interesting properties, such as excellent electrical conductivity, high surface-to-volume ratio, and thermostability (Salvetat et al., 1999; Kang et al., 2007). Studies indicate that gas molecules as either charge donor or a charge acceptor can be weakly adsorbed by SWNTs, which can cause a significant change in the electronic transport properties of SWNTs in view of charge transfer and charge fluctuation (Britz and Khlobystov, 2006; Giraldo et al., 2014). However, the low sensitivity and poor selectivity of bare SWNT-based sensors limit the ability of an individual sensor to analyze a multi-component gas mixture. Surface modifications that occur when SWNTs are functionalized with gas-sensitive materials can enhance sensing performance (Martin et al., 2013; Hijazi et al., 2014). MPs have flat and planar structures that efficiently bind with the SWNTs through π - π interactions (Bassiouk et al., 2013).

Huanglongbing (HLB), also called citrus greening or yellow shoot disease, is a bacterial disease of citrus caused by a vector-transmitted pathogen (Sagaram et al., 2009) that threatens the multi-billion dollar citrus industry all over the world (Bassanezi et al., 2011). There are two general means of propagation:

(i) transmission from infected citrus trees to the surrounding trees by citrus psyllid insects (Grafton-Cardwell et al., 2013); (ii) grafting of an infected scion on a healthy citrus tree. In reality, if a citrus tree is infected by HLB, the disease will incubate for several years without any symptoms (Lee et al., 2015) and then exhibit visible symptoms, including yellowing of the veins, splotchy mottling of the entire leaf, dieback of twigs, and decay of feeder rootlets and lateral roots (Johnson et al., 2014). There are few effective and cheap treatments to cure this disease. The most frequently used method is to remove infected trees selectively, halting the spread of HLB, wherefore early detection of this disease is vital. In 2020, an approach to eradicate the bacteria responsible for Huanglongbing disease using silver nanoparticles (AgNPs) achieved remarkable results, providing a new method to cure this disease (Stephano-Hornedo et al., 2020). However, it is especially challenging to diagnose HLB at an early stage due to the infected trees lacking symptoms while still acting as reservoirs to transmit the disease. Current detection methods for HLB are based on qualitative assessment of disease symptoms and molecular analysis methods such as visible-near infrared spectroscopy (Sankaran et al., 2011), mid-infrared (MIR) spectroscopy (Sankaran et al., 2010), enzyme-linked immunosorbent assay (ELISA) (Rapala et al., 2002), and polymerase chain reaction (PCR) (Ananthakrishnan et al., 2010). These techniques are susceptible to error and require expensive, time-consuming processes, which makes them unsuitable for rapid, on-site detection at the asymptomatic stage. Previous research has demonstrated that the VOCs released by the trees are closely associated with plant metabolism, which offers a new means for detecting the status of plant health at any stage. Aksenov et al. (2014) used gas chromatography/differential mobility spectrometry (GC/DMS) to analyze the VOCs released by the Huanglongbing infected citrus tree. Hundreds of independent VOC measurements were collected and analyzed through GC/DMS. Based on changes in the concentrations of characteristic VOCs, the infection process was divided into four stages: healthy, asymptomatic, mild, and severe. They found that the contents of VOCs (tetradecene, linalool, nonadecane, phenylacetaldehyde, and ethylhexanol) changed dramatically at the asymptomatic stage. The levels of tetradecene and ethylhexanol decreased, and the rest increased. They established VOC-based disease detection with high accuracy. But GC/DMS is an expensive device that requires professional operation. To overcome this limitation, this paper proposes an electronic gas sensor to replace GC/DMS so as to determine the VOC concentrations at high sensitivity and low cost.

Here, hybrid chemiresistive sensor arrays based on SWNTs non-covalently functionalized with MPs was fabricated that is easy to use and low-cost and which is suitable for the detection of VOCs released from Huanglongbing infected citrus trees at the asymptomatic stage. The characteristics of MP-SWNTs were measured by optical and electrical methods, including UV-vis absorption spectroscopy, Raman, atomic force microscopy, current-voltage (I-V), and field-effect transistor (FET) measurement. The sensor arrays were applied to monitor the concentrations of the VOCs tetradecene, linalool, phenylacetaldehyde, and ethylhexanol. To discriminate the four VOCs qualitatively and quantitatively, partial least squares (PLS)

and an artificial neural network (ANN) were further selected to process the data recorded by the sensor arrays.

MATERIALS AND METHODS

Chemicals and Materials

Dispersed single-walled carbon nanotube solution (0.01 mg/ml, 95% semiconducting) was obtained from Nano-Integris Inc. (USA). Chemical reagents (dimethylformamide, acetone, propanol, and ammonium hydroxide) were purchased from Fisher Scientific Company (USA). Three volatile organic compounds (2-Ethyl-1-hexanol, 1-tetradecene, and phenylacetaldehyde) and 3-aminopropyltriethoxysilane (APTES) were purchased from Sigma Aldrich (USA). The MPs, namely tetraphenyl porphyrin (TPP), iron porphyrin (FeTPP), copper porphyrin (CuTPP), zinc porphyrin (ZnTPP), copper octamethyl porphyrin (CuOEP), and manganese OEP (MnOEP), were provided by two chemical companies, Sigma-Aldrich (USA) and Frontier Scientific (USA). Deionized water was used throughout the experiments.

The dispersed solutions of MPs (TPP, FeTPP, ZnTPP, and MnOEP) were prepared by dissolving a certain weight into 10 ml N, N-dimethylformamide (DMF) under ultrasonication. Saturated solutions of CuTPP and CuOEP were prepared for further use.

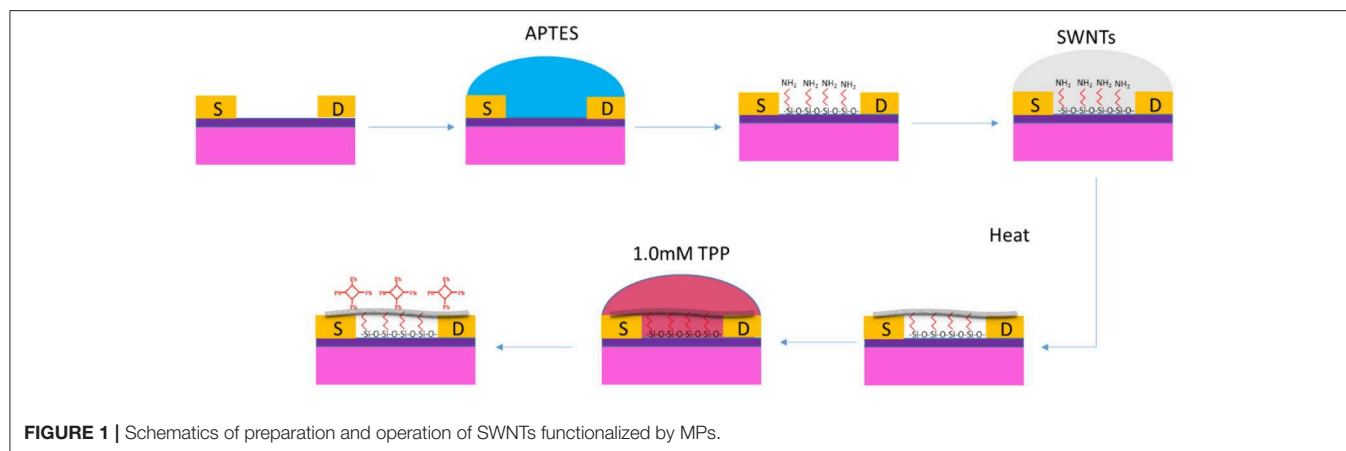
Apparatus

The spectral, morphological, and electrical characteristics of SWNTs before and after being functionalized by MPs were investigated by atomic force microscopy (AFM), Raman, UV-Vis spectrometry, current-voltage (I-V), and field-effect transistor (FET) measurement. AFM images were obtained using an atomic force microscope (Veeco Innova, Santa Barbara, CA, USA). Raman spectra were measured with a Nicolet Omega XR Dispersive microscope with 532-nm laser excitation. The UV spectrum was acquired by a Beckman DU640 UV/Vis spectrophotometer (Beckman Coulter, Inc. USA). Electrical measurements were made using a semiconductor parameter analyzer (Keithley 2636, USA).

For FET measurements, the Si substrate was covered with gold film, which served as the base, and charged with a linear voltage ranging from -60 V to $+20$ V. The two gold electrodes etched on the SiO_2 surface acted as the drain and source, to which a constant voltage (0.1 V) was applied. A dielectric layer of 100-nm thick SiO_2 was used to separate the base from the source-drain.

Fabrication of MPs-SWNTs

The sensor was designed with a single-gap structure because this offers a large area over which to react with gas molecules, and electrical conductivity can be controlled easily in comparison with an interdigital electrode. Highly p-doped silicon with a 100-nm SiO_2 layer was employed to fabricate the single gap microelectrode (10 μm in width and 10 μm in length) by photolithography using the positive photoresist AZ-5214. A 20-nm Cr layer and a 180-nm Au layer were uniformly deposited and etched on the surface of the Si/SiO_2 via e-beam evaporation. Finally, the photoresist residual was cleaned away with acetone solution.



The modification was shown in **Figure 1**. The single-gap electrode was flushed successively with acetone and isopropanol and then blow-dried in streaming air to remove surface impurities before use. The electrode was immersed into ammonium hydroxide for 30 min, and the residue was rinsed off with sufficient deionized water. The cleaned electrode was incubated in 0.5 mL APTES for 60 min, washed with deionized water, and blow-dried using a nitrogen stream as quickly as possible. After that, a 5- μ L SWNT solution was added to cover the microelectrode, and it was incubated with a high-humidity and dark condition for 60 min. The residual SWNTs were then carefully cleaned away with deionized water, and the electrode was annealed in ambient air at 250°C for 60 min. For MP immobilization, the single-gap electrode decorated with SWNTs (SWNTs-FET) was immersed in different MPs and placed in the dark for 4 h. Finally, the MP-SWNTs was annealed at 90°C under inert gasses in a protected condition for 60 min.

Gas Sensing Setup

The gas sensing setup shown in **Figure S1** was designed and integrated to perform VOC determination. This device can generate different concentrations of VOCs by mixing different proportions of air and saturated vapors of VOCs, which flowed through a 1.2 cm³ sealed glass dome covering the sensor array. A Keithley 2636 was used as a data-collecting device, connecting to the sensor arrays via three meters (bias, drain, and source) and recording output voltage and input current. All devices were controlled by the software installed in the computer that was programmed with the Laboratory Virtual Instrument Engineering Workbench (Lab VIEW). For experimental measurement, a voltage of +0.1 V was applied between the drain and the source without the base voltage. Before detecting a desired concentration of VOC, the sensor array was exposed to dry air until it reached a stable baseline.

RESULTS AND DISCUSSION

Characteristics of MP-SWNTs

Electrical characteristics (I_{DS} - V_{DS} and I_{DS} - V_G), AFM, UV spectrometry, and Raman were used to investigate the

characteristics of SWNTs before and after functionalization with MPs.

Electrical characterization is an effective method for distinguishing the changes in conductivity or resistance of SWNTs before and after each modification. As shown in **Figure 2A**, the I_{DS} - V_{DS} curves of bare SWNTs and CuTPP-SWNTs presented good linear relationships, but the current decreased dramatically with CuTPP-SWNTs. As shown in **Figure S2**, the resistance values of bare SWNTs and CuTPP-SWNTs were 28 and 318 k Ω , respectively; thus, with the addition of CuTPP, the resistance increased 11 times in comparison with bare SWNTs. The poor conductivity of CuTPP-SWNTs illustrated that the molecules of CuTPP had interacted with the carbon nanotube sidewalls, forming specific π - π -interactions through non-covalent interactions (Li et al., 2004; Shirakawa et al., 2005). The change in conductivity may be attributed to a couple of different causes (Zhao and Stoddart, 2009): (i) the carrier concentration (n) may be changed by an electron/charge-transfer between CuTPP and SWNTs; (ii) CuTPP may act as a randomly distributed scattering potential, transforming the mobility (μ) of the charge carrier. The FET curves of bare SWNTs before and after functionalization with CuTPP are shown in **Figure 2B**, for which the two electrodes were exposed to the air. We found that the threshold gate voltage (V_{TH}) of bare SWNTs was about -13.5 V, while when the SWNTs were functionalized with CuTPP, the FET curves shifted in the negative direction and the V_{TH} value was -20 V. According to the mobility equation, the mobility values of bare SWNT and CuTPP-SWNTs are 176 and 136 cm²/Vs, respectively, which is in agreement with the I_{DS} - V_{DS} results. The results remarkably demonstrate that the positive hole of the p-type semiconductor SWNTs was occupied by the electron, resulting in a lower barrier concentration and carrier mobility.

The morphology of bare SWNTs and CuTPP-SWNTs was studied by AFM observation in **Figure 3**. It was clear that the height of bare SWNTs was about 1.7 nm, approximately equal to the theoretical value (Bandow et al., 1998), which also matched the diameter value for the SWNTs offered by the producer. The height of the CuTPP-functionalized SWNTs was noticeably increased to 4 nm as a consequence of the attachment of porphyrin to the SWNTs' surface.

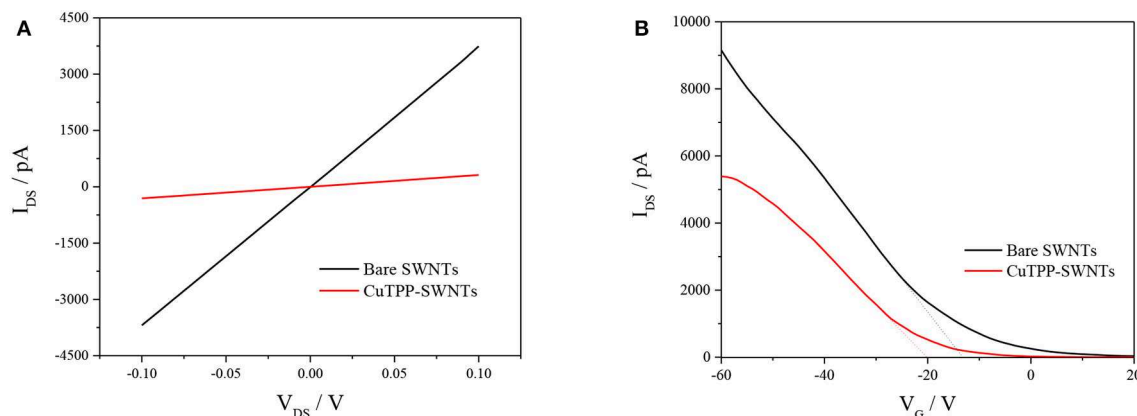


FIGURE 2 | Electrical and FET transfer characteristics of a CuTPP-functionalized bare SWNT device: **(A)** I_{DS} - V_{DS} at $V_{GS} = 0$ V and **(B)** V_G - I_{DS} at $V_{DS} = 0.1$ V.

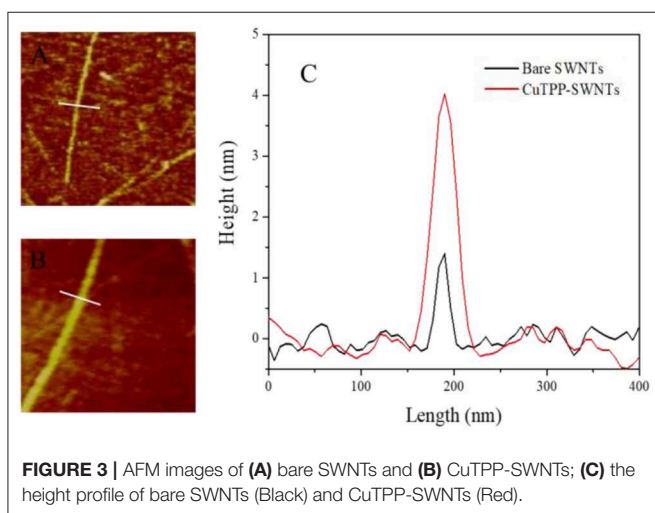


FIGURE 3 | AFM images of **(A)** bare SWNTs and **(B)** CuTPP-SWNTs; **(C)** the height profile of bare SWNTs (Black) and CuTPP-SWNTs (Red).

The formation of CuTPP-SWNTs is further confirmed by UV absorbance because most MPs have a strong near-UV band [a sharp, intense Soret band (B band)] in the near UV region and two weak Q bands responsible for the red to purple color in the visible region. Here, we chose a quartz plate to replace the silicon substrate due to its good optical transparency. Compared to blank Quartz in **Figure 4**, SWNTs-Quartz had an absorption peak at 273 nm and an increasing absorbance intensity in the whole spectral range, suggesting that the opaque material of SWNTs had attached to the Quartz (Ryabenko et al., 2004). The network structure formed by this attachment hampers parts of light from moving through it. After SWNTs were functionalized with CuTPP, a transmitting B band at 418 nm and one Q band at 541 nm were observed, which demonstrate that CuTPP was covalently attached to the surface of the SWNTs (Mammanna et al., 2008; Wang et al., 2011).

The interactions between the SWNTs and CuTPP were characterized using Raman spectroscopy, and the results are shown in **Figure 5**. The Raman spectrum of SWNTs shows four

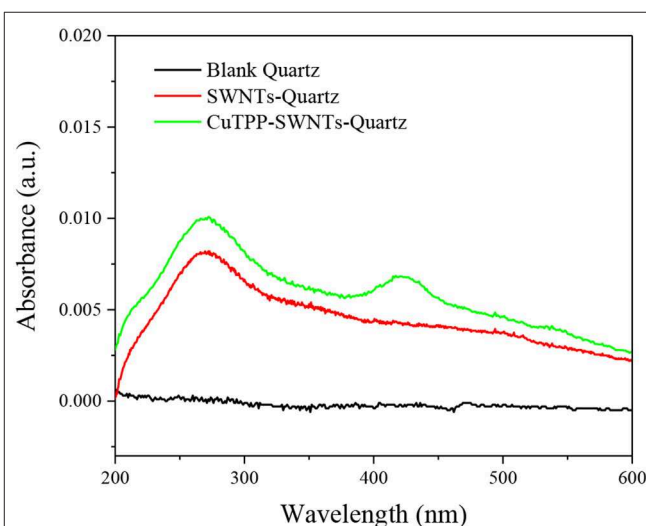


FIGURE 4 | UV-vis spectra of blank Quartz (Black), SWNTs-Quartz (Red), and CuTPP-SWNTs-Quartz (Green).

peaks at $1,351\text{ cm}^{-1}$ (a small D band), $1,579\text{ cm}^{-1}$ (a G^- band), $1,600\text{ cm}^{-1}$ (a sharp G^+ band), and $2,680\text{ cm}^{-1}$ (2D band). After CuTPP was non-covalently linked to SWNTs, the G^+ band peak becomes narrower, and the G^+ band shifts to $1,598\text{ cm}^{-1}$, suggesting that it can be ascribed to electron doping between SWNTs and CuTPP. Meanwhile, the D/G intensity ratio of CuTPP-SWNTs increase in comparison with SWNTs, indicating the conversion of sp^2 carbons to sp^3 carbons on the SWNTs surfaces due to the functionalization (Geng and Jung, 2010).

Gas Sensing Performance

As discussed earlier, the VOCs can serve as biomarkers to diagnose whether a citrus tree is infected by HLB. To evaluate the sensing performance of MP-functionalized SWNTs devices, we measured the real-time electrical response of the hybrid chemiresistor sensor arrays to phenylacetaldehyde, tetradecene,

linalool, and ethylhexanol vapors with concentrations varying from 5 to 100% of saturated vapors at room temperature. A normalization method was adopted to process the electrical signal, reducing the differences caused by the modification. The normalized response is defined as a relative change in resistance:

$$\Delta R/R_0 \% = (R - R_0)/R_0 \times 100\% \quad (1)$$

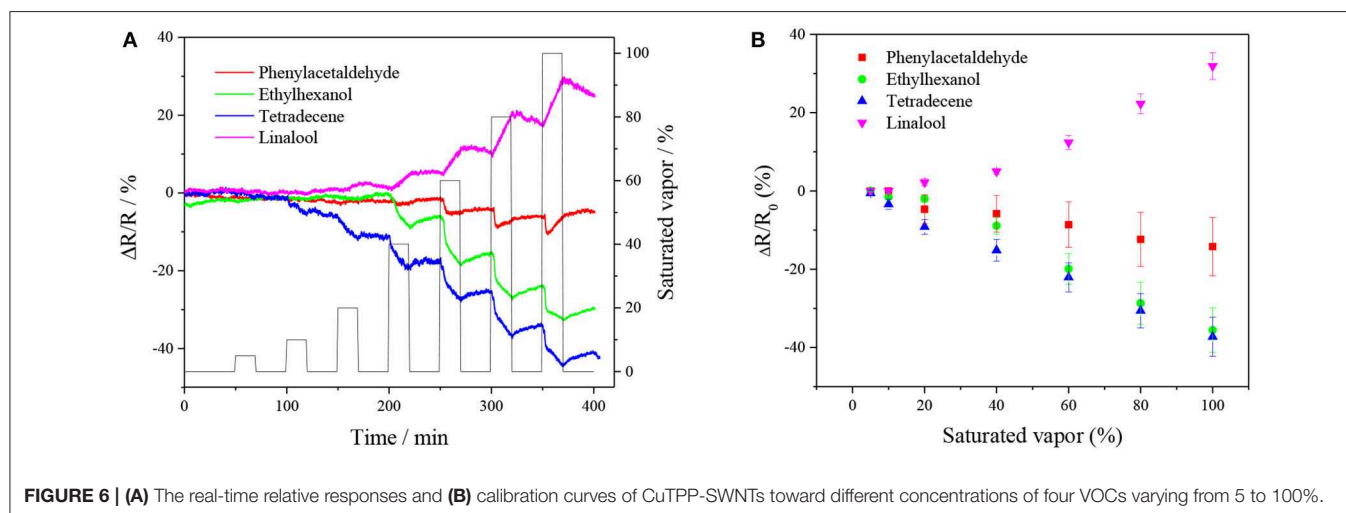
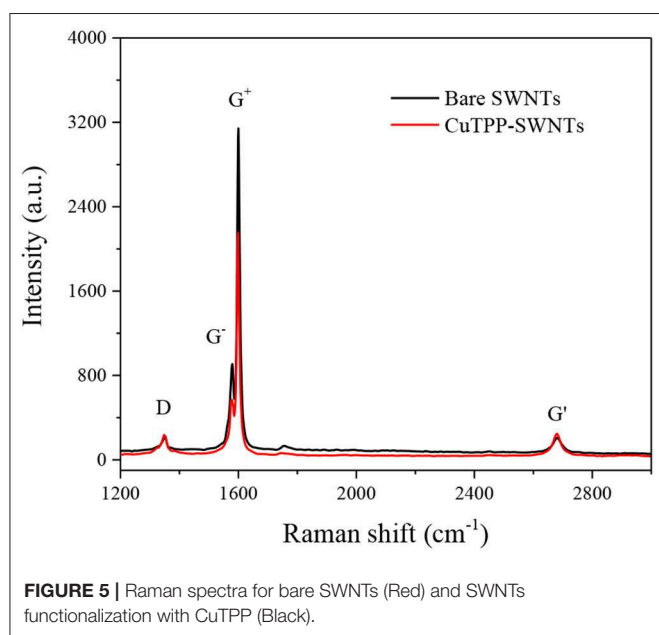
where R_0 is the value of initial baseline resistance before MP-SWNTs are exposed to VOCs and R is the value of resistance after MP-SWNTs are exposed to VOCs.

Figure 6A shows the normalized resistance of CuTPP-SWNTs toward the four VOCs (tetradecene, linalool, phenylacetaldehyde, and ethylhexanol) released by infected citrus trees at the asymptomatic stage. The normalized resistance

of CuTPP-SWNTs displayed a correlation with the VOC concentrations in the **Figure 6B**. The conductivity of CuTPP-SWNTs was increased after CuTPP-SWNTs had been exposed to tetradecene, ethylhexanol, and phenylacetaldehyde, while, in CuTPP-SWNTs exposed to linalool, the conductivity decreased. The reason for this is discussed in Mechanism section. Compared with the sensing responses of bare SWNTs shown in **Figure S3**, the sensitivity of CuTPP-SWNTs to the VOCs (except for phenylacetaldehyde) was improved to different degrees. For 100% saturated tetradecene vapor, the normalized response of bare SWNT is only 0.83%, with the response reaching 50% of the maximum in 4 min, as shown in **Figure S4**. However, the normalized response of CuTPP-SWNTs was 45 times higher than that of bare SWNTs at the same concentration, and 50% of the maximum response was reached in <5 min. Similar fast responses were observed using the rest of the MP functionalized SWNT devices to test the four VOCs; the related data are shown in **Tables S1–S4**. This indicates that the modification of SWNTs with MPs can enhance sensitivity, selectivity, and response time in detecting gas concentration. As shown in **Table S5**, the lowest detection limits were 4.86, 10.15, 0.18, and 0.61 ppm for phenylacetaldehyde, ethylhexanol, tetradecene, and linalool, respectively. After each experiment, we found that the sensor arrays needed a long time to recover to the baseline, but it was possible to shorten the recovery time by exposing the sensor arrays to UV light or a high-temperature environment in an oven, which can enhance the rate of desorption.

Mechanism

The sensing mechanism for the field-effect transistor includes four aspects: electrostatic gating, changes in gate coupling, Schottky barrier effects, and carrier mobility changes (Heller et al., 2008). CuTPP-SWNTs were selected to investigate the sensing mechanism upon interaction with organic gas molecules. Prior to FET detection, CuTPP-SWNTs were exposed to steaming air or saturated VOC vapors for 60 min to ensure that the gas molecules could interact adequately with the gas-sensitive material of CuTPP-SWNTs. **Figure 7** shows the transfer



characteristics (I_{DS} - V_G) curves. Compared to the FET curve in dry air, the I_{DS} - V_G curves of phenylacetaldehyde shifted in the negative direction, and the threshold gate voltage (V_{TH}) was

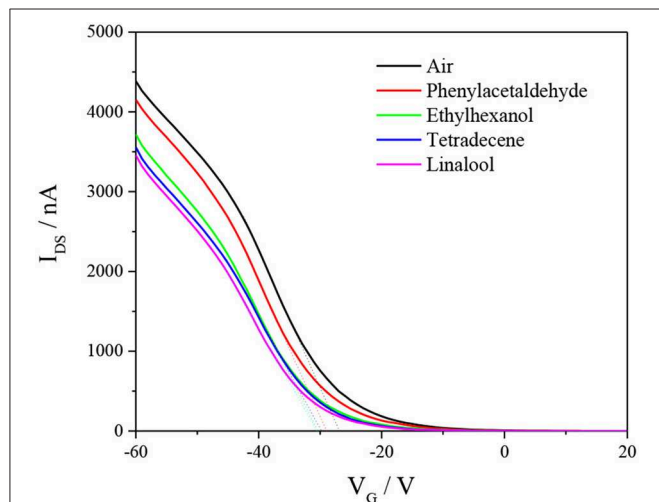


FIGURE 7 | Transfer characteristics (I_{DS} - V_G curves at $V_{DS} = -0.1$ V) of CuTPP-SWNTs in the presence of air and different saturated VOCs.

decreased, which was mainly ascribed to the electrostatic gating effect. According to the mobility equation, the values of carrier mobility of ethyl hexanol, tetradecane, and linalool reduced compared to the mobility for dry air. Thus, a threshold voltage shift and change in carrier mobility in the case of exposure of the CuTPP-SWNT hybrid to ethyl hexanol, tetradecane, and linalool indicate that the sensing mechanism is mainly governed by electrostatic gating and carrier mobility changes in combination.

Mathematical Model for VOC Analysis

Pattern recognition tools can provide powerful multivariate analysis methods to extract specific non-related information from complex correlations and have been widely applied in the multisensory field. Herein, we chose linear and non-linear models to process the data collected by the hybrid chemiresistor sensor arrays for the qualitative and quantitative analysis of the four VOCs. Principal component analysis (PCA) was performed, and the results are shown in **Figure S5** and **Table S6**.

Partial Least Square Regression (PLSR)

PLSR (Mehmood et al., 2012), a multivariate calibration model, was used to deal with the two multivariable matrices (X_0 and Y_0) with significantly redundant variations. It is realized by extracting predictor variables (X and Y) from the block X_0 -matrix and

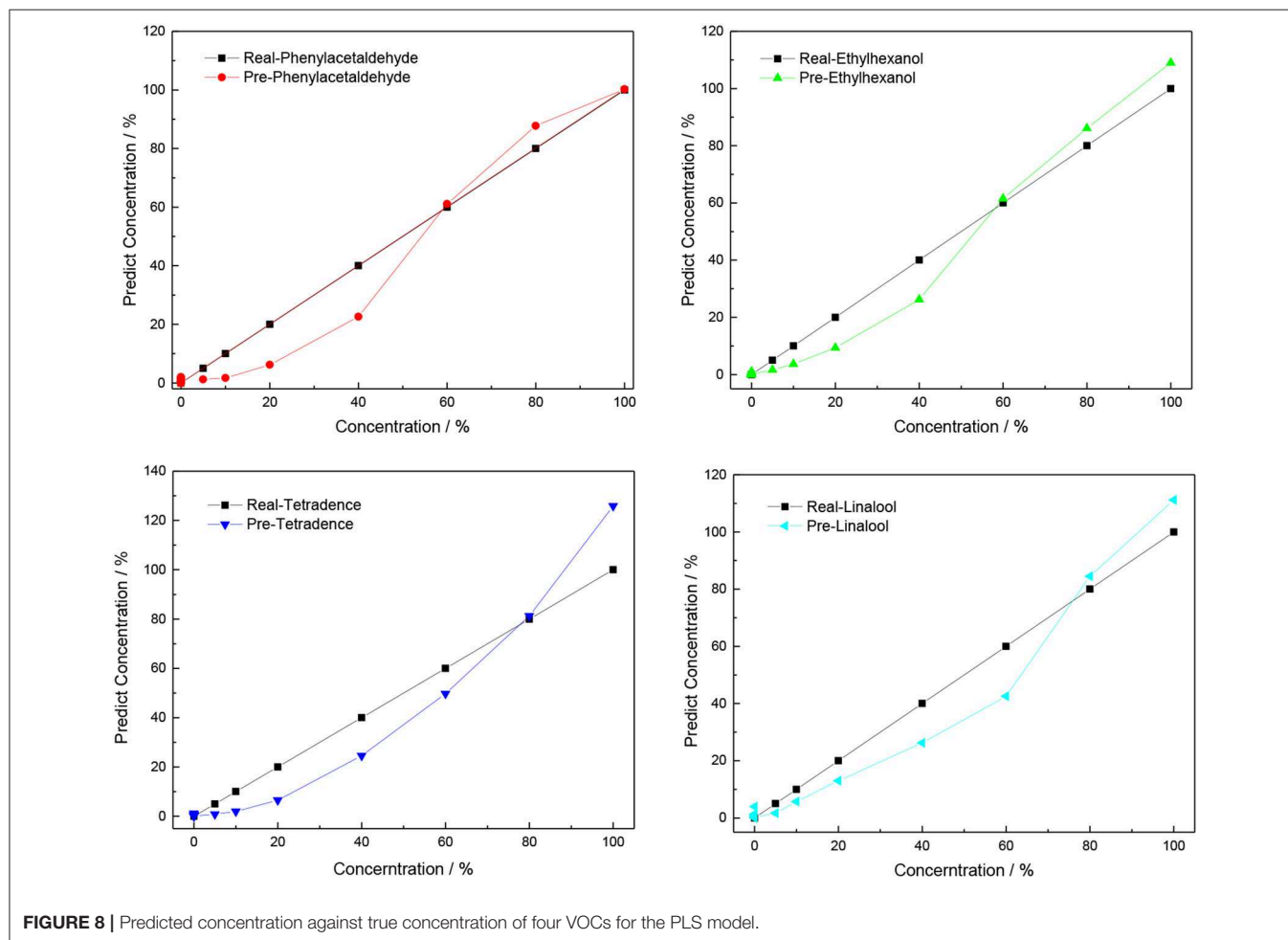
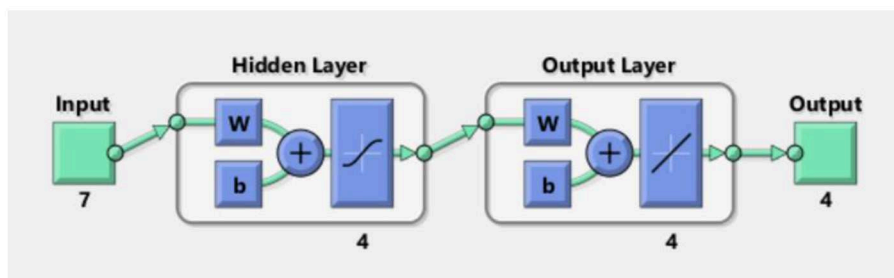
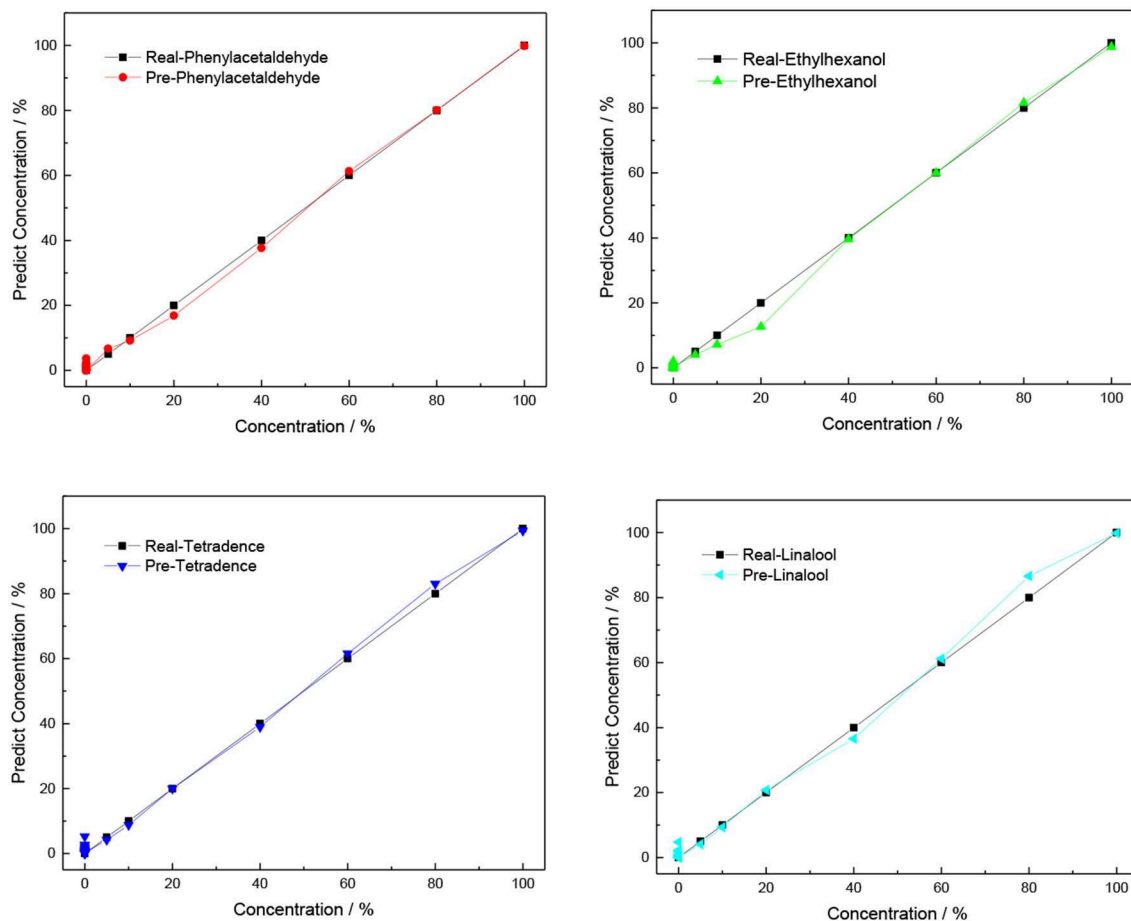


FIGURE 8 | Predicted concentration against true concentration of four VOCs for the PLS model.

TABLE 1 | The correlation coefficient (R_0) and root mean square error (R_{SMT}) between real concentrations and predicted concentrations.

	Phenylacetaldehyde		Ethylhexanol		Tetradecene		Linalool	
	R_0	R_{SMT}	R_0	R_{SMT}	R_0	R_{SMT}	R_0	R_{SMT}
PLSR	0.92816	9.58762	0.98718	4.11176	0.98303	4.72537	0.9762	5.58669
SPLS	0.98321	4.82493	0.98924	4.12993	0.9734	6.75741	0.98067	5.14909
ANN	0.99883	1.33108	0.99784	1.69709	0.99861	1.53506	0.99794	1.80906

**FIGURE 9** | Type of architecture of the neural network.**FIGURE 10** | Predicted concentration against true concentration of four VOCs for the ANN model.

the block Y_0 -matrix and then analyzing and establishing the relationship between the block X -matrix and the block Y -matrix. PLSR combines the merits of principal component analysis and multiple linear regression. This analysis also suits small samples with a simplified data structure.

For this experiment, the X_0 -matrix consists of 28 columns and 7 rows, with different concentrations (corresponding to 5, 10, 20, 40, 60, 80, and 100% saturated vapors) of four VOCs as the columns and normalized responses of MP-functionalized SWNTs (bare SWNTs, TPP-SWNTs, CuTPP-SWNTs, FeTPP-SWNTs, ZnTPP-SWNTs, CuOEP-SWNTs, MnOEP-SWNTs) as rows, and the Y_0 -matrix consists of 28 columns and 4 rows by using the real concentration as the columns and the four VOCs as the rows. As the normalized responses (X_0 -matrix) are non-linear with the concentrations of VOCs (Y_0 -matrix), these data matrices need to be pre-processed prior to use: $X = X_0$, $Y = \text{Sqrt}(Y_0)$. After the pre-treatment, the relationship between X and Y approximates linearity. The X -matrix and Y -matrix are inputted into the PLSR model, and the result is shown in **Figure S6** and **Figure 8**. We found that the correlation coefficient between the real concentration and fit concentration was much higher and the standard deviation was lower than the matrix without pretreatment; the data are presented.

Artificial Neural Network

An artificial neural network (ANN) (Asilturk and Cunkas, 2011) is a flexible mathematical structure that is capable of identifying complex non-linear relationships between input and output data sets. ANN models have been found to be useful and efficient, particularly in problems for which the characteristics of the processes are difficult to describe using physical equations. The overall structure is shown in **Figure 9**. The procedures of ANN are divided into three main parts: an input layer, hidden layers, and an output layer. In this model, the X matrix is the input layer, which consists of 28 columns and 7 rows filled by using different concentrations (corresponding to 5, 10, 20, 40, 60, 80, and 100% saturated vapors) of four VOCs as the columns and normalized responses of MP-functionalized SWNTs (bare SWNTs, TPP-SWNTs, CuTPP-SWNTs, FeTPP-SWNTs, ZnTPP-SWNTs, CuOEP-SWNTs, and MnOEP-SWNTs) as rows. The Y matrix is selected as an output layer, which consists of 4 columns and 28 rows, with the four concentrations in each row corresponding to each column of X . The data of the X matrix are divided randomly into three sets: 60% as training samples, 10% as validation samples, and 30% as testing samples. During learning, output values from the ANN are compared to true values, and the coupling weights are adjusted to give a minimum sum of square errors. After testing and comparing, we found that four nodes of the hidden layer can cause the average relative error to reach a minimum, shown in **Figure S7** and **Figure 10**.

Among the three mathematical models, PCA is used only for qualitative analysis of VOCs emitted by infected citrus trees, and it is hard to acquire accurate results when the gas concentration of any VOC is below 20%. Both PLSR and ANN are simple methods that can offer qualitative and quantitative information, which is widely employed in stoichiometry. The correlation coefficient (R_0) and root mean square error (R_{SMT}) between

real concentrations and predicted concentrations are shown in **Table 1**. We found that the best result is achieved with the utilization of the ANN model because the values of R_0 for these VOCs are higher and the R_{SMT} is lower than with PLS and SPLS. This demonstrates that a non-linear regression model is well-suited for non-linear data processing.

CONCLUSIONS

Volatile organic compounds (VOCs; phenylacetaldehyde, tetradecene, linalool, and ethylhexanol) released by infected citrus trees are associated with plant metabolism and can serve as biomarkers for the detection of Huanglongbing disease (HLB). In conclusion, we have fabricated hybrid chemiresistor sensor arrays based on SWNTs functionalized with different MPs to determine changes in the concentrations of four VOCs emitted by infected citrus trees, which are used to diagnose HLB at an asymptomatic stage. Optical and electrochemical approaches have been applied to examine the electrical characterization of SWNTs before and after functionalization with MPs and have shown that MPs can attach to SWNTs to form a stable membrane. MP-SWNTs improved the sensitivity to the various VOCs tested, and are shown to have differences in sensing performance. To obtain accurate concentrations, the test data collected by the hybrid chemiresistor sensor arrays were analyzed using the PCA, PLSR, and ANN techniques. By comparing these three results, it was found that ANN was much better suited to the non-linear data processing required.

DATA AVAILABILITY STATEMENT

The raw data supporting the conclusions of this article will be made available by the authors, without undue reservation, to any qualified researcher.

AUTHOR CONTRIBUTIONS

HW: data curation, formal analysis, methodology, software, writing—original draft, reviewing, and editing. PR, TP, CV, and XY: formal analysis and methodology. GL: supervision, reviewing, and editing. AM: conceptualization, funding, resources, supervision, methodology, reviewing, and editing.

FUNDING

This work was supported by grants from the United States Department of Agriculture (No. 2014-67021-21589) to AM, the Chinese National Natural Science Foundation (No. 31671578), and Key Realm R&D Program of Guangdong Province (Nos. 2019B020215002 and 2019B020215004). AM acknowledges the financial support of W. Ruel Johnson Chair.

SUPPLEMENTARY MATERIAL

The Supplementary Material for this article can be found online at: <https://www.frontiersin.org/articles/10.3389/fchem.2020.00362/full#supplementary-material>

REFERENCES

- Aksenov, A. A., Pasamontes, A., Peirano, D. J., Zhao, W., Dandekar, A. M., Fiehn, O., et al. (2014). Detection of Huanglongbing disease using differential mobility spectrometry. *Anal. Chem.* 86, 2481–2488. doi: 10.1021/ac403469y
- Ananthakrishnan, G., Venkataprasanna, T., Roy, A., and Bransky, R. N. (2010). Characterization of the mixture of genotypes of a Citrus tristeza virus isolate by reverse transcription-quantitative real-time PCR. *J. Virol. Methods* 164, 75–82. doi: 10.1016/j.jviromet.2009.12.001
- Asilturk, I., and Cunkas, M. (2011). Modeling and prediction of surface roughness in turning operations using artificial neural network and multiple regression method. *Expert Syst. Appl.* 38, 5826–5832. doi: 10.1016/j.eswa.2010.11.041
- Auwarter, W., Eciija, D., Klappenberger, F., and Barth, J. V. (2015). Porphyrins at interfaces. *Nat. Chem.* 7, 105–120. doi: 10.1038/nchem.2159
- Bandow, S., Asaka, S., Saito, Y., Rao, A. M., Grigorian, L., Richter, E., et al. (1998). Effect of the growth temperature on the diameter distribution and chirality of single-wall carbon nanotubes. *Phys. Rev. Lett.* 80, 3779–3782. doi: 10.1103/PhysRevLett.80.3779
- Bassanezi, R. B., Montesino, L. H. M., Gasparoto, C. G., Bergamin, A., and Amorim, L. (2011). Yield loss caused by huanglongbing in different sweet orange cultivars in so Paulo, Brazil. *Eur. J. Plant Pathol.* 130, 577–586. doi: 10.1007/s10658-011-9779-1
- Bassiouk, M., Basiuk, V. A., Basiuk, E. V., Álvarez-Zauco, E., Martínez-Herrera, M., Rojas-Aguilar, A., et al. (2013). Noncovalent functionalization of single-walled carbon nanotubes with porphyrins. *Appl. Surf. Sci.* 275, 168–177. doi: 10.1016/j.apsusc.2012.12.167
- Britz, D. A., and Khlbystov, A. N. (2006). Noncovalent interactions of molecules with single walled carbon nanotubes. *Chem. Soc. Rev.* 35, 637–659. doi: 10.1039/b507451g
- Geng, J. X., and Jung, H. (2010). Porphyrin functionalized graphene sheets in aqueous suspensions: from the preparation of graphene sheets to highly conductive graphene films. *J. Phys. Chem. C* 114, 8227–8234. doi: 10.1021/jp1008779
- Giraldo, J. P., Landry, M. P., Faltermeier, S. M., McNicholas, T. P., Iverson, N. M., Boghossian, A. A., et al. (2014). Plant nanobionics approach to augment photosynthesis and biochemical sensing. *Nat. Mater.* 13, 400–408. doi: 10.1038/nmat3890
- Grafton-Cardwell, E. E., Stelinski, L. L., and Stansly, P. A. (2013). Biology and management of asian citrus psyllid, vector of the huanglongbing pathogens. *Annu. Rev. Entomol.* 58, 413–432. doi: 10.1146/annurev-ento-120811-153542
- Gutiérrez-Cerón, C., Páez, M. A., and Zagal, J. H. (2016). Reactivity descriptors for iron porphyrins and iron phthalocyanines as catalysts for the electrooxidation of reduced glutathione. *J. Solid State Electrochem.* 20, 3199–3208. doi: 10.1007/s10008-016-3396-z
- Heller, I., Janssens, A. M., Mannik, J., Minot, E. D., Lemay, S. G., and Dekker, C. (2008). Identifying the mechanism of biosensing with carbon nanotube transistors. *Nano Lett.* 8, 591–595. doi: 10.1021/nl072996i
- Hijazi, I., Bourgeteau, T., Cornut, R., Morozan, A., Filoramo, A., Leroy, J., et al. (2014). Carbon nanotube-templated synthesis of covalent porphyrin network for oxygen reduction reaction. *J. Am. Chem. Soc.* 136, 6348–6354. doi: 10.1021/ja500984k
- Johnson, E. G., Wu, J., Bright, D. B., and Graham, J. H. (2014). Association of 'Candidatus Liberibacter Asiaticus' root infection, but not phloem plugging with root loss on huanglongbing-affected trees prior to appearance of foliar symptoms. *Plant Pathol.* 63, 290–298. doi: 10.1111/ppa.12109
- Kang, S., Pinault, M., Pfefferle, L. D., and Elimelech, M. (2007). Single-walled carbon nanotubes exhibit strong antimicrobial activity. *Langmuir* 23, 8670–8673. doi: 10.1021/la701067r
- Lee, J. A., Halbert, S. E., Dawson, W. O., Robertson, C. J., Keesling, J. E., and Singer, B. H. (2015). Asymptomatic spread of huanglongbing and implications for disease control. *P. Natl. Acad. Sci. U S A* 112, 7605–7610. doi: 10.1073/pnas.1508253112
- Li, H. P., Zhou, B., Lin, Y., Gu, L. R., Wang, W. K., Fernando, S., et al. (2004). Selective interactions of porphyrins with semiconducting single-walled carbon nanotubes. *J. Am. Chem. Soc.* 126, 1014–1015. doi: 10.1021/ja037142o
- Liu, H. M., Xu, Z., Wang, N., Yu, C., Gao, N. Y., Zhao, J. W., et al. (2010). Theoretical investigation on the chemical sensing of metalloporphyrin-based molecular junction. *J. Chem. Phys.* 132:244702. doi: 10.1063/1.3456542
- Mammana, A., Asakawa, T., Bitsch-Jensen, K., Wolfe, A., Chaturantabut, S., Otani, Y., et al. (2008). Synthesis and characterization of water-soluble free-base, zinc and copper porphyrin-oligonucleotide conjugates. *Bioorgan. Med. Chem.* 16, 6544–6551. doi: 10.1016/j.bmc.2008.05.041
- Martin, K. E., Tian, Y., Busani, T., Medforth, C. J., Franco, R., van Swol, F., et al. (2013). Charge effects on the structure and composition of porphyrin binary ionic solids: ZnTPPS/SnTMePyP nanomaterials. *Chem. Mater.* 25, 441–447. doi: 10.1021/cm303595s
- Mehmood, T., Liland, K. H., Snipen, L., and Saebø, S. (2012). A review of variable selection methods in Partial Least Squares Regression. *Chemometr. Intell. Lab. Syst. J.* 118, 62–69. doi: 10.1016/j.chemolab.2012.07.010
- Peng, G., Wu, S., Ellis, J. E., Xu, X., Xu, G., Yu, C., et al. (2016). Single-walled carbon nanotubes templated CuO networks for gas sensing. *J. Mater. Chem. C* 4, 6575–6580. doi: 10.1039/C6TC01722C
- Penza, M., Rossi, R., Alvisi, M., Signore, M. A., Serra, E., Paolesse, R., et al. (2010). Metalloporphyrins-modified carbon nanotubes networked films-based chemical sensors for enhanced gas sensitivity. *Sensor. Actuat. B-Chem.* 144, 387–394. doi: 10.1016/j.snb.2008.12.060
- Rapala, J., Erkkö, K., Kukkonen, J., Sivonen, K., and Lahti, K. (2002). Detection of microcystins with protein phosphatase inhibition assay, high-performance liquid chromatography-UV detection and enzyme-linked immunosorbent assay - comparison of methods. *Anal. Chim. Acta* 466, 213–231. doi: 10.1016/S0003-2670(02)00588-3
- Ryabenko, A. G., Dorofeeva, T. V., and Zvereva, G. I. (2004). UV-VIS-NIR spectroscopy study of sensitivity of single-wall carbon nanotubes to chemical processing and Van-der-Waals SWNT/SWNT interaction. Verification of the SWNT content measurements by absorption spectroscopy. *Carbon* 42, 1523–1535. doi: 10.1016/j.carbon.2004.02.005
- Sagaram, U. S., DeAngelis, K. M., Trivedi, P., Andersen, G. L., Lu, S. E., and Wang, N. (2009). Bacterial diversity analysis of huanglongbing pathogen-infected citrus, using phylochip arrays and 16S rRNA gene clone library sequencing. *Appl. Environ. Microb.* 75, 1566–1574. doi: 10.1128/AEM.02404-08
- Salvetat, J. P. G., Briggs, A. D., Bonard, J. M., Bacsá, R. R., Kulik, A. J., Stockli, T., et al. (1999). Elastic and shear moduli of single-walled carbon nanotube ropes. *Phys. Rev. Lett.* 82, 944–947. doi: 10.1103/PhysRevLett.82.944
- Sankaran, S., Ehsani, R., and Etxeberria, E. (2010). Mid-infrared spectroscopy for detection of huanglongbing (greening) in citrus leaves. *Talanta* 83, 574–581. doi: 10.1016/j.talanta.2010.10.008
- Sankaran, S., Mishra, A., Maja, J. M., and Ehsani, R. (2011). Visible-near infrared spectroscopy for detection of Huanglongbing in citrus orchards. *Comput. Electron. Agric.* 77, 127–134. doi: 10.1016/j.compag.2011.03.004
- Shirakawa, M., Fujita, N., and Shinkai, S. (2005). A stable single piece of unimolecularly pi-stacked porphyrin aggregate in a thixotropic low molecular weight gel: a one-dimensional molecular template for polydiacetylene wiring up to several tens of micrometers in length. *J. Am. Chem. Soc.* 127, 4164–4165. doi: 10.1021/ja042869d
- Shirsat, M. D., Sarkar, T., Kakoullis, J., Myung, N. V., Konnanath, B., Spanias, A., Mulchandani, A. (2012). Porphyrin-functionalized single-walled carbon nanotube chemiresistive sensor arrays for VOCs. *J. Phys. Chem. C* 116, 3845–3850. doi: 10.1021/jp210582t
- Song, F. F., Ma, P., Chen, C. L., Jia, J. N., Wang, Y. C., and Zhu, P. H. (2016). Room temperature NO₂ sensor based on highly ordered porphyrin nanotubes. *J. Colloid Interf. Sci.* 474, 51–57. doi: 10.1016/j.jcis.2016.04.012
- Stephano-Hornedo, J. L., Torres-Gutiérrez, O., Toledano-Magaña, Y., Gradilla-Martínez, I., Pestryakov, A., Sánchez-González, A., et al. (2020). ArgovitTM silver nanoparticles to fight huanglongbing disease in Mexican limes (*Citrus Aurantifolia* Swingle). *RSC Adv.* 10, 6146–6155. doi: 10.1039/C9RA09018E
- Wang, B., Zuo, X., Wu, Y. Q., Chen, Z. M., He, C. Y., and Duan, W. B. (2011). Comparative gas sensing in copper porphyrin and copper phthalocyanine spin-coating films. *Sensor. Actuat. B-Chem.* 152, 191–195. doi: 10.1016/j.snb.2010.12.006

- Xie, H., Li, Y. T., Lei, Y. M., Liu, Y. L., Xiao, M. M., Gao, C., et al. (2016). Real-time monitoring of nitric oxide at single-cell level with porphyrin-functionalized graphene field-effect transistor biosensor. *Anal. Chem.* 88, 11115–11122. doi: 10.1021/acs.analchem.6b03208
- Zahou, I., Hassen, L. B., Mlika, R., Ben Chaabane, R., Nasri, H., and Ben Ouada, H. (2016). Synthesis and investigation on optical and electrical properties of a triflate iron porphyrin: application as an optical BPA sensor. *Synthetic Met.* 221, 75–85. doi: 10.1016/j.synthmet.2016.07.020
- Zhao, Y. L., and Stoddart, J. F. (2009). Noncovalent functionalization of single-walled carbon nanotubes. *Accounts Chem Res.* 42, 1161–1171. doi: 10.1021/ar900056z

Conflict of Interest: The authors declare that the research was conducted in the absence of any commercial or financial relationships that could be construed as a potential conflict of interest.

Copyright © 2020 Wang, Ramnani, Pham, Villarreal, Yu, Liu and Mulchandani. This is an open-access article distributed under the terms of the Creative Commons Attribution License (CC BY). The use, distribution or reproduction in other forums is permitted, provided the original author(s) and the copyright owner(s) are credited and that the original publication in this journal is cited, in accordance with accepted academic practice. No use, distribution or reproduction is permitted which does not comply with these terms.



Interface Design of SnO₂@PANI Nanotube With Enhanced Sensing Performance for Ammonia Detection at Room Temperature

Anqiang Jia^{1,2,3}, Bitao Liu^{2*}, Haiyan Liu³, Qiufeng Li³ and Yingxia Yun^{1*}

¹ Department of Urban and Rural Planning, School of Architecture, Tianjin University, Tianjin, China, ² Research Institute for New Materials Technology, Chongqing University of Arts and Sciences, Chongqing, China, ³ Institute of Urban and Rural Construction, College of Science, College of Animal Science and Technology, Hebei Agricultural University, Baoding, China

OPEN ACCESS

Edited by:

Weiwei Wu,
Xidian University, China

Reviewed by:

Ning Tang,
Xidian University, China
Xu Yan,
Tianjin University, China

*Correspondence:

Bitao Liu
liubitao007@163.com
Yingxia Yun
jiaanqiang111@163.com

Specialty section:

This article was submitted to
Nanoscience,
a section of the journal
Frontiers in Chemistry

Received: 26 February 2020

Accepted: 14 April 2020

Published: 03 June 2020

Citation:

Jia A, Liu B, Liu H, Li Q and Yun Y
(2020) Interface Design of
SnO₂@PANI Nanotube With
Enhanced Sensing Performance for
Ammonia Detection at Room
Temperature. *Front. Chem.* 8:383.
doi: 10.3389/fchem.2020.00383

Gas sensors with excellent stability and a high response at room temperature has drawn a great deal of attention and demand for them is huge. Surface designs provide inspiration toward making more useful sensor devices. The facile electrospinning process and Ar plasma treatment are used to fabricate rich and stable oxygen vacancies that contain a core-shell structured SnO₂ polyaniline (PANI) nanotube. It shows that the induced surface oxygen vacancies would accelerate the PANI shell to generate more protons, which can enhance its sensor responsibility through reacting with the target Ammonia (NH₃) gas. It was also found that the obtained oxygen vacancies can be well-protected by the coated PANI shell, which enhance and stabilize the gas response. It shows that the room temperature for the gas response of NH₃ can reach up to 35.3 at 100 ppm. Finally, its good stability is demonstrated by the response-recovery performances carried out over 3 months and multiple cycles. This work indicates that this well-designed PANI-coated plasma-treated SnO₂ is a potential way to design ammonia gas sensors.

Keywords: ammonia sensor, room temperature, oxygen vacancies, PANI-T-SnO₂, interface design

INTRODUCTION

Ammonia (NH₃), a colorless, strong, volatile gas, which can have a huge impact on the respiratory tract and eyes at a concentration below 50 ppm, has drawn much attention (Timmer et al., 2005; Li et al., 2016). It is generally known that human body's long-term allowable limit of NH₃ in an indoor environment is lower than 25 ppm (Li et al., 2018). Thus, it is critical for environmental protection and human health to detect NH₃ gas at room temperature. Oxide semiconductors have been extensively studied to detect dangerous and various toxic gases, especially in harsh environments (Cheng et al., 2017; Lupan et al., 2018). Dioxide (SnO₂), which has a superior thermal stability (the melt point is 1,127°C), non-toxicity, and a low cost, has been proved to be an outstanding candidate for gas sensing (Wang et al., 2010; Das et al., 2014; Lee et al., 2015; Singkammo et al., 2015). Different morphologies of SnO₂ have been synthesized for various gas detection, especially for the 1D nanostructured (Das et al., 2014; Lee et al., 2015; Singkammo et al., 2015). However, the optimized response is usually performed at a relatively high temperature of more than 200°C, which means that is not suitable for gas sensing at a room temperature (Das et al., 2014; Lee et al., 2015; Singkammo et al., 2015). Thus, it is still a challenge to reduce the working temperature.

Many attempts aimed at improving the properties of the gas sensor, like element doping (Wang et al., 2010), composites with RGO (Su and Yang, 2016; Chen et al., 2017) and MWCNT (Tyagi et al., 2017), and using a heterostructure design (Chen et al., 2015; Lee et al., 2015; Liu et al., 2016; Yuan et al., 2020), have been conducted. More importantly, inorganic and organic composites have drawn much attention for they can overcome the shortcomings of each other in gas sensor performance. Specifically, the conductive polymers can work effectively at room temperature, and among these, PANI has been considered a better NH₃ sensor at room temperature (Shin et al., 2008; Wen et al., 2013; Li et al., 2016; Syrovoy et al., 2016; Kumar et al., 2017; Bai et al., 2018; Liu B. T. et al., 2018; Nie et al., 2018; Tang et al., 2018, 2019; Santos et al., 2019). Several PANI and oxide semiconductors composites, like V₂O₅@PANI (Santos et al., 2019), CeO₂@PANI (Liu C. H. et al., 2018), SiO₂@PANI (Nie et al., 2018), SnO₂@PANI (Bai et al., 2018), etc., have been reported as effective room temperature gas sensors. However, the recovery time for these PANI-based composites is usually long due to their hydrophilic surface. Additionally, PANI is a p type material that needs a fast electron speed to provide protons for the target gas effectively and provide a higher gas-sensitivity (Kumar et al., 2017). Thus, composites of PANI to an n-type oxide semiconductor material with an efficient electron speed could provide an opportunity to improve their gas-sensitive response through separating the accepted electrons (Wang et al., 2017; Chen et al., 2020a,b). Oxygen vacancies, an ideal electron acceptor, usually exist in many n-type oxide semiconductor materials, which can enhance the sensor properties and decrease the working temperature (Pacchioni, 2003; Trani et al., 2009). It has been reported that oxygen vacancies with rich oxide semiconductors, such as WO₃ (Qin and Ye, 2016; Wang et al., 2017), W₁₈O₄₉ (Chen et al., 2020a), CeO₂ (Soni et al., 2018) etc., would strengthen the interaction between vacancy-terminated surface and gas molecules remarkably, subsequently reducing the optimized work temperature and enhancing the sensitivity. Thus, developing oxygen vacancies with rich SnO₂ through combining them with PANI should be an efficient way to obtain high sensitivity room temperature gas sensors.

As far as we know, there has been little research into the oxygen vacancies that contain SnO₂-PANI for gas sensing at room temperature. Herein, in this work, we fabricated a nanotube core-shell structured SnO₂-PANI nanotube with rich and stable oxygen vacancies to operate an NH₃ sensor under room temperature. The oxygen vacancies were ingeniously introduced on the interface between the SnO₂ nanotube and the PANI shell by Ar plasma treatment (Jia et al., 2019; Liu et al., 2019), which would promote the shell coated with PANI to produce more protons for the target NH₃ gas and enhance its sensitivity.

EXPERIMENT

The chemicals used in this experiment were of analytical purity; no further purification was required. The electrode was composed of glass substrate and gold. The schematic diagram of the samples synthesis process was shown in **Figure 1**.

Synthesis of SnO₂ Nanotube

Electrospinning was used to obtain the SnO₂ nanotube according to ref (Wang et al., 2017). 0.4 g PVP and 2 g SnCl₄·5H₂O were dissolved in a mixture solution of 4.4 g DMF and ethanol, and this was then stirred for 6 h. A syringe with an inner diameter of 1.01 mm was used, the voltage was 18 kV, and the distance was 15 cm. The fibers were collected and dried for 12 h at 100°C, and then annealed at 600°C for 2 h.

Plasma Treatment of SnO₂ Nanotube and Electrode (T-SnO₂)

The obtained SnO₂ nanotube was treated with Ar plasma at a flow rate of 30 ccm, powered at 100 V for 30 min. The glass substrate was treated with O plasma for 10 min to make the substrate more hydrophilic.

Synthesis of SnO₂@PANI on Electrode (PANI -T-SnO₂)

28.6 ul aniline monomer was injected into 18 ml hydrochloric acid (1M), and then stirred for 30 min. After that, 0.0873 g of T-SnO₂ was added and stirred for 30 minutes. Subsequently, 18 ml hydrochloric acid (1M) containing 0.3 g ammonium persulfate (APS) was added in to the solution, and stirred for another 30 minutes. Finally, these two solutions were mixed and kept at a temperature of 0-4°C for 6 h in an ice bath. An Au-electrode was immersed for 2, 4, 8, and 10 minutes (denoted as 1-PANI-T-SnO₂, 2-PANI-T-SnO₂, 3-PANI-T-SnO₂, 4-PANI-T-SnO₂) in the solution until it turned dark blue, and then froze and dried it in a vacuum for 8 h.

MATERIAL CHARACTERIZATION

The X-ray diffraction patterns (XRD) of serious samples were measured on the Dandong TD-3500 (Cu K α radiation, 30 kV, 20 mA). The morphology was tested by the scanning electron microscope (SEM, Hitachi, SU-8010). The surface structure information was recorded with X-ray photoelectron spectroscopy (XPS) equipment (ESCA Lab MKII). The surface oxygen vacancy was characterized by Electron spin resonance (ESR) on Japanese electronics (JEOLFA200).

Sensor Fabrication and Test

The gas sensing performances were tested as the same as our former work (Chen et al., 2020a), which were measured in an intelligent gas sensor analysis system (CGS-8, Beijing Elite Tech Co., Ltd.). To make sure the gas flow was smooth and steady, a self-made chamber (50 ml) and gas supply system were used. The test platform was shown in **Figure 1B**. All the tests were conducted at a room temperature of 25°C. The sensor response was defined as response = R_g/R_a, where R_a is the resistance in air and R_g is the measured resistance in the presence of the test gas.

RESULTS AND DISCUSSION

The XRD pattern for different samples was shown in **Figure 2**. All the diffraction peaks could be ascribed to the rutile structure of SnO₂ (JCPDS: 41-1445). As can be seen in **Figure 2A**, several

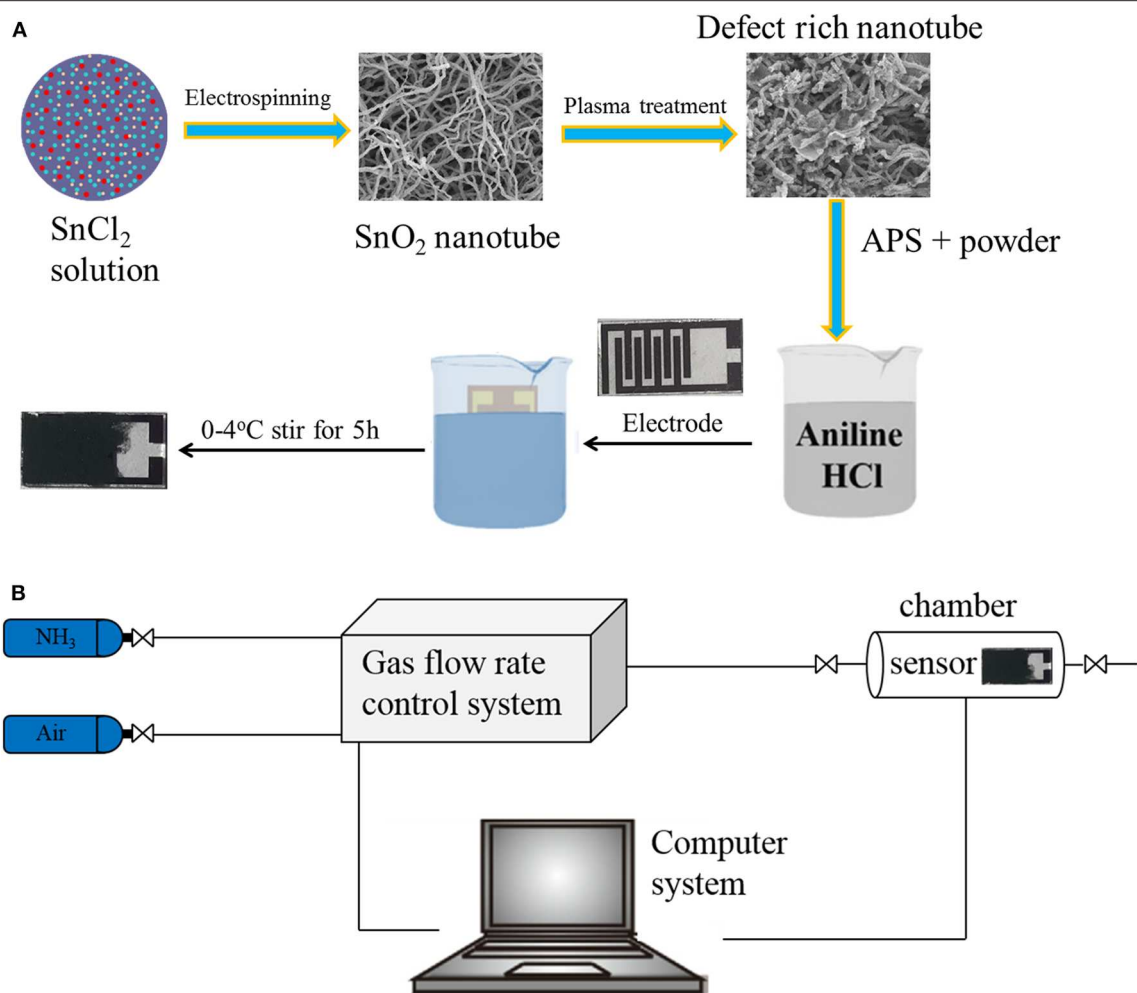


FIGURE 1 | Schematic illustration of the deposition process of nanocomposite thin film **(A)**. Schematic diagram illustrating the gas-sensing test platform **(B)**.

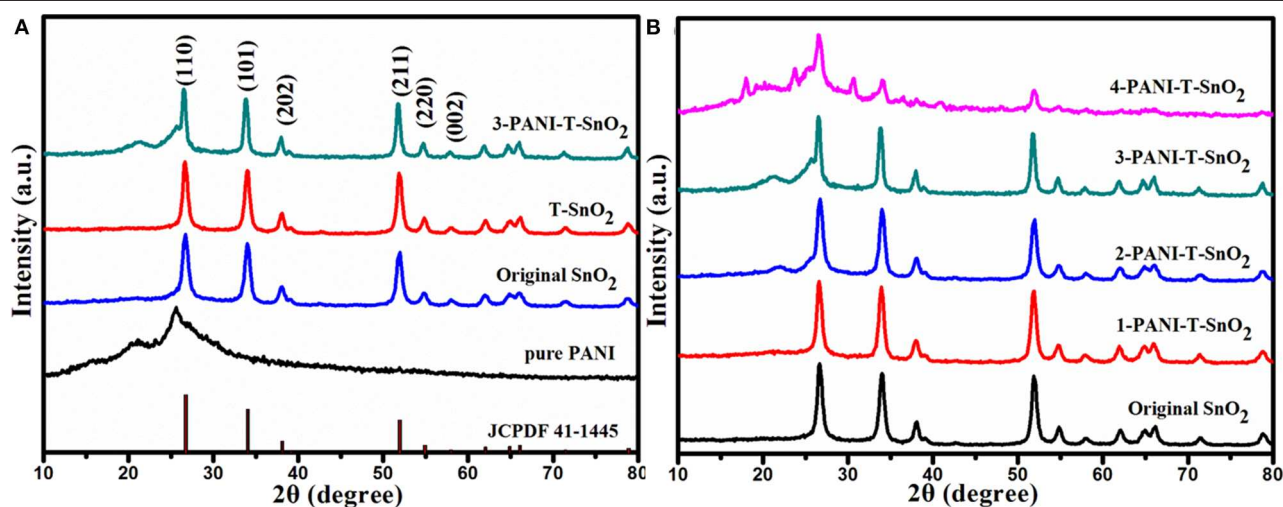


FIGURE 2 | XRD pattern of different samples **(A)** different samples **(B)** SnO₂ with different content of PANI. (T denoted as Ar plasma treatment, 1,2,3,4 denoted as different content of PANI).

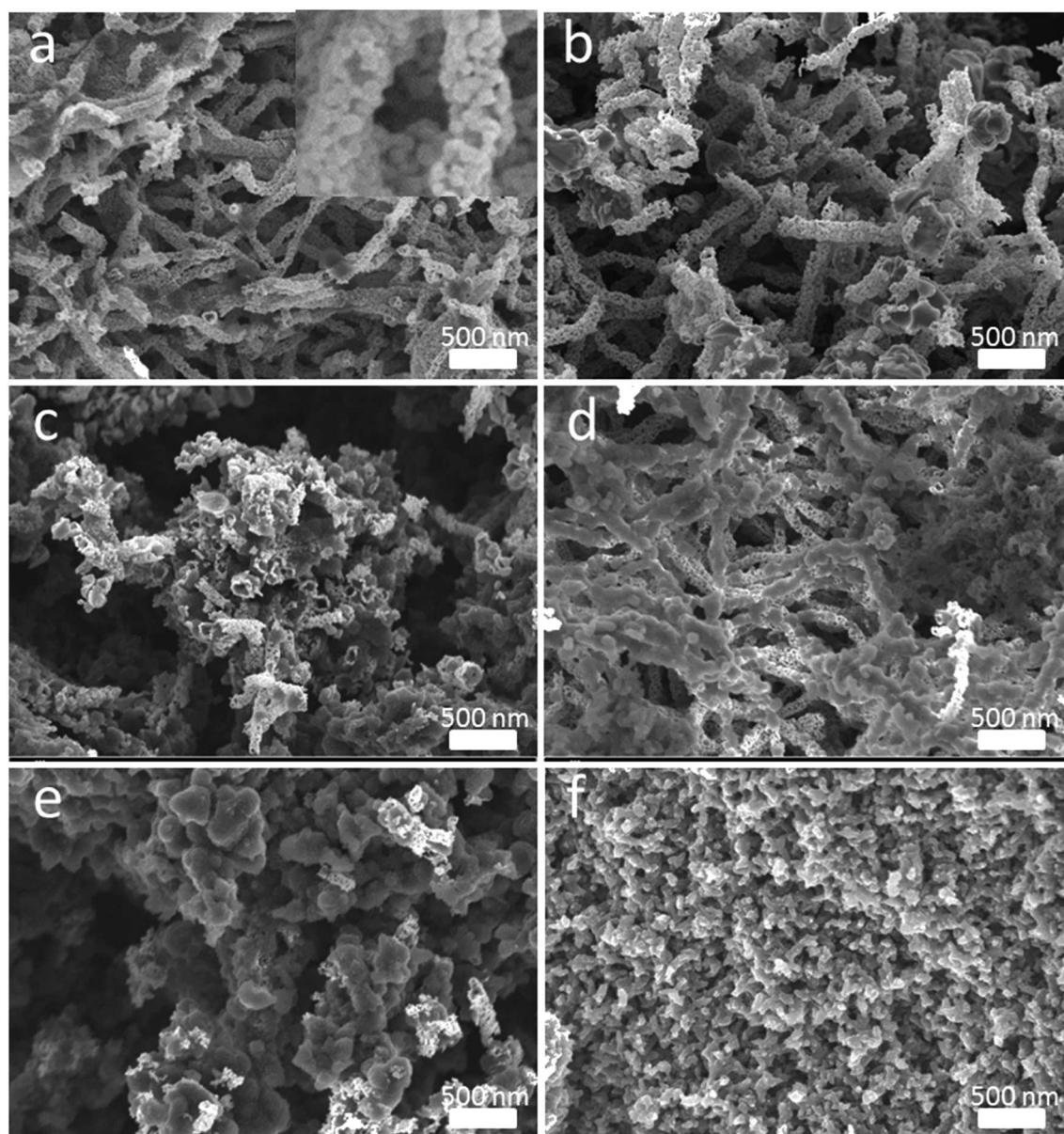


FIGURE 3 | Morphology and surficial characteristics revealed by SEM images with different magnifications (a) Original SnO_2 , (b) T- SnO_2 , (c) 1-PANI-T- SnO_2 , (d) 2-PANI-T- SnO_2 , (e) 3-PANI-T- SnO_2 , (f) 4-PANI-T- SnO_2 .

characteristic peaks at 27.1° , 34.3° , 40.6° , and 52.1° should be ascribed to the crystal planes of (110), (101), (202), and (211) (Li et al., 2016; Su and Yang, 2016). No peak shift or new peaks could be found in the sample treated by Ar plasma, which implied that the Ar plasma treatment would not destroy the phase structure. The reason for this should be that the treatment only occurred on the surface and on a few destroyed atom layers, which would result in many surface defects like oxygen vacancies (Liu B. T. et al., 2018; Wu et al., 2018; Chen et al., 2020a). It was also found that there was little change on the diffraction peaks for the PANI coated samples, which should be due to the thinner

PANI shell coating on the serious SnO_2 samples. As the thickness of the PANI shell increased, the PANI peaks at 22.5° and 26.5° became much more obvious, as shown in **Figure 2B**. Obviously, these PANI shells encapsulate on the surface of SnO_2 and could efficiently protect the surface defects. SEM was carried out as shown in **Figure 3** for further research.

The SEM images of different SnO_2 -based samples were shown in **Figure 3**. Nanotube morphology, which was composited with many little grains, could be seen in the original SnO_2 as shown in **Figure 3a**. The diameter of the nanotube was about 60–80 nm. **Figure 3b** showed the sample with Ar plasma treatment;

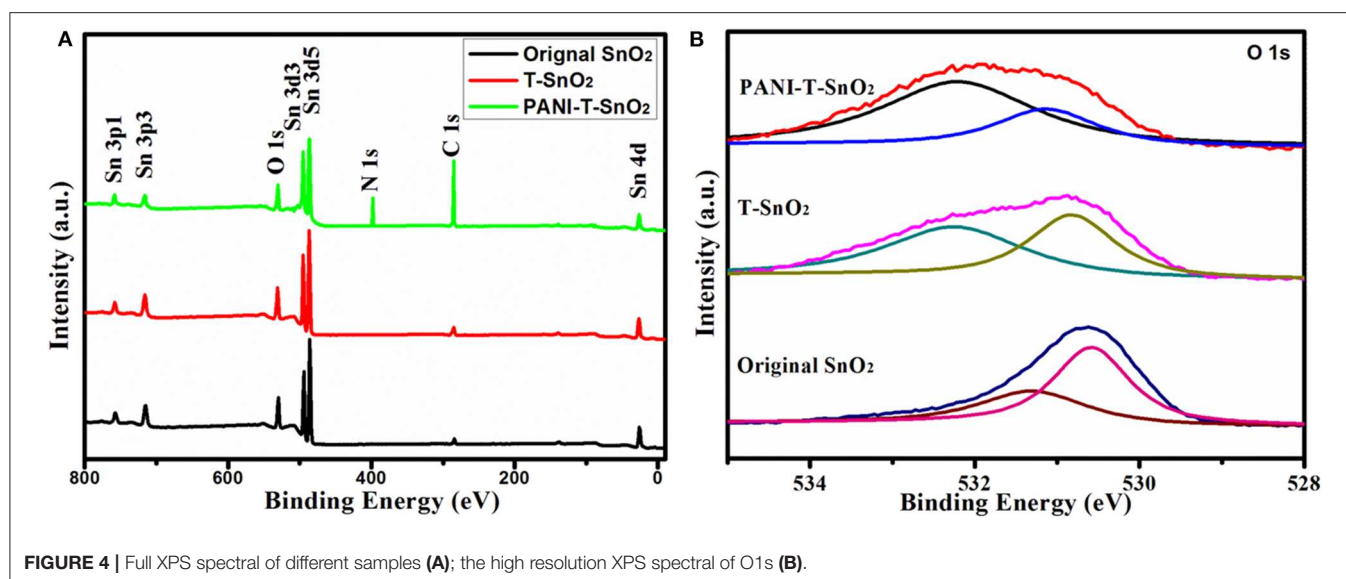


FIGURE 4 | Full XPS spectral of different samples (A); the high resolution XPS spectral of O 1s (B).

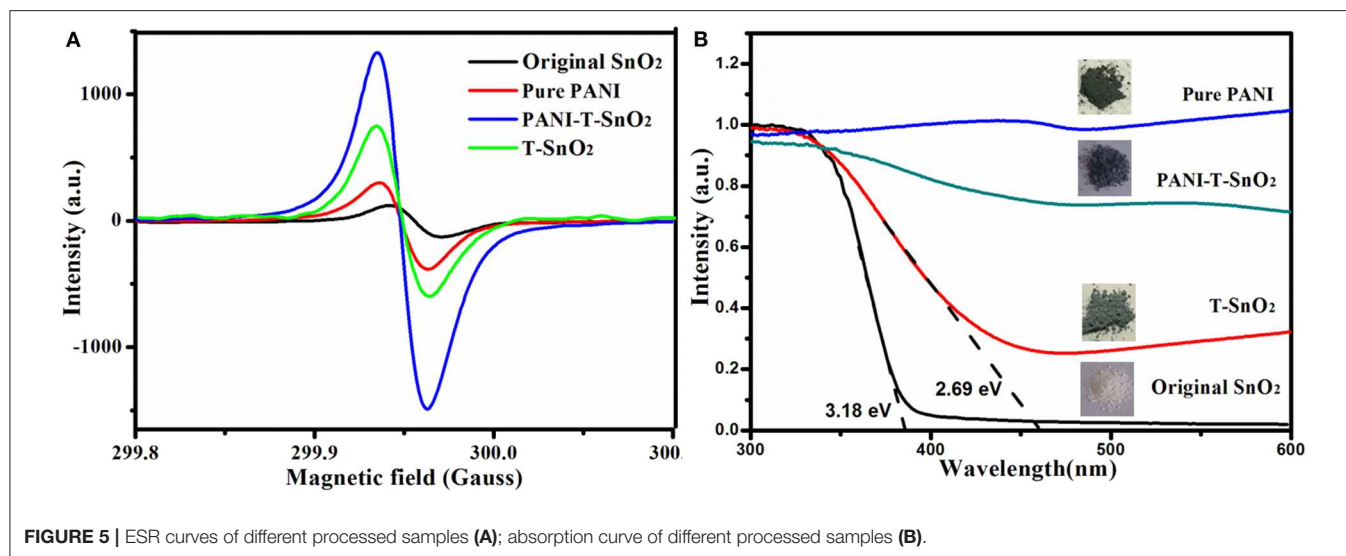


FIGURE 5 | ESR curves of different processed samples (A); absorption curve of different processed samples (B).

no change could be found in it. This was consistent with the XRD results in **Figure 2**, which showed that the plasma could not affect the SnO₂ crystalline structure. However, if the T-SnO₂ sample was coated with the PANI shell, as shown in **Figures 3c–f**, the surface would become rough and irregular as the diameter increased. Additionally, if too many PANI were shown in **Figure 3f**, the morphology of the nanotube could not be found. XPS tests were performed in **Figure 4** for detailed surface structure information.

The full XPS spectra of SnO₂, T-SnO₂, and PANI-T-SnO₂ were list in **Figure 4A**. All the samples were composed of Sn, O, and C. However, the C peak in PANI-T-SnO₂ was much higher than that in the other two uncoated samples, and there was also an N species peak, which implied that PANI is coated successfully. In addition, it was also found that the full XPS spectral of T-SnO₂ seems to be unrelated with the original SnO₂. For a deep

investigation, the oxygen vacancies were further investigated by the O 1s spectra in **Figure 4B**. It could be clearly seen that the binding energy at 530.63 and 531.25 eV in the original SnO₂ could represent the lattice oxygen in chemical groups Sn-O-Sn and adsorbed oxygen in Sn-OH and -OH, respectively (Li et al., 2016; Su and Yang, 2016). Compared with the original SnO₂, the absorbed oxygen in O 1s curve for T-SnO₂ and PANI-T-SnO₂ exhibited a significant drift from 531.25 to 532 eV, which indicated the existence of oxygen vacancies (Chen et al., 2020a). Meanwhile, this peak in T-SnO₂ was relatively lower than that in PANI-T-SnO₂, which meant that some surface oxygen vacancies obtained by Ar plasma treatment in T-SnO₂ would re-oxidate without any protective effect from the PANI shell. Obviously, it can be concluded that the PANI-T-SnO₂ has a higher ratio and stable oxygen vacancies, which is beneficial for sensor properties.

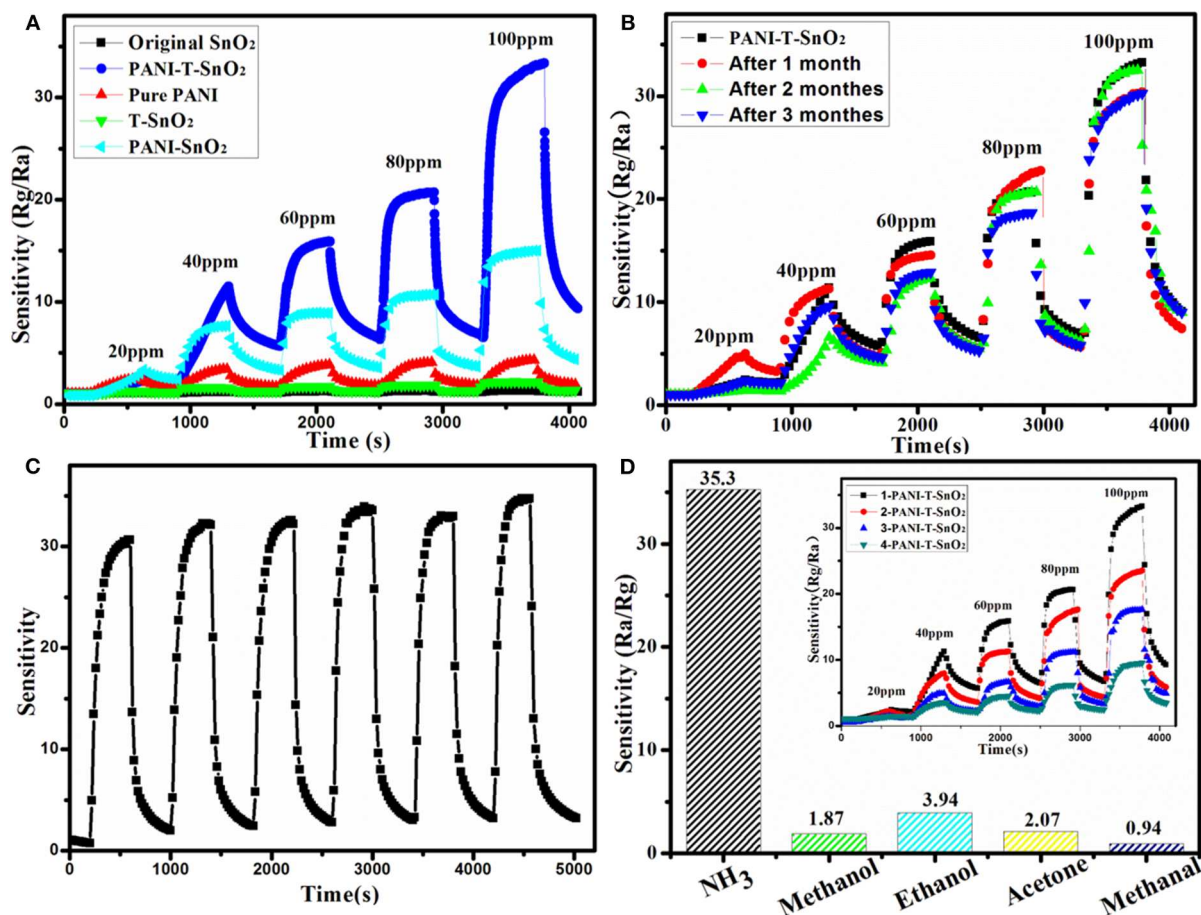


FIGURE 6 | Resistance variation in gas sensing tests of different samples (A), 3-months cycle stability test for PANI-T-SnO₂ (B), 100 ppm 6-time cycle test for PANI-T-SnO₂ (C), gas selectivity testing (D) (the inset is the gas sensing coated with different PANI layer).

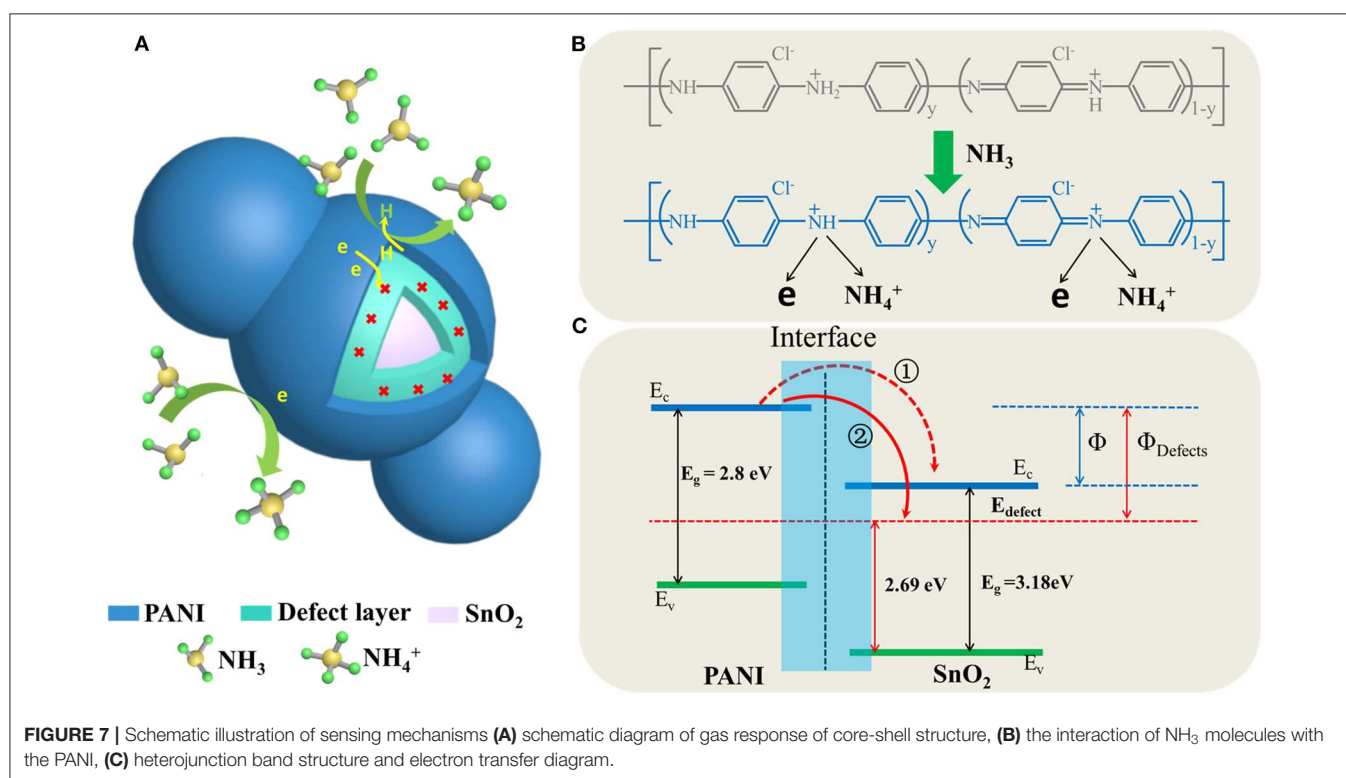
An ESR test was used for a further study of the surface oxygen vacancies. It is generally known that the peak intensity at around $g=2$ in ESR curves usually represents the concentration of the surface oxygen vacancies (Xu et al., 2016; Chen et al., 2020a). That is to say, the Ar plasma treatment can result in many oxygen vacancies in T-SnO₂, while the original SnO₂ only contains limited defects (Xu et al., 2016; Chen et al., 2020a). Surprisingly, when T-SnO₂ was coated with the PANI shell, the ESR signal of the surface oxygen vacancies was much higher than the uncoated samples. After considering that pure PANI only showed a weak signal, it could be concluded that this enhancement cannot be ascribed to the intrinsic properties of the coated PANI shell. The reason for this would be that the coated PANI shell can use air oxygen to protect the oxygen vacancies re-oxidization effectively. Of course, the relatively weak ESR signal in T-SnO₂ should be ascribed to the fact that the test was not conducted in time, causing the re-oxidizing process to suffer (Chen et al., 2020a). The oxygen vacancies structure was also performed by absorption spectral as shown in Figure 5B. As shown, the absorption edge of the original SnO₂ was 390 nm (3.18 eV), while it extended to 460 nm (2.69 eV) for T-SnO₂. It

is generally known that if the oxygen vacancies can broaden the absorption spectral, subsequently, the oxygen vacancies would affect its gas sensor properties (Wang et al., 2010; Xu et al., 2016; Cheng et al., 2017; Chen et al., 2020a), and for the sample coated PANI shell, the band gap would decrease further. This should be ascribed to the conductive properties of PANI, and implied that an effective hetero structure was constructed. It also showed that it can accelerate electron transfer during the sensing process (Chen et al., 2020a).

The whole gas sensing test was carried out at 25°C with a relative constant humidity of 50%. In order to evaluate the response properties of different samples more intuitively, the gas response curves were shown in Figure 6A. As it shows clearly, the original SnO₂ and T-SnO₂ have nearly no sensitivity toward NH₃ at room temperature and the pure PANI shows a relative lower sensitivity of about 4.5 at 100 ppm of NH₃. However, the synergistic effect of surface oxygen vacancies and PANI coating could be observed, which could significantly enhance the sensitive response as we expected in PANI-T-SnO₂. The result showed that the PANI-T-SnO₂ has a higher response at 35.3 of 100 ppm, which was 7.8 times higher than pure PANI, and also

TABLE 1 | Comparison of the performances of the sensor developed here and the other reported.

Material	Gas	Temperature (°C)	The formula of response	Response	Concentration(ppm)	Reference
Sb-doped SnO ₂	NH ₃	150	Rg/Ra	30	40 ppb	10.3
WO ₃ @SnO ₂	NH ₃	200	Rg/Ra	25	50	13
RGO@SnO ₂	NH ₃	RT	Rg/Ra	22	100	10
RGO@SnO ₂	NH ₃	RT	Rg/Ra	1.3	100	11
MWCNT@SnO ₂	NH ₃	RT	Rg/Ra	5	100	12
PANI	NH ₃	RT	(Z-Z ₀)/Z	0.7	10	20
PANI	NH ₃	RT	Rg/Ra	2.2	10	21
PANI	NH ₃	RT	(Rg-Ra)/Ra (%)	7.90%	10	22
SnO ₂ @PI	NH ₃	RT	Rg/Ra	33	100	18
SnO ₂ @PANI	NH ₃	RT	Rg/Ra	25	80	27
CeO ₂ @PANI	NH ₃	RT	(Rg-Ra)/Ra (%)	250%	50	29



better than most reported PANI-based materials as shown in **Table 1**. Obviously, the surface oxygen vacancies play the key role in the sensitive response that can rapidly separate and remove the surface electrons induced by the target gas (Chen et al., 2020a). An untreated sample coated with PANI was also listed for comparison; the response was about 15 at 100 ppm, which demonstrated our design concept that PANI can bring a room temperature response and the oxygen vacancies make it more sensitive, that is to say, that simply introducing surface defects or a coating of PANI it is not an efficient way to increase the gas sensor properties (Chen et al., 2020a). A 3-months multi-time stability gas response test and long cycle response performance

were respectively listed in **Figures 6B,C** to investigate the stability of surface oxygen vacancies protected by the outer PANI layer. It showed that there were only a few tiny fluctuations for the sensor response after 3 months or after being retested six times, and remains at more than 90% sensitive at 100 ppm. This result further confirmed the PANI shell can protect the inner oxygen vacancies well and bring a stable gas response. There was nearly no change in the long cycle response performance under a concentration of 100 ppm. The response remained in a stable level, which illustrated a better stability, as we expected. In addition, this PANI shell had a thin layer which can exhibit a better sensor process as shown in the inset. And as shown in

Figure 6D, there is substantially no response to the redox gas other than NH₃, which shows an excellent selectivity for the target gas.

The schematic diagram of the detailed gas sensor mechanism was shown in **Figure 7**. It can be seen that the PANI shell acted as a better recognition center for electrons sensitive to NH₃ since the SnO₂ nanotubes encapsulate with PANI, a heterojunction will be formed at their interface (Hu et al., 2002; Gumpu et al., 2014; Kumar et al., 2017; Chen et al., 2020a). If the PANI was active with HCl, it could efficiently generate more protons to gain conductive properties on the basis of a protonation reaction, as shown in **Figure 7B**. Thus, when it suffered a protonation reaction, it would form many more N⁺-H bonds, which would result in many positive centers, and then facilitate the free electrons in the valence band to move to these positive centers (Ikeda et al., 2012). The reaction process between the PANI shell and NH₃ molecules was shown in **Figure 7B**, this chemisorption process is reversible, as equation (1) shows:



The PANI shell would lose an H proton, and then recombine an electron from an H atom. With the reaction preceded, the electron generated by the PANI shell would gradually increase. Therefore, it would form a relatively high potential barrier, which would make the electron transfer more difficult, and then result in a lower response property. Thus, if the oxygen vacancies were introduced in the interface, it would recombine with the redundant electron, which could separate the generated electrons in PANI efficiently, and then accelerate the gas-sensitive reaction (Wang et al., 2017; Chen et al., 2020a). More importantly, the electron transfer ratio in Path 2 would be more efficient than

that in Path 1, as the energy potential difference between the introduced oxygen vacancies energy level and the conduction band (CB) of PANI was relatively high, as shown in **Figure 7C**. It would also lead to higher sensitivity properties (Qin and Ye, 2016; Chen et al., 2020a).

CONCLUSION

In conclusion, a PANI-T-SnO₂ nanotube with rich and stable surface oxygen vacancies was constructed. The result shows that the surface oxygen vacancies act as an efficient electron acceptor, and generates more protons in the coated PANI shell that react with the target NH₃. It was found that the gas response of NH₃ would be enhanced to 35.4 at 100 ppm at room temperature and concluded that the PANI shell can also protect the oxygen vacancies from re-oxidation, which results in a stable and enhanced NH₃ gas responsibility at room temperature. It can also lead to a stable response performance in multiple cycles of 3 months and multiple cycles.

AUTHOR CONTRIBUTIONS

All experimental work was performed by AJ under guidance of BL. HL, QL, and YY contributed to the analysis of the results and to the writing of the paper.

FUNDING

This work was funded by the project no. 2018YFD0501805, supported by National Key R&D Program of China. Funding for the project no. A201901046, was supported by the talent training project of Hebei province.

REFERENCES

- Bai, S. L., Tian, Y. L., Cui, M., Sun, J. H., Tian, Y., Luo, R. X., et al. (2018). Polyaniline@SnO₂ heterojunction loading on flexible PET thin film for detection of NH₃ at room temperature. *Sens. Actuators B* 226, 540–547. doi: 10.1016/j.snb.2015.12.007
- Chen, Y., Chen, D. L., Chen, J. F., Lu, Q. J., Zhang, M., Liu, B. T., et al. (2015). Facile synthesis of Bi nanoparticle modified TiO₂ with enhanced visible light photocatalytic activity. *J. Alloys Compounds* 651, 114–20. doi: 10.1016/j.jallcom.2015.08.119
- Chen, Y., Zhang, W., and Wu, Q. S. (2017). A highly sensitive room-temperature sensing material for NH₃: SnO₂-nanorods coupled by RGO. *Sens. Actuators B* 242, 1216–1226. doi: 10.1016/j.snb.2016.09.096
- Chen, Y. F., Li, C., Ma, X. L., Qiang, Q. P., Liu, B. T., Cao, S. X., et al. (2020a). Interface defect engineering induced drastic sensing performance enhancement of W18O₄₉@PANI nanowires for ammonia detection at room temperature. *Appl. Surface Sci.* 506:144816. doi: 10.1016/j.apsusc.2019.144816
- Chen, Y. F., Ma, X. L., Li, C., Wu, Q. Y., Wang, Y. B., Huang, M. J., et al. (2020b). Oxygen vacancies-contained SnO₂ nanotubes with enhanced ethanol gas sensing properties. *Int. J. Modern Phys. B* 34:2040003. doi: 10.1142/S0217979220400032
- Cheng, J., Yan, X. L., Mo, Q. H., Liu, B. T., Wang, J., Yang, X., et al. (2017). Facile synthesis of g-C₃N₄/BiVO₄ heterojunctions with enhanced visible light photocatalytic performance. *Ceram. Int.* 43, 301–307. doi: 10.1016/j.ceramint.2016.09.156
- Das, A., Bonu, V., Prasad, A. K., Panda, D., Dhara, S., and Tyagi, A. K. (2014). The role of SnO₂ quantum dots in improved CH₄ sensing at low temperature. *J. Mater. Chem. C* 2, 164–171. doi: 10.1039/C3TC31728E
- Gumpu, M. B., Nesakumar, N., Sethuraman, S., Krishnan, U. M., and Rayappan, J. B. (2014). Development of electrochemical biosensor with ceria-PANI core-shell nano-interface for the detection of histamine. *Sens. Actuators B* 199, 330–338. doi: 10.1016/j.snb.2014.04.009
- Hu, H., Trejo, M., Nicho, M. E., Saniger, J. M., and Garcia-Valenzuela, A. (2002). Adsorption kinetics of photochemical NH₃ gas sensing with semiconductor polyaniline films. *Sens. Actuators B* 82, 14–23. doi: 10.1016/S0925-4005(01)00984-4
- Ikeda, K., Takahashi, K., Masuda, T., Kobori, H., Kanehara, M., Teranishi, T., et al. (2012). Structural tuning of optical antenna properties for plasmonic enhancement of photocurrent generation on a molecular monolayer system. *J. Phys. Chem. C* 116, 20806–20811. doi: 10.1021/jp308290v
- Jia, L. N., Li, C., Zhao, Y. R., Liu, B. T., Cao, S. X., Mou, D. D., et al. (2019). Interfacial engineering of Mo₂C-Mo₃C₂ heteronanowires for high performance hydrogen evolution reaction. *Nanoscale* 11, 23318–23329. doi: 10.1039/C9NR08986A
- Kumar, L., Rawal, I., Kaur, A., and Annapoorani, S. (2017). Flexible room temperature ammonia sensor based on polyaniline. *Sens. Actuators B* 40, 408–416. doi: 10.1016/j.snb.2016.08.173
- Lee, J. H., Katoch, A., Choi, S. W., Kim, J. H., Kim, H. W., and Kim, S. S. (2015). Extraordinary improvement of gas-sensing performances in SnO₂ nanofibers due to creation of local p-n heterojunctions by loading reduced graphene oxide nanosheets. *ACS Appl. Mater. Interf.* 7, 3101–3109. doi: 10.1021/am5071656

- Li, H. Y., Lee, C. S., Kim, D. H., and Lee, J. H. (2018). Flexible room-temperature NH₃ sensor for ultrasensitive, selective, and humidity-independent gas detection. *ACS Appl. Mater. Interf.* 10, 27858–27867. doi: 10.1021/acsami.8b09169
- Li, Y., Ban, H. T., and Yang, M. J. (2016). Highly sensitive NH₃ gas sensors based on novel polypyrrole-coated SnO₂ nanosheet nanocomposites. *Sens. Actuators B* 224, 449–457. doi: 10.1016/j.snb.2015.10.078
- Liu, B. T., Mo, Q. H., Zhu, J. L., Zhupei H, Peng, L. L., Tu, Y. J., et al. (2016). Synthesis of Fe and N Co-doped Bi₂Ti₂O₇ nanofiber with enhanced photocatalytic activity under visible light irradiation. *Nanoscale Res. Lett.* 11:391. doi: 10.1186/s11671-016-1610-7
- Liu, B. T., Wang, S. W., Mo, Q. H., Peng, L. L., Cao, S. X., Wang, J., et al. (2018). Epitaxial MoS₂ nanosheets on nitrogen doped graphite foam as a 3D electrode for highly efficient electrochemical hydrogen evolution. *Electrochim. Acta* 292, 407–418. doi: 10.1016/j.electacta.2018.09.160
- Liu, B. T., Wu, C. R., Chen, G., Chen, W. B., Peng, L. L., Yao, Y. C., et al. (2019). All-in-one surface engineering strategy on nickel phosphide arrays towards a robust electrocatalyst for hydrogen evolution reaction. *J. Power Sources* 429, 46–54. doi: 10.1016/j.jpowsour.2019.04.119
- Liu, C. H., Tai, H. L., Zhang, P., Yuan, Z., Du, X. S., Xie, G. Z., et al. (2018). A high-performance flexible gas sensor based on self-assembled PANI-CeO₂ nanocomposite thin film for trace-level NH₃ detection at room temperature. *Sens. Actuators B* 261, 587–597. doi: 10.1016/j.snb.2017.12.022
- Lupan, O., Postica, V., Hoppe, M., Wolff, N., Polonskyi, O., Pauporté, T., et al. (2018). PdO/PdO₂ nanocluster-functionalized ZnO: Pd films for lower operating temperature hydrogen gas sensing. *Nanoscale* 10, 14107–14127. doi: 10.1039/C8NR03260B
- Nie, Q. X., Pang, Z. Y., Li, D. W., Zhou, H. M., Huang, F. L., Cai, Y. B., et al. (2018). Facile fabrication of flexible SiO₂/PANI nanofibers for ammonia gas sensing at room temperature. *Colloids Surf. A* 537, 523–539. doi: 10.1016/j.colsurfa.2017.10.065
- Pacchioni, G. (2003). Oxygen vacancy: the invisible agent on oxide surfaces. *ChemPhysChem* 4, 1041–1047. doi: 10.1002/cphc.200300835
- Qin, Y. X., and Ye, Z. H. (2016). DFT study on interaction of NO₂ with the vacancy-defected WO₃ nanowires for gas-sensing. *Sens. Actuators B* 222, 499–507. doi: 10.1016/j.snb.2015.08.040
- Santos, M. C., Hamdan, O. H. C., Valverde, S. A., Guerra, E. M., and Bianchi, R. F. (2019). Synthesis and characterization of V₂O₅/PANI thin films for application in amperometric ammonia gas sensors. *Organic Electron.* 65, 116–120. doi: 10.1016/j.orgel.2018.11.013
- Shin, M. K., Kim, Y. J., Kim, S. I., Kim, S. K., Lee, H., Spinks, G. M., et al. (2008). Enhanced conductivity of aligned PANi/PEO/MWNT nanofibers by electrospinning. *Sens. Actuators B* 134, 122–126. doi: 10.1016/j.snb.2008.04.021
- Singkammo, S., Wisitsoraat, A., Sriprachubwong, C., Tuantranont, A., Phanichphant, S., and Liewhiran, C. (2015). Electrolytically exfoliated graphene-loaded flame-made Ni-doped SnO₂ composite film for acetone sensing. *ACS Appl. Mater. Interf.* 7, 3077–3092. doi: 10.1021/acsami.5b00161
- Soni, S., Kumar, S., Dalela, B., Kumar, S., Alvie, P. A., and Dalel, S. (2018). Defects and oxygen vacancies tailored structural and optical properties in CeO₂ nanoparticles doped with Sm³⁺ cation. *J. Alloys Compounds* 752, 520–531. doi: 10.1016/j.jallcom.2018.04.157
- Su, P. G., and Yang, Y. L. (2016). NH₃ gas sensor based on Pd/SnO₂/RGO ternary composite operated at room-temperature. *Sens. Actuators B* 223, 202–208. doi: 10.1016/j.snb.2015.09.091
- Syrový, T., Kuberský, P., Sapurina, I., Pretl, S., Bober, P., Syrová, L., et al. (2016). Gravure-printed ammonia sensor based on organic polyaniline colloids. *Sens. Actuators B* 225, 510–516. doi: 10.1016/j.snb.2015.11.062
- Tang, N., Jiang, Y., Qu, H. M., and Duan, X. X. (2018). Graphene oxide-doped conducting polymer nanowires fabricated by soft lithography for gas sensing applications. *IEEE Sensors J.* 18, 7765–7771. doi: 10.1109/JSEN.2018.2833146
- Tang, N., Zhou, C., Xu, L. H., Jiang, Y., Qu, H. M., and Duan, X. X. (2019). A fully integrated wireless flexible ammonia sensor fabricated by soft nanolithography. *ACS Sensors* 4, 726–732. doi: 10.1021/acssensors.8b01690
- Timmer, B., Olthuis, W. W., and Berg, A. (2005). Ammonia sensors and their applications—a review. *Sens. Actuators B* 107, 666–677. doi: 10.1016/j.snb.2004.11.054
- Trani, F., Causà, M., and Lettieri, S. (2009). Role of surface oxygen vacancies in photoluminescence of tin dioxide nanobelts. *Microelectron. J.* 40, 236–238. doi: 10.1016/j.mejo.2008.07.060
- Tyagi, P., Sharma, A., Tomar, M., and Gupta, V. (2017). A comparative study of RGO-SnO₂ and MWCNT-SnO₂ nanocomposites based SO₂ gas sensors. *Sens. Actuators B* 248, 980–986. doi: 10.1016/j.snb.2017.02.147
- Wang, Y. D., Mu, Q. Y., Wang, G. F., and Zhou, Z. L. (2010). Sensing characterization to NH₃ of nanocrystalline Sb-doped SnO₂ synthesized by a nonaqueous sol-gel route. *Sens. Actuators B* 145, 847–853. doi: 10.1016/j.snb.2010.01.070
- Wang, Z. B., Wang, D., and Sun, J. (2017). Controlled synthesis of defect-rich ultrathin two-dimensional WO₃ nanosheets for NO₂ gas detection. *Sens. Actuators B* 245, 828–834. doi: 10.1016/j.snb.2017.02.038
- Wen, Y., Liu, B. T., Zeng, W., and Wang, Y. H. (2013). Plasmonic photocatalysis properties of Au nanoparticles precipitated anatase/rutile mixed TiO₂ nanotubes. *Nanoscale* 5, 9739–9746. doi: 10.1039/c3nr03024e
- Wu, C. R., Liu, B. T., Wang, J., Su, Y. Y., Yan, H. Q., Ng, C. T., et al. (2018). 3D structured Mo-doped Ni₃S₂ nanosheets as efficient dual-electrocatalyst for overall water splitting. *Appl. Surface Sci.* 441, 1024–33. doi: 10.1016/j.apsusc.2018.02.076
- Xu, L., Jiang, Q. Q., Xiao, Z. H., Li, X. Y., Huo, J., Wang, S. Y., and Dai, L. M. (2016). Plasma-engraved Co₃O₄ nanosheets with oxygen vacancies and high surface area for the oxygen evolution reaction. *Angew. Chem. Int. Edn.* 55, 5277–5281. doi: 10.1002/anie.201600687
- Yuan, K. P., Zhu, L. Y., Yang, J. H., Hang, C. Z., Tao, J. J., Ma, H. P., et al. (2020). Precise preparation of WO₃@SnO₂ core shell nanosheets for efficient NH₃ gas sensing. *J. Colloid Interf. Sci.* 568, 81–88. doi: 10.1016/j.jcis.2020.02.042

Conflict of Interest: The authors declare that the research was conducted in the absence of any commercial or financial relationships that could be construed as a potential conflict of interest.

The reviewer XY declared a shared affiliation, though no other collaboration, with the authors AJ, YY to the handling Editor.

Copyright © 2020 Jia, Liu, Li and Yun. This is an open-access article distributed under the terms of the Creative Commons Attribution License (CC BY). The use, distribution or reproduction in other forums is permitted, provided the original author(s) and the copyright owner(s) are credited and that the original publication in this journal is cited, in accordance with accepted academic practice. No use, distribution or reproduction is permitted which does not comply with these terms.



Anisotropic Thermal Expansion in an Anionic Framework Showing Guest-Dependent Phases

Zhu Zhuo^{1,2}, You-Gui Huang^{1,2*}, Krista S. Walton^{3*} and Osamu Sato^{4*}

¹ CAS Key Laboratory of Design and Assembly of Functional Nanostructures, and Fujian Provincial Key Laboratory of Nanomaterials, Fujian Institute of Research on the Structure of Matter, Chinese Academy of Sciences, Fuzhou, China,

² Xiamen Institute of Rare Earth Materials, Haixi Institutes, Chinese Academy of Sciences, Xiamen, China, ³ School of Chemical & Biomolecular Engineering, Georgia Institute of Technology, Atlanta, GA, United States, ⁴ Institute for Materials Chemistry and Engineering, Kyushu University, Fukuoka, Japan

OPEN ACCESS

Edited by:

Jiandong Pang,
Texas A&M University, United States

Reviewed by:

Kecai Xiong,
Jiangsu Normal University, China
Yanzhou Li,
Henan University, China

*Correspondence:

You-Gui Huang
yghuang@fjirsm.ac.cn
Krista S. Walton
krista.walton@chbe.gatech.edu
Osamu Sato
sato@cm.kyushu-u.ac.jp

Specialty section:

This article was submitted to
Nanoscience,
a section of the journal
Frontiers in Chemistry

Received: 31 January 2020

Accepted: 15 May 2020

Published: 18 June 2020

Citation:

Zhuo Z, Huang Y-G, Walton KS and
Sato O (2020) Anisotropic Thermal
Expansion in an Anionic Framework
Showing Guest-Dependent Phases.
Front. Chem. 8:506.
doi: 10.3389/fchem.2020.00506

Crystalline materials generally show small positive thermal expansion along all three crystallographic axes because of increasing anharmonic vibrational amplitudes between bonded atoms or ions pairs on heating. In very rare cases, structural peculiarities may give rise to negative, anomalously large or zero thermal expansion behaviors, which remain poorly understood. Host–guest composites may exhibit such anomalous behavior if guest motions controllable. Here we report an anionic framework of helical nanotubes comprising three parallel helical chains. The anisotropic interaction between the guest and the framework, results in anisotropic thermal expansion in this framework. A series of detailed structural determination at 50 K intervals enable process visualization at the molecular level and the observed guest-dependent phases of the framework strongly support our proposed mechanism.

Keywords: thermoresponsive, anisotropic, anionic framework, host–guest interaction, phase

INTRODUCTION

Actuators based on materials that reversibly change shape and/or size in response to external stimuli are highly desirable (Otsuka and Wayman, 1998; Yu et al., 2003). Photo-responsive materials, which enable remote operation without direct contact with the actuators, have attracted particular interest, some exceptional cases have also been shown (Kobatake et al., 2007; Kumpfer and Rowan, 2011). Most of these materials exploit the photo-isomerization of constituent molecules, which induces molecular motion and thereby deforms the bulk material (Kobatake et al., 2007; Nabetani et al., 2011; Yamaguchi et al., 2012). Thermal expansion also exemplifies the impact of external stimuli on material properties. Indeed, solid-state materials typically expand along all three crystallographic axes with increasing temperature (positive thermal expansion (PTE), $0 < \alpha < 20 \times 10^{-6} \text{ K}^{-1}$, where α is the axial thermal expansion coefficient), however a few materials show little response (zero thermal expansion (ZTE), $\alpha \approx 0 \text{ K}^{-1}$) or shrink (negative thermal expansion (NTE), $\alpha < 0 \text{ K}^{-1}$) along a specific crystallographic direction upon heating (Salvador et al., 2003; Goodwin et al., 2008; Long et al., 2009; Greve et al., 2010; Phillips et al., 2010; Azuma et al., 2011; Fortes et al., 2011; Yamada et al., 2011; Huang et al., 2013). Materials exhibiting ZTE or NTE are technologically useful in areas such as heat-engine components, structural engineering applications, and thermomechanical actuators or sensors, etc (Peter et al., 2011). Characteristic NTE-type materials include a small number of inorganic oxides and zeolites (Evans, 1999; Lightfoot et al., 2001), a family of cyanide coordination frameworks (Goodwin and Kepert, 2005;

Goodwin et al., 2005, 2008; Korčok et al., 2009) and some organic compounds (White and Choy, 1984; Birkedal et al., 2002; Das et al., 2010). Goodwin et al. have shown that $\text{Ag}_3[\text{Co}(\text{CN})_6]$ exhibits “colossal” positive and negative thermal expansion by flexing like lattice fence (Goodwin et al., 2008). Barbour et al. have reported that (S,S)-octa-3,5-diyn-2,7-diol displays exceptionally large positive and negative anisotropic thermal expansions because the molecules pack down on heating (Das et al., 2010). de Pedro et al. have observed colossal and highly anisotropic thermal expansion on several imidazolium salts (de Pedro et al., 2015). Very recently, some metal-organic frameworks (MOFs) have shown such anomalous thermal expansion behavior, which usually stems from a hinged movement around the metal center (Wu et al., 2008; Zhou et al., 2008; Miller et al., 2009; Yang et al., 2009; de Vries et al., 2011; Grobler et al., 2013; Shang et al., 2014; Pang et al., 2016). Elucidating the mechanisms governing this behavior becomes a fascinating subject because it offers information on new design principles for thermoresponsive materials. Host–guest composites may provide good examples of NTE-type materials and the mechanisms can easily be rationalized at the molecular level if guest motion can be visualized and controlled. The state of guest molecules confined in a host is expected to be readily modified under extra stimuli, which may drive the host to respond. For instance, Chen et al. have directly visualized the crystal deformation of a MOF triggered by guest rotation (Zhou et al., 2013). The challenge is rationally translating guest motion into crystal lattice deformation because the thermodynamic energy changes of these flexibilities usually differ significantly in magnitude. To address this issue, a flexible porous anionic framework with counter cations strongly confined by hydrogen bonds was designed. Sites interacting with the guest may perceive guest motions and properly transfer these local molecule motions into bulk mechanical response because of the flexibility of the confinement.

EXPERIMENTAL SECTION

Materials

All reagents, except H_4BPTC , were purchased from commercial sources and used without purification.

Synthesis

H_4BPTC : H_4BPTC was synthesized by a modified literature procedure (Lin et al., 2009). 3,3',5,5'-tetramethylbiphenyl (1.0 g, 0.0047 mol) was oxidized using KMnO_4 (6.5 g, 0.112 mol) in tert-butanol/water (v/v = 1:1; 50 mL) containing NaOH (0.4 g, 0.01 mol). Yield: 1.12 g 72.2%. Anal. Calcd (Found) for $\text{C}_{16}\text{O}_8\text{H}_{10}$: C, 58.19 (58.10); H, 3.05 (3.09) %.

$[\text{Me}_2\text{NH}_2] \cdot [\text{Mg}_2(\text{BPTC})(\text{NO}_3)(\text{H}_2\text{O})]$ (**1**) A mixture of $\text{Mg}(\text{NO}_3)_2 \cdot 6\text{H}_2\text{O}$ (0.052 g, 0.2 mmol), H_4BPTC (0.033 g, 0.1 mmol), 4,4'-azopyridine (0.018 g, 0.1 mmol) and HCl (1 mL 1 mol/L) in DMF (5 mL) was heated at 120°C in a sealed 20 mL glass vial for 1 day, and cooled to room temperature. Colorless needle crystals of compound **1** were filtrated, washed using methanol and air-dried (0.041 g, Yield: 80% based on Mg). Anal. Calcd (Found) for $\text{MgNC}_9\text{O}_6\text{H}_8$: C, 43.12 (43.03); H, 3.19 (3.11); N 5.59 (5.63) %.

$[\text{EtNH}_3] \cdot [\text{Mg}_2(\text{BPTC})(\text{NO}_3)(\text{H}_2\text{O})]$ (**2**) A mixture of $\text{Mg}(\text{NO}_3)_2 \cdot 6\text{H}_2\text{O}$ (0.052 g, 0.2 mmol), and H_4BPTC (0.033 g, 0.1 mmol) in NEF (5 mL) was heated at 120°C in a sealed 20 mL glass vial for one day, and cooled to room temperature. Colorless needle crystals of compound **2** were filtrated, washed using methanol, and air-dried (0.035 g, Yield: 70% based on Mg). Anal. Calcd (Found) for $\text{MgNC}_9\text{O}_6\text{H}_8$: C, 43.12 (43.06); H, 3.19 (3.09); N 5.59 (5.51) %.

Measurements

Elemental analyses were performed using a Vario EL elemental analyzer. IR (KBr pellet) spectra were recorded in the range of 400–4,000 cm^{-1} on a JASCO FT/IR-600 Plus spectrometer. Thermogravimetric analyses (TGA) were performed using a TG/DTA6300 system at a rate of 5°C/min under N_2 atmosphere. Powder X-ray diffraction (PXRD) patterns were acquired using a Rigaku 2100 diffractometer with $\text{Cu K}\alpha$ radiation in flat plate geometry. The temperature increased at a rate of 10°C/min and was held constant for 5 min at each targeted temperature before measurement.

Single-Crystal X-Ray Diffraction

Diffraction data were collected on a Rigaku-CCD diffractometer with $\text{Mo K}\alpha$ radiation. The temperature was changed at a rate of 10°C/min and was maintained at each targeted temperature for 5 min before measurement. Structures were solved by direct method and refined by full-matrix least-squares analysis on F^2 using the SHELX program. Hydrogen atoms were generated geometrically and refined in a riding model. For compound **1**, anisotropic thermal parameters were applied to all non-hydrogen atoms. Guest cations in compound **2** were isotropically refined. NO_3^- and guest cations in compound **1** as well as guest cations in compound **2** were restrained by several DFIX instructions. The occupancies of $\mu\text{-NO}_3^-$, $\mu\text{-H}_2\text{O}$ and guests in all structures were refined to be consistent with the results of elemental analyses.

RESULTS AND DISCUSSION

The solvothermal reaction of $\text{Mg}(\text{NO}_3)_2 \cdot 6\text{H}_2\text{O}$, biphenyl-3,3',5,5'-tetracarboxylic acid (H_4BPTC) and 4,4'-azopyridine (AZPY) in dimethylformamide (DMF) afforded $[\text{Me}_2\text{NH}_2] \cdot [\text{Mg}_2(\text{BPTC})(\text{NO}_3)(\text{H}_2\text{O})]$ (**1**) as colorless needle-shaped crystals. Single-crystal X-ray crystallography revealed that compound **1** consists of a three dimensional (3D) chiral anionic framework assembled from nanotubes comprising parallel triple helices. Charge neutrality is achieved by protonated dimethylamine cations $[\text{Me}_2\text{NH}_2]^+$, NO_3^- anions and H_2O molecules present a statistical distribution in the anionic framework (Figure S1). Therefore, the formula of compound **1** was determined by combining single-crystal X-ray crystallography, thermogravimetry (TG) and elemental analysis, results. Compound **1** crystallizes in the chiral orthorhombic space group $I2_12_12_1$ and the asymmetric unit contains a Mg^{2+} ion, half a BPTC^{4-} ligand, half a $\mu\text{-NO}_3^-$ anion and $\mu\text{-H}_2\text{O}$ in statistical distribution and half a $[\text{Me}_2\text{NH}_2]^+$ cation. Each Mg^{2+} ion is coordinated with six O atoms in an octahedral geometry, four of which from four different BPTC^{4-} ligands and the other

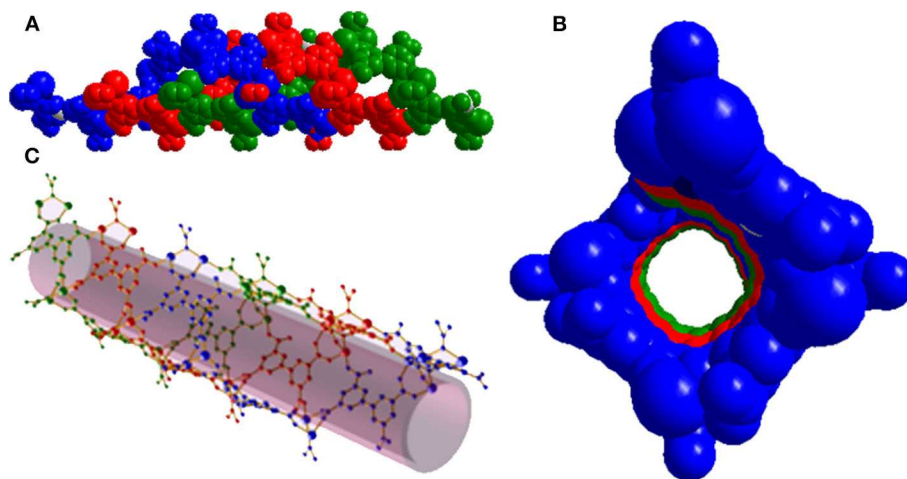


FIGURE 1 | (A) Side view of the helical nanotube of triple helices in compound **1**. (B) Top view of the helical nanotube. (C) Perspective view of the helical nanotube. Helices are differentiated by their colors (blue, red, and green).

two from two different $\mu\text{-NO}_3^-$ or $\mu\text{-H}_2\text{O}$ (Figure S2). All four carboxylate groups of BPTC^{4-} ligand adopt a $\mu_2\text{-}\eta_1\text{-}\eta_1$ bridging mode to ligate to two Mg^{2+} ions (Figure S3). Two Mg^{2+} ions are bridged by $\mu\text{-NO}_3^-$ or $\mu\text{-H}_2\text{O}$ to form $\{\text{Mg}\}_2$ dinuclear units which are further linked together by BPTC^{4-} ligands giving rise to a helical chain running along the crystallographic a axis (Figure S4). Three homochiral helices associate in parallel to generate the wall of a helical nanotube with an opening of about $11 \times 11 \text{ \AA}^2$ (Figure 1). As mentioned above, the Mg^{2+} ions favor a hexacoordinated environment, while five of these sites are dedicated to the nanotube, the remaining one provides an additional binding site for nanotube assembly into a 3D array. Specifically, each nanotube serves as a tertiary building unit and is further linked to its four adjacent neighbors to generate a 3D chiral anionic framework. The $[\text{Me}_2\text{NH}_2]^+$ cations stacking in helical template are confined in the nanotube strongly by hydrogen bond formation with a BPTC^{4-} ligand O atom in the framework (Figure S5). As a result, the channel is predominantly obstructed leaving an effective void volume of only $\sim 12.3\%$ as $[\text{Me}_2\text{NH}_2]^+$ cations could not be removed by simple activation.

Thermogravimetry and variable temperature powder X-ray diffraction (PXRD) showed that compound **1** can retain framework integrity up to 363 K before irreversibly changing to another unknown phase (Figures S1, S6, S7). The helical nanotube of compound **1** is orthorhombic, but slightly deviates from a tetragonal geometry. Its crystallographic b axis is $\sim 9\%$ shorter than its c axis at 123 K, which may be attributed to the anisotropic interaction between the guest and the framework. Figure 2 shows a structural representation of the helical chain that can be used to analyze the flexibility of compound **1**. Angles θ , ϕ , α , β , and γ (Figure 2) are key parameters in the nanotube flexibility. Because of the orthorhombic symmetry of the space group $I2_12_12_1$, b and c cell parameters can be expressed by simple trigonometric formulas involving the angle θ and the distance between MgB and MgC (d_1), or the angle ϕ and the distance

between MgD and MgE (d_2), respectively (Figure 2A). Therefore, $b = 2d_1 \sin \theta / 2$ and $c = 2d_2 \sin \phi / 2$. The guest $[\text{Me}_2\text{NH}_2]^+$ cation is attached to the ligand part which is directly related to the b cell parameter by hydrogen bonding. In contrast, no apparent interaction can be observed for the ligand part related to the c cell parameter. Consequently, this host-guest interaction is highly anisotropic, straining the ligands on the framework leading to the angle θ being smaller than the angle ϕ , and b smaller than c . The anisotropic host-guest interaction may be easily modified by heating, causing the angle θ to change. Two flexible sites exist in the helical nanotube of compound **1**: (i) the torsion angle between the two phenyl groups in BPTC^{4-} ligand has been shown to be variable (Suh et al., 2006), (ii) on the turning of the helical nanotube, the Mg-Mg axis of the $\{\text{Mg}\}_2$ dinuclear unit acts as a “knee cap,” around which the BPTC^{4-} ligands can change their angular orientations, allowing the moieties to rotate, like that observed in MIL-88 (Serre et al., 2007). These flexible features enable the angle ϕ to change oppositely with the angle θ . As a result, anisotropic thermal expansion may be anticipated in the nanotube of compound **1**.

To verify this hypothesis, temperature-dependent single-crystal X-ray diffraction experiments were performed on compound **1** from 123 K to 373 K at 50 K intervals. All lattice parameters change almost linearly with increasing temperature. Interestingly, b - and c -axes change by $+1.52\%$ and -0.52% over a 250 K temperature range, while the a -axis remains relatively unchanged (Figure 3A). Over the measured temperature range, the thermal expansion coefficients α_b and α_c for compound **1** amount to ca. $+76 \times 10^{-6} \text{ K}^{-1}$ and $-26 \times 10^{-6} \text{ K}^{-1}$, respectively. The large PTE along the b -axis is near an order of magnitude larger than conventional PTE (Krishnan et al., 1979) and comparable to the highest values reported for solid frameworks (Goodwin et al., 2008; de Vries et al., 2011; Grobler et al., 2013). Therefore, the thermal response of compound **1** is highly anisotropic, characterized by near zero expansion along

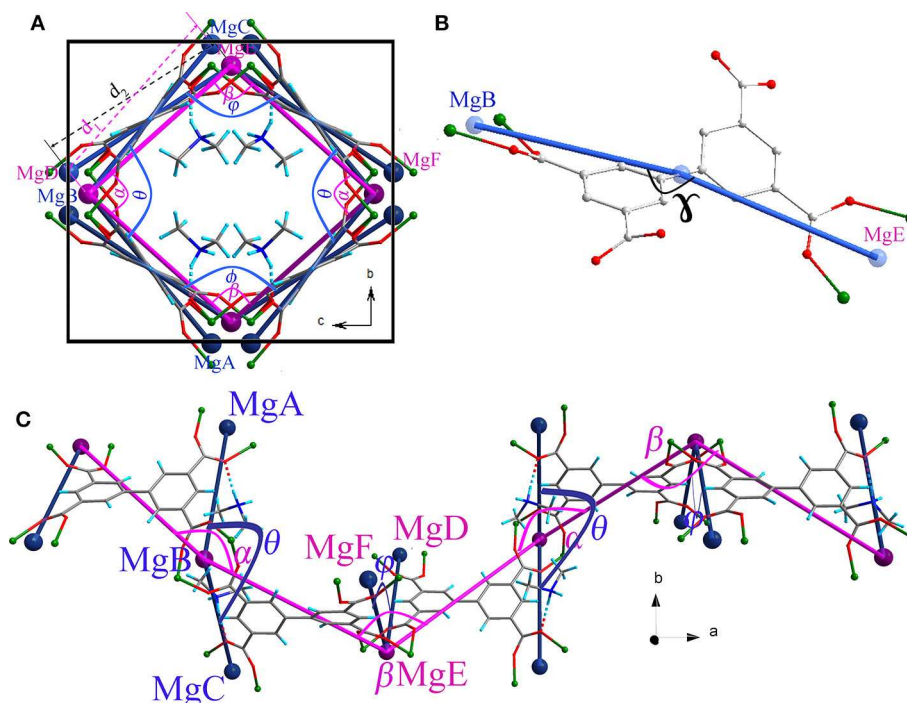


FIGURE 2 | Structure of the helical chain in compound **1** (A) viewed along the *a* axis (C) viewed along the *c* axis showing the hinge angle θ , ϕ , α , and β . (B) Structure of the ligand BPTC^{4-} showing the angle γ . (MgA, MgB, MgC, MgD, MgE, and MgF are simplified nodes located on the centers of $\{\text{Mg}\}_2$ dinuclear units.

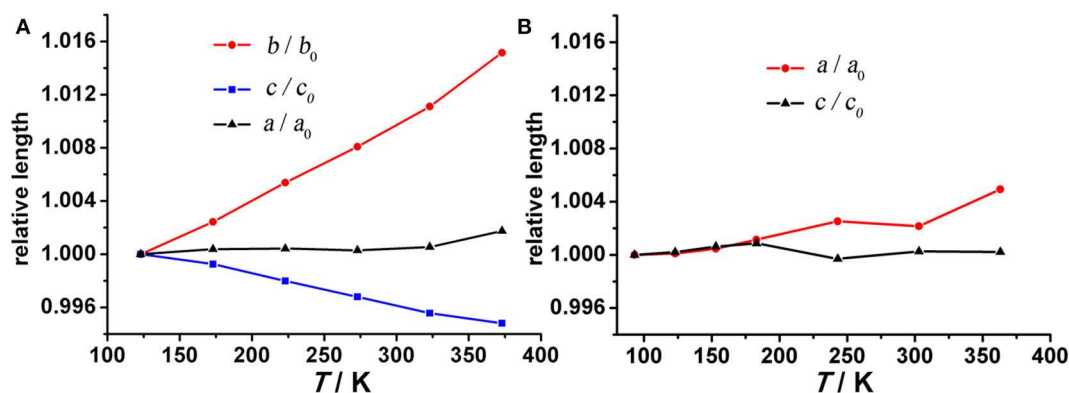


FIGURE 3 | Temperature dependent unit cell parameters for (A) compound **1** and (B) compound **2**. Due to the absolute value offset, all values are normalized to 123 and 93 K for compounds **1** and **2**, respectively.

the *a*-axis and large positive expansion along the *b*-axis coupled with negative expansion along the *c*-axis, leading to an overall volumetric expansion β_v of $+58 \times 10^{-6} \text{ K}^{-1}$ (Figure S8). In addition to this anisotropy, the thermal expansion behavior of compound **1** is highly desirable because its PTE/NET coefficients remain constant over wide temperature range which is beneficial for sensors and similar applications (Barrera et al., 2005; Zhou et al., 2013).

As anticipated, when the temperature rises from 123 to 373 K, the angle θ linearly increases from 100.47° to 102.18° whereas the angle ϕ linearly decreases from 113.95° to 112.64° (Figure 4A),

which may be attributed to the hydrogen bonding interaction being significantly weakened. From 123 to 323 K, the hydrogen bond length increases from 1.91 Å to 1.98 Å (Table S1). On the other hand, as mentioned above, the helical nanotube in compound **1** consists of three parallel helices. The significant structural transformation can be illustrated in Figure 2C either. On the turning of the helix, the hinge angles α , β change according to the same trend with θ and ϕ , respectively. When the temperature increases from 123 to 373 K, the angle α linearly increases from 115.65° to 116.48° whereas the angle β linearly decreases from 123.54° to 122.61° (Figure 4B), consequently, the

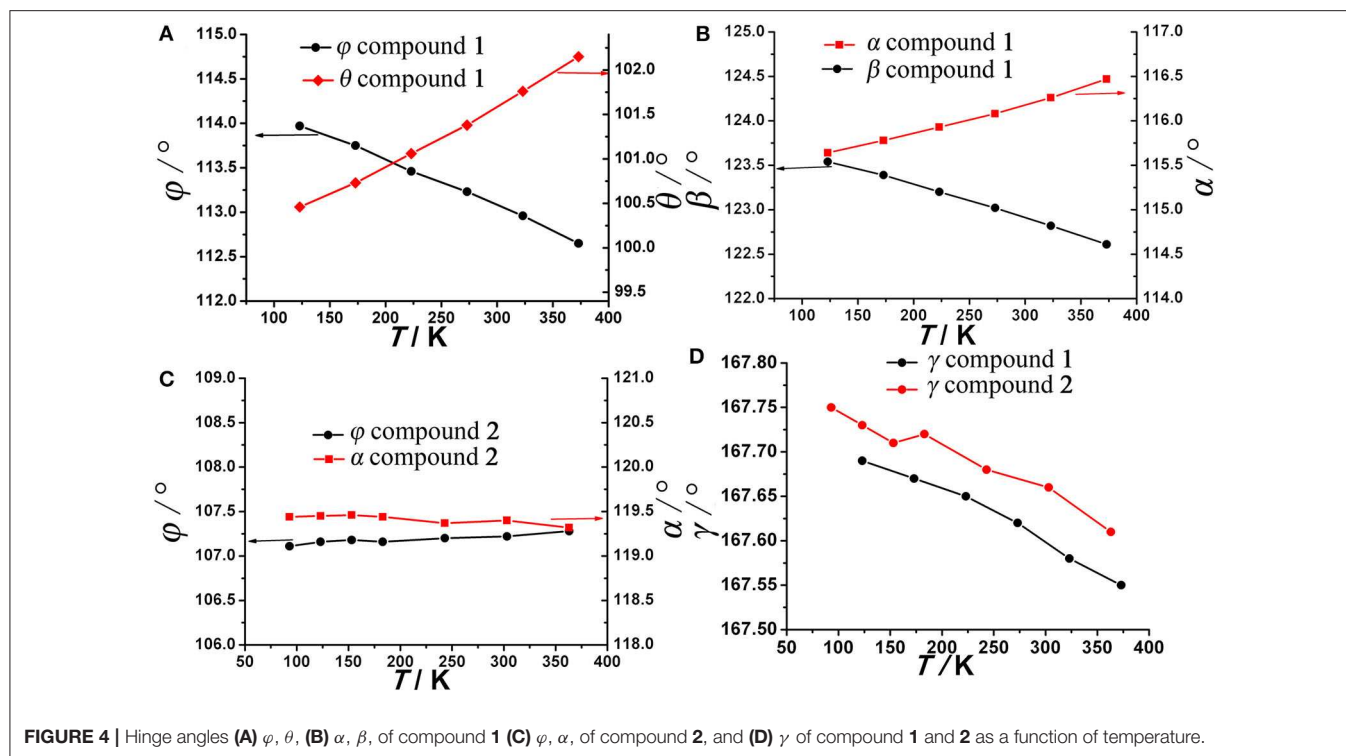


FIGURE 4 | Hinge angles (A) ϕ , θ , (B) α , β , of compound 1 (C) ϕ , α , of compound 2, and (D) γ of compound 1 and 2 as a function of temperature.

helical nanotube in compound **1** becomes more round on heating (Figure 5). Unexpectedly, the a -axis shows near zero thermal expansion rather than a conventional small positive expansion. Close examination of the helical nanotube revealed that the helical pitch corresponds to $3a$, i.e., the projection of distance between MgB and MgE along the a -axis is $0.75a$ (Figure 2B). The ZTE along the a -axis may result from the slight rotation of phenyl rings of BPTC⁴⁻ ligand. The angle γ displays a slight linear decrease from 167.69° to 167.55° , when the temperature rises from 123 to 373 K (Figure 4D), counteracting the increasing of anharmonic vibrational amplitudes. To test the reversibility of the hinged movement of compound **1**, the unit cell was determined from 123 K to 373 K and then back to 123 K, where it showed an almost complete return to the original cell (Table S2).

Because the anisotropic interaction between the guest and the framework play a key role in the orthorhombic phase formation and its anisotropic thermal expansion behavior, to the extreme, a tetragonal phase of the anionic framework exhibiting normal isotropic thermal expansion behavior can be expected in case of the interactions being isotropic or completely avoided. To confirm this hypothesis, we performed the similar reaction in N-Formylethylamine (NEF) and obtained the tetragonal phase of the anionic framework $[\text{EtNH}_3]^+[\text{Mg}_2(\text{BPTC})(\text{NO}_3)(\text{H}_2\text{O})]$ (**2**) with $[\text{EtNH}_3]^+$ cations confined in the tetragonal nanotube. Schröder et al. Hong et al., and Feng et al. have recently reported neutral frameworks with similar structure (Ibarra et al., 2011; Lin et al., 2011; Qian et al., 2012; Yang et al., 2012). In addition to $\mu\text{-H}_2\text{O}$, $\mu\text{-NO}_3^-$ was also incorporated giving rise to the anionic framework. The IR spectra of compounds **1** and **2** are shown in Figure S9, the strong absorption at 1,573 and around

$1,650\text{ cm}^{-1}$ for both compounds can be assigned to $\nu_{\text{C=O}}$ of BPTC⁴⁻. Temperature variable powder X-ray diffraction (PXRD) showed that compound **2** can retain framework integrity up to 443 K (Figure S10). In compound **2**, the $[\text{EtNH}_3]^+$ cations are confined in the center of the nanotube without notable hydrogen bond interaction with the entire framework, specifically, the nearest N...O distance between the guest and the framework is about 3.573 \AA too far for the formation of hydrogen bond. As a result the nanotubes in compound **2** are considerably more round than in compound **1** (Figure 6). On the turning of the nanotube, the hinge angle θ becomes the same as ϕ with a unique value of 107.18° , and the hinge angle α also becomes identical to β with a value of 119.46° at 93 K (Figure 4C). As expected, compound **2** shows no notable structural transformation and exhibits isotropic small positive thermal expansion behavior like common materials as revealed by temperature-dependent single-crystal X-ray diffraction experiments (Figure 3B). The thermal expansion coefficients $\alpha_{a,b}$ and α_c equal ca. $+18 \times 10^{-6}\text{ K}^{-1}$ and $+0.8 \times 10^{-6}\text{ K}^{-1}$, respectively, in the 93–363 K temperature range. Similarly to compound **1**, the near ZTE along the c axis is attributed to the slight rotation of the BPTC⁴⁻ phenyl rings with the angle γ slightly decreasing from 167.75° to 167.61° when the temperature rises from 93 to 363 K (Figure 4D). Compared to the significant heat induced change in hinge angles observed in compound **1**, the hinge angles θ and α remain almost constant in compound **2**, implying that its framework remains almost unchanged (Figure 4C). These results strongly support that the anisotropic thermal expansion in compound **1** is because of the highly anisotropic interaction between the guest and the framework.

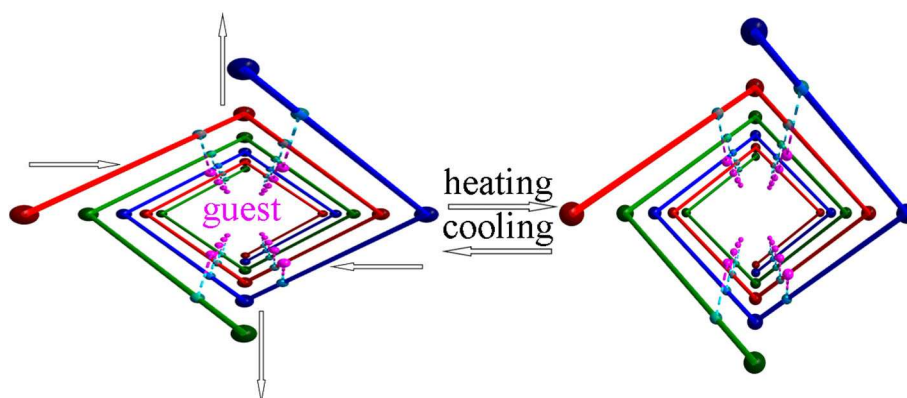


FIGURE 5 | Illustration showing heat induced hinged movements of the helical nanotube.

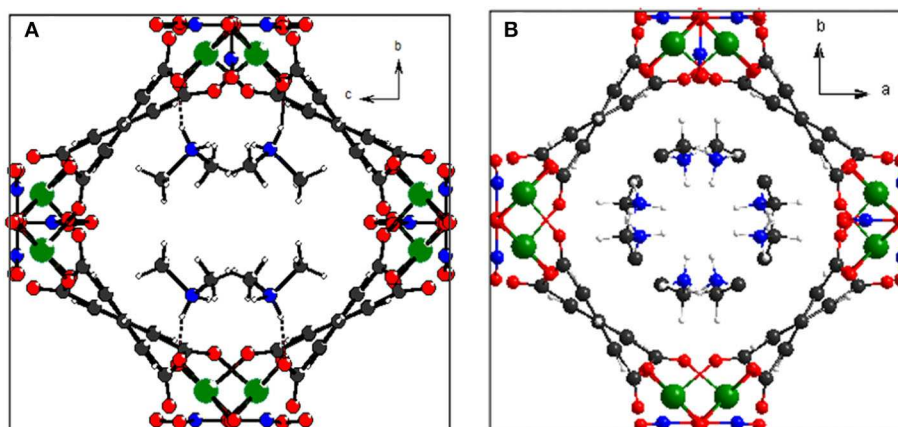


FIGURE 6 | Top view of the helical nanotube in compounds **1** (A) and **2** (B). Color code: Mg, green; C, gray; N, blue; O, red; H, white.

CONCLUSION

In conclusion, an anionic framework exhibiting guest dependent phases was designed. The anisotropic thermal expansion observed in the orthorhombic phase stems from the anisotropic hydrogen bonding between the guest and the framework. This is strongly supported by the observation of normal thermal expansion of the tetragonal phase in the absence of notable hydrogen bond interaction between guest and framework. This mechanism offers a new way to transfer guest motions to host in host–guest composites. A detailed understanding of the mechanisms governing this unusual thermal expansion behavior at the molecular level may provide key information on new design principles for sensitive thermo-mechanical actuators.

DATA AVAILABILITY STATEMENT

The X-ray crystallographic coordinates for structures reported in this article have been deposited at the Cambridge Crystallographic Data Centre (CCDC), under deposition numbers CCDC 1021857–1021862 for compound **1** and 1021863–1021869 for compound **2**. These data can be obtained

free of charge from the Cambridge Crystallographic Data Center via www.ccdc.cam.ac.uk/data_request/cif.

AUTHOR CONTRIBUTIONS

ZZ: synthesized the compounds and performed PXRD measurements. Y-GH: designed this study, conducted the experiments, and wrote the manuscript. KW: designed this study. OS: designed this study and wrote the manuscript. All authors read and approved the final manuscript version to be submitted.

FUNDING

This work was supported by the NSFC (21871262, 21805275, 21901242), and the Recruitment Program of Global Youth Experts.

SUPPLEMENTARY MATERIAL

The Supplementary Material for this article can be found online at: <https://www.frontiersin.org/articles/10.3389/fchem.2020.00506/full#supplementary-material>

REFERENCES

- Azuma, M., Chen, W. T., Seki, H., Czapski, M., Olga, S., Oka, K., et al. (2011). Colossal negative thermal expansion in BiNiO_3 induced by intermetallic charge transfer. *Nat. Commun.* 2:347. doi: 10.1038/ncomms1361
- Barrera, G. D., Bruno, J. A. O., Barron, T. H. K., and Allan, N. L. (2005). Negative thermal expansion. *J. Phys.-Condens. Mat.* 17, R217–R252. doi: 10.1088/0953-8984/17/4/R03
- Birkedal, H., Schwarzenbach, D., and Pattison, P. (2002). Observation of uniaxial negative thermal expansion in an organic crystal. *Angew. Chem. Int. Ed.* 41, 754–756. doi: 10.1002/1521-3773(20020301)41:5<754::AID-ANIE754>3.0.CO;2-R
- Das, D., Jacobs, T., and Barbour, L. J. (2010). Exceptionally large positive and negative anisotropic thermal expansion of an organic crystalline material. *Nat. Mater.* 9, 36–39. doi: 10.1038/NMAT2583
- de Pedro, I., García-Saiz, A., Dupont, J., Migowski, P., Vallcorba, O., Junquera, J., et al. (2015). On the colossal and highly anisotropic thermal expansion exhibited by imidazolium salts. *Cryst. Growth Des.* 15, 5207–5212. doi: 10.1021/acs.cgd.5b00633
- de Vries, L. D., Barron, P. M., Hurley, E. P., Hu, C., and Choe, W. (2011). “Nanoscale lattice fence” in a metal-organic framework: interplay between hinged topology and highly anisotropic thermal response. *J. Am. Chem. Soc.* 133, 14848–14851. doi: 10.1021/ja2032822
- Evans, J. S. O. (1999). Negative thermal expansion materials. *J. Chem. Soc. Dalton. Trans.* 3317–3326. doi: 10.1039/a904297k
- Fortes, A. D., Suard, E., and Knight, K. S. (2011). Negative linear compressibility and massive anisotropic thermal expansion in methanol monohydrate. *Science* 331, 742–746. doi: 10.1126/science.1198640
- Goodwin, A. L., Calleja, M., Conterio, M. J., Dove, M. T., Evans, J. S. O., Keen, D. A., et al. (2008). Colossal positive and negative thermal expansion in the framework material $\text{Ag}_3[\text{Co}(\text{CN})_6]$. *Science* 319, 794–797. doi: 10.1126/science.1151442
- Goodwin, A. L., Chapman, K. W., and Kepert, C. J. (2005). Guest-dependent negative thermal expansion in nanoporous prussian blue analogues ($\text{M}^{\text{IV}}\text{Pt}^{\text{II}}(\text{CN})_6 \cdot x[\text{H}_2\text{O}]$) ($0 \leq x \leq 2$; $\text{M} = \text{Zn}, \text{Cd}$). *J. Am. Chem. Soc.* 127, 17980–17981. doi: 10.1021/ja056460f
- Goodwin, A. L., and Kepert, C. J. (2005). Negative thermal expansion and low-frequency modes in cyanide-bridged framework materials. *Phys. Rev. B* 71:140301. doi: 10.1103/PhysRevB.71.140301
- Greve, B. K., Martin, K. L., Lee, P. L., Chupas, P. J., Chapman, K. W., Wilkinson, A. P., et al. (2010). Pronounced negative thermal expansion from a simple structure: cubic ScF_3 . *J. Am. Chem. Soc.* 132, 15496–15498. doi: 10.1021/ja106711v
- Grobler, I., Smith, V. J., Bhatt, P. M., Herbert, S. A., and Barbour, L. J. (2013). Tunable anisotropic thermal expansion of a porous zinc(II) metal-organic framework. *J. Am. Chem. Soc.* 135, 6411–6414. doi: 10.1021/ja401671p
- Huang, R. J., Liu, Y. Y., Fan, W., Tan, J., Xiao, F. R., Qian, L. H., et al. (2013). Giant negative thermal expansion in NaZn_{13} -type $\text{La}(\text{Fe}, \text{Si}, \text{Co})_{13}$ compounds. *J. Am. Chem. Soc.* 135, 11469–11472. doi: 10.1021/ja405161z
- Ibarra, I. A., Yang, S. H., Lin, X., Blake, A. J., Rizkalah, P. J., Nowell, H., et al. (2011). Highly porous and robust scandium-based metal-organic frameworks for hydrogen storage. *Chem. Commun.* 47, 8304–8306. doi: 10.1039/c1cc11168j
- Kobatake, S., Takami, S., Muto, H., Ishikawa, T., and Irie, M. (2007). Rapid and reversible shape changes of molecular crystals on photoirradiation. *Nature* 446, 778–781. doi: 10.1038/nature05669
- Korčok, J. L., Katz, M. J., and Leznoff, D. B. (2009). Impact of metalophilicity on “colossal” positive and negative thermal expansion in a series of isostructural dicyanometallate coordination polymers. *J. Am. Chem. Soc.* 131, 4866–4871. doi: 10.1021/ja809631r
- Krishnan, R. S., Srinivasan, R., and Devanarayanan, S. (1979). *Thermal Expansion of Crystals*. Pergamon: Oxford.
- Kumpfer, J. R., and Rowan, S. J. (2011). Thermo-, photo-, and chemo-responsive shape-memory properties from photo-cross-linked metallo-supramolecular polymers. *J. Am. Chem. Soc.* 133, 12866–12874. doi: 10.1021/ja205332w
- Lightfoot, P., Woodcock, D. A., Maple, M. J., Villaescusa, L. A., and Wright, P. A. (2001). The widespread occurrence of negative thermal expansion in zeolites. *J. Mater. Chem.* 11, 212–216. doi: 10.1039/b002950p
- Lin, Q. P., Wu, T., Zheng, S. T., Bu, X. H., and Feng, P. Y. (2011). A chiral tetragonal magnesium-carboxylate framework with nanotubular channels. *Chem. Commun.* 47, 11852–11854. doi: 10.1039/c1cc14836b
- Lin, X., Telepeni, I., Blake, A. J., Daily, A., Brown, C. M., Simmons, J. M., et al. (2009). High capacity hydrogen adsorption in $\text{Cu}(\text{II})$ tetracarboxylate framework materials: the role of pore size, ligand functionalization, and exposed metal sites. *J. Am. Chem. Soc.* 131, 2159–2171. doi: 10.1021/ja806624j
- Long, Y. W., Hayashi, N., Saito, T., Azuma, M., Muranaka, S., and Shimakawa, Y. (2009). Temperature-induced A-B intersite charge transfer in an A-site-ordered $\text{LaCu}_3\text{Fe}_4\text{O}_{12}$ perovskite. *Nature* 458, 60–63. doi: 10.1038/nature07816
- Miller, W., Smith, C. W., Mackenzie, D. S., and Evans, K. E. (2009). Negative thermal expansion: a review. *J. Mater. Sci.* 44, 5441–5451. doi: 10.1007/s10853-009-3692-4
- Nabetani, Y., Takamura, H., Hayasaka, Y., Shimada, T., Takagi, S., Tachibana, H., et al. (2011). A photoactivated artificial muscle model unit: reversible, photoinduced sliding of nanosheets. *J. Am. Chem. Soc.* 133, 17130–17133. doi: 10.1021/ja207278t
- Otsuka, K., and Wayman, C. M. (1998). *Shape Memory Materials*; Cambridge Univ. Press: Cambridge.
- Pang, J. D., Liu, C. P., Huang, Y. G., Wu, M. Y., Jiang, F. L., Yuan, D. Q., et al. (2016). Visualizing the dynamics of temperature- and solvent-responsive soft crystals. *Angew. Chem. Int. Ed.* 55, 7478–7482. doi: 10.1002/anie.201603030
- Peter, S. C., Chondroudi, M., Milliakas, C. D., Balasubramanian, M., and Kanatzidis, M. G. (2011). Anomalous thermal expansion in the square-net compounds RE_4TGe_8 ($\text{RE} = \text{Yb}, \text{Gd}$; $\text{T} = \text{Cr}-\text{Ni}, \text{Ag}$). *J. Am. Chem. Soc.* 133, 13840–13843. doi: 10.1021/ja204971n
- Phillips, A. E., Halder, G. J., Chapman, K. W., Goodwin, A. L., and Kepert, C. J. (2010). Zero thermal expansion in a flexible, stable framework: tetramethylammonium copper(I) zinc(II) cyanide. *J. Am. Chem. Soc.* 132, 10–11. doi: 10.1021/ja906895j
- Qian, J. J., Jiang, F. L., Yuan, D. Q., Wu, M. Y., Zhang, S. Q., Zhang, L. J., et al. (2012). Highly selective carbon dioxide adsorption in a water-stable indium-organic framework material. *Chem. Commun.* 48, 9696–9698. doi: 10.1039/c2cc35068h
- Salvador, J. R., Guo, F., Hogan, T., and Kanatzidis, M. G. (2003). Zero thermal expansion in YbGaGe due to an electronic valence transition. *Nature* 435, 702–705. doi: 10.1038/nature02011
- Serre, C., Mellot-Draznieks, C., Surble, S., Audebrand, N., Flinchuk, Y., and Férey, G. (2007). Role of solvent-host interactions that lead to very large swelling of hybrid frameworks. *Science* 315, 1828–1831. doi: 10.1126/science.1137975
- Shang, R., Xu, G. C., Wang, Z. M., and Gao, S. (2014). Phase transitions, prominent dielectric anomalies, and negative thermal expansion in three high thermally stable ammonium magnesium-formate frameworks. *Chem. Eur. J.* 20, 1146–1158. doi: 10.1002/chem.201303425
- Suh, M. P., Moon, H. R., Lee, E. Y., and Jang, S. Y. (2006). A redox-active two-dimensional coordination polymer: preparation of silver and gold nanoparticles and crystal dynamics on guest removal. *J. Am. Chem. Soc.* 128, 4710–4718. doi: 10.1021/ja056963l
- White, G. K., and Choy, C. L. (1984). Thermal-expansion and gruneisen parameters of isotropic and oriented polyethylene. *J. Polym. Sci. Polym. Phys. Ed.* 22, 835–846. doi: 10.1002/pol.1984.180220505
- Wu, Y., Kobayashi, A., Halder, G. J., Peterson, V. K., Chapman, K. W., Lock, N., et al. (2008). Synthesis, structure, and photophysical properties of highly substituted 8,8a-dihydrocyclopenta[a]indenes. *Angew. Chem. Int. Ed.* 47, 8929–8932. doi: 10.1002/anie.200802560
- Yamada, I., Tsuchida, K., Ohgushi, K., Hayashi, N., Kim, J., Tsuji, N., et al. (2011). Giant negative thermal expansion in the iron perovskite $\text{SrCu}_3\text{Fe}_4\text{O}_{12}$. *Angew. Chem. Int. Ed.* 50, 6579–6582. doi: 10.1002/anie.201102228
- Yamaguchi, H., Kobayashi, Y., Kobayashi, R., Takashima, Y., Hashidzume, A., and Harada, A. (2012). Photoswitchable gel assembly based on molecular recognition. *Nat. Commun.* 3:603. doi: 10.1038/ncomm31617
- Yang, C., Wang, X. P., and Omary, M. A. (2009). Crystallographic observation of dynamic gas adsorption sites and thermal expansion in a breathable fluorine metal-organic framework. *Angew. Chem. Int. Ed.* 48, 2500–2505. doi: 10.1002/anie.200804739

- Yang, S. H., Sun, J. L., Ramirez-Cuesta, A. J., Callear, S. K., David, W. I. F., Anderson, D. P., et al. (2012). A partially interpenetrated metal-organic framework for selective hysteretic sorption of carbon dioxide. *Nature Chem.* 4, 887–894. doi: 10.1038/NMA T3343
- Yu, Y., Nakano, M., and Ikeda, T. (2003). Directed bending of a polymer film by light - Miniaturizing a simple photomechanical system could expand its range of applications. *Nature* 425, 145–145. doi: 10.1038/425145a
- Zhou, H. L., Lin, R. B., He, C. T., Zhang, Y. B., Feng, N. D., Wang, Q., et al. (2013). Direct visualization of a guest-triggered crystal deformation based on a flexible ultramicroporous framework. *Nat. Commun.* 4:2534. doi: 10.1038/ncomms3534
- Zhou, W., Wu, H., Yildirim, T., Simpson, J. R., and Walker, A. R. H. (2008). Origin of the exceptional negative thermal expansion in metal-organic framework-5 $\text{Zn}_4\text{O}(\text{1,4-benzenedicarboxylate})(3)$. *Phys. Rev. B* 78:054114. doi: 10.1103/PhysRevB.78.054114
- Conflict of Interest:** The authors declare that the research was conducted in the absence of any commercial or financial relationships that could be construed as a potential conflict of interest.

Copyright © 2020 Zhuo, Huang, Walton and Sato. This is an open-access article distributed under the terms of the Creative Commons Attribution License (CC BY). The use, distribution or reproduction in other forums is permitted, provided the original author(s) and the copyright owner(s) are credited and that the original publication in this journal is cited, in accordance with accepted academic practice. No use, distribution or reproduction is permitted which does not comply with these terms.



Low-Dimension Nanomaterial-Based Sensing Matrices for Antibiotics Detection: A Mini Review

Yucan Dong^{1,2}, Fengting Li^{1,2} and Ying Wang^{1,2*}

¹ State Key Laboratory of Pollution Control and Resources Reuse, College of Environmental Science and Engineering, Tongji University, Shanghai, China, ² Shanghai Institute of Pollution Control and Ecological Security, Shanghai, China

OPEN ACCESS

Edited by:

Mingshui Yao,
Kyoto University, Japan

Reviewed by:

Liwei Wang,
Guangxi University, China
Xiaochuan Duan,
Xiamen University, China

*Correspondence:

Ying Wang
yingwang@tongji.edu.cn

Specialty section:

This article was submitted to
Nanoscience,
a section of the journal
Frontiers in Chemistry

Received: 10 February 2020

Accepted: 28 May 2020

Published: 24 July 2020

Citation:

Dong Y, Li F and Wang Y (2020)
Low-Dimension Nanomaterial-Based
Sensing Matrices for Antibiotics
Detection: A Mini Review.
Front. Chem. 8:551.
doi: 10.3389/fchem.2020.00551

Antibiotics, a kind of secondary metabolite with antipathogen effects as well as other properties, are produced by microorganisms (including bacterium, fungi, and actinomycetes) or higher animals and plants during their lives. Furthermore, as a chemical, an antibiotic can disturb the developmental functions of other living cells. Moreover, it is impossible to avoid its pervasion into all kinds of environmental media via all kinds of methods, and it thus correspondingly becomes a trigger for environmental risks. As described above, antibiotics are presently deemed as a new type of pollution, with their content in media (for example, water, or food) as the focus. Due to their special qualities, nanomaterials, the most promising sensing material, can be adopted to produce sensors with extraordinary detection performance and good stability that can be applied to detection in complicated materials. For low-dimensional (LD) nanomaterials, the quantum size effect, and dielectric confinement effect are particularly strong. Therefore, they are most commonly applied in the detection of antibiotics. This article focuses on the influence of LD nanomaterials on antibiotics detection, summarizes the application of LD nanomaterials in antibiotics detection and the theorem of sensors in all kinds of antibiotics detection, illustrates the approaches to optimizing the sensitivity of sensors, such as mixture and modification, and also discusses the trend of the application of LD nanomaterials in antibiotics detection.

Keywords: nanomaterials, antibiotics detection, low-dimension, fluorescent, electrochemical

INTRODUCTION

Since their discovery in 1929, antibiotics have been extensively adopted for many decades. At present, there is abundant research on the content of antibiotics in water bodies and food as well as the transportation, transformation, and degeneration patterns of antibiotics in nature. Although most antibiotics do not have long half-lives, they can be regarded as chronic organic pollutants due to their long-term and lasting use. Antibiotics are harmful to the human body as they can alter the microbial community inside it, disturb the human metabolism, and produce antibiotic-resistant genes and antibiotic-resistant bacteria in the environment (Kuemmerer, 2009; Ben et al., 2019). The concentration of antibiotics in wastewater ranges from a few ng to tens of thousands of μg . Nonetheless, antibiotics are rarely detected in other environmental media such as air, and the residue in soil mainly comes from irrigation (Mohammad-Razdari et al., 2019a).

At present, detection of the amount of antibiotics has already achieved a relatively low limit of quantitation. For example, by combining solid-phase extraction with liquid chromatography,

the quantitation limit can be taken to an order of magnitude lower than 10^{-12} M. However, the instrument mentioned above is bulky and difficult to operate (Netea et al., 2019). In terms of innovation, nanomaterials have four distinctive properties, namely their surface effect, quantum size effect, quantum tunnel effect, and dielectric confinement effect. LD materials have a high specific surface area, with quick electron conduction. Moreover, the high abundance of surface defects helps them to emit high-intensity fluorescence, which is an excellent characteristic for both the detector of the sensor and the signal sensing module (Coleman et al., 2006). Sensors produced with this kind of material are easy to operate, quick in detection, and highly sensitive, making them the primary direction of development in this field at present. This article summarizes work on the application of 0-, 1-, and 2-dimensional nanomaterials in antibiotics detection, respectively, explores the application mechanism of nanomaterials, and puts forward the development trend in this field.

THE ROLE OF NANOMATERIALS IN ANTIBIOTICS DETECTION

The concept of nanomaterials began with nanocrystalline research by Gleiter and Marquardt (1984), Gleiter (1989), Gleiter (2000), and since then, nanomaterials have gradually become a hot topic of research. Nanomaterials can be divided into 0-dimensional (0D), 1-dimensional (1D), 2-dimensional (2D), and 3-dimensional (3D) in terms of dimensional characteristics. Dimensions refer to the number of dimensions where the material is not within the size boundary of 0.1–100 nm. Because their dimensions and structures are different, the sensitivity of sensors made of different nanomaterials is different according to the surface effect and the properties of the dielectric region (Figure 1).

The types of nanomaterials adopted for the determination of antibiotics are as follows. Among them, 0D materials include nanoclusters (Zang et al., 2013), nanoparticles (Wu et al., 2018), and quantum dots (QDs) (Malik et al., 2019); the 1D materials include nanowires (Shad et al., 2019), nanotubes (Xiao et al., 2007), and nanorods (Roushani and Ghanbari, 2018); the 2D materials include nanoflakes (Zeng et al., 2018) and nanofilms (Velusamy et al., 2018).

There are two common types of antibiotic detection sensors at present. One is an electrochemical (EC) sensor (Liu et al., 2019), and the other is a fluorescence (FL) sensor (Peng et al., 2018). The common characteristics of these two types of sensors are fast response, convenient operation, portability, and a low limit of detection (LOD). An EC sensor reflects the concentration of the measured object with electrical signals, so nanomaterials are commonly used to promote conductivity. Nanomaterials are often adopted in an FL as fluorescent materials or as fluorescence quenching materials, such as carbon quantum dots (CQDs) (Chen et al., 2018). The details of the types, detection limits, and

measurement properties of nanomaterial sensors are given in Table 1.

In the next section, we will introduce the application of 0D, 1D, and 2D nanomaterials in the two types of sensors, FL and EC. We will then summarize and forecast the status and trends of research in related fields in the third section.

LD NANOMATERIAL-BASED SENSORS FOR ANTIBIOTICS DETECTION

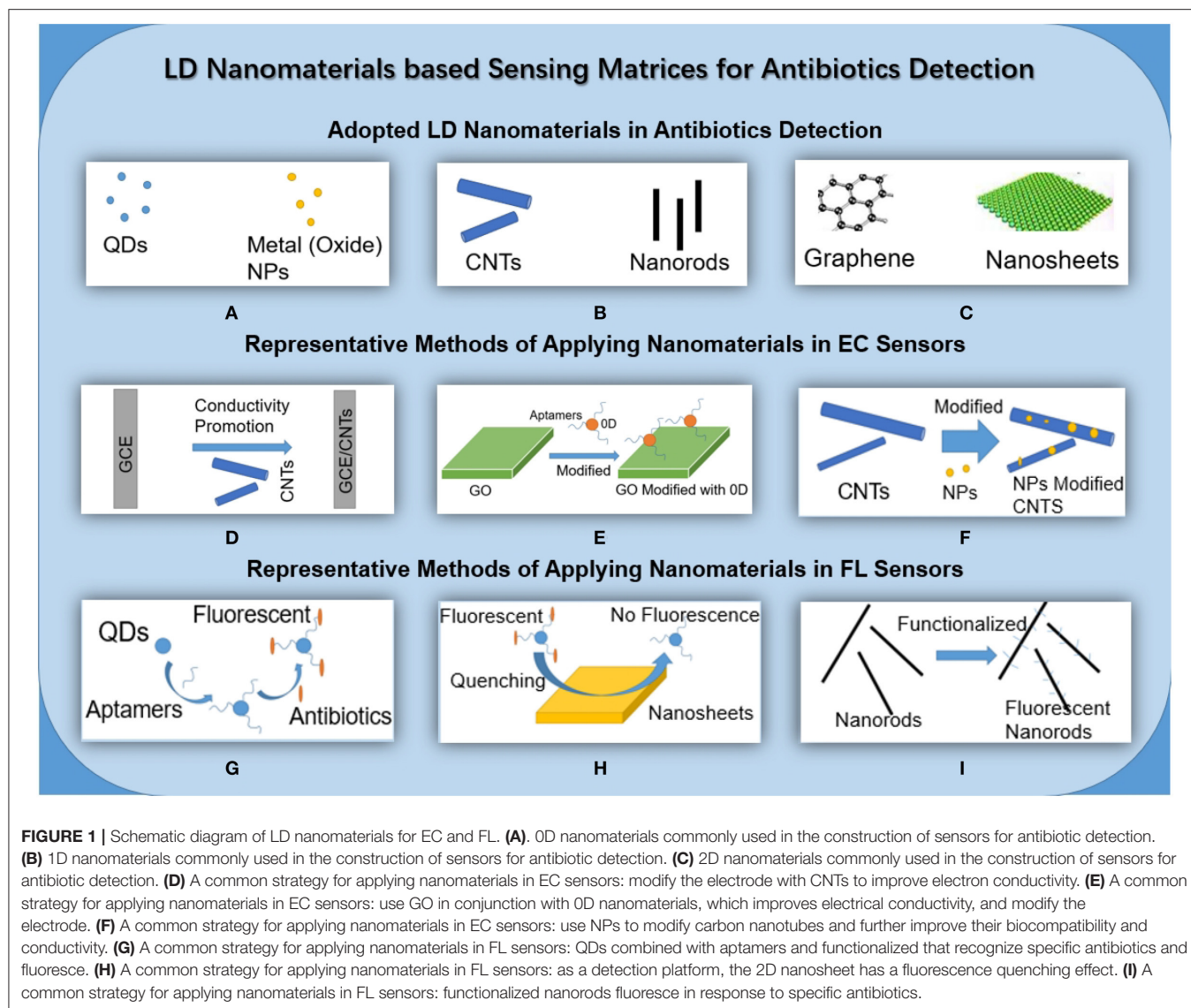
LD Nanomaterial-Based FL Sensors

FL sensors have high selectivity because the occurrence and quenching of fluorescence have specificity. Therefore, the use of FL sensors for the detection of antibiotics in complex media (such as milk, honey, etc.) has high research value, and it is one of the hot spots in the research field in recent years.

The most common 0D nanomaterials adopted in FL sensors are QDs (Liu et al., 2009). This is because of the long-term photostability, high-quantum yield, narrow emission, and broad excitation spectra of CdX QDs (Leptihn et al., 2010; Hou et al., 2011). QDs are generally composed of elements from groups III to V or II to IV in the periodic table of the elements (Zhang and Wei, 2016). QDs were applied as early as 2006. At that time, CdX (X = S, Se, etc.) QDs were mainly adopted (Qie Gen et al., 2007; Wang et al., 2009, 2010).

For example, Ding et al. adopted CdSe QDs and competitive fluorescence-linked immunosorbent assay (cFLISA) for the detection of sulfamethazine (Ding et al., 2006). QDs were applied as a fluorescence label in the cFLISA method. The combination of the cFLISA method and QDs has great specificity, so it can be used for the determination of antibiotic residues in chicken muscle. The LOD is as low as 3.6×10^{-9} M. In addition to QDs, other nanoparticles are also widely adopted in the design of antibiotic sensors. Berlina et al. integrated lateral flow assay with fluorescent labels, which provides the opportunity to achieve simple and sensitive control of milk contamination by chloramphenicol. This method also illustrates the high specificity of the combination of QDs and immunization methods. The LOD of chloramphenicol is 9.3×10^{-9} M (Berlina et al., 2013). NPs are also widely adopted in the design of antibiotic sensors. Mesoporous silica nanoparticles are an example of non-metal oxide nanoparticles that can be used (Wang C. et al., 2018). Wang et al. adopted aggregation-induced emission luminogens to functionalize silica nanoparticles. Because of the restricted intramolecular vibration and rotation in rigid silica networks, the material emitted strong blue fluorescence, which showed highly sensitive fluorescence-quenching responses toward nitrofurant antibiotics. The LOD of nitrofurazone reached 7.2×10^{-6} M.

1D nanomaterials have relatively few applications in the fluorescence detection of antibiotics. 1D nanomaterials like nanotubes or nanorods are more applied in EC sensors, which will be described in detail in the next section. Liu et al. developed a semiconductor of ZnO nanomaterials as a fluorescence sensor without leakage toxicity. ZnO nanomaterials have desirable optical and electronic properties, a large excitation binding energy of 60 meV, and a wide bandgap. Liu adopted molecular



imprinting polymer technology and ZnO nanomaterials to realize specific selectivity, high stability, and easy operation, which exhibited promising application in sensors (Liu et al., 2020).

Due to the superiority of 2D nanomaterials on the macro scale, they are easily adopted in sensing platforms. For example, Qin et al. made a fluorescent sensing platform for bleomycins by using WS₂ nanosheets. In the presence of Fe(II), bleomycin forms a BLM·Fe(II) complex that reacts with oxygen to generate a BLM·Fe(III)OOH species. BLM·Fe(III)OOH can catalyze the incision of DNA. WS₂ nanosheets exhibit different affinity toward single-stranded DNA (ssDNA) with different length and excellent fluorescence quenching ability. BLM catalyzes the incision of long ssDNA and restores fluorescence, Different fluorescence intensities correspond to different BLM concentrations. Using the above-described detection principle, the LOD of BLM is 3.0×10^{-10} M. Using rolling circle amplification to amplify the signal is an important factor in this

method, and using ssDNA as a signal has good biological activity (Qin et al., 2015).

According to the literature summarized above, the nanomaterials used in FL are mainly 0D and 2D. 0D materials like QDs are rich in surface defects and are easy to modify and synthesize. They will emit high-intensity fluorescence when they encounter specific substances, which has good application value for antibiotics detection in complex environments. Compared with CdX QDs, CQDs are less biotoxic and have better biocompatibility. 2D materials are more suitable for building platforms, as they have good fluorescence quenching performance.

LD Nanomaterial-Based EC Sensors

The characteristics of EC sensors are that they are fast, low-cost, high-sensitivity, and relatively portable, and they have hence been one of the development directions in environmental pollutant detection in recent years. In this part, we will mainly introduce

TABLE 1 | Characteristics of the different nanomaterials applied.

Type	Nanomaterials	Role of nanomaterial	Analyte	References
FL	0D CdSe–ZnS QDs	Sensitivity enhancement	Sulfamethazine	Ding et al., 2006
EC	1D MWCNTs	Sensitivity, selectivity enhancement	Oxytetracycline	Vega et al., 2007
EC	0D/1D AuNPs/SWCNTs	Sensitivity and stability enhancement	Chloramphenicol	Xiao et al., 2007
FL	0D CdSe–ZnS QDs	Sensitivity enhancement	Enrofloxacin	Chen et al., 2009
FL	0D CdTe QDs	Sensitivity enhancement	Etimicin	Wang et al., 2010
EC	2D GOs	Sensitivity and stability enhancement	Alpha fetoprotein	Wei et al., 2010
EC	0D/1D AuNCs/AuNRs	Selectivity enhancement	Ofloxacin	Zang et al., 2013
EC	1D/2D MWCNTs/GOs	Simplicity, stability enhancement	Azithromycin	Zhang et al., 2013
EC	2D CuO nanosheets	Sensitivity enhancement	Vancomycin	Khataee et al., 2014
EC	2D rGO nanosheet	Sensitivity enhancement	Rifampicin	Rastgar and Shahrokhian, 2014
EC	0D gold@silver nanoparticles	Sensitivity enhancement	Kanamycin	Zengin et al., 2014
FL	2D WS ₂ nanosheet	Selectivity and sensitivity enhancement	Bleomycin	Qin et al., 2015
EC	1D/2D MWCNTs/MoS ₂ nanosheets	Reproducibility and stability enhancement	Chloramphenicol	Govindasamy et al., 2017
EC	0D AuNPs	Sensitivities and specificity	Chloramphenicol	Huang et al., 2018
FL	0D CdTe QDs	Sensitivity enhancement	Sulfadiazine	Chen et al., 2018
EC	0D/2D g-C ₃ N ₄ QDs/rGOs	Sensitivity enhancement	Sulfadimethoxine	Dang et al., 2018
EC	2D graphene	Stability and repeatability enhancement	Erythromycin	Huang et al., 2018
EC	0D Silver NPs	Speed and sensitivity enhancement	Ampicillin	Rosati et al., 2019
EC	0D CdS QDs	Selectivity and sensitivity enhancement	Chloramphenicol	Wang Y. et al., 2018
FL	0D g-C ₃ N ₄ QDs	Sensitivity enhancement	Amikacin	Hassanzadeh et al., 2019
EC	0D/1D AuNPs/MWCNTs	Sensitivity enhancement	Oxytetracycline	He et al., 2019
EC	0D/2D AuNPs/GOs	Speed and sensitivity enhancement	Penicillin	Mohammad-Razdari et al., 2019b
EC	0D/2D AuNPs/rGOs	Reproducibility and selectivity enhancement	Sulfadimethoxine	Mohammad-Razdari et al., 2019a

FL, fluorescence sensor; EC, electrochemical sensor; QDs, quantum dots; CNTs, carbon nanotubes; MWCNTs, multi-walled carbon nanotubes; SWCNTs, single-walled nanotubes; GOs, graphene oxides; AuNCs, gold nanoclusters; AuNPs, gold nanoparticles; AuNRs, gold nanorods; rGOs, redox graphene oxides.

the ways in which 0D, 1D, and 2D nanomaterials are used to improve the performance of EC sensors.

For 0D materials, QDs can be taken as an example. QDs can be used as stabilizers (Xu et al., 2018). Besides being adopted as stabilizers, Dang et al. adopted g-C₃N₄ QDs modified with redox graphene oxides (rGOs) in photoelectric sensors to measure sulfadimethoxine (SDM). g-C₃N₄ QDs possess good optical and electrical properties as compared to other carbon-based QDs (Dang et al., 2018). Due to their lower intrinsic conductivity, they need to be modified with materials with high conductivity and hydrophilic ability for better performance in the detection of antibiotics. By modifying g-C₃N₄ QDs with rGOs, a linear calibration range for SDM of 5.0×10^{-10} M– 1.4×10^{-15} M was obtained, with a LOD of 1.0×10^{-10} M.

1D materials perform well in EC sensors. The general method of applying 1D nanomaterials in antibiotics sensing is through electrode surface modifications (Vega et al., 2007). Zhang et al. combined the hydrophilic properties of rGOs and the excellent electronic and antifouling properties of multi-walled carbon nanotubes (MWCNTs) for azithromycin detection. Compared with a bare glassy carbon electrode (GCE), the GCE modified with MWCNTs has a larger active surface area. The LOD of tetracyclines in a water sample was 1.1×10^{-9} – 6×10^{-9} M under pre-concentration (Zhang et al., 2013). P-type semiconductor-based transition metal oxide nanoparticles have received much attention due to their

excellent physicochemical properties, which make them suitable for catalysis, energy storage, and electrochemical conversion applications. The integration of metal oxides and their synergistic effects enhance selectivity and activity. Chen et al. synthesized a CuO NPs@MWCNTs nanocomposite (Chen et al., 2019). AuNPs have also been introduced to anchor on MWCNTs, not only providing a large number of biological binding sites but also effectively improving the electron transfer rate (He et al., 2019).

In terms of cost or difficulty of preparation, carbon nanotubes are excellent choices, but nanorods and nanowires also have unique properties due to their morphologies. Nanowires can be easily synthesized to achieve a multisegment structure, which will enable the nanowire to be used for multifunctional applications, especially as high sensitivity, multitasking electrochemical biosensors (Li et al., 2019). Nanorods have a relatively small specific surface area but also have excellent electronic conductivity and are more stable.

0D, 1D, and 2D nanomaterials are used to improve the performance of electrochemical sensors. Herein, by viewing the reported studies, it can be seen that combinations of 0D (such as NPs) and 2D (rGOs) nanoparticles have attracted a lot of attention in this research field. Mohammad et al. fabricated an electrochemical aptamer-based biosensor on a pencil graphite electrode (PGE). The bare PGE was modified with rGOs and AuNPs for SDM determination. This optimizes the linear

range of the electrode as well as stability and reproducibility (Mohammad-Razdari et al., 2019b).

CONCLUSION AND OUTLOOK

Supplementary Notes on Methods of Applying LD Nanomaterials in Antibiotic Detection

For 0D materials, QDs are often used as fluorophores with excellent performance, and metal or metal oxide nanoparticles are often used to modify other materials to further improve electronic conductivity. For 1D materials, nanotubes, nanowires, and nanorods are often used to enhance sensor performance, or to form microelectrode arrays; 2D materials, meanwhile, are more convenient for constructing platforms (Wang et al., 2017; He and Yan, 2018). Sensitivity is usually enhanced by means of signal amplification and enhancement (Wei et al., 2010). In order to improve the performance of the sensor, combination of nanomaterials in various dimensions is a very common method, such as using AuNPs to modify rGOs to improve the electronic conductivity of the sensor, which promotes the stability and sensitivity of the sensor. Good electron transfer capabilities and conductivity can also promote selectivity (Munawar et al., 2018).

When designing sensors, fluorescence immunoassay (FIA) is one of the promising technologies for antibiotics detection based on LD nanomaterials. In order to cope with complex environments, the sensors need to have good selectivity (Govindasamy et al., 2017). For example, FIA, a type of immunoassay, has two models: competitive type and sandwich type. The competitive type refers to a competitive mechanism that enables unlabeled antigens to compete with labeled antigens by binding to a limited antibody. For the competitive type, unlabeled antigens, and labeled antigens compete with antibodies that are bound to QDs. The fluorescence intensity varies with different antigen concentrations (Chen et al., 2009; Zhu et al., 2011).

For the sandwich type, the reaction principle is illustrated as follows. An excess of antibody is fixed on the immune reaction carrier, and subsequently, a certain amount of antigen is added. After the immune reaction, an excess of labeled antibody is added to form a “sandwich” immune complex. The more antigens in the sample and the more labeled antibodies bound, the stronger the labeled fluorescent signal of the sandwich immune complex is. Zengin et al. adopted this method and made a sensor on the basis of gold and silver nanoparticles. Accordingly, the LOD of kanamycin can reach 3.4×10^{-12} M (Zengin et al., 2014).

This method can be adopted in high-precision detection of antibiotics in complex media; such applications have been introduced above in the 0D section.

Summary and Outlook

Due to their different morphologies and dimensions, different nanomaterials have different beneficial properties.

The development of antibiotics sensors in the next few years can be roughly divided into the following directions: the pursuit

of high-sensitivity detection, the pursuit of low-cost and fast on-site detection, and the pursuit of multi-functional integration. Among them, the gradual realization of low-cost and rapid monitoring should be the most noteworthy, and this fits with the advantages of EC. According to the 57 articles cited in this article, we concluded that, in FL, 0D is currently used most, followed by 2D, and 1D is used least. 0D is represented by various types of QDs that can be used as fluorophores. In EC, 1D is the most used type, and 2D and 0D are used relatively little. In the future, researchers who want to improve FL performance can pay more attention to new quantum dots and NPs, and researchers who want to improve EC performance can pay more attention to materials with good electron conduction properties such as CNTs. At the same time, the performance improvement brought about by NP modification of other nanomaterials should also be considered. Finally, when the wish is to build a platform, 2D materials have advantages in terms of morphology. At present, there are few related studies, and in the coming decades, these may be hot research topics (Rastgar and Shahrokhian, 2014; Kokulnathan and Chen, 2020; Liu et al., 2020; Roushani et al., 2020).

In order to further optimize the performance of antibiotics sensors based on LD nanomaterials, the following suggestions are proposed according to the application status:

1. Fluorescence immunoassay method can be better applied to the detection of low levels of antibiotics in complex media, such as chicken muscle, milk, and honey. This is because quantum dots can be well combined with antibody immunoassay. This method has great specificity, lower LOD, and good biocompatibility. In order to achieve specific functions for various antibiotics, different immunoassays combined with QDs need to be designed.
2. Pay attention to the portability, fastness of measurement, and cooperation with smart devices (Tian et al., 2015). Taking the research by Yu et al. As an example, the electrodes were printed by screen printing technology to achieve rapid response measurement within 30 s (Yu et al., 2019). The research of Wang et al. in 2020 realized online monitoring through the color selection application of the mobile phone and the fluorescence reaction. These studies have good application value.
3. Build a platform that can detect multiple antibiotics at the same time. The platformization of the sensor depends on 2D nanomaterials or MOF. MOF is often used in combination with metal nanoparticles to obtain better performance. To achieve the simultaneous measurement of multiple antibiotics, microarray electrode technology can achieve this complex function.
4. In addition to the combination with MOF, the combination of NPs and other materials can also achieve better performance, which is a breakthrough direction for high-precision research.

AUTHOR CONTRIBUTIONS

YW and FL supervised this work. YW established the conceptualization of this work and acquired the funding. YD did

research on methodology, collected the data, edited, and wrote this review. All of the authors read and approved the manuscript.

FUNDING

This work was supported by the National Natural Science Foundation of China (NSFC, Nos. 21876132

and 21577100), the National Program for Support of Top-Notch Young Professionals, Shanghai Rising-Star Program (18QA1404300), the Fundamental Research Funds for the Central Universities (22120180102), and Young Excellent Talents in Tongji University (2015KJ001), Science and Technology Commission of Shanghai Municipality (18DZ1204400).

REFERENCES

- Ben, Y., Fu, C., Hu, M., Liu, L., Wong, M. H., and Zheng, C. (2019). Human health risk assessment of antibiotic resistance associated with antibiotic residues in the environment: a review. *Environ. Res.* 169, 483–493. doi: 10.1016/j.envres.2018.11.040
- Berlina, A. N., Taranova, N. A., Zherdev, A. V., Vengerov, Y. Y., and Dzantiev, B. B. (2013). Quantum dot-based lateral flow immunoassay for detection of chloramphenicol in milk. *Anal. Bioanal. Chem.* 405, 4997–5000. doi: 10.1007/s00216-013-6876-3
- Chen, J., Xu, F., Jiang, H., Hou, Y., Rao, Q., Guo, P., et al. (2009). A novel quantum dot-based fluoroimmunoassay method for detection of Enrofloxacin residue in chicken muscle tissue. *Food Chem.* 113, 1197–1201. doi: 10.1016/j.foodchem.2008.08.006
- Chen, T.-W., Rajaji, U., Chen, S.-M., Muthumariyappan, A., Mogren, M. M. A., Jothi Ramalingam, R., et al. (2019). Facile synthesis of copper(II) oxide nanospheres covered on functionalized multiwalled carbon nanotubes modified electrode as rapid electrochemical sensing platform for super-sensitive detection of antibiotic. *Ultrasonics Sonochem.* 58, 104596–104596. doi: 10.1016/j.ultrasonch.2019.05.013
- Chen, X., Luan, Y., Wang, N., Zhou, Z., Ni, X., Cao, Y., et al. (2018). Ratiometric fluorescence nanosensors based on core-shell structured carbon/CdTe quantum dots and surface molecularly imprinted polymers for the detection of sulfadiazine. *J. Separation Sci.* 41, 4394–4401. doi: 10.1002/jssc.201800866
- Coleman, J. N., Khan, U., Blau, W. J., and Gun'ko, Y. K. (2006). Small but strong: a review of the mechanical properties of carbon nanotube-polymer composites. *Carbon* 44, 1624–1652. doi: 10.1016/j.carbon.2006.02.038
- Dang, X., Zhao, H., Wang, X., Sailijiang, T., Chen, S., and Quan, X. (2018). Photoelectrochemical aptasensor for sulfadimethoxine using g-C₃N₄ quantum dots modified with reduced graphene oxide. *Microchim. Acta* 185:4. doi: 10.1007/s00604-018-2877-4
- Ding, S., Chen, J., Jiang, H., He, J., Shi, W., Zhao, W., et al. (2006). Application of quantum dot-antibody conjugates for detection of sulfamethazine residue in chicken muscle tissue. *J. Agri. Food Chem.* 54, 6139–6142. doi: 10.1021/jf0606961
- Gleiter, H. (1989). Nanocrystalline materials. *Progr. Mater. Sci.* 33, 223–315. doi: 10.1016/0079-642590001-7
- Gleiter, H. (2000). Nanostructured materials: basic concepts and microstructure. *Acta Mater.* 48, 1–29. doi: 10.1016/s1359-645400285-2
- Gleiter, H., and Marquardt, P. (1984). Nanocrystalline structures - an approach to new materials. *Zeitschrift Metallkunde* 75, 263–267.
- Govindasamy, M., Chen, S.-M., Mani, V., Devasenathipathy, R., Umamaheswari, R., Joseph Santharaj, K., et al. (2017). Molybdenum disulfide nanosheets coated multiwalled carbon nanotubes composite for highly sensitive determination of chloramphenicol in food samples milk, honey and powdered milk. *J. Colloid Interface Sci.* 485, 129–136. doi: 10.1016/j.jcis.2016.09.029
- Hassanzadeh, J., Moghadam, B. R., Sobhani-Nasab, A., Ahmadi, F., and Rahimi-Nasrabadi, M. (2019). Specific fluorometric assay for direct determination of amikacin by molecularly imprinting polymer on high fluorescent g-C₃N₄ quantum dots. *Spectrochim. Acta* 214, 451–458. doi: 10.1016/j.saa.2019.02.067
- He, B., Wang, L., Dong, X., Yan, X., Li, M., Yan, S., et al. (2019). Aptamer-based thin film gold electrode modified with gold nanoparticles and carboxylated multiwalled carbon nanotubes for detecting oxytetracycline in chicken samples. *Food Chem.* 300, 125179–125179. doi: 10.1016/j.foodchem.2019.125179
- He, B.-S., and Yan, S.-s. (2018). Electrochemical aptasensor based on aptamer-complementary strand conjugate and thionine for sensitive detection of tetracycline with multi-walled carbon nanotubes and gold nanoparticles amplification. *Anal. Methods* 10, 783–790. doi: 10.1039/c7ay02728a
- Hou, M., Xiong, L., and Liu, G. (2011). Determination of sparfloxacin with fluorescence probe of CdSe/CdS quantum dots. *Phys. Test. Chem. Anal.* 47, 1387–1390. doi: 10.1016/j.jlumin.2014.08.006
- Huang, S., Gan, N., Li, T., Zhou, Y., Cao, Y., and Dong, Y. (2018). Electrochemical aptasensor for multi-antibiotics detection based on endonuclease and exonuclease assisted dual recycling amplification strategy. *Talanta* 179, 28–36. doi: 10.1016/j.talanta.2017.10.016
- Khataee, A. R., Hasanzadeh, A., Iranifam, M., Fathinia, M., Hanifehpour, Y., and Joo, S. W. (2014). CuO nanosheets-enhanced flow-injection chemiluminescence system for determination of vancomycin in water, pharmaceutical and human serum. *Spectrochim. Acta* 122, 737–743. doi: 10.1016/j.saa.2013.12.014
- Kokulnathan, T., and Chen, S.-M. (2020). Robust and selective electrochemical detection of antibiotic residues: the case of integrated lutetium vanadate/graphene sheets architectures. *J. Hazardous Mater.* 384, 121304–121304. doi: 10.1016/j.jhazmat.2019.121304
- Kuemmerer, K. (2009). Antibiotics in the aquatic environment—a review—part I. *Chemosphere* 75, 417–434. doi: 10.1016/j.chemosphere.2008.11.086
- Leptihn, S., Guo, L., Frece, V., Ho, B., Ding, J. L., and Wohland, T. (2010). Single molecule resolution of the antimicrobial action of quantum dot-labeled sushi peptide on live bacteria. *Virulence* 1, 42–44. doi: 10.4161/viru.1.1.10229
- Li, Z., Liu, C., Sarpong, V., and Gu, Z. (2019). Multisegment nanowire/nanoparticle hybrid arrays as electrochemical biosensors for simultaneous detection of antibiotics. *Biosensors Bioelectr.* 126, 632–639. doi: 10.1016/j.bios.2018.10.025
- Liu, X., Hu, M., Wang, M., Song, Y., Zhou, N., He, L., et al. (2019). Novel nanoarchitecture of Co-MOF-on-TPN-COF hybrid: ultralowly sensitive bioplatfrom of electrochemical aptasensor toward ampicillin. *Biosens. Bioelectr.* 123, 59–68. doi: 10.1016/j.bios.2018.09.089
- Liu, X., Zhou, Z., Wang, T., Xu, Y., Lu, K., and Yan, Y. (2020). Molecularly imprinted polymers-captivity ZnO nanorods for sensitive and selective detecting environmental pollutant. *Spectrochim. Acta A Mol Biomol Spectr.* 228:e117785. doi: 10.1016/j.saa.2019.117785
- Liu, Z., Liu, S., Wang, L., Peng, J., and He, Y. (2009). Resonance Rayleigh scattering and resonance non-linear scattering method for the determination of aminoglycoside antibiotics with water solubility CdS quantum dots as probe. *Spectrochim. Acta A Mol. Biomol. Spectr.* 74, 36–41. doi: 10.1016/j.saa.2009.04.026
- Malik, R., Pinnaka, A. K., Kaur, M., Kumar, V., Tikoo, K., Singh, S., et al. (2019). Water-soluble glutathione-CdS QDs with exceptional antimicrobial properties synthesized via green route for fluorescence sensing of fluoroquinolones. *J. Chem. Technol. Biotechnol.* 94, 1082–1090. doi: 10.1002/jctb.5855
- Mohammad-Razdari, A., Ghasemi-Varnamkhashi, M., Izadi, Z., Ensafi, A. A., Rostami, S., and Siadat, M. (2019a). An impedimetric aptasensor for ultrasensitive detection of Penicillin G based on the use of reduced graphene oxide and gold nanoparticles. *Mikrochim Acta* 186, 372–372. doi: 10.1007/s00604-019-3510-x
- Mohammad-Razdari, A., Ghasemi-Varnamkhashi, M., Izadi, Z., Rostami, S., Ensafi, A. A., Siadat, M., et al. (2019b). Detection of sulfadimethoxine in meat samples using a novel electrochemical biosensor as a rapid analysis method. *J. Food Composition Anal.* 82:e103252. doi: 10.1016/j.jfca.2019.103252
- Munawar, A., Tahir, M. A., Shaheen, A., Lieberzeit, P. A., Khan, W. S., and Bajwa, S. Z. (2018). Investigating nanohybrid material based on 3D CNTs@Cu nanoparticle composite and imprinted polymer for highly

- selective detection of chloramphenicol. *J. Hazardous Mater.* 342, 96–106. doi: 10.1016/j.jhazmat.2017.08.014
- Netea, S. A., Messina, N. L., and Curtis, N. (2019). Early-life antibiotic exposure and childhood food allergy: a systematic review. *J. Allergy Clin. Immunol.* 144:1445. doi: 10.1016/j.jaci.2019.08.001
- Peng, J., Huang, Q., Zhuge, W., Liu, Y., Zhang, C., Yang, W., et al. (2018). Blue-light photoelectrochemical sensor based on nickel tetra-aminated phthalocyanine-graphene oxide covalent compound for ultrasensitive detection of erythromycin. *Biosens. Bioelectr.* 106, 212–218. doi: 10.1016/j.bios.2018.02.009
- Qie Gen, L., Yuan Fang, L., and Cheng Zhi, H. (2007). A light scattering and fluorescence emission coupled ratiometry using the interaction of functional CdS quantum dots with aminoglycoside antibiotics as a model system. *Talanta* 71, 567–572. doi: 10.1016/j.talanta.2006.04.035
- Qin, Y., Ma, Y., Jin, X., Zhang, L., Ye, G., and Zhao, S. (2015). A sensitive fluorescence turn-on assay of bleomycin and nuclease using WS2 nanosheet as an effective sensing platform. *Anal. Chim. Acta* 866, 84–89. doi: 10.1016/j.aca.2015.01.049
- Rastgar, S., and Shahrokhian, S. (2014). Nickel hydroxide nanoparticles-reduced graphene oxide nanosheets film: layer-by-layer electrochemical preparation, characterization and rifampicin sensory application. *Talanta* 119, 156–163. doi: 10.1016/j.talanta.2013.10.047
- Rosati, G., Ravarotto, M., Scaramuzza, M., De Toni, A., and Paccagnella, A. (2019). Silver nanoparticles inkjet-printed flexible biosensor for rapid label-free antibiotic detection in milk. *Sens. Actuators B-Chem.* 280, 280–289. doi: 10.1016/j.snb.2018.09.084
- Roushani, M., and Ghanbari, K. (2018). A novel aptasensor based on gold nanorods/ZnS QDs-modified electrode for evaluation of streptomycin antibiotic. *Anal. Methods* 10, 5197–5204. doi: 10.1039/c8ay01815d
- Roushani, M., Rahmati, Z., Farokhi, S., Hoseini, S. J., and Fath, R. H. (2020). The development of an electrochemical nanoaptasensor to sensing chloramphenicol using a nanocomposite consisting of graphene oxide functionalized with (3-Aminopropyl) triethoxysilane and silver nanoparticles. *Mater. Sci. Eng. C Mater. Biol. Appl.* 108, 110388–110388. doi: 10.1016/j.msec.2019.110388
- Shad, N. A., Bajwa, S. Z., Amin, N., Taj, A., Hameed, S., Khan, Y., et al. (2019). Solution growth of 1D zinc tungstate (ZnWO₄) nanowires; design, morphology, and electrochemical sensor fabrication for selective detection of chloramphenicol. *J. Hazard. Mater.* 367, 205–214. doi: 10.1016/j.jhazmat.2018.12.072
- Tian, Q., Wang, Y., Deng, R., Lin, L., Liu, Y., and Li, J. (2015). Carbon nanotube enhanced label-free detection of microRNAs based on hairpin probe triggered solid-phase rolling-circle amplification. *Nanoscale* 7, 987–993. doi: 10.1039/c4nr05243a
- Vega, D., Agui, L., Gonzalez-Cortes, A., Yanez-Sedeno, P., and Pingarron, J. M. (2007). Voltammetry and amperometric detection of tetracyclines at multi-wall carbon nanotube modified electrodes. *Anal. Bioanal. Chem.* 389, 951–958. doi: 10.1007/s00216-007-1505-7
- Velusamy, V., Palanisamy, S., Kokulnathan, T., Chen, S. W., Yang, T. C. K., Banks, C. E., et al. (2018). Novel electrochemical synthesis of copper oxide nanoparticles decorated graphene-beta-cyclodextrin composite for trace-level detection of antibiotic drug metronidazole. *J. Colloid Interface Sci.* 530, 37–45. doi: 10.1016/j.jcis.2018.06.056
- Wang, C., Li, Q., Wang, B., Li, D., and Yu, J. (2018). Fluorescent sensors based on AIEgen-functionalised mesoporous silica nanoparticles for the detection of explosives and antibiotics. *Inorg. Chem. Front.* 5, 2183–2188. doi: 10.1039/c8qi00622a
- Wang, L., Peng, J., Liu, Z., and He, Y. (2010). Resonance Rayleigh-scattering spectral method for the determination of some aminoglycoside antibiotics using CdTe quantum dots as a probe. *Luminescence* 25, 424–430. doi: 10.1002/bio.1170
- Wang, Y., Bian, F., Qin, X., and Wang, Q. (2018). Visible light photoelectrochemical aptasensor for chloramphenicol by using a TiO₂ nanorod array sensitized with Eu(III)-doped CdS quantum dots. *Mikrochim. Acta* 185, 161–161. doi: 10.1007/s00604-018-2711-z
- Wang, Y., Lu, J., Tang, L., Chang, H., and Li, J. (2009). Graphene oxide amplified electrogenerated chemiluminescence of quantum dots and its selective sensing for glutathione from thiol-containing compounds. *Anal. Chem.* 81, 9710–9715. doi: 10.1021/ac901935a
- Wang, Y., Ma, T., Ma, S., Liu, Y., Tian, Y., Wang, R., et al. (2017). Fluorometric determination of the antibiotic kanamycin by aptamer-induced FRET quenching and recovery between MoS₂ nanosheets and carbon dots. *Microchim. Acta* 184, 203–210. doi: 10.1007/s00604-016-2011-4
- Wei, Q., Mao, K., Wu, D., Dai, Y., Yang, J., Du, B., et al. (2010). A novel label-free electrochemical immunosensor based on graphene and thionine nanocomposite. *Sensors Actuators B Chem.* 149, 314–318. doi: 10.1016/j.snb.2010.06.008
- Wu, C., Cheng, R., Wang, J., Wang, Y., Jing, X., Chen, R., et al. (2018). Fluorescent molecularly imprinted nanoparticles for selective and rapid detection of ciprofloxacin in aquaculture water. *J. Separation Sci.* 41, 3782–3790. doi: 10.1002/jssc.201800418
- Xiao, F., Zhao, F., Li, J., Yan, R., Yu, J., and Zeng, B. (2007). Sensitive voltammetric determination of chloramphenicol by using single-wall carbon nanotube-gold nanoparticle-ionic liquid composite film modified glassy carbon electrodes. *Anal. Chim. Acta* 596, 79–85. doi: 10.1016/j.aca.2007.05.053
- Xu, J., Yu, C., Feng, T., Liu, M., Li, F., Wang, Y., et al. (2018). N-Carbamoylmaleimide-treated carbon dots: stabilizing the electrochemical intermediate and extending it for the ultrasensitive detection of organophosphate pesticides. *Nanoscale* 10, 19390–19398. doi: 10.1039/c8nr05098h
- Yu, C., Yu, J., Zhang, H., He, Z., Sha, Y., Liu, B., et al. (2019). A facile approach for rapid on-site screening of nicotine in natural tobacco. *Environ. Pollution* 259:113841. doi: 10.1016/j.envpol.2019.113841
- Zang, S., Liu, Y., Lin, M., Kang, J., Sun, Y., and Lei, H. (2013). A dual amplified electrochemical immunosensor for ofloxacin: polypyrrole film-Au nanocluster as the matrix and multi-enzyme-antibody functionalized gold nanorod as the label. *Electrochim. Acta* 90, 246–253. doi: 10.1016/j.electacta.2012.12.021
- Zeng, R., Tang, Y., Zhang, L., Luo, Z., and Tang, D. (2018). Dual-readout aptasensing of antibiotic residues based on gold nanocluster-functionalized MnO₂ nanosheets with target-induced etching reaction. *J. Mater. Chem. B* 6, 8071–8077. doi: 10.1039/c8tb02642d
- Zengin, A., Tamer, U., and Caykara, T. (2014). Extremely sensitive sandwich assay of kanamycin using surface-enhanced Raman scattering of 2-mercaptobenzothiazole labeled gold/silver nanoparticles. *Anal. Chim. Acta* 817, 33–41. doi: 10.1016/j.aca.2014.01.042
- Zhang, K., Lu, L., Wen, Y., Xu, J., Duan, X., Zhang, L., et al. (2013). Facile synthesis of the necklace-like graphene oxide-multi-walled carbon nanotube nanohybrid and its application in electrochemical sensing of azithromycin. *Anal. Chim. Acta* 787, 50–56. doi: 10.1016/j.aca.2013.05.037
- Zhang, Y., and Wei, Q. (2016). The role of nanomaterials in electroanalytical biosensors: a mini review. *J. Electroanal. Chem.* 781, 401–409. doi: 10.1016/j.jelechem.2016.09.011
- Zhu, K., Li, J., Wang, Z., Jiang, H., Beier, R. C., Xu, F., et al. (2011). Simultaneous detection of multiple chemical residues in milk using broad-specificity antibodies in a hybrid immunosorbent assay. *Biosens. Bioelectr.* 26, 2716–2719. doi: 10.1016/j.bios.2010.09.01

Conflict of Interest: The authors declare that the research was conducted in the absence of any commercial or financial relationships that could be construed as a potential conflict of interest.

Copyright © 2020 Dong, Li and Wang. This is an open-access article distributed under the terms of the Creative Commons Attribution License (CC BY). The use, distribution or reproduction in other forums is permitted, provided the original author(s) and the copyright owner(s) are credited and that the original publication in this journal is cited, in accordance with accepted academic practice. No use, distribution or reproduction is permitted which does not comply with these terms.

Advantages of publishing in Frontiers



OPEN ACCESS

Articles are free to read
for greatest visibility
and readership



FAST PUBLICATION

Around 90 days
from submission
to decision



HIGH QUALITY PEER-REVIEW

Rigorous, collaborative,
and constructive
peer-review



TRANSPARENT PEER-REVIEW

Editors and reviewers
acknowledged by name
on published articles

Frontiers

Avenue du Tribunal-Fédéral 34
1005 Lausanne | Switzerland

Visit us: www.frontiersin.org

Contact us: frontiersin.org/about/contact



REPRODUCIBILITY OF RESEARCH

Support open data
and methods to enhance
research reproducibility



DIGITAL PUBLISHING

Articles designed
for optimal readership
across devices



FOLLOW US

@frontiersin



IMPACT METRICS

Advanced article metrics
track visibility across
digital media



EXTENSIVE PROMOTION

Marketing
and promotion
of impactful research



LOOP RESEARCH NETWORK

Our network
increases your
article's readership